A Theoretical and Experimental Study of the Thermal Degradation of Biomass

by
Morten Gunnar Grønli

A thesis submitted to
The Norwegian University of Science and Technology
for the degree of

Doktor Ingeniør

November 1996
The Norwegian University of Science and Technology
Faculty of Mechanical Engineering
Division of Thermal Energy and Hydro Power
7034 Trondheim, Norway

NTNU

Norges Teknisk-Naturvitenskapelige Universitet
The Norwegian University of Science and Technology

Report no:
NTNU 1996:115

Classification
Open

POSTADRESSE
NTNU
INSTITUTT FOR TERMISK ENERGI OG VANNKRAFT
Kolbjørn Hejes vei 1A
N-7034 Trondheim - NTNU

TELEFONER
Sentralbord NTNU: 73 59 40 00
Instituttkontor: 73 59 27 00
Vannkraftlaboratoriet: 73 59 38 57

TELEFAX
Instituttkontor: 73 59 83 90
Vannkraftlaboratoriet: 73 59 38 54

Title of report:	Date
A THEORETICAL AND EXPERIMENTAL STUDY OF THE THERMAL DEGRADATION OF BIOMASS	November 1996
	No. of pages/appendices 282/60
Author (s): Morten G. Grønli	Project manager (sign) Otto K. Sønju
Division: Faculty of Mechanical Engineering Dept. of Thermal Energy and Hydropower	Project no.:
ISBN no.: Doctoral Thesis	Price group:

Client/sponsor of project:	Client's ref.:

Abstract:
In the first part of this thesis, experimental and modeling work on the pyrolysis of biomass under regimes controlled by chemical kinetics are presented. The pyrolysis of three Scandinavian wood species (birch, pine, pineroot and spruce); five different celluloses, and hemicellulose and lignin isolated from birch and spruce have been studied by thermogravimetry. The celluloses exhibited sharp, single DTG curves which could be well described by a single first order reaction model. The kinetic analysis gave activation energies between 210 and 280 kJ/mole for all the celluloses. The thermograms of the wood species revealed different weight loss characteristics which can be attributed to their different chemical composition. In the kinetic analysis, a model of independent parallel reactions was successfully used to describe the thermal degradation. The main advantage of this modeling approach is that the in situ decomposition of cellulose in wood can be studied. A mean activation energy of 260 kJ/mole with a standard deviation ±16 kJ/mole was calculated.

In the second part of this thesis, experimental and modeling work on the pyrolysis of biomass under regimes controlled by heat and mass transfer are presented. Particles (D=20 mm, L=30 mm) prepared from the same wood species were one-dimensionally heated. The effect of heating conditions (heat flux, grain orientation) on the product yields distribution and reacted fraction was investigated. The experiments show that heat flux alters the pyrolysis products as well as the intraparticle temperatures to the greatest extent. A comprehensive mathematical model which can simulate drying and pyrolysis of moist wood is presented. The thermal degradation of wood involves the interaction in a porous media of heat, mass and momentum transfer with chemical reactions. Heat is transported by conduction, convection and radiation and mass transfer is driven by pressure and concentration gradients. The simulation of these processes involves the simultaneous solution of the partial differential, conservation equations for mass, energy and momentum with kinetic expressions describing the rate of reaction. By using three parallel competitive reactions to account for primary production of gas, tar and char, and a consecutive reaction for the secondary cracking of tar, the predicted intraparticle temperature profiles, ultimate product yields distribution and reacted fraction agreed well with the experimental results.

	Indexing terms: English	Indexing terms Norwegian
Group 1	Heat Engineering	Varmeteknikk
Group 2	Solid fuels	Faste Brensler
Selected by author	Pyrolysis	Pyrolyse
	Drying	Tørking
	Biomass	Biomasse

PREFACE

First, I wish to thank my academic advisor, Professor Otto K. Sønju, for introducing me to the field of solid fuel combustion and for making it possible for me to meet and work with leading authorities and environments within this field. Even though he has been quite busy during these years, he has in his way managed to keep track of what I was doing and guided me if it was needed. I am especially indebted to my two scientific advisors, Professor Johan E. Hustad and Professor Morten C. Melaaen. Their patience, guidance and moral support have been outstanding.

This work was initiated in January 1991 through a scholarship from the Nordic Council of Ministers' Energy Research Programme, Solid Fuel Committee. My first introduction to the science of biomass pyrolysis was at a Nordic Seminar arranged at NTH by Professor Sønju in February 1991. Although, I did not understand too much of what was presented, I was fortunate to meet one of the authorities within the field, Dr. Abraham Broido, and researchers from other Nordic universities and research organisations. Nordic Seminars have been arranged annually since then, and my Nordic colleagues deserves thanks for their many inspiring discussions and critical views.

In June 1991, I spent two weeks together with Dr. Jaakko Saastamoinen at VTT's laboratory in Jyväskylä, Finland, to get familiar with his modelling work. His insight in the science of mathematical modeling inspired me to begin working within this particular field.

In spring 1992, I attended my first international conference "Advances in Thermochemical Biomass Conversion" in Interlaken, Switzerland. This was a good opportunity for me to get an overview of what was going on and to meet researchers working within the same field. Two of them have in particular to be mentioned, Professor Michael Jerry Antal, Jr, from University of Hawaii, USA, and Professor Barbara Krieger Brockett from Washington State University, USA. Through his many publications jointly with Dr. Gabor Varhegyi from the Hungarian Academy of Sciences, Hungary, Professor Antal introduced me to the science of thermogravimetry. Both Professor Antal and Dr. Varhegyi deserve thanks for their many valuable discussions and suggestions. Professor Krieger-Brockett has been visiting our Department several times and is acknowledged for her inspiring attitude and for trying to teach me about experimental design.

In July 1992, I spent two month at Department of Combustion Research, Risø National Laboratory, Denmark to carry out pyrolysis experiments in their thermogravimetric analyzer. I have visited Risø at several occasions thereafter and wish to thank Dr. Lasse Holst Sørensen for organizing my countless stays, and for the many stimulating and fruitful discussions we have had during his parallel work with coke and char reactivity.

In 1993, we finally managed to finance the building of an experimental rig for studying pyrolysis of larger particles. The support from the technical group in our laboratory, particularly from Nils Skei, in the design, building up, and modification is acknowledged. I am especially indebted to Mr. Stefan Wessling from the Technical University of Aachen, Germany, who took his diploma thesis working with me on these experiments. We spent countless days (and nights) together in the laboratory and without his support, the comprehensive experimental program carried out in this part of the thesis would not have been possible.

The staff at the Department and my colleagues at SINTEF and NTNU, especially Anders Austegaard (our MATLAB expert), deserves thanks for their help and support. My employer, SINTEF, is acknowledged for the financial support through the last two and a half years of this work.

Most of all, I wish to thank my wife, Sissel, for her understanding and moral support. Sissel and my children, Lise and Hanne, have unselfishly given up much to allow me to do this dissertation.

Morten G. Grønli
Trondheim, November 1996

DEDICATION

This work is dedicated to the memory of my sister, Bente

TABLE OF CONTENTS

LIST OF FIGURES

LIST OF TABLES

NOMENCLATURE

a_i	coefficients used in the pyrolysis models	
A_i	pre-exponential factor in the pyrolysis model	[1/s]
b_i	coefficients used in the pyrolysis models	
c_i	coefficients used in the pyrolysis models	
C_{Pi}	specific heat capacity at constant pressure	[J/kg K]
d_{por}	pore diameter	[m]
D_b	diffusivity of bound water	[m^2/s]
D_{eff}	effective diffusivity in gas mixture phase	[m^2/s]
E_i	activation energy in the pyrolysis model	[J/mole]
F	incident heat flux to surface	[W/m^2]
h	relative humidity	
h_m	mass transfer number	[m/s]
h_T	heat transfer number	[W/m^2 K]
Δh_i	heat of reaction	[J/kg]
Δh_l	latent heat of evaporation of liquid water	[J/kg]
Δh_{sorp}	heat of sorption of bound water	[J/kg]
k	thermal conductivity	[W/m K]
k_i	reaction rate constant	[1/s]
K	intrinsic permeability	[m^2]
K_r	relative permeability	
m	mass	[kg]
M	moisture content	
M	molecular weight	[kg/mole]
n	reaction order	
N_g	number of components in the gas mixture phase	
P	pressure	[N/m^2]
$<P_g>^g$	pressure in the gas mixture phase	[N/m^2]
$<P_l>^l$	pressure in the liquid phase	[N/m^2]
P_C	capillary pressure	[N/m^2]
R	universal gas constant (= 8.3144)	[J/mole K]
T, <T>	temperature	[K]
$<v_i>$	superficial velocity of component *i*	[m/s]
V	volume	[m^3]
$<\dot{w}_i>$	rate of production of component or phase *i* in phase γ	[kg/m^3 s]
x	cartesian coordinate	[m]

Greek letters

α	conversion fraction	
β	heating rate	
η	interpolation factor	
ξ	"bridge" factor	
λ	photon mean free path	[m]
μ	dynamic viscosity	[kg/m s]
ε	volume fraction	
$<\rho_\gamma>$	(phase average) density of phase γ	[kg/m^3]
$<\rho_\gamma>^\gamma$	intrinsic (phase average) density of component or phase *i* in phase γ	[kg/m^3]
σ	Stefan-Boltzmann constant (= $5.67 \cdot 10^{-8}$)	[W/m^2 K^4]
σ	surface tension	[N/m]
σ	constriction factor	
τ	tortuosity	
ω	emissivity	
φ	general variable	

Subscript and Superscript

b	bound water phase
C	char
eff	effective
fsp	fiber saturation point
g	gas mixture phase
G	gas in the gas mixture phase
$H_2O_{(v)}$	water vapour
$H_2O_{(b)}$	bound water
i	component or phase i
l	liquid water phase
L, $\parallel$	longitudinal (parallel) direction
R, $\perp$	radial (perpendicular) direction
s	solid phase
s	surface
S	virgin (unreacted) solid
SD	dry solid
sat	saturation

rad	radiation
T	tar in gas mixture phase
T	tangential direction
v	water vapour
0	initial conditions
∞	ambient

Abbreviations

SP	spruce
BI	birch
PI	pine
LH	low heat flux (80 kW/m^2)
HH	high heat flux (130 kW/m^2)
RD	radial direction
LD	longitudinal direction
C&G	Chan and Glaister
T&M	Thurner and Mann
D&R	Di Blasi and Russo

CHAPTER 1
INTRODUCTION

1.1 INTRODUCTION

The major alternatives to the conventional fossil fuels are nuclear power and renewables. Renewables cover sources of energy such as wind, wave, hydro-electric-power, tidal, direct solar and biomass, and are in general more evenly dispersed over the earths surface compared to fossil fuels and uranium. The renewable energy sources thus increase the possibilities for local, regional or national energy self-supply relatively isolated from international fluctuations and availability of fossil fuels. In addition, renewables are not in the same manner associated with environmental pollutions as the fossil fuels or kind of risks linked to nuclear power [Hustad and Sønju (1992)].

1.1.1 BIOMASS AS A RENEWABLE SOURCE OF ENERGY

Biomass is all the matter that can be derived directly or indirectly from plant photosynthesis, but may be in many forms, vegetable or animal. Annually, around 220 billion dry tonnes of new biomass is produced or approximately 10 times as much energy in biomass as man currently consumes from all energy sources. Much of this is harvested for food or forest products and less than 1.5% is currently used for energy purpose [Hall (1991)]. If grown at the same average rate as it is consumed, bioenergy would make no net contribution to atmospheric CO_2, since carbon released in consuming the biomass for energy would be photosynthesized by new plant growth. Worldwide, biomass accounts for around 15% of primary energy consumption but the global exploitation is unevenly distributed among the industrialized and developing world. In industrial countries, biomass contributes with an average of 3% to the primary energy consumption compared with 35% for the third world countries. However, much of the present activity in biomass exploitation is unsustainable. Fuelwood gathering and charcoal making have caused considerable environmental damage like deforestation followed by soil erosion and loss of biological diversity in many regions of Africa, Latin and South-America and Asia.

In 1990, the use of biomass for energy accounted for approximately 144 TWh (516 PJ) in the nordic countries which was about 9% of the total energy consumption. In Finland and Sweden the major consumers of biofuels are the power companies and the pulp and paper industry using bark, peat and black liquor. In Denmark, combustion of straw bales in small boilers for district heating is essential, while in Norway, about one million wood stoves and fireplaces are in practical use in households. These small units (less then 20 kW) account for approximately 50% of the total biomass energy consumption in Norway.

Table 1.1 Biomass energy consumption in the nordic countries, [Hustad and Sønju (1992)].

Country	Biomass Energy Used [TWh]	Potential [TWh]	% of Total Energy Used
Denmark	8.4	35.0	4.0
Finland	60.0		17.0
Norway	10.0	140	3.6
Sweden	65.0	150	11.3

1.1.2 BIOENERGY UTILISATION

A very large number of biomass species or crops has been and is being considered as energy sources. These fall into several groups, depending on crop type and on the type of fuel which it is to be converted [The European Renewable Energy Study]:

- The first group is perennial lignocellulosic crops, primarily woody species and includes long term (15-50 year rotation) and short term (6-15 year rotation) single stem forestry and short rotation (3-5 years) multiple stem coppicing of perennial crops. Willow and poplar are two species being considered for energy production in northern and temperate zones of Europe.
- The second group is the herbaceous annual crops, including miscanthus and sweet sorghum.
- A third group is the high sugar/starch crops, some of which are already used for ethanol production in some countries. Examples are sugar-cane, maize and sugar beet, together with a large number of conventional food crops such as wheat.
- A fourth group is the oil-containing crops such as oil seed rape and sunflower, from which vegetable oils (bio-diesel) can be extracted.

In addition, energy can be reclaimed from the following biomass wastes:

- Residues from conventional forestry, including branches and tops from clear felling; storm damaged trees and thinnings.

- Solid agricultural residues, mainly straw from cereal crops.
- Residues from manufacturing of wood based products such as bark, sawdust, planner shavings and off-cuts from sawmills; and bark and black liquor from pulp and paper production.
- Municipal and industrial solid waste

Thus, the resource base is highly diverse in terms of its availability and its physical and chemical properties. Compared with fossil fuels, biomass has usually only a modest energy content. The physical form is rarely homogeneous and free flowing and when harvested, the moisture content is often very high. In its solid form, biomass is therefore difficult to use in many applications without substantial modification (comminution, drying, storage and feeding systems). However, technologies for converting and upgrading the biomass into more convenient energy forms, namely gaseous and liquid fuels, may be introduced to adapt the fuel to a particular end use. There are in principle three classes of conversion processes which can be used: biochemical via microbiological action; thermochemical via heat treatment; and physical/chemical processing. The components of bioenergy utilization are summarized in Figure 1.1. In the following, a short presentation of the different thermochemical conversion technologies will be given.

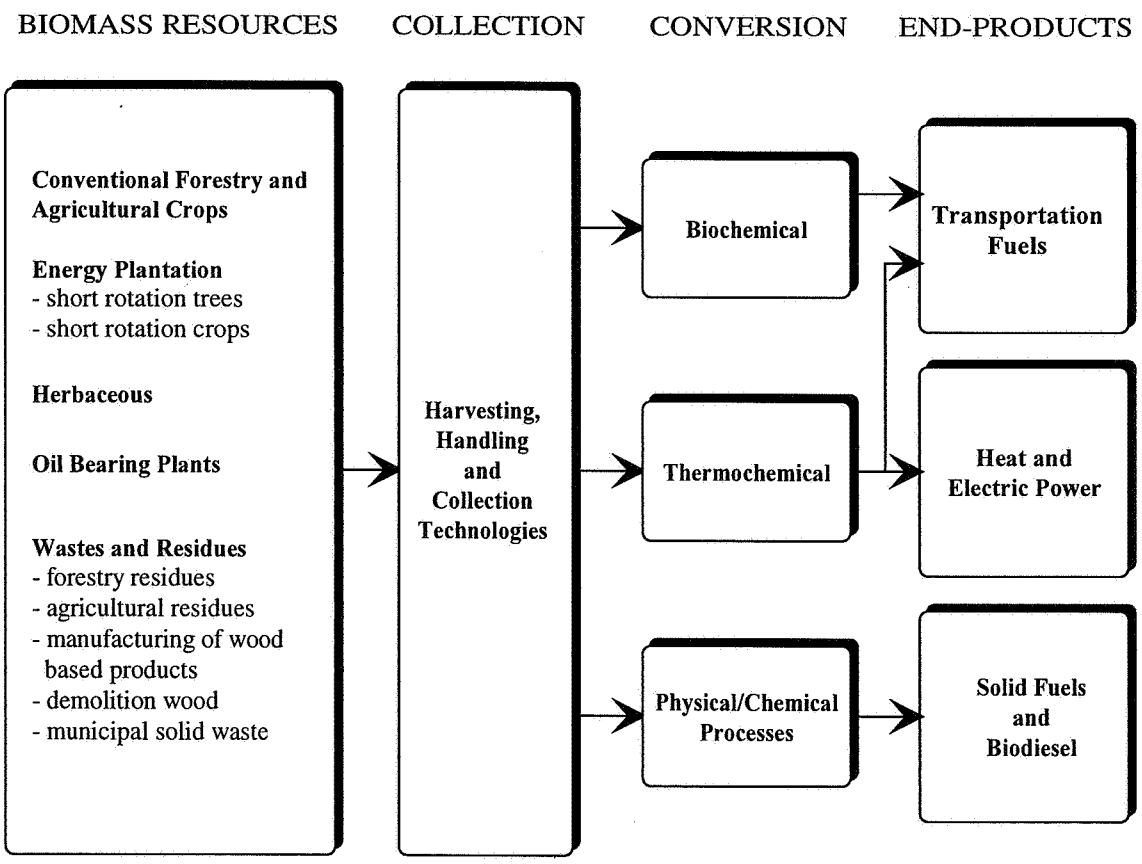

Figure 1.1 The components of bioenergy utilization.

1.1.3 THERMOCHEMICAL CONVERSION TECHNOLOGIES

There are four thermochemical methods suitable for the conversion of biomass: pyrolysis, gasification, liquefaction or direct combustion, and the primary products can be gas, liquid, solid char and/or heat dependent on conversion technology employed. Secondary higher value products may be produced by additional processing. In principle, most of the petroleum derived chemicals currently being used can be produced from biomass, but some will require rather circuitous synthesis routes [Bridgewater (1991)].

Pyrolysis is the thermal degradation (devolatilization) in the absence of an oxidizing agent at temperatures of 200-500°C. This leads to the formation of a mixture of liquid (tarry composition), gases and a highly reactive carbonaceous char of which the relative proportions depend very much on the method used. Temperature, pressure, heating rate and reaction time can be used to influence and determine the proportions and characteristics of the main products of the process. The products can be used in a variety of ways. The char can be upgraded to activated carbon, used in the metallurgical industry, as a domestic cooking fuel or for barbecuing. Pyrolysis gas can be used for power generation or heat, or synthesised to produce methanol or ammonia. The tarry liquid, pyrolysis oil or bio-oil can be upgraded to high grade hydrocarbon liquid fuels for combustion engines (e.g. transportation), or used directly for power generation or heat.

Gasification, also called pyrolysis by partial oxidation is a conversion process which goal is to maximize the gaseous product-yield. Relatively higher temperatures are used 800-1100°C, compared to 200-500°C in pyrolysis. The gaseous mixture produced contains CO, CO_2, H_2, H_2O, CH_4, N_2 (if air is used as oxidizing agent) and various contaminants such as small char particles, small amount of ash and tars. The partial oxidation can be carried out using air, oxygen, steam or a mixture of these. Air gasification produces a low heating value (LHV) gas (4-7 MJ/Nm^3 higher heating value), while oxygen gasification produces a medium heating value (MHV) gas (10-18 MJ/Nm^3 higher heating value). The fuel gas can through synthesis be upgraded to methanol, be burned externally in a boiler for producing hot water or steam, be burned in a gas turbine for electricity production or be burned in internal combustion engines such as diesel and spark ignition engine for the same purpose. Before the fuel gas can be used in gas turbines or internal combustion engines, the contaminants (tar, char-particles, ash) has to be removed. The hot gas from the gas turbine can be used to raise steam to be utilized in a steam turbine (Integrated Gasification Combined Cycle).

Combustion is complete oxidation of the biomass feedstock. Combustion provides very hot gases that can be used to heat a boiler and raise steam, as a source of process or space heat, or as the energy source for Stirling engines. Drying and pyrolysis will always be the first step in any gasification or combustion process.

Liquefaction is low temperature (250-350°C), high pressure (100-200 bar) thermochemical conversion in the liquid phase, usually with a high hydrogen partial pressure and also a catalyst to enhance the rate of reaction and/or to improve the selectivity of the process. The main goal is to maximise the liquid-yield, and the product is a higher quality liquid than from the pyrolysis process in terms of higher heating value (35-40 MJ/kg compared to 20-25 MJ/kg) and lower oxygen content. In addition, the lower oxygen content makes the fuel more stable and requires less upgrading to a hydrocarbon product.

A somewhat simplified overview of the thermochemical conversion processes, products and potential end-use is depicted in Figure 1.2.

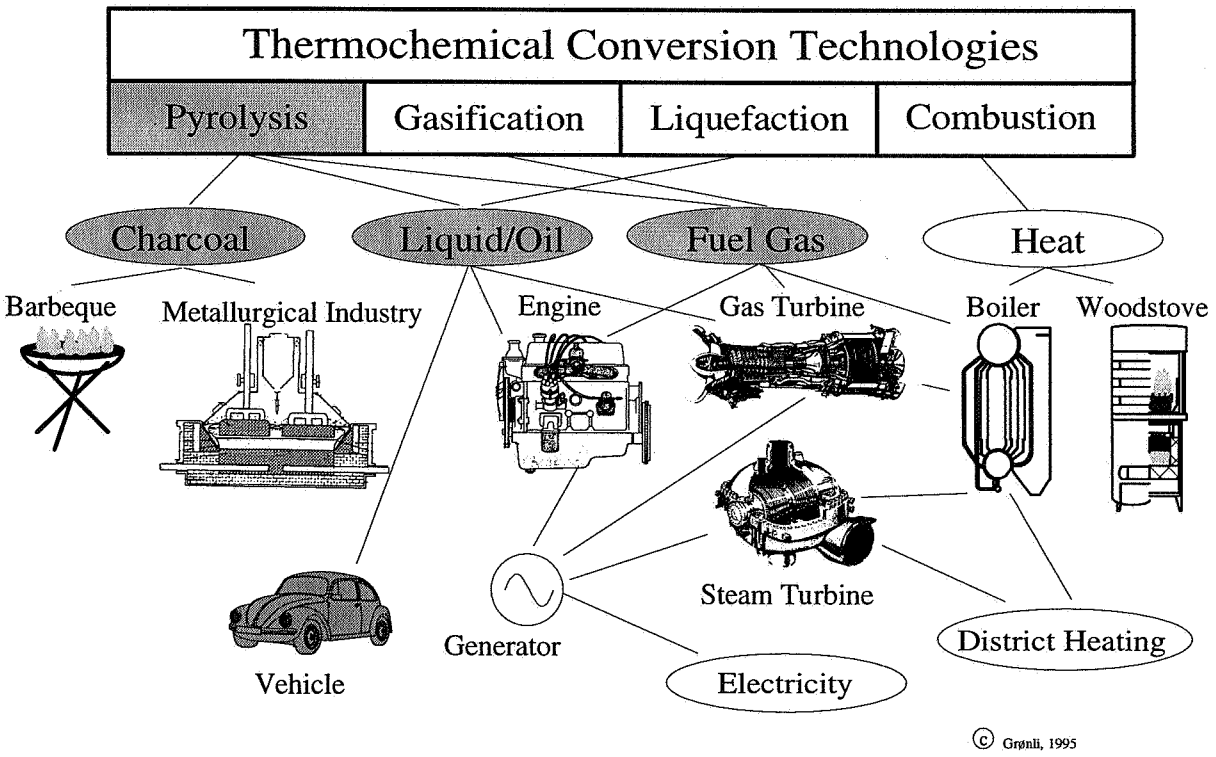

Figure 1.2 Thermochemical conversion technologies, products and potential end-use.

Except for combustion for which well established technologies exist, the present state of the art in these processes is still some way from commercialisation. There are more than 20 plants operating or planned in each of the pyrolysis [Elliot *et al.* (1991)] and gasification [Bridgwater (1995)] categories. However, todays low prices of petroleum has slowed dramatically the research activity in producing liquid fuels from biomass. Pressurized gasification is being demonstrated in the Värnamo plant in Sweden with an Ahlström circulating fluidized bed (CFB) gasifier and a European Gas Turbine 4 MW_e machine operating in combined cycle and cogeneration mode. Atmospheric gasification (CFB) with an engine has been demonstrated at 500 kW_e at TPS Termiska Processor, Sweden. A World Bank funded 30 MW_e biofuel power plant based on TPS gasification technology and a combined cycle based on the GE LM 2500 is planned to be built in Brazil.

1.2 OBJECTIVES OF THIS STUDY

The development of thermochemical processes for biomass conversion and proper equipment design requires knowledge and good understanding of the several chemical and physical mechanisms which are interacting in the thermal degradation process. Mathematical modelling and simulation of single particle pyrolysis represent a very useful tool for the understanding of some of these processes. Then one can focus on the solid phase internal processes such as heat and mass transfer that control the release of products, results which can be used in the design and control of large scale converters.

A substantial amount of fundamental research has been done within this field in the past decades (over 200 articles have been collected during this study). This work can generally be divided in two groups, where the first group cover those who have studied the thermal degradation of very small ("thermally thin") particles like sawdust, powder etc. in attempt to understand the detailed mechanisms of the chemical kinetics. The second group cover the researchers who have made detailed studies on the thermal degradation of large ("thermally thick") particles like logs, chips, dowels etc. by including as many thermo-physical processes as possible, such as heat, mass and momentum transfer with multistep reaction schemes describing the chemical kinetics.

The present study comprises experimental and modelling work on pyrolysis of both small and large particles. Since biomass is rarely completely dried before entering any thermal converter, it has been emphasized to understand the complex mechanisms of drying which will occur prior to, and simultaneously with the thermal degradation process. Three typical Scandinavian wood species have been selected as fuels. These are birch, spruce and pine.

1.3 ORGANISATION OF THE THESIS

The thesis is divided into two parts. The first part is entitled: "Pyrolysis of small biomass particles controlled by chemical kinetics", and the second: "Pyrolysis of large biomass particles controlled by heat and mass transfer". These can be read separately from each other or together.

However, before treating wood as a fuel, some knowledge about its physical as well as its chemical properties is of great importance. Physical properties deal with the relationship between the solid wood and moisture content, and the chemical properties refer to carbohydrate and lignin structures that are related to the decomposition and reactivity of the fuel. In **Chapter 2**, a general introduction to the wood structure and chemical composition which are relevant for this study will be given. This is an extraction of some excellent books of Skaar (1988); Siau (1984); Sjöström (1981); and Wenzl (1970) ,which are highly recommended. In addition, some of the properties and characteristics of the Scandinavian wood species selected will be given.

Chapter 3, presents experimental and modelling work on the pyrolysis of biomass under regimes controlled by chemical kinetics. The chapter comprises a review part where some of the previous work within this field will be summarized. It is not made any attempt to do any extensive review but rather quote some phenomenological models where kinetic parameters have been reported. Considerations will also be limited to the pyrolysis of wood and its main constituents: cellulose, hemicellulose and lignin. In Section 3.3, nonisothermal pyrolysis experiments of wood and different forms of cellulose, hemicellulose and lignin will be presented and discussed. These experiments have been carried out in a thermogravimetric analyzer (thermobalance, TGA). Next, the kinetic model and the technique used for the kinetic evaluation of these experiments will be described. In the last section of Chapter 3, the results from the kinetic analysis will be presented and discussed.

In **Chapter 4**, experimental and modelling work on the drying and pyrolysis of large particles of wood will be presented. This chapter comprises also a review part, where some of the main features in the modelling development will be drawn; from the very first numerical model presented in 1946 until today, where computers and numerical techniques have allowed the development of more complex and accurate models. In Section 4.3, a transient, one-dimensional mathematical model which can be used to simulate drying and pyrolysis of wood will be presented. The general equations for mass and energy are described; different pyrolysis reaction models are discussed together with necessary property relations and thermo-physical

data. In Section 4.4, the results from pyrolysis experiments on large wood particles (pellets) will be presented and discussed along with the details of the test facility, diagnostic system and the experimental program. In the final section of Chapter 4, the theoretical predictions from the mathematical model will be presented. First, predictions will be compared with the experiments to assess the validity of the mathematical model. Second, the model will be used to study pyrolysis of moist wood. Finally, the sensitivity of the model to some of the important thermo-physical and kinetic parameters will be discussed together with the applicability of the model.

In the final **Chapter 5**, the summary and conclusions from the work; the present contribution and recommendations for further work will be given

CHAPTER 2

WOOD STRUCTURE AND CHEMICAL COMPOSITION

2.1 INTRODUCTION

Before treating wood as a fuel it is important to understand the anatomical and physical properties as well as the chemical properties. Anatomical properties identify the macroscopic structures which are related to transport mechanisms inside the wood. Physical properties deal with the relationship between wood and moisture content, and the chemical properties refer to carbohydrate and lignin content and structures and are related to the decomposition and reactivity of the fuel.

Wood is obtained from two broad categories of plants known commercially as softwoods (gymnosperms) and hardwoods (angiosperms). The softwoods are also referred to as conifers because many produce seed cones, pollen cones, or both. The conifers have needlelike (e.g. pine, spruce) or scalelike (e.g. cedar) leaves and appear to be evergreen in that they retain new leaves for up to several years. Hardwoods have leaves that are generally broad or bladelike, and most commercial species are deciduous, which means they commonly shed their leaves each fall at the end of the tree's growing season.

2.2 THE MACROSCOPIC STRUCTURE OF WOOD

The structure of wood and the location and amount of water in wood influence its drying characteristics. Wood is composed of elongated cells, most of which are oriented in the longitudinal direction of the stem. They are connected with each other through openings, referred to as pits. These cells, varying in their shape according to their functions, provide the mechanical strength to the tree and also perform the function of liquid transport as well as the storage of reserve food supply. Figure 2.1 shows the macroscopic structure of wood. The centrally located pith is discernible as a dark stripe in the middle of the stem or branches. It represents the tissues formed during the first year of growth. The xylem or wood is organized in concentric growth rings (annual increments). It also contains rays in horizontal files,

extending from the outer bark either to the pith (primary rays) or to the annual ring (secondary rays). Some softwood also contain resin canals. The inner part of a tree usually consists of dark-colored heartwood. The outer part, or sapwood, is lighter in colour and conducts water from the roots to the foliage of the tree. The cambial zone is a very thin layer consisting of living cells between the wood (xylem) and the inner bark (phloem). The tree grows through the division of the cells and is always continuous, although it becomes slower in the course of time.

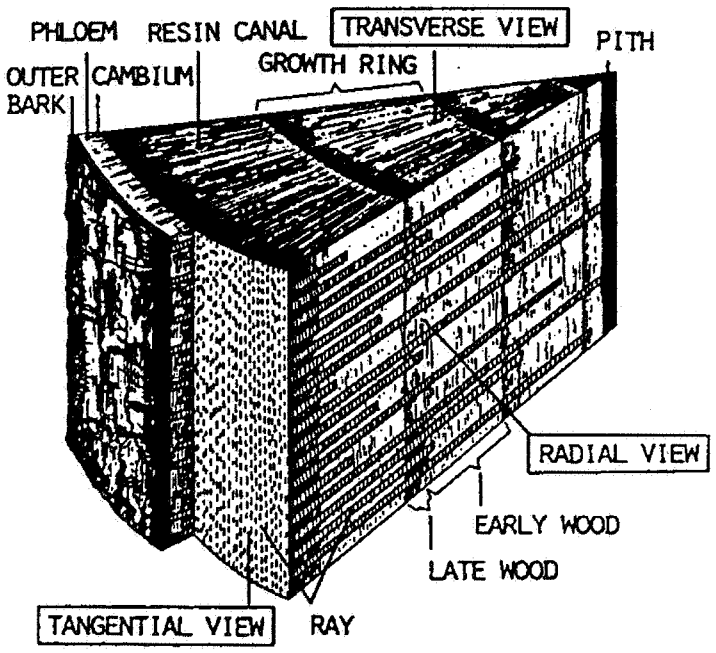

Figure 2.1 Section of a four-year-old stem, [Sjöström (1981)].

Longitudinal growth (primary growth), which take place in the early season, proceeds at the end of the stem, branches and roots. The growth points are located inside the buds, which have been formed during the preceding autumn. Radial growth begins in the cambium, which is composed of a single layer of thin-walled living cells (initials) filled with protoplasm. The cambial zone consists of several rows of cells, which all process the ability to divide. On division, the initial cell produces a new initial cell and a xylem mother cell, which in turn gives rise to two daughter cells; each of the latter is capable of further division. More cells are produced toward the xylem on the inside than to the phloem on the outside; phloem cells divide less frequently than xylem cells. For this reason trees always contains much more wood than bark. Each year a layer of wood grows over the preceding year's growth, adding a growth ring as portrayed in Figure 2.1. There is a basic similarity in the arrangement of cells and cell wall structure in wood and most other land plants.

2.3 THE WOOD CELL

The wood cell consists mainly of cellulose, hemicellulose and lignin. A simplified picture is that cellulose forms a skeleton which is surrounded by other substances functioning as matrix (hemicellulose) and encrusting (lignin) materials. The organization of a softwood tracheid or hardwood fiber is shown schematically in Figure 2.2.

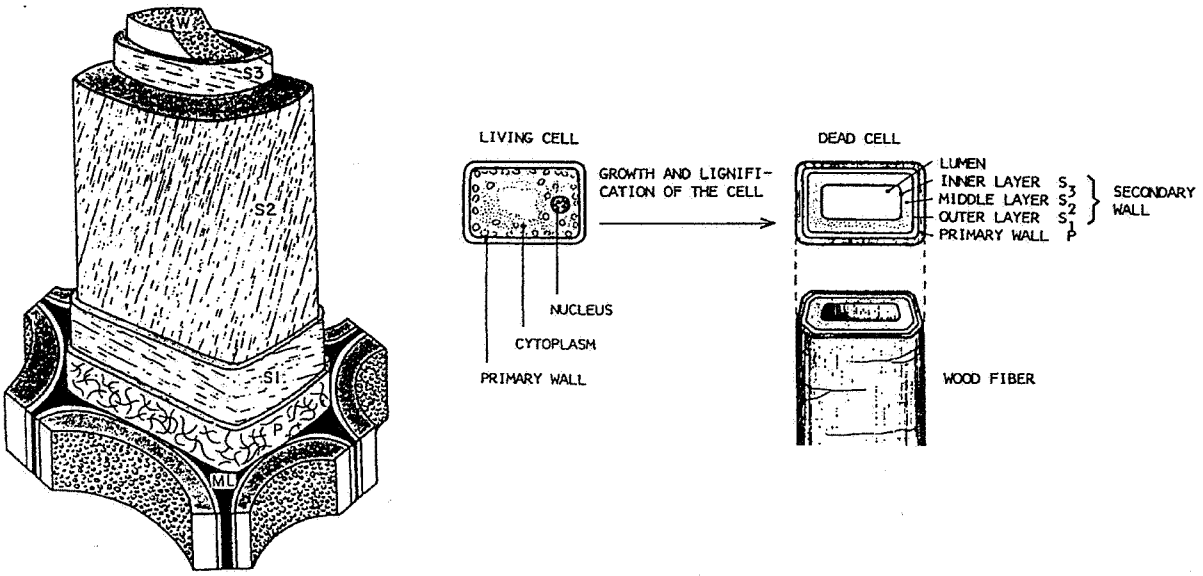

Figure 2.2 Simplified structure of a woody cell, [Sjöström (1981)].

The cell wall is built up of several layers, namely middle lamella (ML), primary wall (P), outer (S1), middle (S2) and inner (S3) layer of the secondary wall, and warty layer (W). The middle lamella is located between the cells and serves the function of binding the cells together. At an early stage of the growth it is mainly composed of pectic substances, but it eventually becomes highly lignified. Its thickness is 0.2-1.0 μm. The primary wall is a thin layer 0.1-0.2 μm thick, consisting of cellulose, hemicelluloses and protein. The secondary wall consists of three layers. A thin outer layer (0.2-0.3 μm), a thick middle layer (1-5 μm) and a thin inner layer (0.1 μm). These layers are built up by lamella formed by almost parallel microfibirils between where lignin and hemicelluloses are located.

2.4 STRUCTURE OF SOFTWOODS

The wood substance in softwoods is composed of two different cells: tracheids (90-95%) and ray cells (5-10%). Tracheids give softwoods the mechanical strength required (especially the thick-walled latewood tracheids) and provide for water transport, which occurs through the

thin-walled earlywood tracheids with their large cavities. The length and width of the tracheids ranges from 2.5 to 7 mm and 30 to 45μm, respectively. In the paper technology the softwood tracheids are normally just called fibers. A typical softwood structure is depicted in Figure 2.3 [Siau (1984)] and Figure 2.4 [Butterfield *et.al.* (1980)]

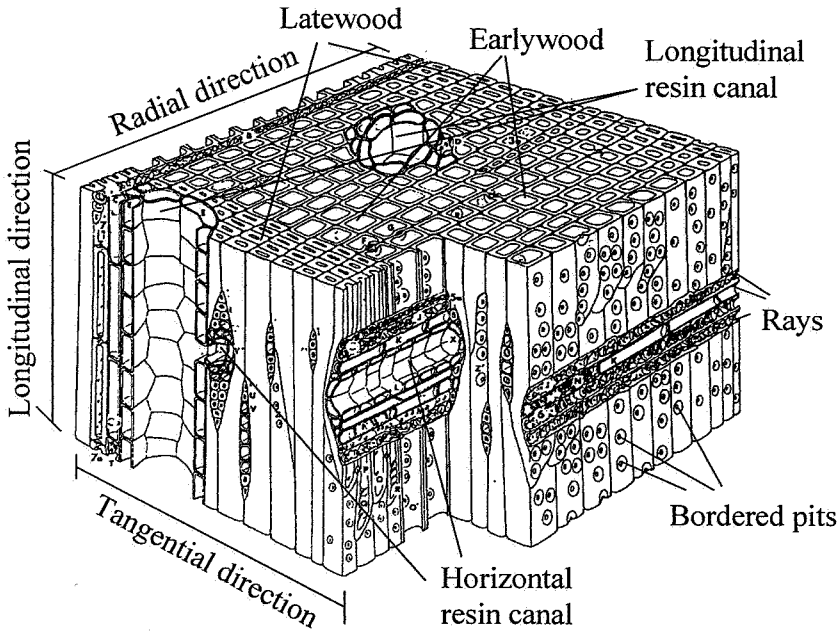

Figure 2.3 Gross structure of softwood, [Siau (1984)].

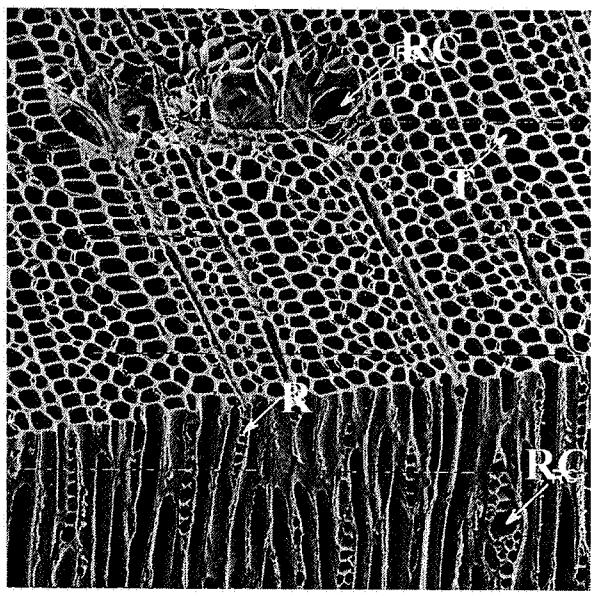

Figure 2.4 Transverse and longitudinal faces of a softwood [Butterfield *et.al.* (1980)]. T:Tracheid, R:Rays, RC:Resin canals.

The liquid transport from one tracheid to another takes place through the bordered pits; their amount in earlywood tracheids is about 200 per tracheid, most of them located in the radial walls in one to four lines. Latewood tracheids have only 10 to 50 rather small bordered pits. The bordered pit is constructed to act as a valve to keep the water flow under control and to

prevent air and vapour bubbles to get into the liquid flow. The pit opening (aperture) is built up by a membrane (torus) constructed from the middle lamella, and protected by the fiber wall formed as an overlapping concentric ring (Figure 2.5).

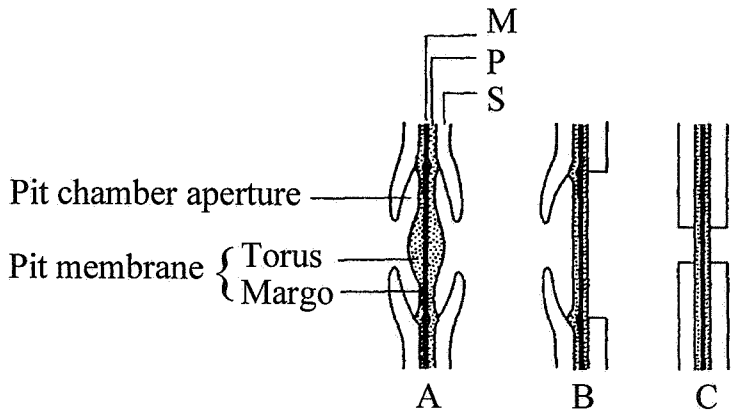

Figure 2.5 Types of pit pairs. A: bordered pit pair; B: half bordered pit pair; C: simple pit pair; M: middle lamella; P: primary wall; S: secondary wall.

Another major type of cells in softwoods are the parenchyma cells. They are non-fibrous living cells, brick-like and very small compared to the fibers. They are arranged in radial strands, referred to as ray parencyma, and are storing extraneous material in the wood, such as starch, oils, fat etc. Similar in size to the parenchyma cells are the ray tracheids. They transport water horizontally and are connected to the tracheids by bordered pits, which size varies with species. Spruce has very small bordered pits between the ray tracheids and the fibers compared to pine. By this reason, and due to the fact that the pits will be closed or aspirated after the wood has been dried, it is almost impossible to impregnate spruce. Another feature of the softwoods are the resin ducts or canals, which are intercellular spaces building up a uniform channel network in the tree. Horizontal canals are always located inside the rays which appear together in several files. Pine wood contains more and larger resin canals than spruce wood does. In pine they are concentrated in the heartwood and root, whereas in spruce they are evenly distributed throughout the whole wood. The diameters of the resin canals in pine are on the average about 80 μm (vertical) and 30 μm (radial).

2.5 STRUCTURE OF HARDWOODS

Hardwoods grow in almost all regions of the world, from temperated to tropical zones. They have to be adaptable to variable growing conditions and have therefore a more complicated morphology than the softwoods with vessel elements, fiber tracheids and longitudinal parenchyma (Figure 2.6-2.7). Hardwoods are rapidly growing trees and consequently they need an effective conducting system. The water conducting function is undertaken by the vessel

elements. The vessels are non-fibrous tube-like elements running vertically in the tree. They have large diameter compared to the fibers and are joined together end-to-end and appears as pores in the cross (tangential) view. The length of the vessel elements ranges from 0.18 mm to 1.33 mm for the most common hardwoods. In the heartwood of hardwoods the vessel elements are usually closed, being plugged by a gumlike substance. The fiber tracheids are thick walled with a small lumen, typical fiber lengths range from 0.9 mm to 2.0 mm. The rays, although more complex, provide the same function as in softwoods.

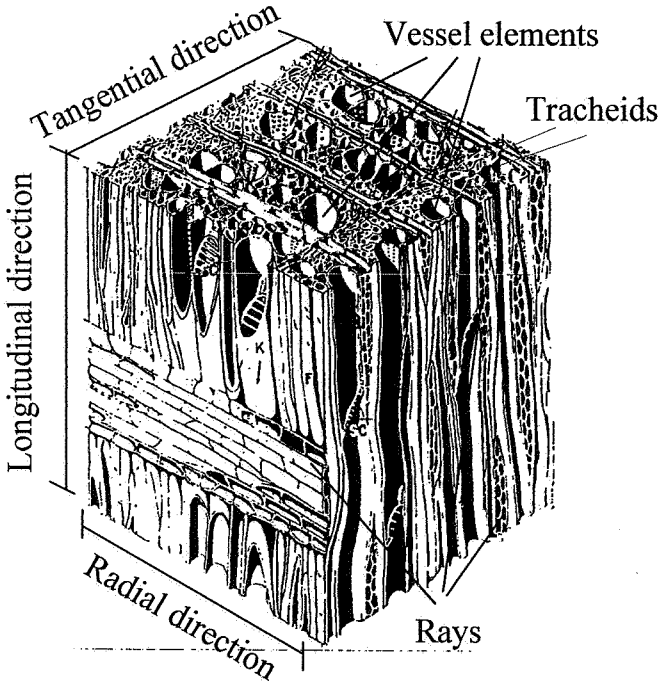

Figure 2.6 Gross structure of hardwood, [Siau (1984)].

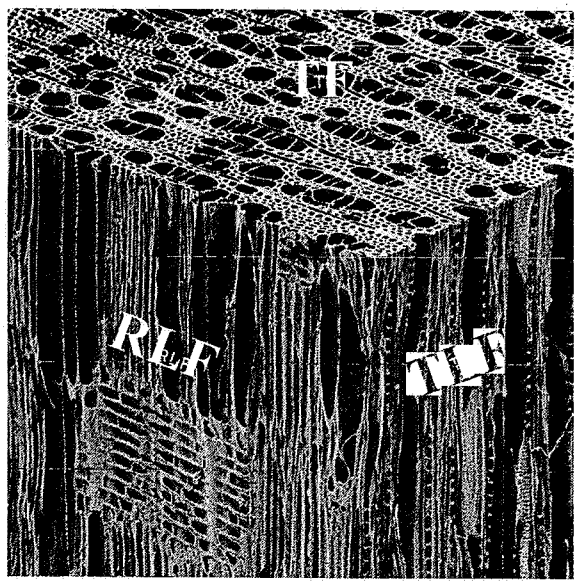

Figure 2.7 The three basic planes: (TF) transverse; (TLF) tangential longitudinal; and (RLF) radial longitudinal of a hardwood tree [Butterfield *et.al.* (1980)].

2.6 CHEMICAL COMPOSITION OF WOOD

Cellulose, hemicelluloses, and lignin generally constitute from 95% to 98% of wood. Additionally, wood contains many low-molecular-weight organic compounds known as extractives or extraneous substances and small amounts of mineral matter known as ash.

Cellulose is the main component of the cell wall, with the elementary formula $(C_6H_{10}O_5)_n$. It is a linear polysaccharide composed of β-D glucopyranose units connected to each other by (1→4) glucosidic bonds (Figure 2.8). The degree of polymerization (DP), which is the numbers of units (glucose in this case) that make up the polymer, is above 10 000 in unaltered wood.

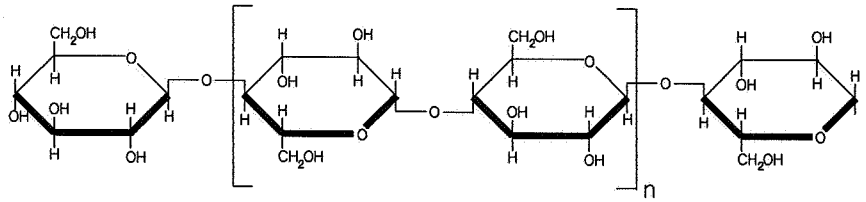

Figure 2.8 Structural formula of cellulose.

Cellulose molecules are completely linear and have a strong tendency to form intra- and intermolecular hydrogen bonds. Aggregation of the linear chains of molecules within microfibriles provides a highly crystalline structure. As a consequence of its fibrous structure and strong hydrogen bonding, cellulose has a high tensile strength and is insoluble in most solvents.

All noncellulosic polysaccharides and related substances comprise the **hemicelluloses**. Like cellulose most hemicelluloses function as supporting material in the cell walls. Hemicelluloses chemically are a class of polymers of sugars including the six-carbon sugars mannose, galactose, glucose and 4-O-methyl-D-glucuronic acid and the five-carbon sugars xylose and arbinose (Figure 2.9). The structure is similar to that of cellulose except that the hemicellulose polymers generally contain 50 to 200 monomer units and exhibit a branched rather than a linear structure. The hemicelluloses are much more soluble and susceptible to chemical degradation than cellulose.

Lignins, the encrusting substance which binds the cells together and gives rigidity to the cell wall are complex three dimensional polymers of phenylpropane units (Figure 2.10) and seem to be totally insoluble in most solvents. The polymeric lignin that one isolates from wood is chemically altered, which means that many lignin bonds are broken in order to separate the

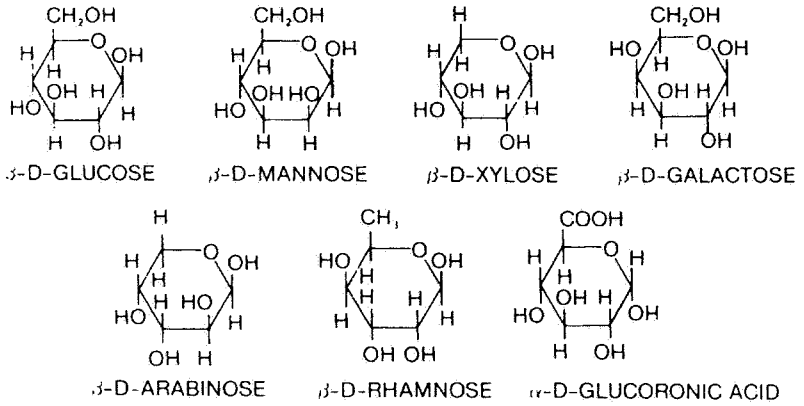

Figure 2.9 Monomers of hemicellulose, [Wenzl (1970)].

lignin from the wood, and the resultant lignin is often called by the name of the process ("Kraft lignin", "Klason lignin", "Thermomechanical lignin" ..). These lignins have different molecular weights, different chemical structures and different trace organic species.

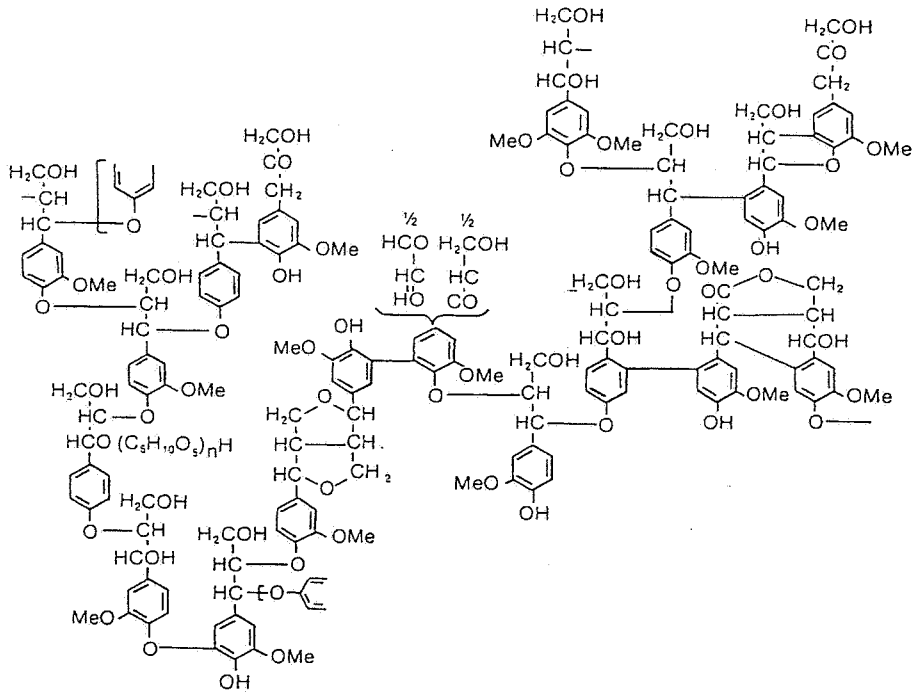

Figure 2.10 A hypothetical depiction of softwood lignins [Siau (1984)].

The **extraneous components** of wood include aliphatic, aromatic and alicyclic compounds, hydrocarbons, alcohols, ketones and various acids, esters, phenolic compounds, resins, terpenes and so on. These components are easily extracted from the wood using organic solvents or water.

Inorganic constituents or **ash** in wood contains sodium and potassium cations, carbonate, phosphate, sulphate, chlorite anions, silicates, etc. The ash content in wood seldom exceed 0.5 to 1.0 %.

Generally, hardwoods contain a larger portion of holocellulose (cellulose + hemicellulose) and less lignin as compared to softwoods. The composition of some softwoods and hardwoods by the class of compounds is given in Table 2.1

Table 2.1 Chemical composition of some selected wood species [Wenzl (1970)]

Species	Cellulose	Hemicellulose	Lignin	Extractives
Softwoods				
Scandinavian Spruce	43	27	29	1.8
Scandinavian Pine	44	26	29	5.3
Douglas Fir	39	23	29	5.3
Scots Pine	40	25	28	3.5
Hardwoods				
Scandinavian Birch	40	39	21	3.1
Silver Birch	41	30	22	3.2
American Beech	48	28	22	2.0

2.7 WATER IN WOOD

Wood contains water in three forms: bound (hygroscopic or adsorbed) water; liquid (free or capillary) water; and water vapour.

Bound water (M_b) is found in the cell wall and is believed to be hydrogen bonded to the hydroxyl groups of primarily the cellulose and hemicelluloses, and to a lesser extent also to the hydroxyl groups of lignin. Bound-water moisture content is limited by the number of sorption sites available and by the number of molecules of water which can be held on a sorption site. When only bound water is present, an equilibrium exists between the moisture content of the wood and the relative humidity of the surrounding air.

Free water (M_l) in liquid form is found in the lumens or voids of the wood. The amount of free water which wood may hold is limited by the fractional void space or porosity of the wood. There is no hydrogen bonding and therefore free water is held only by weak capillary forces and cannot cause swelling or shrinking or changes in most other physical properties because the cell wall is already saturated with much more tightly bonded hygroscopic water.

The **Moisture content (M)** is the quantity of moisture in wood, expressed as a percentage of oven-dry mass. The latter is defined as the constant mass obtained after wood has been dried

in an air oven maintained at 102 ± 3°C.

$$M = \frac{m_s - m_{sd}}{m_{sd}} = M_b + M_l \qquad (2.1)$$

where : m_s = green or moist mass

m_{sd} = oven-dry mass.

When a tree is harvested, the moisture content may range from 30 to nearly 200 percent (dry basis), depending on species and sapwood or heartwood. Sapwood is usually higher in moisture content than heartwood. As wood dries, water leaves cell cavities first. When cell cavities are empty, the cell wall begins to dry. The **fiber saturation point (M_{fsp})** has been defined as the moisture content at which the cell walls are saturated with bound water with no free water in the lumens. The fiber saturation point has a great importance in wood science, since it is related to abrupt changes in physical properties of wood such as shrinkage, mechanical strength, electrical conductivity and heat of wetting. An average FSP of 30% may be assumed for most woods at 25°C. The FSP of wood decreases approximately 0.1% per 1°C rise in temperature:

$$M_{fsp} = [M^0_{fsp} + 0.298] - 0.001T \qquad (2.2)$$

where: M^o_{fsp} = Fiber saturation point at 298 K

T = Temperature [K]

A schematic diagram and a graphical presentation illustrating the three different kinds of water in wood are given in Figure 2.11. The moisture content in equilibrium with a given relative humidity is called the equilibrium moisture content (EMC). The relationship between EMC and relative humidity at a given temperature is called the sorption isotherm. Numerous theories have been derived for sorption of gases on solids, many of which can be applied to the sorption of water vapour by wood. Characteristic for moisture sorption on wood is that more than one layer of vapour is formed on the solid where the forces of attraction between the vapour and solid are large. Sorption isotherms are generally temperature-dependent. As temperature increases, the amount of vapour adsorbed at any given vapour pressure or relative humidity decreases as shown in Figure 2.11.

The three forms of water found in wood differ in their energy level, as shown schematically in Figure 2.12. Water vapour has the highest level, followed by liquid water in the cell cavities with essentially the same energy as ordinary liquid water. Bound water in the cell walls of wood is in the lowest energy state, the level decreasing with decreasing moisture content below M_{fsp}. The energy needed to evaporate liquid water is equal to the latent heat

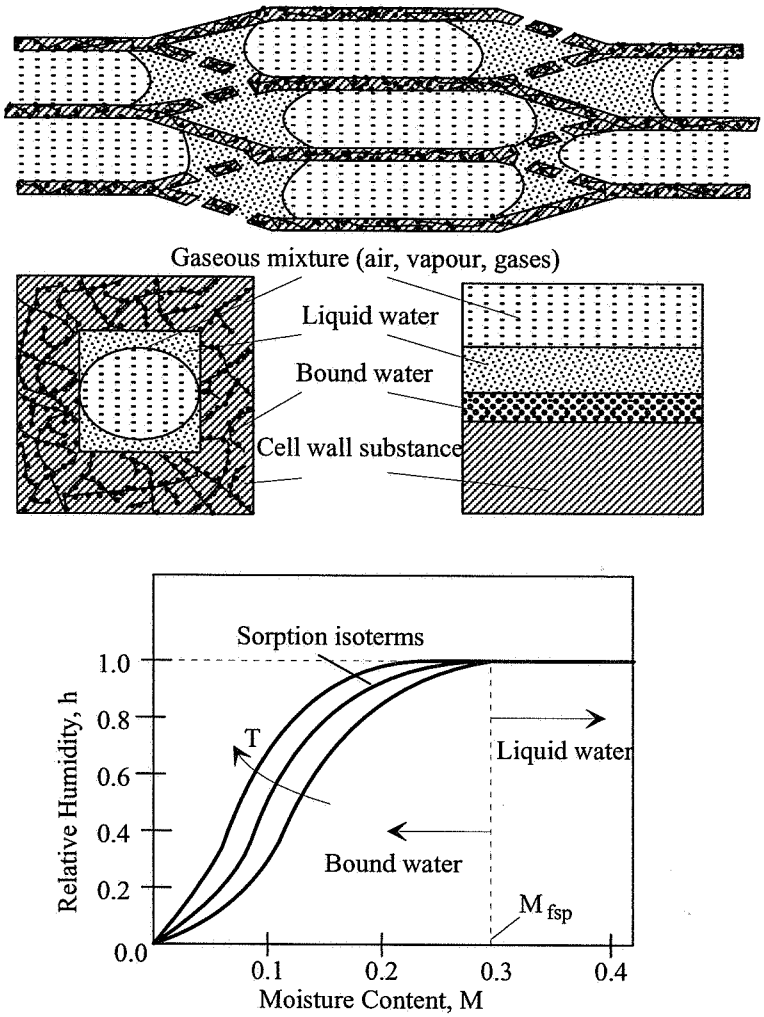

Figure 2.11 Various forms of water found in wood.

of evaporation, which is a function of temperature: $\Delta h^{\circ}_{l} = \Delta h^{\circ}_{lat}(T)$. The energy needed to release bound water to form liquid water is a function of temperature and moisture content: $\Delta h^{\circ}_{b} = \Delta h^{\circ}_{sorp}(T, M_b)$.

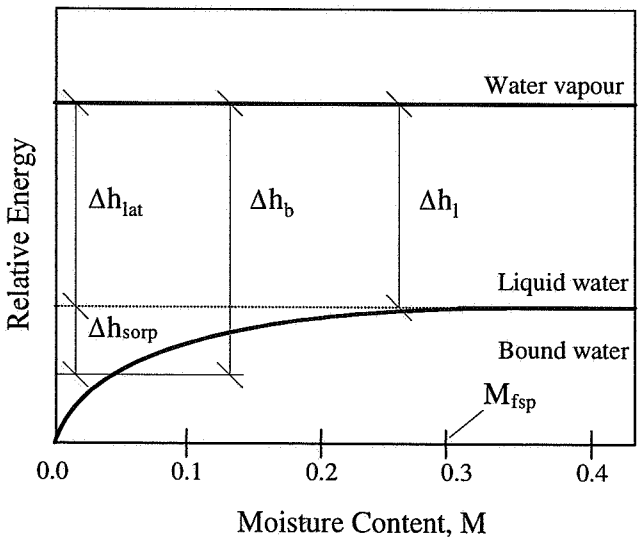

Figure 2.12 Relative energy levels in wood as functions of moisture content.

Wood changes dimension as it gains or loses moisture below the fiber saturation point. It shrinks when losing moisture from the cell walls and swells when gaining moisture in the cell walls. Wood is an anisotropic material in shrinkage characteristics. It shrinks most in the direction of the annual growth rings (tangentially), about one-half as much across the rings (radially), and only slightly along the grain (longitudinally). The combined effect of radial and tangential shrinkage can distort the shape of wood pieces because of the difference in shrinkage and the curvature of annual rings, as illustrated in Figure 2.13.

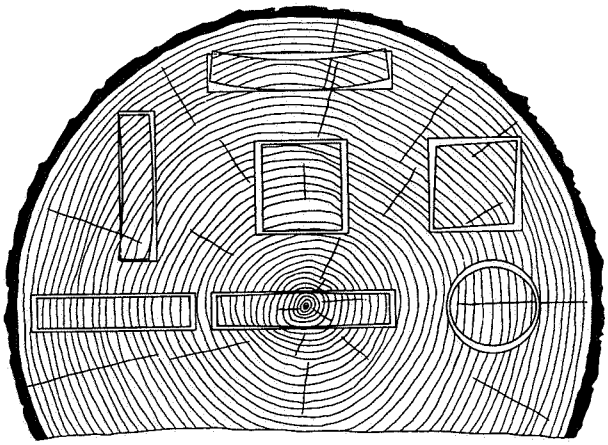

Figure 2.13 Characteristic shrinkage as affected by the direction of the annual rings. [The Encyclopedia of Wood (1980)].

The shrinkage from green to oven-dry moisture content may range from 2 to 8 % in radial direction, from 4 to 13 % in tangential direction, from 0 to 0.5 % in longitudinal direction while the volumetric shrinkage is reported between 7 and 20 %. Shrinkage values reported for some typical wood species found in the scandinavian countries, expressed in percentage of the green dimension, are summarized in Table 2.2.

Table 2.2 Shrinkage values and densities of some typical scandinavian wood species [Esping (1992)]

Species	Shrinkage from green to oven-dry moisture content			Density	
	Tangential β_t [%]	Radial β_r [%]	Volumetric β_v [%]	Oven-dry ρ_{sd} [kg/m^3]	Green ρ_s [kg/m^3]
Softwoods					
Spruce	7.8	3.6	11.4	430	385
Pine	7.7	4.0	12.4	490	430
Hardwoods					
Ash	8.0	5.0	13.6	650	550
Birch	7.8	5.3	14.2	610	516
Oak	7.8	4.0	13.6	650	550

2.8 WOOD SPECIES USED IN THIS STUDY

The three most common wood species growing in Norway were chosen, including one hardwood: **birch (*Betula Verrucosa*)** and two softwoods: **spruce (*Picea Abies*)** and **pine (*Pinus Silvestris*)**.

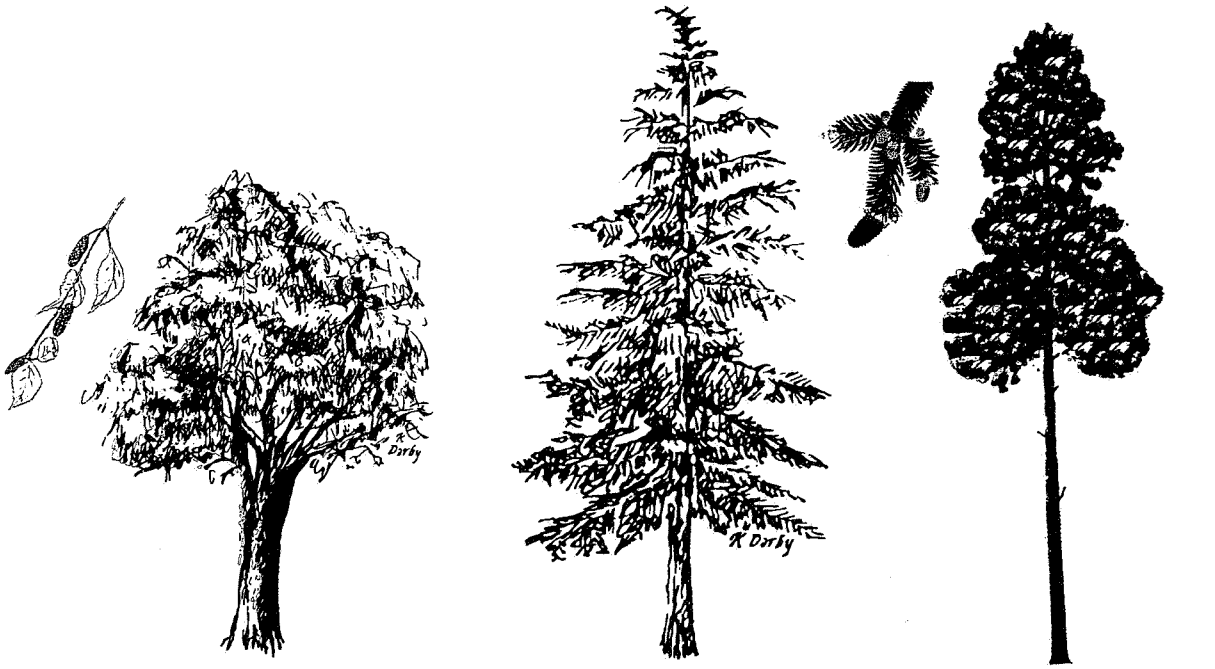

Birch (*Betula Verrucosa*) Spruce (*Picea Abies*) Pine (*Pinus Silvestris*)

Figure 2.14 Depiction of the wood species investigated in this study.

Birch is a very robust tree and grows farther north and at higher altitudes than any other European trees. It grows on almost any soil, as scrub under poor conditions in the mountains (dwarf birch ~ *betula nana*), and can be found almost everywhere in Norway. The timber is white or pale brown and has high strength. Birch is the most commonly used firewood in Norway. It is easy to process and hold some excellent qualities for wood carving and is used for furniture, tools and small household articles. Spruce and pine, being the two most abundant wood species, cover respectively one half and one fourth of the Norwegian forests. Spruce can grow to a height of 30-40 m with maximum diameters of 1 m. Pines are often grown crowded together in order to discourage branch growth and increase the length and girth of the trunk, and attains a normal height of 20-30 m with the same diameter as spruce. Spruce and pine timber are always in good demand, as they are the general utility wood species of the builder for joists, roofing, flooring, indoors and outdoors panelling, and are largely used in the manufacture of paper pulp. Wood waste (bark, sawdust, side pieces, off-cuts) from sawmills and paper manufacturing is used as raw material in the manufacture of

particle boards and to some extent as fuel. The root of the pine is abound in turpentine and resins and has for hundreds of years been utilized for the production of tar to impregnate wood in boats and houses.

Wenzl (1970) has reported the following chemical composition of Scandinavian birch, spruce and pine:

Table 2.3 Chemical composition of Scandinavian birch, spruce and pine, [Wenzl (1970)]

	Birch	Spruce	Pine	Pineroot
Cellulose (wt%)	40	44	43	---
Hemicellulose (wt%)	39	27	27	---
Lignin (wt%)	21	29	30	---
Extractives (wt%)	3	2	5	20

The extractable fraction of pineroot was found by using the pre-extraction procedure recommended by Browning (1967). (*see Chapter 3.3.1.1*). Birch contains more hemicellulose and less lignin compared to the two softwood species, and as expected, the highly resinous pineroot contains considerable more extractives (light molecular weight compounds).

Their proximate analysis were found by using the standard procedure for TGA-proximative analysis, recommended by Elder (1983). The elemental composition (ultimate analysis) was measured at the University of Vienna, Department of Physical Chemistry, by using the *EA 1108 CHNS-O, Carlo Erba Instrument*, while their higher heating values were measured at NTNU, Department of Thermal Energy and Hydropower by using a high precision calorimeter.

Table 2.4 Proximate and ultimate analysis of the selected wood species.

	Birch	Spruce	Pine	Pineroot
Volatile Matter (wt%)	90.4	86.7	87.6	89.9
Fixed Carbon (wt%)	9.4	13.2	12.3	10.1
Ash (wt%)	0.2	0.1	0.1	<0.1
C (wt%)	47.1	47.4	46.9	53.6
H (wt%)	6.2	6.3	6.3	6.5
N (wt%)	0.11	0.07	0.07	0.10
O (wt%)	46.6	46.2	46.7	38.5
HHV (MJ/kg)	19.13	19.30	19.03	21.90

Birch and pineroot contains less fixed carbon while having more volatile matter than spruce and pine. The elemental composition is fairly constant with the exception of pineroot which has less oxygen and higher carbon content, which is reflected in its higher heating value.

Charcoal was prepared from birch and spruce by pyrolysing 10 mm sided cubes in an oven purged with nitrogen at a heating rate of 5°C/min from ambient temperature to 600°C. The charcoal yield obtained, based on original dry matter was 19% and 22% for birch and spruce, respectively. Scanning electron microscopy (SEM) pictures of the transverse faces of the charcoals, shown in Figure 2.15, were taken at SINTEF Material Technology, and reveals that the characteristic cellular structure of the hardwood and softwood is intact after the pyrolysis.

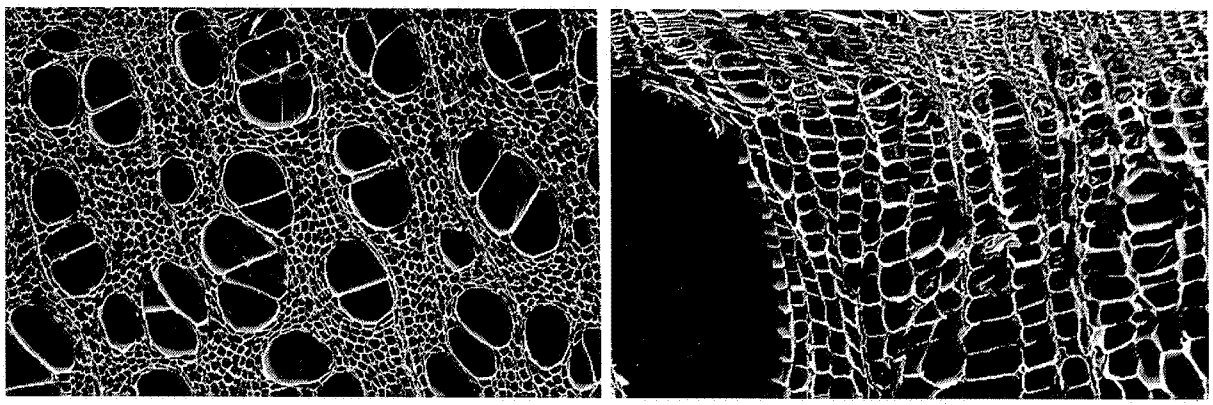

(a) (b)

Figure 2.15 Transverse faces of charcoals from (a) birch and (b) spruce (x 150)

Density, internal surface area and pore volume distribution of origin dry birch and spruce and their charcoals were measured at NTNU, Department of Industrial Chemistry, by using pycnometry, N_2-adsorption and mercury porosimetry. The results are presented in Table 2.5 and Figures 2.16 and 2.17.

The solid (apparent) density, $\langle\rho_s\rangle$, which is based on the volume defined by the external surface of the species was determined by using mercury as a displacement fluid. (At 1 atm, mercury cannot penetrate pores with diameter less than 15 μm). The specific (absolute or true) density, $\langle\rho_s\rangle^s$, eliminates that portion of the total volume occupied by pores and was determined by using helium as a displacement fluid. (Helium can penetrate all pores larger than 40 nm in diameter). By using $\langle\rho_s\rangle$ and $\langle\rho_s\rangle^s$, one can calculate the total internal volume, V_g [m^3/kg], and porosity, ε_g:

$$V_g = \frac{1}{\langle\rho_s\rangle} - \frac{1}{\langle\rho_s\rangle^s} \qquad \varepsilon_g = 1 - \frac{\langle\rho_s\rangle}{\langle\rho_s\rangle^s} \tag{2.3}$$

The internal (meso pore) surface area was determined by N_2 adsorption. The amount of gas physically adsorbed on a surface can be related to the pressure at a given temperature via the BET isotherm. By calculating the amount of gas adsorbed in the first monolayer, the internal surface area can be determined. The pore volume distribution was determined by forcing mercury into the pores at successively higher pressure. By varying the pressure between 1 and 1000 atm, one can examine the 0.01-10 μm (macro) pore size range.

Table 2.5 Density, porosity and surface area of birch and spruce.

Species	Solid density		Specific density	Pore volume	Porosity	Surface area
	$<\rho_s>^*$ [kg/m^3]	$<\rho_s>^{**}$ [kg/m^3]	$<\rho_s>^{s\dagger}$ [g/cm^3]	$V_g^{\dagger\dagger}$ [cm^3/g]	$\varepsilon_g^{\dagger\dagger}$	$S_g^{\ddagger}$ [m^2/g]
Birch	540	580	1.45	1.02	0.60	0.30
Birch char	---	390	1.57	1.99	0.77	410
Spruce	420	470	1.39	1.41	0.66	0.19
Spruce char	---	290	1.54	2.82	0.81	459

*Based on weight/volume measurements; **_Carlo Erba Porosimeter 2000_; †_Micrometrics AccuPyc 1330_; ††Equation (2.3); ‡ _Coulter SA 3100 Surface Area Analyzer_.

Both in its native and charcoal state, birch has higher density and lower porosity than spruce. The solid density calculated from carefully weight/volume measurements are somewhat lower (~ 10%) than the one obtained by mercury pycnometry. Since mercury can penetrate the largest pores (>15 μm) of the substances, the pycnometric densities are probably too high. Especially for the charcoal states, where the pore volume has been enlarged. This can be seen in Figures 2.16 and 2.17, where the macro pore volume distribution over pore radius of the birch and spruce and their charcoals are presented. Birch exhibits two peaks in pore volume, one peak located in the 0.5-1.0 micron range and one in the 5-20 micron range. For spruce, the pore volume is more evenly distributed over the pore radius, however, a small peak can be observed for the charcoal in the 0.1-0.5 micron range.

Determination of the the specific density gives a measure of the density of the cell wall substance of the native wood and the carbon skeleton of the charcoal. For the two wood species and charcoals analyzed, these densities seems to be quite equal in size.

At the end of the pyrolysis, a large area with large macropores (feeding pores) make the charcoal easy accessible for reactant gases. Hence, the charcoal from wood is an excellent

basis material for the manufacturing of active carbon.

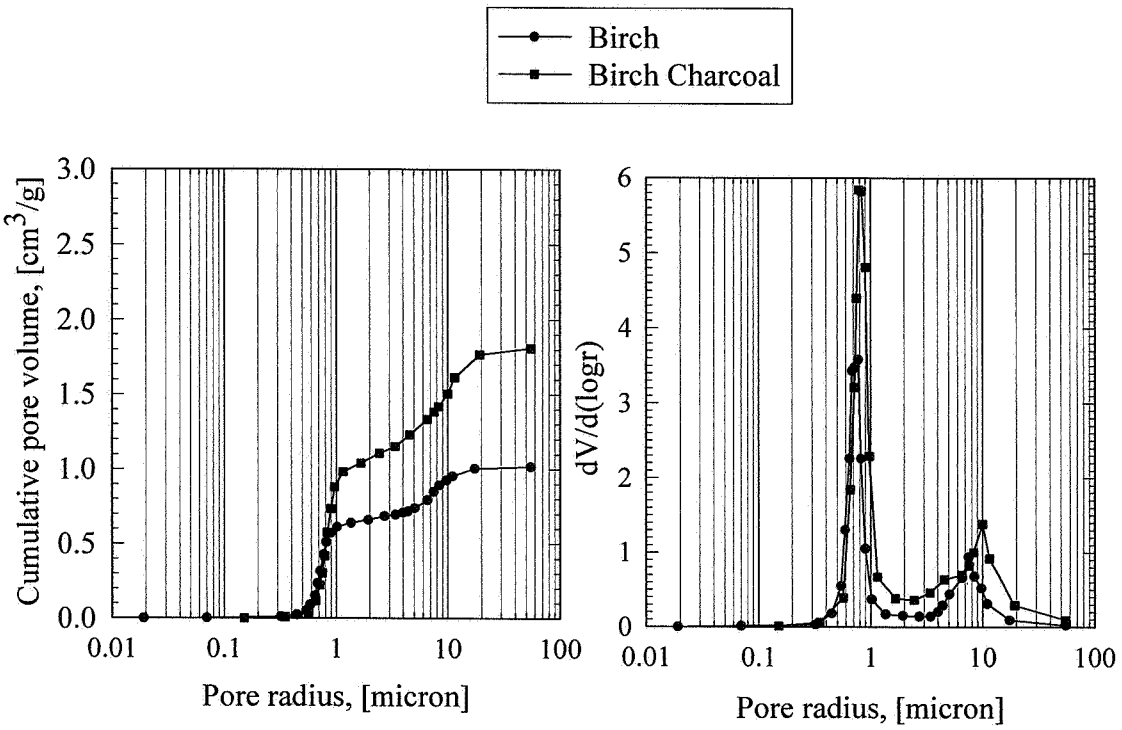

Figure 2.16 Cumulative and relative pore volume of birch and charcoal from birch.

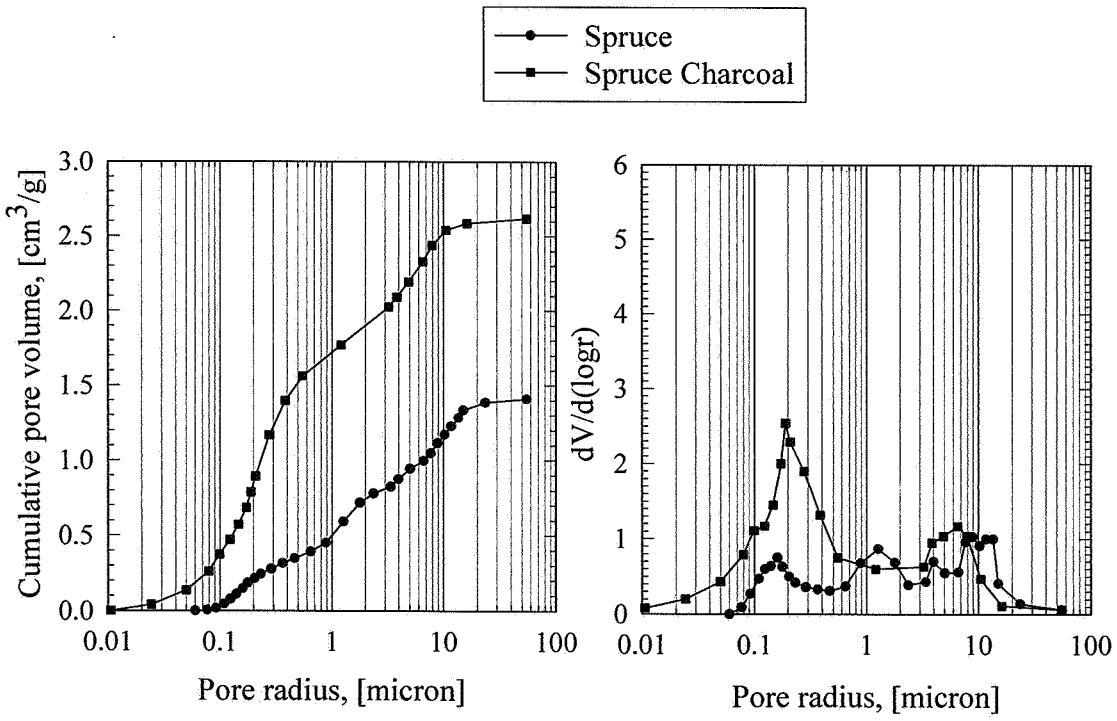

Figure 2.17 Cumulative and relative pore volume of spruce and charcoal from spruce.

CHAPTER 3

PYROLYSIS OF SMALL BIOMASS PARTICLES CONTROLLED BY CHEMICAL KINETICS

3.1 INTRODUCTION

The chemistry of biomass pyrolysis has been the subject of intense scientific research for many decades, and several review-articles are available in the literature [Beall and Eickner (1970); Roberts (1970); Milne (1979); Antal (1983, 1985); Agrawal (1984), Antal and Varhegyi (1995)]. Pyrolysis of biomass is a complex process which produces a host of chemical species, generally grouped into three major yields: gases; tar and char. It is influenced by a variety of factors, such as: heating rate; temperature history; particle size, shape and density; pressure, moisture content and chemical composition.

The determination of kinetic mechanisms and rate constants for the pyrolysis process has been mainly carried out under regimes controlled by chemical kinetics, by using very small samples in powder form so that effects of transport phenomena such as heat and mass transfer can be neglected. This will be the subject of this chapter, where experimental and modeling work on the pyrolysis of biomass under regimes controlled by chemical kinetics will be presented. The chapter comprises a review part, where some of the previous work done within this field will be discussed. It has not been made any attempt to do any extensive review but rather quote some phenomenological models where kinetic parameters have been reported. Considerations will also be limited to the pyrolysis of wood and its main constituents: cellulose, hemicellulose and lignin. Next, the results from pyrolysis experiments on the selected Scandinavian wood species and different forms of cellulose, hemicellulose and lignin will be presented and discussed. These experiments have been carried out in a thermogravimetric analyzer. In the last section of this chapter, the kinetic model that have been used will be described and the results obtained from the kinetic evaluation of these experiments will be presented and discussed.

3.2 REVIEW OF RELATED LITERATURE

3.2.1 EXPERIMENTAL TECHNIQUES

A large variety of experimental techniques have been adopted for the study of pyrolysis. The most frequently applied techniques used to study biomass pyrolysis are: thermogravimetric analysis (TGA) [Tang (1967); Broido and Weinstein (1970, 1971); Shafizadeh and McGinnis (1971); Havens *et al.* (1972); Lee (1982); Varhegyi *et al.* (1988, 1989)], differential thermal analysis (DTA) and differential scanning calorimeter (DSC) [Arseneau (1961); Akita and Kase (1967); Havens *et al.* (1972); Mok and Antal (1983)], heated grid apparatus [Hajaligol *et al.* (1982); Nunn *et al.* (1985)] and evolved gas analysis (EGA).

Thermal Gravimetric Analysis (TGA). The TGA apparatus is a highly automated instrument that yields continuous data on the mass loss of a sample as a function of either temperature or time as the sample is heated at a programmed rate. The basic requirements for making a thermogravimetric analysis are a precision balance and a furnace which can be programmed to maintain a constant temperature (isothermal or static), to effect a controlled linear temperature rise (dynamic) or a combination of these two. The results of a TGA run may be presented as a mass vs temperature or time curve and/or as a rate of mass loss vs temperature or time curve, the latter is usually referred to as a differential thermogravimetric curve (DTG). A schematic drawing of a thermobalance and a graphical presentation illustrating the read out from a typical TGA-run are shown in Figure 3.1.

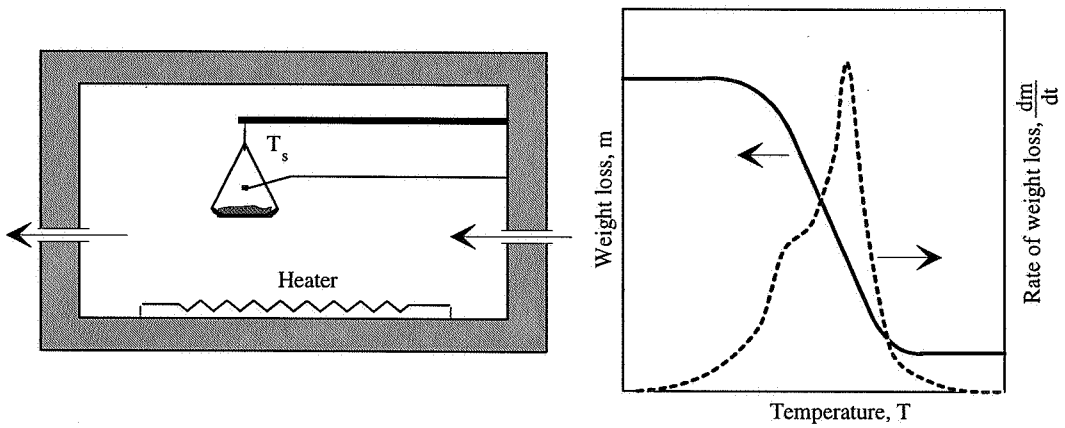

Figure 3.1 TGA.

Since the mass of the sample is continuously recorded, the actual sample temperature is usually recorded by a thermocouple located near the sample. Three examples of thermocouple location are shown in Figure 3.2 [from left to right: (a) *DuPont 951 TGA*, (b) *Perkin Elmer TGS-2*, (c) *SDT 2960* from *TA Instruments*). Hence, even for a properly calibrated instrument,

the recorded temperature often lags or leads the true sample temperature. For example, a DuPont instrument can have a 100°C temperature error [Antal (1995)].

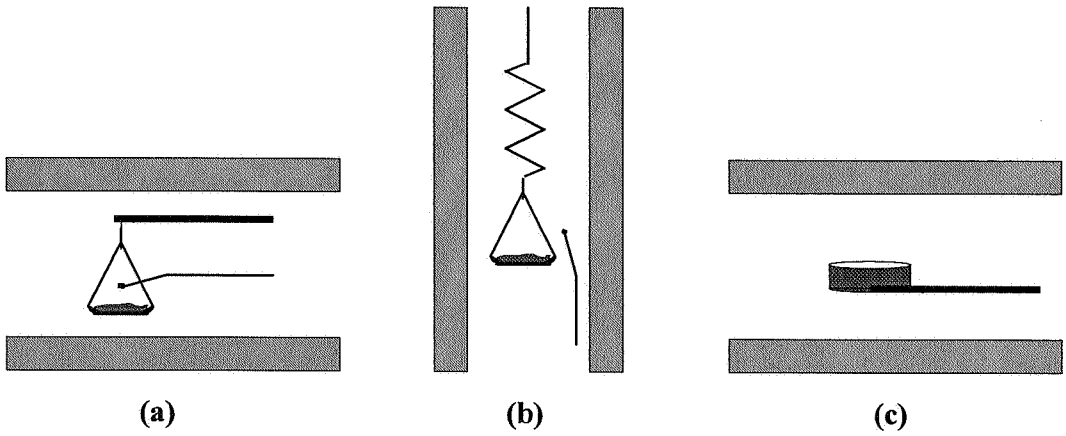

Figure 3.2 Thermocouple location in: (a) *DuPont 951 TGA*, (b) *Perkin Elmer TGS-2*, (c) *SDT 2960* from *TA Instruments*

Other factors which may affect the read out from a TGA-system includes: heating rate, pressure, purge gas flow-rate, characteristics of sample holder and sample size and packing density.

Differential Thermal Analysis (DTA) is a thermal technique in which the temperature of a sample is compared to the temperature of a thermally inert material. The temperature difference is recorded as a function of the temperature measured in the furnace which is heated at constant heating rate. Temperature changes in the sample are due to endothermic or exothermic enthalphic transitions or reactions such as those caused by vaporization/ condensation and decomposition reactions. Hence, the DTA signal gives a qualitative measure of the sign and magnitude of energy absorption or evolution. A schematic presentation of DTA and a graphical presentation illustrating the difference in temperature between the sample and reference holder heated at a constant rate are shown in Figure 3.3.

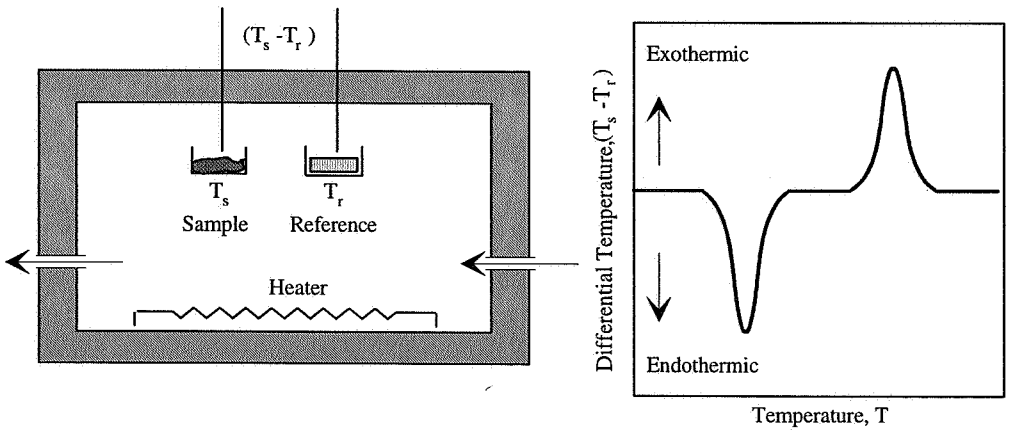

Figure 3.3 DTA.

The critical variables in DTA are related to the size and form of the sample and reference material. The sample has to be so small that effects of temperature gradients within the sample can be neglected. The optimum reference material is one which has thermal characteristics similar to that of the sample, undergoes no appreciable thermal transitions, does not react with or catalyze reactions with the sample and has uniform porosity. The apparatus which has been used in this study, combines the method of TGA and DTA and allows simultaneous measure of mass loss and differences in temperature between a reference material and a sample which are heated at a constant or linearly increasing temperature.

Differential Scanning Calorimetry (DSC). At least two types of DSC instruments have been developed which are based on entirely different designs: the heat flux DSC which is actually a DTA (developed by DuPont) and the power compensation DSC (developed by Perkin-Elmer). The primary functional part of the power compensation DSC consist of a sample holder and a reference holder each having an independently controllable platinum resistance heater imbedded in its base. The principle of operation of the DSC is to maintain the reference and sample holders, and their contents, at the same temperature during the analysis by add heat to, or subtract heat from the sample. The readout from the DSC represents the difference in electrical power (heat), dissipated in the sample and reference holders, which is required to maintain the holders and their contents at the same temperature. This is illustrated in Figure 3.4. Hence, the power compensation DSC provides more direct (quantitative) information relating to changes in enthalpy than does DTA.

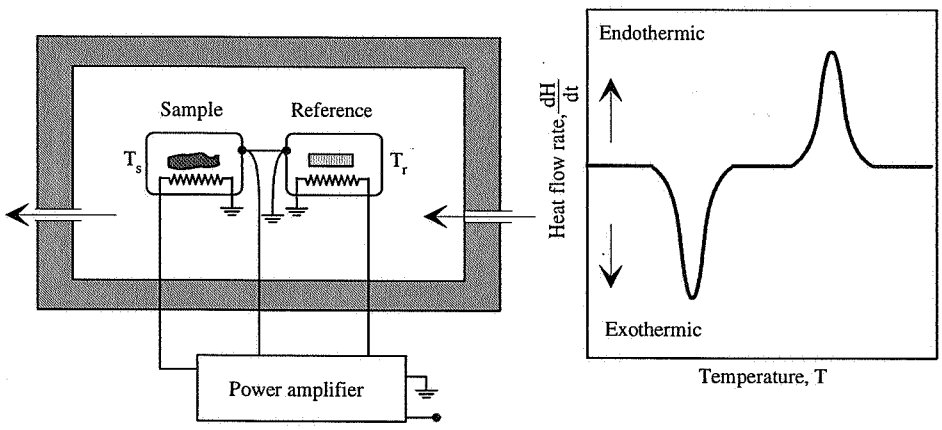

Figure 3.4 Power compensation DSC.

Evolved Gas Analysis (EGA) is used to qualitatively characterize the gases produced during degradation. It may be used in conjunction with other methods, such as TGA or DSC, enabling both qualitative and quantitative analysis. The gases may be analyzed in an intermittent or continuous manner by various techniques. Analytical techniques usually employed are gas chromatography (GC), high performance liquid chromatography (HPLC),

mass spectrometry (MS) or infrared spectrometry (IR). Sometimes it can be troublesome to measure the high molecular products known as tar, since these may deposit in the apparatus. If the transfer line is too hot, secondary reactions will occur. If the transfer line is not enough heated, the tars will not reach the analyzer.

Heated Grid Apparatus is an apparatus developed to study coal devolatilization under very high heating rates (100-100 000°C/s). The sample is placed in a wire screen heated to a preselected temperature by DC or AC current. Mass loss is measured by weighting the sample before and after the run. In conjunction with EGA, the apparatus can be used to study the product composition and ultimate char, gas, tar-yields as a function of final sample temperature, heating rate and residence time. A principle drawing of the apparatus is shown in Figure 3.5.

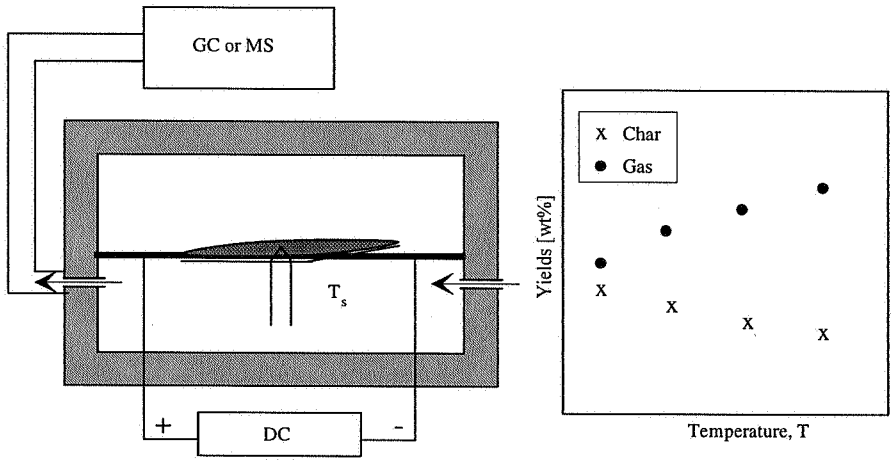

Figure 3.5 Heated grid apparatus.

3.2.2 PHENOMENOLOGICAL MODELS AND KINETIC PARAMETERS

The pyrolysis of wood and related lignocellulosic substances is frequently describe by a single reaction:

$$\text{solid} \xrightarrow{k_1} \text{volatiles + char}$$

where the rate of mass loss depends on mass and temperature according to the following equation:

$$\frac{d\alpha}{dt} = k(T)\ f(\alpha) \qquad (3.1)$$

α, t, T, and k defines the reacted (converted) fraction, time, temperature, and the rate constant, respectively. The variation of the rate constant with temperature is approximated by the

Arrhenius equation:

$$k(T) = A \exp(-E/RT) \tag{3.2}$$

where A, E, R, T denotes the frequency (pre-exponential) factor, activation energy, gas constant and temperature, respectively. $f(\alpha)$ is usually approximated by:

$$f(\alpha) = (1 - \alpha)^n \tag{3.3}$$

where n is the formal reaction order. If the initial sample mass, the actual sample mass and the relative char yield is denoted by m_0, m and m_{char}, then the conversion fraction α can be defined as follows:

$$\alpha = \frac{(m_0 - m)}{(m_0 - m_{char})} \tag{3.4}$$

Several methods leading to the determination of the kinetic parameters (E, A, n) are available in the literature. These can be classified into three categories: integral, differential and special methods. Integral methods are based on the mass loss data while differential methods require data for both the mass loss and rate of mass loss. Special methods are generally based on particular couples of experimental data, e.g. data from different heating rates, or they need data evaluated from graphical plots. By assuming a first order rate of reaction, equation (3.1) to (3.3) can be written in the following form:

$$\frac{d\alpha}{dt} = A \exp(-E/RT)\ (1 - \alpha) \tag{3.5}$$

Dynamic thermogravimetry is often carried out at constant heating rates. In such case:

$$T = T_0 + \beta t \quad \Rightarrow \quad \beta = \frac{dT}{dt} \tag{3.6}$$

When the natural logarithm of equation (3.5) is taken and the resulting equation is rearranged, one obtains the traditional and often applied differential method [Lee (1982), Williams and Besler (1992), Grønli *et al.* (1992)]:

$$\ln\left[\frac{d\alpha/dt}{(1 - \alpha)}\right] = \ln(A) - \frac{E}{RT} \tag{3.7}$$

By using experimental values for α and $d\alpha/dt$ as a function of temperature, a plot of $\ln[(d\alpha/dt)/(1-\alpha)]$ versus 1/T should ideally give a straight line with a slope of (-E/R) with an intercept of ln(A). Difficulties arise when computing kinetic parameters by means of integral methods. This is due to a temperature-containing integral which turns up when equation (3.5) is integrated

$$\int_0^{\alpha} \frac{d\alpha}{(1 - \alpha)} = \frac{A}{\beta} \int_{T_0}^{T} \exp(-E/RT)\,dT \tag{3.8}$$

Since the temperature-containing integral on right-hand side of equation (3.8) has no exact

solution, several expansions and semi-empirical approximations have been suggested: Van Krevelen approximation and asymptotic expansion [Broido and Williams (1973)]; and Doyle's approximation [Flynn (1983)]. Carrasco (1993) made an extensive review of solution methods and compared the results obtained by using a general analytical solution based on a recurrent series equation with those evaluated by means of twelve established integral, differential and special methods. The kinetic parameters for a given polymeric substance varied considerably, with reaction order between 0.8-1.4, activation energy between 100-160 kJ/mol, and frequency factors between $2.07 \cdot 10^8$-$9.38 \cdot 10^8$ s^{-1}. The most accurate methods were the general analytical solution together with the traditional differential method. As expected, the special methods gave the worst accuracy. With todays computers and software, however, there is no need for simplifying approximations. If α and $d\alpha/dt$ is known, one can easily calculate the kinetic parameters by non-linear curve-fitting of equation (3.5).

Table 3.1 gives a survey of kinetic data for different biomass species where a single step reaction model have been used.

Table 3.1 A survey of kinetic data for biomass pyrolysis.

Reference	Feedstocks		n	log(A) [log s^{-1}]	E [kJ/mole]	Conditions
Akita and Kase (1967)	Cellulose	250-330°C	1.0	15.0	224.0	TGA and DTA, 0.23-5°C/min, N_2 and vacuum
Tang (1967)	Pine	280-325°C	1.0	5.5	96.3	TGA, 200-460°C, 3°C/min, vacuum
		325-350°C	1.0	16.8	226.1	
	Cellulose	240-308°C	1.0	9.8	146.5	
		308-360°C	1.0	17.6	234.5	
	Lignin	280-344°C	1.0	5.2	87.9	
		344-435°C	1.0	-0.03	37.7	
Leu (1976)	Spruce	α>54%	1.1	18.4	217.3	TGA, 250-450°C 10-160°C/min, N_2
		α<54%	1.3	16.1		
	Redwood	α>54%	1.3	17.7	185.0	
		α<54%	1.4	14.2		
Leu (1976)	Spruce	α>54%	1.1	18.4	217.3	TGA, 250-450°C 10-160°C/min, N_2
		α<54%	1.3	16.1		
	Redwood	α>54%	1.3	17.7	185.0	
		α<54%	1.4	14.2		
Lewellen *et al.* (1977)	Cellulose	250-1000°C	1.0	9.8	139.8	Heated grid, 400-10 000°C/s, He

Table 3.1 *(cont)* A survey of kinetic data for biomass pyrolysis.

Reference	Feedstocks		n	log(A) [log s^{-1}]	E [kJ/mole]	Conditions
Fairbridge *et al.* (1978)	Cellulose*	284-337°C	1.0	18.6	248.0	TGA, 7°C/min, * N_2 ** Air
	Cellulose**	290-360°C	1.0	27.5	343.0	
Rogers *et al.* (1980)	Whatman filter paper		0.5	11.3	153.2	TGA, 200-400°C, 1-5°C/min N_2
Lee (1982)	Spruce	10°C/min	1.0	5.8	98.4	TGA, 220-460°C, 10-160°C/min N_2
		160°C/min	1.0	5.5	86.3	
	Redwood	10°C/min	1.0	2.8	63.2	
		160°C/min	1.0	3.2	58.6	
Hajaligol *et al.* (1982)	Cellulose		1.0	8.3	133.1	Heated grid, 300-1100°C 100-15 000°C/s, He
Cooley *et al.* (1988)	Cellulose*		1.13	16.6	213.0	TGA, 200-600°C, He, *1°C/min,**2°C/min,*** 5°C/min
	Cellulose**		0.99	16.8	216.3	
	Cellulose***		1.02	17.5	225.5	
Cordero *et al.* (1989)	Holm oak	5°C/min	1.0	3.0	68.0	TGA, 25-900°C, 5-20°C/min He
		20°C/min	1.0	4.3	70.6	
Varhegyi *et al.* (1989)	Cellulose	10°C/min	1.0	17.6	234.0	TGA, 200-400°C, Argon
		80°C/min	1.0	15.1	205.0	
Grønli *et al.* (1992)	Pine	230-360°C	1.0	4.7	87.6	TGA, 150-500°C, He, 5°C/min
	Spruce	220-400°C	1.0	7.2	92.4	
Williams *et al.* (1994)	Pine <300°C	5°C/min	1.0	5.5	84.5	TGA, 200-500°C, 5-80°C/min N_2
	<300°C	80°C/min	1.0	4.1	77.1	
	Cellulose	5°C/min	1.0	19.8	260.4	
		80°C/min	1.0	13.2	187.6	
	Hemicellulose	5°C/min	1.0	22.3	258.8	
		80°C/min	1.0	9.2	125.1	
	Lignin	5°C/min	1.0	7.4	124.3	

The activation energy in Table 3.1 ranges from 130 to 260 kJ/mole for cellulose, from 125 to 260 for hemicellulose, from 37 to 125 kJ/mole for lignin and from 60 to 240 kJ/mole for wood. The reason for this diversity may be attributed to different experimental conditions, e.g.: sample size; temperature measurements; heating rate and atmosphere. To different extraction procedures and to lack of accuracy caused by the approximations used in the different computational methods.

Even though reported activation energies and frequency factors vary greatly, their combined effect in the rate constants is quite consistent. This is known as the kinetic compensation effect [Zsakó (1976), Chornet and Roy (1980) and Pokol and Varhegyi (1988)]. This effect consists of a correlation between the kinetic parameters and the main analytical feature of this compensation effect is that any variation in the experimental conditions that causes the activation energy to change will be compensated by a change in frequency factor. A family of reactions that will all exhibit the same rate at a characteristic temperature can be described by:

$$\ln(A) = mE + \ln(k_0) \tag{3.9}$$

where the constant $m=1/(RT_i)$ is the slope of a plot of ln(A) vs E and is related to the isokinetic temperature T_i, the temperature at which all reactions of the group proceed at the same reaction rate k_0. In Figure 3.6 a plot of the kinetic data listed in Table 3.1 are shown from which an isokinetic temperature of 318°C (591 K) with k_0 equals to $1.65 \cdot 10^{-1}$ min^{-1} ($2.75 \cdot 10^{-3}$ s^{-1}) can be calculated.

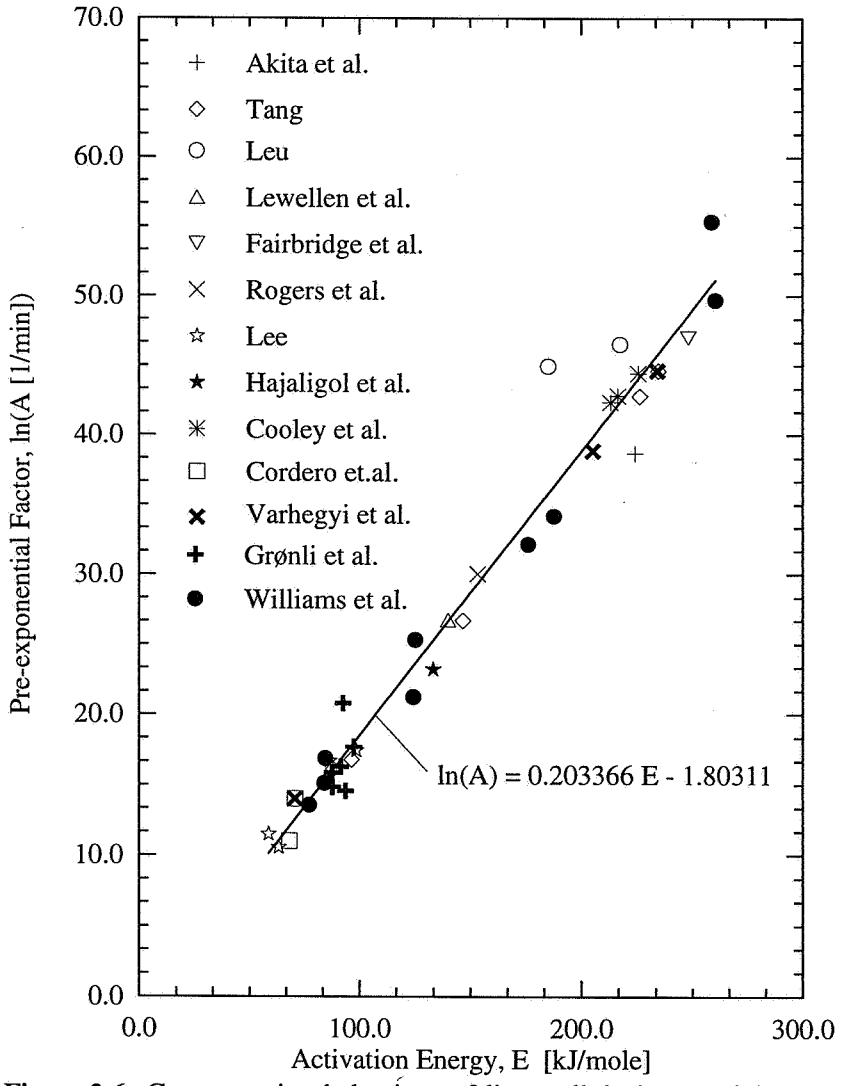

Figure 3.6 Compensation behaviour of lignocellulosic materials.

Narayan and Antal (1996) have shown by using a simple mathematical model that the most likely reason for this compensation behaviour of lignocellulosic materials is due to inaccurate temperature measurements in the experiments, i.e., undetected thermal lag caused by the usual thermocouple lag and thermal lag caused by the fusion like endothermic heat of reaction.

Other workers have undertaken a more complicated analysis to describe the thermal degradation of biomass. Vovelle *et al.* (1982) modeled the pyrolysis of different wood species by considering the wood to consist of 50% cellulose and 50% so called "secondary constituent" (hemicellulose+lignin). A similar approach was used by Varhegyi *et al.* (1989) who modeled the decomposition of sugar cane bagasse by two independent parallel first order reactions, one reaction describing the hemicellulose decomposition and the second describing the cellulose decomposition. This modeling approach is a mathematical expression of the hypothesis of Shafizadeh and McGinnis (1971) who assumed that the major components in a lignocellulosic material decomposes independently from each other.

It has long been known that the presence of inorganic materials (metals, salts) either as additives or natural alter the pathways of biomass pyrolysis. The influence of inorganic materials has been extensively investigated in flame-proofing and fire prevention studies [Akita and Kase (1967), Shafizadeh (1985)]. In this context, the term "catalytic effect" has frequently been used since some of these additives (potassium, lithium, ferrous ($FeSO_4$) and ferric ($Fe_2(SO_4)_3$) salts) act as a catalyst reducing the temperature threshold at which the pyrolysis starts, and in general increases the yield of char, water, carbon monoxide and carbon dioxide while decreasing the fraction of tar and non-flammable volatile products. Recently, the goal of this type of research, i.e., adding inorganics or other additives to the biomass material, has become the thermochemical conversion of biomass to fuel and chemicals [Varhegyi *et al.* (1988), Richards and Zheng (1991), Skille (1995)].

Among the shortcomings of employing single step reaction models to describe the kinetics of biomass pyrolysis are that only total volatiles are predicted by difference. Not how they are distributed among combustible and non-combustible gases, char and tar and the results are often related to highly specified experimental conditions and biomass species. In 1975 Broido and Nelson published results involving thermal pretreatments of cellulose between 230 and 275°C prior to isothermal pyrolysis at 350°C. Depending upon the temperature and the duration of the pretreatment, the char yield from cellulose varied from 11.0 to 27.6 %. Broido explained this result by a competitive degradation mechanism involving a depolymerization reaction which formed no char and a dehydration reaction which formed 36% char. Based on these findings, Broido (1976) proposed the following multistep reaction scheme for the thermal degradation of cellulose:

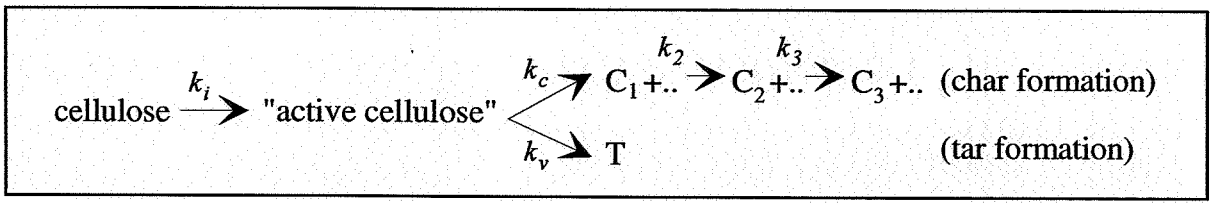

When cellulose is heated it undergoes a rapid decrease in DP to form a so-called low DP "active cellulose". The active cellulose subsequently decomposes by two competitive mechanisms, producing either tar (without char), or solid intermediates (char, C_i) via a sequence of consecutive reactions. The ellipses with the plus sign, "+..", indicate accompanying gas formation. Later, Bradbury, Sakai and Shafizadeh (1979) modified Broido's reaction scheme into what today is known as the "Broido-Shafizadeh model":

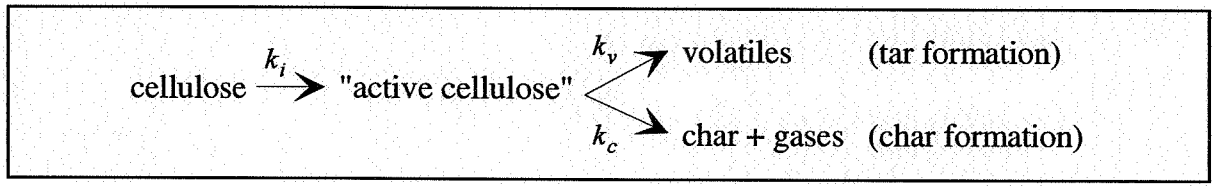

Broido (1976, 1992) and Bradbury *et al.* (1979) reported the following rate constants: $k_v = 1.70 \cdot 10^{16} \exp(-221.6/RT)$ [s^{-1}] and $k_v = 3.17 \cdot 10^{14} \exp(-198.0/RT)$ [s^{-1}] for the depolymerization and $k_c = 1.60 \cdot 10^{11} \exp(-169.6/RT)$ and $k_c = 1.32 \cdot 10^{10} \exp(-150.7/RT)$ for the char-forming sequence, respectively. The temperature at which the char formation rate is equal to the volatile production rate can be found when the ratio of the volatile and char formation rates is equal to one

$$(k_v/k_c) = (A_v/A_c)\exp\left(-(E_v - E_c)/RT\right) = 1 \qquad (3.10)$$

This temperature, below which char formation dominates volatile production is: T=267°C for Broido's and T=291°C for Bradbury *et al.* rate constants, respectively. This means that low temperatures and slow heating rates favours char production while high temperatures and fast heating rates favours tar production. Similar reaction schemes involving competitive and consecutive degradation mechanisms have been proposed for the thermal degradation of cellulose [Arseneau (1971), Agrawal (1988a, 1988b), Alves and Figueiredo (1988, 1989a, 1989b)] and also for the whole wood [Thurner and Mann (1981), Agrawal (1984b), Koufopanos *et al.* (1989)].

Experimental studies of the influence of prolonged thermal pretreatments on char yields from pure cellulose were the foundation of Broido's modeling efforts. However, in attempt to improve the yield of charcoal from biomass pyrolysis, Antal *et al.* (1990) reported that various thermal pretreatments of 16-46 h at 172 to 260°C on bagasse offered no improvements in charcoal yields. Similar observations were, among others, reported by Zaror and Pyle (1986) and Piskorz *et al.* (1989). In a recent publication, Varhegyi *et al.* (1994) tried to reproduce or

confirm the findings of Broido, Shafizadeh and co-workers (B-S) by using a modern thermobalance and modern computer hardware/software which permit better data acquisition and more precise numerical treatment than for almost twenty years ago. They were happy to confirm some of the most significant findings of B-S, that prolonged, low temperature isothermal treatments really affected the final char yield indicating a competitive reaction mechanism in the thermal degradation of cellulose. However, no evidence was found to support the inclusion of the initiation 'cellulose → active cellulose' step. B-S assumed that this reaction occurred in the same temperature domain as the reactions leading to mass loss. Varhegyi *et al.* proved that this was not the case, but did not exclude the possibility for this reaction to occur at lower temperatures before the mass loss start. Besides, the solid residue (char) yields were considerably lower than those observed by B-S. This was attributed to the very large samples (90-250 mg) used by B-S which enhanced the pyrolytic vapour-solid interactions leading to char formation. Varhegyi *et al.* (1994) calculated the following rate constants: $k_v=1.26\cdot10^{18}\exp(-238/RT)$ and $k_c=3.16\cdot10^{9}\exp(-147/RT)$ for the depolymerization and char-forming sequence, respectively. However, their conclusion was that complicated models which processes more than one reaction step are not needed to simulate the mass loss behaviour of cellulose at heating rates of 2°C/min or more. Under regimes controlled by chemical kinetics, the depolymerization step is rate limiting and a first-order single-step model with an activation energy of 238 kJ/mol can be used.

By using a heated grid apparatus, Lewellen, Hajaligol, Nunn and co-workers [Lewellen *et al.* (1977), Hajaligol *et al.* (1982), Nunn *et al.* (1985)] studied the effects of temperature (250-1100°C), solid residence time (0-75600 s), ambient pressure (0-1 atm) and heating rate (≤100-15000°C/s) on the yields, compositions and rates of evolution of the major volatile products from rapid (flash) pyrolysis of cellulose and lignin. Their main observations were as follows: For cellulose, temperature and sample residence time were the most important reaction conditions in determining the pyrolysis behaviour. A heavy liquid tar accounted for 40 to 83 wt% of the volatiles above 400°C. Secondary cracking of this material increased with increasing residence time or temperature and was a significant pathway for producing several light combustible gases. At a heating rate of 1000°C/s and temperatures above 750°C, CO was dominating the product gases and attained a yield above 23 wt% at 1000°C. For lignin, the total mass loss increased strongly to an asymptotic value of 86 wt% at 780°C. Tar was the major pyrolysis product above 530°C with a maximum yield of 53 wt% at 630°C. Secondary cracking of the tar to light gases above 680°C and CO was dominating the product gases and attained a yield of 19 wt% at 1170°C. Lewellen *et al.* (1977) used the coal devolatilization model of Anthony *et al.* (1974), and assumed that the pyrolysis of cellulose occurs through an infinite series of parallel reactions. A continuous Gaussian distribution of activation energies about a mean E_0 with a standard deviation σ was assumed, along with a common

value for the frequency factor. The total mass loss in this model was described by:

$$m = 1 - \left[[\sigma (2\pi)^{1/2}]^{-1} \int_{-\infty}^{\infty} \exp\left(- \int_{0}^{t} k(E)\,dt \right) \exp\left(\frac{-(E - E_0)^2}{2\sigma^2} \right) dE \right] \qquad (3.11)$$

Use of a single reaction model with an activation energy of E=140 kJ/mole and a frequency factor of $6.79 \cdot 10^9$ s^{-1} correlated well with their data. Use of equation (3.11) yielded a slightly improved correlation with a mean activation energy of E_0=155 kJ/mole, a standard deviation of σ=4.6 kJ/mole and a frequency factor of $7.67 \cdot 10^{10}$ s^{-1}.

Hajaligol *et al.* (1982) and Nunn *et al.* (1985) assumed that cellulose and milled wood lignin decomposed directly to each reaction product *i* by a single independent reaction pathway:

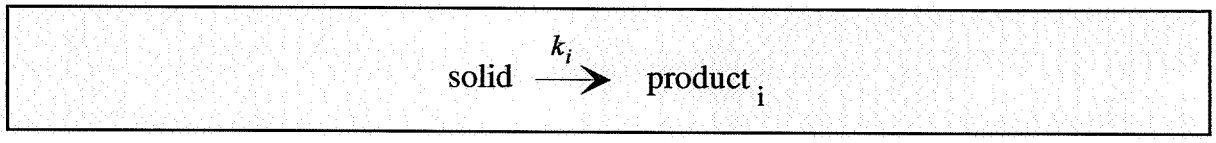

and that the kinetics of the individual products could be modeled by the following unimolecular first-order reaction

$$\frac{dV_i}{dt} = (V_i^* - V_i) A_i \exp(-E_i/RT) \qquad (3.12)$$

where V_i, A_i and E_i are the yield, pre-exponential factor and activation energy of product *i*, respectively. The quantity V_i^* is the ultimate attainable yield of product *i* (high temperature and long residence time). Theoretical curves, obtained by best fit values of the kinetic parameters, correlated well with their experimental data for temperatures up to 1000°C. Their results are given in Table 3.2.

Table 3.2 Kinetic data of Hajaligol *et al.* (1982) and Nunn *et al.* (1985).

Species	Product	log (A_i) [log s^{-1}]	E_i [kJ/mole]	V_i^* [%]
Cellulose	mass loss	8.30	133.1	94.08
	CO	11.75	221.0	21.64
	CO_2	5.39	98.1	3.08
	CH_4	13.00	251.4	2.41
	H_2O	6.71	103.1	8.04
Lignin	mass loss	5.53	82.1	84.35

3.2.3 HEAT OF REACTION

Finally, some reflections about the sign and magnitude of the heat of pyrolysis which is involved in the thermal degradation of wood and its major components. The two types of

experimental techniques that have been used to study this effects are the DTA and DSC, their main features have been discussed previously. The heat of reaction of cellulose, hemicellulose, lignin and wood has been reported in the literature as exothermic, endothermic and a combination of the two. This confusion can be attributed to sample size, atmospheric conditions (inert or oxidizing) and impurities.

Broido (1966) studied the thermal decomposition of "ash-free" cellulose (ash content <0.01%), "pure" cellulose (ash content ~0.15%) and "treated" cellulose (1.5% $KHCO_3$ added) by using a commercial DTA unit. Thermograms were obtained in flowing nitrogen and air atmosphere. About 5 grams of shredded paper were used. The results indicated that for both "ash-free" and "pure" cellulose, the pyrolysis was endothermic up to approximately 325°C and exothermic from 325°C to 500°C in both atmospheres. For the "treated" cellulose, no sharp endotherm could be observed in nitrogen while an almost continuous exotherm could be observed in air. While Broido's results on "pure" cellulose in air are in agreement with the results of Akita and Kase (1967), they could not observe any exothermic reaction above 325°C in nitrogen.

Arseneau (1961) compared the effect of sample layer thickness on the heat of pyrolysis of ash-free cellulose by using a commercial DSC unit. By increasing the sample thickness from 0.46 to 0.9 mm, he could observe that from being a purely endothermic reaction over the entirely temperature region for the 0.46 mm case, the heat of reaction became exothermic above 350°C when the sample thickness was doubled.

Havens *et al.* (1971) developed an experimental procedure to separate the heat effects related to the decomposition from the specific heat of pine and oak pyrolysis by combining the results obtained separately from TGA and DSC experiments. By assuming the sensible heat portion of the total energy capacity measured by the DSC to be proportional to the amount of solid material left, the total energy capacity was multiplied by the TGA mass loss curve. By measuring the area of the energy capacity curve laying above the sensible heat portion, the endothermic heat of pyrolysis was estimated to be 200 kJ/kg and 112 kJ/kg of original mass for pine and oak, respectively. This is shown as the shaded area in Figure 3.7

Mok and Antal (1983) used a Setram DSC to study the effects of pressure and purge gas flow rate (residence time) on char yield and heat of reaction of cellulose pyrolysis. Experiments were conducted at pressures from 10^{-2} to 25 atm with volumetric flows from 1 to 20 cm^3/min. Whatman No 1, filter paper cut into rectangular strips (10 mm x 2 mm) was used. The results revealed that with increasing pressure and decreasing flow rate, the char yield increased while the heat of pyrolysis decreased and became exothermic. This was assumed to be due to secondary repolymerization reactions of the tar. The same apparatus was later used to study

char formation and heat of pyrolysis of biomass within sealed crucibles [Mok *et al.* (1992)]. Very high yields of charcoal, from 40% for cellulose to 48% for *Eucalyptus gummifera* (containing 37% lignin), were obtained. In the absence of oxygen, the pyrolytic charcoal formation was entirely exothermic. Under certain conditions, the reaction released enough heat to raise the solid substrate from room temperature to reaction temperature.

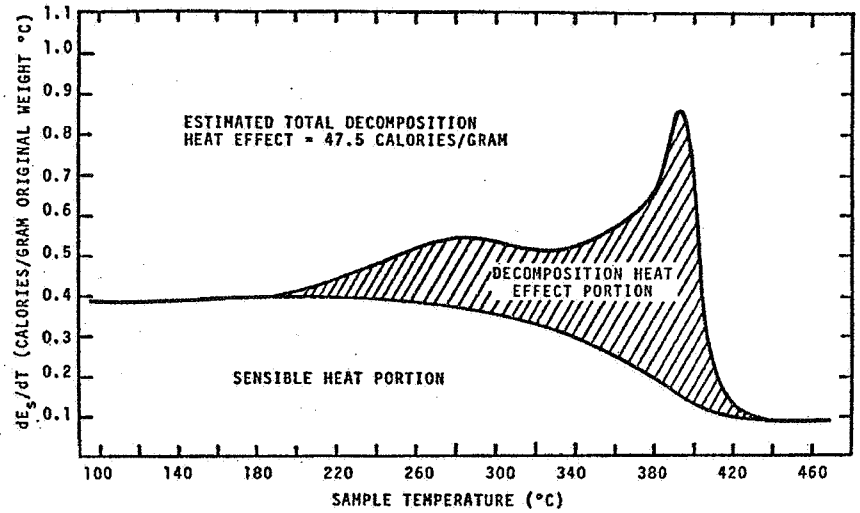

Figure 3.7 Energy capacities of pine, [Havens *et al.* (1971)].

CONCLUDING REMARKS

To summarize, the kinetics of the pyrolysis of wood and related lignocellulosic substances are extremely complex. The major research has been concentrated on single mass loss reaction modeling with large variations in kinetic data reported. This may be attributed to different experimental conditions, e.g.: sample size; temperature measurements; heating rates and atmosphere; and to different computational methods used. Prolonged thermal pretreatment have indicated that there exist a competitive degradation mechanism in the pyrolysis of cellulose, a depolymerization reaction leading to tar formation and a dehydration reaction forming char. Based on these findings, many kinetic models involving parallel and consecutive reactions have been proposed both for cellulose and wood. However, recent works have shown that the pyrolysis of cellulose, with no pretreatment, impurities or secondary reactions involved can be well described by a first-order single-step model. The pyrolysis of the whole wood can be described by two or more parallel reactions, each reaction describing the individual decomposition of the major components found in wood.

It has been proved that the pyrolysis of wood and its components, at least in the absence of impurities and in an inert atmosphere, is entirely endothermic. If impurities (catalysts) are added, oxygen/air is used, the sample size is too large or the pyrolysis vapours (tars) have time to react (secondary charring reactions), exothermic heat effects may be observed.

3.3 THERMOGRAVIMETRIC ANALYSIS AND KINETIC STUDY OF THE PYROLYSIS OF CELLULOSE, HEMICELLULOSE, LIGNIN AND WOOD

3.3.1 EXPERIMENTAL SECTION

3.3.1.1 SAMPLES AND SAMPLE PREPARATION

Birch, pine, spruce and pineroot were powdered from knot and bark-free logs and carefully screened by a sonic shifter. Particle sizes used for the experiments were below 100 microns sieve size. Cellulose, hemicellulose and lignin were isolated from both birch and spruce by the Norwegian Pulp and Paper Research Institute by using the following procedure [Browning (1967)]. The air-dried wood meal was pre-extracted for 6 hours with acetone in a Soxlet extractor and dried for 24 hours at a temperature of 103±2°C. Lignin was isolated from the pre-extracted wood meal by using the standard test method for acid-insoluble lignin using sulphuric acid. Another part of the pre-extracted wood meal was treated with sodium chlorite ($NaClO_2$) to remove the lignin. The resulting holocellulose was treated with 10% potassium hydroxide (KOH) for four hours, filtered, washed, dried and the cellulose part of the holocellulose was obtained. The filtrate from this treatment was added ethanol and the precipitate forms the hemicellulose which was isolated by means of decanting, centrifuging and washing with alcohol. A pure (99.5 %) cellulose (A-cellulose) and a cellulose containing 15 % hemicellulose (B-cellulose) was obtained from a Norwegian pulp and paper company (Borregaard A/S). In addition, Whatman No 42 ash free filter paper (W-cellulose) was studied. The proximative analysis of the celluloses, hemicelluloses and lignins found by using the method recommended by Elder (1983) are listed in Table 3.3.

Table 3.3 Proximative analysis of the celluloses, hemicelluloses and lignins used.

	Volatile Matter* [wt%]	Fixed Carbon [wt%]	Ash [wt%]
A- cellulose	95	5	0
B-cellulose	88	11.5	0.5
W-cellulose	94	6	0
Birch cellulose	90	10.5	0.5
Spruce cellulose	93	6.5	0.5
Birch hemicellulose	85	12.5	2.5
Spruce hemicellulose	76	19	5
Birch lignin	60	39.5	0.5
Spruce lignin	58	41.5	0.5

*At a temperature of 900°C

As mentioned earlier, impurities such as salts and components in the ash is known to alter the pathways of biomass pyrolysis. However, the amount of impurities can be reduced by a dilute acid or hot-water washing procedure. The following procedures (*P1-P3*) recommended by Varhegyi *et al.* (1994a) for removing the minerals and the procedure (*P4*) recommended by Browning (1967) for removing the extractives were applied on some of the wood species (see Table 3.4):

P1. *Acid washing at room temperature by 0.1 mol/l hydrochloric acid (HCl) as proposed by DeGroot and Shafizadeh (1984): A 1 g sample was placed in 20 ml of 0.1 mol/l HCl and stirred for 4 h at room temperature. The suspension was filtered and washed with distilled water until neutrality.*

P2. *The same procedure with 1 mol/l acetic acid instead of HCl.*

P3. *A similar washing by pure, twice distilled, 80°C water for two hours. (In this latter case 120 ml water was used for 1 g sample.)*

P4. *Pre-extraction for 6 hours with acetone in a Soxlet extractor.*

KCl and other salts will be dissolved and part of the -COOK groups will be replaced by -COOH when hot water is used. In addition, CaC_2O_3 will be solved when the acids are used. However, one must be aware of that some hydrolysis, especially of the hemicellulose, may occur during these pretreatments [Varhegyi (1994a)].

Table 3.4 Washing procedures applied on the different wood species.

Method	Birch	Spruce	Pine	Pineroot
P1			*x*	
P2			*x*	
P3	*x*	*x*	*x*	*x*
P4				*x*

3.3.1.2 EXPERIMENTAL APPARATUS

The experimental apparatus consists of a SDT 2960 Simultaneous TGA-DTA from *TA Instruments*, supported by an IBM PC and software for control and data handling. The schematic of the SDT 2960 is shown in Figure 3.8. The system is based on a dual beam horizontal design in which each ceramic beam (balance arm) functions as one half of a DTA thermocouple pair, as well as part of a horizontal null-type balance. One arm accommodates the sample and measures its property changes. The other arm accommodates the reference and is used to generate the DTA (ΔT) measurement, as well as to correct the TGA measurement

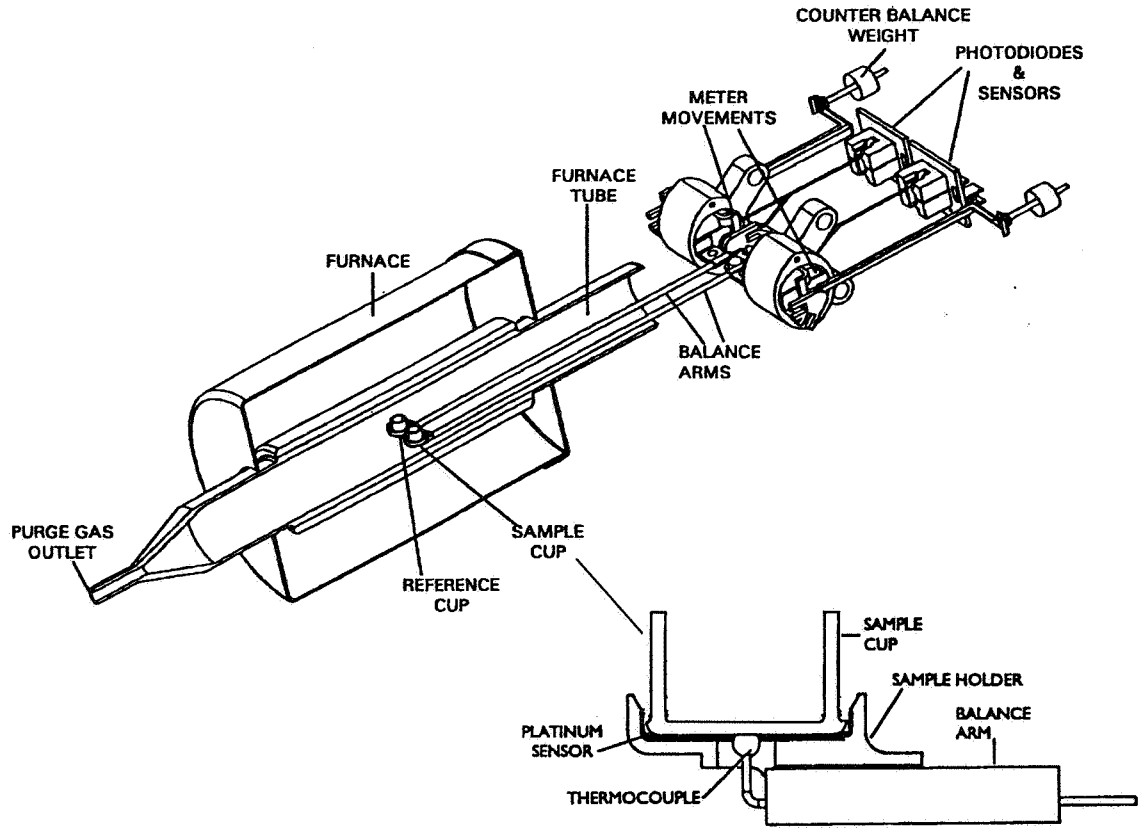

Figure 3.8 Schematic diagram of the SDT 2960 Simultaneous TGA-DTA from *TA Instruments.*

for temperature effects like beam growth. The TGA mass change is measured by a taut-band meter movement located at the rear of each ceramic arm. An optical activated servo loop maintains the balance arm in the horizontal reference (null) position by regulating the amount of current flowing through the transducer coil. An infrared LED light source and a pair of photosensitive diodes detect movement of the arm. A flag at the end of the balance arm controls the amount of light reaching each photo sensor. As mass is lost or gained, the beam becomes unbalanced, causing unequal light to strike the photodiodes. A restoring current is generated to eliminate this imbalance and reattain the null position. The amount of restoring current is a direct measure of the mass change. The DTA (ΔT) measurement is made by a pair of matched platinum/platinum-rhodium thermocouples which are contained inside the ceramic arms and welded to platinum sensors located in the bottom of the sample and reference holder (see Figure 3.8). The thermocouple in contact with the sample cup is used to measure the sample temperature. A bifilar-wound furnace provides uniform controlled heating up to 1500°C. The SDT 2960 has a sample capacity of (max) 200 mg with a balance sensitivity of 0.1 μg. Heating rates from 0.1 to 100°C/min can be used from ambient temperature up to 1000°C, while 0.1 to 25°C/min can be used from ambient temperature up to 1500°C. Although, the response time of the SDT has been reported to be in the order of hundredth of a second, the minimum log-interval which can be used is one point per 0.5 seconds.

3.3.1.3 EXPERIMENTAL PROCEDURE

One important task when doing TGA-experiments for kinetic studies is to decide the heating rate with an appropriate sample size (m_0). The optimal condition which causes minimal heat and mass transfer problems, can be obtained by using very low heating rates and very small sample size. It is well known that the maximum reaction rate $(-dm/dt)_{max}$ of the reactions controlled by, or consisting of a single rate controlling step, is approximately proportional to the linear heating rate (dT/dt). As a rough estimate, the sample thickness should be inversely proportional to heating rate to avoid heat and mass transfer problems. Hence, one can use large m_0 at relatively low dT/dt while m_0 has to be reduced when the heating rate is increased [Varhegyi (1994b)]. On the other hand, it is difficult to measure small sample masses at low heating rates due to the signal to noise ratio and base line uncertainties. With a limited amount of time available to carry out approximately 30 experiments (access to the SDT-apparatus), a heating rate of 5°C/min with a log-interval of one point per second was chosen. After some initial test runs, which will be discussed in the next subsection, it was decided to use a sample size of approximately 5 mg for all the experiments. The effect of heating rate on the pyrolysis of A-cellulose was studied by using 2, 5, and 10°C/min with sample sizes of 5, 5 and 4 mg, respectively.

A typical run was carried out as follows. The sample material was spread in a uniform layer in a ceramic sample cup which was placed on the sample holder attached to the balance arm. The purging (99.99% pure nitrogen with a flow rate of 500 ml/min) was switched on and after 30 minutes isothermal hold at ambient temperature, the temperature was raised to 120°C and maintained for 30 minutes to ensure an atmosphere free of oxygen and that no moisture was left in the sample. The sample was then heated up to 550°C at the preselected heating rates and maintained for 5 minutes after which the experiment was terminated.

3.3.2 RESULTS AND DISCUSSION

The traditional way to present results from non-isothermal thermogravimetric measurements of biomass and related substances has been to show the mass loss vs temperature (integral or TG) curve. From the integral curve one can quantitatively obtain the char-yield at the final temperature and see at which temperatures the thermal decomposition occur. However, the characteristic behaviour of a substance and distinction between different substances becomes more visible in the rate of mass loss vs temperature (differential or DTG) curve. Since both curves contain a piece of information which are relevant for the understanding of the thermal behaviour, both will be presented in the following discussion.

3.3.2.1 SAMPLE SIZE, REPEATABILITY AND EFFECT OF HEATING RATE

To decide which sample size should be used in the experiments, three separate 5°C/min runs with sample sizes of 2, 5 and 10 mg were done. The resulting thermograms which are shown in Figure 3.9 proves that for a heating rate of 5°C/min, it is indifferent which sample size below 10 mg is used. However, by using as much as 10 mg, almost one third of the sample cup will be filled with material and one cannot exclude the possibility of the pyrolysis vapours formed in the bottom of the sample cup to react with the overburden char layer. In order to avoid signal/noise problems which may arise when small sample sizes are used at low heating rates, it was decided to use between 4 and 5 mg for all the experiments at a heating rate of 5°C/min.

In Figure 3.10, results from four identical runs for A-cellulose (5 mg at 5°C/min) are presented. The repeatability is satisfying with some variation in the final char yield at 450°C. This may be explained by irreproducibilities in the experimental procedures, such as the placement of the sample in the sample pan and the subsequent placement of the sample pan on the sample holder. The temperature for which the maximum rate of reaction occur (T_{peak}) is between 325.7 and 328.0°C for all the runs. Based on these findings and the previous experience with the biomass species analyzed [Grønli *et al.* (1994)], it was decided to carry out one experiment only for each species.

The effect of different heating rates on the thermal decomposition of A-cellulose is shown in Figure 3.11 and Figure 3.12. In the latter case, the DTG curves have been scaled to an equal height (normalized by $(dm/dt)_{max}$). Most of the decomposition occurs between 275-325°C at 2°C/min. As the heating rate is increased, this domain moves towards a higher temperature and the rate of mass loss curves (dm/dt) becomes broader. This lateral shift or delayed decomposition may be attributed to the residence time of the sample. A higher heating rate will shorten the time of exposure to a given temperature or temperature zone. Thus, a higher heating rate process means that the sample must reach a higher temperature to assure having enough time for completion of the overall reaction.

3.3.2.2 PYROLYSIS OF CELLULOSE, HEMICELLULOSE AND LIGNIN

A comparison between the different cellulose species are presented in Figure 3.13 and in Figure 3.14 where the DTG curves have been scaled to an equal height. Cellulose loses weight in a narrow temperature range and yields a sharp, single DTG peak. This is consistent

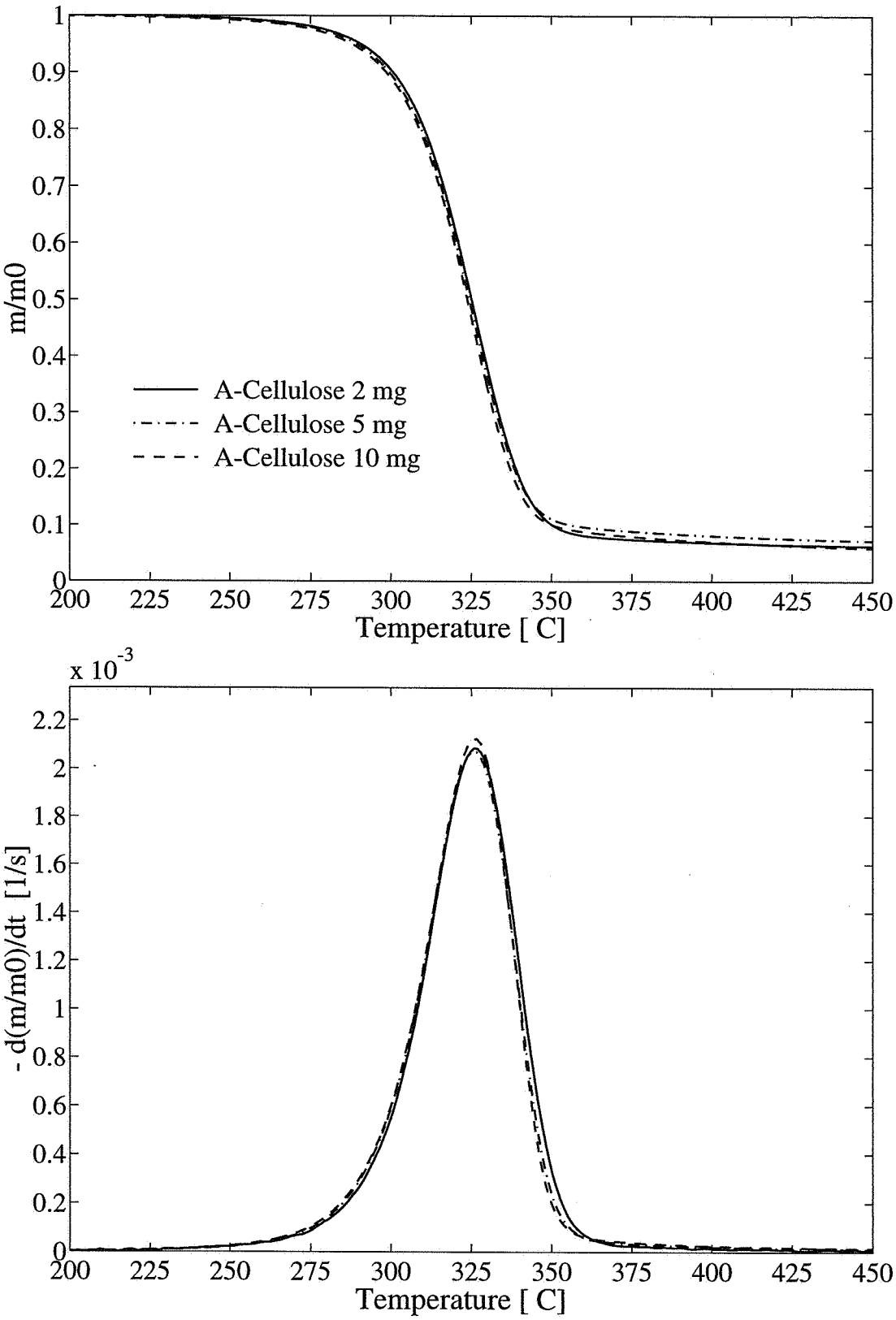

Figure 3.9 The effect of sample size at a heating rate of 5°C/min.

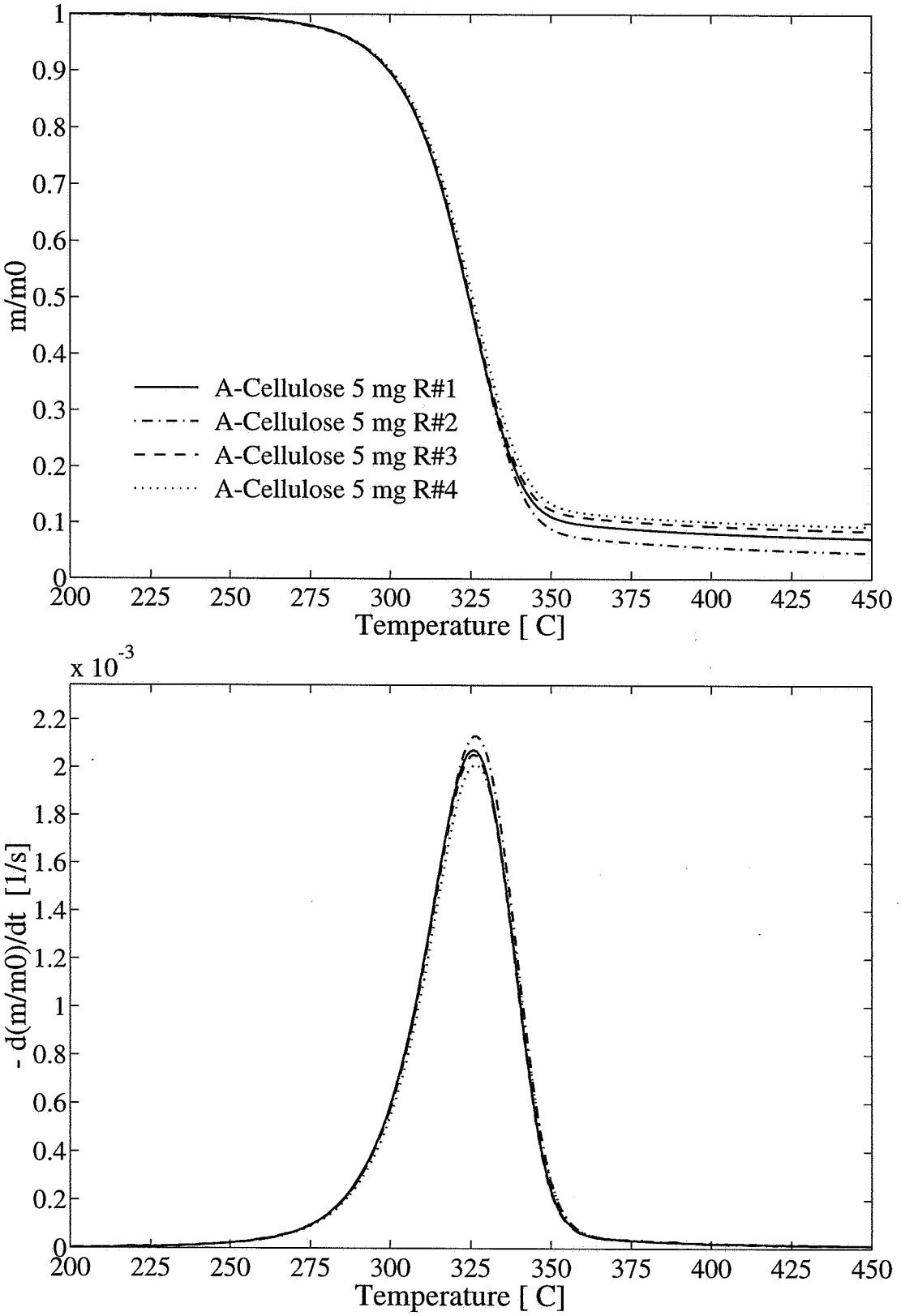

Figure 3.10 Repeatability test with sample size of 5 mg and a heating rate of 5°C/min.

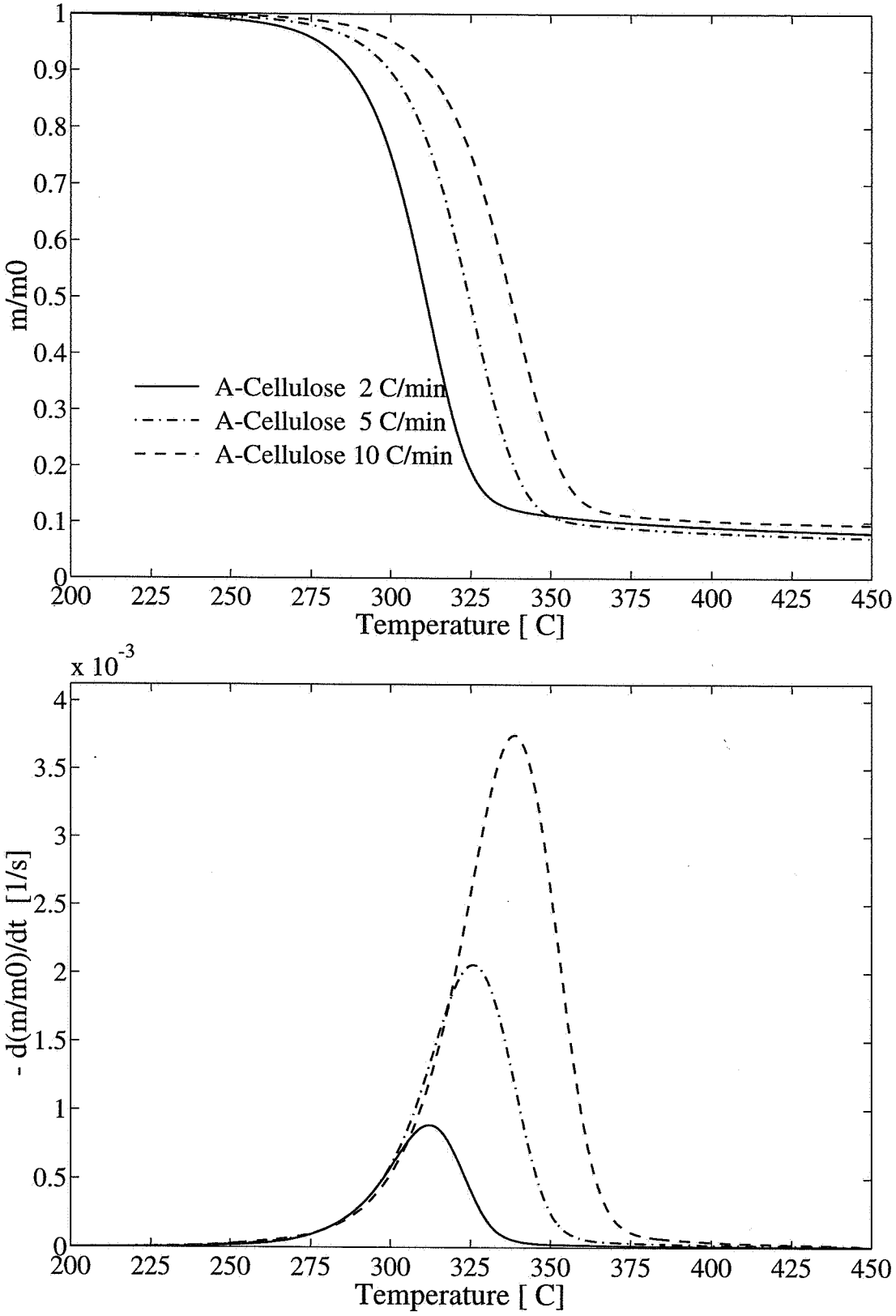

Figure 3.11 The effect of different heating rates on the thermal decomposition of A-cellulose.

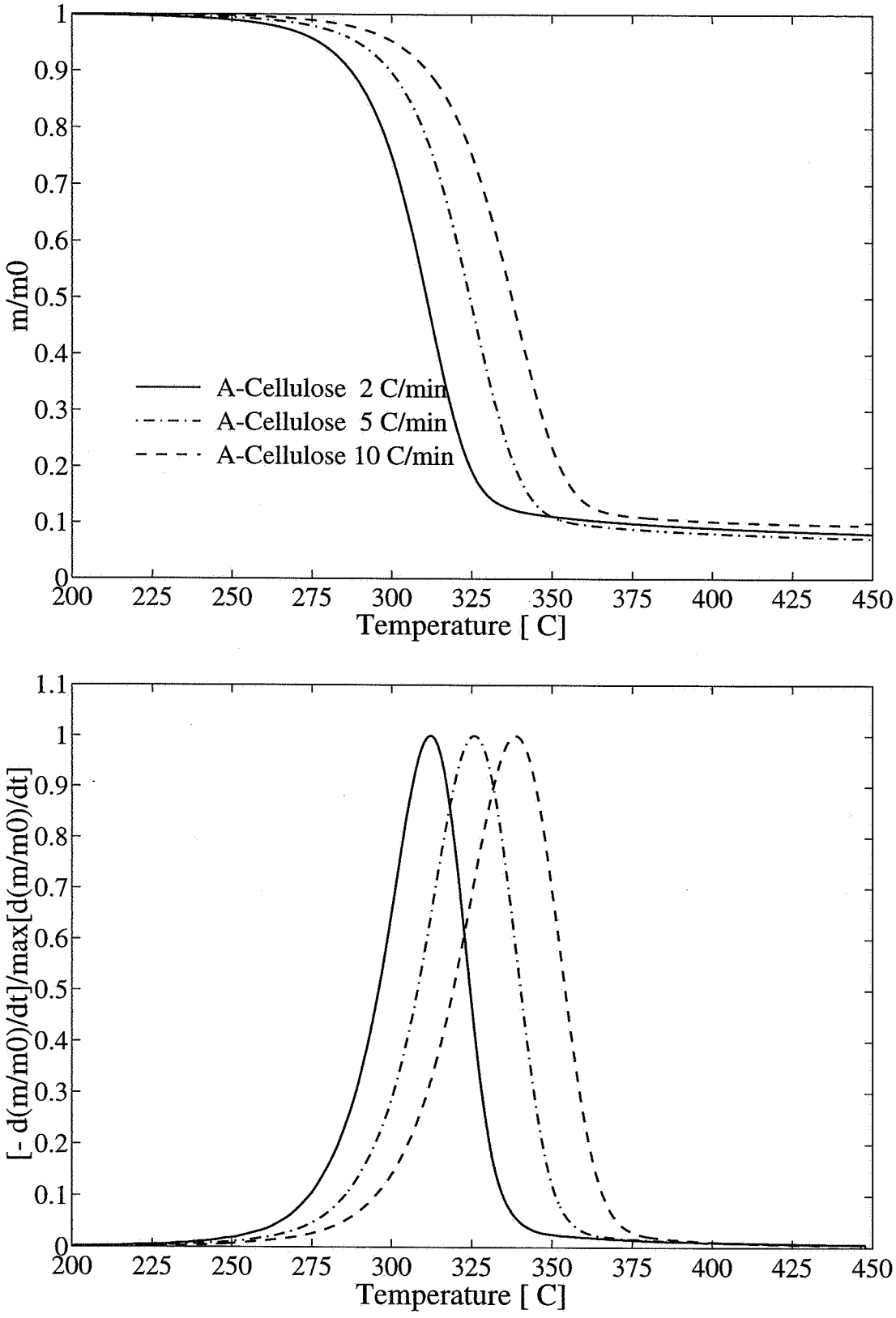

Figure 3.12 The effect of different heating rates on the thermal decomposition of A-cellulose. DTG-curves scaled to an equal height.

with the relatively simple chemical structure of cellulose (shown in Figure 2.8). However, some differences may be observed with respect to: 1) the width of the DTG peaks; 2) the temperature where the maximum rate of decomposition occur (T_{peak}); and 3) the final char yield among the different celluloses analyzed. While A-cellulose and cellulose extracted from spruce have their T_{peak} around 325°C, Whatman filter paper, B-cellulose and cellulose extracted from birch have their T_{peak} around 340°C. B-cellulose has the broadest DTG peak followed by spruce and A-cellulose, while the width of the Whatman filter paper and cellulose extracted from birch are of approximately equal size. B-cellulose contains about 14% hemicellulose so its broad thermoanalytical curve and its early start is not surprising, since hemicellulose is less stable than cellulose and starts to decompose at lower temperatures. A-cellulose and cellulose extracted from spruce may be contaminated with some salts or ash which, as previously discussed, may alter the pyrolysis pathway causing the decomposition to start at lower temperatures and increasing the final char yield. These results clearly reveal that the source, extraction procedure and the presence of impurities have impact on the pyrolysis behaviour of cellulose.

The thermograms of lignin extracted from birch and spruce are shown in Figure 3.15. In contrast to cellulose, lignin shows a gradual loss of weight from about 200°C to the final temperature of 500°C consistent with the wide variety of functional groups and hence bond strengths exhibited in the "representative" structure of lignin (see Figure 2.10). The weight or percentage char at the final temperature is approximately 50% of the original lignin substance, which means that the lignin part of wood is mainly responsible for the char portion of the products. Similar observations of lignin pyrolysis have been reported by Shafizadeh *et al.* (1971) and Williams *et al.* (1992). However, one have to have in mind that the lignin that one isolates from wood is chemically altered and is not the same as which is chemically bound in the wood structure.

In Figure 3.16, a comparison between the hemicelluloses extracted from birch and spruce are presented. For the birch hemicellulose, two main areas of weight loss can be observed, one between 200-300°C and one between 400-450°C while spruce hemicellulose has its main weight loss between 200-300°C. The weight percentage of the remaining residue is as high as 50-55 % for birch 30-35% for spruce hemicellulose, respectively. Proximative analysis of the hemicelluloses (see Table 3.3) gave an ash content of 2.5 and 5% which may be sulphated ash that was not properly washed out after the extraction procedure. As mentioned before, ash and minerals have significant catalytic effects on the thermal decomposition of biomass leading to higher char-yields. The same washing procedures applied on wood (see Table 3.4) were used on hemicellulose, but unfortunately, the material was completely dissolved and disappeared in the solution. As for lignin, the isolation of hemicellulose is problematic and

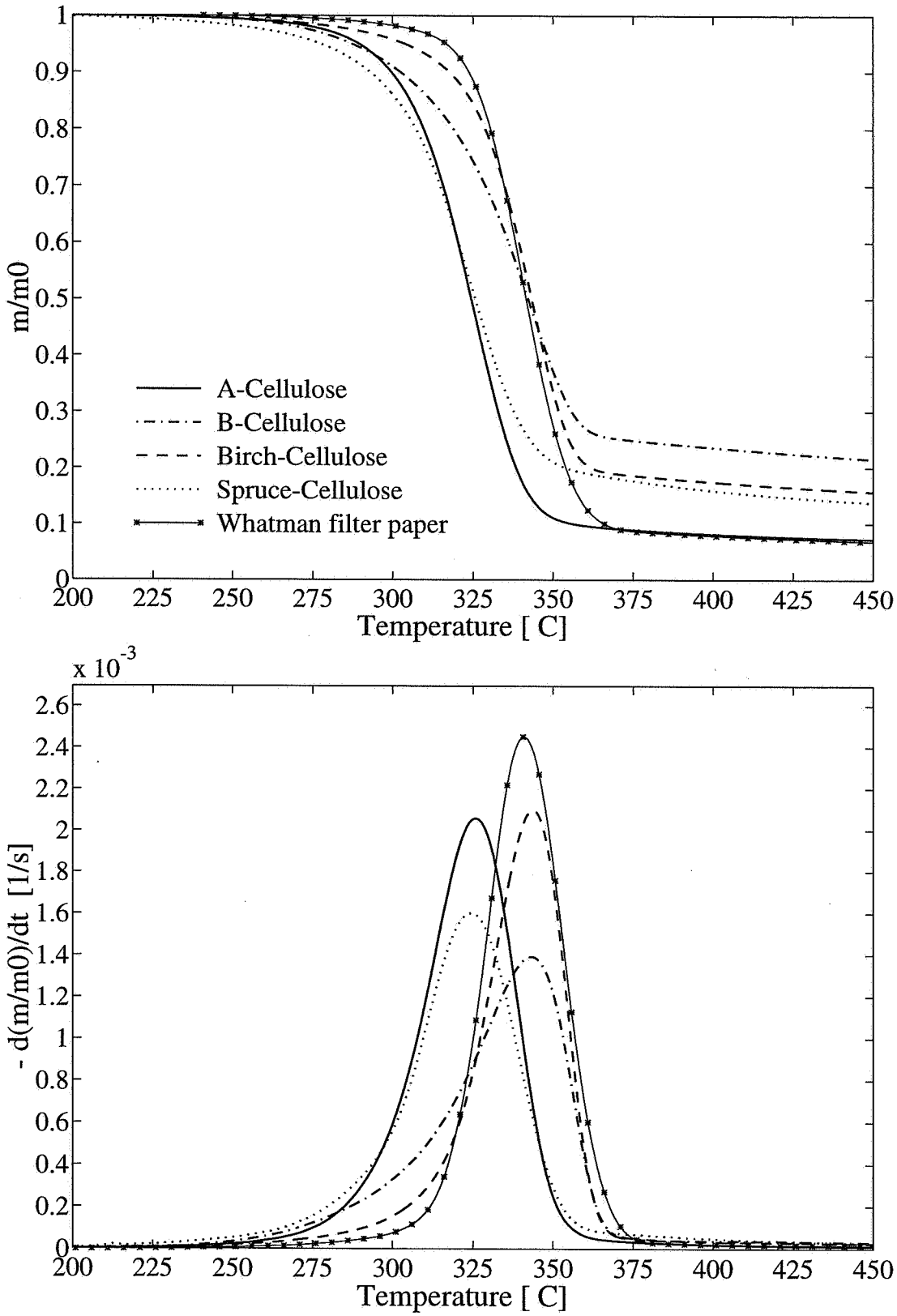

Figure 3.13 Comparison between different celluloses, 5°C/min.

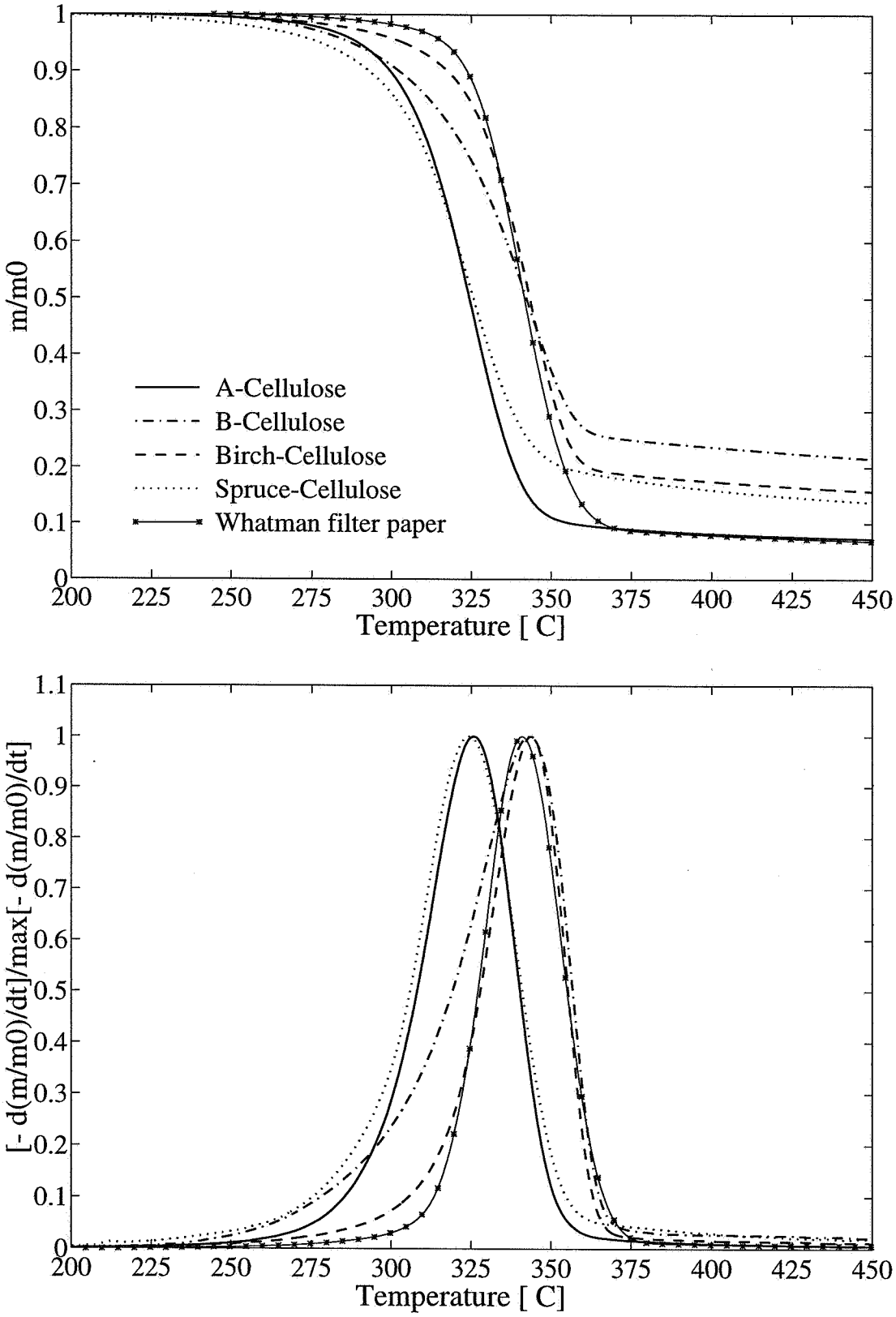

Figure 3.14 Comparison between different celluloses. DTG peaks scaled to an equal height.

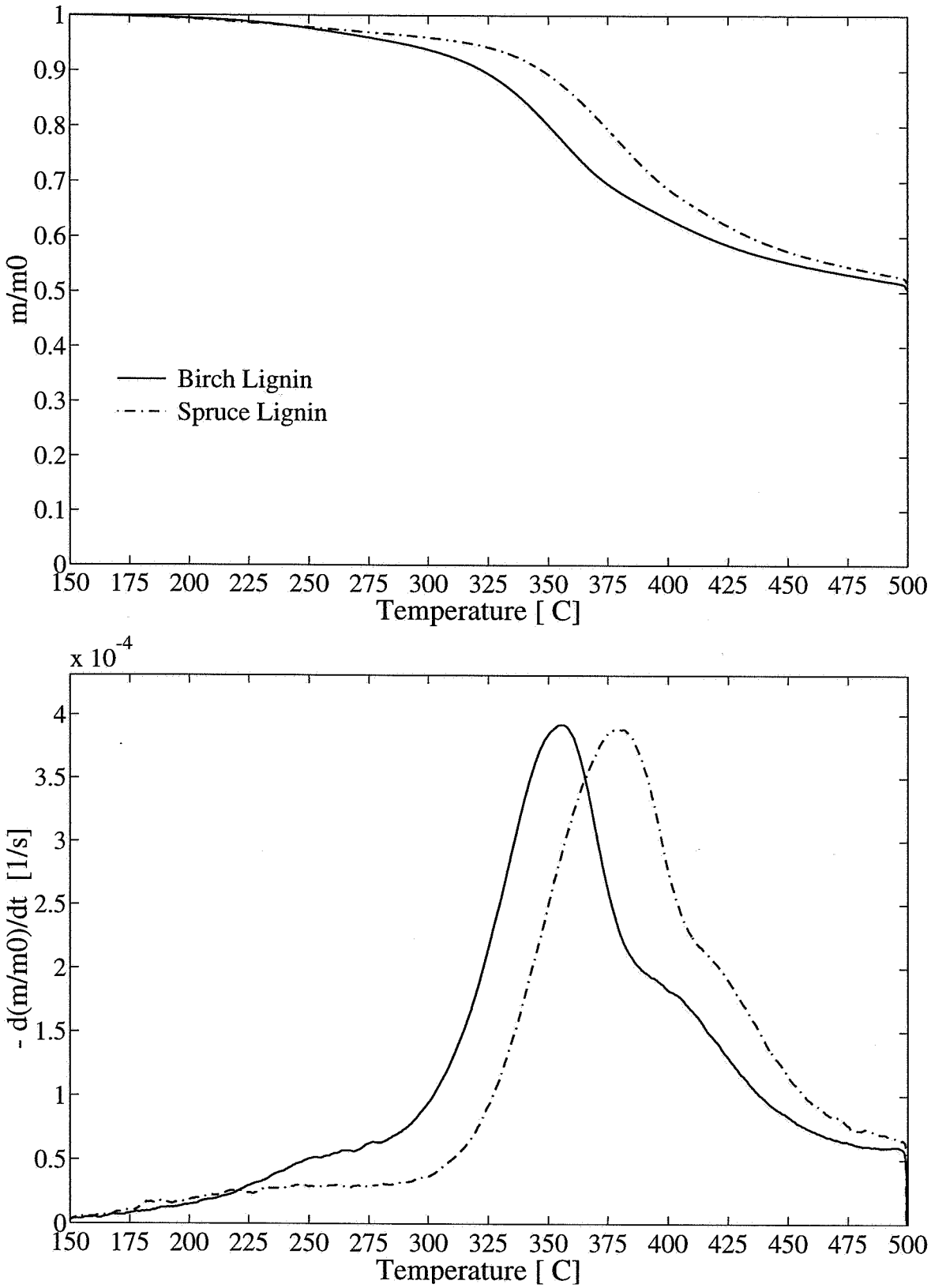

Figure 3.15 Comparison between lignins isolated from birch and spruce, 5°C/min.

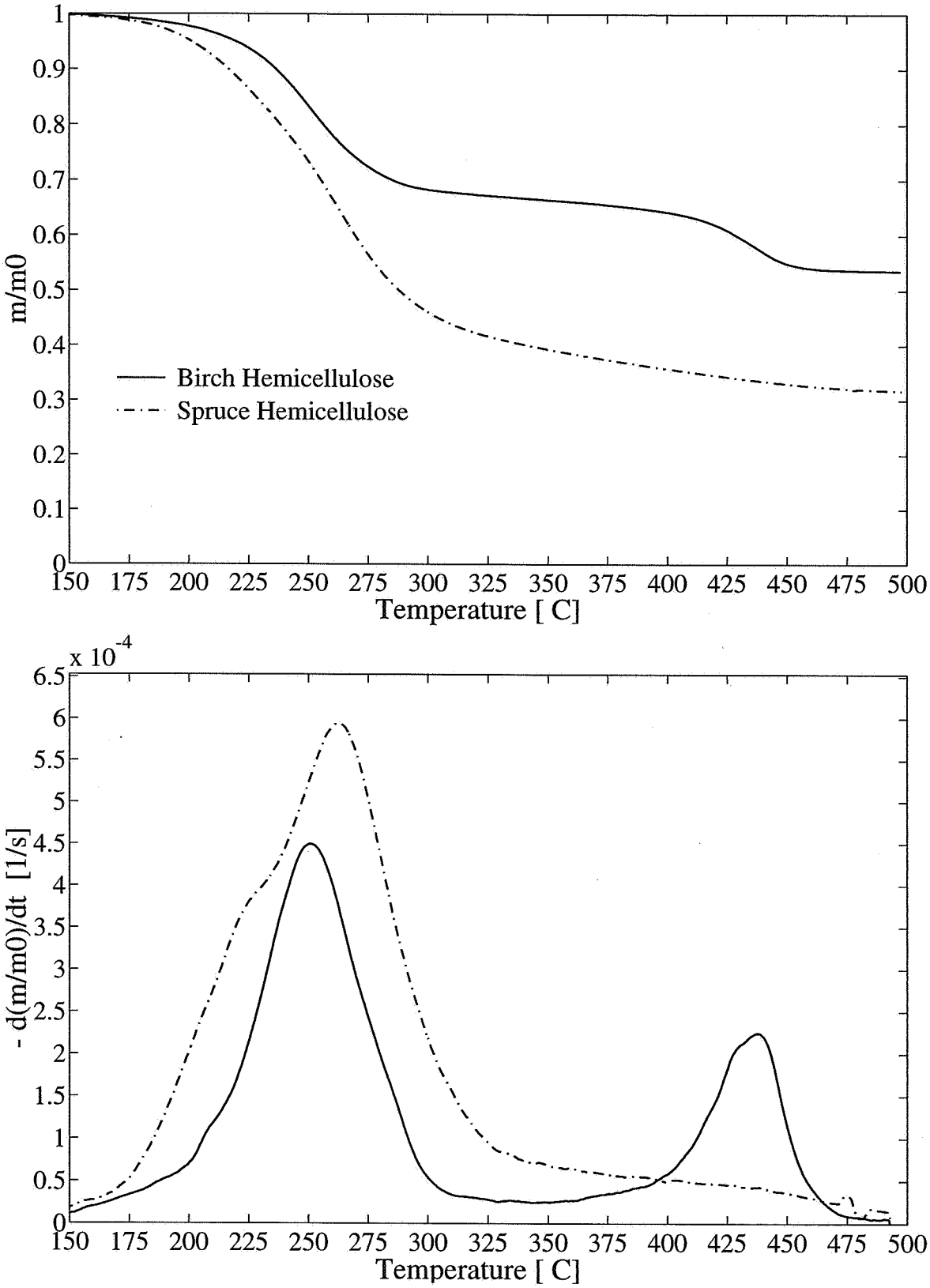

Figure 3.16 Comparison between hemicellulose isolated from birch and spruce, 5°C/min.

the extraction will always change its chemistry. Other studies of xylan [Shafizadeh *et al.* (1971), Simkovic *et al.* (1988) and Williams *et al.* (1992)] have indicated a much lower char-yield for the hemicelluloses and that they are the least thermal stable major component of wood. This is probably due to their lack of crystallinity.

3.3.2.3 PYROLYSIS OF WOOD

A comparison of the thermal behaviour of the selected untreated wood species is presented in Figure 3.17. The temperature threshold for which the pyrolysis of wood starts is around 200°C at a heating rate of 5°C/min. The exception is pineroot which starts to decompose at a lower temperature, around 150°C. For birch, spruce and pine one can see that there are two areas of weight loss producing a single DTG peak with a plateau or shoulder located at the lower temperature region. Pineroot has an additional DTG peak located around 200°C which may be decomposition of the large extractive fraction found in pineroot (~ 20 wt%) or some low molecular weight sugars. For all the species, there is a flat tailing section at higher temperature (> 375°C) responding to the slow charring process of the solid residue. Pine and spruce have almost similar chemical composition, which is reflected by their almost similar thermal fingerprints.

It has been debated in the literature that the two different regions of weight loss observed for wood pyrolysis may be represented as a combination of the individual decomposition of hemicellulose and cellulose, i.e., the lower temperature shoulder representing the decomposition of hemicellulose and the higher temperature peak representing the decomposition of cellulose. Birch, and hardwoods in general contains more hemicellulose than the softwood species (pine and spruce) does, causing the "hemicellulose" shoulder to be more visible. Lignin decomposition occurs throughout the whole temperature range, but the main area of weight loss occurs at higher temperatures which means that lignin is mainly responsible for the flat tailing section which can be observed for all the wood species at higher temperatures. In addition, birch having the highest hemicellulose and lowest lignin content yields the lowest char-residue. Consequently the results show, at least qualitatively, that the thermal decomposition of wood can be represented as the combination of the thermal degradation of the individual major components, i.e. cellulose, hemicellulose and lignin as suggested by Shafizadeh *et al.* (1971). In the kinetic analysis that follows, it will be investigated if it is possible to model the rate of pyrolysis of the whole wood by the sum of the corresponding rates and weighted mass fractions of its major components.

To minimize the aforementioned catalytic effects which minerals may cause, the washing procedures described in section 3.3.1.1 were used. Another purpose of these pretreatments were to try to single out or separate the partial overlapping peaks of hemicellulose and cellulose and by this making the kinetic modeling work much easier. Varhegyi *et al.* (1994a) observed that for a featureless, single-peaked DTG curve of wheat straw, pretreatements resulted in well separated double peaks.

The effects of different pretreatements on pine are shown in Figure 3.18. The most visible effects are that pretreated pine decomposes at a slightly higher temperature and that the char-yield at the final temperature (450°C) is reduced. The reason for this delayed decomposition may be that some of the hemicellulose has been washed out, or that the catalytic effect of the minerals that have been washed out are diminished. In the opinion of the author, the latter explanation is the most likely reason, since the char-yield is decreased and not increased as would be expected if the hemicellulose content is decreased. Another effect of the pretreatements seen in Figure 3.19, where the DTG curves have been scaled to an equal height, is the enhanced sharpness of the cellulose peak. However, separation of the hemicellulose shoulder from the cellulose peak as demonstrated by Varhegyi *et al.* (1994a) for wheat straw, was not possible for pine. The most likely reason for this is the very low ash content found in pine which is less than 0.5 %. The ash content in the native wheat straw used by Varhegyi *et al.* (1994a) was for comparison almost 10 % (!).

As shown in Figures 3.20 and 3.21, hot water washing of birch and spruce had similar effects as for pine, i.e. delaying the decomposition, reducing the char-yield and enhancing the sharpness of the cellulose peak. In addition, hot water washing of birch gave a more visible separation of the hemicellulose shoulder from the cellulose peak.

As shown in Figure 3.22, hot water washing was not sufficient to remove the first peak at 220°C of the pineroot, while the peak disappeared when the pineroot was treated with acetone. Since acetone is known to totally remove the extractives from wood, i.e., it used in the pre-extraction procedure, this suggests that the first DTG peak is decomposition of the large extractive fraction (~ 20%) found in the roots of pine.

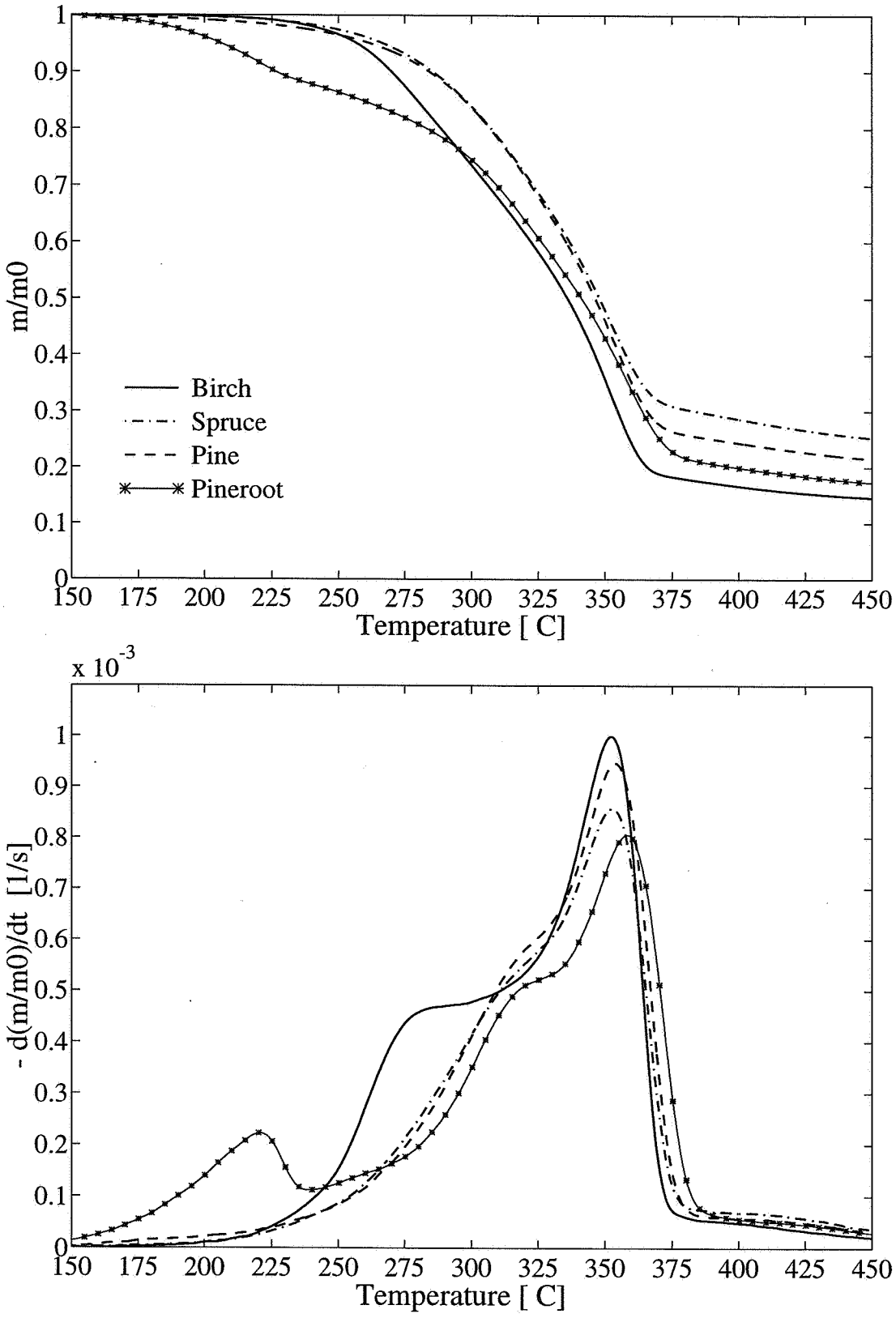

Figure 3.17 Thermal behaviour of birch, spruce, pine and pineroot, 5°C/min.

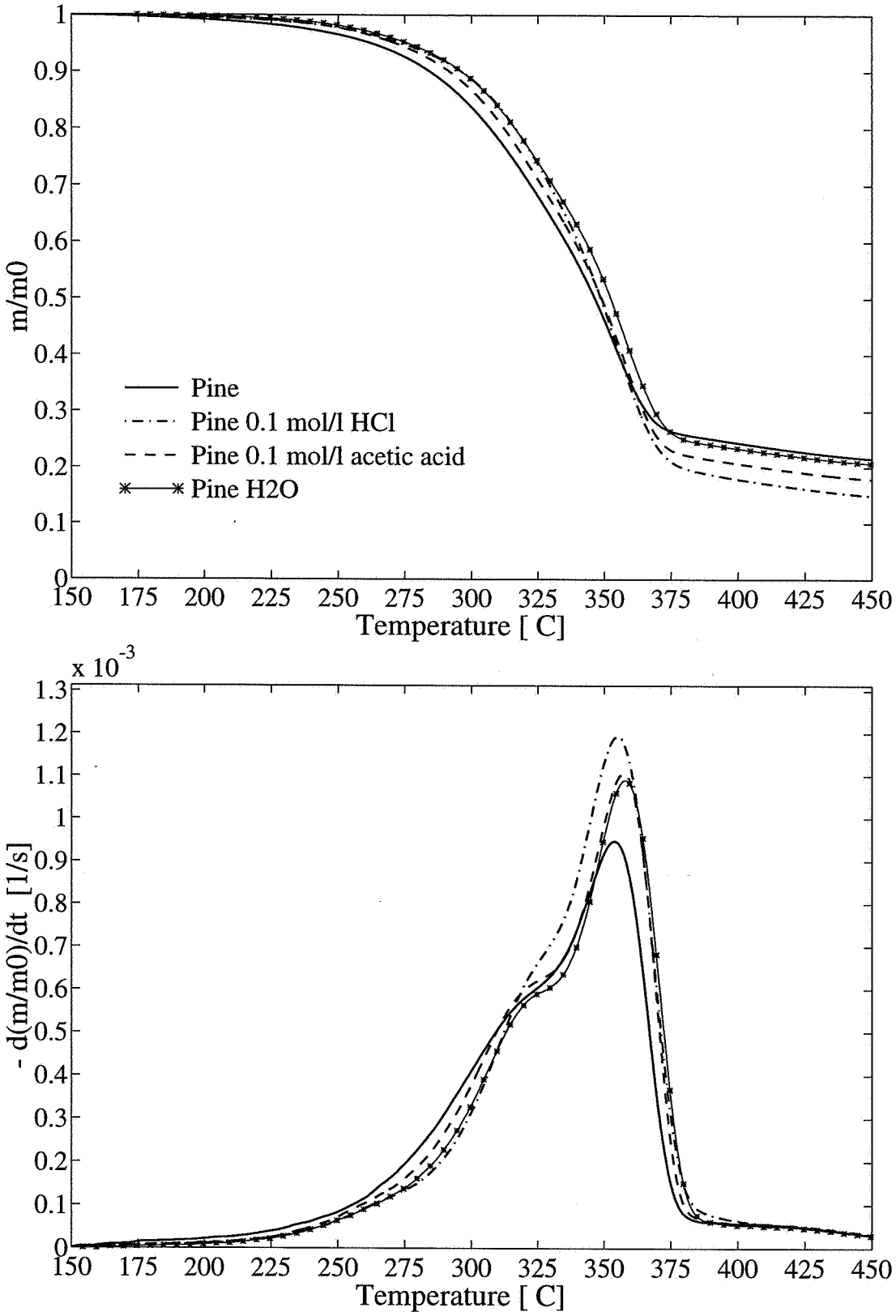

Figure 3.18 Effect of different pretreatements on pine, 5°C/min.

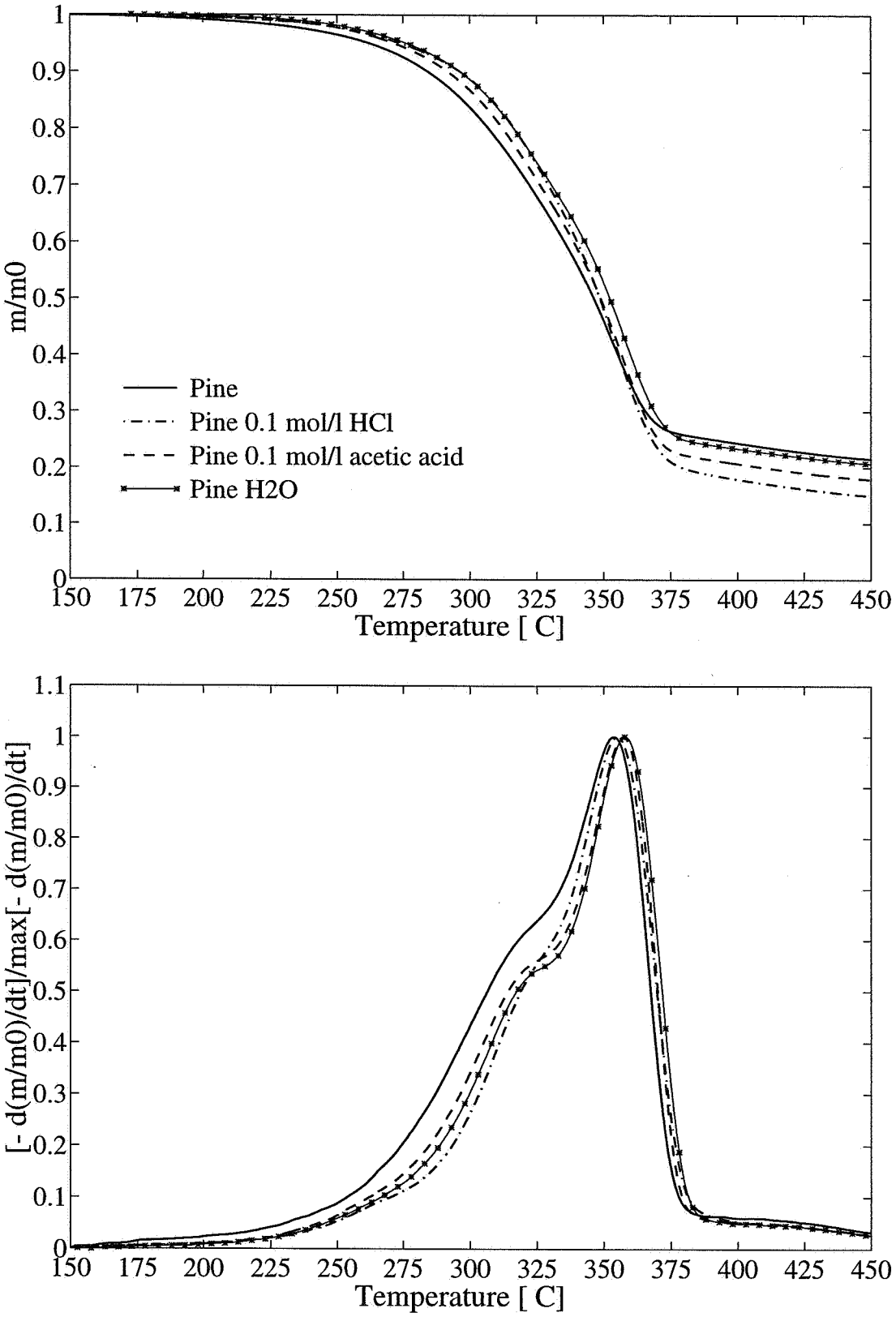

Figure 3.19 Effect of different pretreatements on pine, DTG curves scaled to an equal height.

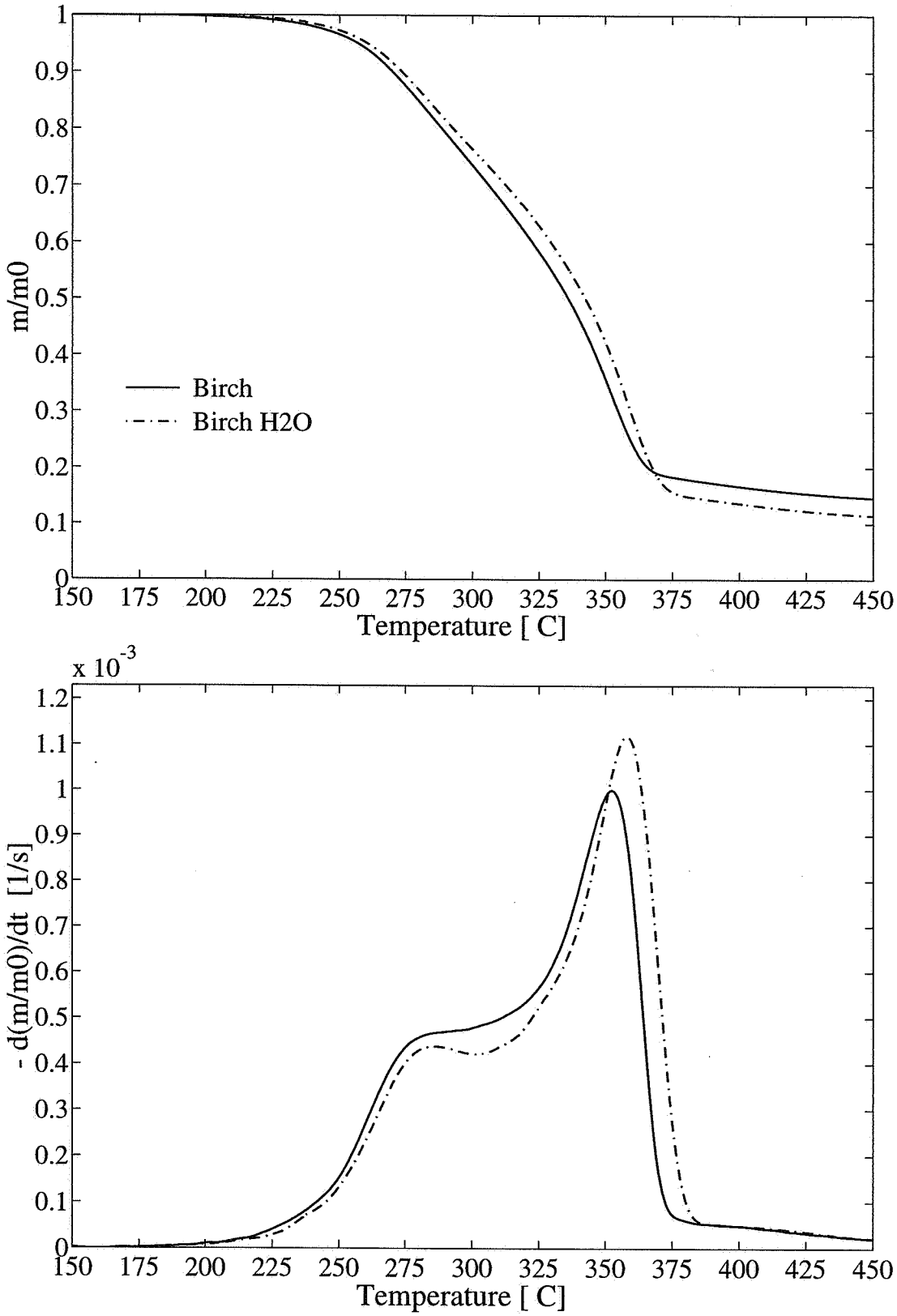

Figure 3.20 Effect of hot water washing of birch, 5°C/min.

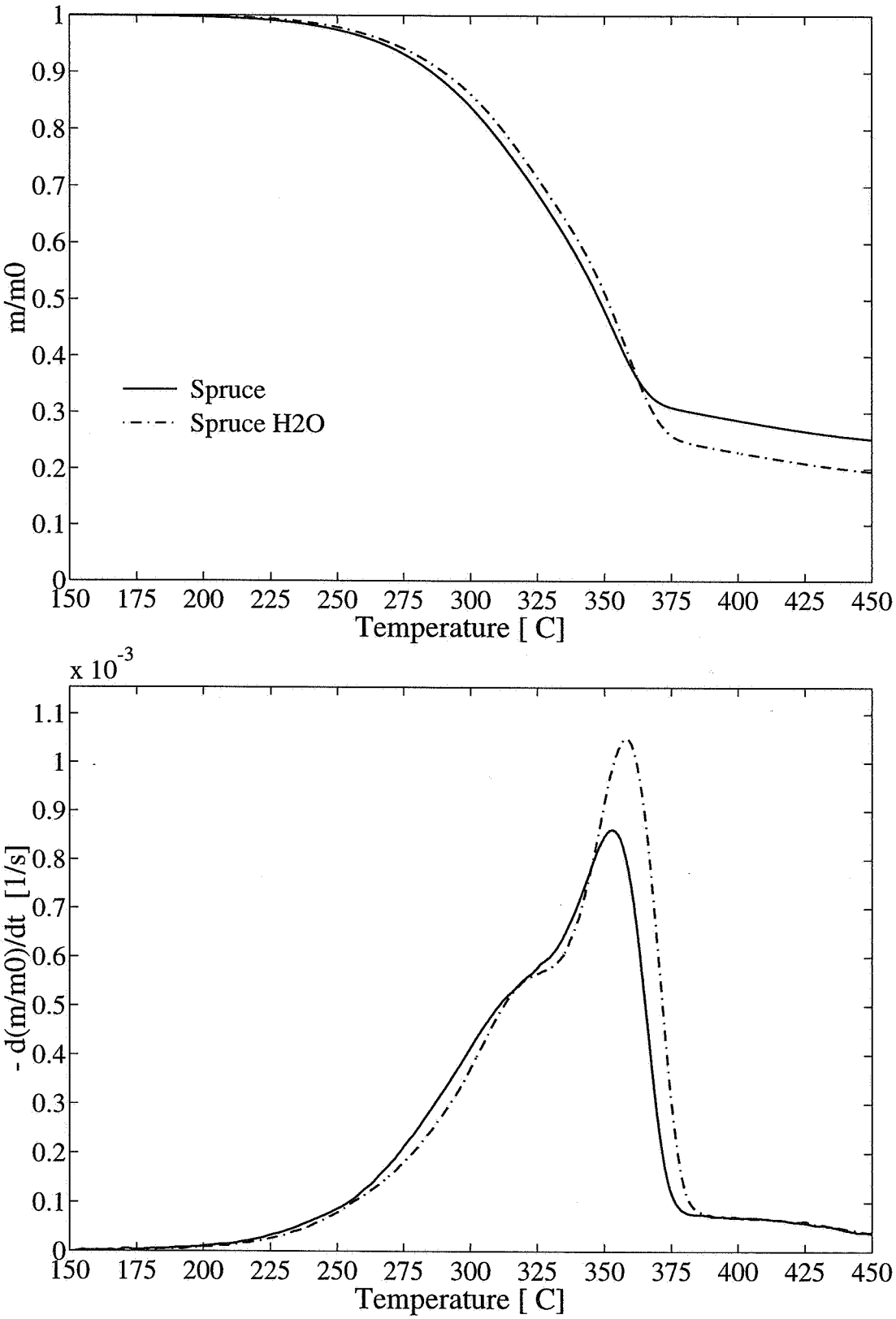

Figure 3.21 Effect of hot water washing of spruce, 5°C/min.

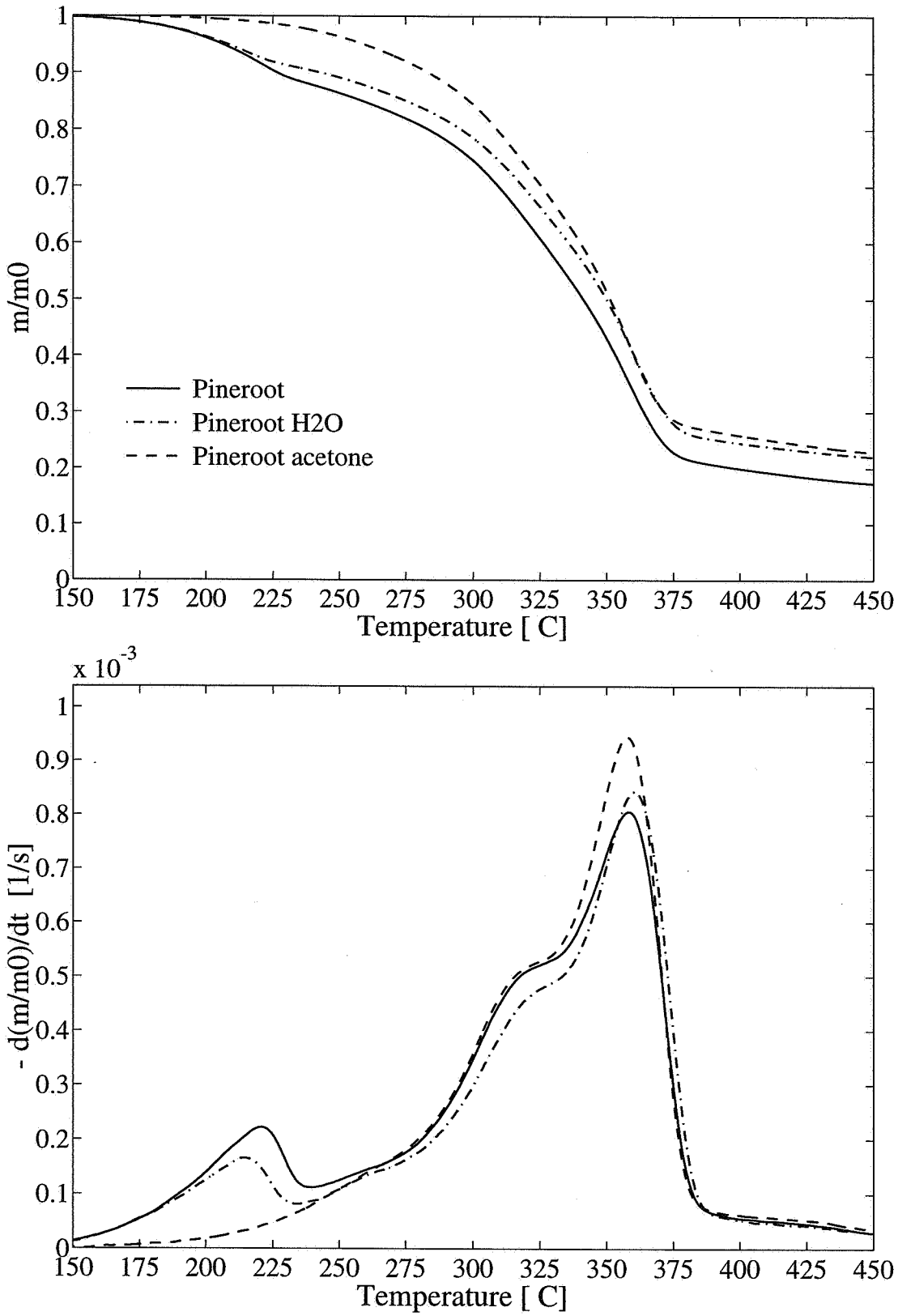

Figure 3.22 Effect of different pretreatements on pineroot, 5°C/min.

3.3.3 KINETIC ANALYSIS

Even though the pyrolysis of wood and its main constituents (cellulose, hemicellulose and lignin) takes place through a reaction network of parallel and competitive reactions, the DTG curves observed are quite simple and can be described by relatively simple mathematical models. Cellulose exhibits a sharp single DTG curve which can be well described by a single reaction model. For the whole wood, however, the DTG curves contain shoulders and/or double peaks indicating that more than one reaction are involved. In this case, the modeling approach of Varhegyi *et al.* (1989) has been adopted in an attempt to describe the overall decomposition by means of independent parallel reactions. In this section, the mathematical models applied will be outlined and the results from the kinetic evaluation will be presented.

SINGLE REACTION MODEL

For the single reaction model, the rate of conversion can be described by:

$$\frac{d\alpha}{dt} = A \exp(-E/RT)\ (1-\alpha)^n \tag{3.13}$$

where A, E, n are the frequency factor, activation energy and reaction order, respectively. α is the conversion (reacted fraction) which can be expressed by:

$$\alpha = \frac{1-m}{1-m_{char}} \tag{3.14}$$

where m and m_{char} are the actual sample mass and char yield, normalized by the initial sample mass m_0, respectively. For constant heating rate experiments ($dT/dt=\beta$), equation (3.13) can be rearranged to:

$$\int_0^{\alpha} \frac{d\alpha}{(1-\alpha)^n} = I, \quad \text{where} \quad I = \frac{A}{\beta}\int_{T_0}^{T} \exp(-E/RT)\,dT \tag{3.15}$$

Equation (3.15) has two general solutions:

$$n = 1 \qquad \int_0^{\alpha} \frac{d\alpha}{(1-\alpha)^n} = -\ln(1-\alpha) = I \tag{3.16}$$

$$n \neq 1 \qquad \int_0^{\alpha} \frac{d\alpha}{(1-\alpha)^n} = \frac{1-(1-\alpha)^{1-n}}{1-n} = I \tag{3.17}$$

By rearranging equation (3.16) and (3.17), the conversion can be singled out:

$$n = 1 \qquad \alpha = 1 - \exp[-I] \tag{3.18}$$

$$n \neq 1 \qquad \alpha = 1 - [1 - (1 - n)I]^{\frac{1}{1-n}} \tag{3.19}$$

The reaction order (n) is strongly connected to the degree of asymmetry of the DTG curves. If the reaction order is larger than one, the descending part of the DTG curve is less steep than in the case of a pure first-order reaction. If the reaction order is lower than one, the descending part becomes steeper than in the case of a pure first-order reaction [Kissinger (1957)].

MODEL OF INDEPENDENT PARALLEL REACTIONS

If the sample consists of more than one component and one assumes that each component decomposes independently from each other, then the overall conversion and rate of conversion for *N* reactions can be described by:

$$m = 1 - \sum_i c_i \alpha_i$$

$$i = 1, 2, 3 \ldots N \tag{3.20}$$

$$-\frac{dm}{dt} = \sum_i c_i \frac{d\alpha_i}{dt}$$

The separate conversion (reacted fraction) α_i for each component is given by:

$$\alpha_i = \frac{(m_{0,i} - m_i)}{(m_{0,i} - m_{char,i})} \tag{3.21}$$

where $m_{0,i}$, m_i and $m_{char,i}$ are the initial sample mass, the actual sample mass and the final char yield (normalized with m_0) of component *i*, respectively. The components are all assumed to decompose individually according to:

$$\frac{d\alpha_i}{dt} = A_i \exp(-E_i/RT)\ (1 - \alpha_i) \tag{3.22}$$

Here, the reaction order is assumed equal one (n=1) for all the reactions. Coefficient c_i express the contribution of the partial processes to the overall mass loss, m_0-m_{char}:

$$c_i = m_{0,i} - m_{char,i} \tag{3.23}$$

TECHNIQUE OF THE KINETIC EVALUATION

From a mathematical point of view the integral (TG) and differential (DTG) curves have identical information content. The least squares evaluation of an experiment can be based either on the TG curve:

$$S_{TG} = \sum \left[(m)_j^{exp} - (m)_j^{calc} \right]^2 \tag{3.24}$$

or on the DTG curve:

$$S_{DTG} = \sum \left[\left(\frac{dm}{dt} \right)_j^{exp} - \left(\frac{dm}{dt} \right)_j^{calc} \right]^2 \tag{3.25}$$

As it will be discussed later, the minimization of S_{TG} and S_{DTG} leads to different results due to the different fit criteria. Equation (3.24) and (3.25) is minimized by searching for the optimal set of parameters by using a SIMPLEX search algorithm together with the Newton method. Here, $(m)^{exp}$ and $(dm/dt)^{exp}$ stands for the experimentally observed TG and DTG curves and $(m)^{calc}$ and $(dm/dt)^{calc}$ stands for the TG and DTG curves obtained by numerical solution of the kinetic differential equation at the given set of parameters. Subscript *j* indicates the discrete values of a given (m) or (dm/dt) curve. The SIMPLEX search algorithm can find the local minimum of equation (3.24) or (3.25), however, due to the non-linear form of the kinetic differential equations more than one local minima can be found. Hence, special care is needed to properly choose the initial values of the unknown parameters and to ensure convergence. An algorithm which can handle these problems has been developed by Austegard (1996) and programmed in MATLAB. The main features of this algorithm and the main steps to find the initial values are given in the following two examples, where A-cellulose is evaluated by a single first-order reaction and birch is evaluated by three independent parallel reactions.

Initial values for A-cellulose evaluated by a single first-order reaction

The initial values for A and E is found by using equations (3.20) and (3.22) at N=1:

$$-\frac{dm}{dt} = c\frac{d\alpha}{dt} = (m - m_{char}) A \exp(-E/RT) \tag{3.26}$$

As sketched in Figure 3.23, a plot of $\ln[-(dm/dt)/(m-m_{char})]$ versus 1/T gives a straight line of -E/R slope with an intercept of ln(A). The initial value for c is easily calculated from equation (3.23). The initial values obtained for A-cellulose are listed in Table 3.5.

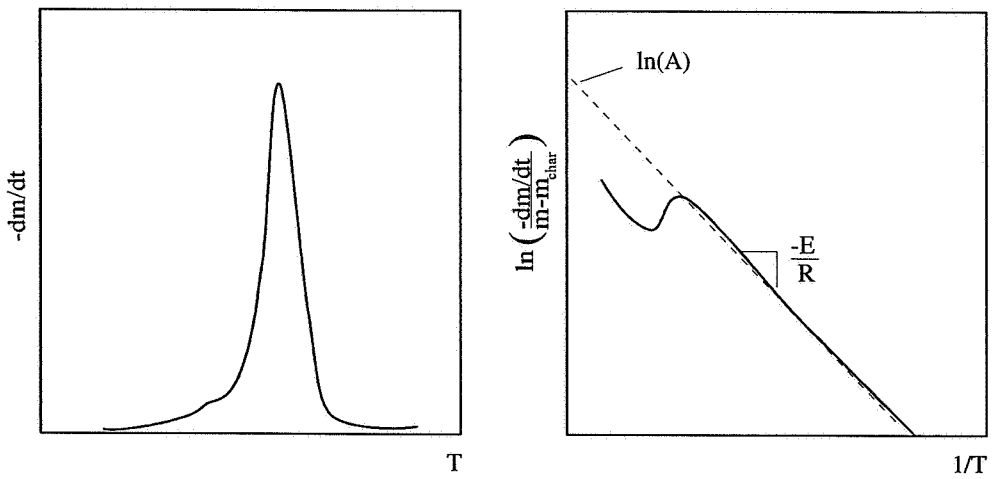

Figure 3.23 The differential curve of A-cellulose with the resulting logarithmic plot.

Table 3.5 Initial values for A-cellulose evaluated by a single first-order reaction model.

	E [kJ/mole]	log(A) [log s^{-1}]	c [%]
A-cellulose	194.0	4.62	91.1

Initial values for birch evaluated by three independent parallel first order reactions

In this case, one set of initial values are required for each of the three reactions. These are found by using the following procedure:

Step 1: By looking at the DTG curve, the temperature domains where each of the three reactions dominate are found.

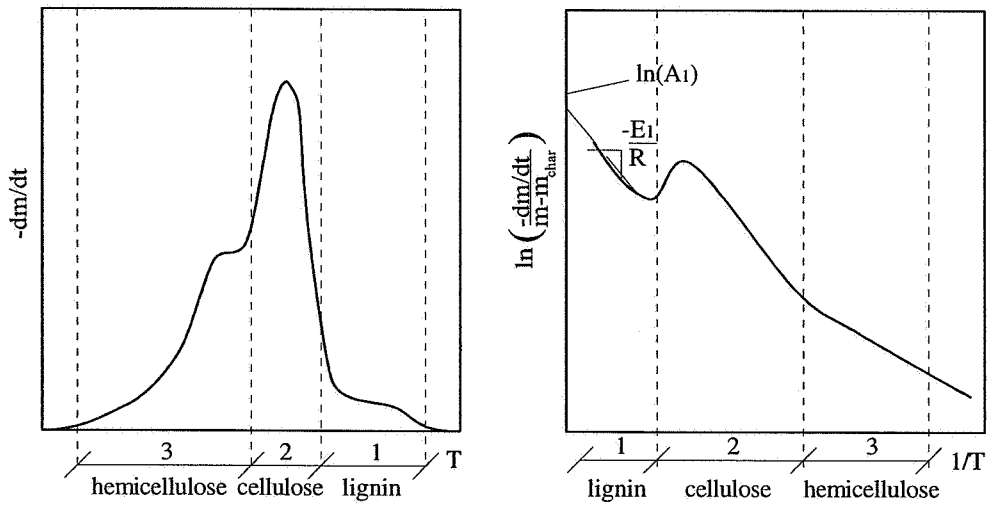

Figure 3.24 The differential curve of birch with the resulting logarithmic plot.

Step 2: The initial values for *reaction 1*, which occurs at the highest temperature (lignin) is found by the following procedure.

A) Initial values for A_i and E_i

The frequency factor and activation energy for lignin can be found by rewriting equation (3.20) into the following form:

$$-\frac{dm}{dt} = c_1 \frac{d\alpha_1}{dt} = (m - m_{char}) A_1 \exp(-E_1/RT) \tag{3.27}$$

A plot of $\ln[-(dm/dt)/(m-m_{char})]$ versus 1/T gives a straight line of $-E_1/R$ slope with an intercept of $\ln(A_1)$ in the domain where *reaction 1* is dominating (see Figure 3.24).

B) Initial values for c_i

c_1 for *reaction 1* is found by linear regression of:

$$m = 1 - c_1 \alpha_1, \quad \text{and} \quad \alpha_1 = 1 - \exp(-I_1) \tag{3.28}$$

where the integral I_1 (see equation (3.15)) is solved numerically by using the trapezoide rule.

Step 3: By using the following relations:

$$\begin{aligned} m^{new} &= m^{old} + c_1 \alpha_1 \\ m_{char}^{new} &= m_{char}^{old} + c_1 \\ \left(\frac{dm}{dt}\right)^{new} &= \left(\frac{dm}{dt}\right)^{old} - c_1 \left(\frac{d\alpha_1}{dt}\right) \end{aligned} \tag{3.29}$$

reaction 1 is removed from the TG and DTG curves and *A)* and *B)* in step 2 is repeated for *reaction 2* which describes the cellulose and *reaction 3* which describes the hemicellulose decomposition. The initial values for the three reactions for birch are listed in Table 3.6.

Table 3.6 Initial values for birch evaluated by three independent parallel reactions.

	E_i [kJ/mole]	$\log(A_i)$ [log s^{-1}]	c_i [%]
Reaction 1 (lignin)	59.4	1.82	4.4
Reaction 2 (cellulose)	262.0	19.68	38.2
Reaction 3 (hemicellulose)	142.9	10.91	43.8

Optimizing A_i, E_i and c_i by non-linear regression analysis

The initial values are used in the first iteration step to calculate:

$$(m)^{calc} = 1 - \sum_i c_i \alpha_i \qquad i = 1, 2, \ldots\ldots N \tag{3.30}$$

$$\left(-\frac{dm}{dt}\right)^{calc} = \sum_i c_i \frac{d\alpha_i}{dt} \qquad i = 1, 2, \ldots\ldots N \tag{3.31}$$

where:

$$\alpha_i = 1 - \exp\left[-\frac{A_i}{\beta}\int_{T_0}^{T} \exp(-E_i/RT)\,dT\right]$$
$$\frac{d\alpha_i}{dt} = A_i \exp(-E_i/RT)\,(1 - \alpha_i) \tag{3.32}$$

Equation (3.30) to (3.32) are further used in the non-linear regression analysis searching for the optimal set of parameters for a given $(m)^{exp}$ or $(dm/dt)^{exp}$ curve.

The deviation between the experimental and the calculated differential curves at the optimal set of parameters is given in percentage of the highest measured (dm/dt) value:

$$dev1\,(\%) = 100 \cdot \frac{\sqrt{S_{DTG}/(Z - N)}}{\max\left[(-\,dm/dt)^{exp}\right]} \tag{3.33}$$

where Z is the number of data points and N is the number of parameters employed in the model (A_i, E_i, c_i). The deviation between the observed and calculated char fraction is given by:

$$dev2\,(\%) = 100 \cdot abs\left[\frac{(m_{char})^{exp} - (m_{char})^{calc}}{(m_{char})^{exp}}\right] \tag{3.34}$$

The final results from the kinetic evaluation of A-cellulose and birch are presented on the following two pages.

NOTE: ***In all figures that follows, dots, the bold solid line and thin solid lines represents the experimental data $(m)^{exp}$ and $(-\,dm/dt)^{exp}$, the calculated data $(m)^{calc}$ and $(-\,dm/dt)^{calc}$ and the contributions of the partial reactions to $(-\,dm/dt)^{calc}$, respectively.***

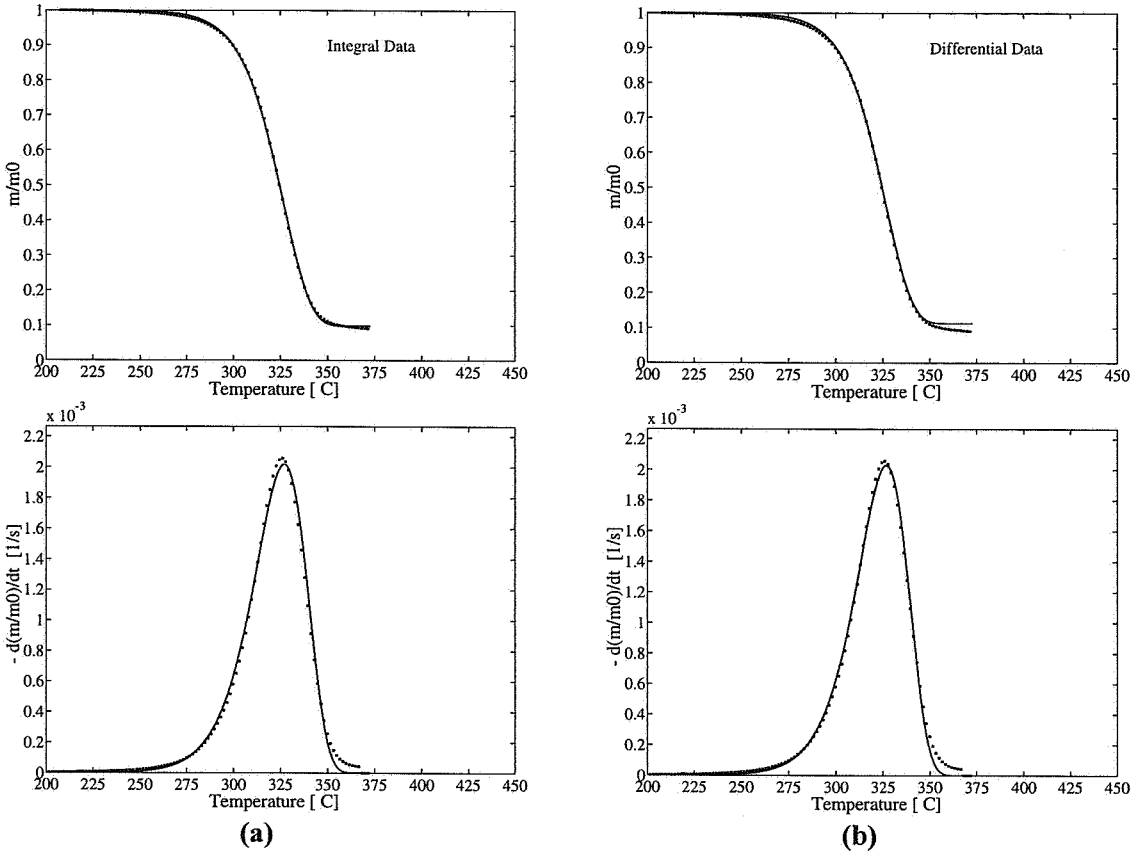

Figure 3.25 Kinetic evaluation of A-cellulose assuming a single first order reaction. Evaluation methods: (a) Fit of TG curve (b) fit of DTG curve.

Table 3.7 Kinetic parameters for A-cellulose evaluated by a single first order reaction.

	first peak	
Evaluated Curve	E_1 (kJ/mole) $\log A_1$ [log s^{-1}] c_1 (%)	dev1 (%) dev2 (%) $(T_{peak})^{calc}$ $(T_{peak})^{exp}$
TG	211.1 16.14 90.2	1.5 7.6 327.1 326.8
DTG	215.6 16.56 88.8	1.4 19.7 327.1 326.8

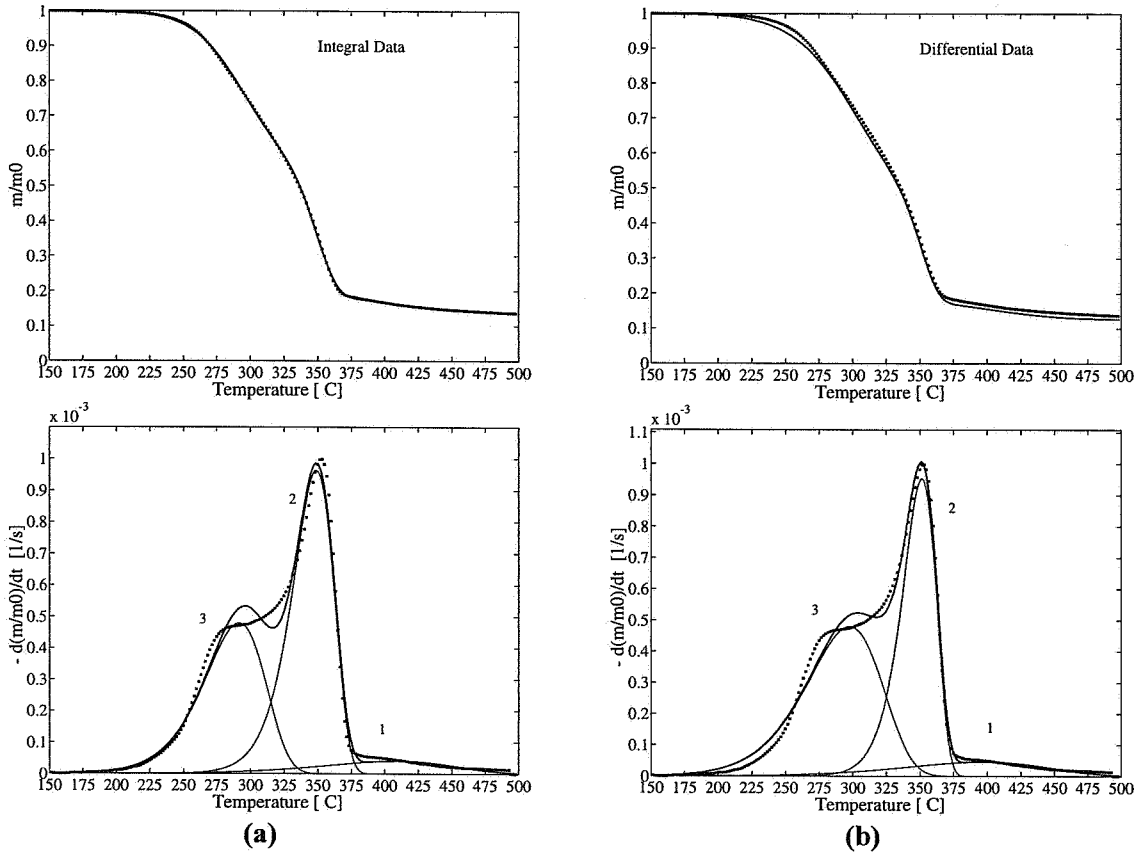

Figure 3.26 Kinetic evaluation of birch assuming three independent parallel first order reactions. Evaluation methods: (a) Fit of TG curve; (b) fit of DTG curve.

Table 3.8 Kinetic parameters for birch evaluated by three independent parallel first order reactions.

	first peak (reaction 3)	second peak (reaction 2)	third peak (reaction 1)	
Evaluated Curve	E_3 (kJ/mole) $\log A_3$ [log s^{-1}] c_3 (%) $(T_{peak,\,3})^{calc}$	E_2 (kJ/mole) $\log A_2$ [log s^{-1}] c_2 (%) $(T_{peak,\,2})^{calc}$	E_1 (kJ/mole) $\log A_1$ [log s^{-1}] c_1 (%) $(T_{peak,\,1})^{calc}$	dev1 (%) dev2 (%) $(T_{peak})^{exp}$
TG	113.2 8.03 33.9 291.2	209.1 15.30 46.3 349.1	75.6 3.01 6.0 408.1	2.8 1.4 352.3
DTG	92.4 5.91 42.0 297.6	256.4 19.26 38.0 351.1	65.6 2.29 7.4 396.2	2.1 7.2 352.3

A fit to the integral data of A-cellulose resulted in practically the same kinetic parameters as a fit to the differential data, with an activation energy and a frequency factor of E_{TG}=211.1 kJ/mole, $\log A_{TG}$=16.14 (log) s^{-1} and E_{DTG}=215.6 kJ/mole, $\log A_{DTG}$=16.56 (log) s^{-1}, respectively. (Here, subscript TG and DTG refers to TG and DTG evaluation, respectively). The small difference may be explained by the deviation in the char-yield (dev2). While the calculated TG curve almost hit the char-yield of the experimental TG curve, the char-yield is over-estimated by 20% when the DTG data are evaluated. In the latter case, the resulting TG&DTG curves becomes more narrow (not easy to see) and the kinetic parameters somewhat higher. Another interesting observation which can be made is that by using the traditional differential method with linear regression of equation (3.7) to calculate the initial values of A-cellulose, see Table 3.5, the activation energy increases with almost 20 kJ/mole compared to when non-linear regression of the TG or DTG data are used.

For birch, however, the kinetic parameters obtained from the fit to the TG data to that of the DTG data varied considerably more. By using the same initial values, a fit to the DTG data resulted in an activation energy of $E_{2,DTG}$=256.4 kJ/mole for *reaction 2* (describing the cellulose decomposition), while the evaluation of the TG data resulted in an activation energy of $E_{2,TG}$=209.1 kJ/mole. The corresponding c_i-values were $c_{2,DTG}$=38.0 % and $c_{2,TG}$=46.3 %, respectively. There is no easy explanation to this, obviously, the approximation of the TG and DTG curves represent quite different mathematical criteria for optimization. Based on their experience, Pokol and Varhegyi (1988) formulated the following two empirical rules for the kinetic evaluation of partial overlapping DTG and DSC curves:

- ***When the overlap is slight and the three fundamental geometric characteristics of the peaks can clearly be distinguished, it is possible to calculate four independent parameters (A_i, E_i, n_i and c_i) for each peak from a single thermoanalytical curve.***
- ***When shoulders can only be distinguished on the overlapped thermoanalytical curves, there is no unique solution.***

However, by choosing proper initial values for the kinetic parameters of each of the individual reactions and domains or intervals where these reactions are dominating, as outlined here, meaningful fits can be obtained for both the TG and DTG curve. By looking at the shape, width and position of the partial curves one can judge which fit gives the most realistic picture of the decomposition.

The results from the kinetic evaluation of all the species, presented in a similar form as for A-cellulose and birch, i.e. with two plots and one table, are given in Appendix A. All the calculations have been carried out on a *90 MHz Pentium PC*. The overall time of the calculations varied between 10 and 300 seconds, depending on the number of reactions used.

KINETICS OF CELLULOSE DECOMPOSITION

The results obtained from the kinetic evaluation of all the cellulose experiments are listed in Table 3.9 and 3.10 (see page A3-A21 Appendix A). At a heating rate of 5°C/min, the single reaction model gave a formal reaction order of 1.018 which reveals that the decomposition of A-cellulose can be described by a first order reaction. Evaluation of the TG curves with a fixed reaction order (n=1) gave for the six 5°C/min experiments a mean value of E_{TG}=211 kJ/mol with a standard deviation of ±1 kJ/mol for the activation energy and $\log A_{TG}$=16.1±0.1 (log) s^{-1} for the frequency factor. The corresponding activation energy and frequency factor obtained by evaluating the DTG curves were E_{DTG}=216±4 kJ/mol and $\log A_{DTG}$=16.6±0.3 (log) s^{-1}, respectively. The activation energy for a single first order reaction is inversely proportional to the peak width. Hence, if anything widens a thermoanalytical peak the corresponding activation energy will be lower. When the heating rate is increased from 2 to 10°C/min, the thermoanalytical peaks shown in Figure 3.12 for A-cellulose becomes wider and the resulting activation energy calculated becomes lower.

Table 3.9 Kinetic parameters for A-cellulose evaluated by a single reaction model.

Species	Evaluated Curve	dT/dt [°C/min]	E [kJ/mol]	logA [log s^{-1}]	n	dev1 [%]	dev2 [%]
A-Cellulose	TG	2	216.3	16.69	1	1.8	6.3
A-Cellulose	DTG	2	227.8	17.75	1	1.4	20.7
A-Cellulose†	TG	5	211±1	16.1±0.1	1	1.6±0.2	8.3±1.6
A-Cellulose†	DTG	5	216±4	16.6±0.3	1	1.4±0.2	22.1±4.9
A-Cellulose	TG	5	212.5	16.27	1.018	1.4	7.1
A-Cellulose	TG	10	212.2	16.15	1	1.3	4.2
A-Cellulose	DTG	10	208.4	15.82	1	1.1	12.1

† Means of 6 experiments with sample sizes of 2, 5 and 10 mg.

As seen in Figure 3.27-3.28, a single first order reaction modeling of B-cellulose resulted in bad fits with activation energies of E_{TG}=153.4 kJ/mol and E_{DTG}=184.5 kJ/mol, respectively. This is not surprising since B-cellulose contains almost 15% hemicellulose which starts to decompose at a lower temperature and makes the ascending part of the DTG curve less steeper than a "pure" cellulose. As expected, modeling of B-cellulose by two independent parallel reactions resulted in much better fits, with activation energies of: E_{TG}=232.4 kJ/mol and E_{DTG}=258.8 kJ/mol for the reaction describing the cellulose decomposition. By looking at the peak area of the two reactions in Figures 3.29-3.30 which reflects the partial contribution (*c_i-values*) to the overall mass loss. It appears that a fit to the TG data give the most realistic parameters, since this fit resulted in c_H=14% for the reaction describing the

decomposition of hemicellulose. The corresponding c_H-value was almost 32% when the DTG curve was evaluated. A single first order reaction modeling of Whatman filter paper and cellulose extracted from spruce and birch resulted in acceptable fits. The wider thermoanalytical curve of spruce-cellulose resulted in lower activation energy compared to that obtained for A-cellulose with same location of T_{peak}. The higher activation energy for Whatman filter paper and birch-cellulose may be attributed to the combined effect of narrower thermoanalytical curves and that the T_{peak}'s are located at higher temperatures. By varying the reaction order, the fits resulted in *n* greater than one and a very high activation energy for Whatman filter paper, and *n* lower than one for the celluloses extracted from birch and spruce.

Table 3.10 Kinetic parameters for the different celluloses evaluated by a single reaction model.

Species	Evaluated Curve	E [kJ/mol]	logA [log s^{-1}]	n	dev1 [%]	dev2 [%]
B-Cellulose	TG	153.4	10.69	1	5.0	4.2
B-Cellulose	DTG	184.5	13.39	1	3.4	14.2
B-Cellulose†	TG	232.4	17.39	1	0.6	0.9
B-Cellulose†	DTG	258.8	19.72	1	0.3	0.2
B-Cellulose	TG	126.1	8.18	0.481	3.4	3.2
Birch-Cellulose	TG	235.5	17.75	1	2.7	0.1
Birch-Cellulose	DTG	269.4	20.67	1	1.3	18.8
Birch-Cellulose	TG	199.9	14.57	0.588	3.7	4.7
Spruce-Cellulose	TG	166.4	12.18	1	3.4	5.0
Spruce-Cellulose	DTG	186.4	13.98	1	2.4	21.7
Spruce-Cellulose	TG	155.0	11.11	0.816	3.9	7.4
Whatman ‡	TG	278±9	21.4±0.8	1	3.6±0.0	3.1±1.2
Whatman‡	DTG	263±8	20.2±0.6	1	3.2±0.1	11.0±1.4
Whatman R#1	TG	334.1	26.32	1.452	1.2	1.7

† Evaluated by two independent parallel reactions. ‡ Means of 2 identical experiments.

KINETICS OF HEMICELLULOSE AND LIGNIN DECOMPOSITION

Since the extraction of hemicellulose from birch and spruce was problematic leading to unusual thermoanalytical curves, no effort was made to calculate their kinetics. The extraction of lignin was also problematic, however, similar thermoanalytical curves have been observed by others [Tang (1967), Faix *et al.* (1988), Williams and Bessler (1994)]. Hence, the broad TG curves of the two lignins were formally approximated by a single first order reaction. This resulted in very low activation energies and frequency factors of E=63.4 kJ/mol, logA =2.33 (log) s^{-1} for lignin extracted from birch and E=74.7 kJ/mol, logA =3.09 (log) s^{-1} for lignin extracted from spruce.

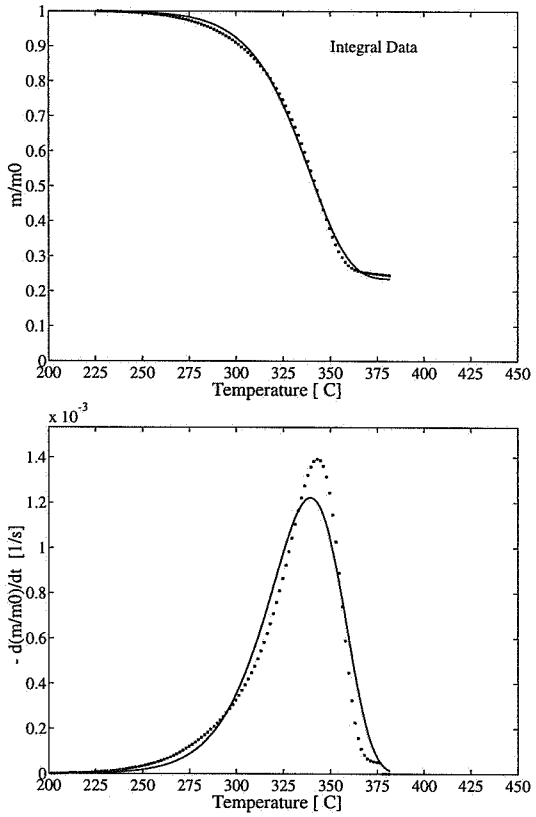

Figure 3.27 TG curve of B-cellulose fitted by a single first-order reaction

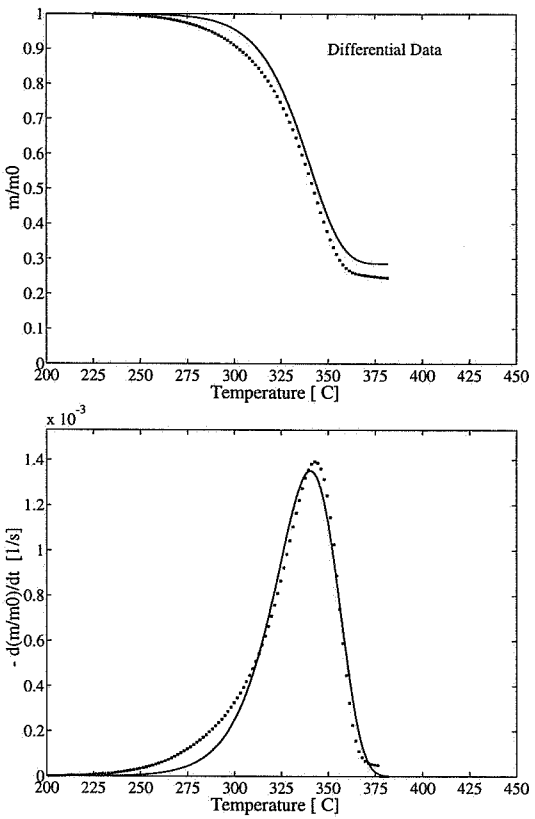

Figure 3.28 DTG curve of B-cellulose fitted by a single first-order reaction

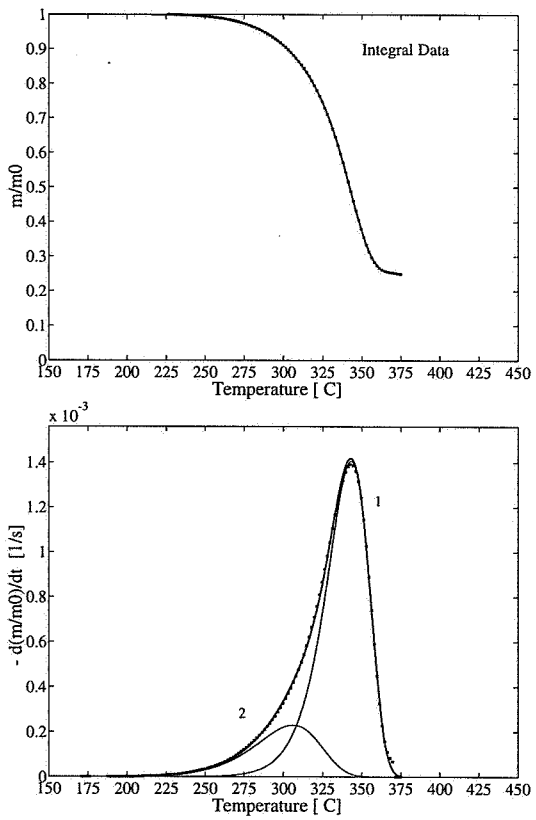

Figure 3.29 TG curve of B-cellulose fitted by two parallel reactions.

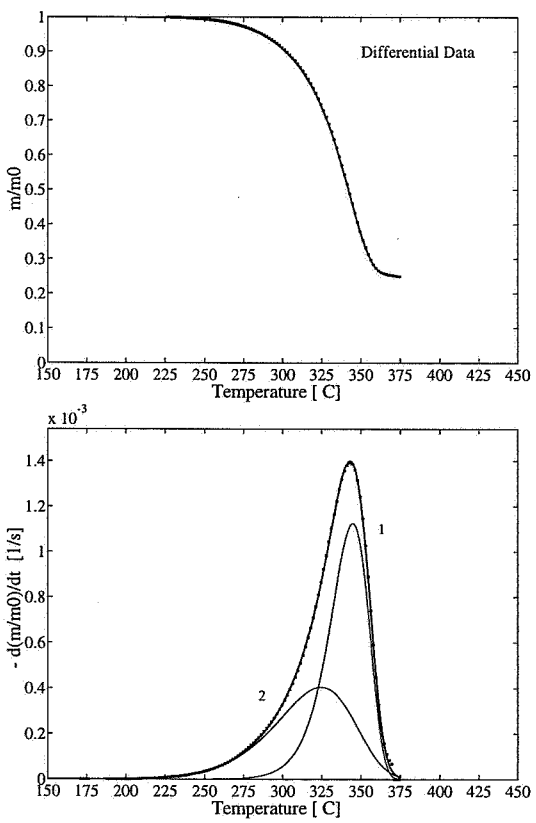

Figure 3.30 DTG curve of B-cellulose fitted by two parallel reactions.

KINETICS OF WOOD DECOMPOSITION

As a first approximation, the TG curve of the different wood species were evaluated by a single first order reaction. The results from such an evaluation are shown for birch in Figure 3.31. By looking at the TG curve only, one can argue that the fit is quite good since the calculated TG curve fits the experimental TG curve tolerably. However, when the calculated TG curve is differentiated, the resulting DTG curve confirm that a single reaction model is not sufficient to describe the decomposition of wood. In Figures 3.32-3.34, one can see how the fits are successively improved by adding two, three and finally four reactions. In the latter case, the first two peaks represent the decomposition of hemicellulose, the third peak represents the decomposition of cellulose and the low, very wide peak is intended to represent the decomposition of lignin. The corresponding kinetic parameters obtained from the fits presented in Figure 3.31-3.34 are listed in Table 3.11.

Table 3.11 Kinetic parameters for birch evaluated by a one, two, three and four parallel reactions.

		1st peak of hemicellulose	2nd peak of hemicellulose	cellulose	lignin	
Species	Evaluated Curve	E logA c	E logA c	E logA c	E logA c	dev1 dev2
Birch	TG	---	---	77.8	---	9.0
		---	---	4.03	---	6.9
		---	---	85.3	---	
Birch	DTG	93.7	---	243.1	---	2.8
		6.06	---	18.13	---	19.5
		41.8	---	41.3	---	
Birch	DTG	92.4	---	256.4	65.6	2.1
		5.91	---	19.26	2.29	7.2
		42.0	---	38.0	7.4	
Birch	TG	159.2	118.2	287.6	49.9	0.7
		12.86	8.10	21.88	1.05	1.27
		11.5	31.4	34.0	9.5	

The units of: E is [kJ/mole]; A is [s^{-1}]; c, *dev1* and *dev2* is [%].

Table 3.12 summarizes the "best-fit" parameters obtained from an evaluation of the DTG curves of untreated and pretreated birch, spruce, pine and pineroot. The corresponding fits are shown in Figure 3.35-3.44. Spruce and pine have been modeled by three parallel reactions. Hot water washed birch, untreated pineroot and pineroot treated with acetone have been modeled by four parallel reactions and finally, hot water washed pineroot has been modeled

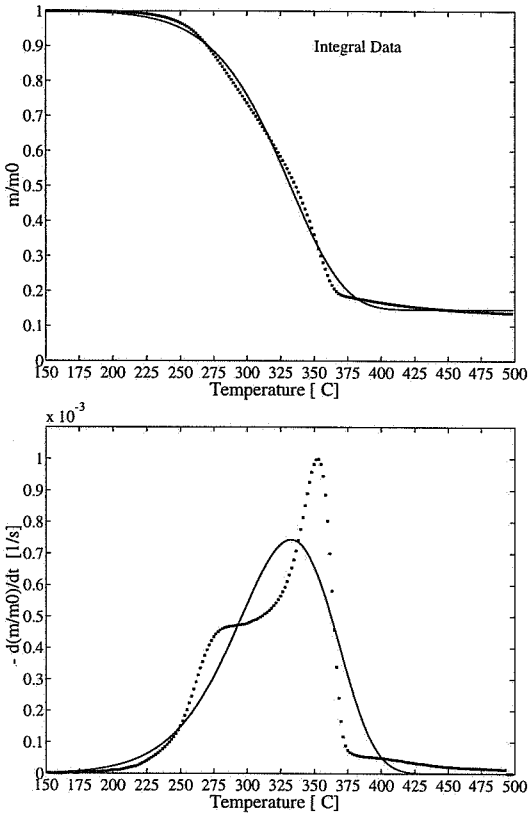

Figure 3.31 TG curve of birch fitted by a single first-order reaction.

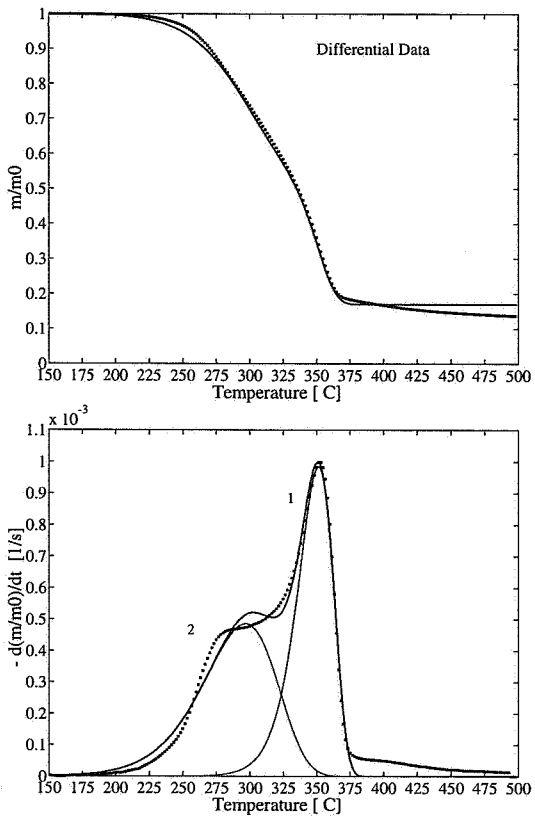

Figure 3.32 DTG curve of birch fitted by two parallel reactions.

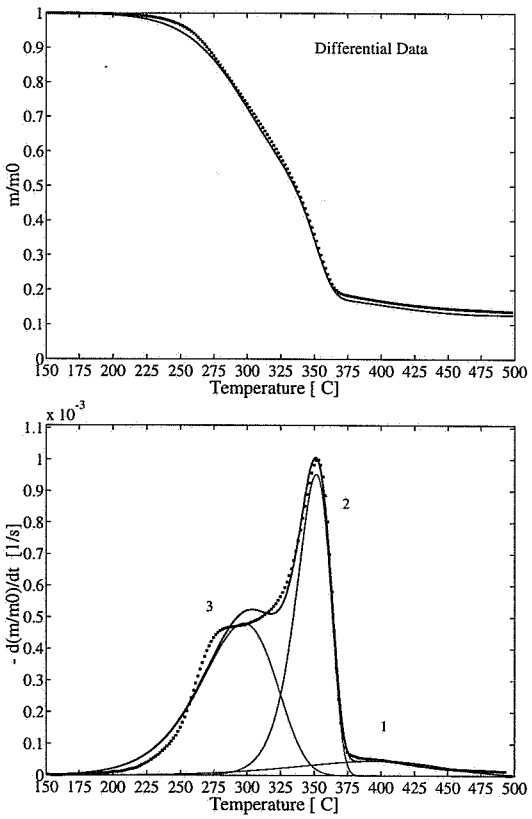

Figure 3.33 DTG curve of birch fitted by three parallel reactions.

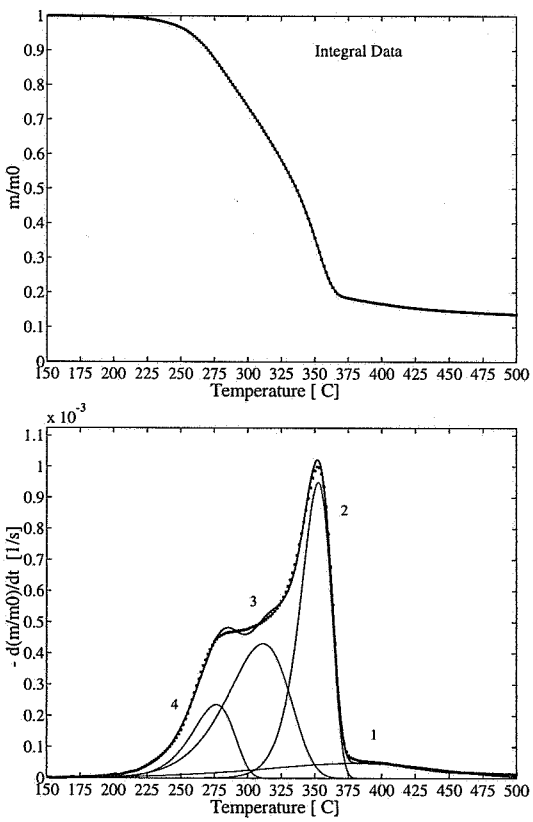

Figure 3.34 TG curve of birch fitted by four parallel reactions.

Table 3.12 Kinetic parameters for wood and pretreated wood based on fits of DTG curves.

	extractives	1st peak of hemicellulose	2nd peak of hemicellulose	cellulose	lignin	
Species Pretreat-ments	E logA c	E logA c	E logA c	E logA c	E logA c	dev1 dev2
			Three Parallel Reactions			
Spruce	---	106.9	---	276.5	44.2	0.3
none	---	6.98	---	20.86	0.56	0.1
	---	34.2	---	26.2	15.9	
Spruce	---	122.8	---	273.2	40.0	0.6
80°C H_2O	---	8.43	---	20.43	0.24	1.1
	---	28.3	---	36.3	18.1	
Pine	---	122.7	---	267.8	32.8	0.3
none	---	8.42	---	20.10	-0.32	0.1
	---	29.6	---	32.3	18.3	
Pine	---	114.0	---	318.8	40.2	1.0
0.1 M HCl	---	7.23	---	24.26	0.24	1.0
	---	48.8	---	23.0	14.8	
Pine	---	137.9	---	280.8	36.3	0.5
0.1 M acetic acid	---	9.78	---	21.09	-0.02	1.1
	---	28.4	---	38.1	17.2	
Pine	---	150.3	---	257.5	36.2	0.6
80°C H_2O	---	10.91	---	19.12	-0.01	1.5
	---	22.9	---	41.2	16.9	
			Four Parallel Reactions			
Birch	---	152.3	117.9	279.7	54.2	0.4
80°C H_2O	---	12.11	7.96	20.98	1.42	0.1
	---	12.9	28.4	38.9	9.4	
Pineroot	145.8	145.1	---	261.4	28.8	0.9
none	13.53	10.39	---	19.35	-0.50	0.0
	4.3	17.4	---	30.2	27.4	
Pineroot	111.2	140.6	---	255.4	40.2	0.3
acetone	8.55	10.10	---	18.96	0.24	0.1
	4.0	23.6	---	35.8	15.7	
			Five Parallel Reactions			
Pineroot	114.5	128.9	139.9	252.1	31.2	0.5
80°C H_2O	10.08	10.29	9.96	18.57	-0.45	0.2
	6.5	3.0	20.4	32.4	17.2	

The units of: E is [kJ/mole]; A is [s^{-1}]; c, *dev1* and *dev2* is [%].

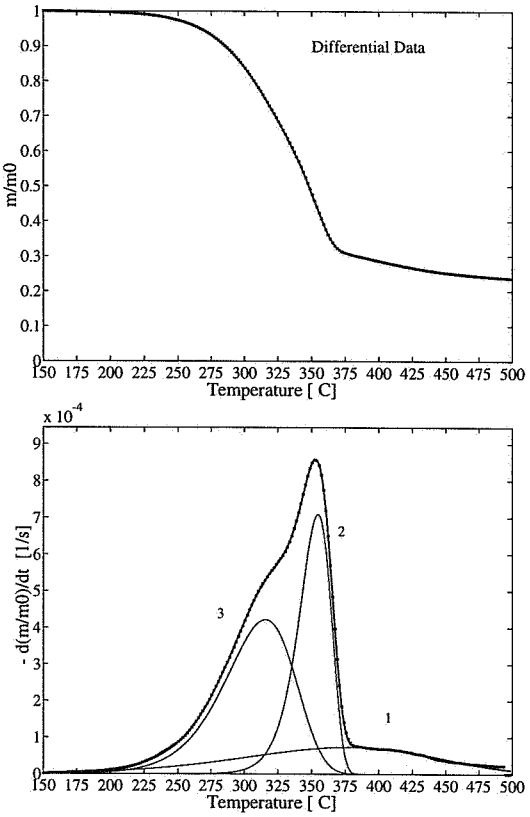

Figure 3.35 DTG curve of spruce fitted by three parallel reactions.

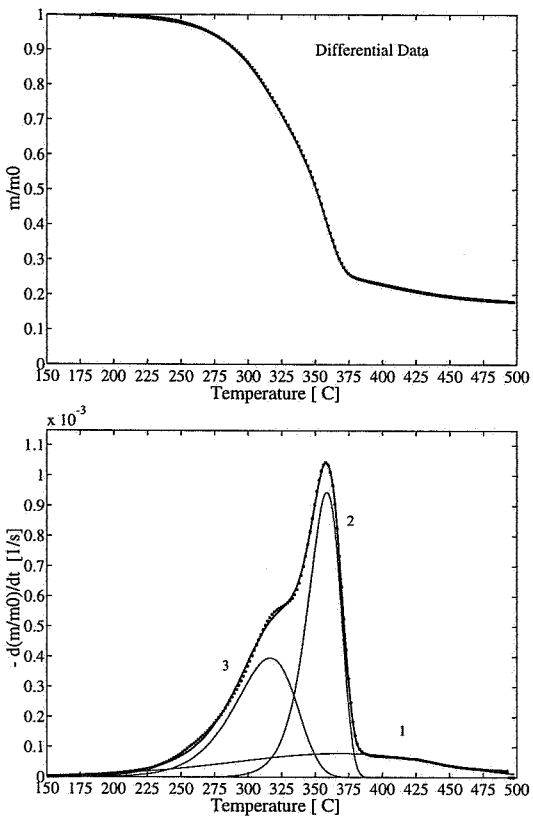

Figure 3.36 DTG curve of H_2O treated spruce fitted by three parallel reactions.

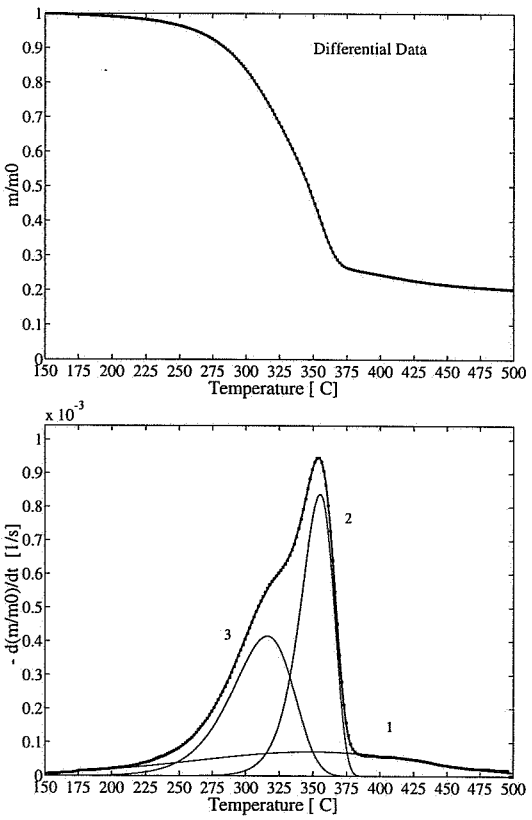

Figure 3.37 DTG curve of pine fitted by three parallel reactions.

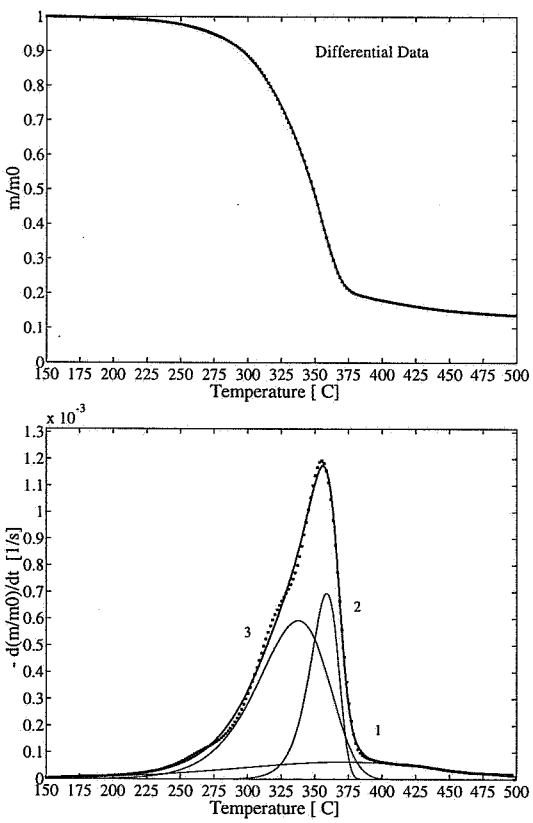

Figure 3.38 DTG curve of HCl treated pine fitted by three parallel reactions.

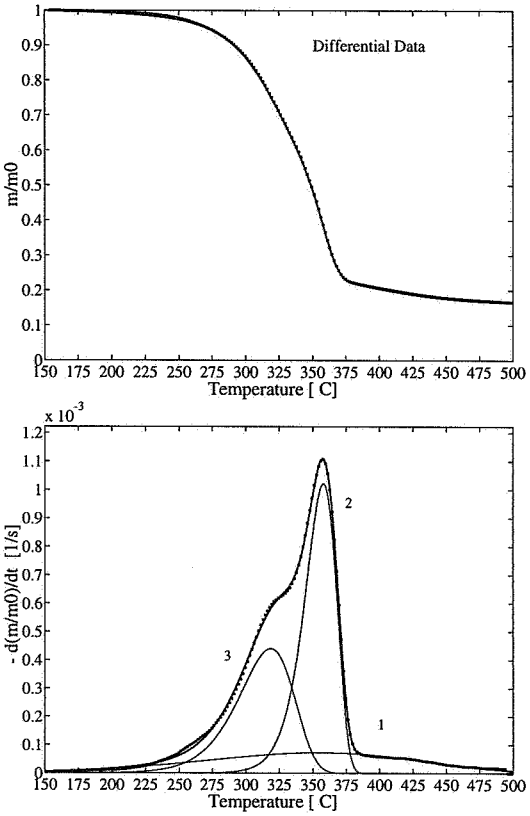

Figure 3.39 DTG curve of acetic acid treated pine fitted by three parallel reactions.

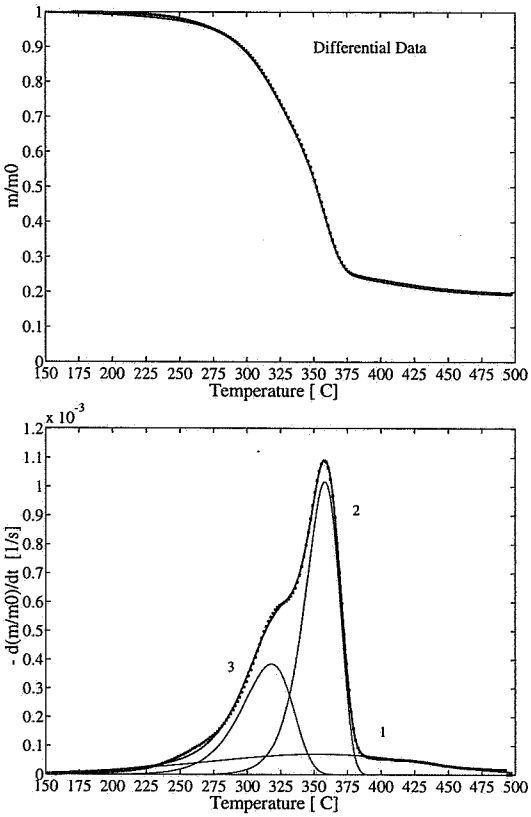

Figure 3.40 DTG curve of H_2O treated pine fitted by three parallel reactions.

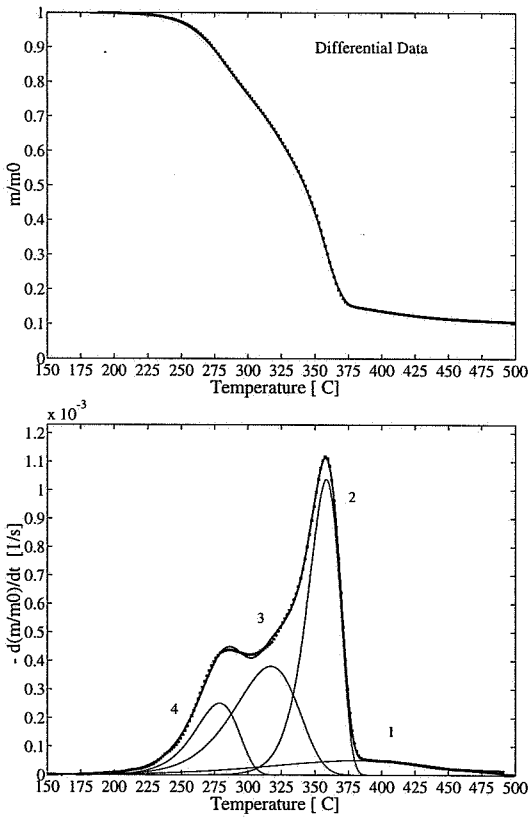

Figure 3.41 DTG curve of H_2O treated birch fitted by four parallel reactions.

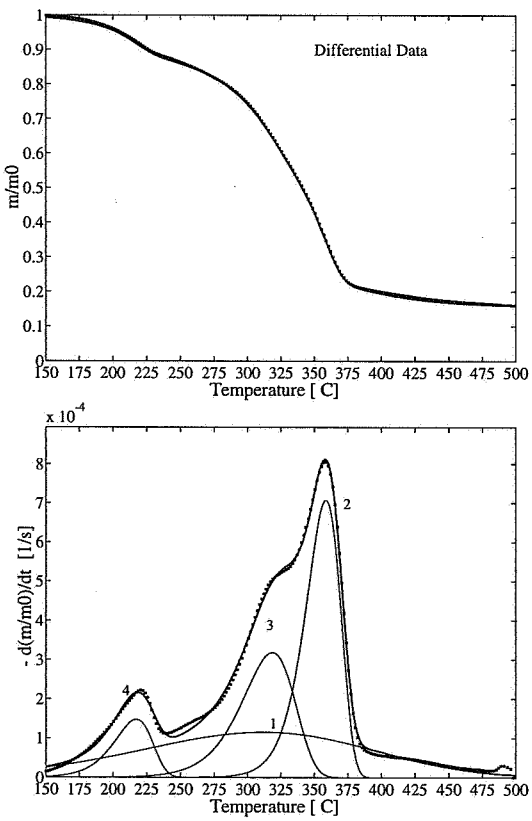

Figure 3.42 DTG curve of pineroot fitted by four parallel reactions.

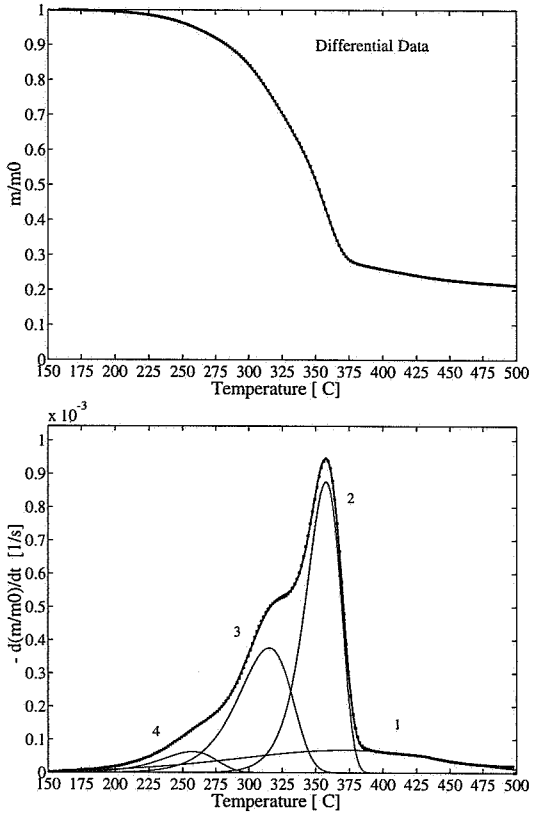

Figure 3.43 DTG curve of acetone treated pine-root fitted by four parallel reactions.

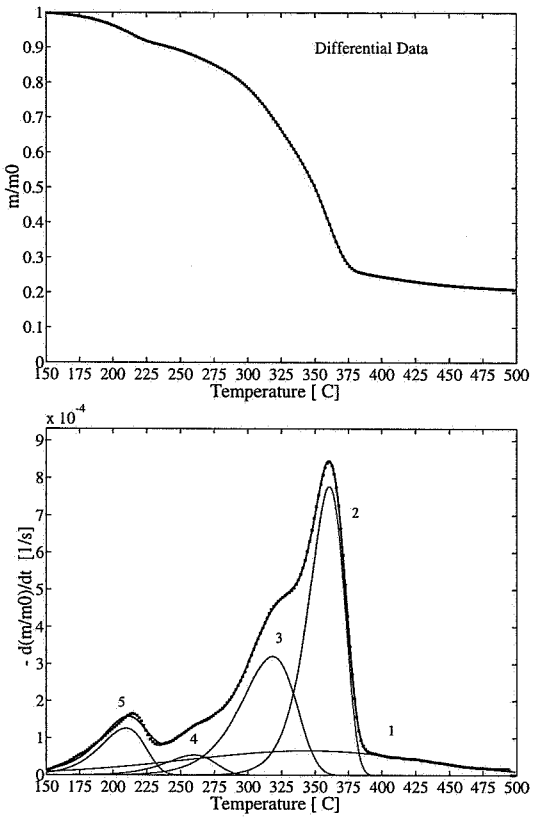

Figure 3.44 DTG curve of H_2O treated pineroot fitted by five parallel reactions.

by five reactions. In the latter case, the first peak intends to represent the decomposition of extractives. The next two peaks represent the decomposition of hemicellulose, the fourth peak represents the decomposition of cellulose and the low, very wide peak represents the decomposition of lignin.

Unfortunately, there is no hope of establishing a quantitative relationship between the c_i-values calculated and the actual mass fractions (here denoted C_i) of extractives, hemicellulose, cellulose and lignin found in wood. The c_i express the contribution of the partial processes to the overall mass loss and thereby the volatile part of each component. The following relation between C_i and c_i can be derived:

$$\sum_i C_i = \sum_i c_i + m_{char} = \sum_i (m_{0,i} - m_{char,i}) + \sum_i m_{char,i} = 1 \qquad (3.35)$$

If a comparison between the c_i-values calculated and the actual mass fractions should be possible, one needs to know either the char fraction, $m_{char,i}$, for each component that decomposes independently from each other or assume that each component yields the same char-fraction. The latter is not true since the lignin in wood is assumed to be responsible for most of the char formed. Hence, this type of modeling cannot be used to estimate the amount of the individual components of the biomass material. However, this modeling approach

makes it possible to study the in situ decomposition of cellulose and to some extent the decomposition of hemicellulose in wood. Table 3.13 displays the kinetic parameters for cellulose decomposition in the wood species analyzed, from which a mean value of E=260 kJ/mol with a standard deviation of ±16 kJ/mol has been calculated for the activation energy and logA=19.4±1.1 (log) s^{-1} for the frequency factor. All the data are based on least squares evaluation of the DTG curves. Untreated birch evaluated by four reaction and HCl washed pine evaluated by three reactions (put in brackets) resulted in logA and E significantly higher than the corresponding means, hence these were excluded from the calculation of the means and standard deviation. The mean activation energy and frequency factor estimated for cellulose decomposition in wood is comparable to those obtained from the least squares evaluation of Whatman filter paper and cellulose extracted from birch.

Table 3.13 Kinetic parameters for cellulose decomposition in wood based on fit of DTG curve.

Species	Pretreatments	Number of reactions	E [kJ/mol]	logA [log s^{-1}]	c [%]	dev1 [%]
Birch	none	2	243.1	18.13	41.3	2.8
Birch	none	3	256.4	19.26	38.0	2.1
Birch†	none	4	(294.0)	(22.41)	(31.8)	(0.6)
Birch	80°C H_2O	2	237.6	17.47	47.7	2.6
Birch	80°C H_2O	3	248.6	18.40	44.5	2.1
Birch	80°C H_2O	4	279.7	20.98	38.9	0.4
Spruce	none	3	276.5	20.86	26.2	0.3
Spruce	80°C H_2O	3	273.2	20.43	36.3	0.6
Pine	none	3	267.8	20.10	32.3	0.3
Pine†	0.1 M HCl	3	(318.8)	(24.26)	(23.0)	(1.0)
Pine	0.1 M acetic acid	3	280.8	21.09	38.1	0.5
Pine	80°C H_2O	3	257.5	19.12	41.2	0.6
Pineroot	none	4	254.3	18.83	29.0	1.1
Pineroot	80°C H_2O	4	261.4	19.35	30.2	0.9
Pineroot	80°C H_2O	5	252.1	18.57	32.4	0.5
Pineroot	acetone	4	255.4	18.96	35.8	0.3
Mean (std‡)			260 (±14)	19.4 (±1.1)		1.1 (±0.9)

† not included in the calculation of the means, ‡ std - standard deviation.

The reaction describing hemicellulose decomposition in wood has been obtained by fitting the shoulder at the ascending part of the DTG curves. For some of the wood species analyzed, it is difficult to separate the DTG shoulder of hemicellulose decomposition from the more protuberant DTG peak of celluloses decomposition (see for instance HCl washed pine in

Figure 3.38). With the two empirical rules for the kinetic evaluation of partial overlapping DTG curves in mind [Pokol and Varhegyi (1988)], this reaction must be regarded only as a formal approximation of the hemicellulose decomposition. In Table 3.14, the kinetics estimated for the hemicellulose decomposition in wood are listed from which a mean value of E=119 kJ/mol with a standard deviation of ±23 kJ/mol has been calculated for the activation energy and logA=8.2±2.0 (log) s^{-1} for the frequency factor. Even though this mean activation energy and frequency factor is close to the values reported by Ramiah (1979) and Min (1977) who described "pure" hemicellulose decomposition by a single first-order reaction, they must be regarded as less reliable compared to those obtained for the cellulose decomposition in wood.

Table 3.14 Kinetic parameters for hemicellulose decomposition in wood based on fit of DTG curve.

Species	Pretreatments	Number of reactions	E [kJ/mol]	logA [log s^{-1}]	c [%]	devl [%]
Birch	none	2	93.7	6.06	41.8	2.8
Birch	none	3	92.4	5.91	42.0	2.1
Birch	80°C H_2O	2	91.1	5.78	39.1	2.6
Birch	80°C H_2O	3	89.7	5.63	39.3	2.1
Spruce	none	3	106.9	6.98	34.2	0.3
Spruce	80°C H_2O	3	122.8	8.43	28.3	0.6
Pine	none	3	122.7	8.42	29.6	0.3
Pine	0.1 M HCl	3	114.0	7.23	48.8	1.0
Pine	0.1 M acetic acid	3	137.6	9.78	28.4	0.5
Pine	80°C H_2O	3	150.3	10.91	22.9	0.6
Pineroot	none	4	144.3	10.36	19.7	1.1
Pineroot	80°C H_2O	4	145.1	10.39	17.4	0.9
Pineroot	acetone	4	140.6	10.10	23.6	0.3
Mean (std‡)			119 (±23)	8.2 (±2.0)		1.1(±0.9)

‡ std - standard deviation.

The lignin in wood decomposes in the same temperature areas as the hemicellulose and cellulose and does not give a separate DTG peak. The only part of the DTG curves which can be used to create a reaction for the lignin decomposition has been the flat tailing section at the descending part of the DTG curves. This very formal approximation of lignin decomposition in wood resulted in extremely low "activation energies" in the range of 28 to 55 kJ/mole with corresponding frequency factors in the range of -0.50 to 1.42 (log) s^{-1}. These values are somewhat lower than those obtained for the isolated lignins.

3.3.4 ERRORS IN MEASUREMENTS, CALIBRATION ROUTINES AND RELATED QUESTIONS

The experimental errors of a TG curve obtained by a modern thermoballance are neither random nor independent quantities since random errors (noise) are filtered out by the analog filter of the instrument. The numerical differentiation and integration methods used in the least squares evaluation do not add significant random errors to the data. Hence, the methods of the mathematical statistics cannot be used for the estimation of the reliability of the kinetic parameters calculated [Pokol and Varhegyi (1988); Varhegyi *et al.* (1989)]. However, the possible sources of error in thermogravimetry are many [Wendlandt (1974)]. The two most important errors are connected to weight and temperature measurements, although, these can be minimized by calibrating the instrument properly.

In the weight calibration of the SDT, two standard weights of 292.795±0.1 mg and 291.79±0.1 mg were used for the sample and reference balance arms, respectively. During a linear temperature increase to 600°C and 900°C, the baseline drifts caused by buoyancy effects and beam growth were measured to 0.04 mg and 0.06 mg, respectively.

The temperature calibration of the SDT was performed by using the phase change of five NBC-ICTA standard reference materials (indium, tin, lead, zinc and aluminium). The standard reference material was heated at linear heating rate until the phase-change temperature. Then the reference holder temperature still increased linearly while the sample holder temperature increased much slower. The measured temperature difference defines an extrapolated onset temperature which is compared with the phase-change temperature, i.e. the melting point of the given reference material. The measured extrapolated onset temperatures for a number of metals are shown in Table 3.15. A heating rate of 5°C/min was used.

Table 3.15 Calibration of *SDT 2969* from *TA Instruments*. Heating rate 5°C/min.

Metal	Melting point	Heat of fusion	Onset temperature
	T_m [°C]	H_f [J/g]	T_{onset} [°C]
Indium (In)	156.59	28.57	156.36
Tin (Sn)	231.93	60.6	231.57
Lead (Pb)	327.50	23.1	327.03
Zinc (Zn)	419.53	108	420.91
Aluminum (Al)	660.33	396.0	662.88

One way to get a picture of the errors in the experiments is a study of their repeatability. In Table 3.16, the peak temperatures (T_{peak}) and char fractions (defined at 450°C) for the six A-cellulose experiments are listed together with the kinetic parameters calculated from a fit to the TG and DTG curves.

Table 3.16 Repeatability of an A-cellulose experiment. Heating rate 5°C/min.

Species	Sample mass [mg]	T_{peak} [°C]	m_{char} [%]	Evaluated Curve	E [kJ/mol]	logA [log s^{-1}]
A-Cellulose	2	326.7	7.5	TG	211.3	16.13
				DTG	211.5	16.16
A-Cellulose$^{R\#1}$	5	325.7	9.0	TG	211.1	16.14
				DTG	215.6	16.56
A-Cellulose$^{R\#2}$	5	326.4	6.5	TG	210.4	16.07
				DTG	216.7	16.64
A-Cellulose $^{R\#3}$	5	326.6	10.2	TG	212.0	16.22
				DTG	217.1	16.69
A-Cellulose $^{R\#4}$	5	328.0	10.8	TG	208.8	15.92
				DTG	214.6	16.45
A-Cellulose	10	327.0	8.0	TG	211.0	16.15
				DTG	222.3	17.16
Mean (std†)		327 (±1)	9 (±2)		214 (±4)	16.4 (±0.4)

† std - standard deviation

The location of peak temperatures, i.e. the temperature where the maximum rate of decomposition occur are almost identical for the 6 experiments with a standard deviation of ±1°C from a mean temperature of 327°C. The reasons for the irregularity in char fraction are not known. It can be irreproducibilities in the experimental procedures, such as the placement of the sample in the sample pan. The subsequent placement of sample pan on the sample holder or simply because of very small impurities in the samples. It is difficult to see which influence T_{peak} and m_{char} have on the kinetic parameters since it seems to be incoherence between them. A standard deviation for the 6 experiments of ±4 kJ/mole from a mean value of 214 kJ/mole for the activation energy and ±0.3 (log) s^{-1} from a mean vale of 16.4 (log) s^{-1} for the frequency factor must, however, be regarded as satisfactory.

Another way of studying the experimental errors is by making a reproducibility (round robin) test, i.e., by studying the same specimen in different thermobalances. Four thermobalances of which two are similar have been used. These include a *DuPont 951 TGA* and a *Perkin Elmer TGS-2* in addition to the *SDT 2960* from *TA Instruments* (see Figure 3.2). However, the heating rate and specimen used were not same in all the experiments. Table 3.17 summarizes which experiment (sample, heating rate) were done in which instrument; where they have been done and when. Figures 3.45 to 3.47 present the TG and DTG comparisons while the results from the kinetic evaluation are presented in Table 3.18.

Table 3.17 Thermobalances, specimens and heating rates used for the reproducibility test.

Instrument	Where & When	Specimen	Heating rate
DuPont 951 TGA	Risø National Laboratory, Denmark, December 1993	A-cellulose	5°C/min
Perkin Elmer TGS-2	Hungarian Academy of Science Hungary, March 1996	Avicel cellulose	10°C/min
TA Instruments SDT 2960	Risø National Laboratory, Denmark, July 1995	Whatman No 42 A-cellulose	5°C/min 5°C/min
TA Instruments SDT 2960	Norwegian University of Science and Technology, Norway, October 1996	Whatman No 42 Avicel cellulose	5°C/min 10°C/min

The two comparisons: *DuPont 951 TGA* and *Perkin Elmer TGS-2* versus *SDT 2960* in Figures 3.45 and 3.46 reveal a difference in peak temperatures of about 8°C and 10°C, respectively. The different peak temperatures may be attributed to the different methods used in the temperature calibration of the instruments. A 10°C difference in T_{peak} must be regarded as quite normal [Varhegyi (1996)]. The DTG curves of the two Whatman No 42 filter paper experiments shown in Figure 3.47 coincide fairly well. The difference in peak temperature is only 3°C, which is not very surprising since similar instruments (*SDT 2960*) with similar calibration routines have been used. However, as the kinetic evaluation of the TG and DTG curves presented in Table 3.18 reveals, a higher peak temperature does not necessarily mean that the activation energy is getting higher. As previously discussed, one must also take into consideration the shape and width of the individual TG and DTG curves. The standard deviation of the activation energies calculated for the two Whatman filter paper experiments having almost similar peak temperatures is at the same level (±5-6 kJ/mole) as calculated for the two A-cellulose and Avicel cellulose experiments, where the differences in peak tempera-

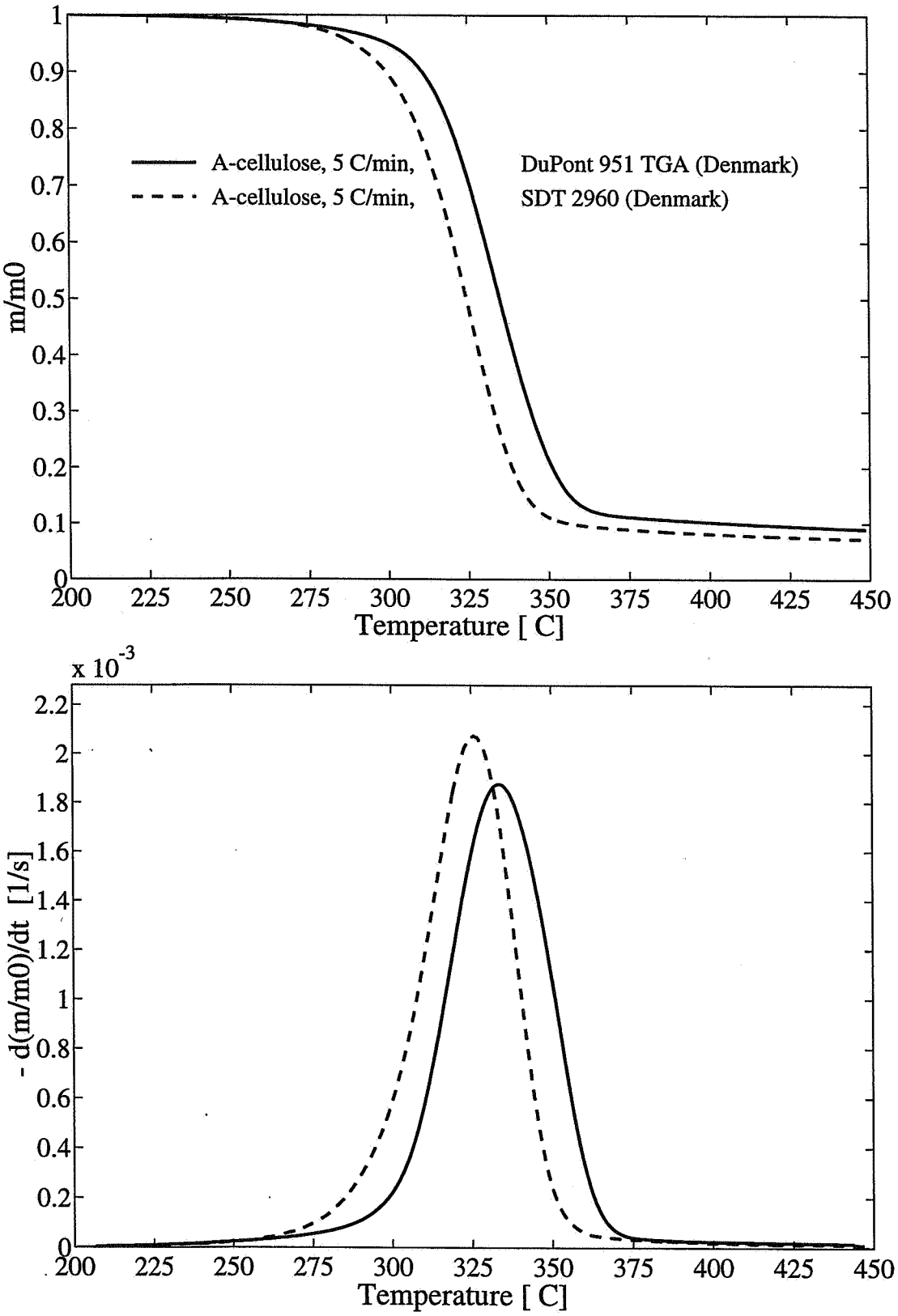

Figure 3.45 Comparison of two 5°C/min A-cellulose experiments: (——) *DuPont 951 TGA* (Denmark); (– – –) *SDT 2960* (Denmark).

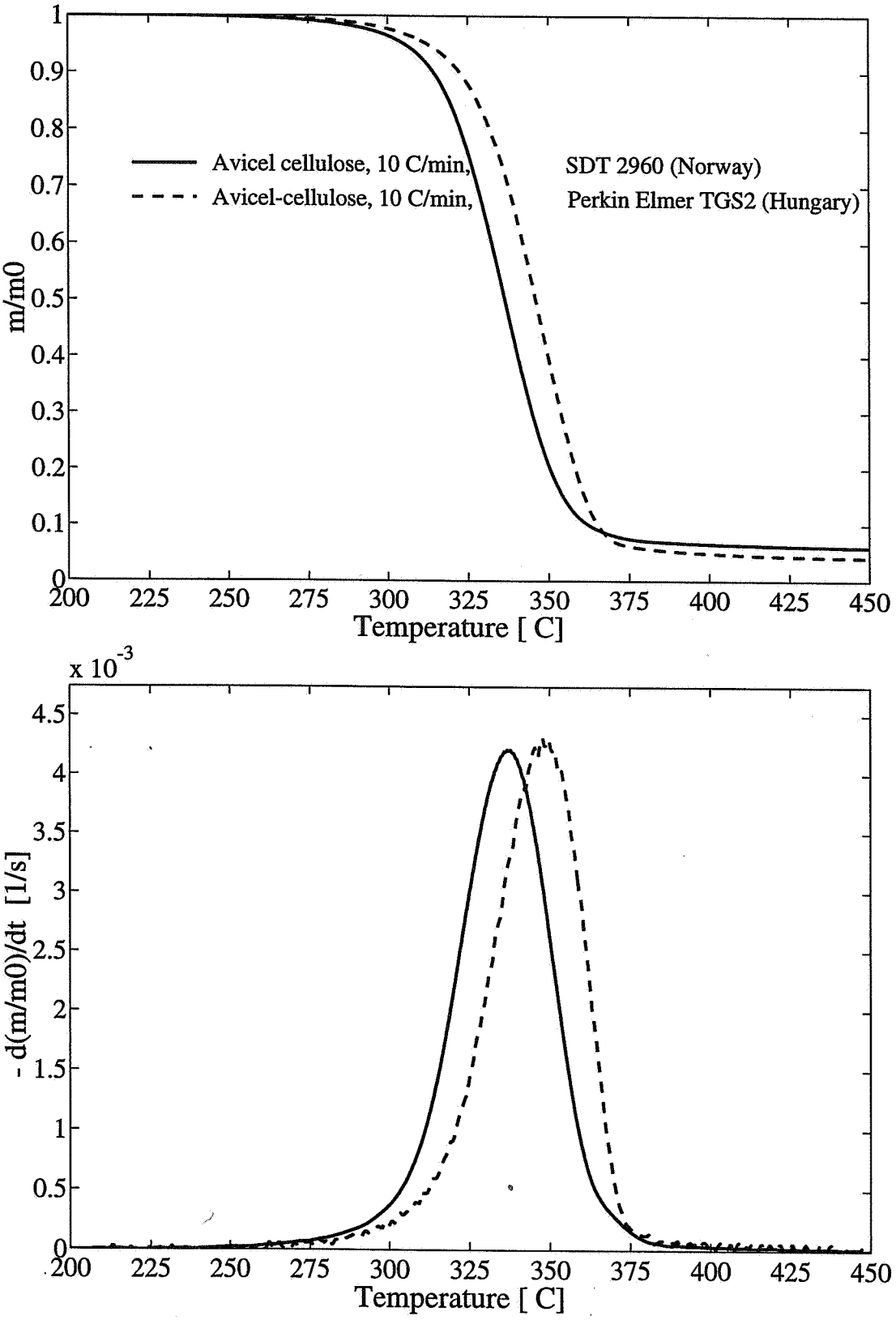

Figure 3.46 Comparison of two 10°C/min Avicel-cellulose experiments: (——) *SDT 2960* (Norway); (– – –) *Perkin Elmer TGS-2* (Hungary).

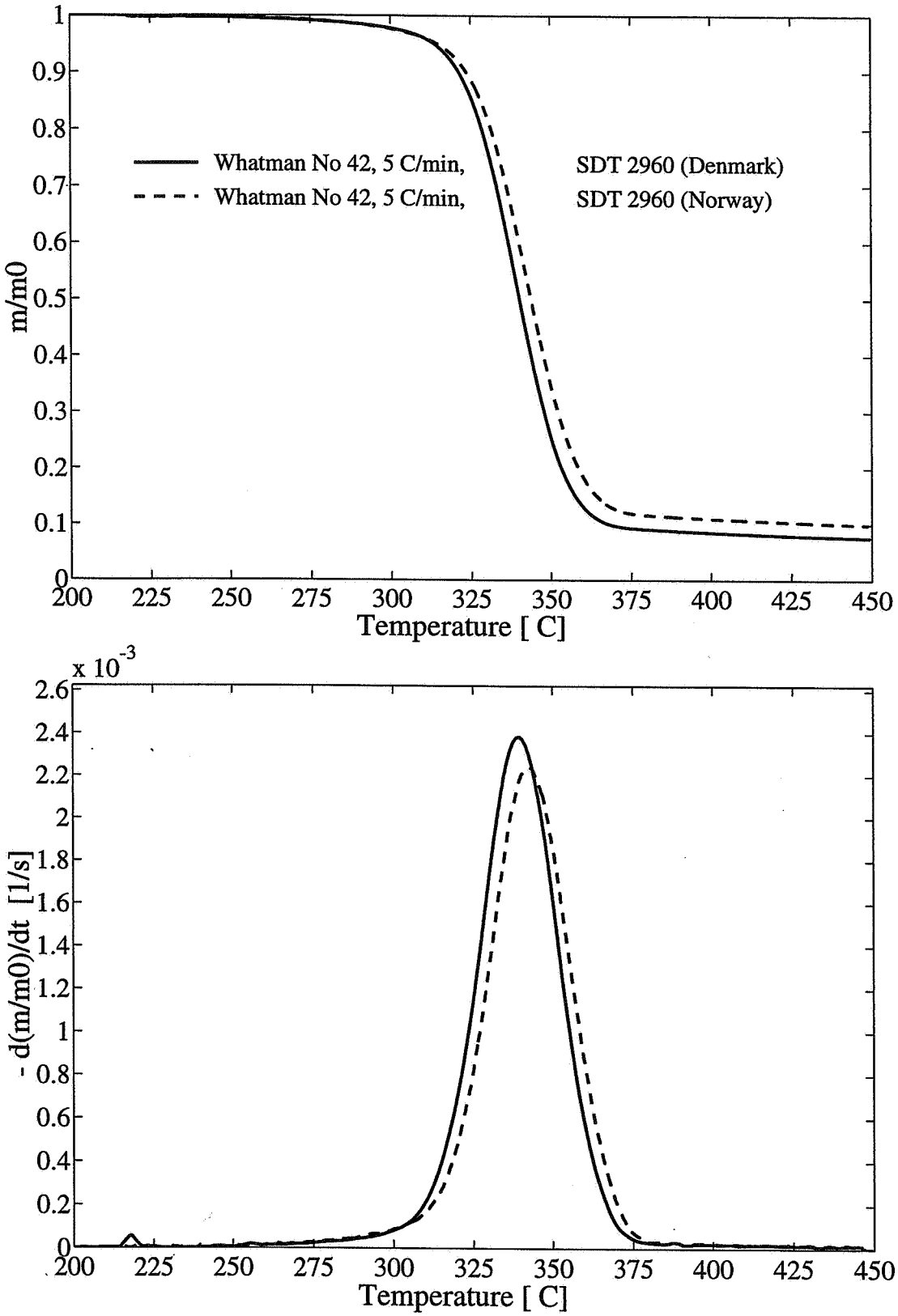

Figure 3.47 Comparison of two 5°C/min Whatman No 42 filter paper experiments: (——) *SDT 2960* (Denmark); (– – –) *SDT 2960* (Norway).

tures are much higher. Since the standard deviation of the activation energies calculated is at the same level as for two repeated run carried out in the same thermobalance, the reproducibility of the experiments must be regarded as satisfactory.

Table 3.18 Kinetic parameters for the celluloses tested in different thermobalances.

Specimen/ Instrument	dT/dt [°C/min]	T_{peak} [°C]	m_{char} [%]	Evaluated Curve	E [kJ/mol]	logA [log s^{-1}]
A-Cellulose						
DuPont 951 TGA	5	333.0	11.2	TG	212.0	15.91
				DTG	205.8	15.38
SDT 2960 (Risø)	5	325.5	8.7	TG	210.1	16.05
				DTG	217.4	16.71
Mean (std†)		329 (±5)	10 (±2)		211 (±5)	16.0 (±0.6)
Avicel cellulose						
Perkin Elmer TGS-2	10	348.3	5.0	TG	235.1	17.81
				DTG	239.2	18.17
SDT 2960 (Norway)	10	338.0	6.7	TG	228.3	17.55
				DTG	226.2	17.40
Mean (std†)		343 (±7)	6 (±1)		232 (±6)	17.7 (±0.3)
Whatman No 42 filter paper						
SDT 2960 (Risø)	5	340.0	8.5	TG	266.5	20.44
				DTG	260.7	19.99
SDT 2960 (Norway)	5	342.7	11.0	TG	256.2	19.44
				DTG	253.6	19.25
Mean (std†)		341 (±2)	10 (±2)		259 (±6)	19.8 (±0.5)

† std - standard deviation

3.4 CONCLUDING REMARKS

A thermogravimetric and kinetic study of the pyrolysis of three Scandinavian wood species (birch - *Betula Verrucosa*, pine and pineroot - *Pinus Silvestris*, spruce - *Picea Abies*); five different celluloses (99.5 % pure cellulose, cellulose containing 15 % hemicellulose, Whatman No 42 ash free filter paper, cellulose isolated from birch and spruce); and hemicellulose and lignin isolated from birch and spruce have been presented. The following main conclusions can be drawn:

- All the cellulose species lost weight in a narrow temperature range shown as sharp, single peaks on the DTG curve. However, some differences in shape, width and location of the DTG peak temperature were observed. This may be attributed to their different DP and crystallinity, impurities such as mineral matter or the presence of hemicellulose in the samples. In contrast to cellulose, lignin had a gradual loss of weight from about 200°C to the final temperature of 550°C, consistent with the wide variety of functional groups found in lignin. The "unusual" thermal behaviour of hemicellulose isolated from birch and spruce may be attributed to inorganic impurities which had not been properly washed out during the extraction procedure.

- The thermograms (TG&DTG curves) of the wood species revealed different weight loss characteristics which must be attributed to their different chemical composition. For birch, being a hardwood with a hemicellulose content of about 40 wt%, two main areas of weight loss were observed producing a single DTG peak (resulting from the decomposition of cellulose) with a broad plateau or shoulder (owing to hemicellulose decomposition) located at the ascending part of the curve. For the two softwoods, pine and spruce, having a hemicellulose content less than 30 wt%, this shoulder was hardly visible and more or less overlapped with the more protuberant DTG peak of cellulose decomposition. The highly resinous pineroot had an additional DTG peak located in the lower temperature region resulting from the decomposition of the very high (~20 wt%) fraction of extractives found in the roots of pine.

- Pretreatments, such as washing with hot water, diluted hydrochloric acid or diluted acetic acid did not give any better resolution or separation of the hemicellulose shoulder and cellulose peak as observed by other workers, especially on herbaceous plants. The very low ash and mineral contents in the wood species analyzed are the most plausible reason for not seeing any significant effect of these pretreatments.

Even though the pyrolysis of wood and its main constituents cellulose, hemicellulose and lignin takes place through a reaction network of parallel and competitive reactions, the DTG (and TG) curves observed were quite simple and could be described by relatively simple mathematical models.

- The celluloses exhibited sharp, single DTG curves which could be well described by a single first order reaction. With the exception of cellulose extracted from spruce (probably because of contamination), the kinetic analysis gave activation energies between 210 and 280 kJ/mole for all the celluloses. This reveals that the pyrolysis of "pure" cellulose under the regimes studied, i.e., small sample masses and relatively slow heating rates, is a low temperature high activation energy process. Hence, complicated models that processes more than on reaction step, e.g., the Broido-Shafizadeh model, are superfluous to describe the mass loss behaviour of cellulose. In light of the findings presented in this work, as well as earlier analysis of Varhegyi *and co-workers* (1988, 1989, 1994), measurements of activation energies below 150 kJ/mole for cellulose pyrolysis are questionable. Either are these related to heat transfer limitations, such as the MIT-studies [Lewellen *et al.* (1977), Hajaligol *et al.* (1982)] discussed by Antal and Varhegyi (1995); Narayan and Antal (1996), or lack of accuracy caused by the approximations used in the different computational methods, e.g., the use of equation (3.7).

- The wood species evidenced a distinct DTG peak with shoulders or double peaks. By assuming the components of wood to decompose independently of one another, the pyrolysis process could be described by using a model of independent parallel reactions. Spruce and pine were successfully described by three reactions while birch and pineroot required four independent reactions. The main advantage of this modeling approach is that the in situ decomposition of cellulose in wood can be studied. From such an analysis of all the treated and untreated wood species used, a mean activation energy of 260 kJ/mole with a standard deviation ±16 kJ/mole was calculated. This activation energy is in accordance with those obtained for Whatman filter paper and the cellulose isolated from birch.

- Four thermobalances of which two were similar were used to check the reproducibility of the experiments. Although, differences in peak temperatures of about 10°C were obtained, the standard deviation of the activation energies calculated was at the same level as for two repeated run from the same thermobalance.

CHAPTER 4

PYROLYSIS OF LARGE BIOMASS PARTICLES CONTROLLED BY HEAT AND MASS TRANSFER

4.1 INTRODUCTION

The previous chapter dealt with the pyrolysis of small samples, i.e. thermally thin particles with negligible temperature gradient within the solid, where the chemical kinetics were the rate-controlling process. Beside pulverized fuel combustors, however, there are not many thermochemical conversion processes that use biomass in the form of sawdust or powder as feedstock. Grate firing units, fluidized bed combustors/gasifiers and wood-stoves use feedstock with a certain size (i.e. thermally thick) such as pellets, chips or logs which all have an effective temperature gradient within the solid during the thermal degradation. In this case, the chemistry of decomposition is influenced by heat and mass transfer effects. Since the fuel is seldom completely dried before it enters the conversion unit, it is of importance to have knowledge about the effect of moisture on the rate of conversion.

This will be the subject of this chapter, where theoretical and experimental work on the pyrolysis of large particles of wood will be presented. This chapter comprises a review part where some of the previous work done within this field will be discussed. A theoretical part where a transient, one-dimensional mathematical model for the drying and pyrolysis of wood has been derived. An experimental part where pyrolysis experiments of wooden cylinders will be presented, and a final part where the experimental results will be compared with modelling predictions. At first, however, a qualitative description of the successive events that take place within wood during the thermal degradation process will be given (see Figure 4.1).

When moist wood is heated, it first undergoes an initial drying period. Intraparticle temperature profiles found in laboratory experiments of moist pellets or slabs show always definite inflection points or plateaus located near 100°C [White and Schaffer (1981), Fredlund (1988)]. During this initial drying period, most of the energy received by the pellet is consumed by heating and evaporating water. If the initial moisture content is above the fiber saturation point ($M>M_{fsp}\approx30\%$), the pores contain liquid water and the internal moisture transfer is mainly attributable to capillary flow of free water through the voids. As drying proceeds, the surface moisture content reaches its maximum sorptive value ($M=M_{fsp}$), and the evaporation front

begins to travel into the solid leaving behind a sorption zone ($M<M_{fsp}$). Inside the evaporation front, the material will still contain liquid water in the pores. Outside the evaporation front, no liquid water exists and the main transfer mechanisms are bound water diffusion and convective and diffusive transport of water vapour. Evaporation takes place at the front as well as in the whole sorption zone.

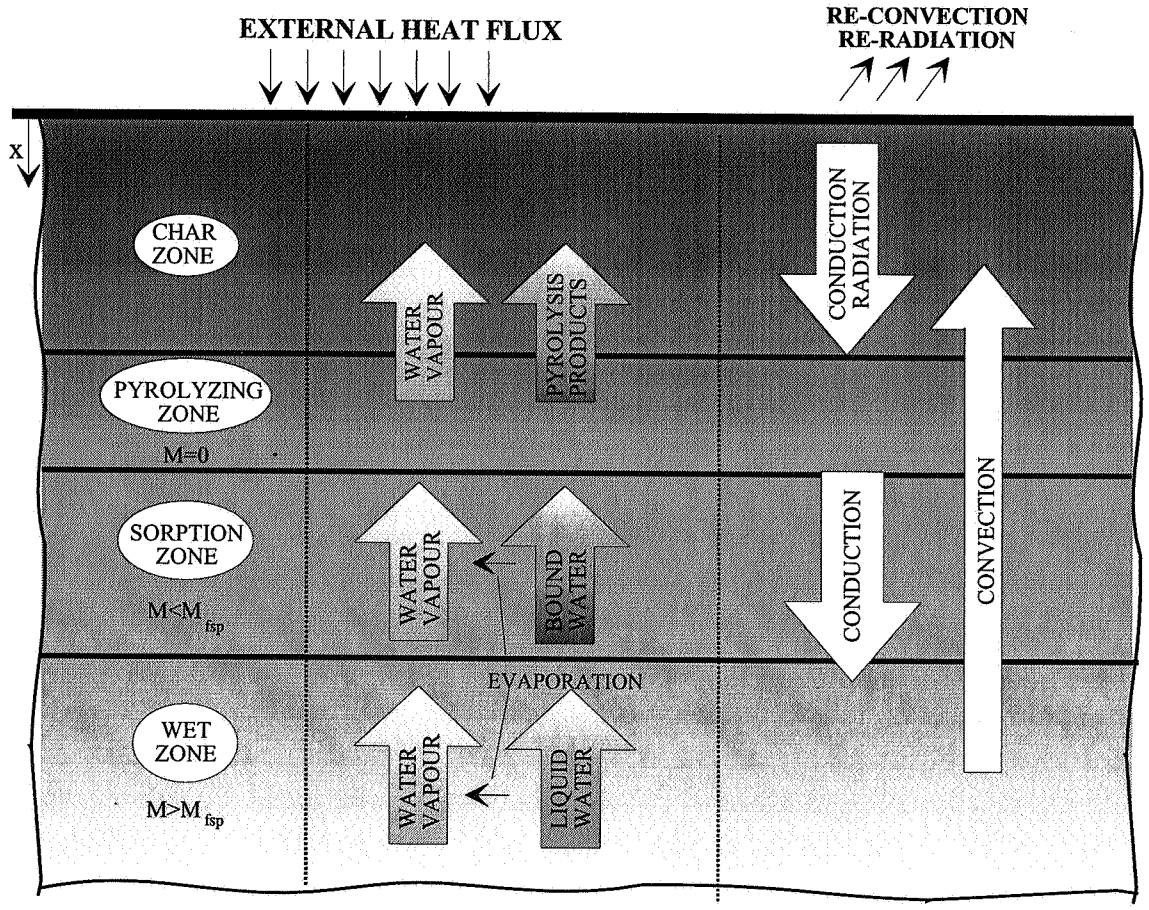

Figure 4.1 Schematic diagram of the thermal degradation process

As time proceeds, the solid reaches the temperature at which the thermal decomposition takes place at the surface, forming a pyrolysing zone. After a certain period the pyrolysing solid losses all of its volatiles and the pyrolysing zone propagates slowly into the interior of the solid, leaving behind a thermally insulating layer of char. As volatiles (tar, water vapour and gases) from the pyrolysis and water vapour formed during drying in the interior flow out through this high temperature char layer, secondary reactions may occur both homogeneously and heterogeneously. Homogeneously in the gas phase where the heavy tar components crack into lighter hydrocarbons and heterogeneously, which can be endo-/exothermic char gasification/combustion reactions of the oxygen-rich part of the volatiles. Wood loses up to 80% of its mass during the pyrolysis and its quite obvious that this leads to changes in the physical structure such as internal shrinkage, surface recession and formation of surface fissures. If oxygen is available at the surface, oxidation reactions of the volatiles leads to flaming

combustion while char-oxidation leads to smouldering or glowing combustion. Hence, the thermal degradation of wood involves the interaction in a porous media of heat and mass transfer with chemical reactions, where heat is transported by conduction, convection and radiation and mass transfer is driven by pressure and concentration gradients. The simulation of these processes involves the simultaneous solution of the partial differential, conservation equations for mass, energy and momentum with kinetic expressions describing the rate of reaction.

A lot of effort has been made through the years both experimentally and theoretically in attempt to better understand the complex mechanisms interacting in the thermal degradation of "thermally thick" particles of wood and related substances. However, the driving force for doing such research have been somewhat different. Some have developed models for use in the field of fire prevention for studying ignition [Bamford *et al.* (1946)], flame spread [Atreya (1983)] or fires in loadbearing building structures [Fredlund (1988)]. These have used very simple, one-step global expressions for the chemical reactions. Other have developed models to study the effect of different process-parameters on the product composition such as tar-/gas-/char-yields in attempt to establish guidelines for optimizing conversion processes [Chan (1983), Di Blasi (1993a)]. In this case, more complex reaction schemes including parallel, consecutive and/or competitive reactions have been used for the chemical kinetics. What is common for all the models independent of purpose and reaction scheme employed is that the solution of partial differential equations for heat and mass transfer requires some sort of numerical treatment. Through the years, the modeller has often been limited by the access to modern computerized numerical solution techniques, and very simple models which offer analytical solutions have been developed. However, todays computers and numerical solvers have allowed the development of more complex and accurate models. In the following section, some of the work done within this field will be reviewed. This is an extraction of a more extensive review given in Grønli (1995). The objective of this review is to present the main features in the development rather than in detail describe all the equations used. Simplifying assumptions often employed by the modellers are listed in Table 4.1.

Table 4.1 Simplifying assumptions used by the modellers

(A1)	No shrinkage and cracks of the solid
(A2)	No heat transfer by convection within the solid matrix
(A3)	No heat transfer by radiation within the solid matrix
(A4)	Local thermal equilibrium between the solid and gas phase
(A5)	Constant thermo-physical properties (specific heat, thermal conductivity etc)
(A6)	Instantaneous outflow of gas species from the solid matrix
(A7)	No secondary reactions
(A8)	No moisture effect

By discussing literature work it will be referred to assumption (A1) to (A8) in this table. The thermo-physical properties and kinetic data used by the modellers will be presented separately in later sub-sections.

4.2 REVIEW OF RELATED LITERATURE

Bamford *et al.* (1946) in their study of spontaneous ignition and subsequent burning of wood, were the first to construct and utilize a mathematical model for comparison with experimental results. In their experiments, sheets of deal wood 23 cm square and 2 to 4 cm thick placed in a vertical position, were exposed on both sides to gas-flames from batswing burners. Temperatures in the centre of the specimen were measured by thermocouples. By assuming (A1) to (A8), they suggested that the transient temperature response could be described by a one-dimensional heat conduction equation with a source term to account for the heat of decomposition. The rate of decomposition was described by a first order Arrhenius equation. As part of the same study, a numerical technique was developed by Crank and Nicholson to solve the set of differential equations. Various values for the activation energy and frequency factor were tried until an acceptable fit to the data was obtained. The heat of reaction was believed to be exothermic due to the sudden rise in temperature observed. The calculations gave temperature and density profiles and mass flux histories. They predicted that a self-sustainable flame will be established if the mass flux from the wood surface is at least $2.5 \cdot 10^{-7}$ kg/m^{2}s. The only experimental data available for comparison was the temperature history at the centreline of the sample. The calculated temperature response was predicted with good accuracy, considering the simplicity of the model.

In **Roberts and Clough's (1963)** experiments, cylinders of beech approximately 2 cm in diameter and 15 cm long were heated radially in a furnace at temperatures between 275 and 435°C. The temperature at the surface and inside the cylinders were measured by thermocouples at six different positions. The furnace was sealed, except for an opening for a balance arm to which the sample was attached, and inlet and outlet ports for purge gas (nitrogen) flow. Their experimental results showed that the mass loss vs time data depended significantly on the heating conditions and that the centre temperature exceeded the surface temperature. This was believed to be due to exothermic reactions inside the sample. A first order Arrhenius equation was fitted to the weight-loss data to calculate the kinetic parameters. With assumption (A1) to (A8), a transient, one-dimensional heat conduction equation with a source term derived in cylindrical coordinates was used together with experimental data to estimate the heat of reaction in different annulus inside the cylinders. The low temperature experiments showed a systematic increase in heat of reaction with increasing distance from

the centre and out to the surface. This was assumed to be due to increasing residence time and secondary (exothermic) reactions catalyzed by the solid residue of the volatiles when they were transported from the centre of the cylinder and out to the surface.

In addition to weight-loss, centre and surface temperature measurements, **Tinney (1965)** measured the centre pressure during the thermal degradation of small oven-dried white-fir cylinders (D≈0.6-1.3 cm L≈13 cm). The pre-dried cylinders were horizontally inserted into a preheated furnace, which was kept at a constant temperature in the range of 300-650°C. At furnace temperatures below 350°C, the exothermic heat of reaction did not contribute significantly to the centre temperature until several minutes after exposure. During this time, nearly 60% of the weight of the dowel had been consumed. At higher furnace temperatures, the centre temperature rose rapidly to well beyond the furnace temperatures, indicating significant exothermic heat generation. The experiments on centre-pressure revealed an interesting correlation between flaming, centre-pressure and structural-failure. At furnace temperatures below 350°C, there was no visible flaming. The centre pressure rose to an average value of 14 kPa. After a while the surface cracked, longitudinal channels were developed in the interior and the centre pressure dropped back to zero. At higher temperatures, jets of flame were observed at the surface while the centre pressure rose rapidly to a peak value of 28 kPa. Suddenly structural failures was developed and the pressure dropped quickly back to zero.

Blackshear and Kanury (1965, 1967) made detailed experimental studies to evaluate the temperature and density distribution inside a burning specimen. Cylinders of α-cellulose, 3.5 cm in diameter, was uniformly heated around its radial surface by a rotating copper tube. Thermocouples were employed at varying levels beneath and on the surface to measure the temperature-time histories. Mass evolution was measured from the change in density determined from successive X-ray photographs and by continuously weighing the sample. From the temperature-time profiles they observed that the temperature within the cellulose tends to plateau, first at about 125°C and later at about 375°C, indicating apparent sinks of energy at these two stages. The plateau at 125°C was assumed to be due to evaporation of water, and the reduced slope near 375°C was associated with the endothermic pyrolysis reaction. Beyond 400°C the rise in temperature was very steep indicating a source of energy. Low temperature experiments permitted the determination of the thermal diffusivity from the internal temperature histories, and was used to predict the local heat source and sink strengths within the specimen in the same manner as Roberts and Clough (1963). By graphing the heat evolution as a function of radius and temperature, they made the following two observations. I) For most of the reactions which occurred in the interior of the sample, the heat of pyrolysis was endothermic. It was only for those reactions which occurred at temperatures higher than 400°C that the heat of pyrolysis was exothermic. II) A strong exothermic process in the char

layer near the surface of the cylinder, which was assumed to be due to cracking reactions in the char-layer of the outflowing pyrolysis products and homogeneous oxidation reactions between the products and oxygen which had diffused into the char from the surroundings. From the density and temperature-distribution profiles they could predict apparent activation energies and pre-exponential factors at different radii inside the cylinder by assuming a first-order Arrhenius equation. The increasing activation energy from 54.4 kJ/mole in the interior layers to 92.1 kJ/mole in the exterior layers was assumed to be related to the effect of incubation and rearrangement of the molecular structure of the original α-cellulose in the interior layers leading to easier decomposition.

Panton and Rittmann (1970) were the first to incorporate variable thermo-physical properties and a multiple reaction scheme in the heat conduction problem as a slab of porous material was exposed to an external heat flux. The material making up the solid matrix was assumed to maintain a constant volume while the consuming reactions resulted in increased void volume and a decrease in the bulk density. The thermal conductivity was then assumed to be proportional to the bulk density which was decreasing during the decomposition. The reaction scheme was chosen as a model of cellulose decomposition and consisted of two competing and one consecutive reaction. However, no comparison was made with experimental data, so the model was used strictly for a parametric study.

Havens *et al.* (1972) developed a model which differed from the previous models in the way that a lumped parameter, E(T), was derived which described the internal energetics including the reactions and the variation in thermal properties. This quantity, E(T), was only a function of temperature and eliminated the need for an explicit kinetic reaction scheme. The input data required for the model could be obtained directly from DSC and TGA measurements along with measured values of the thermal conductivity. The model required the assumption of no shrinkage and no internal convection. In their experiments, a resistance wire was applied as a heat source to the interior of a hollow wooden cylinder. The measured values for temperature histories at selected radial positions, temperature profiles across the cylinder and mass loss rate coincided well with the predicted values. However, critics would argue that the model was only an empirical curve fitting of the DSC and TGA data obtained.

Kung (1972); Kung and Kalelkar (1973) returned to model with Arrhenius decomposition kinetics. The physical processes in the model included transient conduction and internal convection of volatiles, and the chemistry was described by a single global first-order reaction model. The specific heats and thermal conductivity was assumed to vary continuously from their values for the virgin wood to their values for the final char. The outward flow and convection of volatile products in the interior of the solid were accommodated by adding the term $\partial(m_g h_g)/\partial x$ to the energy equation, where m_g and h_g represented the outward mass flux

and specific enthalpy of the gases, respectively. In addition, assumption (A1), (A3-A4) and (A6-A8) was used. Model predictions were compared with the experimental results of Roberts and Clough (1963). Because complete data was not recorded, the authors were forced to estimate the rate of heat transfer to the specimen and thermo-physical properties were estimated or taken from the literature. There was good agreement between calculations and data obtained from the experiments, both for weight loss curves and temperature profiles. Roberts and Clough concluded from their work that the heat of reaction was exothermic, but by including all the essential mechanisms in the pyrolysis process, Kung and Kalelkar showed that the heat of reaction was apparently endothermic.

Kansa *et al.* (1977) were the first to include Darcy's momentum equation for the transport of the pyrolysis products through the porous medium and to account for the anisotropicity of the wood structure. Also included in the model were: radiant and convective heat transport to and from the surface; a linear functional dependence between the virgin wood and char of the system parameters (density, specific heat, thermal conductivity, porosity, permeability and molecular weight); and a first-order global Arrhenius pyrolysis reaction. The authors initially separated the energy conservation equation for the gas from that of the solid. However, by assuming local thermal equilibrium between gas and the solid, the energy conservation equations were combined into one. Like Kung (1972), they made no effort to account for moisture effects, diffusion and secondary reactions of pyrolysis products in the char. The inclusion of Darcy's momentum equation permitted calculations of pressure histories in addition to the regular temperature and density information. Calculations were compared with the experimental results of Lee *et al.* (1976), who pyrolysed cylinders of maple using a CO_2-laser as a radiant heat source. Along with gathering temperature and density data, they measured pressure at a number of locations. Kansa's calculation of the pressure history accurately predicted the magnitude of the maximum of the pressure history from Lee's experiments but failed to predict its time of occurrence. The predicted temperature profiles were in good agreement with the experiments, but the model exhibited poor quantitative prediction of mass loss histories. At heat fluxes typical of fires (about 83.7 kW/m^2), the model failed to predict correct temperature, mass loss, and pressure histories. Through a sensitivity analysis, they found the mass loss rate to be fairly insensitive to changes in permeability and heat capacity, but much more sensitive to heat of reaction and thermal conductivity of the char. The authors recommended: inclusion of a more complex multistep reaction scheme similar to that proposed by Panton and Rittmann (1970) to account for secondary reactions of volatiles in the char-zone and condensation of vapour in the colder zones; moisture effects; and shrinkage in the next generation of mathematical models.

Saastamoinen and Aho (1984) presented a mathematical model for the simultaneous drying and pyrolysis of single particles and pellets made of biomass. The model included assumption

(A1), (A4), (A6), (A7). Moisture transfer in the liquid phase was not considered. The pyrolysis was assumed to be controlled by diffusion of heat, with negligible effects of chemical kinetics, and as Havens *et al.* (1972) they did not apply any Arrhenius expression for the pyrolysis. The authors pointed out that the most common used one step first order reaction scheme is physically incorrect for larger particles since a local point inside the particle cannot "know" in advance its final density that depends on the temperature history. Another reason for not using any Arrhenius expression for the pyrolysis was the disagreement and uncertainties in reported values for the activation energy and frequency factor. The equilibrium density $\rho_s(T)$ was described by a temperature dependent function: $e(T) = \rho_s(T)/\rho_{s0}$, which was found experimentally for different materials by using a thermobalance. By using this approach, the local solid density was uniquely defined by the local temperature according to the measured equilibrium curve $\rho_s(T) = \rho_{s0}e(T)$, and the local generation of volatiles or the local sink of the solid matter could be expressed as $\partial\rho_s/\partial t = -\rho_{s0}(de(T)/dT)(\partial T/\partial t)$. Evaporation of liquid water, pyrolysis and heat storage were all approximated as phase change processes in the numerical treatment. The idea of these approximations was that instead of calculating the temperature distribution as a function of time, the locations of successive isotherms could be calculated as a function of time. These isotherms or moving boundaries were chosen in advance with a suitable interval, i.e. one moving core where the evaporation of liquid water takes place (T=100°C) and several moving cores where the generation of pyrolysis products takes place (T=200.....500°C). The energy equation could then be separated into boundary conditions for the moving cores and equations that were valid between the moving cores. These equations were solved numerically, and the following transients could be predicted: temperature, moisture, and density distribution inside the particle; the local generation of water vapour and volatiles inside the particle; and the flow rate of water vapour and volatiles from the particle surface.

A more complex multistep reaction scheme was included in the mathematical model of **Chan *et al.* (1985)**. In their experiments, one face of a uniform and well-characterized 1 cm-diameter cylinder of biomass (wood, compressed sawdust, cellulose or lignin) was radiatively heated in a single-particle Pyrex reactor. A variable-power xenon arc lamp capable of combustion level heat fluxes was used as a heat source. The progress of the temperature front was continuously monitored by three thermocouples located 2, 4 and 6 mm from the surface. The surface temperature was measured with an infrared pyrometer. Density profiles along the length of the pellet were taken intermittently by X-ray photos. Outflowing volatiles were rapidly quenched and collected in a cold trap where water and tars were analyzed in detail as a single time-integrated sample. Uncondensed gases were analyzed by using gas chromatography. Thus instantaneous density, four temperature-profiles and numerous compositions as functions of time (only batch sample of tar) were available for validation of the mathematical model. In order to study variable effects on devolatilization, the external heat flux (83.6, 167.2

and 250.8 kW/m^2), pellet length (0.5, 1.0 and 1.5 cm) and wood grain orientation relative to the heat flux, were systematically varied through their experiments. The mathematical model derived included assumption (A1), (A4), (A6) and (A7). One of the most important contributions of this model was the inclusion of a char forming reaction. Unlike the previous models where a constant char yield had been assumed, this model was able to predict the char yield under various pyrolysis conditions throughout the length of the pellet. The model divided the devolatilization into a gas, tar and char forming reaction and the kinetic scheme included three parallel and one consecutive reaction which all were of Arrhenius type. Desorption of water was treated as an additional Arrhenius reaction. Predicted temperature profiles, mass flux of non-condensable gases and ultimate yields of char, gas and tar, were in good agreement with the results obtained from the experiments.

A more extensive examination of the moisture evaporation was given by **Fredlund (1988)**. The main objective of his work was to calculate the fire resistance of building materials on the basis of analytical treatment and develop a model for simulating heat and mass transfer inside constructions of timber exposed to fire conditions. The original moist wood was divided into four phases: active wood which could decompose to form volatiles; char which could be oxidized at the surface; water in the liquid phase and water vapour. A single first order Arrhenius equation was assumed for the pyrolysis reaction while an expression for the evaporation of liquid water was derived from the saturation vapour pressure. The energy transfer inside the specimen was assumed to occur by conduction in the solid part, and by convection due to outflow of volatile pyrolysis products and water vapour in the pore system. Darcy's momentum equation was used to calculate the transport of water vapour and volatiles, while mass transfer in the liquid phase was neglected. The thermal conductivity was given as a function of moisture content, density and temperature for the wood and a function of density and temperature for the char. Specific heat of the solid and gas species was given as a function of temperature and the variation in permeability was a function of the local density. In addition, Fredlund included an Arrhenius type expression for the surface recession due to char-oxidation. Thus, time and space histories of temperature, total pressure, density and the moisture distribution could be predicted. In order to verify the model, cubes of 13.5 cm sides were horizontally exposed by a cone heater with constant heat-fluxes of 78 to 90 kW/m^2. The specimens were made of pine, spruce and chipboard, conditioned to an initial moisture content of 0.0%, 12.0% and 24.0% (dry basis). The temperature and pressure history was measured at 10 and 6 different depths, respectively. The density was measured by a gamma ray assembly, the total weight loss by a balance, and the evolved gases by conventional gas-analysis equipment. The length of the experiments was approximately 60 minutes, with all the above quantities being recorded once every two minutes. One-dimensional simulation evidenced that the distribution of temperature in the specimens was very well predicted both for moist and dry material. It was seen from the experiments that the internal pressure build-

up was very sensitive to cracking in the char layer. This prevented the model from giving good prediction of the pressure distribution. The model gave a satisfactory description of the penetration of the char-layer, the recession of the surface and the total reduction in weight.

Alves and Figueiredo (1989) assumed the drying rate to be controlled by equilibrium between liquid water and water vapour. By neglecting bound and liquid water movement, no diffusion or pressure driven flow of water vapour, the transport mechanism for the vapour and pyrolysis products was assumed to be due to temperature driven convection. These simplifying assumptions reduced the model validity to high temperature drying, only. A "moisture boiling point", T_b, was defined as the temperature at which the liquid water is in equilibrium with water vapour at atmospheric pressure. At moisture contents below 14% and temperatures above 100°C, a third-degree polynomial was derived for the moisture boiling point, $T_b(M)$. For moisture contents above 14%, the moisture boiling point was assumed to be constant T_b=100°C. Based on these simplifying assumptions, three zones in the drying-pyrolysing solid were defined: I) the inner most part of the solid where the temperature is below T_b. By assuming constant moisture content in this zone, the solid temperature could be determined by a simple heat balance; II) the "drying" zone where the temperature has reached T_b and there exist equilibrium between the liquid water and water vapour. The temperature in this region could be determined by using the equation for $T_b(M)$, and the heat balance gave the amount of water which was evaporated; III) the outer most part of the particle, where the solid is completely dry and the temperature is above T_b. The solid temperature is again determined by a heat balance and the temperature can be high enough for pyrolysis to occur. At any point inside the particle, pyrolysis reactions and reaction kinetics were assumed not to depend on the previous drying history. The reaction scheme and corresponding kinetics were experimentally determined for very small samples of dry pine wood sawdust with negligible internal temperature gradients. Six independent parallel reactions were identified and used in the pyrolysis model. By assuming thermal equilibrium between the gases and solid matrix, heat accumulation, conduction through the solid, convection of volatile gases and water vapour, chemical reaction and water evaporation, a proper energy equation together with initial and boundary was derived. The pine wood thermal conductivity was experimentally measured for moisture contents up to 66% and temperatures between 35-118°C. It was found not to be sensitive to temperature in this range. The char thermal conductivity was measured in the range of 30 to 220°C. The thermal conductivity and specific heat of the pyrolysing solid were interpolated between those of wood and char. In order to verify the model, thermogravimetric experiments were carried out inside a vertical cylindrical refractory steel reactor 50 mm in diameter surrounded by a furnace. The temperature-controlled reactor was continuously swept with 3 l/min of pure nitrogen, and the samples used were cylinders of pine wood of variable diameter and length at least 3 times greater than the diameter. The furnace was heated up to the desired temperature and the sample, suspended from a balance, was quickly lowered to

the constant temperature zone of the reactor. Three sets of experiments were performed: 1) pyrolysis of dry-wood cylinders of about 18.0 mm in diameter at furnace temperatures between 300-786°C; 2) high-temperature drying at 150°C of wood cylinders with moisture contents between 0-60% and diameters between 7.5-18.5 mm; 3) pyrolysis of moist cylinders of about 18.5 mm in diameter in the temperature range between 298-780°C. Good agreement was found between simulated and experimentally measured weight loss curves, both for dry and wet wood pyrolysis without any parameter optimization. The effect of some of the model simplifications was apparent in the simulation of the drying curves. Since the model had to wait for the solid to reach the "boiling temperature" before drying could start, there was a delay in the beginning of the simulations. In reality, drying starts at time zero since water can reach the particles outer surface by several other mechanisms not described in the model.

The effect of secondary reactions were also included in the model of **Di Blasi and Russo (1994)**. The authors developed a one-dimensional model for the thermal degradation of dry wood in an inert atmosphere subjected one side to a radiative heat flux. In addition to (A1) and (A4) the following assumptions were made. No diffusive transport of volatile species generated during the reaction and no condensation of volatile species in the virgin solid region. The thermal degradation was assumed to follow a competitive reaction scheme to form gas, tar and char. The tar could further go through secondary reactions in the hot char-layer to either form lighter hydrocarbons or more char through a repolymerization step. All the reactions were assumed to follow an Arrhenius type expression and Darcy's law for the transport of gases and tars through the porous wood was assumed. Radiative heat transfer inside the solid was described through an radiative contribution term to the effective thermal conductivity. In addition, a linear variation of the conductive contribution of the effective thermal conductivity and permeability between the virgin wood and the char was assumed. The simulations were compared with the experimental results of Lee *et al.* (1976) showing fairly good agreement for the total gas production and for the temperature and pressure spatial distributions in the first period of the experiments. For longer times, the agreement changed only to qualitative for the temperature distribution and was completely lost for the pressure. The disagreement was assumed to be due to the structural changes (shrinkage, crack-formation and surface recession) observed in the experiments which were not accounted for in the model. In addition, the large uncertainties in the kinetic data and bad knowledge about the thermo-physical properties made an qualitative comparison very difficult.

CONCLUDING REMARKS:

The chemical kinetics of the thermal degradation of "thermally thick" samples made of wood and related substances have in most cases been modeled according to a one-step, first order Arrhenius reaction [Bamford *et al.* (1946), Roberts and Clough (1963), Tinney (1965), Kung (1972), Kansa *et al.* (1977), Fredlund (1988)]. Among the shortcomings of employing such simple kinetics are that only total volatiles are predicted, not how they are distributed among combustible and non-combustible gases and the inability to account for the variation in char-yield dependence of operating conditions. Another approach that has been quite successfully used to model the chemical kinetics is the so-called lumped parameter approach, where the reaction products have been grouped into classes of products such as non-condensable gases, condensable gases (tars) and char [Chan *et al.* (1985) and Di Blasi and Russo (1994)].

A different degree of approximations have also been used in modelling of the physical processes, with constant thermo-physical properties and neglecting the convective transport of heat [Bamford *et al.* (1946), Roberts and Clough (1963), Tinney (1965), Panton and Rittmann (1971)] and quasi steady-state approximation for the gas-phase with no mass transfer within the porous structure [Kung (1972), Chan *et al.* (1985)]. With the exception of Fredlund (1988), all the modellers have assumed no shrinkage and surface recession.

The effects of moisture and drying on the thermal degradation have either been neglected or treated in a very simple way. Chan *et al.* (1985) described the drying process as an additional chemical reaction. Saastamoinen and Aho (1984) and Alves and Figueiredo (1989) inserted a boiling temperature at which the evaporation of moisture took place while Fredlund (1988) described the evaporation by a local moisture-vapour equilibrium relation. None of them have included the transport of bound and liquid water.

A quantitative comparison between model predictions and experimental data has proved to be rather difficult because of:

- The widely varying property values (solid density, specific heat, thermal conductivity, porosity, permeability) among the different wood species used in the experiments.
- The large uncertainty on the properties of the charred and partially charred solid including structural failure and shrinkage.
- The different chemical composition of wood, i.e. the different percentage of cellulose, hemicellulose and lignin, the different amount and composition of inorganic matter which leads to different yields of primary pyrolysis products.
- The high uncertainty on the kinetic model and rate constants to be used for semi-global reaction mechanisms.

4.3 A MATHEMATICAL MODEL FOR DRYING AND PYROLYSIS OF WOOD

As pointed out in the foregoing discussion, the effects of moisture on the thermal degradation of biomass has either been neglected or treated in a very simple and often un-physical way. Hence, the main objective of this modelling work has been to focus on the mechanisms of drying, i.e. evaporation/desorption and transport of moisture, which will occur prior to and simultaneously with the pyrolysis process. Among the work related to this question, one have to cite the detailed theoretical description of drying in non-hygroscopic porous media given by Whitaker (1967, 1969, 1977), and the modelling and experimental work of Spolek (1981), Ouelhazi *et al.* (1992) and Perre *and co-workers* (1990, 1991, 1993).

In the analysis of drying and pyrolysis of wood one is interested in knowing how the operational conditions (temperature/heating rate) and moisture content influences the internal heat and mass transfer processes which again controls the release of products (tar, gases, char) and the total time of conversion. In order to investigate these quantities, appropriate conservation equations for mass and energy has to be derived. Moist wood contains four different phases: a solid, bound water, liquid water and a gas mixture phase (initially water vapour and air), which means that each phase must be identified and analyzed. This can be done by assuming that every portion of each phase constitutes a continuum within the local boundaries that separate it from the neighbouring phases. Within this domain, the continuum conservation laws must be satisfied. At the phase interfaces, certain boundary conditions must be met. In Whitaker (1977), a complete set of differential point equations for each phase as well as interfacial boundary conditions has been derived. If the wood structure is known, the boundaries of each phase can be identified so that for given initial conditions a solution to the equations can theoretically be generated. However, the complicated geometrical structure of wood makes it impossible to keep track of all surfaces at all times. A more desirable set of equations would be one that is valid everywhere within the wood structure regardless of position. This can be done by volume averaging the conservation equations over a representative elementary volume that contains all phases, as illustrated in Figure 4.2. One pass from a microscopic view where the size of the representative volume is small with regard to the pores, to a macroscopic view where the size of the representative volume is large with regard to the pores.

There are three types of averages that are useful in the analysis of transport phenomena in porous media. The *spatial average* of a quantity φ defined everywhere in space is averaged over the total volume V containing all phases. This average is defined by:

$$<\varphi> = \frac{1}{V}\int_{V} \varphi \, dV \tag{4.1}$$

If the average of a quantity φ is solely associated with a single phase γ, then we define the *phase average* as:

$$<\varphi> = \frac{1}{V}\int_{V_\gamma} \varphi \, dV \tag{4.2}$$

where V_γ is the volume occupied by phase γ in V. An *intrinsic phase average* of a quantity φ, which represents the averaged value inside phase γ is also defined:

$$<\varphi>^\gamma = \frac{1}{V_\gamma}\int_{V_\gamma} \varphi \, dV \tag{4.3}$$

The *phase average* quantity and *intrinsic phase average* quantity are related by:

$$<\varphi> = \varepsilon_\gamma <\varphi>^\gamma \tag{4.4}$$

where ε_γ is the volume fraction occupied by phase γ:

$$\varepsilon_\gamma = \frac{V_\gamma}{V} \tag{4.5}$$

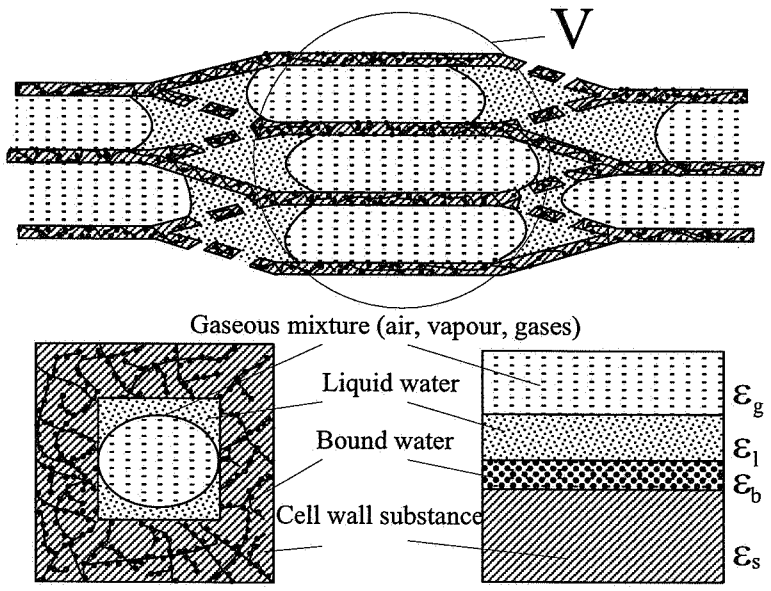

Figure 4.2 Averaging volume (V) and volume fractions of the different phases found in wood.

The total volume V of moist wood is made of the volume of each phase:

$$V_s + V_l + V_b + V_g = V \tag{4.6}$$

where subscripts s, l, b and g denotes solid, liquid, bound and gas phase, respectively. The volume fraction of each phase can then be written as follows:

$$\varepsilon_s = V_s/V \quad [m_s^3/m^3] \qquad \varepsilon_l = V_l/V \quad [m_l^3/m^3]$$
$$\varepsilon_b = V_b/V \quad [m_b^3/m^3] \qquad \varepsilon_g = V_g/V \quad [m_g^3/m^3]$$

so that

$$\varepsilon_s + \varepsilon_l + \varepsilon_b + \varepsilon_g = 1 \tag{4.7}$$

The mass concentrations or densities represented in moist wood can either be given as *intrinsic phase average* densities ($<\rho_i>^\gamma$), or *phase average* densities ($<\rho_i>$). Between these densities the following relations exist:

$$<\rho_i> = \varepsilon_\gamma <\rho_i>^\gamma , \qquad <\rho_\gamma> = \varepsilon_\gamma <\rho_\gamma>^\gamma \tag{4.8}$$

from which the following densities can be derived:

Solid:

$<\rho_s>^s$	kg of solid/ volume of solid phase	$[kg/m_s^3]$
$<\rho_s> = \varepsilon_s<\rho_s>^s$	kg of solid/ total volume	$[kg/m^3]$

Liquid water:

$<\rho_l>^l$	kg of liquid water/ volume of liquid phase	$[kg/m_l^3]$
$<\rho_l> = \varepsilon_l<\rho_l>^l$	kg of liquid water/ total volume	$[kg/m^3]$

Bound water:

$<\rho_b>^b$	kg of bound water/ volume of bound phase	$[kg/m_b^3]$
$<\rho_b> = \varepsilon_b<\rho_b>^b$	kg of bound water/ total volume	$[kg/m^3]$

Gas mixture:

$<\rho_g>^g$	kg of gas mixture/ volume of gas phase	$[kg/m_g^3]$
$<\rho_g> = \varepsilon_g<\rho_g>^g$	kg of gas mixture/ total volume	$[kg/m^3]$

Water vapour:

$<\rho_v>^g$	kg of water vapour/ volume of gas phase	$[kg/m_g^3]$
$<\rho_v> = \varepsilon_g<\rho_v>^g$	kg of vapour/ total volume	$[kg/m^3]$

Gas species (gases, tar):

$<\rho_i>^g$	kg of gas species *i*/ volume of gas phase	$[kg/m_g^3]$
$<\rho_i> = \varepsilon_g<\rho_i>^g$	kg of gas species *i*/ total volume	$[kg/m^3]$

Hence, the volume fractions of the dry solid, liquid water and bound water is given by the following expressions:

$$\varepsilon_s = \frac{\langle \rho_s \rangle}{\langle \rho_s \rangle^s}, \qquad \varepsilon_l = \frac{\langle \rho_l \rangle}{\langle \rho_l \rangle^l}, \qquad \varepsilon_b = \frac{\langle \rho_b \rangle}{\langle \rho_b \rangle^b} \tag{4.9}$$

By substituting equation (4.9) into equation (4.7), the following expression yields the void, or the volume fraction occupied by the gas mixture in moist wood:

$$\varepsilon_g = 1 - \left(\frac{\langle \rho_s \rangle}{\langle \rho_s \rangle^s} + \frac{\langle \rho_l \rangle}{\langle \rho_l \rangle^l} + \frac{\langle \rho_b \rangle}{\langle \rho_b \rangle^b} \right) \tag{4.10}$$

where the intrinsic phase average density or specific density of the cell wall substance ($\langle \rho_s \rangle^s$), liquid water ($\langle \rho_l \rangle^l$) and bound water ($\langle \rho_b \rangle^b$) has to be specified.

The specific density of oven-dry cell-wall substance has been measured using displacement methods by many investigators with the values obtained being influenced by the properties of the displacing fluid (water, benzene, helium, etc). By using helium as a displacing fluid, the specific densities of birch and spruce analyzed in Chapter 2.8 were 1450 kg/m^3 and 1390 kg/m^3, respectively. Siau (1984) proposed that an average value of $\langle \rho_s \rangle^s$=1500 kg/m$_s^3$ can be used for most wood species. Stamm and Seborg (1934) measured the specific density of cell wall substance at different moisture content from which they calculated the specific density of bound water over the hygroscopic range. The values extended from $\langle \rho_b \rangle^b$=1113 kg/m$_b^3$ at fiber saturation point (M_{fsp}) to about $\langle \rho_b \rangle^b$=1300 kg/m$_b^3$ under oven-dry conditions. For simplicity, an average value of $\langle \rho_l \rangle^l$=1000 kg/m$_l^3$ will be used for the liquid water in this model, and the specific density of bound water will be approximated by the liquid water density $\langle \rho_b \rangle^b \approx \langle \rho_l \rangle^l$.

After having identified the phases and found the connection between them, the mass conservation equation for the phases together with the energy conservation equation will be presented. A more detailed description of the progress in the deduction of the equations, the numerical treatment and the simulation program, FLOWPOR, is given in Melaaen and Grønli (1994); Melaaen (1994); Melaaen (1996); and Melaaen and Grønli (1996). The simulation program has been made general so it can simulate pure drying, pure pyrolysis and problems where both drying and pyrolysis occur. During drying (below M_{fsp}) and pyrolysis the wood will shrink, however, this is not accounted for in the model. In addition, the formation of cracks and surface recession is not considered.

4.3.1 CONSERVATION EQUATIONS

The transport of fluids through wood may be divided in two main classifications. The first is the bulk flow through the interconnected voids of the wood structure under the influence of a static or capillary pressure gradient. This is sometimes designated as momentum transfer because it can be attributed to a momentum-concentration gradient. The magnitude of the bulk flow is determined by its permeability, which is a measure of the ease which fluids are transported through a porous medium under the influence of a pressure gradient (Darcy's law). If there are two fluids, such as gas and liquid flowing simultaneously, then each fluid has its own, so-called, relative permeability which are dependent on the relative saturation of each fluids. The second transport mechanism is diffusion consisting of two types, intergas diffusion between the different gas species in the gas mixture phase and bound water diffusion which takes place within the cell walls of wood. Hence, the following mass and energy conservation equations can be derived.

Mass conservation of solid substance:

$$\frac{\partial}{\partial t}\langle \rho_s \rangle = \langle \dot{w}_s \rangle \tag{4.11}$$

where $\langle \dot{w}_s \rangle$ is the rate of consumption or production of solid matter. The solid wood is consumed while char is produced during the thermal degradation. The chemical reaction scheme describing the thermal decomposition will be given in the next subsection.

Mass conservation of liquid water:

$$\frac{\partial}{\partial t}\langle \rho_l \rangle + \frac{\partial}{\partial x}(\langle \rho_l v_l \rangle) = \langle \dot{w}_l \rangle \qquad \langle \rho_l v_l \rangle = \langle \rho_l \rangle^l \langle v_l \rangle \tag{4.12}$$

where the first term accounts for the accumulation, the second term accounts for the transport and the third therm accounts for the rate of evaporation or condensation of the liquid water. The superficial velocity of liquid water is given by Darcy's law:

$$\langle v_l \rangle = - \frac{K_l K_r^l}{\mu_l} \frac{\partial}{\partial x} \langle P_l \rangle^l \tag{4.13}$$

where the effect of body forces (gravity) has been neglected. K_l, K_r^l and μ_l are the intrinsic permeability, relative permeability and dynamic viscosity for the liquid phase, respectively. $\langle P_l \rangle^l$ is the liquid pressure which is connected to the gaseous pressure by capillarity:

$$\langle P_l \rangle^l = \langle P_g \rangle^g - P_C \,, \qquad P_C \sim P_C(M_l, T) \tag{4.14}$$

Mass conservation of bound water:

$$\frac{\partial}{\partial t}<\rho_b> + \frac{\partial}{\partial x}(<\rho_b v_b>) = <\dot{w}_b> \tag{4.15}$$

where $<\dot{w}_b>$ is the rate of desorption or adsorption of bound water and:

$$<\rho_b v_b> = -<\rho_{SD}> D_b \frac{\partial}{\partial x}\frac{<\rho_b>}{<\rho_{SD}>}, \qquad D_b \sim D_b(M_b, T) \tag{4.16}$$

is the average mass flux of bound water which is modeled as a diffusion process.

Mass conservation of component *i* in the gas mixture phase:

$$\frac{\partial}{\partial t}(\varepsilon_g <\rho_i>^g) + \frac{\partial}{\partial x}(<\rho_i v_i>) = <\dot{w}_i>, \qquad <\rho_i v_i> = <\rho_i>^g <v_g> + <\rho_i U_i> \tag{4.17}$$

where $<\dot{w}_i>$ is the rate of production or consumption of component *i*, i.e. water vapour, tar and gases formed during drying and pyrolysis. The superficial velocity of the gas mixture is given by:

$$<v_g> = -\frac{K_g K_r^g}{\mu_g}\frac{\partial}{\partial x}<P_g>^g \tag{4.18}$$

where K_g, K_r^g and μ_g are the intrinsic permeability, relative permeability and dynamic viscosity of the gas mixture, respectively. Binary diffusion is assumed and the diffusive flux of component *i* in the gas mixture phase is given by:

$$<\rho_i U_i> = -<\rho_g>^g D_{eff}\frac{\partial}{\partial x}\left(\frac{<\rho_i>^g}{<\rho_g>^g}\right) \tag{4.19}$$

where D_{eff} is an effective diffusion coefficient.

Energy conservation:

By assuming thermal equilibrium between the solid, bound water, liquid water and gas mixture phase and neglecting dispersion, the energy conservation equation is given by:

$$\begin{aligned}&\left(<\rho_s>C_{P,s} + <\rho_l>C_{P,l} + <\rho_b>C_{P,l} + \varepsilon_g <\rho_g>^g C_{P,g}\right)\frac{\partial <T>}{\partial t}\\ &+\left(<\rho_l v_l>C_{P,l} + <\rho_b v_b>C_{P,l} + <\rho_g v_g>C_{P,g} + \sum_{i=1}^{N_g} C_{P,i}<\rho_i U_i>\right)\frac{\partial <T>}{\partial x}\\ &= \frac{\partial}{\partial x}\left(k_{eff}\frac{\partial <T>}{\partial x}\right) - \sum_i <\dot{w}_i>\Delta h_i - <\dot{w}_v>\Delta h_v + <\rho_b v_b>\frac{\partial}{\partial x}(\Delta h_{sorp})\end{aligned} \tag{4.20}$$

The first term accounts for the accumulation of energy; the second term is the convective and diffusive heat transfer caused by moisture and volatile movement; the third term accounts for

the conductive heat transfer which is represented by an effective thermal conductivity. The last three terms accounts for the net heat of reaction due to pyrolysis reactions; the energy consumed during evaporation and desorption of liquid and bound water and the variation in heat of desorption.

4.3.2 BOUNDARY CONDITIONS

The boundary conditions presented here are implemented on the left hand side of the calculation domain. Infinity or symmetry is assumed on the right hand side. Hence, the velocities are zero and the gradients of the dependent variables are zero.

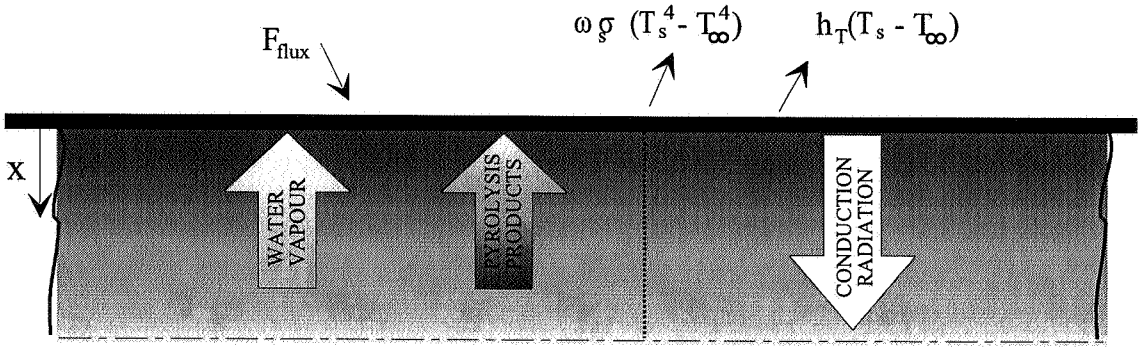

Figure 4.3 Boundary conditions used on left hand side of the calculation domain.

Energy:

The left surface is subjected to a radiative heat flux (F) which balance the convective and radiative heat losses, the inward conduction and the evaporation and desorption of liquid and bound water at the surface:

$$F_{flux} - h_T(<T_s> - <T_\infty>) - \omega_s \sigma(<T_s^4> - <T_\infty^4>) = -k_{eff}\frac{\partial <T>}{\partial x} - <\rho_l v_l>\Delta h_l - <\rho_b v_b>\Delta h_b \quad (4.21)$$

Here, subscript '∞' denotes ambient (surrounding) conditions and 's' denotes surface conditions.

Moisture:

$$-(<\rho_l v_l> + <\rho_b v_b> + <\rho_v v_v>) = h_m(<\rho_v>_s^g - <\rho_v>_\infty^g) \quad (4.22)$$

Pressure:

$$<P_g>_s^g = <P_g>_\infty^g \quad (4.23)$$

h_T and h_m are the heat and mass transfer coefficients, respectively. In addition, initial conditions for temperature, density, pressure, moisture content and velocities have to be specified. These will be discussed more thoroughly in the sub-section were the simulations are presented.

4.3.3 PYROLYSIS MODELS

As previously discussed in the reviews, different reaction schemes or kinetic models have been proposed for the thermal decomposition of biomass. In the following, some of the reaction schemes used in the modelling of "thermally thick" particles will be presented. All these reaction schemes have been implemented in the simulation program in addition to the model of independent parallel reactions described in the previous chapter. The reaction rate constants have all been modeled by an Arrhenius equation of the form:

$$k_i = A_i \exp(-E_i/RT) \tag{4.24}$$

where A_i is the pre-exponential factor and E_i is the activation energy for reaction *i*.

The most applied pyrolysis model is the one-step global model where the dry solid material (S) decomposes into volatiles (V) and char (C).

$$S \xrightarrow{k_1} V + C$$

The consumption of solid material can be written as:

$$\frac{\partial}{\partial t}\langle\rho_S\rangle = -k_1(\langle\rho_S\rangle - \langle\rho_{C\infty}\rangle) \tag{4.25}$$

The main disadvantages of this model is that: 1) the char density $\langle\rho_{C\infty}\rangle = c\langle\rho_{SD}\rangle$ is assumed constant and is not dependent on operating conditions; and 2) the term volatiles does not give any information about the distribution between tar and gases. However, if a constant distribution between tar and gases is assumed, the following source terms for the tar and gases in equation (4.17) can be used:

$$\langle\dot{w}_T\rangle = ak_1(\langle\rho_S\rangle - c\langle\rho_{SD}\rangle), \qquad \langle\dot{w}_G\rangle = (1-a)k_1(\langle\rho_S\rangle - c\langle\rho_{SD}\rangle) \tag{4.26}$$

where c and a are the stoichiometric coefficient for char and tar, respectively. As Table 4.2 shows, different values for the pre-exponential factor, activation energy and heat of reaction have been used by the modellers.

An improvement from the one-step global model with a single rate constant would be to separate the wood into it's main constituents, i.e., hemicellulose, cellulose and lignin, and assume these to decompose independently from each other. By doing so, it is possible to use the rate constants obtained from the TGA evaluation in Chapter 3. In this case, the wood is

Table 4.2 Global reaction rate constants, heats of reaction, densities and stoichiometric coefficients used in the modelling of "thermally thick" particles.

Reference	Species	A_1 [s^{-1}]	E_1 [kJ/mole]	Δh_1 [kJ/kg]	$<\rho_S>$ [kg/m^3]	c
Bamford *et al.*	deal wood	$5.3 \cdot 10^8$	138.8	- 360.0	375.0	---
Kung *et al.*	beech	$2.0 \cdot 10^3$	63.4	203.0	600.0	0.25
Kansa *et al.*	oak	$2.5 \cdot 10^4$	74.4	418.0	580.0	0.40
Atreya	maple	$2.5 \cdot 10^8$	125.0	0.0	676.0	0.24
Fredlund	pine	0.45	23.6	0.0	470.0	0.32-0.43

separated into three fractions which decompose independently from each other to form volatiles (V_i) and char (C_i). The volatiles formed from the hemicellulose, cellulose and lignin decomposition can further be separated into a tar and gas fraction by the stoichiometric coefficient b_i.

$$S = \sum_i S_i \qquad i = 1,2,3$$

$$S_i \xrightarrow{k_i} V_i + C_i$$

The consumption of solid material is then the sum of the individual consumption of component *i* according to:

$$\frac{\partial}{\partial t}<\rho_S> = \sum_i \frac{\partial}{\partial t}<\rho_{S,i}> = -\sum_i k_i(<\rho_{S,i}> - <\rho_{C\infty,i}>) \tag{4.27}$$

where c_i is the stoichiometric coefficient of char from component *i*. The rate of production of tar and gases can then be written as follows:

$$\begin{aligned} <\dot{w}_T> &= \sum_i k_i b_i (<\rho_{S,i}> - <\rho_{C\infty,i}>) \\ <\dot{w}_G> &= \sum_i k_i (1 - b_i) (<\rho_{S,i}> - <\rho_{C\infty,i}>) \end{aligned} \tag{4.28}$$

This model has, however, the same disadvantages as the one-step global model, that is, the stoichiometric coefficients have to be decided in advance, and this time not only two, but six (!) coefficients must be specified. In Table 4.3, the mean activation energy and frequency factor calculated in Chapter 3 for the decomposition of cellulose and hemicellulose are listed together with a reasonable rate constant for the lignin decomposition. a_1 to a_3 represent the mass fractions of hemicellulose, cellulose and lignin found in spruce. c_1 to c_3 represent the char fraction of each of these components, where the lignin is supposed to account for most of the char formed. The heat of reactions and the stoichiometric coefficients, b_i, for the tar fractions for the three reactions have been arbitrary chosen.

Table 4.3 Reaction rate constants, heats of reaction and stoichiometric coefficients.

Reaction *i*	Component	A_i [s^{-1}]	E_i [kJ/mole]	Δh_i [kJ/kg]	a_i	c_i	b_i
1	hemicellulose	$1.56 \cdot 10^{8}$	119.0	150.0	0.27	0.2	0.31
2	cellulose	$2.51 \cdot 10^{19}$	260.0	150.0	0.44	0.2	0.31
3	lignin	$5.01 \cdot 10^{3}$	81.0	150.0	0.29	0.5	0.31

The Broido & Shafizadeh model previously described in Chapter 3 has been included in a heat transfer problem by Wichman and Melaaen (1994) in the modelling of cellulose pyrolysis

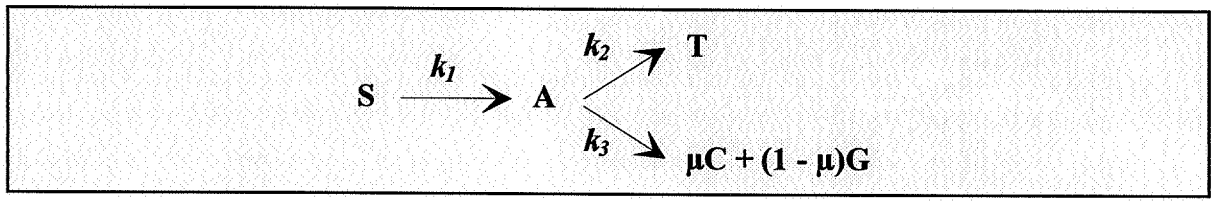

from which the following conservation equations for the solid substances can be derived:

$$\frac{\partial}{\partial t}\langle \rho_S \rangle = -k_1 \langle \rho_S \rangle \tag{4.29}$$

$$\frac{\partial}{\partial t}\langle \rho_A \rangle = k_1 \langle \rho_S \rangle - (k_2 + k_3)\langle \rho_A \rangle \tag{4.30}$$

$$\frac{\partial}{\partial t}\langle \rho_C \rangle = \mu k_3 \langle \rho_A \rangle \tag{4.31}$$

The source term in the mass conservation equations get the following form:

$$\begin{aligned} \langle \dot{w}_T \rangle &= k_2 \langle \rho_A \rangle \\ \langle \dot{w}_G \rangle &= (1 - \mu) k_3 \langle \rho_A \rangle \end{aligned} \tag{4.32}$$

The kinetic data given in Table 4.4 with a stoichiometric coefficient, μ=0.35, were determined by Bradbury *et al.* (1979) and the authors assumed the heat of reaction to be slightly endothermic for all the reactions.

Table 4.4 Reaction rate constants proposed by Bradbury *et al.* (1979).

Reaction *i*	A_i [s^{-1}]	E_i [kJ/mole]	Δh_i [kJ/kg]
1	$2.83 \cdot 10^{19}$	242.8	endothermic
2	$3.17 \cdot 10^{14}$	198.0	endothermic
3	$1.32 \cdot 10^{10}$	150.7	endothermic

The reaction scheme proposed by Chan (1983); Chan *et al.* (1985) included three parallel and one consecutive reaction. Unreacted wood reacts through three competitive paths to form char (C); primary gases (G_1) e.g. CO_2, CO and CH_4; and primary tars (T_1) e.g. phenols, levoglucosane. The primary tars can further cracks to form secondary gases (G_2) and secondary tar (T_2). This reaction scheme was further improved by Glaister (1987), to account for water production as a primary product from pyrolysis of wood. Desorption of bound water ($H_2O_{(b)}$) was modeled as an additional Arrhenius type expression.

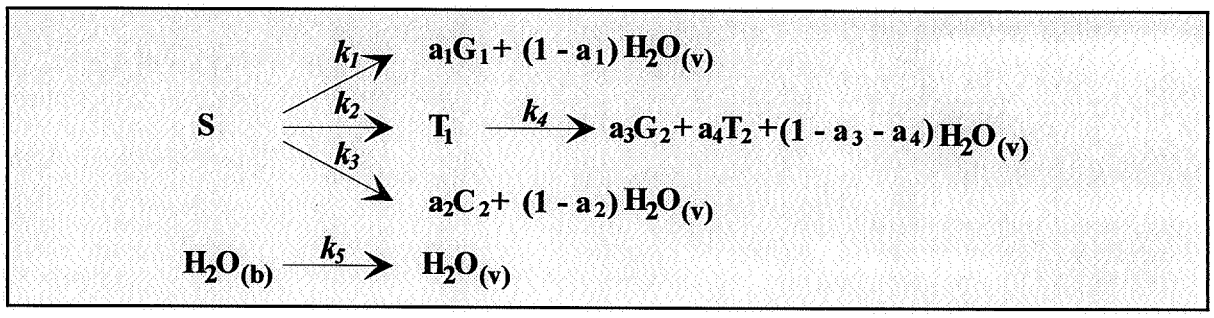

From this reaction scheme, the following conservation equations for the solid fractions can be derived:

$$\frac{\partial}{\partial t}\langle \rho_S \rangle = -(k_1 + k_2 + k_3)\langle \rho_S \rangle \tag{4.33}$$

$$\frac{\partial}{\partial t}\langle \rho_C \rangle = a_2 k_3 \langle \rho_S \rangle \tag{4.34}$$

As the tar and gases was separated into primary (T_1, G_1) and secondary (T_2, G_2) products, one conservation equation with a source term has to be derived for each of the components:

$$\langle \dot{w}_{T1} \rangle = k_2 \langle \rho_S \rangle - k_4 \varepsilon_g \langle \rho_{T1} \rangle^g \tag{4.35}$$

$$\langle \dot{w}_{T2} \rangle = a_4 k_4 \varepsilon_g \langle \rho_{T1} \rangle^g \tag{4.36}$$

$$\langle \dot{w}_{G1} \rangle = a_1 k_1 \langle \rho_S \rangle \tag{4.37}$$

$$\langle \dot{w}_{G2} \rangle = a_3 k_4 \varepsilon_g \langle \rho_{T1} \rangle^g \tag{4.38}$$

$$\langle \dot{w}_{H2O_{(v)}} \rangle = k_5 \langle \rho_{H2O_{(b)}} \rangle + (1 - a_1) k_1 \langle \rho_S \rangle + (1 - a_2) k_3 \langle \rho_S \rangle + (1 - a_3 - a_4) k_4 \varepsilon_g \langle \rho_{T1} \rangle^g \tag{4.39}$$

Glaister (1987) used the kinetic data, heat of reactions and stoichiometric coefficients listed in Table 4.5 to model the pyrolysis of lodgepole pine.

Table 4.5 Reaction rate constants, heats of reaction and stoichiometric coefficients used by Glaister (1987).

Reaction *i*	A_i [s^{-1}]	E_i [kJ/mole]	Δh_i [kJ/kg]	a_i
1	$1.3 \cdot 10^8$	140.3	209.3	0.7
2	$2.0 \cdot 10^8$	133.1	209.3	0.9
3	$1.1 \cdot 10^7$	121.4	209.3	0.65
4	$1.5 \cdot 10^6$	114.3	-2009.7	0.25
5	$4.0 \cdot 10^2$	25.1	2260.9	

Di Blasi and Russo (1994) used the model proposed by Thurner and Mann (1981) for the primary reactions, where the thermal degradation of wood was assumed to follow a competitive reaction scheme to form gases, tar and char. In addition, Di Blasi and Russo included a competitive secondary reaction step for the tar species, which could either lead to the formation of lighter hydrocarbons (gases) through a cracking reaction or to the formation of char through a repolymerization process:

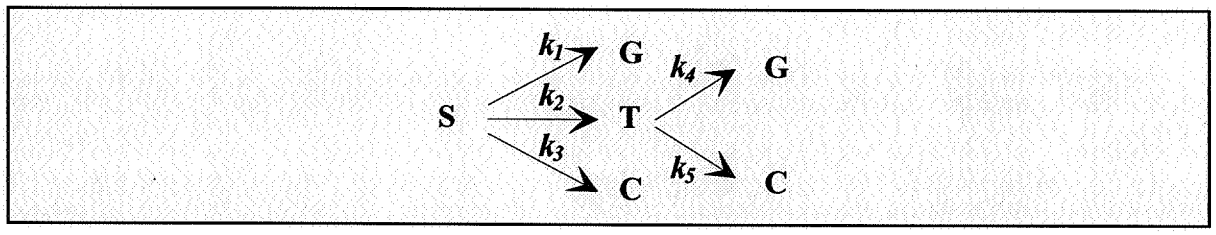

The following conservation equations for the solid fraction can be derived:

$$\frac{\partial}{\partial t}\langle \rho_S \rangle = -(k_1 + k_2 + k_3)\langle \rho_S \rangle \tag{4.40}$$

$$\frac{\partial}{\partial t}\langle \rho_C \rangle = k_3 \langle \rho_S \rangle + k_5 \varepsilon_g \langle \rho_T \rangle^g \tag{4.41}$$

Since the gases produced in the primary and secondary reaction were assumed to be made of the same components, it is only necessary to solve one equation for the gases. Hence, the following source terms for the tar and gases can be derived:

$$\langle \dot{w}_T \rangle = k_2 \langle \rho_S \rangle - (k_4 + k_5)\varepsilon_g \langle \rho_T \rangle^g \tag{4.42}$$

$$\langle \dot{w}_G \rangle = k_1 \langle \rho_S \rangle + k_4 \varepsilon_g \langle \rho_T \rangle^g \tag{4.43}$$

Di Blasi and Russo (1994) used the kinetic data of Thurner and Mann (1981) for reaction 1 to 3. [Note: In the paper, Di Blasi and Russo (1994) have miscalculated the frequency factors

originally presented by Thurner and Mann (1981)]. The data reported by Liden *et al.* (1988) were used for the secondary tar cracking reaction (reaction 4) while the reaction rate of the secondary char forming reaction (reaction 5) was assumed forty times slower than the tar cracking reaction.

Table 4.6 Reaction rate constants and heats of reaction used by Di Blasi and Russo (1994).

Reaction *i*	A_i [s^{-1}]	E_i [kJ/mole]	Δh_i [kJ/kg]	$A_i^{\dagger}$ [s^{-1}]
1	$5.16 \cdot 10^6$	88.6	418.0	$1.435 \cdot 10^4$
2	$1.48 \cdot 10^{10}$	112.7	418.0	$4.125 \cdot 10^6$
3	$2.66 \cdot 10^{10}$	106.5	418.0	$7.377 \cdot 10^5$
4	$4.280 \cdot 10^6$	108.0	-42.0	
5	$1.000 \cdot 10^6$	108.0	-42.0	

†Frequency factors reported by Thurner and Mann (1981)

All the pyrolysis models presented above have been implemented in the simulation program, FLOWPOR. The number of mass conservation equations to be solved for the different reaction schemes are summarized in Table 4.7.

Table 4.7 Number of mass conservation equations to be solved for the different pyrolysis models.

Model	Solid phase	Gas phase
One-step global reaction model	1	1
Three independent parallel reactions	3	1
Broido & Shafizadeh's model	3	2
Chan and Glaisters's model	2	5
Di Blasi and Russo's model	2	2

In addition to conservation equations for mass and energy and an appropriate reaction scheme for the pyrolysis process, the mathematical model requires relations between the moisture content and densities, and data for the thermo-physical properties. The latter comprises expressions for: saturation, capillary and total pressure; heat of evaporation and desorption of liquid and bound water; intrinsic and relative permeabilities; thermal conductivity; specific heat; diffusion constants for bound water and gas diffusion; and dynamic viscosity. These are all given as algebraic expressions and will be presented in the following subsections. Absolute temperature in Kelvin [K], will consistently be used in the case where temperature is a variable in the equations.

4.3.4 PROPERTY RELATIONS AND THERMO-PHYSICAL DATA

4.3.4.1 MOISTURE CONTENT

By neglecting the contribution of the vapour fraction ($<\rho_v>$), the moisture content (M) in wood is given by:

$$M = M_b + M_l = \frac{<\rho_b> + <\rho_l>}{<\rho_{SD}>} \tag{4.44}$$

where M_b and M_l are the bound and liquid moisture content, respectively. The fiber saturation point is a function of temperature [Siau (1984)]:

$$M_{fsp} = [\, M^0_{fsp} + 0.298\,] - 0.001T \tag{4.45}$$

where $M^0_{fsp} \approx 0.3$ can be used for most wood species. If the temperature is high, M_{fsp} can be un-physical low or even negative, so regardless of temperature it is assumed that M_{fsp} is not less than 0.2. By using equation (4.44) and (4.45), the following expressions can be derived for the bound and liquid moisture content:

$$M_b = \frac{<\rho_b>}{<\rho_{SD}>} = \min(M_{fsp}, M) \tag{4.46}$$

$$M_l = \frac{<\rho_l>}{<\rho_{SD}>} = \max(M - M_{fsp}, 0) \tag{4.47}$$

If the lumens or pore-system of the wood is completely filled with water , then the maximum moisture content M_{sat} is given by:

$$M_{sat} = M_{fsp} + M_{lsat} \tag{4.48}$$

where M_{lsat} is the maximum liquid water content which can be absorbed by the wood. In this case, the volume fraction occupied by the gas phase will be zero ($\varepsilon_g=0$) and by applying equation (4.10) and (4.44), the following expression can be derived for M_{sat}:

$$M_{sat} = <\rho_l>^l \left(\frac{1}{<\rho_{SD}>} - \frac{1}{<\rho_s>^s} \right) \tag{4.49}$$

4.3.4.2 PRESSURE RELATIONS

Gas Mixture Pressure

The gas mixture is assumed to be an ideal mixture of perfect gases:

$$<P_i>^g = \frac{<\rho_i>^g RT}{M_i}, \qquad <P_g>^g = \frac{<\rho_g>^g RT}{M_g} \tag{4.50}$$

$$<P_g>^g = \sum_i <P_i>^g, \qquad <\rho_g>^g = \sum_i <\rho_i>^g \tag{4.51}$$

from which a mean molecular weight of the gas mixture, M_g,can be derived:

$$M_g = \left(\sum_i \frac{<\rho_i>^g}{<\rho_g>^g M_i} \right)^{-1} \tag{4.52}$$

The molecular weights of water vapour and dry air is M_v=0.018 kg/mole and M_a=0.029 kg/mole, respectively. The molecular weights of the gases and tars from the pyrolysis are not easily determined since these consist of a large number of components. Based on Chan's (1983) experiments, Fredlund (1988) estimated a mean value of M_g=0.076 kg/mole for the volatiles (gases, tars, water vapour). In the present model, however, the molecular weight of benzene, M_T=0.110 kg/mole, has been chosen to represent the tars while an average value between carbon monoxide and carbon dioxide, M_G=0.038 kg/mole, has been assumed for the gases.

Vapour Pressure

The partial vapour pressure inside the porous wood structure is assumed to be equal its equilibrium (saturated) pressure:

$$\begin{aligned} M > M_{fsp} \qquad & <P_v>^g = P_v^{sat}(T) \\ M < M_{fsp} \qquad & <P_v>^g = P_v^{sat}(T)\, h(M_b, T) \end{aligned} \tag{4.53}$$

where $h(M_b,T)$ is the relative humidity. Generally speaking, the saturated vapour pressure inside a porous structure is made of two parts. The first part is the pressure that exists when the gas-liquid interface is flat. Clausius-Clapeyron's equation gives then the equilibrium vapour pressure in terms of the latent heat of evaporation of the free bulk water surface. The second part described by Kelvin's equation is the pressure caused by the curvature of the menisci formed, and the surface tensions that exist between the gas-liquid interface. In the present model, however, a somewhat simplified expression based on a fit to the vapour data (over a flat plate) found in Raznjevic (1976) are used for the saturated vapour pressure :

$$P_v^{sat}(T) = \exp(24.1201 - 4671.3545/T) \qquad [N/m^2] \tag{4.54}$$

As previously discussed in Chapter 2, different models for water sorption in wood can be found in the literature [Simpson (1980)]. For modelling purposes, an analytical expression is needed which reliably relate the moisture content and temperature to the relative humidity and which fulfil the following constrains:

$$h(M_b = 0) = 0, \quad h(M_b = M_{fsp}) = 1, \quad \left(\frac{\partial h}{\partial M_b} \right)_{M_b = M_{fsp}} = 0, \quad M_{fsp} = 0.598 - 0.001T \tag{4.55}$$

Based on the measured sorption isotherms given in The Encyclopedia of Wood (1980), the

following model has been derived for the relative humidity in wood:

$$h(M_b,T) = 1 - \left(1 - \frac{M_b}{M_{fsp}}\right)^K, \qquad K = 6.453 \cdot 10^{-3} T \tag{4.56}$$

Figure 4.4 presents the comparison between the measured data and the best-fit prediction results given by equation (4.56).

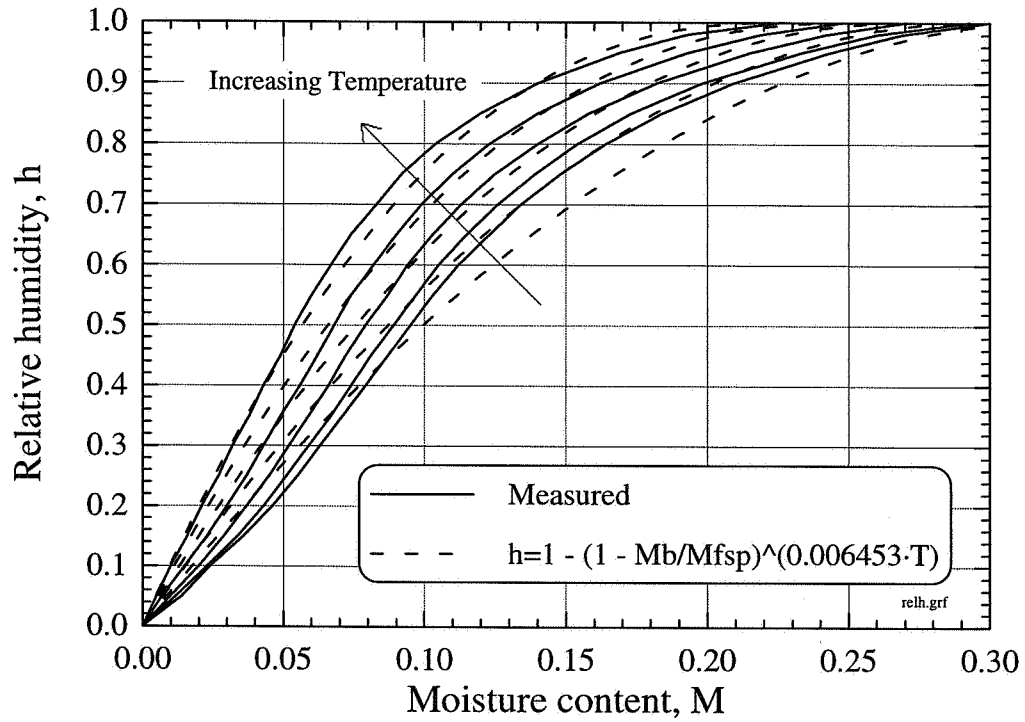

Figure 4.4 Comparison between the measured and predicted sorption isotherms for wood.

Capillary Pressure

To predict the pressure driven transport of liquid water, it is important to know which effect the moisture content and temperature have on the capillary pressure. In any lumen partially filled with liquid, a meniscus is formed between the liquid and gas phase due to surface tension forces which exist between the water molecules and the cell wall material. This is illustrated in Figure 4.5.

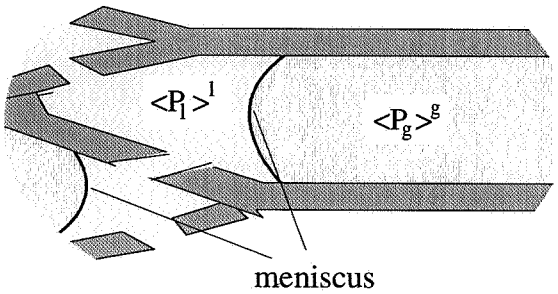

Figure 4.5 Meniscus between the gas and liquid phase.

A balance of the mechanical forces at this phase interface will show that the gas phase pressure exceeds the pressure in the liquid according to the following equation [Spolek and Plumb (1981)]:

$$\langle P_g \rangle^g = \langle P_l \rangle^l + \sigma\left(\frac{1}{r_1} + \frac{1}{r_2}\right) \tag{4.57}$$

The last term in equation (4.57) is known as the capillary pressure:

$$P_C = \sigma\left(\frac{1}{r_1} + \frac{1}{r_2}\right) \tag{4.58}$$

σ is the surface tension between the two phases and is a material property which depends on temperature. r_1 and r_2 are the principal radii of curvature and depends on the liquid water content, contact (wetting) angle and the structure of the porous matrix. The capillary pressure in wood has been measured by centrifugal techniques by Spolek and Plumb (1981) and Choong and Tesoro (1989). Based on the work of Spolek and Plumb (1981), Perre and Degiovanni (1990) derived the following expression for the capillary pressure in softwoods:

$$\begin{aligned} P_C &= 1.364 \cdot 10^5 \, \sigma (M_l + 1.2 \cdot 10^{-4})^{-0.63} && [N/m^2] \\ \sigma &= (128.0 - 0.185\,T)\,10^{-3} && [N/m] \end{aligned} \tag{4.59}$$

In Figure 4.6, where equation (4.59) is drawn, it can be seen that the capillary pressure, and the absolute value of the gradient of the capillary pressure, increases rapidly when the liquid water content goes to zero ($M_l \to 0 \Rightarrow M \to M_{fsp}$).

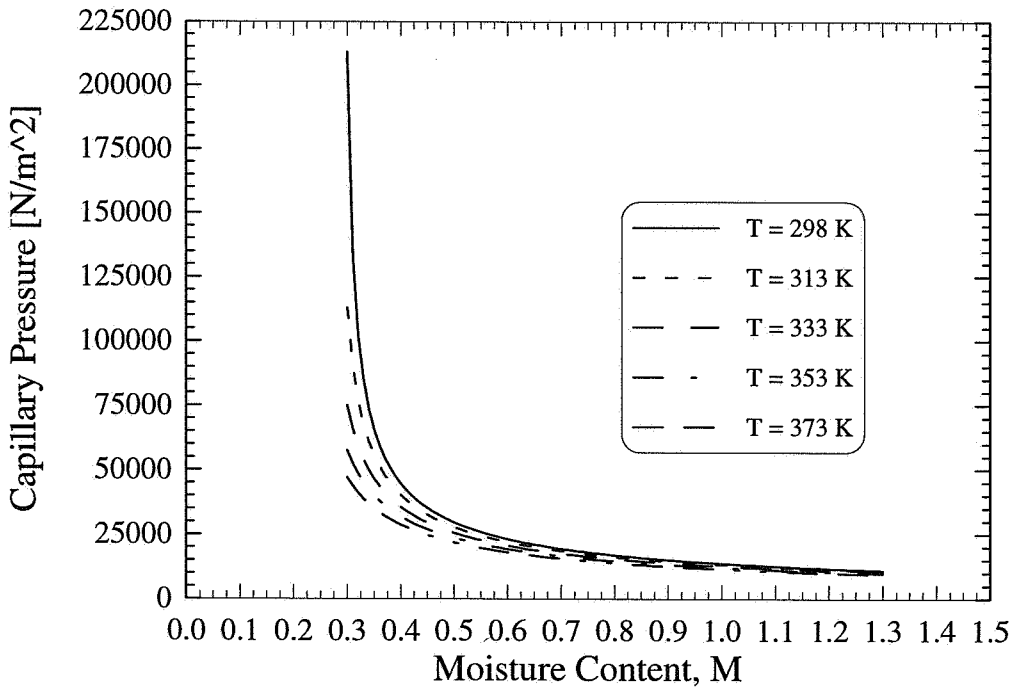

Figure 4.6 Capillary pressure as a function of temperature and moisture content.

According to Darcy's law, higher pressure gradients should lead to higher velocities of the liquid water. However, this is not the case since, as it will be shown later, the relative permeability of liquid water (K_r^l) is decreasing and will approach zero when the liquid water content goes to zero. The moisture content, which below no liquid transport due to capillary action exist, is called the irreducible saturation point (M_{irr}). This irreducible saturation point is always somewhat higher than the fiber saturation point.

4.3.4.3 HEAT OF EVAPORATION/DESORPTION OF LIQUID AND BOUND WATER

The three forms of water found in wood differ in their energy level. Water vapour has the highest level, followed by liquid water in the cell cavities with essentially the same energy as ordinary liquid water. Bound water in the cell walls of wood is in the lowest energy state, the level decreasing with decreasing moisture content below fiber saturation point (see Figure 2.12). Hence, the energy needed to form water vapour from liquid and bound water is:

$$\begin{aligned} M \geq M_{fsp} \qquad & \Delta h_v = \Delta h_l \\ M < M_{fsp} \qquad & \Delta h_v = \Delta h_l + \Delta h_{sorp} \end{aligned} \tag{4.60}$$

The heat of evaporation of liquid water has been obtained by curve-fitting the saturated vapour data in Raznjevic (1976):

$$\Delta h_l = 3179.0 - 2.5T \qquad [kJ/kg] \tag{4.61}$$

Skaar (1989) suggested the following empirical equation for the heat of desorption:

$$\Delta h_{sorp} = 1176.2 \exp(-15 M_b) \qquad [kJ/kg] \tag{4.62}$$

while Stanish *et al.* (1986) assumed Δh_{sorp} to vary quadratically with the bound water content, and at zero bound water content to be equal 40% of the heat of evaporation of liquid water:

$$\Delta h_{sorp} = 0.4 \Delta h_l \left(1 - \frac{M_b}{M_{fsp}} \right)^2 \qquad [kJ/kg] \tag{4.63}$$

This expression has also been used by Perre and Degiovanni (1990) and Ouelhazi *et al.*(1992).

4.3.4.4 INTERPOLATION FACTOR

During the course pyrolysis, the solid structure changes from virgin wood to char. The density decreases while the porosity increases. Hence, the thermo-physical properties which are related to the solid structure, i.e: thermal conductivity, specific heat and intrinsic permeability will also change. Continuous measurements of thermal properties during the thermal decomposition

is extremely complex, since it is difficult to distinguish effects from heat transfer (thermal conductivity, specific heat) from those related to the decomposition (heat of reaction). Havens *et al.* (1972) solved this problem by writing an expression which took into account all the internal energetics including the reactions and the variation in thermal properties. The properties of interest have, however, been measured for the initial (virgin) and final (char) stage. In the present mathematical model, these properties are assumed to follow a linear variation between the virgin wood and char according to:

$$\varphi = \eta\,\varphi_{SD} + (1 - \eta)\,\varphi_{C} \tag{4.64}$$

where the interpolation factor (η) depends on the pyrolysis model used.

For the one-step global model:

$$\eta = \frac{\langle\rho_s\rangle - \langle\rho_{C\infty}\rangle}{\langle\rho_{SD}\rangle - \langle\rho_{C\infty}\rangle} \tag{4.65}$$

where subscript SD and C∞ denotes virgin wood and char, respectively. For the other reaction schemes where the final char density is not assumed in advance, the following equation is used:

$$\eta = \frac{\langle\rho_s\rangle + \langle\rho_A\rangle}{\langle\rho_{SD}\rangle} \tag{4.66}$$

where the density of "active cellulose", $\langle\rho_A\rangle$, must be accounted for in the model of Broido-Shafizadeh, only.

4.3.4.5 PERMEABILITIES

As previously discussed in subsection 4.3.1, the magnitude of the bulk flow through wood is determined by the permeability of wood, which is a measure of the ease which fluids are transported under the influence of a pressure gradient. In other words, the permeability is a measure of the mass-transfer resistance inside the porous wood structure. For two-phase flow, the permeability, sometimes denoted effective permeability, consists of two parts: an intrinsic permeability which is solely connected to the solid structure and a relative permeability which is dependent on the relative saturation of the fluids. Hence, two intrinsic permeabilities and two relative permeabilities have to be defined.

Intrinsic Permeabilities (K_g, K_l)

The intrinsic permeability is an extremely variable property of wood and depends on: 1) type of wood (hardwood/softwood); 2) position inside the stem (heartwood/sapwood); and 3) structural directions of wood (longitudinal/tangential/radial). In general, the intrinsic permea-

bility of softwoods > hardwoods; sapwood > heartwood; and the permeability in longitudinal direction (L) >> radial direction (R) ≥ tangential direction (T) [Siau (1984)]. Comstock (1970) compared softwood gas permeability measurements of several investigators, and found ratios of longitudinal-to-tangential permeabilities (K_{gL}/K_{gT}) between 500 and $8 \cdot 10^4$, whereas ratios of longitudinal-to-radial permeabilities (K_{gL}/K_{gR}) varied between 15 to $5 \cdot 10^5$. Table 4.8 summarizes some intrinsic permeabilities which have been measured or assumed. The intrinsic permeability of liquid (K_l) water is often assumed equal to the gas (K_g), however, a phenomena called pit-aspiration makes K_g somewhat lower than K_l. When wood dries, the water moves from one tracheid to another through border pits (see Figure 2.5). As air takes the place of liquid water, a large percentage of the pits' membranes can be aspirated and become an obstacle to gas movement [Siau (1984)]. Perre *et al.* (1993) have taken this phenomena into account in their model and assumed K_l five times greater than K_g.

Table 4.8 Intrinsic permeabilities of wood.

Reference	Species	Permeability		
		Longitudinal K_{gL} [m^2]	Tangential K_{gT} [m^2]	Radial K_{gR} [m^2]
Comstock (1970)*	Pine (*s*)	$2.98 \cdot 10^{-11}$	$3.65 \cdot 10^{-16}$	$2.07 \cdot 10^{-15}$
	Pine (*h*)	$1.86 \cdot 10^{-12}$	$7.80 \cdot 10^{-17}$	$3.55 \cdot 10^{-16}$
	Spruce (*s*)	$5.72 \cdot 10^{-13}$	$7.80 \cdot 10^{-18}$	$7.50 \cdot 10^{-17}$
	Spruce (*h*)	$2.96 \cdot 10^{-15}$	$1.18 \cdot 10^{-19}$	$1.28 \cdot 10^{-18}$
Perre (1987)*	Spruce	$1.90 \cdot 10^{-14}$	----	$2.90 \cdot 10^{-18}$
	Pine	$7.10 \cdot 10^{-14}$	----	$4.20 \cdot 10^{-17}$
Fredlund (1988)*	Spruce	$9.70 \cdot 10^{-14}$	---	$2.20 \cdot 10^{-16}$
Kansa *et al.*(1977)**	---	$2.00 \cdot 10^{-14}$	---	---
Ouelhazi *et al.*(1992)**	Softwood	$2.00 \cdot 10^{-14}$	$3.00 \cdot 10^{-18}$	---
Di Blasi and Russo (1994)**	---	$1.00 \cdot 10^{-12}$	---	$1.00 \cdot 10^{-17}$

* measured values, ** assumed values, (*s*) sapwood and (*h*) heartwood with 9% moisture content.

The intrinsic permeability and its evolution during the course of pyrolysis is also of great importance. Especially when secondary reactions are considered, since the permeability will influence the residence time of the volatiles in the hot char layer and thereby the possibility for the tars to crack. In addition to the enlargement of the pore system, fissuration in the char layer makes the flow easier, but the modelling work much more complicated. However, pressure measurements of Tinney (1965); Lee *et al.* (1976); and Fredlund (1988) have shown that the pressure at a given position inside the wood drops to zero when the pyrolysis is over, which should indicate that there is no mass transfer resistance in the char layer. In the present model, the intrinsic permeability of the gas mixture is given by:

$$K_g = \eta K_{g,SD} + (1 - \eta) K_{g,C} \tag{4.67}$$

where $K_{g,SD}$ and $K_{g,C}$ are respectively the intrinsic permeability of the virgin solid and char, and the intrinsic permeability of the liquid water is assumed to be equal the gas mixture:

$$K_l = K_{g,SD} \tag{4.68}$$

Relative Permeabilities (K_r^g, K_r^l)

Typical relative permeability curves for softwoods as a function of the water saturation are shown in Figure 4.7.

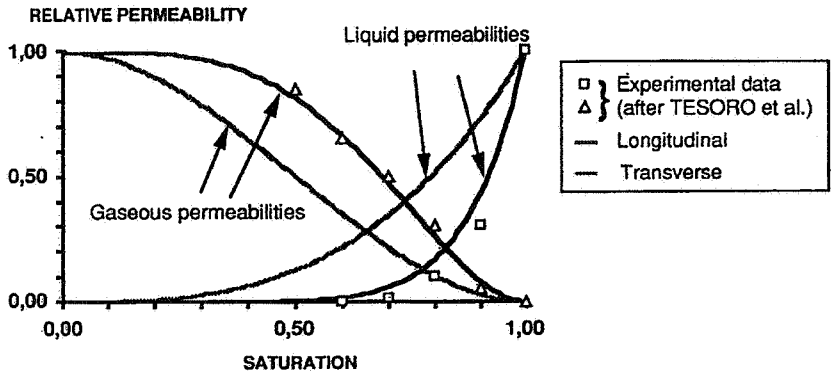

Figure 4.7 Relative permeability measurements of Tesoro *et al.* (1974), modeled by Perre *et al.* (1993).

The water saturation is related to the moisture content by:

$$S = \frac{\text{liquid volume}}{\text{void volume}} = \frac{M - M_{fsp}}{M_{sat} - M_{fsp}} = \frac{M_l}{M_{l,sat}} \tag{4.69}$$

where M_{fsp} is the fiber saturation point and M_{sat} is the wood's moisture content if the entire void structure is filled with liquid water. The main influence on the shapes of the relative permeability curves appears to be the interconnections (pits) between the lumens in the wood structure, which can vary considerably among wood species. Different expressions for the relative permeability have been proposed by different modellers [Spolek and Plumb (1981); Ben Nashrallah and Perre (1988); Ouelhazi *et al.* (1992); Perre *et al.* (1993)]. Based on the experimental measurements of Tesoro *et al.* (1974) in Figure 4.7, Perre *et al.* (1993) derived the two expressions listed in Table 4.9 for the relative permeabilities of softwoods in the longitudinal and tangential direction, respectively.

Table 4.9 Relative permeabilities used by Perre *et al.* (1993).

	K_r^g	K_r^l
longitudinal	$1 + (4S - 5)S^4$	S^8
tangential	$1 + (2S - 3)S^2$	S^3

4.3.4.6 THERMAL CONDUCTIVITY

Wood is an anisotropic material and the thermal conductivity varies with the direction of heat flow with respect to the grain, with temperature, with density and hence the porosity, with kind and quantity of extractives, with defects and especially with moisture content. According to MacLean (1941), the conductivity in tangential direction is from 0.5 to 0.9 times that in the radial direction and in the longitudinal direction, it is 1.75-2.25 times that in the radial direction. Since wood is porous and heat transfer takes place through a complex interaction between several transfer mechanisms, the term effective or equivalent conductivity is often introduced. The effective thermal conductivity ($k_{eff,\,s}$) of moist wood can be expressed as:

$$k_{eff,s} = k_{cond} + k_{rad}, \qquad k_{cond} = f(k_{fiber},\, k_{bl},\, k_{gas}) \tag{4.70}$$

where k_{cond} is the total thermal conductivity which is made of three terms, i.e. the thermal conductivity of the cell wall substance or fibres (k_{fiber}); bound/liquid water (k_{bl}); and gas (k_{gas}). k_{rad} is the radiative thermal conductivity which accounts for the radiation in the pore system.

Table 4.10 presents some data reported for the effective thermal conductivity of dry wood. They reveal that: 1) the conductivity increases slightly with density; 2) the conductivity along or parallel (∥) with the grain is between 1.5 to 2.7 times that perpendicular (⊥) to the grain; and 3) that char has comparatively lower thermal conductivity than wood. Based on a statistical evaluation of data presented in the literature, Maku (1954) calculated the thermal conductivity of the cell-wall substance to be $k_{fiber,\,\parallel} = 0.654$ W/mK along the grain and $k_{fiber,\perp} = 0.421$ W/mK perpendicular to the grain. Siau (1984) reported $k_{fiber,\,\parallel} = 0.878$ W/mK along the grain and $k_{fiber,\,\perp} = 0.439$ W/mK perpendicular to the grain for the cell-wall substance.

The most frequently applied thermal conductivity model for wood pyrolysis is [Kung (1972); Kansa *et al.* (1977); Chan (1983); Fredlund (1988); Di Blasi and Russo (1994)]:

$$k_{eff,\,s} = \varepsilon_g k_g + (\varepsilon_l + \varepsilon_b)k_l + \eta k_{SD} + (1 - \eta)k_C + k_{rad} \tag{4.71}$$

which takes into account all the main heat transfer mechanisms listed above, i.e., heat transfer in the gas; bound/liquid water and solid phase. The latter is successively changing as the virgin wood pyrolyzes to char. Radiation in the pores is believed to play an important role at higher temperatures [Hottel and Sarofim (1967)]. Brown (1972) measured the char thermal conductivity in the temperature range 550-650°C to be three times greater than that measured at room temperature; in fact, it was nearly twice as high as that of the virgin wood.

Another model for the effective thermal conductivity of moist porous or fibrous structures is obtained by assuming a pore (fibre) structure consisting of a mixture of two extreme cases [Kollmann and Cote (1968), Strumillo and Kudra (1986)]. One case comprises a pore system

where heat transfer takes place in parallel layers of gas, liquid and solid phase, which gives the maximum heat transfer. The minimum heat transfer is given by a heat flow which takes place in layers of gas, liquid and solid phase which are connected in series. The thermal conductivity for real porous or fibrous materials lies between these two limiting cases, as illustrated in Figure 4.8. A weighting or "bridge" factor (ξ) is introduced to simulate the real porous (or fibrous) material arrangement, i.e., ξ part of the material is in parallel with heat transfer direction and (1-ξ) part of the material is in series with heat transfer direction. According to this assumption, the effective thermal conductivity model has the following form:

$$k_{eff,s} = \xi k_{par} + (1 - \xi) k_{ser} \tag{4.72}$$

where k_{par} is the effective thermal conductivity in the parallel part (ξ):

$$k_{par} = \varepsilon_s k_{fiber,\parallel} + (\varepsilon_b + \varepsilon_l) k_{bl} + \varepsilon_g (k_{gas} + k_{rad}) \tag{4.73}$$

and k_{ser} is the effective thermal conductivity in the series part (1-ξ):

$$k_{ser} = \frac{1}{\frac{\varepsilon_s}{k_{fiber,\perp}} + \frac{(\varepsilon_b + \varepsilon_l)}{k_{bl}} + \frac{\varepsilon_g}{(k_{gas} + k_{rad})}} \tag{4.74}$$

ε_s, ε_b, ε_l and ε_g are the volume fractions occupied by solid, bound water, liquid water and gas phase, respectively.

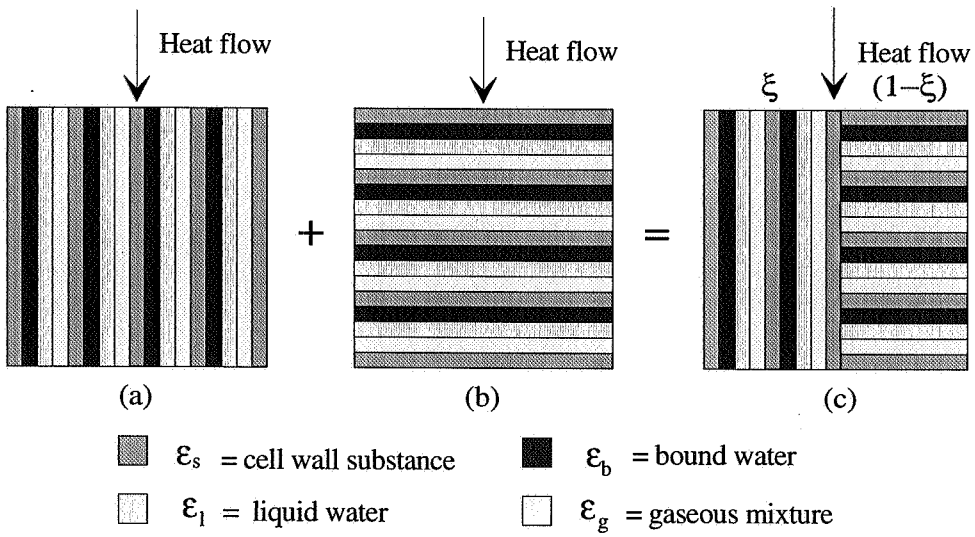

Figure 4.8 Graphical model of heat conduction in moist wood. (a) in parallel, (b) in series and (c) a combination of series and parallel

By using the thermal conductivity of dry air (k_{air}=0.0258 W/mK) at zero wood density and $k_{fiber,\parallel}$ = 0.766 W/mK and $k_{fiber,\perp}$= 0.430 W/mK for the fibers at a density of 1500 kg/m^3, the effective thermal conductivity (k_{eff}) according to equation (4.72) is shown in Figure 4.9 for different "bridge" factors (ξ) and densities together with the data listed in Table 4.10.

Table 4.10 Effective thermal conductivity for dry wood.

Substrate	T [°C]	$<\rho_{SD}>$ [kg/m^3]	Effective Thermal Conductivity [W/m K] $k_{eff,SD\parallel}$	$k_{eff,SD\perp}$	$\parallel / \perp$	References
Balsa	20	200		$8.100 \cdot 10^{-2}$		Raznjevic (1976)
Balsa	20	300		$1.050 \cdot 10^{-1}$		Raznjevic (1976)
Lodg. Pine	20	372	$1.576 \cdot 10^{-1}$	$1.003 \cdot 10^{-1}$	1.57	Chan (1983)
Spruce	20	400	$2.790 \cdot 10^{-1}$	$1.280 \cdot 10^{-1}$	2.18	Raznjevic (1976)
White Pine	20	450	$2.593 \cdot 10^{-1}$	$9.769 \cdot 10^{-2}$	2.65	Maku (1954)
Fir	20	540	$3.396 \cdot 10^{-1}$	$1.384 \cdot 10^{-1}$	2.45	Maku (1954)
Teak	20	640	$3.815 \cdot 10^{-1}$	$1.756 \cdot 10^{-1}$	2.17	Maku (1954)
Beech	20	700	$3.490 \cdot 10^{-1}$	$2.090 \cdot 10^{-1}$	1.67	Raznjevic (1976)
Mahogany	25	700	$3.140 \cdot 10^{-1}$	$1.510 \cdot 10^{-1}$	2.08	Raznjevic (1976)
Maple	30	710	$4.190 \cdot 10^{-1}$	$1.580 \cdot 10^{-1}$	2.65	Raznjevic (1976)
Oak	15	820	$3.605 \cdot 10^{-1}$	$2.093 \cdot 10^{-1}$	1.72	Maku (1954)
Sawdust	20	870	$7.700 \cdot 10^{-2}$			Chan (1983)
Sawdust	20	970	$8.800 \cdot 10^{-2}$			Chan (1983)
Cell wall	20	1500	$6.540 \cdot 10^{-1}$	$4.210 \cdot 10^{-1}$	1.55	Maku (1954)
Cell wall	20	1500	$8.780 \cdot 10^{-1}$	$4.390 \cdot 10^{-1}$	2.00	Siau (1984)
Maple char	90	200	$1.045 \cdot 10^{-1}$	$7.106 \cdot 10^{-2}$		Lee *et al.* (1976)

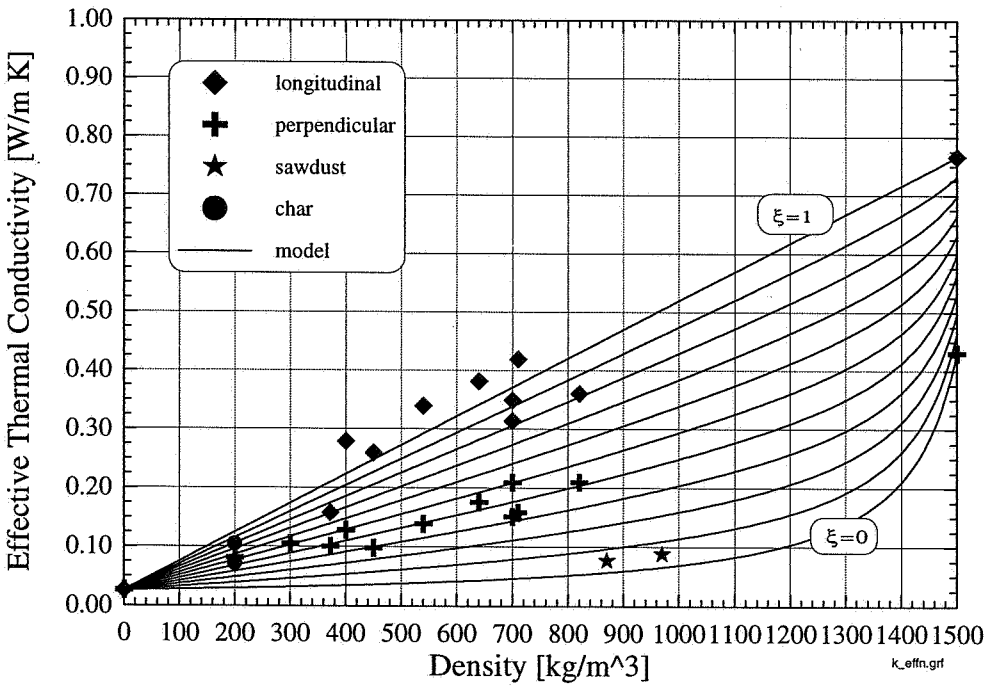

Figure 4.9 Relation between density and effective thermal conductivity

For heat conduction along the grain, ξ is between 0.8 and 1 while for heat conduction perpendicular to the grain, ξ is between 0.35 and 0.6. Kollmann and Cote (1968) calculated $\xi = 1$ for the parallel heating and $\xi = 0.58$ for the perpendicular heating, respectively. For sawdust where fibers are felted in crisscrossing patterns, ξ is less than 0.1.

Effect of Moisture Content

MacLean (1941) measured the effective thermal conductivity of many wood species with a large range of moisture contents and densities. He presented an empirical equation which gave the best agreement with his experimental data perpendicular to the grain:

$$\begin{aligned} M < 0.4: &\quad k_{eff,s\perp} = 2.37\cdot10^{-2} + 2.0\cdot10^{-4}\langle\rho_{SD}\rangle(1.0 + 2.0M) \quad [W/mK] \\ M \geq 0.4: &\quad k_{eff,s\perp} = 2.37\cdot10^{-2} + 2.0\cdot10^{-4}\langle\rho_{SD}\rangle(1.0 + 2.5M) \quad [W/mK] \end{aligned} \tag{4.75}$$

and assumed $k_{eff,s\parallel} = 2.5k_{eff,s\perp}$. Perre and Degiovanni (1990) assumed $k_{eff,s\parallel} = 2.0k_{eff,s\perp}$ in their modelling work and used the following empirical expression for the effective thermal conductivity perpendicular to the grain:

$$\begin{aligned} M < 0.4 &\quad k_{eff,s\perp} = [0.129 - 0.049M][1.0 + 0.001(2.05 + 4M)(T - 273)] \\ &\qquad \cdot[0.986 + 2.695M] \quad [W/mK] \\ M \geq 0.4 &\quad k_{eff,s\perp} = [0.0932 + 0.0065M][1.0 + 0.00365(T - 273)] \\ &\qquad \cdot[0.986 + 2.695M] \quad [W/mK] \end{aligned} \tag{4.76}$$

By using a dry solid density ($\langle\rho_{SD}\rangle$) of 500 kg/m^3, a temperature of 298 K, and by assuming the "bridge" factor (ξ) to be 1.0 for heat conduction parallel to the grain and 0.5 for heat conduction perpendicular to the grain, the empirical equations of MacLean; and Perre and Degiovanni are compared with equation (4.72) in Figure 4.10.

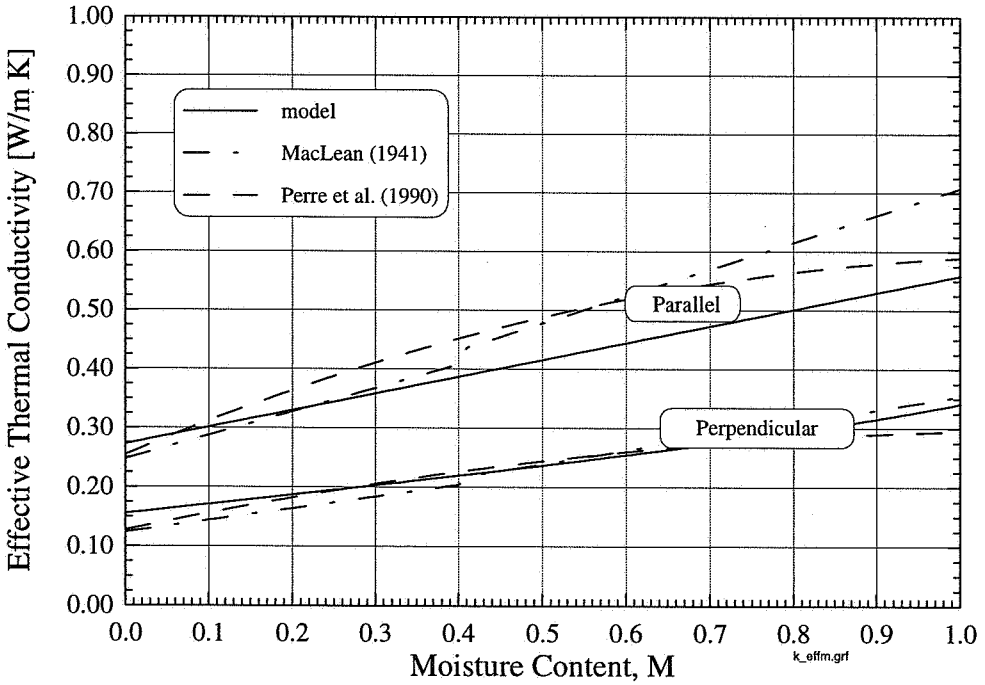

Figure 4.10 Comparison between the effective thermal conductivity models of MacLean (1941), Perre and Degiovanni (1990) and the prediction results of equation (4.72).

The effective thermal conductivity model based on weighting between parallel and serial heat transfer coincide quite well with the empirical expressions of MacLean (1941) and Perre and

Degiovanni (1990) over the whole range of moisture contents when the heating is perpendicular to the grains. In the case of heat transfer parallel with the grains, the model predicts a somewhat lower conductivity compared to those obtained by using MacLean's and Perre and Degiovanni's formulas.

Radiative Heat Transfer

As previously mentioned, radiative heat transfer is assumed to play an important role in the porous char layer at higher temperatures. Radiation through the pores or between the fibres in porous/fibrous substances may be treated as a diffusion process analogous to Knudsen diffusion of gases in pores. Hottel and Sarofim (1967) derived the following general expression for radiative thermal conductivity in porous substances:

$$k_{rad} = \frac{16}{3} n^2 \lambda \sigma T^3 = A \lambda \sigma T^3 \qquad [W/mK] \qquad (4.77)$$

where n^2 is the effective index of refraction of the substance; λ [m] is the photon mean free path or the characteristic length which the radiation passes through; and σ is Stefan Boltzmann constant (= $5.6703 \cdot 10^{-8}$ [$W/m^2 K^4$]). Table 4.11 presents models for the constant (A) and the photon mean free path (λ) used in the modelling of radiative heat transfer through wood and other porous/fibrous materials.

Table 4.11 Models for the constant (A) and the photon mean free path (λ) used in the modelling of radiative heat transfer in porous/fibrous materials.

Reference	A	photon mean free path λ	Comments
Hottel *et al.* (1967)	16/3	d_{pore}	d_{pore} = pore diameter
Birkebak and Ozil (1979)	4.5	$d_{fiber}/(1-\varepsilon_g)\omega$	2-dim. model, randomly distributed fibers in parallel planes, d_{fiber}= fiber diameter, ε_g = porosity, ω = emissivity
Panton and Rittmann (1971)	4	$\varepsilon_g \omega d_{pore}/(1-\varepsilon_g)$	
Chan (1985)	4.5	$3d_{fiber}/\varepsilon_g \omega$	$d_{fiber,wood}= 4 \cdot 10^{-5}$ m
Curtis *et al.* (1988)	16/3	$d_{fiber}/\ln\varepsilon_g$	d_{fiber} = cellulose fiber diameter
Di Blasi and Russo (1994)	1	d_{pore}/ω	$d_{pore} = \eta d_{pore,S} + (1-\eta) d_{pore,C}$ $d_{pore,S}=4 \cdot 10^{-5}$ m, $d_{pore,C}=2 \cdot 10^{-4}$ m

The importance of radiation as a heat transfer process at higher temperatures will be demonstrated in the section where the experiments are compared with theoretical predictions.

4.3.4.7 SPECIFIC HEAT

The energy equation requires data for the specific heat of wood, liquid water and the volatile species. The specific heat of the substances involved in the drying and pyrolysis of wood has in most cases been assumed constant. Table 4.12 presents some data for virgin wood, char and gases which have been assumed and used by different modellers.

Table 4.12 Data for the specific heat reported in the literature.

Virgin wood $C_{P,s}$ [kJ/kg K]	Char $C_{P,C}$ [kJ/kg K]	Gases $C_{P,G}$ [kJ/kg K]	References
2.30	----	----	Bamford *et al.* (1946)
1.38	0.67	1.11	Kung and Kalelkar (1973)
2.30	0.71	1.09	Kansa *et al.* (1977)
2.51	1.05	1.05	Chan *et al.* (1985)
1.67	1.00	----	Pyle and Zaror (1984)
1.95	1.35	1.20	Alves and Figueiredo (1989c)
1.50	1.10	1.10	Di Blasi and Russo (1994)

In the present model, the specific heat of the solid substance is assumed to vary linearly between virgin wood ($C_{P,SD}$) and char ($C_{P,C}$):

$$C_{P,s} = \eta C_{P,SD} + (1 - \eta) C_{P,C} \qquad [kJ/kg\,K] \qquad (4.78)$$

Koch (1969) measured the specific heat of pine at different temperatures by using a differential scanning calorimeter and reported the following equation for the specific heat between 298 and 413 K:

$$C_{P,SD} = -9.12 \cdot 10^{-2} + 4.4 \cdot 10^{-3} T \qquad [kJ/kg\,K] \qquad (4.79)$$

By using a Perkin Elmer DSC, the author has measured the specific heat of spruce between 350 and 500 K. A fit to the data gave the following expression:

$$C_{P,SD} = 1.5 + 1.0 \cdot 10^{-3} T \qquad [kJ/kg\,K] \qquad (4.80)$$

Raznjevic (1976) reported the data listed in Table 4.13 for the specific heat of charcoal, from which the following second order polynomial has been derived:

$$C_{P,C} = 0.42 + 2.09 \cdot 10^{-3} T + 6.85 \cdot 10^{-7} T^2 \qquad [kJ/kg\,K] \qquad (4.81)$$

The specific heat of bound water is slightly higher than that of liquid water. For simplicity they are assumed equal, and constant value of $C_{P,l}$ = 4.2 kJ/kg K at a temperature of 323 K has been chosen.

Table 4.13 Specific heat of charcoal [Raznjevic (1976)].

	Specific heat at different temperatures $C_{P,C}$ [kJ/kg K]				
	273	373	673	1273	[K]
Charcoal	1.005	1.005	1.549	2.010	

Since the gas phase consists of a mixture of different species (air, water vapour, tar, gases) which continuously change during the course of drying and pyrolysis, an average specific heat for the gas phase can be calculated by using the following equation:

$$C_{P,g}\langle\rho_g\rangle = \sum_{i=1}^{N} C_{P,i}\langle\rho_i\rangle \tag{4.82}$$

where N is the number of components in the gas phase. The data from Raznjevic (1976) listed in Table 4.14 have been used to determine the following expressions for the specific heat of the species in the gas mixture phase:

Dry air:	$C_{P,A} = 0.95 + 1.88\cdot10^{-4}\ T$	[kJ/kg K]	(4.83)
Water vapour:	$C_{P,V} = 1.67 + 6.40\cdot10^{-4}\ T$	[kJ/kg K]	(4.84)
Tar:	$C_{P,T} = -0.10 + 4.40\cdot10^{-3}\ T - 1.57\cdot10^{-6}\ T^2$	[kJ/kg K]	(4.85)
Gases:	$C_{P,G} = 0.77 + 6.29\cdot10^{-4}\ T - 1.91\cdot10^{-7}\ T^2$	[kJ/kg K]	(4.86)

As for the calculation of the mean molecular weights, benzene has been chosen to represent the tars and the gases is assumed to consist of fifty-fifty CO_2 and CO by weight.

Table 4.14 Specific heat as a function of temperature [Raznjevic (1976)].

Species	Mol. weight [kg/mole]	Specific heat at different temperatures $C_{P,i}$ [kJ/kg K]							
		273	373	573	723	973	1173	1373	[K]
Dry air	0.029	1.0036	1.0103	1.0446	1.0923	1.1355	1.1702	1.1970	
Water vapour	0.018	1.8594	1.8903	2.0005	2.1319	2.2730	2.4154	2.5456	
Benzene	0.110	0.9433	1.3352	1.9565	2.3694	2.6553	2.8613	3.0128	
Carbon monoxide	0.028	1.0396	1.0446	1.0802	1.1321	1.1790	1.2158	1.2435	
Carbon dioxide	0.044	0.8148	0.9136	1.0567	1.1547	1.2230	1.2715	1.3059	

The specific heats presented above are summarized in Figure 4.11.

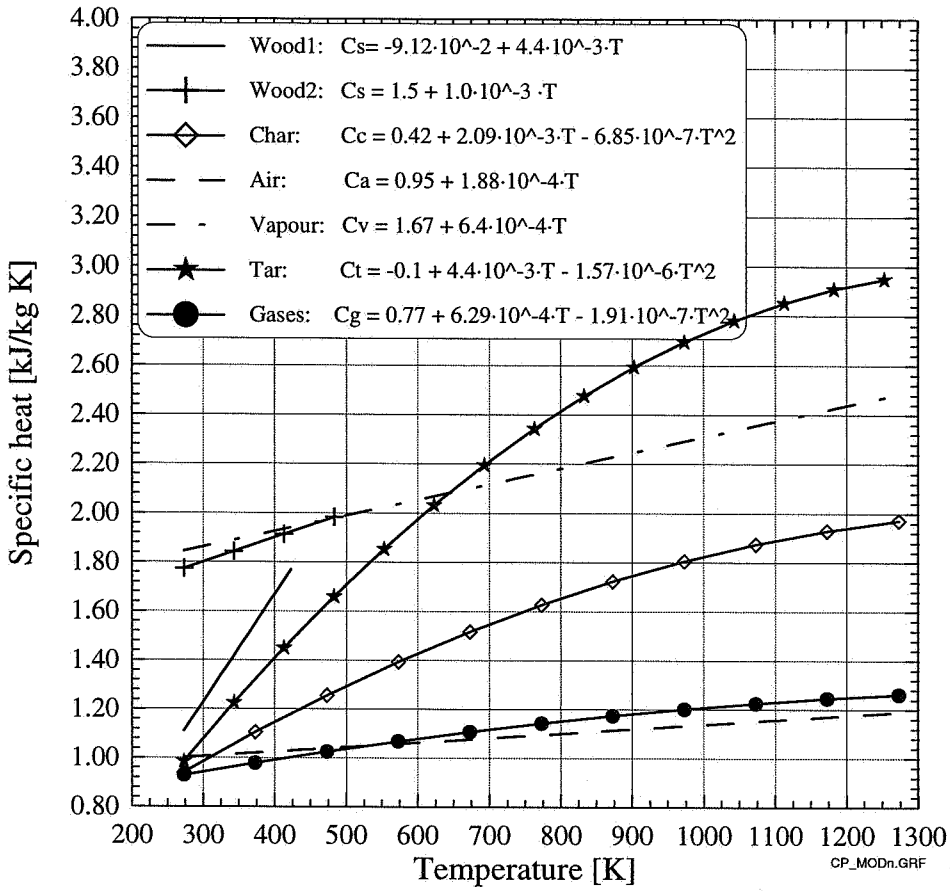

Figure 4.11 Specific heat of the solid and gas species involved in drying and pyrolysis of wood.

4.3.4.8 DIFFUSION COEFFICIENTS

Two diffusion processes i.e., bound water diffusion which takes place within the cell wall and intergas diffusion in the gas mixture phase, have been accounted for in the model (Knudsen diffusion in the gas phase has not been considered).

Bound Water Diffusion Coefficient

Different models have been proposed for the bound water movement in wood. Skaar and Babiak (1982) presented a model based on the assumption that the driving force for bound water movement was the gradient in "spreading" pressure (ϕ), derived from sorption theory. Stanish (1986) used the gradient in chemical potential (μ) of the bound water molecules as a driving force for moisture movement below fiber saturation point. However, in the present model, bound water diffusion is taken into account by a diffusion coefficient which is a function of bound water content (M_b) and temperature. In Siau (1980), an Arrhenius type expression based on the experimental work of Stamm (1964) has been derived:

$$D_{B,T} = 7 \cdot 10^{-6} \exp[(-4633 + 3523 M_b)/T] \qquad [m^2/s] \qquad (4.87)$$

where subscript T denotes tangential direction. Stamm (1964) found that the longitudinal

bound water diffusion coefficient in the cell wall substance was approximately three times that in the tangential; and two times that in the radial direction.

$$D_{B,L} \simeq 3.0 D_{B,T} \simeq 2.0 D_{B,R} \qquad [m^2/s] \qquad (4.88)$$

Perre and Degiovanni (1990), Ouelhazi *et al.* (1992) and Perre *et al.* (1993) used the following expression for the bound water diffusion coefficient in tangential direction:

$$D_{B,T} = \exp[-9.9 + 9.8 M_b - 4300/T] \qquad [m^2/s] \qquad (4.89)$$

which gives about one order of magnitude higher values for $D_{B,T}$ than equation (4.87) does.

Gas Diffusion Coefficient

During drying and pyrolysis, several gas species (air, water vapour, CO, CO_2, tars and lighter hydrocarbons etc.) will exist in the gas mixture phase making the modelling of diffusion very complex. However, gas diffusion is a dominating transport mechanism at low heat fluxes and temperatures. At higher heat fluxes and temperatures, convection will be the dominating transport mechanism and diffusion may be neglected. Anyhow, diffusion is assumed in the gas phase and since diffusion is most important during drying, a binary diffusion model for water vapour in air is used:

$$D_{v-a} = 1.192 \cdot 10^{-4} (T^{1.75}/P) \qquad [m^2/s] \qquad (4.90)$$

For diffusion in porous structures, the diffusion coefficient given above will be reduced due to constrictions and also due to the longer distance the molecules have to travel. An effective diffusion coefficient which takes this into account is often introduced [Fogler (1986)]:

$$D_{eff} = (\varepsilon_g \sigma D_{v-a})/\tau \qquad (4.91)$$

where ε_g is the volume fraction occupied by the gas phase, σ is the constriction factor and τ is the tortuosity. The constriction factor accounts for the variation in the cross-sectional that is perpendicular to the diffusion direction. The tortuosity is defined by the actual distance a molecule travels between two points divided by the shortest distance between these points. However, even if this expression seems to be reasonable it is difficult to determine σ and τ. Perre *et al.* (1993) have for simplicity used the following model for the effective diffusion coefficient:

$$D_{eff,L} = 20 D_{eff,T} = D_{v-a}/50 \qquad (4.92)$$

where subscript L and T denote longitudinal and tangential direction, respectively.

4.3.4.9 DYNAMIC VISCOSITY

Darcy's law calculation of the convective flow requires data for the dynamic viscosity of the liquid (μ_l) and the gas mixture phase (μ_g). The following second order polynomial has been obtained by curve-fitting the data reported in Raznjevic (1976) for the dynamic viscosity of

liquid water between 298 K and 373 K:

$$\mu_l = 1.40 \cdot 10^{-2} - 7.30 \cdot 10^{-5}\, T + 9.73 \cdot 10^{-8}\, T^2 \qquad [\text{kg m/s}] \tag{4.93}$$

The dynamic viscosity of the gas mixture can be determined in the same way as the specific heat:

$$\mu_g \langle \rho_g \rangle = \sum_{i=1}^{N} \mu_i \langle \rho_i \rangle \tag{4.94}$$

where N is the number of components in the gas mixture phase. By using the data from Raznjevic (1976) listed in Table 4.15, the following expressions have been derived for the dynamic viscosity of the gas species between 273 K and 1273 K:

Dry air:	$\mu_A = 9.12 \cdot 10^{-6} + 3.27 \cdot 10^{-8}\, T$	[kg m/s]	(4.95)
Vapour:	$\mu_V = -1.47 \cdot 10^{-6} + 3.78 \cdot 10^{-8}\, T$	[kg m/s]	(4.96)
Tar:	$\mu_T = -3.73 \cdot 10^{-7} + 2.62 \cdot 10^{-8}\, T$	[kg m/s]	(4.97)
Gases:	$\mu_G = 7.85 \cdot 10^{-6} + 3.18 \cdot 10^{-8}\, T$	[kg m/s]	(4.98)

Table 4.15 Dynamic viscosity of gases [Raznjevic (1976)].

Species	Dynamic viscosity at different temperatures $\mu_i \cdot 10^6$ [kg m/s]							
	273	298	400	600	800	1000	1273	[K]
Dry air	17.2	18.2	22.2	29.8	36.5	42.4	49.3	
Water Vapour	8.8	9.6	13.2	21.4	29.5	36.5	46.0	
Benzene	7.0	7.6	9.9	15.0	20.5	26.0	33.0	
Carbon Monoxide	16.6	17.7	21.8	29.0	35.0	41.0	49.0	
Carbon Dioxide	14.6	15.0	19.8	27.6	34.0	39.4	44.6	

4.3.5 NUMERICAL SOLUTION PROCEDURE

The governing set of equations includes: 1) partial differential equations for the conservation of heat, mass and momentum; 2) non-linear equations describing the boundary conditions; and 3) algebraic equations for the thermo-physical properties. The only way in which the model can be solved is by using a numerical solution procedure. The system of equations is solved by the method of finite differences based on the notation of control domain described by Patankar (1980). The domain of integration is partitioned in a set of control volumes in which grid points P_i are placed in the geometrical center (see Figure 4.12). By doing so, the value of any physical quantity φ at point P_i can be regarded as a good representative value for the

control volume. A fixed grid in space with a uniform or a constant expansion ratio can be used. The method consists of integrating the conservation equations over the control volumes *dx* (Δx) and over the time step *dt* (Δt). The convective terms are discretized by first-order upwinding, while central differensing is used for the diffusive terms.

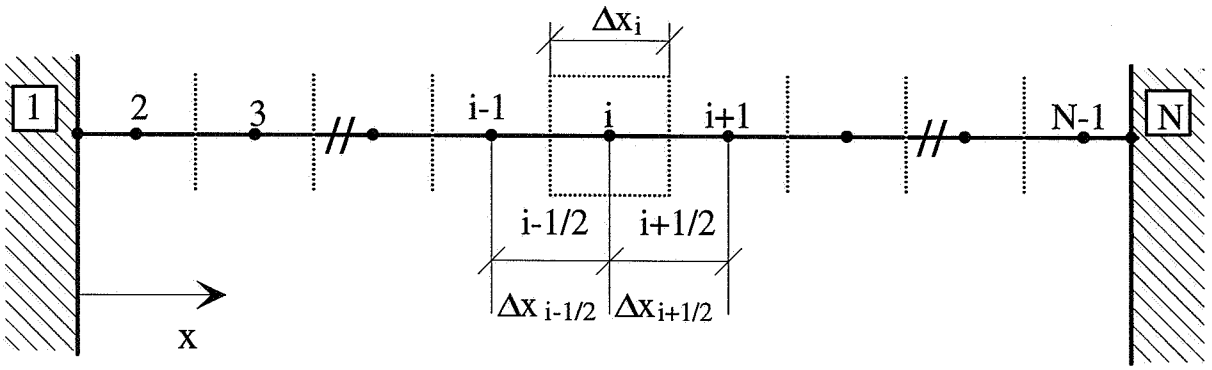

Figure 4.12 Numerical grid arrangement.

The time integrator must handle a system of differential and algebraic equations. The numerical code DASSL has been chosen, which solves implicitly a set of differential and algebraic equations of the form:

$$F\left(t,\ \varphi,\ \frac{\partial \varphi}{\partial t}\right) = 0 \tag{4.99}$$

where φ, $\partial\varphi/\partial t$ and F are vectors of the same size. Initial values for φ and $\partial\varphi/\partial t$ which are consistent, i.e. which satisfy equation (4.99) must be given as input parameters. The backward differentiation formulas of order one to five are used. After $\partial\varphi/\partial t$ in the system of equations have been substituted by backward differentiation formulas, Newton's method is used to solve the resulting equations. On every step in time, the order of the backward difference formula and the step size in time are automatically chosen on the basis of the behaviour of the solution. If the iteration matrix is banded, DASSL can utilize this banded structure to save memory and computational time.

The following partial differential and algebraic equations are solved:

- conservation equation for energy, equation (4.20).
- equation for pressure constraint, equation (4.51), together with equation for the molecular weight of gas mixture, equation (4.52).
- equation for the density constrain, equation (4.51).

- conservation equation for the different components *i* in the gas phase, equation (4.17). This equation is solved for all the components in the gas phase with the exception of water vapour which is treated separately.

- conservation equation for the sum of bound and liquid water:

$$\frac{\partial}{\partial t}(<\rho_b> + <\rho_l>) + \frac{\partial}{\partial x}(<\rho_b v_b> + <\rho_l v_l>) = -<\dot{w}_v> \qquad (4.100)$$

- The production of water vapour $<\dot{w}_v>$ appears in both the equation for water vapour in the gas phase and in the equation for the sum of bound and liquid water, equation (4.100). Since both $<\dot{w}_v>$ and $<\rho_v>^g$ are unknown, equilibrium is assumed between water vapour and bound or liquid water. From equilibrium, the density of water vapour is given by:

$$<\rho_v>^g = f(M_b, T) \qquad (4.101)$$

and $<\dot{w}_v>$ is removed from the equation system by including the conservation equation for water vapour into the conservation of energy equation (4.20), and in the equation for the sum of bound and liquid water (4.100).

- conservation equation for the solid phase, equation (4.11)

- equation for volume fraction constraint, equation (4.7), where ε_g is unknown and ε_s, ε_l and ε_b are given by equation (4.9)

The variables listed in Table 4.16 can be calculated by the simulation program FLOWPOR In addition, the percentage reacted and ultimate product yields of char, gas, tar and water vapour from drying and pyrolysis can be predicted.

Table 4.16 Variables which can be calculated by the simulation program FLOWPOR

Variable	Symbol	
absolute temperature	T	[K]
total pressure in the gas phase	$<P_g>^g$	[N/m^2]
water vapour, capillary and liquid pressure	$<P_v>^g$, P_C, $<P_l>^l$	[N/m^2]
superficial gas mixture and liquid water velocity	$<v_g>$, $<v_l>$	[m/s]
gas mixture and liquid water permeability	$K_g K_g^r$, $K_l K_l^r$	[m^2]
density of solid	$<\rho_s>$	[kg/m^3]
intrinsic density of gas mixture	$<\rho_g>^g$	[kg/m^3]
intrinsic density of component *i* in gas mixture	$<\rho_i>^g$	[kg/m^3]

Table 4.16 *(cont)* Variables which can be calculated by the simulation program FLOWPOR

Variable	Symbol	
density of bound and liquid water	$<\rho_b> + <\rho_l>$	[kg/m^3]
mean molecular weight of gas mixture	M_g	[kg/mole]
rate of production of component i	$<\dot{w}_i>$	[kg/m^3 s]
liquid, bound and total moisture content	M_l, M_b, M	
volume fraction of solid, liquid-, bound water and gas phase	ε_s, ε_l, ε_b, ε_g	
effective, thermal and radiative conductivity	k_{eff}, k_{cond}, k_{rad}	[W/m K]

The history of FLOWPOR (FLOW in PORous media)

The development of a simulation program for biomass pyrolysis started by Melaaen in 1991. In its very simple form (constant thermo-physical properties, instantaneous outflow of gases), the first version was used to simulate pyrolysis of cellulose by using the Broido-Shafizadeh model [Wichman and Melaaen (1994)]. Grønli continued the work in 1993 and assisted by Melaaen, he implemented a model for gas flow (convection, diffusion) in the simulation program. In addition, several kinetic models and new models for thermo-physical properties were included. Melaaen and Grønli continued together and implemented a model for drying in the simulation program [Melaaen and Grønli (1994)]. In the first version of the program, the Tri-Diagonal Matrix Algorithm (TDMA) was used to solve the set of partial differential and algebraic equations. This solver worked well in the pure pyrolysis simulations, however, convergence problems appeared when the drying model was included. This was due to the highly non-linear and strongly coupled equation system which form was not suitable for TDMA. Hence, it was decided to rewrite the program and use DASSL to solve the governing set of equations [Melaaen (1994); Melaaen (1996); Melaaen and Grønli (1996)]. Grønli has thereafter continued to make improvements to the program and derived and implemented new temperature dependent expressions for the thermo-physical properties.

4.4 EXPERIMENTAL SECTION

The purpose of these experiments was to study the pyrolysis of "thermally thick" samples of wood, to see what influence different heating conditions, grain orientation and wood species have on the product yields, and to obtain data which could be compared with theoretical predictions from the mathematical model derived in the previous section.

Cylinders with a diameter of approximately 20 mm and a length of 30 mm made of birch, spruce and pine were one-dimensionally heated in bell-shaped glass reactor using a Xenon arc lamp as a heat source (adopted from Chan (1983)). Two different heat fluxes: 80 kW/m^2 (low) and 130 kW/m^2 (high) were used, and the effect of grain orientation relative to the heat flux (longitudinal and radial direction) were investigated. The following parameters were measured: surface and internal temperature, gas composition, i.e. CO, CO_2 and total hydrocarbons (HC), char-yield, tar/water-yield (condensable gases) and gas-yield (by mass balance), percentage reacted and shrinkage. In some initial experiments, the internal pressure was measured by a hypodermic needle connected to a pressure transducer as described by Tinney (1965) and Lee *et al.* (1977). However, the maximum pressure measured in these initial experiments was only 25 Pa. For this reason, the pressure measurements were excluded since the pellet diameter was probably too small to build up a noticeable pressure.

4.4.1 EXPERIMENTAL APPARATUS AND MEASURING EQUIPMENT

A schematic diagram of the experimental apparatus and pictures showing the reactor and the setup on the optical bench are given in Figure 4.13 to Figure 4.15. In the following, a brief description of the experimental apparatus and procedure employed will be given.

4.4.1.1 XENON ARC LAMP

The xenon arc lamp and its supporting equipment is fabricated by Photon Technology International (Germany). The water-cooled lamp in its housing *"A-5000"* is supported by a 1.1 kW *"LPS-1100"* DC power supply. An external igniter *"LPS 1221 G"* is used to create the high voltages needed for ignition. Light collection and focusing are achieved using the internal reflector in the lamp housing. Thus a spatially uniform, relatively constant and high radiant heat flux is provided. By varying the distance between the xenon arc lamp and the reactor the heat flux can be directly focused onto the pellet surface.

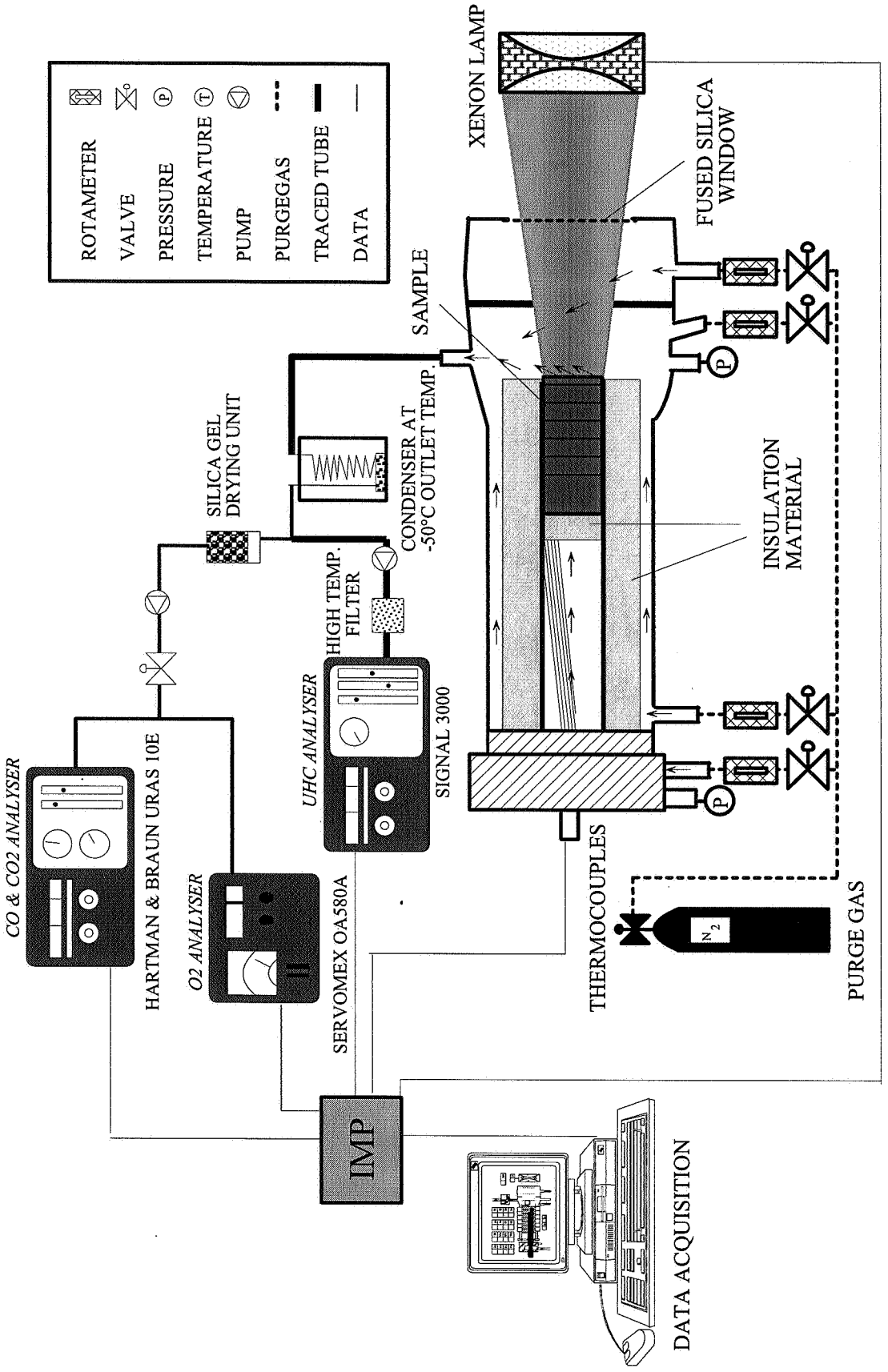

Figure 4.13 Schematic diagram of the pyrolysis experimental apparatus.

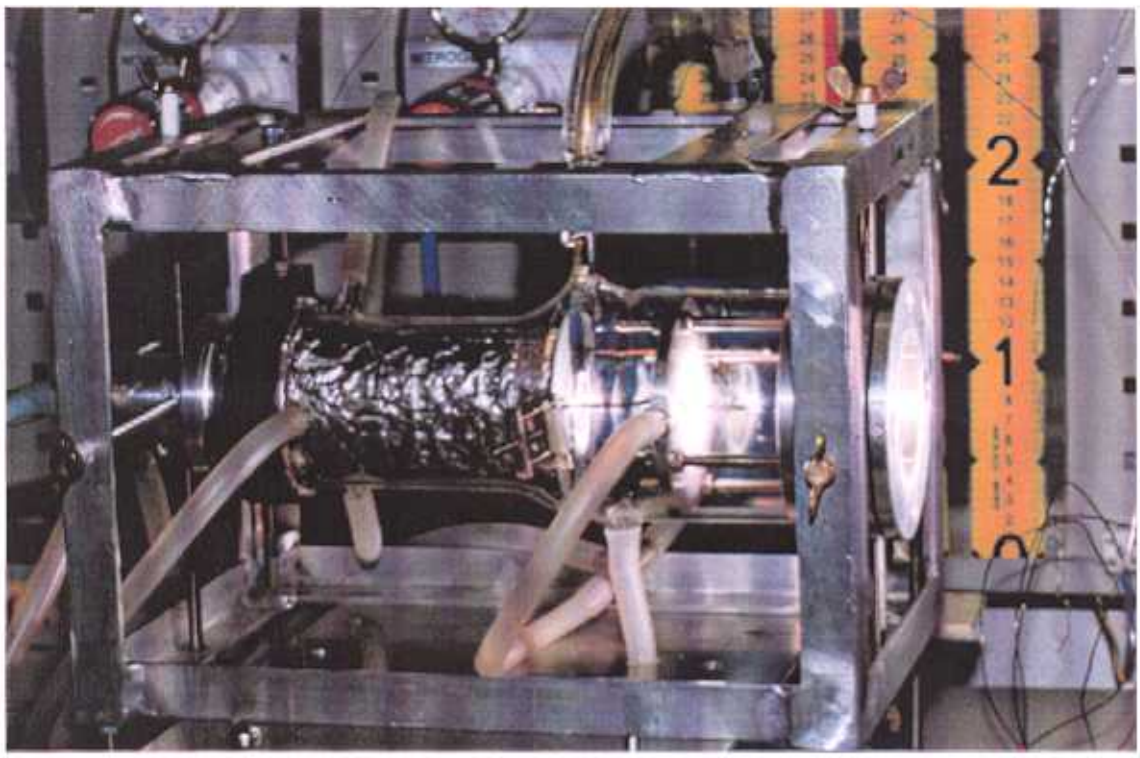

Figure 4.14 The reactor

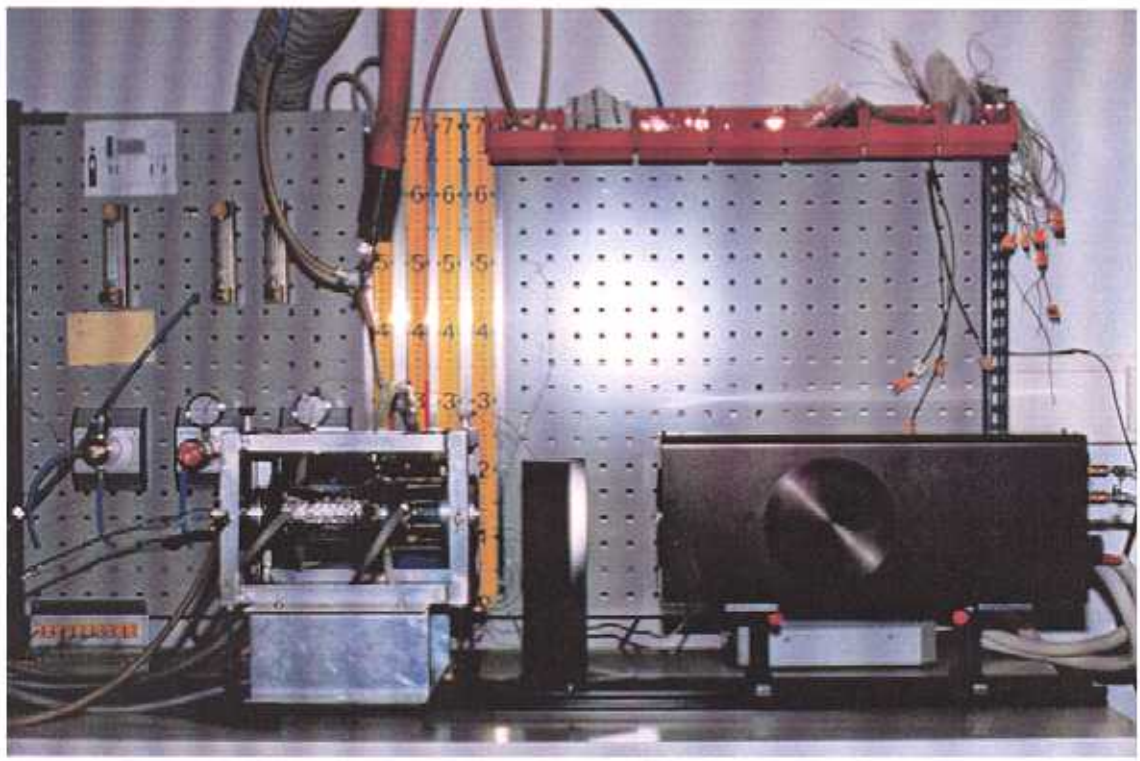

Figure 4.15 The set-up on the optical bench

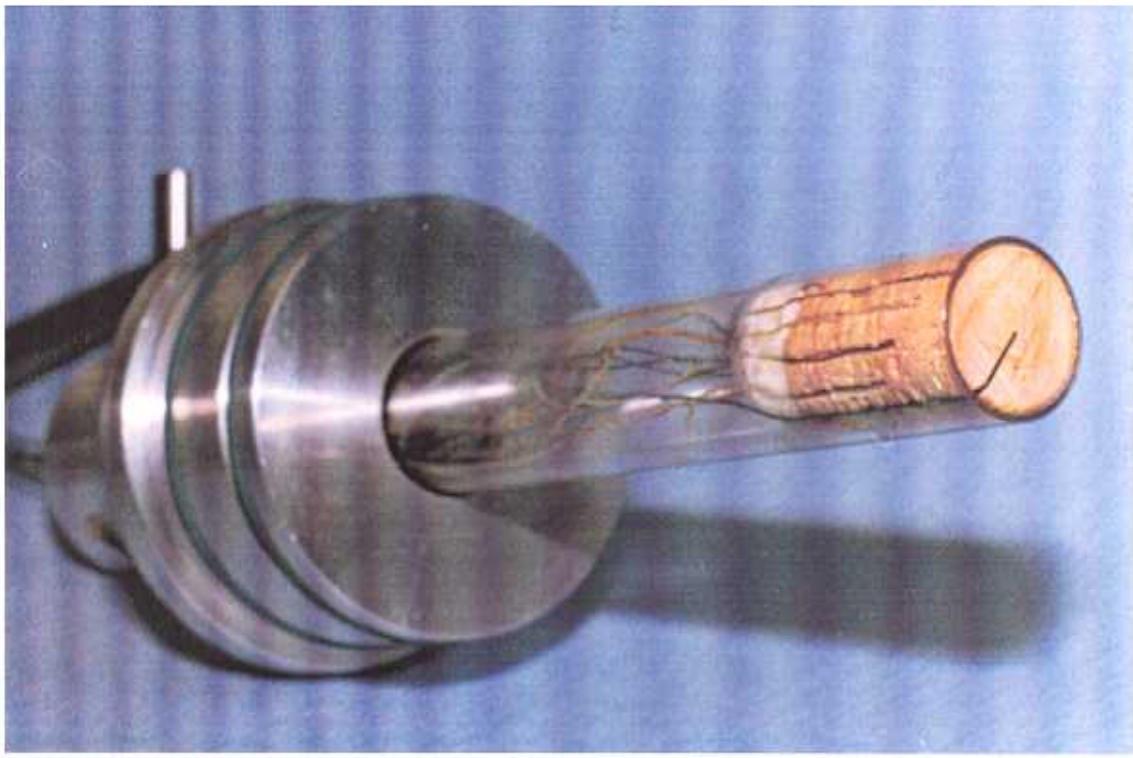

Figure 4.16 Glass tube with prepared sample in the reactor back

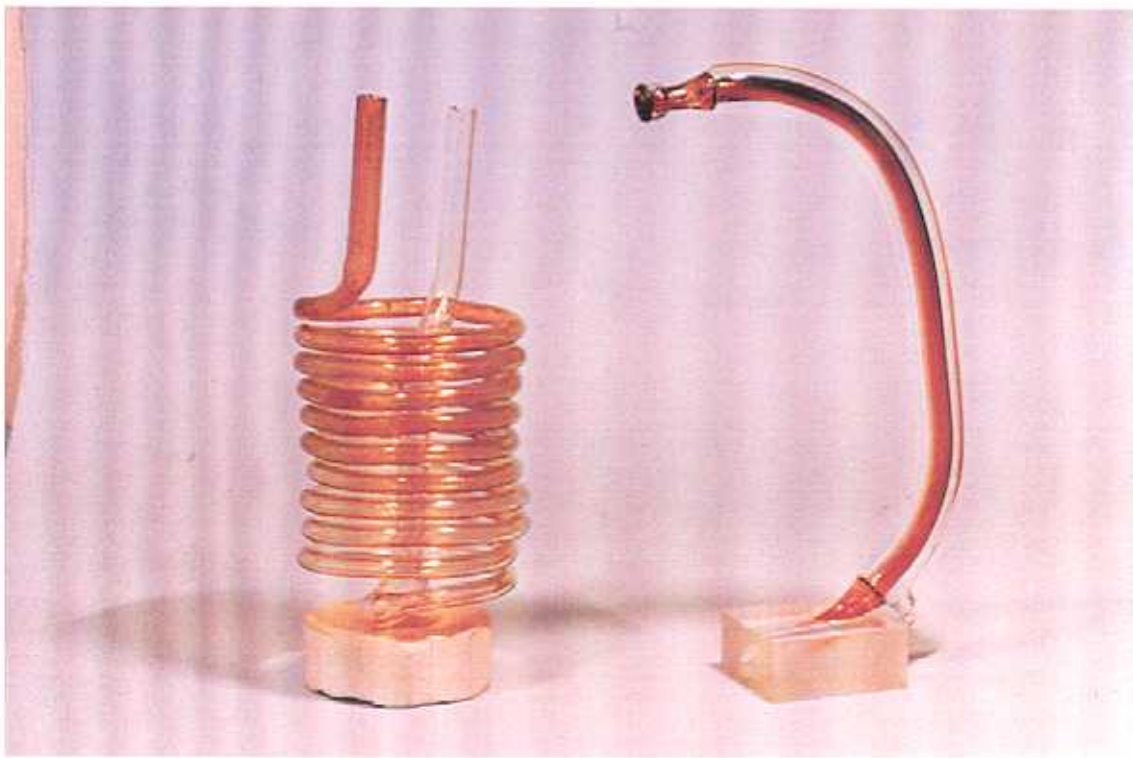

Figure 4.17 Condenser (left) and double-walled outlet tube (right). The dark colour inside the tubes are condensed tar.

4.4.1.2 REACTOR

The reactor consists mainly of two parts: the glass reactor head and the reactor back with a glass tube into which the pellet is tightly fitted. The irradiated front pellet surface is flush with one end of the glass tube. The glass tube in turn is placed inside an aluminium sleeve joining the reactor head (see Figure 4.16). O-rings in this connector seal the back of the reactor. The glass wall and additional insulation around the glass tube ensure one-dimensional heating of the sample. The front face of the bell-shaped reactor head consists of a fused silica window, which allows maximum transmission of radiant energy (loss ≈ 10%). Two of the six inlet ports for the purge gas are located close to the window, three of them at the end of the glass reactor head, and the sixth one is located in the reactor back to purge the gas directly in the glass tube towards the back of the sample. The outlet port is located above and close to the pellet surface. Such a configuration reduces the possibility of volatile condensation on the window and decreases the residence time of the volatiles in the reactor. Nitrogen is used as purge (carrier) gas and for creating an inert atmosphere. A laminar flow of the purge gas is adjusted, so that the volatile products are swept out of the reactor with little back-mixing. The pressure at the back must be so high, that there is a positive gradient towards the heated surface of the pellet. Thus vapour and volatiles leaving the sample are purged immediately to the outlet of the reactor. There they are leaded through a double-walled glass tube (see Figure 4.17) to the condenser. The condenser or cold trap consists of a spiral glass tube (see Figure 4.17), which is located in a thermos bottle filled with dry ice (temperature: -75°C). Some of the gases condense there, and the rest is separated in two parts. One part flows through a heated tube and a heated pre-filter unit (all of them heated to 180°C) to the hydrocarbon analyzer. The second part flows through another tube with three parallel silica gel drying units and a pump to the CO/CO_2 and O_2 analyzers. The pressures in front and in back of the sample are measured with two u-tube manometers. To ensure stable conditions and positioning between the xenon lamp and the reactor, the assembly is mounted on a guide rail and placed on an optical bench (see Figure 4.15).

4.4.1.3 GAS ANALYZERS

There are 3 gas analyzers, all operating on different gas concentration measurement principles. The *"Servomex Oxygen Analyzer OA 580 A"* fabricated by SYBRON/Taylor, UK, measures the paramagnetic susceptibility of the sample gas by means of a proven magneto dynamic type measuring cell. The paramagnetic susceptibility of oxygen is significantly greater then that of other common gases. Because of this, oxygen molecules are attracted much more strongly by

a magnetic field than molecules of other gases, most of which are slightly diamagnetic. The *"URAS 10 E CO/CO_2 Analyzer"* fabricated by Hartmann & Braun, Germany, is a non-dispersive infrared (NDIR) analyzer, using the specific absorption of infrared radiation in the middle infrared spectral range (between 2 and 8 m wavelength). The *"SIGNAL Hydrocarbon Analyzer Modell 3000"* with *"SIGNAL Pre-filter Unit 333"* fabricated in UK is based on the flame ionisation detector (FID). This detector ionises carbon atoms in a hydrogen flame. Normally, a hydrogen flame produces negligible ions; however, most carbon bond containing compounds carried into the flame result in the formation of ions from the carbon atoms. The FID can measure most compounds with a hydrocarbon bond. When a number of different compounds are mixed, the detector will respond to the ppm/carbon number, e.g. 10 ppm CH_4 and 10 ppm C_3H_8 mixed together with an air diluent will produce an approximate reading of 40 ppm CH_4 equivalent. Normally, a response factor is determined for each hydrocarbon of interest. For these experiments, however, propane (C_3H_8) is used because it is the largest normal hydrocarbon constituent found in combustion processes and therefore it is more representative of expected emissions.

Some of the characteristic data of the analyzers are given in Table 4.17

Table 4.17 Some of the characteristic data of the analyzers

	Model and Manufacturer	Range Used	Output Signal	Accuracy and Repeatability	Response Time [s]	Detection Principle
O_2	Servomex OA580 A	0-10 vol%	0-1 V	≤ 1 % FSD	T_{90} = 6 s	Paramagnetic cell, inherently linear
CO	Hartmann & Braun, Uras 10E	0-10 000 ppm	0-10 V	≤ 1 % FSD	T_{90} = 6 s	Infrared absorption, analog, linearisation
CO_2	Hartmann & Braun, Uras 10E	0-5 vol%	0-10 V	≤ 1 % FSD	T_{90} = 6 s	Infrared absorption, analog, linearisation
HC	Signal Model 3000	0 - 4 ppm 0 - 10 ppm 0 - 100 ppm 0 - 1000 ppm 0 - 10 000 ppm	0 - 10 V in each range	≤ 1 % FSD	T_{90} = 1.5 s	Flame ionisation principle, inherently linear

4.4.1.4 TEMPERATURE MEASUREMENTS

The surface temperature of the pellet was measured by a single sheathed 0.5 mm thermo-couple and the internal temperatures were measured by seven two-wire thermocouples, 0.2 mm in diameter coated with Teflon. In addition, the surrounding (room) temperature, the temperature in the thermos bottle (condenser) and the temperature in the gas-flow at the outlet of the condenser were measured. The Chromel-Alumel thermocouples used were comprised of wires of nickel-chromium and nickel-aluminium alloy and are referred to as Type K.

4.4.1.5 DATA ACQUISITION

The signals from the thermocouples as well as the signals of the gas analyzers, the lamp's power supply and the heat flux meter were delivered to two measuring units *"Model 35951C IMP"*, made by SOLARTRON SCHLUMBERGER, UK. The 3595 series of Isolated Measurement Pods (IMPs) are data collecting stations designed for remote operations by a host computer or data logger. For these experiments an *"IBM-PC (386)"* was used as a host computer for monitoring and saving of data. Every 3 seconds all channels of tense were logged by the computer. All communication was via twin-cored cable and conformed to the standard, S-Net (Solartron Network for Distributed Data Acquisition). Each *"35951C IMP"* provided twenty channels of reed-relay switching, which could be used to measure voltage, currency or temperature.

4.4.2 EXPERIMENTAL PROCEDURE

4.4.2.1 SAMPLE PREPARATION

Pellets of birch, spruce and pine were prepared from dry boards by cutting out dowels (D≈22 mm, L≈35 mm) using a hole saw. Figure 4.18 shows the dowel's position in the tree which corresponds to the grain directions used in the experiments. A wood lathe was further used to adjust the diameter of the pellets so they fitted exactly in the glass tube of the reactor back. The length was exactly cut by a high speed grinder.

Holes for thermocouples were carefully drilled through the radial direction by using a 0.5 mm drill. In addition, the holes were enlarged from one side to the centre by using a 0.7 mm drill. By doing so, the welding point of the two wires of one thermocouple, being bigger than 0.5

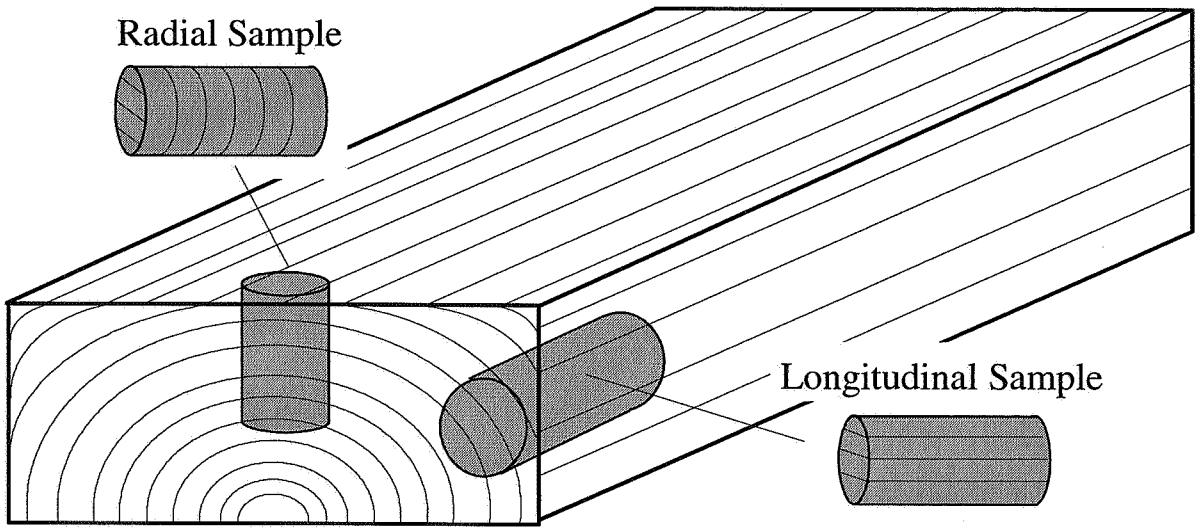

Figure 4.18 Dowel's bored out from a wood board

mm in diameter, could be exactly positioned in the centre of the sample. This procedure also ensured good thermal contact between the welding point where the temperature is measured and the wood. Small tracks were shaped from the outlet of the holes to the back of the sample so the pellet could be fitted into the glass tube even with the thermocouple wires at its side. This was done for all the seven thermocouples in the pellet at distances of 1, 4, 8, 12, 16, 20 and 24 mm from the front as shown in Figure 4.19. An additional track for the sheathed thermocouple (surface temperature) was shaped straight from the front to the back of the pellet.

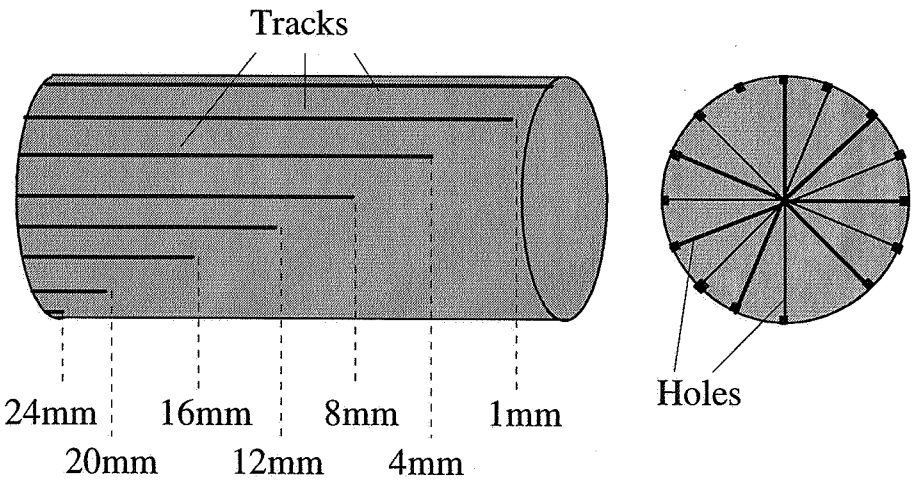

Figure 4.19 Positioning of the holes and tracks for the thermocouples

The pellets were afterwards dried for 24 hours at 105°C and stored in a desiccator until they were used.

4.4.2.2 CALIBRATION ROUTINES

The gas analyzers were calibrated according to the procedures given in the operation manuals (zero and span calibration). One of the most important parts of each experiment, however, was the calibration of the Xenon arc lamp. The goal was to achieve a uniform heat flux on the pellet surface with sufficient intensity. This was done by adjusting the focusing point of the light beam by the reflector within the lamp housing. The focusing point of this light beam is very sensitive to temperature variations. The lamp was therefore ignited and heated for a period of 30 minutes before the adjustments started. For the calibration of the lamp, several testing methods had to be examined. In a first step the beam had to be focused and centred. A piece of wood was used, exactly fixed in that position where the sample surface was located during the experiment. The fraction of the light beam with the highest intensity had to describe a circle centred in the circle of the whole beam, and the electrode reflection of the arc should not be visible on the wood piece. In a second step, the intensity distribution of this centred beam was analyzed. A metal testing plate with three small holes (diameter 2 mm) at certain radii (r = 0, 5 and 9 mm) was fixed in front of the heat flux meter "*MOLECTRON PM 150X*". The distance from the testing plate to the lamp was the same as the distance from the pellet surface to the lamp used in the experiments. To analyze the intensity at one particular position, only one of the three hole was open while the two other were closed by small magnets. The measured heat flux at nine different positions were registered and the intensity distribution was evaluated, as shown in Figure 4.20.

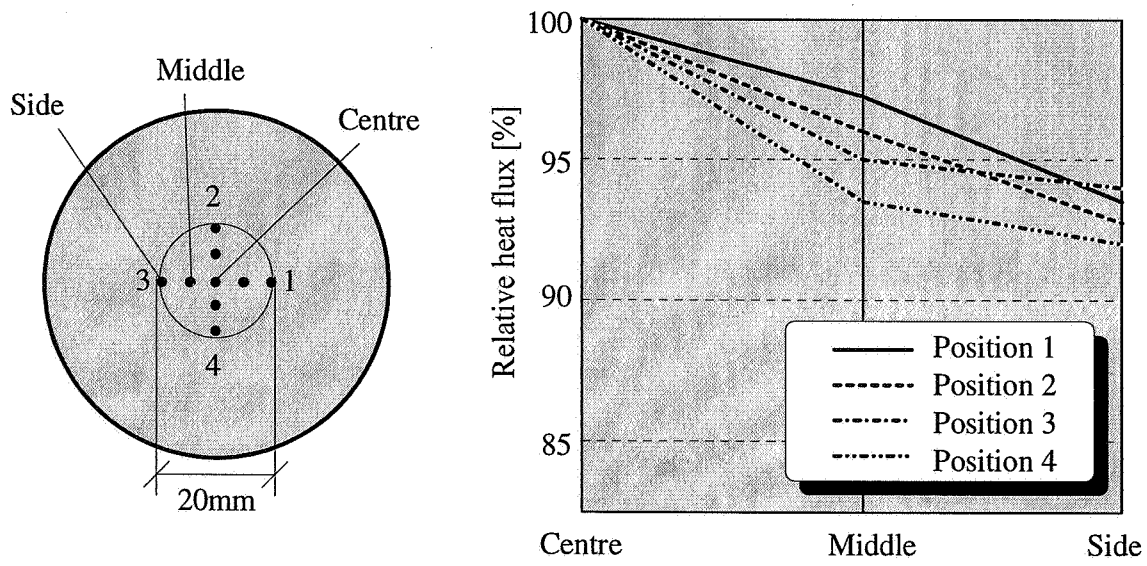

Figure 4.20 Metal testing plate for calibration of heat flux distribution.

If the intensity versus diameter was almost uniform (a maximum of 10% difference between the centre to the sides was allowed), the light was accepted for the experiment. If this was not the case, step one and two had to be repeated until the distribution was satisfactory. In a third step the heat flux versus electrical parameter was measured. An apparatus was used rebuilding the decisive parts of the reactor like front silica window, light reduction shield and a plate with a hole 20 mm in diameter. By using this apparatus, the light beam radiating the sample surface and the glass tube during the experiment could be simulated. It was fixed in front of the heat flux meter and the intensity of the light was measured for different values of the electrical parameter. Hence, the heat flux desired for the experiment could be obtained by simply adjusting the current delivered by the power supply.

4.4.2.3 ACTIVITIES BEFORE, DURING AND AFTER THE RUN

The weight, length and diameter of the sample were measured and recorded in an experimental journal, where all the data were written which were not recorded automatically by the IMPLOG system . The glass tube enclosing the sample was cleaned and weighted. The sheathed thermocouple was fixed onto the front surface of the pellet. The other seven thermocouples, which consisted of two wires, were mounted at certain, well-defined positions in the pellet. One wire of each pair was led through the prepared holes and welded together with the second one. The welding point, which actually measures the temperature, was pulled back into the centre of the sample. The wires of the thermocouples were led towards the back in the tracks and glued to an insulation piece. The insulation piece, which was glued onto the back of the sample, consisted of a 10 mm thick high temperature resistance fibre glass wool cylinder with a diameter being the same as the inner diameter of the glass tube. The sample together with the insulation piece and the thermocouples were then pushed into the glass tube, so that the front surface of the sample was in flush with the front of the glass tube (see Figure 4.16). Finally, the hole where the thermocouple wires left the reactor back was sealed with plasticine to avoid any leakage from behind. The time taken for installation of thermocouples and the insertion of the pellet into the glass tube was approximately one hour. A few percent moisture could be adsorbed from the environment by the pellet during this period of time, so the reactor back including glass tube, sample and thermocouples were placed in an oven until the sample was used. Before each experiment, the glass tube enclosing the sample was insulated by 20 mm of glass wool (fiberfrax).

Before each experiment, all glassware including the reactor, fused silica window, condenser and double-walled outlet tube were cleaned by acetone, dried in an oven and weighted. The gas analyzers and arc lamp were calibrated according to the procedures described previously

and a shield was placed in front of the light beam. The reactor head was mounted in an aluminium frame which was positioned on the optical bench. The reactor back with glass tube, the prepared sample, and the thermocouples was put into the reactor head from behind. The silicon tubes connected to the purge gas system and u-tube manometers were fixed at the reactor's arms. Since it was necessary that the distance of the pellet from the arc lamp be identical for each experiment in order to obtain the desired pre-calibrated heat flux, the reactor was accurately positioned within the frame by using several spatial reference markers. The outlet of the reactor was connected to the inlet of the condenser by a double walled glass tube. The thermos bottle with the condenser inside was filled with dry ice and closed to cool this system down to - 75°C. The condenser outlet was then connected to the gas analyzers.

After the reactor, purge gas, u-tube manometers, condenser and gas analyzers were assembled, pure nitrogen (99.99%) was used to purge the system for at least 10 minutes to make sure that no oxygen was left inside the reactor. If there was still oxygen, indicated by the O_2 - analyzer, there was a leakage somewhere in the system, which had to be eliminated. The total flow rate of nitrogen was set to about 4.4 l/min by two rotameters.

To begin the experiment, the shield was removed from the beam pathway. At the same time the logging programme was activated so the IMPLOG data could be stored on the PC's hard-disk. The pyrolysis time for all experiments was 10 minutes, except for one set which were carried out with 5 minutes. After approximately one minute of exposure, a small amount of purge gas (0.18 l/min) was allowed to flow inside the tube enclosing the sample to ensure that no volatiles could flow backwards and condense there.

When the experiment was over, the shutter was placed between the xenon arc lamp and the reactor to interrupt the light beam and stop the pyrolysis. The condenser was disconnected from the analyzer tubes and the reactor, sealed by cork plugs and taken out of the thermos bottle. The purging of the reactor with nitrogen was continued to cool the sample. The analyzers, the pumps and the heating of the tubes were switched off. After several minutes the reactor had been cooled enough so the reactor back including the inner glass tube and sample could be taken out of the reactor head. The pyrolysed sample was carefully taken out of the glass tube, the thermocouples were removed and the sample weight and length was measured. The black char was removed carefully from the light-colored un-pyrolysed pellet by a scalpel. Both portions were weighed and the length of the un-pyrolysed pellet was measured. The small amount of tar condensed at the outlet of the reactor was carefully cleaned by a cotton-wool stick (Q-tip), which was moistened with acetone. After the spiral-tube condenser reached room temperature, its weight, the weight of the double-walled outlet tube, the weight of the sample tube as well as the weight of the Q-tip was measured. The

increase in weight of all these were equal to the experimental tar and water yield, i.e. the condensable gases.

The data concerning weight and length measurements written in the experimental journal were all typed into a program which calculated the percentage reacted, axial shrinkage and the ultimate product yields, i.e. char, condensable (tar/water) and non-condensable gas fractions. In addition, the program prepared time-dependent plots of temperature profiles and CO, CO_2 and HC concentration profiles.

4.4.3 EXPERIMENTAL RESULTS

The data obtained from the experiments includes: 1) axial shrinkage; 2) reacted fraction (percentage pyrolysed); 3) temperature at 8 locations versus time; 4) CO, CO_2 and HC concentrations versus time; and 5) the ultimate product yields. To get some sort of statistical evidence, at least three, and sometimes four experiments were carried out at each condition, i.e. species/heat flux/grain orientation. The experimental matrix is presented in Table 4.18.

Table 4.18 Pyrolysis experiments on large particles

Species	Heat Flux	Grain Orientation	Number of Experiments	Total Time	Abbreviation
Birch	High	Longitudinal	4	10 min	BIHHLD
Birch	Low	Longitudinal	3	10 min	BILHLD
Birch	High	Radial	4	10 min	BIHHRD
Birch	Low	Radial	4	10 min	BILHRD
Pine	High	Longitudinal	4	10 min	PIHHLD
Pine	Low	Longitudinal	3	10 min	PILHLD
Pine	High	Radial	3	10 min	PIHHRD
Pine	Low	Radial	4	10 min	PILHRD
Spruce	High	Longitudinal	4	10 min	SPHHLD
Spruce	Low	Longitudinal	3	10 min	SPLHLD
Spruce	Low	Longitudinal	3	5 min	SPLHLD-5
Spruce	High	Radial	4	10 min	SPHHRD
Spruce	Low	Radial	4	10 min	SPLHRD

In the following discussion, the abbreviations in Table 4.18 will be used for simplicity:

Character 1+2: BI = birch, PI = pine, SP = spruce

Character 3+4: HH = high heat flux (130 kW/m^2), LH = low heat flux (80 kW/m^2)

Character 5+6: LD = longitudinal direction, RD = radial direction

e.g: birch - high heat flux - longitudinal direction will have the abbreviation BIHHLD. With these numerous measurements, only some of the time dependent data will be presented. For the data concerning axial shrinkage, reacted fraction and ultimate product yields, an average value :

$$\bar{y} = \sum_{i=1}^{n} \frac{y_i}{n} \tag{4.102}$$

with the standard deviation:

$$s = \sqrt{\sum_{i=1}^{n} \frac{(y_i - \bar{y})^2}{n - 1}} \tag{4.103}$$

will be presented, where n is the number of experiments and y_i is one single data point. In Appendix B, the results from all the experiments are tabulated with the calculated means and standard deviations. These are summarized in Table 4.19. Recall that in the evaluation of ultimate product yields, the amount of char and condensable gases (tar/water) have been measured while the total amount of non-condensable gases have been calculated by mass balance.

Table 4.19 Axial shrinkage, reacted fraction and ultimate product yields

Experiment	Axial shrinkage [%]	Reacted fraction [wt%]	Char [wt%]	Condensable gases [wt%]	Non-condensable gases [wt%]
BIHHLD	13.2±2.19	83.7±4.61	21.9±2.70	27.8±0.65	50.4±2.48
BILHLD	5.6±1.02	51.2±3.01	24.7±1.25	28.0±2.24	47.2±2.21
BIHHRD	30.1±2.63	98.5±2.95	21.4±2.61	30.5±5.35	48.1±4.08
BILHRD	18.3±1.52	62.3±3.12	22.6±0.29	40.3±2.41	37.0±2.77
PIHHLD	14.6±2.25	93.1±6.90	24.5±1.18	25.5±1.13	50.0±0.06
PILHLD	6.9±1.01	48.2±2.50	25.7±1.51	34.4±3.25	39.9±2.19
PIHHRD	0.2±0.40	78.8±5.73	24.4±1.16	30.7±1.24	45.0±1.16
PILHRD	2.4±1.19	51.6±5.44	28.8±0.93	40.6±6.41	30.7±7.33
SPHHLD	1.5±0.92	72.1±3.05	27.0±0.06	27.9±0.61	45.2±0.62
SPLHLD	2.7±2.34	45.5±3.61	28.7±1.06	31.3±5.06	40.0±5.45
SPLHLD-5	2.9±0.75	25.7±1.63	26.2±0.53	38.0±1.22	35.9±1.44
SPHHRD	4.1±4.23	82.0±15.18	23.3±0.17	33.0±4.23	43.7±4.36
SPLHRD	12.7±4.59	66.7±4.29	25.6±1.51	38.3±4.72	36.1±3.23

4.4.3.1 SHRINKAGE AND REACTED FRACTION

The average axial shrinkage and reacted fraction are presented in Figure 4.21 accompanied with some photos on the pages that follows showing the origin wood pellets, and the wood pellets after the experiments, - before and after the char layer was cut off.

As the photos indicate, wood is anisotropic in shrinkage characteristics and the deformation of birch, pine and spruce is different. Both at high and low heat fluxes, the axial shrinkage of the radial grain oriented samples of birch and spruce are higher than for the longitudinal ones while the opposite effect can be seen for pine. The deformation of the longitudinal samples is smaller compared to that of the radial ones. Beside shrinkage in the longitudinal direction, a noticeable shrinkage in the diametrical direction can be seen for both the radial and longitudinal samples. In addition, cracks in the front part of the spruce and birch radial samples can be observed. It seems that the total time of pyrolysis (Figure 4.21 d) has no influence on the axial shrinkage of spruce/longitudinal/low heat flux.

Obviously, the reacted or pyrolysed fraction for the high heat flux experiments is higher than for the low heat flux experiments. This is consistent for all wood species and grain orientations. In three out of four experiments on birch/radial/high heat flux, the sample was completely reacted, while in the fourth experiment 94% was reacted. By doubling the total time of pyrolysis from 5 to 10 minutes (Figure 4.21 d), the reacted fraction of spruce/longitudinal/low heat flux increased from 25 to 45 %. However, the most striking results shown in Figure 4.21 are the difference in percent reacted between the longitudinal and radial samples. Heating the radial samples (lower thermal conductivity) would be expected to exhibit a slower pyrolysis rate and therefore a smaller amount of reacted substrate for the same time. Except for pine, the trends indicate the opposite results. This can be explained by the relatively higher axial shrinkage in the char layer of the radial samples. Shrinkage will increase the heat transfer rate through the insulating char layer since its thickness is being reduced.

4.4.3.2 TEMPERATURE

In Figures 4.30-4.35, comparisons have been made of selected temperature distributions inside the pellets for different species, fiber direction and heating conditions.

Figure 4.30 compares low and high heating of longitudinal spruce while low and high heating of radial pine is compared in Figure 4.31. Obviously, the surface and in-depth temperatures

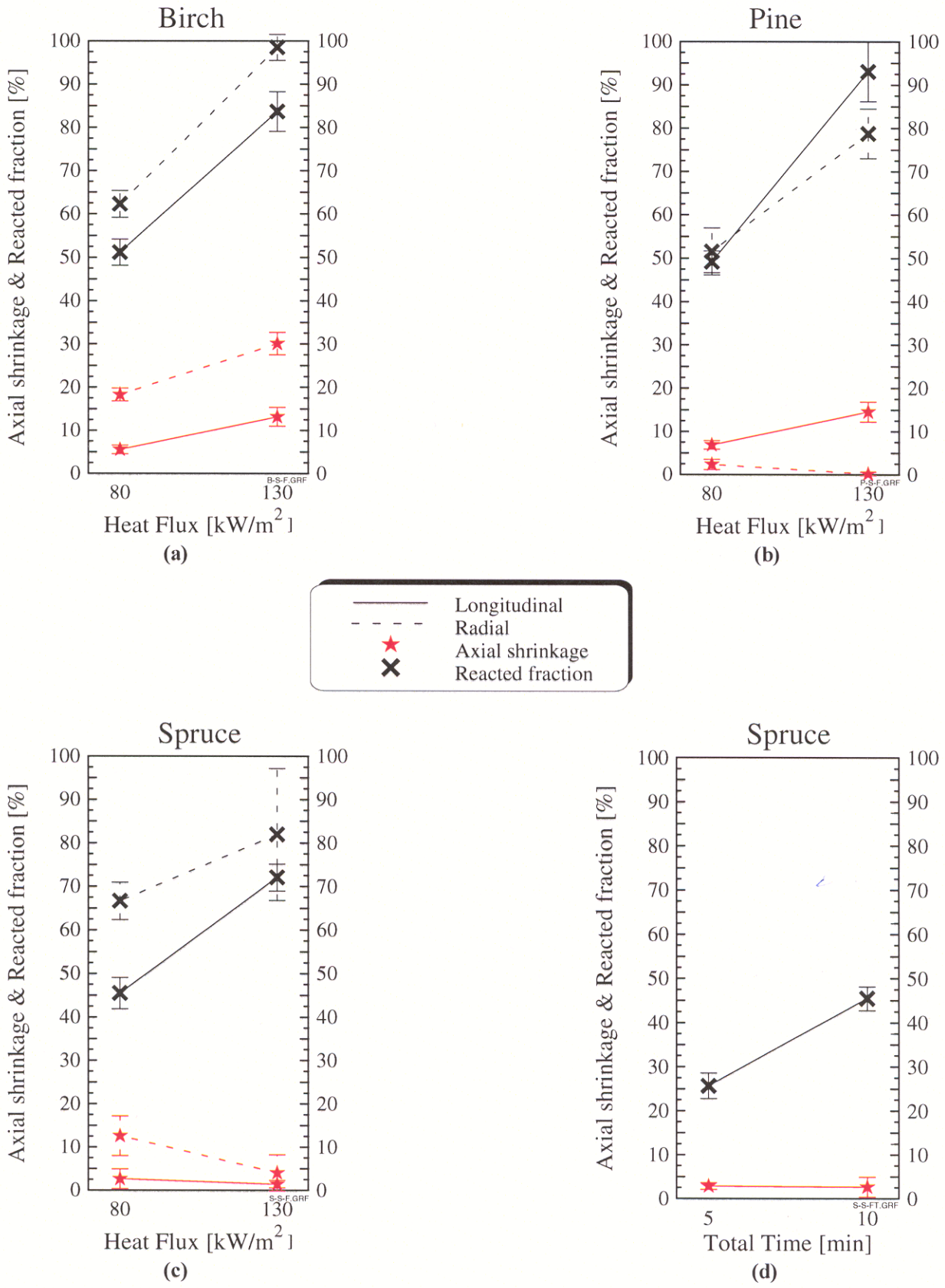

Figure 4.21 Average axial shrinkage and reacted fraction. The effects of grain orientation and heat flux.on (a) birch, (b) pine and (c) spruce. The effect of total time of pyrolysis on (d) spruce, longitudinal fiber direction, low heat flux.

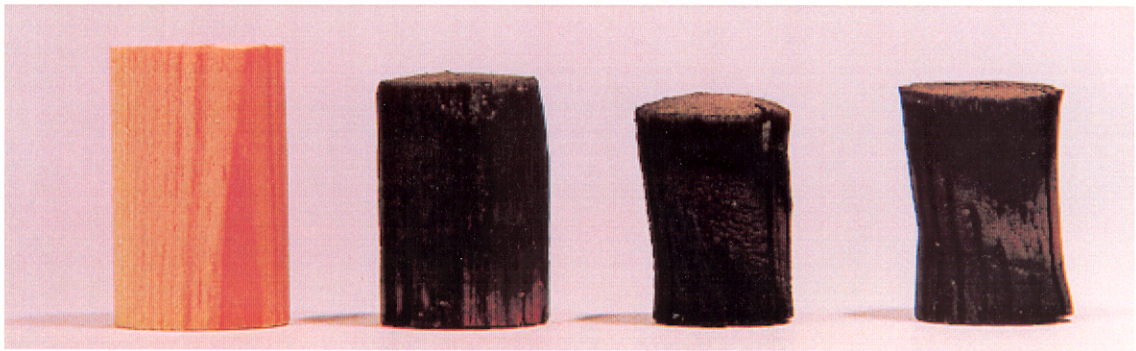

Figure 4.22 Shrinkage at high heat flux for longitudinal samples (REF., **SPHHLD, PIHHLD, BIHHLD**)

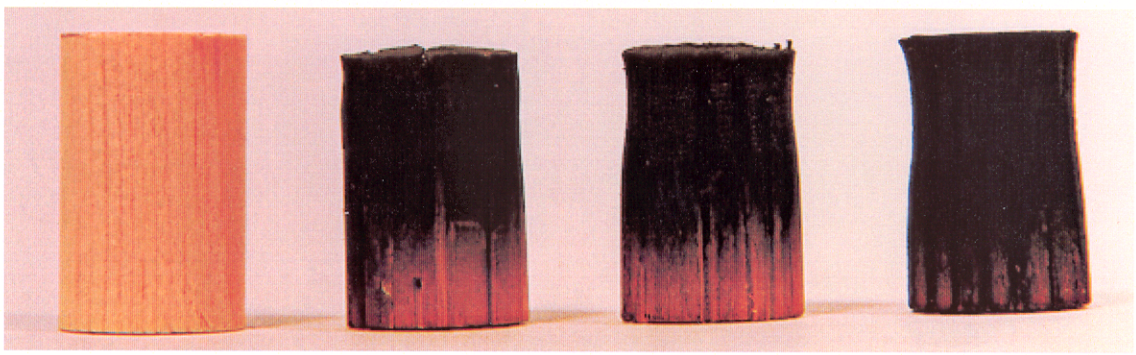

Figure 4.23 Shrinkage at low heat flux for longitudinal samples (REF., **SPLHLD, PILHLD, BILHLD**)

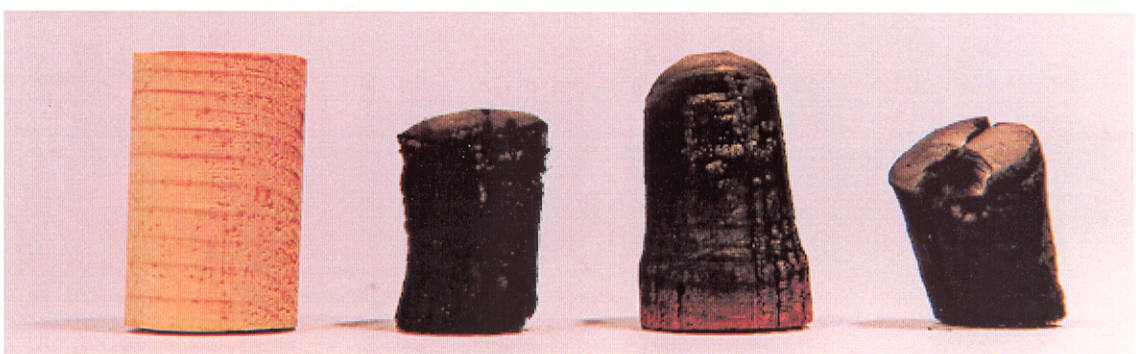

Figure 4.24 Shrinkage at high heat flux for radial samples (REF., **SPHHRD, PIHHRD, BIHHRD**)

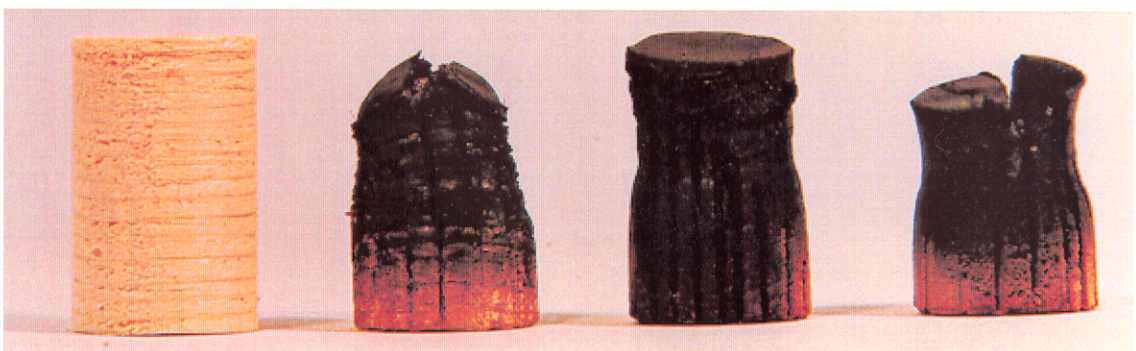

Figure 4.25 Shrinkage at low heat flux for radial samples (REF., **SPLHRD, PILHRD, BILHRD**)

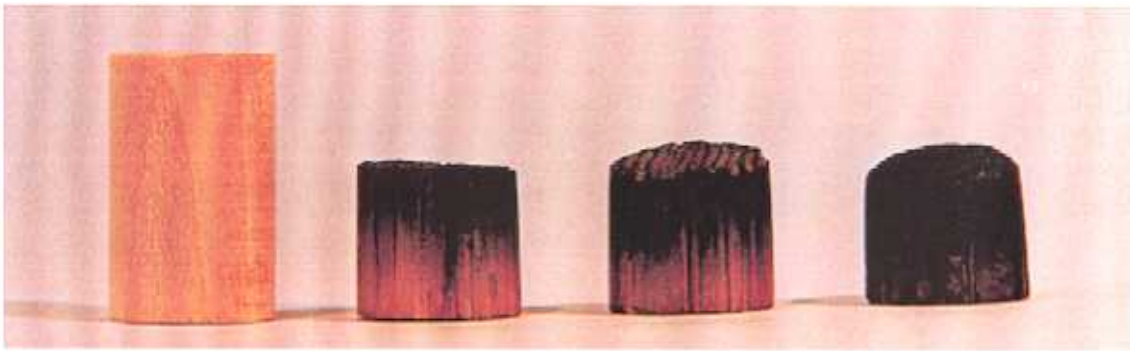

Figure 4.26 Virgin rest of longitudinal samples at low heat flux (REF., **SPLHLD**, **PILHLD**, **BILHLD**)

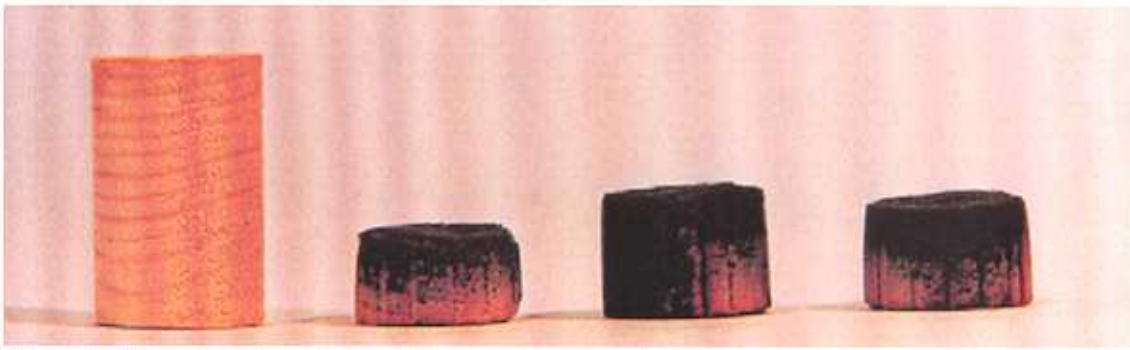

Figure 4.27 Virgin rest of radial samples at low heat flux (REF., **SPLHRD**, **PILHRD**, **BILHRD**)

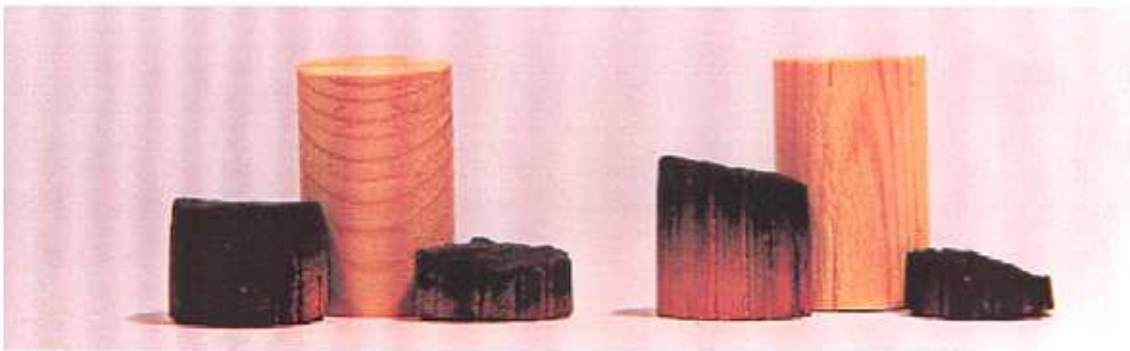

Figure 4.28 Virgin rest of pine samples (**PILHRD**, REF., **PIHHRD**, **PIHHLD**, REF., **PIHHLD**)

Figure 4.29 Virgin rest of birch samples (**BILHRD**, REF., —, **BILHLD**, REF., **BIHHLD**)

of both the longitudinal and radial pellets are significantly higher when exposed to a heat flux of 130 kW/m^2 compared to a heat flux of 80 kW/m^2. The temperature difference close to the surface is about 150°C in both the longitudinal and radial case after 10 minutes heating, but this difference slightly decreases as the temperature wave moves into the pellet. In Figure 4.30, a noticeable temperature plateau around 380°C can be seen for both the low and high heating of spruce. This is found especially at locations 8 and 12 mm from the surface where the temperature gradients are not so steep as at the front surface. A first explanation would be that this plateau is caused by the endothermic heat of pyrolysis. By using the theoretical model, insight into this phenomena was gained. The predictions proved that an endothermic heat of reaction delays the overall decomposition but does not give any sudden change in the temperature gradient as seen in these experiments. The most likely reason for the flattening or slope change of the temperature curves around 380°C is a reduction in the local thermal conductivity. When the substrate changes from wood to a more porous char, the local thermal conductivity decreases in a short period of time until the temperature reaches the level where the radiative contribution to the effective thermal conductivity becomes significant. This will be discussed more thoroughly in a later section where the experiments will be compared with theoretical predictions.

Recall that for the measurement of surface temperature, a sheathed thermocouple was pressed against the front surface of the pellet. Due to shrinkage, this thermocouple always lost contact and after a while, measured the gas temperature in front of the surface rather than the surface temperature itself. This explains why the temperature at 1 mm position in Figure 4.30 exceeds the surface temperature.

Figure 4.32 compares the longitudinal and radial heating of spruce at 130 kW/m^2 heat flux while the longitudinal and radial heating of spruce at a heat flux of 80 kW/m^2 are compared in Figure 4.33. During the first period of heating, the interior temperature of the axially heated pellets are rising faster than the radially heated ones as a result of higher initial thermal conductivity for the axially heated pellet. Although the interior temperature of the radially heated pellet rises more slowly, it reaches higher values at certain positions in the latter period of the experiment as a result of shrinkage. During shrinkage, the char layer thickness is reduced and the heat transfer rate through the char layer increases. In addition, the front surface moves slightly away from the arc lamp, thus getting closer to the focusing point of the lamp so that the intensity of the radiant beam increases.

Figures 4.34 and 4.35 compare the longitudinal heating of birch, pine and spruce at high and low heat flux, respectively. During the first one and a half minute of the experiments, the

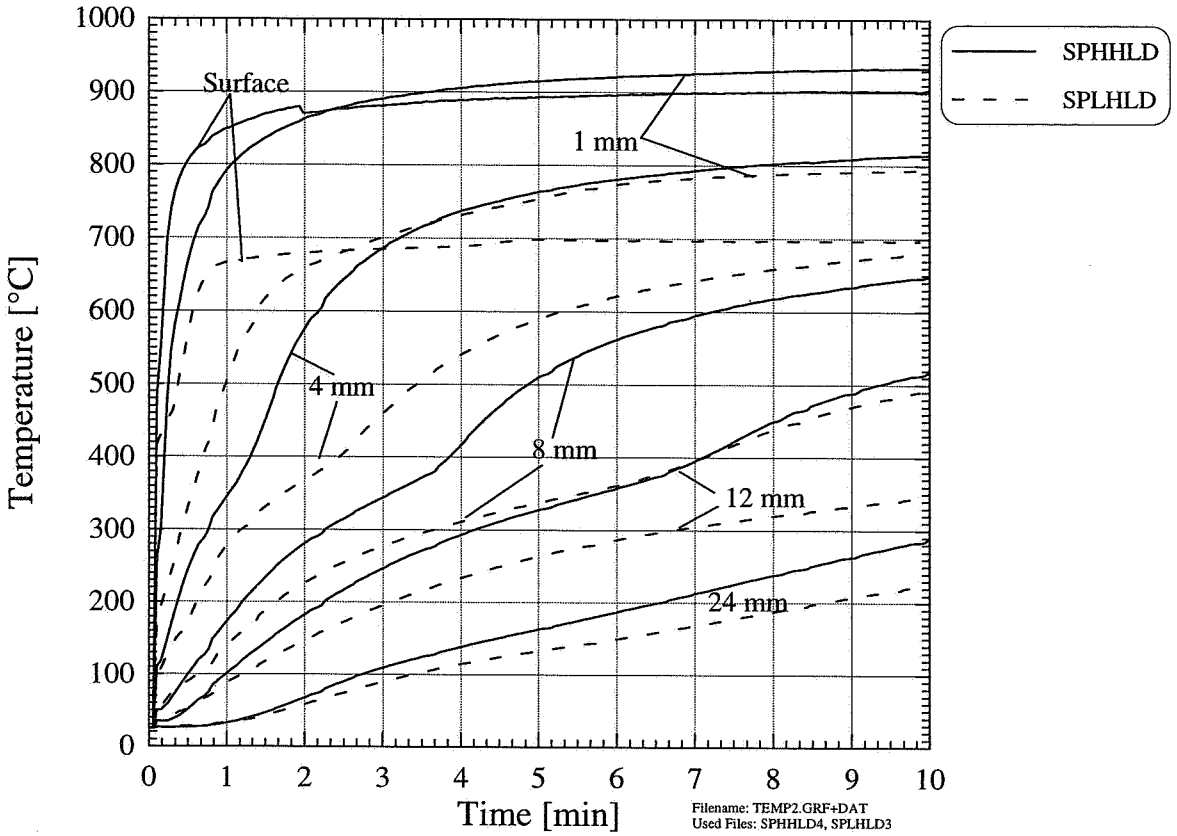

Figure 4.30 Comparison between high and low heating of spruce, longitudinal grain orientation.

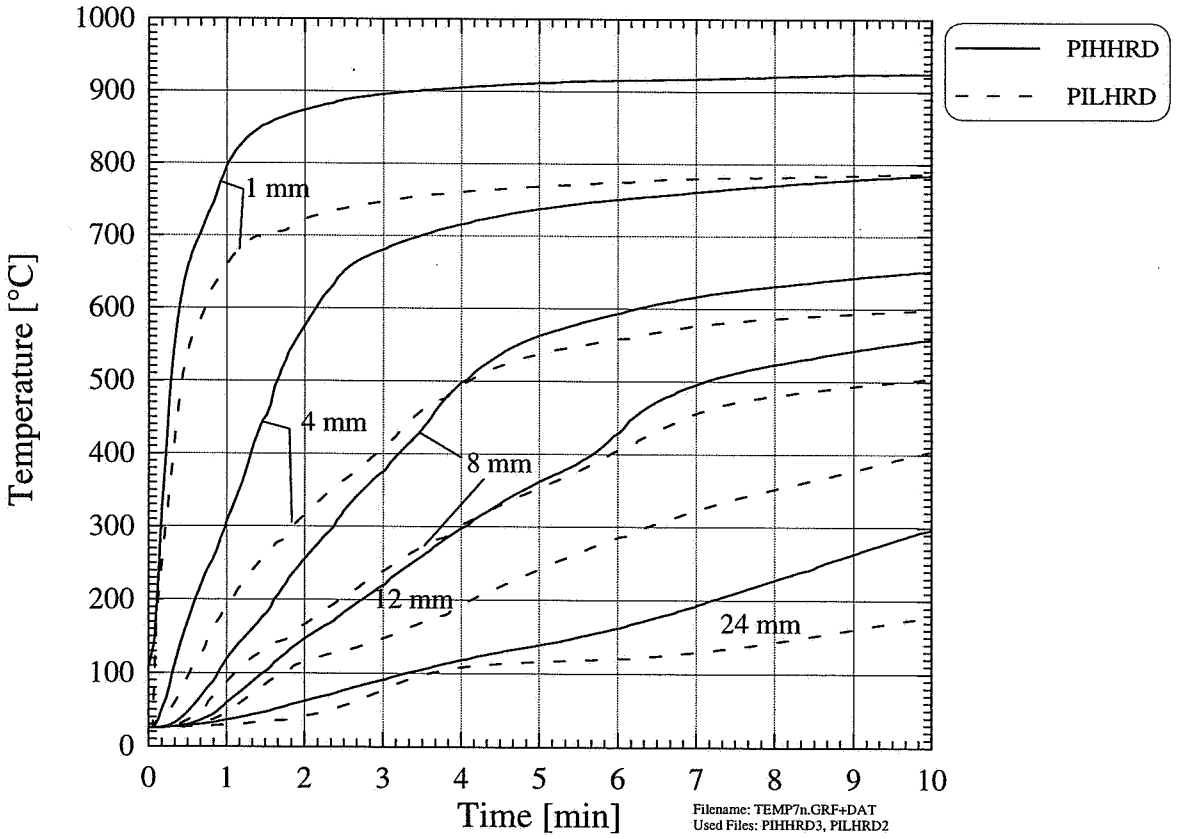

Figure 4.31 Comparison between high and low heating of pine, radial grain orientation.

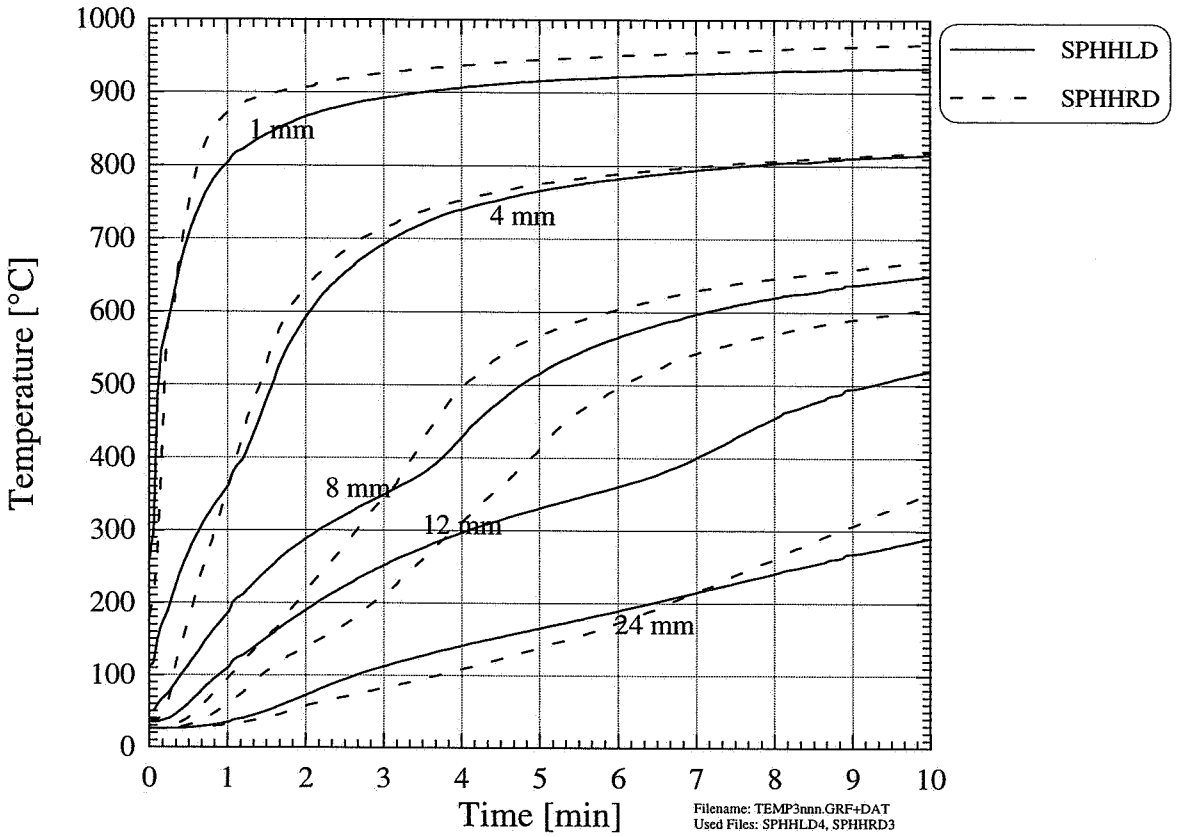

Figure 4.32 Comparison between longitudinal and radial heating of spruce, high heat flux.

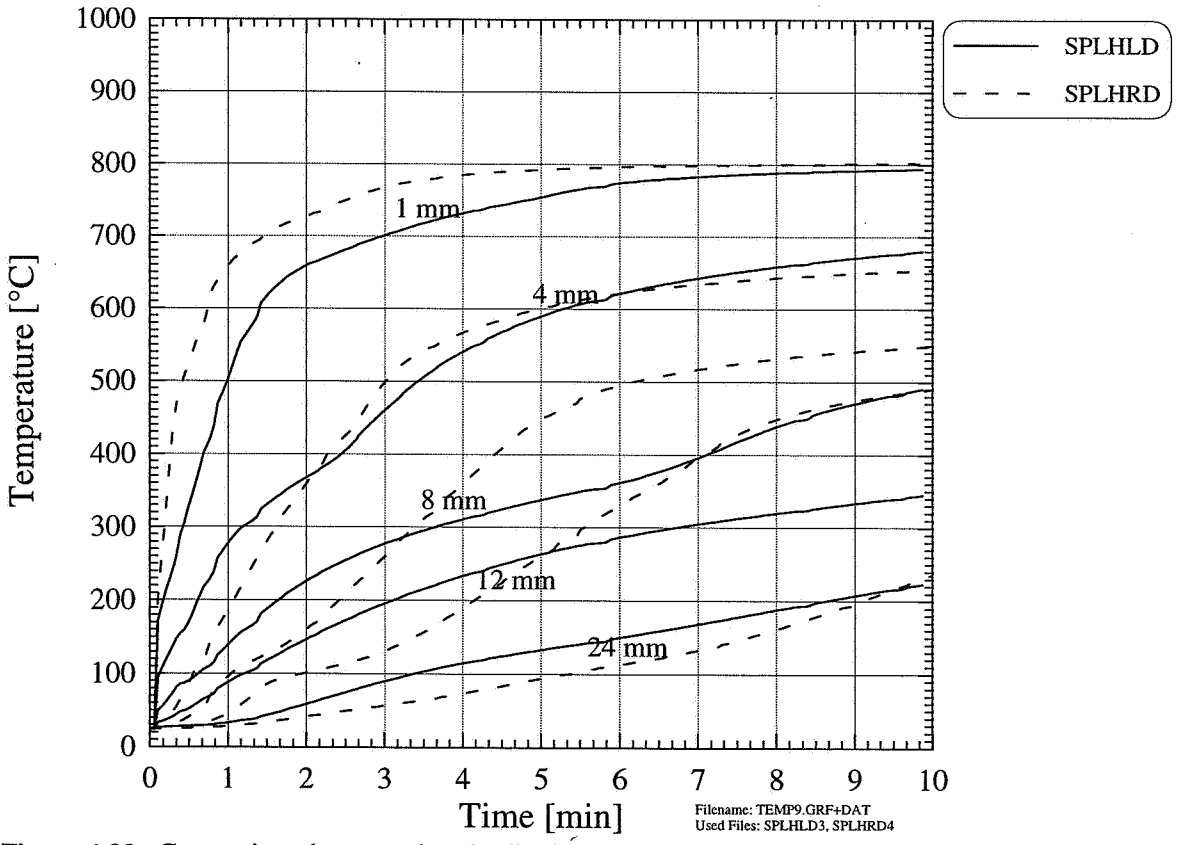

Figure 4.33 Comparison between longitudinal and radial heating of spruce, low heat flux.

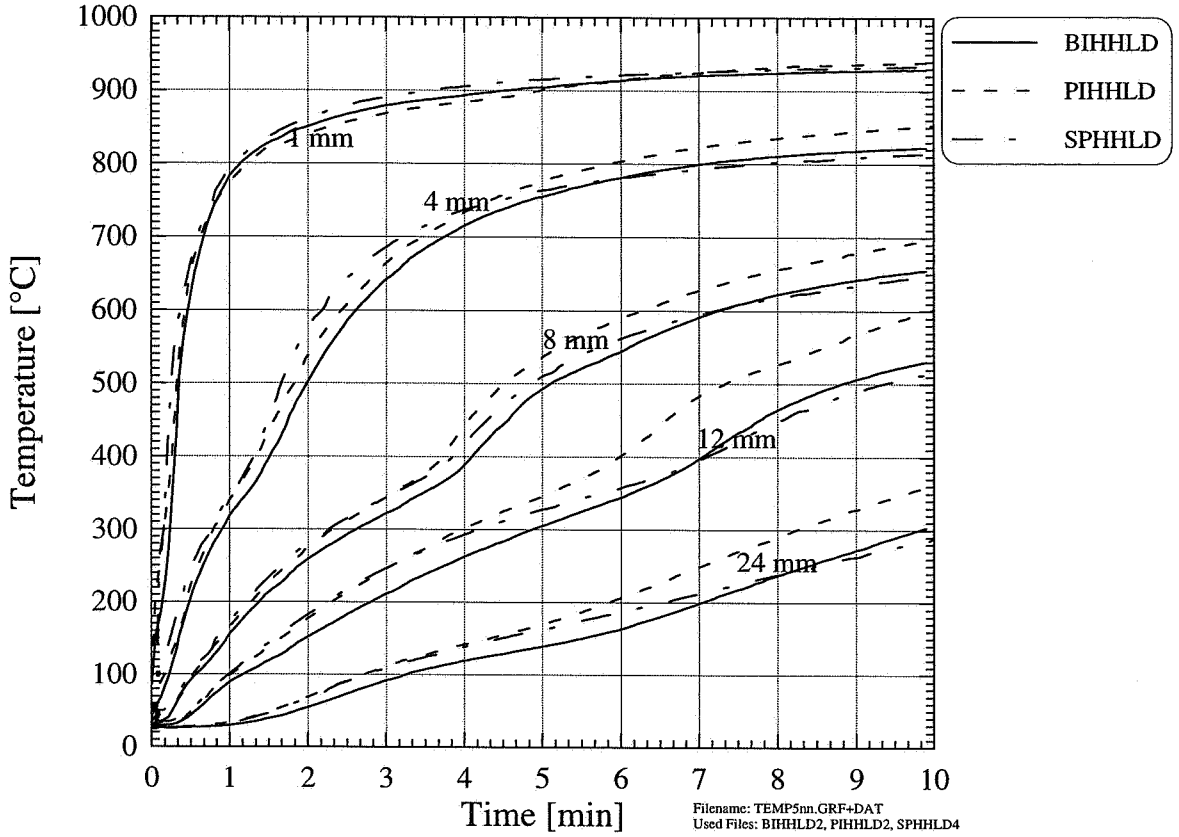

Figure 4.34 Comparison between birch, pine & spruce, longitudinal grain orientation, high heat flux.

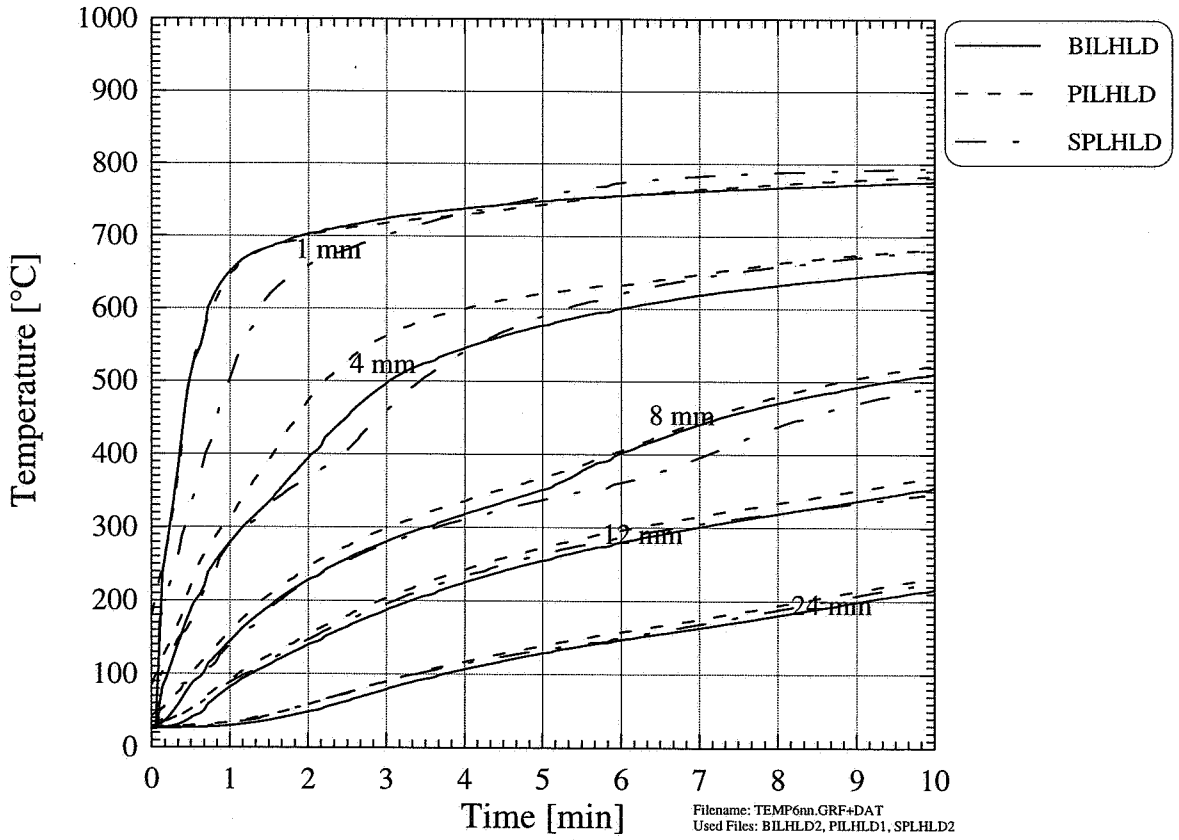

Figure 4.35 Comparison between birch, pine & spruce, longitudinal grain orientation, low heat flux.

differences between the three wood species are comparatively small. After approximately 4 minutes heating, the temperatures of pine at high heat flux (Figure 4.34) increase faster than those of birch and spruce due to greater axial shrinkage. The reason why the temperatures inside birch with a relative high axial shrinkage and initial high thermal conductivity (due to its higher density) lag the temperatures of pine and spruce is not known.

4.4.3.3 ULTIMATE PRODUCT YIELDS AND GAS COMPOSITION

The average ultimate product yields are presented in Figure 4.36. In general, as the heat flux is increased from 80 to 130 kW/m^2 the yields of char and condensable gases (tar/water) decrease while the yield of non-condensable gases increases. Higher heat fluxes means that there are higher temperatures in the char layer and that more of the substance is reacted. Hence, the distance the volatiles must travel, i.e. the residence time in the hot char layer increases as the pyrolysing zone propagates further into the wood, promoting secondary reactions of the heavy tar molecules. The exception is birch samples heated axially for which the condensable fraction is almost unaffected by the heat flux. This cannot easily be explained. An interesting observation, however, is that for both heat fluxes and grain orientations, birch yields a somewhat lower char-fraction than pine and spruce, consistent with lower char-fraction observed in the TGA experiments.

By comparing the two grain orientations for the same species and heat flux, it is evident that the condensable product fractions are lower for the longitudinal than the radially heated samples. From a theoretical point of view, heating the radial samples with lower permeability, i.e. higher mass transfer resistance to volatile outflow, would be expected to promote secondary reactions, thus, increasing the gas yield at the expense of tar. However, this counter intuitive result can again be explained by the relative higher axial and diametrical shrinkage in the char layer of the radial samples which makes it easier for the volatiles to escape. In addition, huge cracks in the char layer of birch and spruce radial samples (see Figures 4.24-4.25) may also shorten the residence time and thus the reaction of the volatiles inside the hot char layer.

By doubling the total time of exposure from 5 minutes to the usual 10 minutes, the ultimate yields of char and non-condensable gases from spruce/longitudinal/low heat flux increase while those of condensable gases decrease. Recall from Figure 4.21 (d) that the axial shrinkage was unaffected while the reacted fraction increased from 25 to 45 wt%. The residence time of tar inside the char layer will nonetheless increase since the char layer becomes thicker as a consequence of longer pyrolysing time. Hence, cracking of the tar components

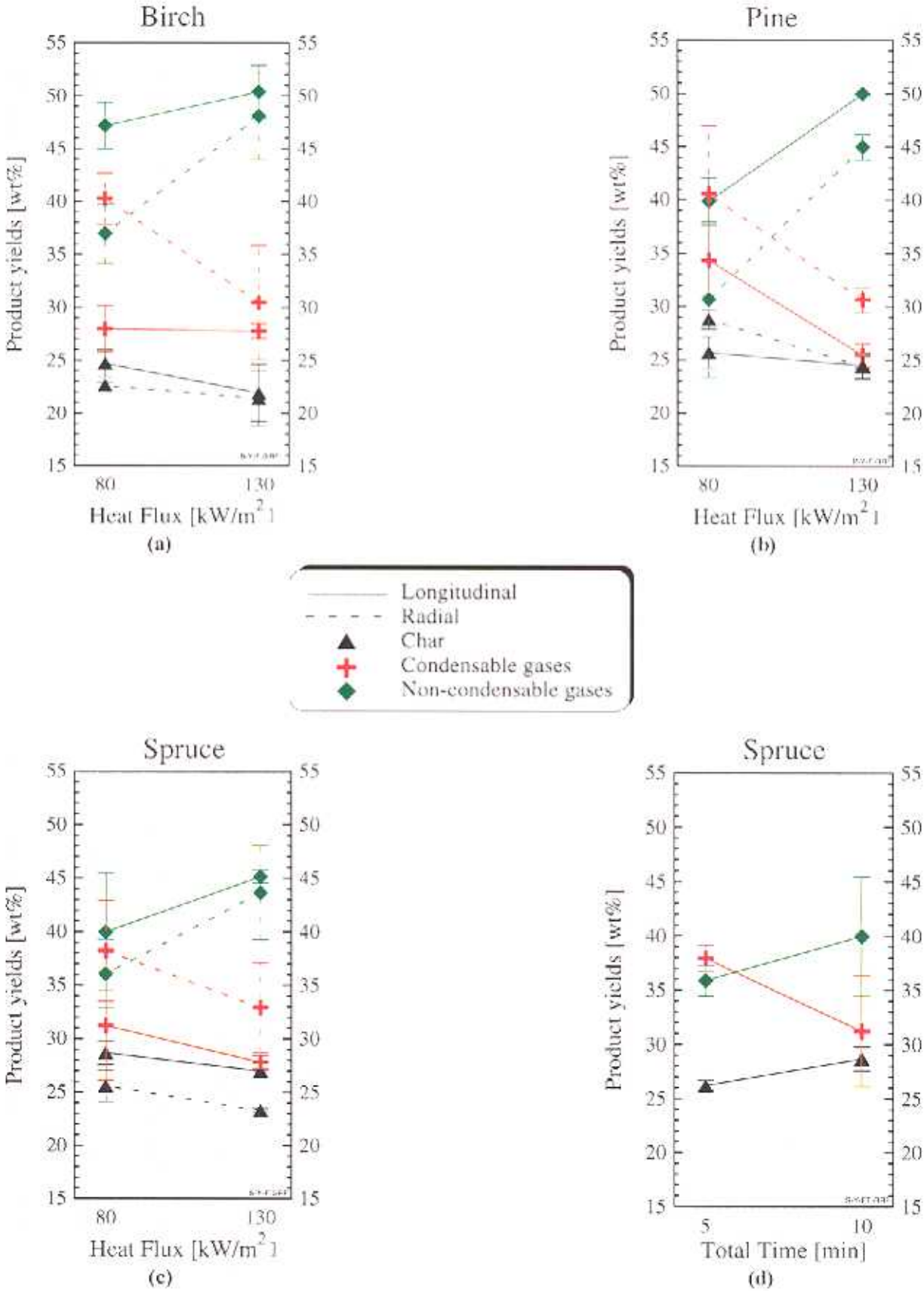

Figure 4.36 Ultimate product yields. The effect of grain orientation and heat flux on: (a) birch, (b) pine and (c) spruce. The effect of total time of pyrolysis on (d) spruce, longitudinal.....

to form gas products may explain the increase in ultimate yield of non-condensable gases. If one assumes that the local char density is dependent on the local temperature history, one may expect that the char density close to the surface going through a very rapid heating (steep temperature gradients) is lower than the char density in the interior of the pellet where the heating rate is much slower. Hence, the local char density will slightly increase with pellet depth and so does the average (integrated) char yield as the pyrolysing front propagates into the wood pellet. Another reason which may explain the increased ultimate char yield in the 10 min. experiment is that more char is formed through a repolymerization reaction of the tar.

For comparison, the ultimate product yields reported in the work of Chan (1983) are listed in Table 4.20. Chan used pellets of Oregon lodgepole pine with an initial density and moisture content of 375 kg/m^3 and 5%, respectively. Chan (1983) studied the effects of: grain orientation (longitudinal, radial and tangential); heat flux (83, 167 and 250 kW/m^2); and pellet length (5, 10 and 15 mm) and the total time of pyrolysis was 12 minutes for all the experiments. While the ultimate char yields are within the same range, the yields of non-condensable gases of the present study are higher and the yield of condensable gases (tar/water) are lower than in the work of Chan (1983). The reasons for this difference may be explained by different experimental conditions (heating, insulation, surface temperatures) and wood species (sample length, diameter and density).

Table 4.20 Comparison of ultimate product yields.

	Present study	Chan (1983)
Pyrolysis temperature [°C]	150-970	150-900
Char [wt%]	21-29	20-26
Tar [wt%]	25-40[†]	33-52
Water [wt%]	---	9-19
Gases [wt%]	30-50	11-27
CO [wt%]	---	5-15
CO_2 [wt%]	---	6-10
CH_4 [wt%]	---	0.3-1.8

[†] Water included in the tar fraction.

Beside collecting the water and tar in the cold trap, Chan (1983) collected the non-condensable gases and analyzed them by gas chromatography. Since some of the volatiles condensed on the reactor wall and was not easily removed, the determination of non-condensable gas and char yields were considered to have a higher accuracy than the yield of condensable gases. The weight of condensable gases collected in the cold trap was always

between 10 and 15 wt% lower than the one calculated by mass balance. Hence, the fraction of condensable gases presented in this study may also be in the range of 10 to 15% too low. By accounting for the 5 % initial moisture content in Chan's pellets, the present ultimate product yields become closer to those obtained by Chan. The CO, CO_2 and CH_4 fractions cover between 97 to 99 wt% of the total gas yield in Chan's work.

The number of gas species measured in the present study was very limited since there was no access to multi-gas analysing equipment (gas/liquid chromatography, FTIR or mass spectrometry). The condensable fraction was not analyzed for composition nor water content and the gas species measured were CO, CO_2, O_2 and total hydrocarbons (HC). Since no oxygen was detected, the oxygen analyzer was only used to check if there was any leakage in the reactor system. The flow rate ($\dot{V}_{flow}$) of purge gas (N_2) was not constant from experiment to experiment. It could even be adjusted within one particular experiment. Since higher flow rates mean higher dilution (and reverse), a comparison between the CO, CO_2 and HC concentrations of the different experiments can only be made if the concentrations are somehow normalized by the flow rate. To do so, the CO, CO_2 and HC concentrations have been multiplied by the flow rate and divided by a fixed constant so their relative values become between zero and one:

$$[CO]_{relative} = \frac{\dot{V}_{flow} \cdot [CO]_{actual}}{5}$$

$$[CO_2]_{relative} = \frac{\dot{V}_{flow} \cdot [CO_2]_{actual}}{5} \qquad (4.104)$$

$$[HC]_{relative} = \frac{\dot{V}_{flow} \cdot [HC]_{actual}}{30\,000}$$

The maximum actual gas concentrations measured are listed in Appendix B.

Figures 4.37 and 4.38 compare the relative gas concentrations from low and high heating of spruce longitudinally heated samples. The corresponding temperature plot is shown in Figure 4.30.

Obviously, the maximum levels of CO, CO_2 and HC for the high heat flux experiments are higher than for low heating due to a higher rate of reaction. Another point is that the total amount of non-condensable gases are higher in the high heat flux experiment. Both the CO and HC concentrations increase and reaches a maximum between 30 and 120 seconds before they decrease and level off at the end of the experiment. The second peak observed on the HC-curve is a consequence of an adjustment of the purge gas. After the first critical 1 to 1.5

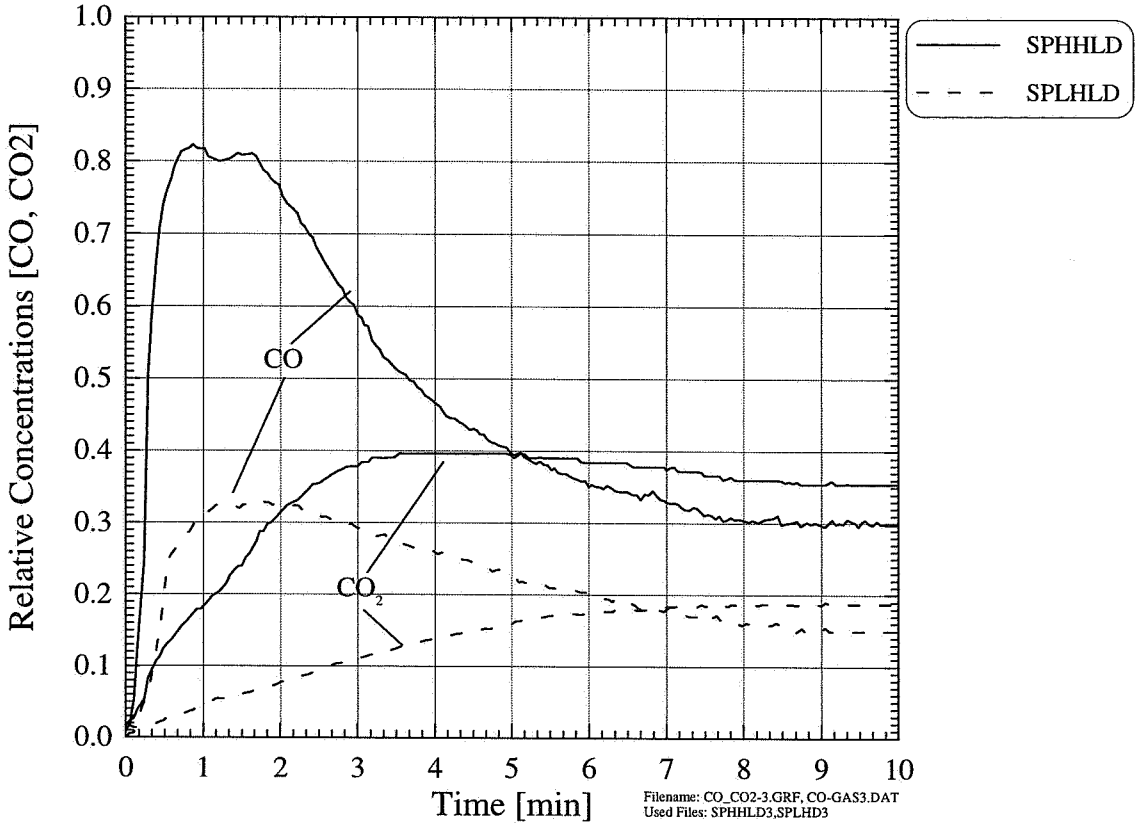

Figure 4.37 Relative CO and CO_2 concentration profiles of spruce, longitudinal grain orientation, exposed to high and low heat flux.

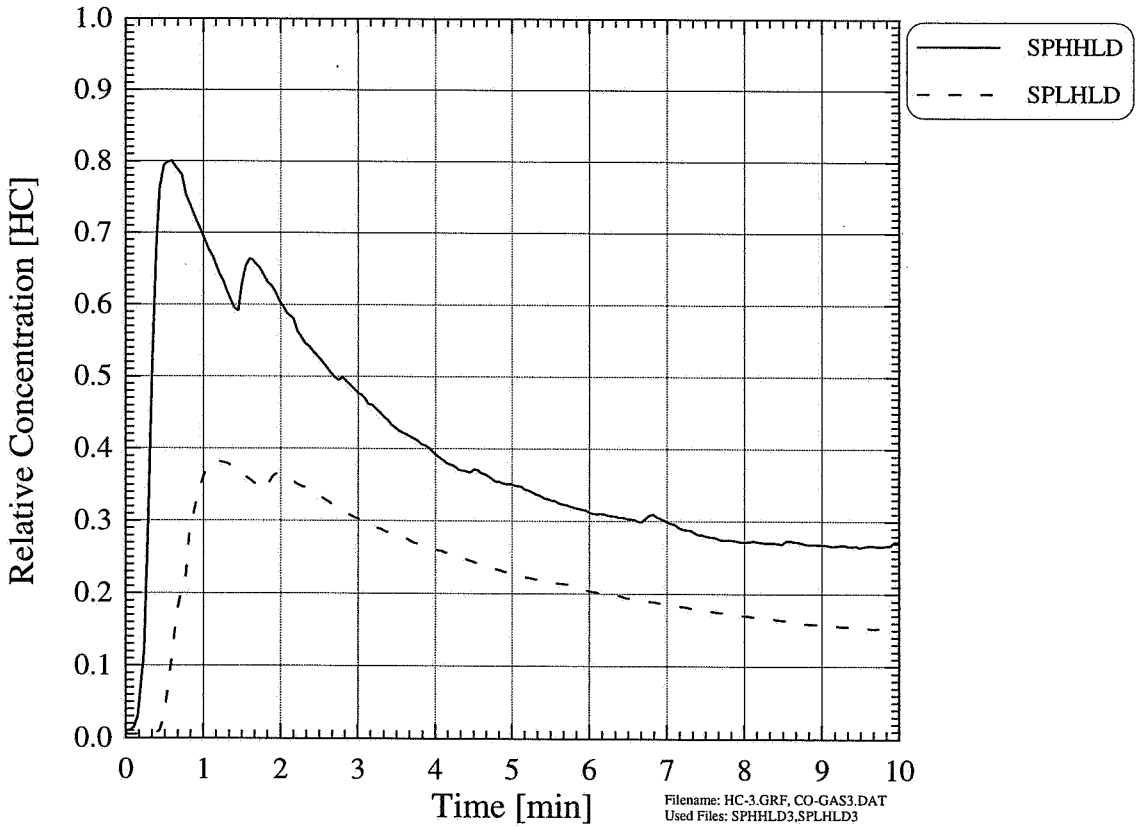

Figure 4.38 Relative HC concentration profiles of spruce, longitudinal grain orientation, exposed to high and low heat flux.

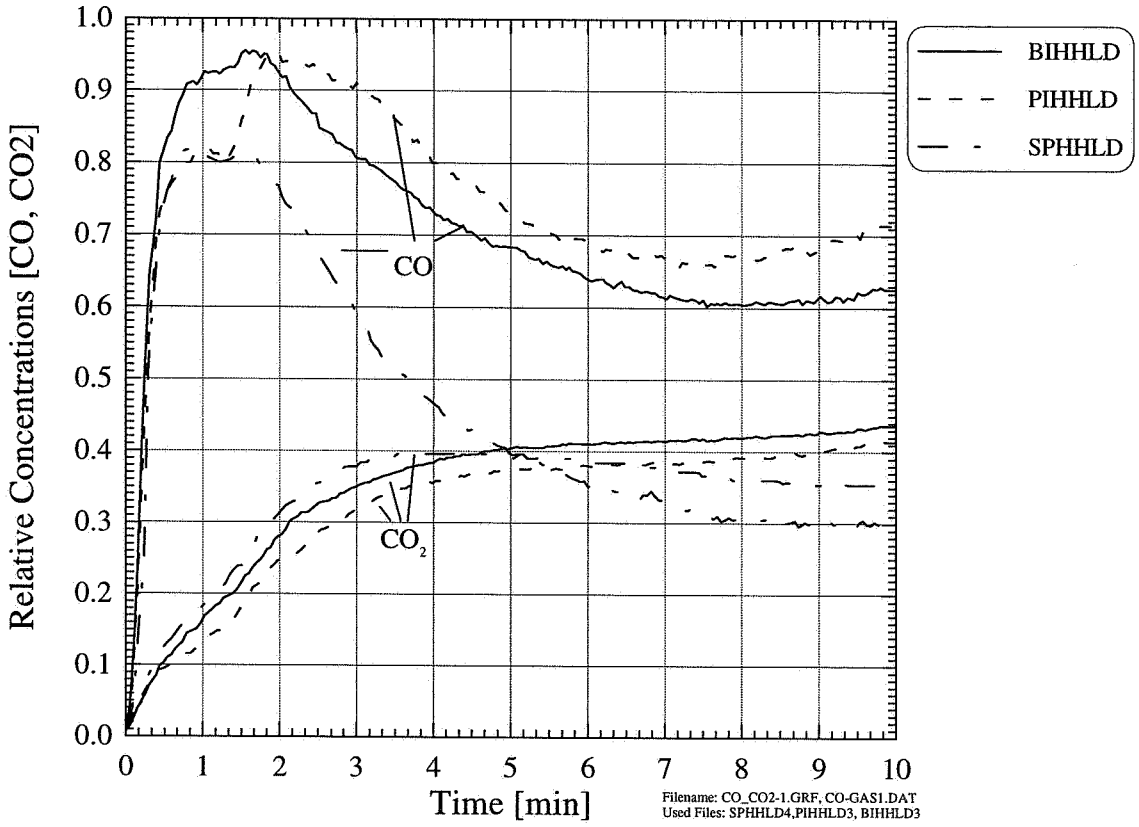

Figure 4.39 Relative CO and CO_2 concentration profiles for birch, pine and spruce, longitudinal grain orientation, high heat flux.

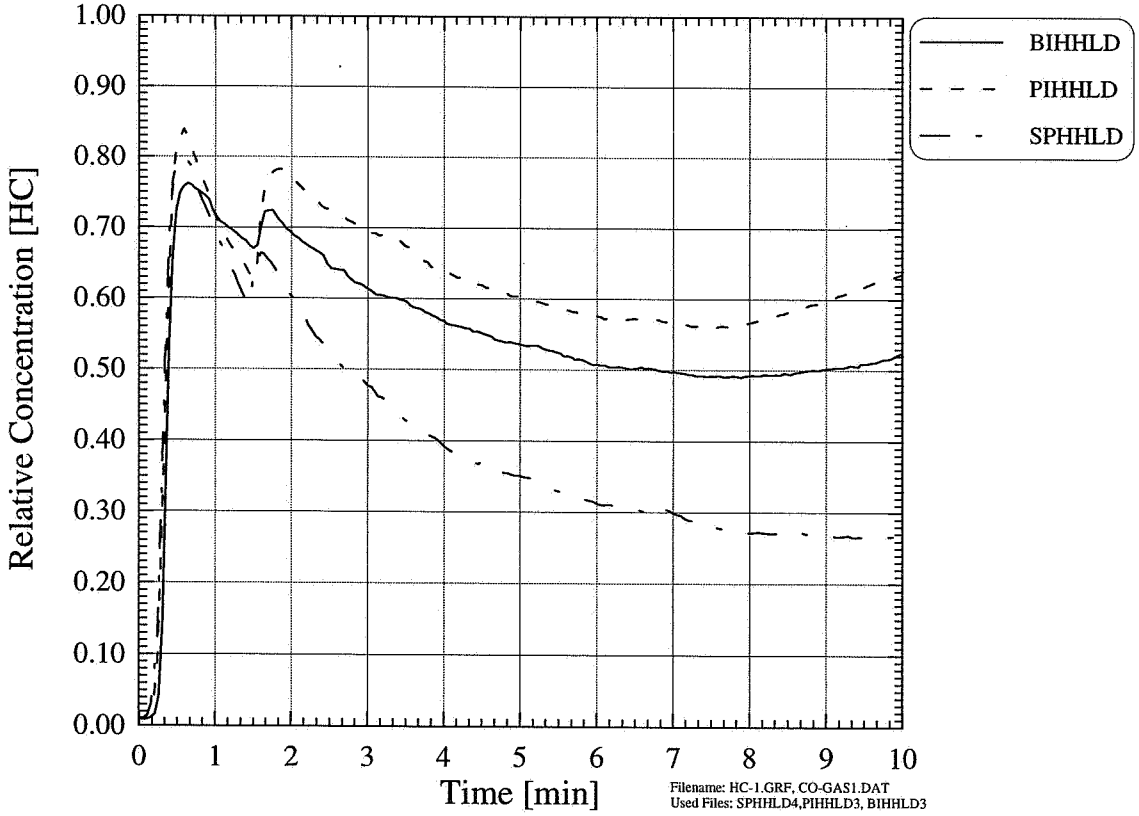

Figure 4.40 Relative HC concentration profiles for birch, pine and spruce, longitudinal grain orientation, high heat flux.

minutes of heating, the pressure at the back of the sample was slightly increased to force the volatiles to flow towards the heated surface. The CO_2 evolves at a much slower rate and reach a maximum at the end of the low heat flux experiment and after approximately 4 minutes in the high heat flux experiment.

Figures 4.39 and 4.40 compare the relative CO_x + hydrocarbon gas concentrations from birch, pine and spruce longitudinal grain orientation at high heat flux. The corresponding temperature plot is shown in Figure 4.34. The CO_2 concentration profiles for all woods are quite similar while the CO and HC concentration profiles of birch and pine differ from that of spruce. Less CO and HC are produced from spruce, especially in the later period of heating where the concentration profiles decrease while the CO and HC concentrations of birch and pine stabilize at a much higher level. The most plausible reason for this is that the total reacted fraction of birch and pine, with an average value of 84 and 93 wt%, respectively, is greater than of spruce for which approximately 72 wt% is reacted.

4.4.4 EXPERIMENTAL PROBLEMS, UNCERTAINTIES IN MEASUREMENTS AND RELATED QUESTIONS

As indicated by the standard deviations in Table 4.19, some uncertainties are inherent in these experiments and some problems had to be overcome during the experiments.

One of the greatest problem was caused by the strange and often unpredictable behaviour of the xenon arc lamp. Its intensity was sometimes not as stable, especially at high heat flux, as promised by the manufacturer. A new bulb was installed and tested; however, this bulb gave even less stable intensity. Even though the lamp was accurately calibrated before each run, the position of the focusing point could sometimes change during the experiment so that the highest intensity was not in the centre of the pellet surface. Radial shrinkage added some more spatial non-uniformity to the radiation since the glass tube did not perfectly insulate the pellet side surface. Hence, the sealing around the pellet was not perfect and some volatiles flowed out and around the sides in the space between the pellet and glass tube. The non-uniform heating condition caused by radial shrinkage and defocused light is revealed by the virgin rest fraction of some of the pellets in Figures 4.28 and 4.29. It can be seen that the non-uniform heated surface is far from being parallel with the backside of the pellet.

Axial shrinkage presents some doubt about the exact position of the thermocouples inside the pellet and since the pellet surface is moved slightly away from the focusing point of the Xenon arc lamp, the heat flux exposing the surface during the whole experiment was not the

same as the pre-calibrated one. Another aspect which makes the temperature comparisons between the different species, grain orientations and heat fluxes difficult, come from drilling of the holes for the thermocouples. Drilling by using a 0.5 mm thin borer in an inhomogeneous substance like wood was very difficult. The borer sometimes followed the track of less resistance rather than the centre line it was supposed to follow. The spruce radial samples were especially difficult since their annual latewood rings are hard compared to the softer parts (earlywood) between them. In this case, the outlet of a hole could deviate several millimetres from the centre line and the positions marked on the temperature plots must be regarded as approximate.

Smoke proved to be another problem, especially during the first minutes after initiation. In some experiments, evolved smoke flowed towards and filled up the space in the front part of the reactor, absorbing some of the radiation from the lamp, thus reducing the inward heat flux to the pellet surface. A lot of tests were made to optimise the flow field in the reactor head by adjusting the three purge gas rotameters. The optimal condition was obtained by not allowing any purge gas to flow through the glass tube sealing of the pellet in the first one and a half minute of heating. Smoke evolving the reactor outlet under optimal conditions are shown in Figure 4.41 while a picture of an unsuccessful experiment is shown in Figure 4.42. In some cases, it was difficult to remove the smoke flowing into the front of the reactor head and the experiment had sometimes to be terminated.

An indication of the reproducibility of the experiments is shown in Figure 4.43, where the temperature histories of three identical (replicated) runs on spruce, longitudinal grain orientation exposed to a low heat flux have been compared. The temperature for replicates are within 50°C of each other for most depths. The ultimate product yields, reacted fraction and axial shrinkage, the replicates' mean and standard deviation are listed in Table 4.21. A similar presentation is given for spruce, longitudinal grain orientation exposed to a high heat flux in Figure 4.44 and Table 4.22. At both heating rates, the temperature profiles coincide fairly well in two out of three runs which must be regarded as satisfactory. The temperature difference between the replicates, at for instance 8 mm from the surface, may be attributed to the positioning of the thermocouples which could slightly vary with a half millimetre or so from pellet to pellet. Differences between replicates are also a reflection of the sample to sample variation of wood. Due to its inhomogeneous grain structure, it is impossible to prepare two or more identical samples from the same log.

Since the axial shrinkage of spruce longitudinal samples is only within a few percent at both low and high heat fluxes, these experiments will be used in the comparison with modeling predictions.

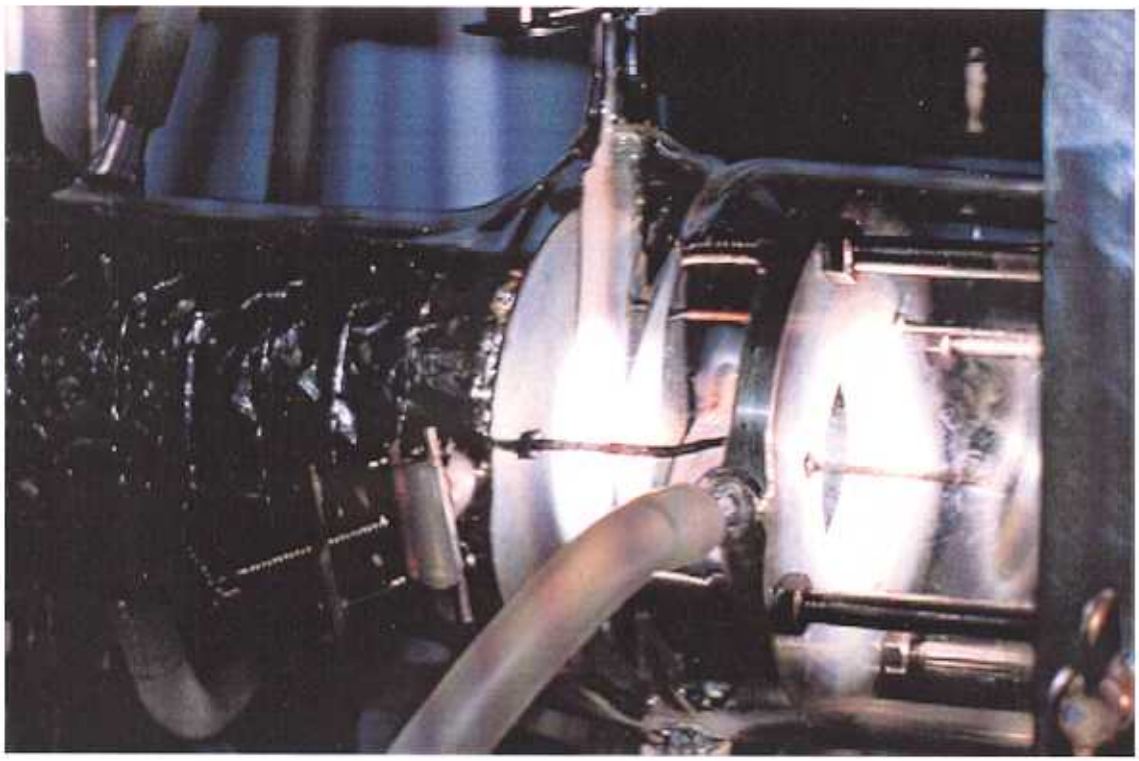

Figure 4.41 Smoke evolving in a laminar flow - optimal conditions.

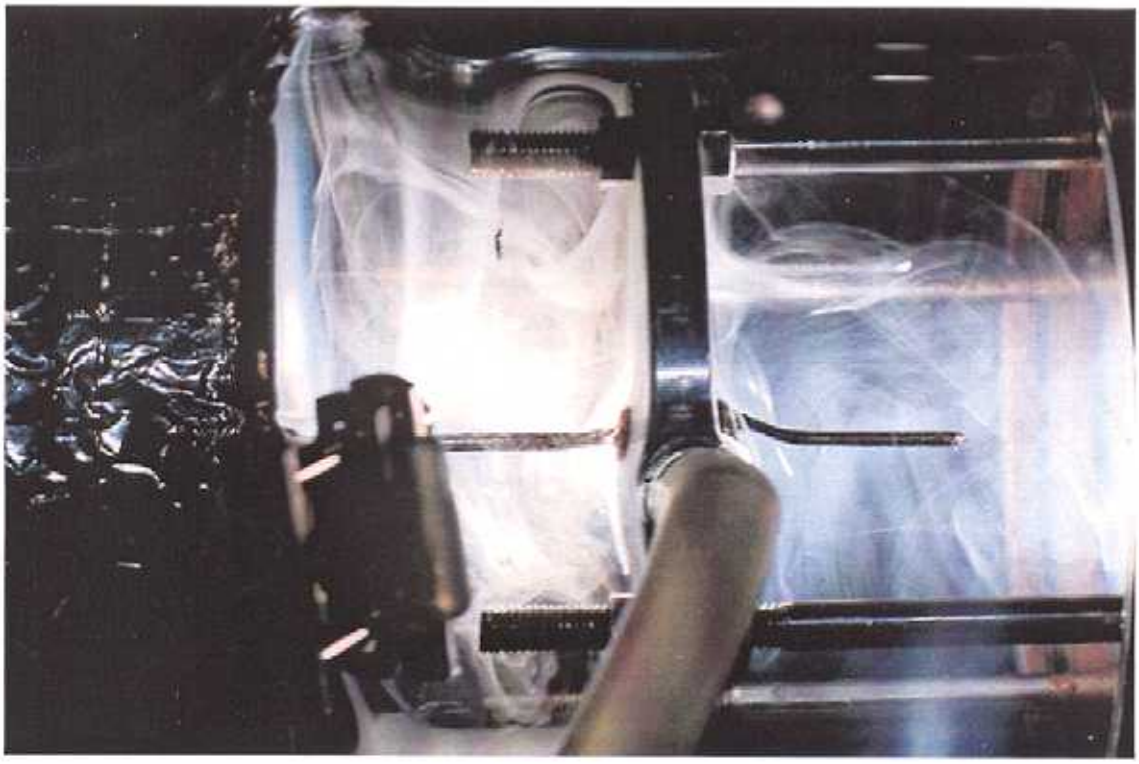

Figure 4.42 Smoke within the front part of the reactor head leading to an unsuccessful experiment.

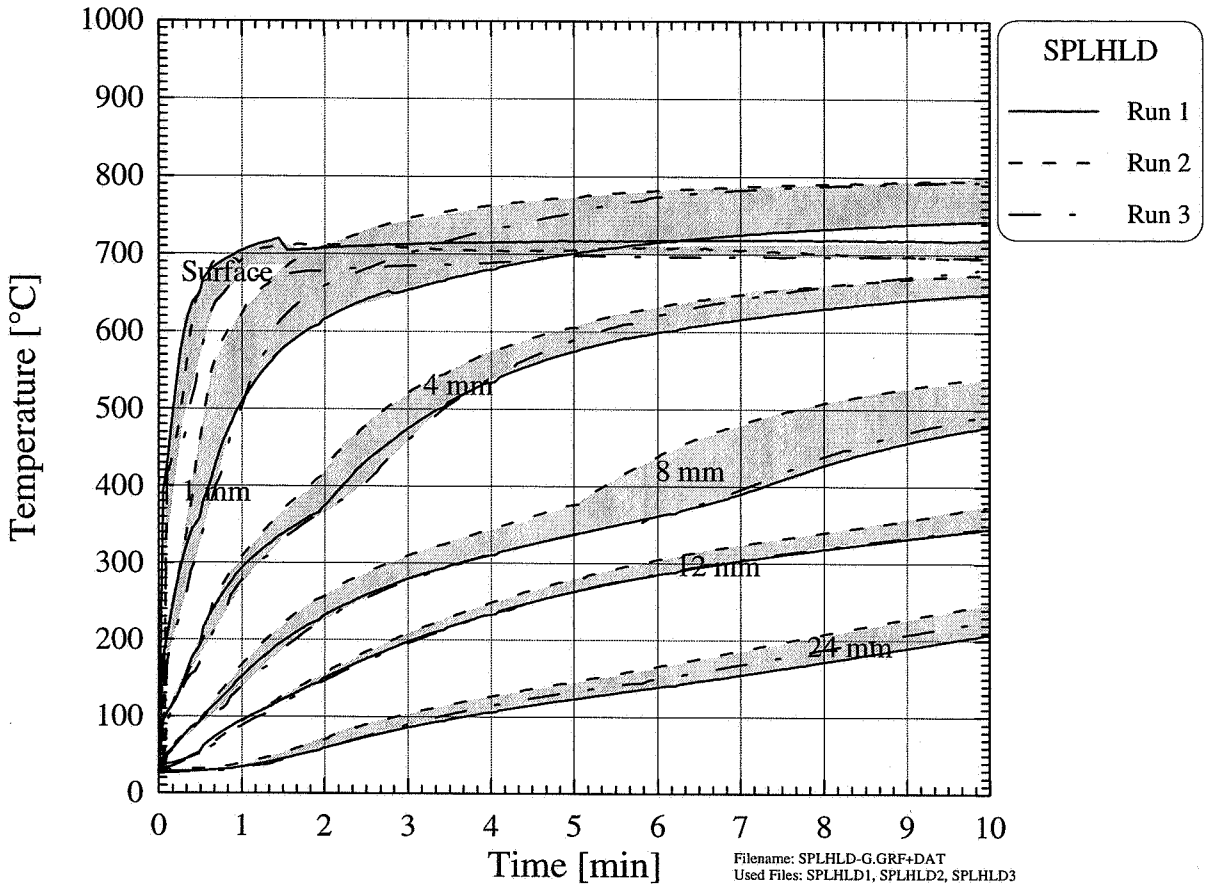

Figure 4.43 Temperature histories of three identical experiments on spruce, longitudinal grain orientation, low heat flux.

Table 4.21 Ultimate product yields, axial shrinkage and reacted fraction of three identical experiments on spruce, longitudinal grain orientation, low heat flux.

	Run 1	Run 2	Run 3	Mean $\bar{y}$	Standard deviation s	Relative deviation 100s/$\bar{y}$
Axial shrinkage [lt%]	4.2	3.9	0.0	2.7	2.34	86.7
Reacted fraction [wt%]	41.6	48.7	46.3	45.5	3.61	7.9
Char-yield [wt%]	29.9	28.3	27.9	28.7	1.06	3.7
Condensable gas-yield [wt%]	34.0	25.5	34.5	31.3	5.06	16.2
Non-condensable gas-yield [wt%]	36.1	46.2	37.6	40.0	5.45	13.6

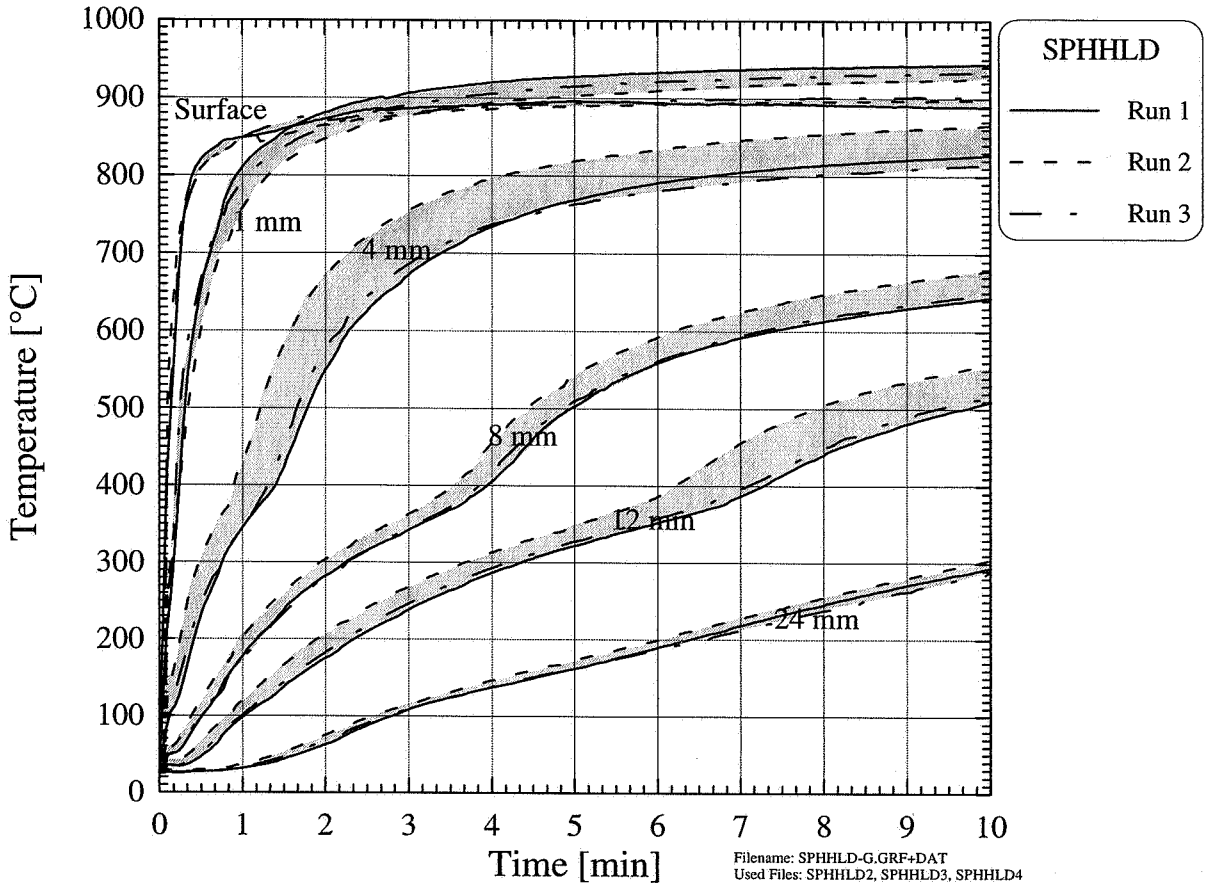

Figure 4.44 Temperature histories of three identical experiments on spruce, longitudinal grain orientation, high heat flux.

Table 4.22 Ultimate product yields, axial shrinkage and reacted fraction of three identical experiments on spruce, longitudinal grain orientation, high heat flux.

	Run 1	Run 2	Run 3	Mean $\bar{y}$	Standard deviation s	Relative deviation 100s/$\bar{y}$
Axial shrinkage [lt%]	0.4	2.0	2.0	1.5	0.92	61.3
Reacted fraction [wt%]	75.2	72.1	69.1	72.1	3.05	4.2
Char-yield [wt%]	27.0	27.0	26.9	27.0	0.06	0.2
Condensable gas-yield [wt%]	28.0	27.2	28.4	27.9	0.61	2.2
Non-condensable gas-yield [wt%]	45.0	45.9	44.7	45.2	0.62	1.4

4.5 DISCUSSION OF THEORETICAL MODEL

In this section, the theoretical predictions from the mathematical model will be presented. First, predictions will be compared with the experiments on spruce, longitudinal samples to assess the validity of the model. Second, the model will be used to study pyrolysis of moist wood. Third, the sensitivity of the model to some of the important thermo-physical and kinetic parameters will be discussed and finally, the effect of particle size and heating condition, i.e., heat flux and grain orientation, on ultimate product yields distribution and total reaction time will be simulated.

In the present model, the slopes of the density, temperature, pressure and moisture profiles along the pellet are strongly dependent on the pellet length and heat flux applied. As previously mentioned in subsection 4.3.5, the calculation domain is partitioned in a set of control volumes in which grid points are placed in the geometrical center. The sizes of the individual control volumes, i.e., the number of grid points, are free to be specified. Obviously, the numerical solutions would be more accurate if more grid points were used. However, if the number of grid points is increased, the total CPU time will also increase.

In the following simulations where predictions will be compared with experiments, two constrains must be satisfied, that is: 1) the pellet length, i.e., the length of the calculation domain is 30 mm; 2) the positions of the grid points must match the locations of the thermocouples used for the temperature measurements. The effect of: 32, 77, 152 and 302 grid points on the solution is shown in Figures 4.45 and 4.46, where the reaction scheme proposed by Chan (1983) and Glaister (1987) has been used to simulate the pyrolysis of a 30 mm pellet. The calculated surface and in-depth temperatures together with the total volatile mass fluxes evolved from the surface are plotted with reaction time for heat fluxes of 130 kW/m^2 and 80 kW/m^2, respectively. The resulting CPU time, percentage reacted and ultimate product yields are presented in Table 4.23, while the positions of the grid points that corresponds to the thermocouple positions used in the experiments are shown in Table 4.24. By using the pyrolysis reaction scheme of Chan and Glaister, two mass conservation equations for the solid phase and five mass conservation equations for the gaseous phase must be solved. The simulations have been carried out on a *90 MHz Pentium PC*.

For 32 grid points, both temperatures and mass fluxes profiles show a series of oscillations early in the pyrolysis. This is believed to be a result of the steepest density, temperature and pressure profiles which occur at the beginning of the pyrolysis. By doubling the number of grid points from 32 to 75, the oscillations disappear but, the CPU time increases from 11 to

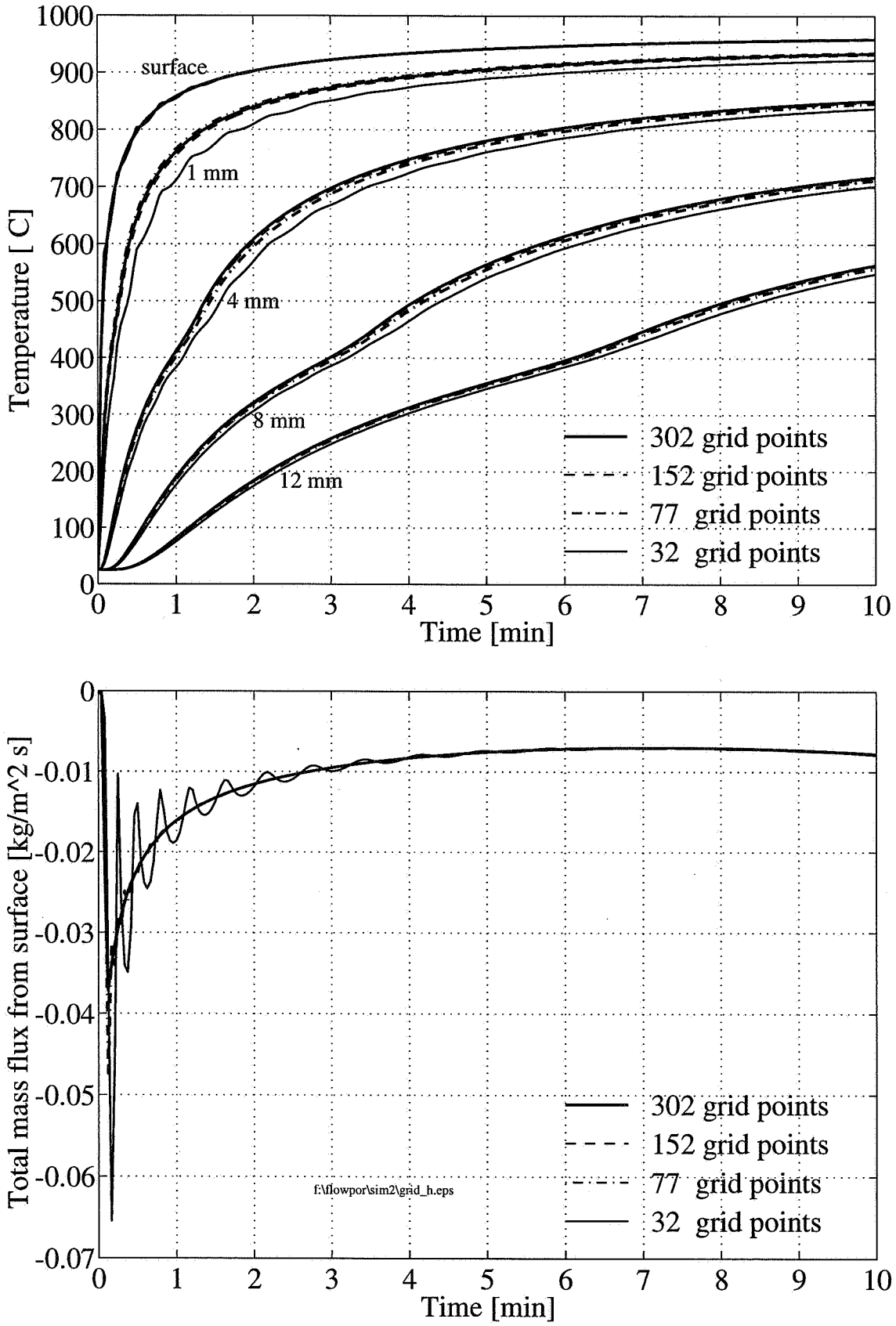

Figure 4.45 The effect of number of grid points on the model predictions [sample size: 30 mm; Chan & Glaisters reaction scheme; heat flux: 130 kW/m^2 (high)].

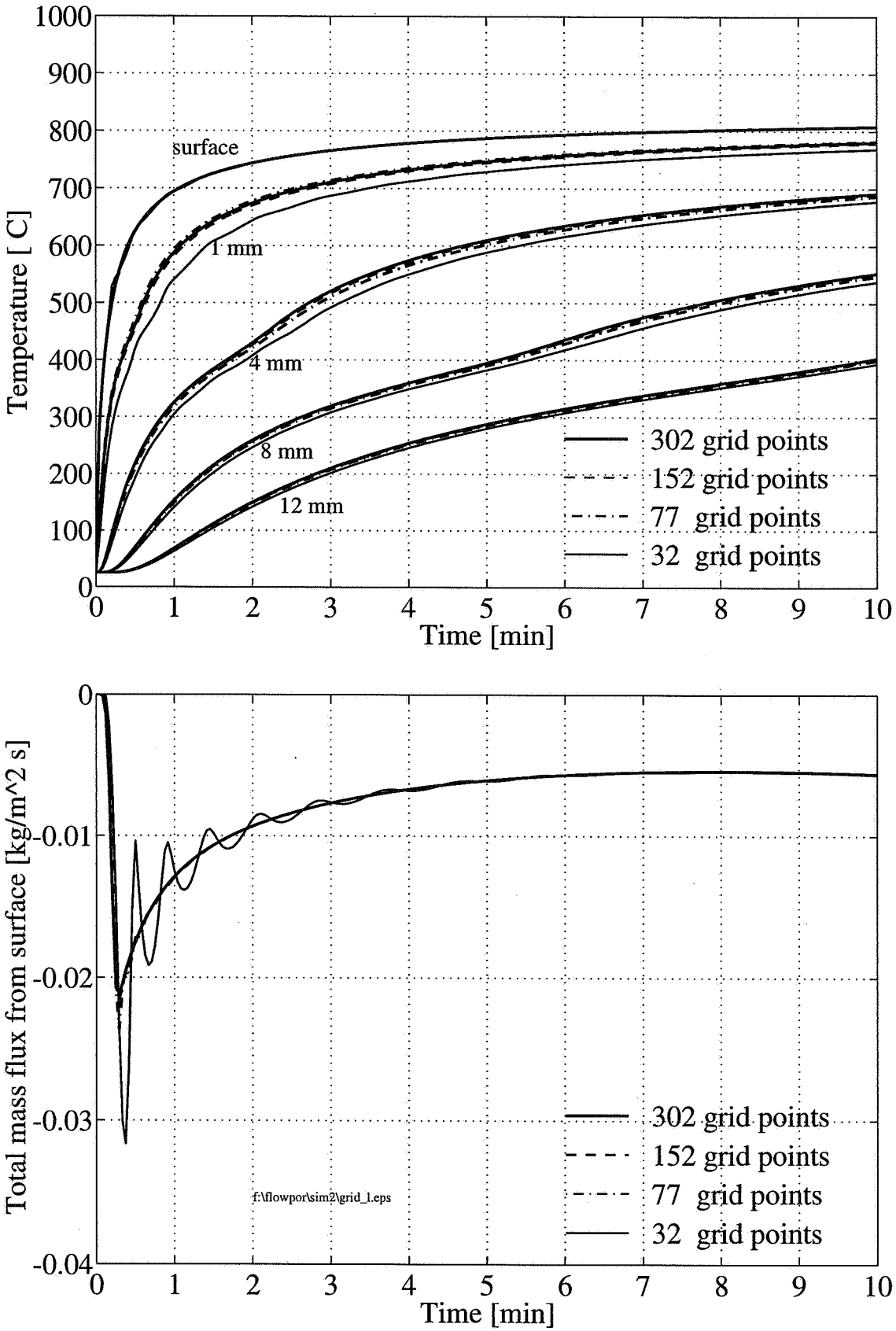

Figure 4.46 The effect of number of grid points on the model predictions [sample size: 30 mm; Chan & Glaisters reaction scheme; heat flux: 80 kW/m^2 (low)].

Table 4.23 The effect of number of grid points on CPU time, percentage reacted and ultimate product yields [sample size: 30 mm; Chan & Glaisters reaction scheme].

	Number of grid points			
	32	77	152	302
Heat flux: 130 kW/m^2 (high):				
CPU time [min]	11.03	39.02	117.69	403.11
%Reacted	57.8	57.4	57.2	57.2
%Tar	35.0	33.9	33.4	33.3
%Gases	31.6	33.9	33.4	33.1
%Vapour from pyrolysis	9.7	9.9	9.9	9.9
%Char	23.7	23.7	23.7	23.7
Heat flux: 80 kW/m^2 (low):				
CPU time [min]	11.03	39.45	118.78	407.18
%Reacted	44.0	43.7	43.6	43.6
%Tar	48.1	47.4	47.2	47.1
%Gases	19.7	20.2	20.4	20.5
%Vapour from pyrolysis	7.9	8.0	8.0	8.0
%Char	24.4	24.4	24.4	24.4

nearly 40 minutes (almost fourfold increase in CPU time). A further increase in the number of grid points to 152 and 302, respectively, gives not much improvements to the temperature and mass flux profiles since they almost overlap with the profiles obtained by using 77 grid points. The reason why the profiles from the calculations with 77, 152 and 302 grid points does not overlap perfectly can be attributed to the grid point positions seen in Table 4.24.

Table 4.24 The grid point positions obtained by using different number of grid points.

Thermocouple location	Grid point position (Number of grid points)			
	32	77	152	302
Surface	0.00 mm	0.00 mm	0.00 mm	0.00 mm
1 mm	1.50 mm	1.00 mm	1.10 mm	1.05 mm
4 mm	4.50 mm	4.20 mm	4.10 mm	4.05 mm
8 mm	8.50 mm	8.20 mm	8.10 mm	8.05 mm
12 mm	12.50 mm	12.20 mm	12.10 mm	12.05 mm
16 mm	16.50 mm	16.20 mm	16.10 mm	16.05 mm
20 mm	20.50 mm	20.20 mm	20.10 mm	20.05 mm
24 mm	24.50 mm	24.20 mm	24.10 mm	24.05 mm

The grid point which should ideally match the thermocouple location for instance 4 mm from the surface is located 4.05 mm from the surface when 302 grid points are used; 4.10 mm from the surface when 152 grid points are used; and 4.20 mm from the surface when 77 grid points are used. By considering the errors found in the experiments, the use of 302 grid points for the simulations must be regarded as a waste of time since the numerical results are not very much improved. Hence, 77 grid points have been used in the trial and error phase of the simulations while 152 grid points have been used for the final presentations.

4.5.1 COMPARISON OF THEORETICAL PREDICTIONS WITH EXPERIMENTAL RESULT

Since the mathematical model does not take shrinkage into account, the experiments on spruce, longitudinal samples have been chosen for comparison with theoretical predictions due to their low axial shrinkage at both low (80 kW/m^2) and high (130 kW/m^2) heating conditions. Data from these experiments which can be used for comparison with model predictions includes: 1) percentage reacted; 2) ultimate product yield distributions, i.e., char, condensable and non-condensable gas yields; and 3) temperature profile histories. Before the comparisons are presented, a short discussion will be given that includes adjustments of the initial and boundary conditions; and justifications of the thermo-physical data used in the simulations.

4.5.1.1 INITIAL CONDITIONS

Pyrolysis of spruce with a pellet length of 30 mm and a dry solid density of $\langle\rho_{SD}\rangle$ = 450 kg/m^3 has been simulated. Recall from subsection 2.8 that the spruce used has a specific density (oven-dry cell-wall substance) of about $\langle\rho_s\rangle^s$ = 1400 kg/m^3 which gives an initial porosity of $\varepsilon_g = 0.68$ ($\varepsilon_g = 1-\langle\rho_{SD}\rangle/\langle\rho_s\rangle^s$). The initial temperature, pressure and moisture content are 298 K (25°C), 1 atm ($1.01325 \cdot 10^5$ N/m^2) and zero, respectively, and the voids or lumens are initially assumed to be filled with air. The total time of pyrolysis is 300 and 600 seconds.

4.5.1.2 BOUNDARY CONDITIONS

The front part of the pyrolysis reactor including the wood sample and the xenon arc lamp which provides the radiant heat flux are depicted in Figure 4.47. Recall from the previous discussion (see Figure 4.17) that the wood sample was tightly fitted into a glass tube which was surrounded by insulation (high temperature resistance glass-wool) material during the

experiments. The irradiated surface is subjected to a heat flux, F_{flux}, that balances the convective and radiative heat losses to the surroundings and the inward conduction of heat. Hence, the boundary condition for the energy equation gets the following form:

$$F_{flux} - h_T(<T_s> - <T_\infty>) - \omega_s \sigma(<T_s^4> - <T_\infty^4>) = -k_{eff}\frac{\partial <T>}{\partial x} \qquad (4.105)$$

where h_T, ω_s, σ are the convective heat transfer coefficient, surface emissivity and Stefan-Bolzmanns constant (=5.6703·10^{-8} W/m^{2}K^4), respectively. Subscript '∞' denotes ambient and 's' denotes surface. The pressure at the irradiated surface is assumed to be equal to the atmospheric pressure:

$$<P_g>^g_s = <P_g>^g_\infty = P_{atm} = 1.01325 \cdot 10^5 \qquad [N/m^2] \qquad (4.106)$$

Recall that an insulation piece, approximately 10 mm thick, was glued onto the non-heated surface (back) of the sample. This makes the boundary adiabatic and impermeable for gas flow. Hence, symmetry can be assumed, i.e., the velocities are zero and the gradients of the dependent variables are zero at the back of the sample.

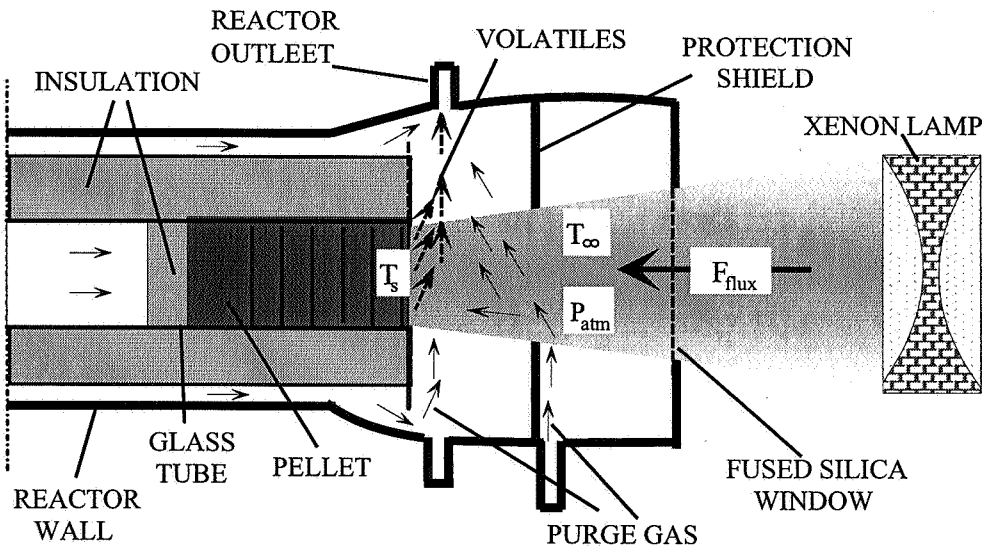

Figure 4.47 Adjustment of boundary conditions for the simulations.

Both the convective heat transfer coefficient, h_T, surface emissivity, ω_s, ambient temperature, T_∞, and obviously, the incident radiation heat flux, F_{flux}, in the boundary condition will affect the surface temperature and, hence, the inward conduction of heat.

Convective Heat Transfer Coefficient

The heated surface of the pellet experiences an outflow of fluids (volatiles) at the same time that it experiences cooling convective heat transfer from the purge gas (nitrogen). This process is called transpirational heating or cooling depending on the direction of heat flow. The

intensity of convective heat flow from the surface to the nitrogen will be reduced if there is another gas flow injected from the surface into the nitrogen flow [Kays and Crawford (1980)]. It is reasoned that during the outflow of fluid, the boundary layer increases, i.e. a thicker layer is created which in turn further insulates the surface from the cooling purge gas flow and results in lower heat transfer. Even though the flow-field in the reactor head is very complex, the convective heat transfer coefficient without transpirational effect can be estimated using the laminar-flow forced heat convection relationship over flat plates [Kreith and Black (1980)]:

$$Nu_L = 0.664 Re_L^{1/2} Pr^{1/3} \tag{4.107}$$

Here, Nu_L, Re_L and Pr are respectively the Nusselt, Reynolds and Prandtl numbers:

$$Nu_L = \frac{h_T L}{k}, \qquad Re_L = \frac{v_\infty \rho L}{\mu}, \qquad Pr = \frac{C_P \mu}{k} \tag{4.108}$$

k, ρ, μ and C_P are purge gas (nitrogen) properties; v_∞ is the free-stream velocity over the flat plate and L is the length of the plate. By using the gas properties of nitrogen between 25 and 350°C [Kreith and Black (1980)]; free-stream gas velocities between 0.01 and 0.5 m/s; and a flat plate length between 0.02 and 0.1 m, a convective heat transfer coefficient between 1.0 and 12.0 W/m^2K can be estimated. As pointed out in the foregoing discussion, these numbers will even be reduced due to transpirational effects caused by outflowing volatiles. In the simulations, however, a constant heat transfer coefficient of: $h_T = 5.0$ W/m^2K has for simplicity been used.

Surface Emissivity

The surface emissivity will continuously change during the course of pyrolysis as the virgin wood changes to char. Raznjevic (1976) has reported emissivities between 0.80 and 0.90 for wood and 0.50 and 0.95 for char (coal, carbon) dependent on temperature, colour and roughness of the surface. In the simulations, a constant surface emissivity of: $\omega_s = 0.85$ has been used.

Ambient Temperature

The ambient temperature in the reactor head, initially at room temperature, comprises the temperature of the surfaces, i.e., the reactor wall and protection shields and the temperature of purge gas in front of the pellet surface. During the experiment, some radiation from the xenon lamp hits the protection shield located in front (see Figure 4.47) which in turn becomes warm and heats up the reactor wall and purge gas. After 10 minutes heating (total pyrolysis time), the glass wall of the reactor head was not touchable. Since the ambient temperature in the reactor head was not measured during the experiments, an average temperature of: T_∞ = 423 K (150°C) has been used in the simulations.

Incident Radiation Heat Flux

The effective heat flux arriving at the heated surface varies slightly during the pyrolysis although constant radiative power is supplied from xenon lamp. This variation (attenuation) of the effective heat flux is believed to be due to several factors. First, the absorptivity of the heated surface varies with its temperature, the energy source temperature, and surface properties such as degree of roughness [Kreith and Black (1980)]. Second, the absorption and scattering of radiation by the outflowing volatiles, which include CO, CO_2, water vapour and various hydrocarbon gases, will further reduce the effective heat flux received at the surface. The latter effect could easily be seen in the unsuccessful experiments where smoke filled the front part of the reactor head (see Figure 4.42). The surface and in-depth temperatures suddenly dropped indicating a reduction in radiation heat flux to the pellet surface. To account for these attenuation effects, Lai (1991) used a Beer's Law expression of the form:

$$(F_{flux})_{eff} = a\,\alpha_s \exp(-b\dot{m}_V)\,F_{flux} \tag{4.109}$$

where a and b are constants; α_s is the absorptivity of the surface and $\dot{m}_V$ is the mass flux of volatiles. However, since the constants (a, b and α_s) in equation (4.109) are not easily determined, the effective heat flux applied in the current simulations has for simplicity been the pre-calibrated one's, i.e., 80 and 130 kW/m^2 for the simulations of the low and high heating experiments, respectively.

4.5.1.3 THERMO-PHYSICAL PROPERTIES

Thermal Conductivity

One of the most important pyrolysis properties is the solid's thermal conductivity. Since the thermal conductivity of spruce has not been measured, data must be taken from the literature. According to Figure 4.9, where the effective thermal conductivity versus density is shown, spruce with a dry solid density of 450 kg/m^3 should have an effective thermal conductivity around 0.25 W/mK parallel with grain and around 0.10 W/mK in it's charcoal state ($<\rho_C> \approx 150$ kg/m^3). However, simulations of the current experiments have indicated that an initial thermal conductivity of 0.25 W/mK for the solid is too low in the early stage of pyrolysis, i.e., before the thermal degradation begin. The in-depth temperatures rise too slow compared to those measured. Hence, the elegant thermal conductivity model based on weighting between parallel and serial heat transfer (equation (4.72)) cannot be used in the current simulations. It remains to see if this model can be used in the simulation of low temperature ($T \approx 100°C$) drying of wood, however, this is beyond the scope of this study. The following effective thermal conductivity model has been used in the simulations:

$$k_{eff,\,s} = \varepsilon_g k_g + \eta\, k_{SD} + (1 - \eta)\, k_C + k_{rad} \tag{4.110}$$

where constant thermal conductivities of: k_g=0.0258 W/mK and k_C=0.1 W/mK have been assumed for the gas mixture and char, respectively. Since the thermal conductivity of solid substances is supposed to slightly increase with temperature, an average thermal conductivity of 0.35 W/mK has been used for the virgin wood between 25°C and 250°C, the latter being approximately the onset temperature of thermal degradation. Recall that Brown (1972) measured the char thermal conductivity in the temperature range 550-650°C to be three times greater than that measured at room temperature; in fact, it was nearly twice as high as that of the virgin wood. Hence, radiation in the pores is believed to play an important role at higher temperatures. This is accounted for in equation (4.110) by introducing a radiative conductivity term of the form:

$$k_{rad} = \frac{4\varepsilon_g}{(1 - \varepsilon_g)} \sigma \omega d_{por} T^3 \tag{4.111}$$

which has been obtained from the work of Panton and Rittmann (1971). ε_g, σ and ω are respectively the porosity, Stefan-Bolzmanns constant and solid emissivity ($\omega \approx 0.9$), while d_{por} is the characteristic length ($\approx$ pore diameter) which the radiation can pass through. As the virgin wood changes to char, the solid becomes more porous and, obviously, the characteristic radiation length will increase. To account for this, a density dependent expression of the form:

$$d_{por} = \eta\, d_{por,SD} + (1 - \eta) d_{por,C} \tag{4.112}$$

is used, where $d_{por,\,SD}$ and $d_{por,\,C}$ are the characteristic radiation length of virgin wood and char, respectively. In the simulations, the "pore diameter" of virgin wood has been approximated by the diameter of a typical softwood lumen which is 50 microns ($50 \cdot 10^{-6}$ m) [Siau (1984)]. The characteristic radiation length in the more porous char is assumed to be two times that of virgin wood, i.e., 100 microns ($100 \cdot 10^{-6}$ m).

Specific Heats

Another important pyrolysis property is the solid's specific heat, which accounts for the accumulation of heat in the energy equation. Less important is the specific heats of volatiles (tars and gases), although they will have certain impact on the convective cooling of the char as they flow towards the heated surface. In the present simulations, the specific heat of the solid substance is assumed to vary linearly between virgin wood and char according to equation (4.78), where $C_{P,SD}$ and $C_{P,C}$ are given by equation (4.80) and (4.81), respectively. For the gas mixture phase, a mass average specific heat calculated by equation (4.82) has been used, where the individual gas components specific heat are given by equation (4.83) to (4.86).

Intrinsic Permeability

Recall from the previous discussion in subsection 4.3.4.5 that the intrinsic permeability of wood is an extremely variable property that depends on type of wood; position inside the stem; and structural directions of wood. As the wood changes to char, one must account for the enlargement of the pores that makes the outflow of volatiles easier. The intrinsic permeability of the gas mixture is assumed to vary linearly between virgin wood and char according to equation (4.67). Since the intrinsic permeability of spruce has not been measured, $K_{g,SD}=1.0\cdot10^{-14}$ m^2 and $K_{g,C}= 1.0\cdot10^{-11}$ m^2 ($K_{g,C}=1000\cdot K_{g,SD}$) have been assumed for the virgin wood and char, respectively.

Dynamic Viscosity

For the Darcy's law calculation of gas mixture velocity, an average dynamic viscosity given by equation (4.94) has been used, where the individual gas components dynamic viscosity are given by equation (4.95) to (4.98)

Finally, diffusion in the gas mixture phase has been neglected in the current simulations, since the diffusive transport of volatiles is assumed to be comparatively smaller than the convective transport.

4.5.1.4 PYROLYSIS REACTION SCHEME

The most difficult task is, however, to choose a reaction scheme with proper rate constants for the thermal degradation process that satisfactory predicts the experimental reacted fraction and ultimate product yields distribution listed in Table 4.25.

Table 4.25 Reacted fraction and ultimate product yields distribution obtained from pyrolysis experiments on spruce, longitudinal samples

	Low heat flux (80 kW/m^2)		High heat flux (130 kW/m^2)
	5 min	10 min	10 min
% Reacted	25.7±1.63	45.5±3.61	72.1±3.05
% Char	26.2±0.53	28.7±1.06	27.0±0.06
% Tar (condensable gases)	38.0±1.22	31.3±5.06	27.9±0.61
% Gas (non-condensable gases)	35.9±1.44	40.0±5.45	45.2±0.62

From the experimental findings summarized in Table 4.25, the following conclusions can be drawn:

- By doubling the total time of exposure (at 80 kW/m^2 heat flux) from 5 to 10 minutes, the reacted fraction increases by almost 77 %; the ultimate yields of char and non-condensable gases increase while the yield of condensable gases (tar/water) decreases. *Explanation:* The char layer thickness will increase as a consequence of longer pyrolysis time. Hence, the distance which the tar molecules must travel before they escape from the surface will also increase. Cracking of the tar components to form gas products may then explain the increase in ultimate yield of non-condensable gases and the decrease in condensable gas yield. If the local char density is assumed to be dependent on the local temperature history, one may expect that the char density close to the surface going through a very rapid heating (steep temperature gradients) is lower than the char density in the interior of the pellet where the heating rate is much slower. Hence, the local char density will slightly increase with pellet depth and so does the average (integrated) char yield as the pyrolysing front propagates into the wood pellet. Another reason which may explain the increase in ultimate char yield is that more char is formed through a repolymerization reaction of the tar.

- By increasing the heat flux (at 10 minutes exposure) from 80 to 130 kW/m^2, the reacted fraction increases by almost 59 %; the ultimate yields of char and condensable gases (tar/water) decrease while the yield of non-condensable gases increases. *Explanation:* Higher heat fluxes means that there are higher temperatures in the char layer and that more of the substance is reacted. Hence, the distance the volatiles must travel, i.e. the residence time in the hot char layer increases as the pyrolysing front propagates into the wood, promoting secondary reactions of the heavy tar molecules. Higher heat fluxes means steeper temperature gradients inside the pellet. By assuming the local char density to be dependent on the local temperature history, a lower char density and, hence, a lower integrated char yield is expected when a higher heat flux is used.

NOTE: ***In the discussion of the experiments, the term "condensable gases" included condensed water vapour and tars. No attempt was made to separate these fractions from each other since no equipment (distillation column) for doing that was available. Hence, the water vapour produced during the pyrolysis process has for simplicity been included in tar fraction in the following discussion.***

One-step Global Model

As a first approach, the one-step global model has been used to model the thermal degradation process. The kinetic data, listed in Table 4.26, have been obtained by evaluating the mass-loss (TG) curve of spruce (see Chapter 3) with a single reaction model. An endotherm heat of reaction has been assumed. The stoichiometric coefficients for the tar and char fractions have been adjusted so they fit the ultimate product yields distribution listed in Table 4.25.

$$S \xrightarrow{k_1} V + C$$

Table 4.26 Kinetic data, heat of reaction and stoichiometric coefficients for the one-step global model.

				Low heat flux		High heat flux	
Component	A [s^{-1}]	E [kJ/mole]	Δh [kJ/kg]	†b	‡c	†b	‡c
Spruce	$7.41 \cdot 10^4$	83.6	150.0	0.48	0.29	0.38	0.27

†b - tar fraction, ‡c - char fraction

Time and space evolution of the pyrolysis process is shown through variable distributions in Figures 4.48 to 4.50 for the heated surface and in position 1, 4, 8, 12, 16, 20 and 24 mm from the heated surface as a function of time; and for every 60 seconds as a function of the distance from the heated surface.

As revealed in Figure 4.48 (upper), the pyrolysis model exhibits an excellent prediction of the experimental temperatures both at high and low heat fluxes. The thick solid lines represent model predictions and the shaded areas represent temperature histories of three identical (replicated) runs. The temperatures follow an exponential growth history with a rapid increase initially. At a depth of 4 mm and deeper, both experimental and predicted temperature curves flatten before they further increase and approach their final temperatures. As previously discussed in the experimental section of this chapter, this sudden change in temperature gradient is due to a reduction in local thermal conductivity. This is revealed in Figure 4.49 where the predicted temperature, effective thermal conductivity and density spatial profiles at several times is presented. The temperature profiles indicate that there is consistently a slope change, or two main temperature gradients along the pellet, where the first slope reflects the thermal properties of the char layer and the second slope, of the unreacted substrate. The effective thermal conductivity decreases from the surface value and has its minimum value at the reaction front which beyond it again increases to the initial value of the solid substrate.

This is confirmed by superimposing the density profiles at the same reaction time. As shown earlier (equations 4.110 and 4.111), the effective thermal conductivity is a function of density (~ porosity) and temperature raised to power 3. The initial decline in effective thermal conductivity happens in the char layer where the density variation is small and the temperature difference is significant, implying that the effective thermal conductivity is mainly temperature-dependent. The location at which the thermal conductivity begins to increase is in the reaction zone, and corresponds to partially reacted substrate. In that region, the temperature gradient is small but the density gradient is steep, and the effective thermal conductivity appears to be mainly density dependent.

The temporal evolution of the reacted fraction and product yields distribution predicted by using the one-step global model is shown in Figure 4.48 (middle). A comparison of the ultimate values obtained from the experiments and those predicted are presented in Table 4.27. While the model over-predicts the reacted fraction with a few percent at low heat flux, the reacted fraction is under-predicted with approximately 10 percent at high heat flux. Since the stoichiometric coefficients for the tar and char fractions have been assumed constant in advance, the one-step global model can neither predict the increase in ultimate char-yield nor the decrease in tar-yield (at low heat flux) as the pyrolysis time is increased from 5 to 10 minutes.

A graph of the local density versus local temperature, as shown in Figure 4.48 (bottom) indicates the relative speed of the chemical kinetic and heat transfer processes. At a depth of 24 mm, heat transfer from the pellet surface is slow, i.e. the temperature rise is much slower than at the surface. Once pyrolysis temperatures are reached, reaction occur over a smaller temperature range (about 250-450°C) than at the surface (about 250-550°C). Thus, in the pellet interior, heat transport is the rate controlling mechanism while the chemical kinetic is the rate controlling mechanism at the pellet surface. A similar behaviour was observed in the TGA-experiments of A-cellulose (see Figure 3.12). By increasing the heating rate from 2 to 10°C/min, a lateral shift towards higher temperatures (delayed decomposition) could be observed on the TG and DTG curves.

The propagation of the pyrolysis front through the virgin wood is also shown in Figure 4.50 where the spatial gas mixture production rate profiles is presented at different times together with the individual profiles for the gas and tar production rate. By superimposing the temperature profiles in Figure 4.49 (upper), it is possible to see that as time proceeds, the maximum reaction rate decreases and occur at lower and lower temperatures. Obviously, higher temperatures and faster heat transfer mechanisms in the high heat flux simulations lead to higher maximum production rates than the low heat flux simulations.

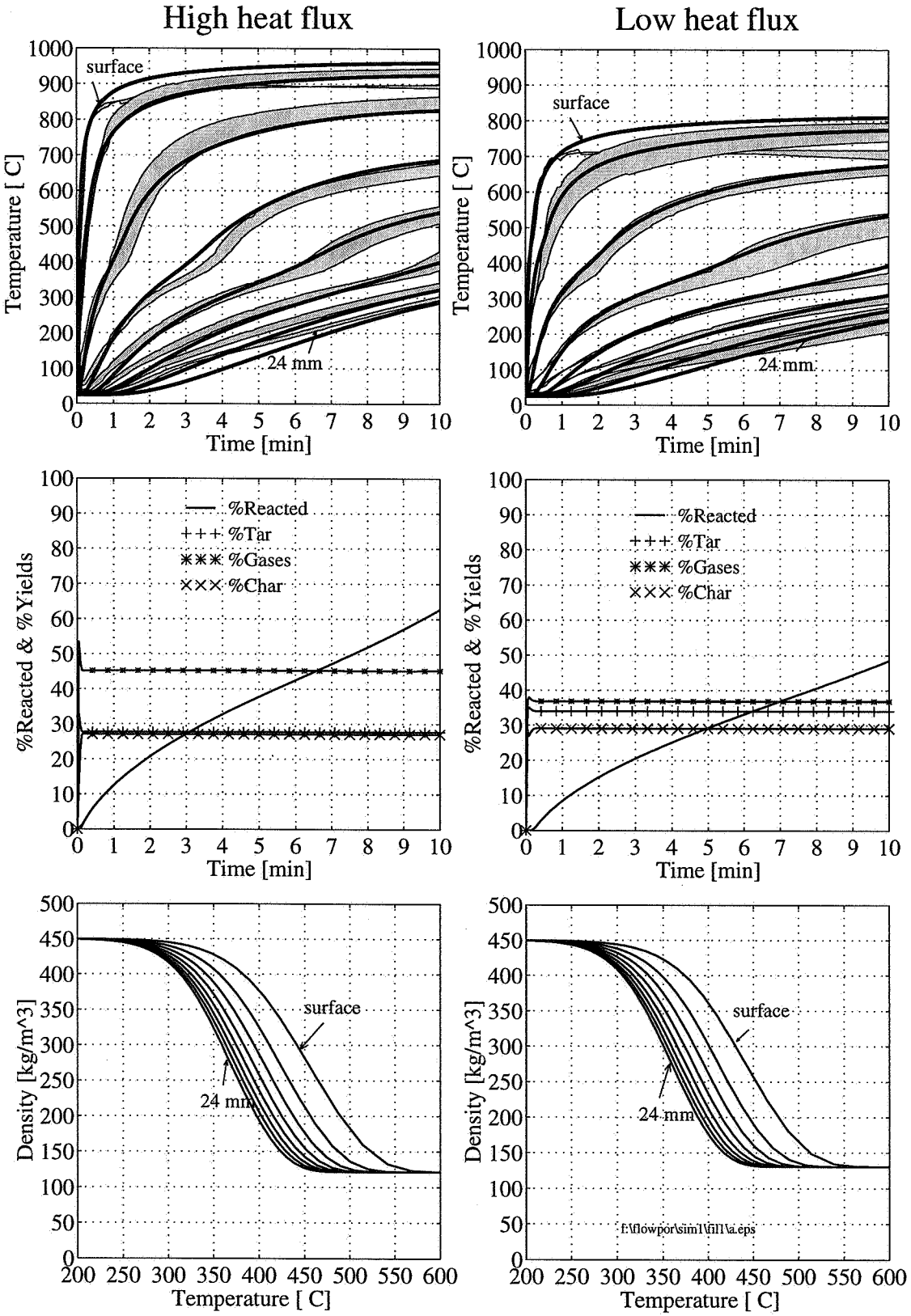

Figure 4.48 *Upper:* Predicted and experimental temperature histories. One-step global model. *Middle:* Predicted percentage reacted and product yields distribution versus time. *Bottom:* Predicted local density versus temperature.

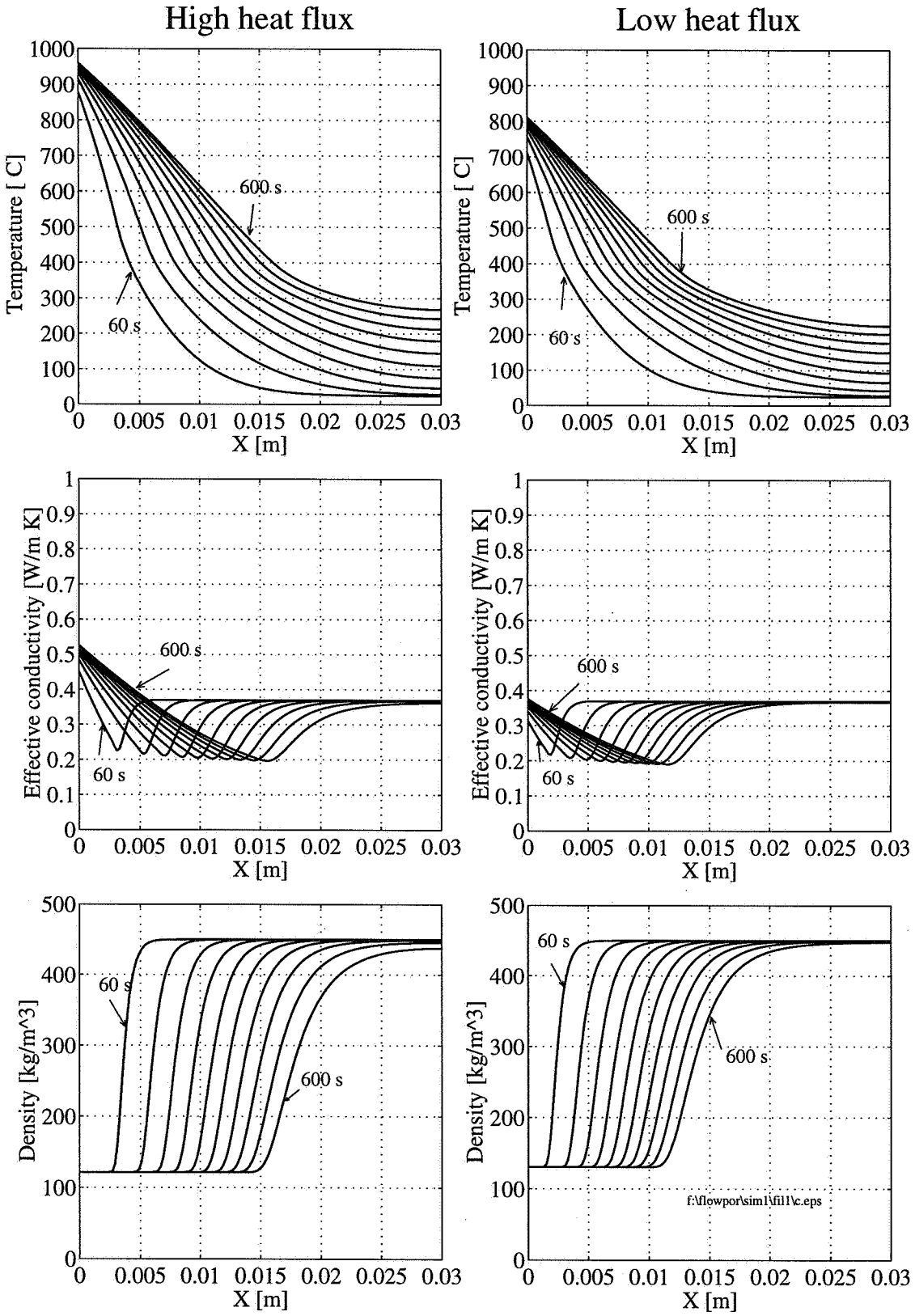

Figure 4.49 *Upper:* Predicted temperature profiles.
Middle: Predicted effective thermal conductivity profiles.
Bottom: Predicted density profiles.

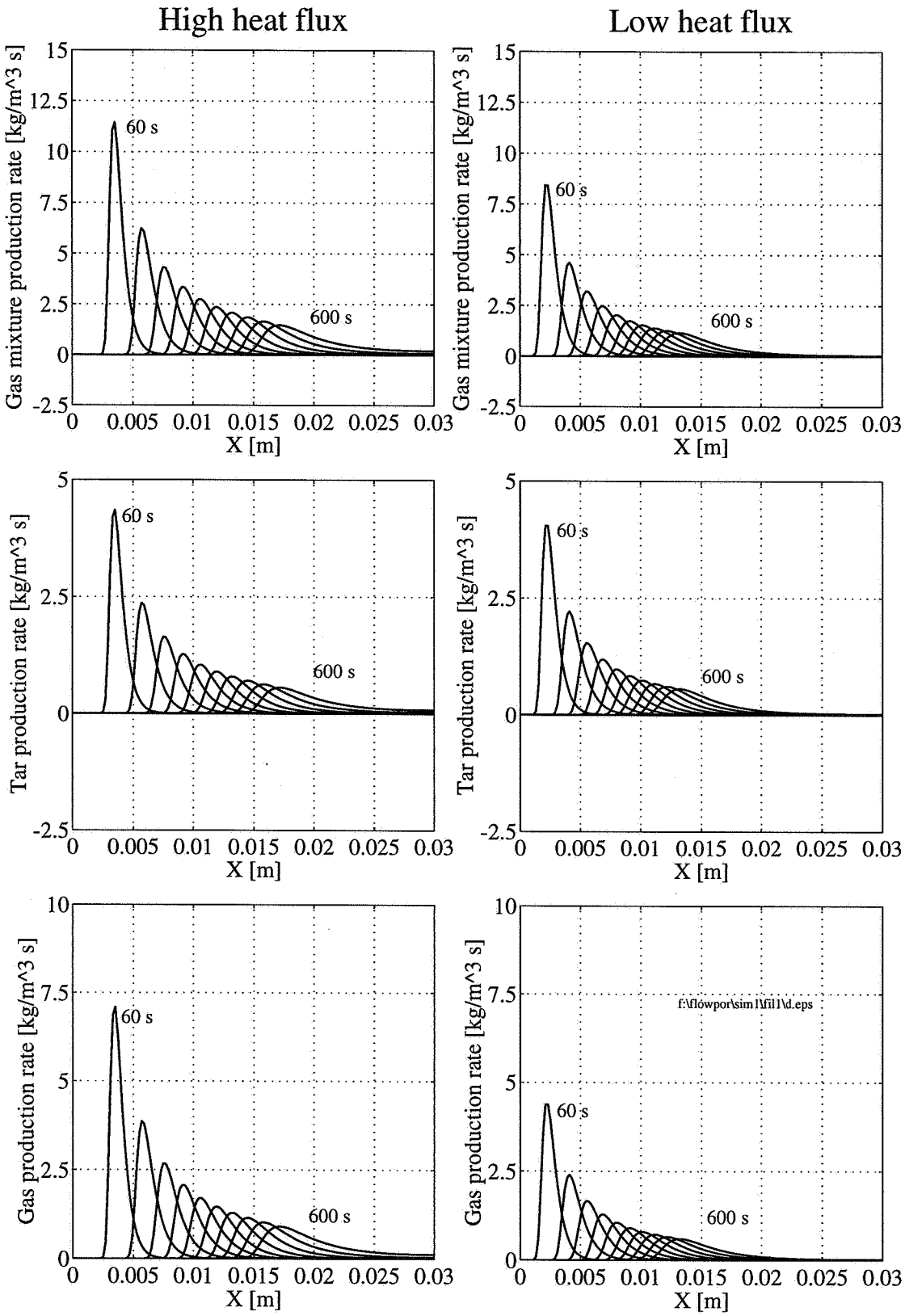

Figure 4.50 *Upper:* Predicted total gas mixture (gas + tar) production rate profiles.
Middle: Predicted tar production rate profiles.
Bottom: Predicted gas production rate profiles.

Table 4.27 Comparison of experimental percent reacted and product yields distribution and those predicted by using a one-step global model

		Low heat flux		High heat flux
		5 min	10 min	10 min
% Reacted	Experimental:	25.7 (±1.63)	45.5 (±3.61)	72.1 (±3.05)
	Predicted:	29.1	48.5	62.7
	Difference‡:	*3.4*	*3.0*	*-9.4*
% Char	Experimental:	26.2 (±0.53)	28.7 (±1.06)	27.0 (±0.06)
	Predicted:	29.1	29.1	27.1
	Difference‡:	*2.9*	*0.4*	*0.1*
% Tar	Experimental:	38.0 (±1.22)	31.3 (±5.06)	27.9 (±0.61)
	Predicted:	34.0	34.0	27.7
	Difference‡:	*-4.0*	*2.7*	*-0.2*
% Gas	Experimental:	35.9 (±1.44)	40.0 (±5.45)	45.2 (±0.62)
	Predicted:	36.9	36.9	45.2
	Difference‡:	*1.0*	*-3.1*	*0.0*

‡ *Difference = Predicted - Experimental*

Model of Three Independent Parallel Reactions

As a second approach, the model of independent parallel reactions outlined in Chapter 3 has been used to describe the thermal degradation process.

$$S = \sum_i S_i \qquad i = 1,2,3$$

$$S_i \xrightarrow{k_i} V_i + C_i$$

The kinetic analysis revealed that spruce with a hemicellulose, cellulose and lignin content of about 27, 44, and 29 wt%, respectively, could be modeled by three independent parallel reactions. In Table 4.28, the mean rate constants calculated in Chapter 3 for the in situ decomposition of cellulose and hemicellulose in wood are listed together with reasonable rate constants for lignin decomposition. a_1 to a_3 represent the mass fractions of hemicellulose, cellulose and lignin in spruce. c_1 to c_3 represent the char fraction of each of these components,

where lignin is supposed to account for most of the char formed. The stoichiometric coefficients for the tar fractions, b_1 to b_3, have been adjusted so they fit the ultimate product yields distribution listed in Table 4.25. An endotherm heat of reaction of 150 kJ/kg has been assumed for all the three reactions.

Table 4.28 Kinetic data, heats of reaction and stoichiometric coefficients for the independent parallel reaction model.

				Low heat flux			High heat flux		
Component *i*	A_i [s^{-1}]	E_i [kJ/mole]	Δh_i [kJ/kg]	$^{\dagger}a_i$	$^{\ddagger}b_i$	$^{¥}c_i$	$^{\dagger}a_i$	$^{\ddagger}b_i$	$^{¥}c_i$
1) hemicellulose	$1.56 \cdot 10^8$	119.0	150.0	0.27	0.48	0.20	0.27	0.38	0.20
2) cellulose	$2.51 \cdot 10^{19}$	260.0	150.0	0.44	0.48	0.20	0.44	0.38	0.20
3) lignin	$5.01 \cdot 10^3$	81.0	150.0	0.29	0.48	0.50	0.29	0.38	0.50

$^{\dagger}a_1$- mass-fraction of hemicellulose in spruce, a_2 - mass-fraction of cellulose in spruce, a_3 - mass-fraction of lignin in spruce, $^{\ddagger}b_i$ - tar fraction of component *i*, $^{¥}c_i$ - char fraction of component *i*

The results from this simulation are presented in Figures 4.51 to 4.53, in a similar manner as for the one-step global model. A comparison of the experimental and predicted ultimate reacted fraction and product yields distribution are presented in Table 4.29.

As seen in Figure 4.51 (upper) the experimental and predicted temperature profiles coincide very well. The model under-predicts the reacted fraction with 15% and 1% at high and low heat flux, respectively. The ultimate product yields distribution are very well predicted, which is not very surprising since the stoichiometric coefficients for the char, tar and gas fractions have been adjusted in advance.

Different from the one-step global model is, however, the way the thermal degradation proceeds, revealed in the density versus temperature profiles in Figure 4.51 (bottom). The thermal degradation proceeds through two steps, where the first step is the very fast decomposition of holocellulose (= hemicellulose+cellulose). The second step is the slow decomposition of lignin. This two steps mechanism is also revealed in the gas, tar and gas mixture production rate profiles in Figure 4.53. Close to the heated surface where the heating rate is fast (after 60 seconds), two peaks may be observed on the gas, tar and gas mixture production rate profiles which means that the lignin decomposition (first peak) is decoupled from the overlapping holocellulose decomposition (second peak). This can be attributed to the very low activation energy and frequency factor used for the lignin decomposition. Such a decoupling of the lignin from the holocellulose pyrolysis has not been observed in any of the experiments.

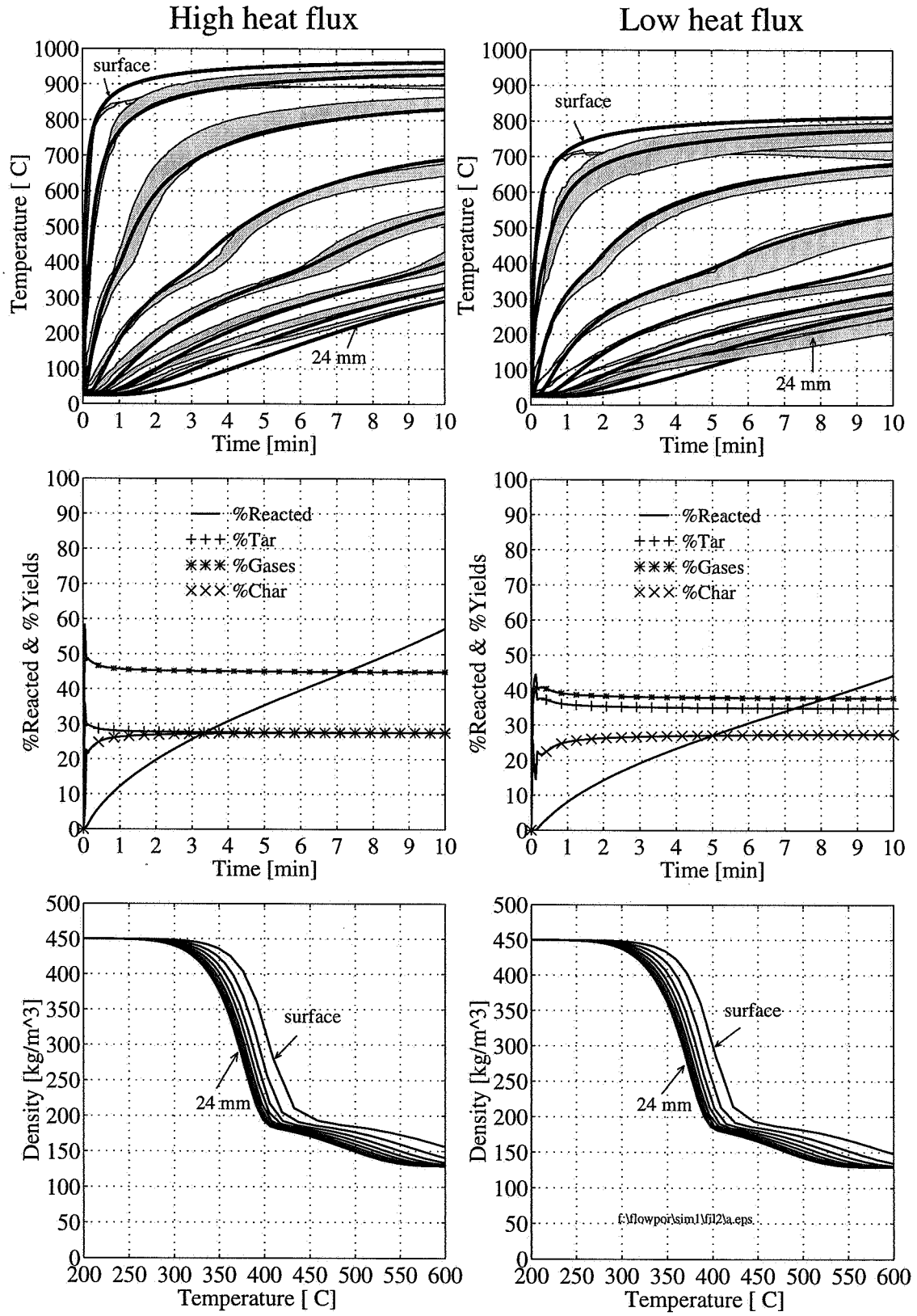

Figure 4.51 *Upper:* Predicted and experimental temperature histories. Three indep. par. reactions. *Middle:* Predicted percentage reacted and product yields distribution versus time. *Bottom:* Predicted local density versus temperature.

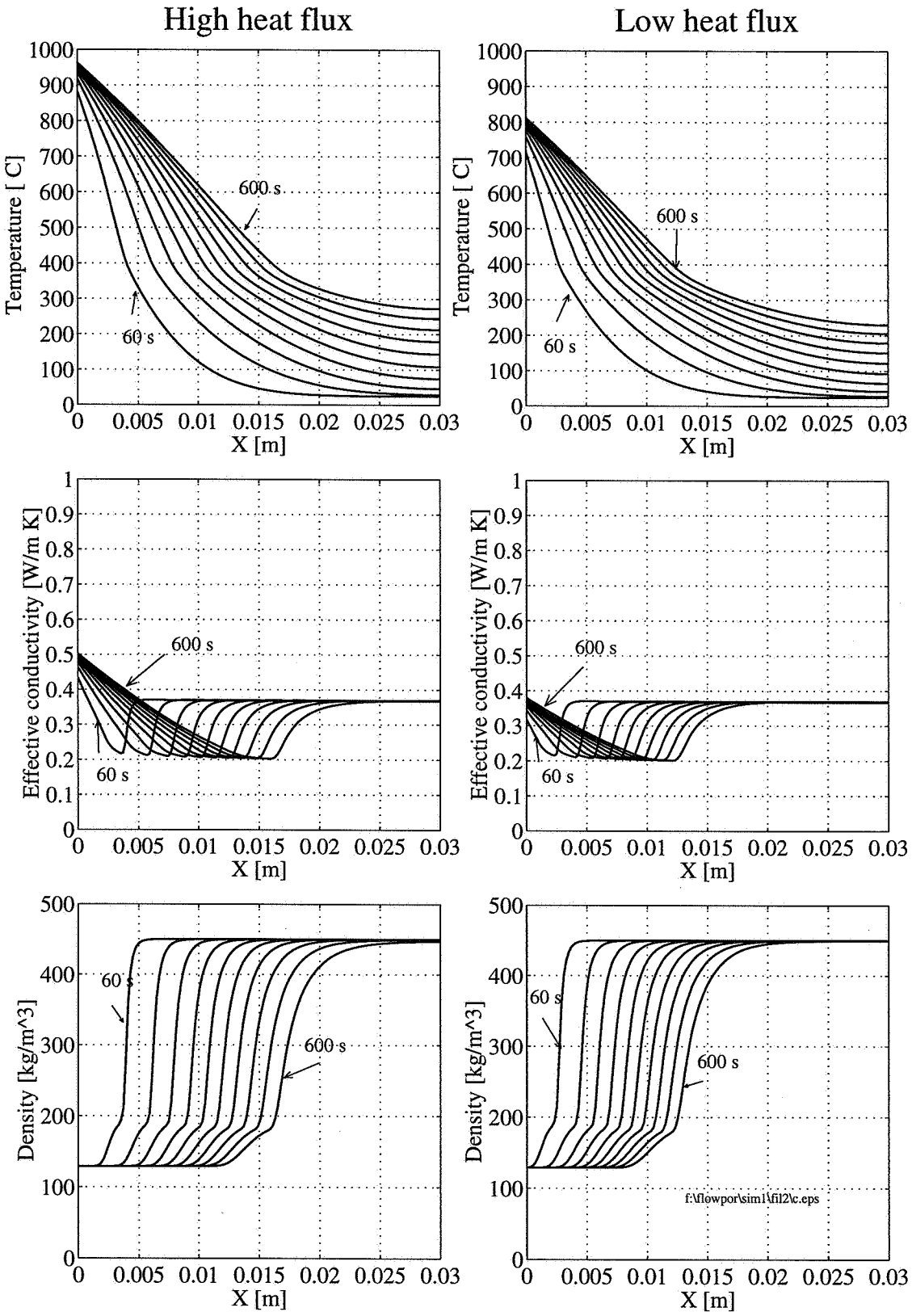

Figure 4.52 *Upper:* Predicted temperature profiles.
Middle: Predicted effective thermal conductivity profiles.
Bottom: Predicted density profiles.

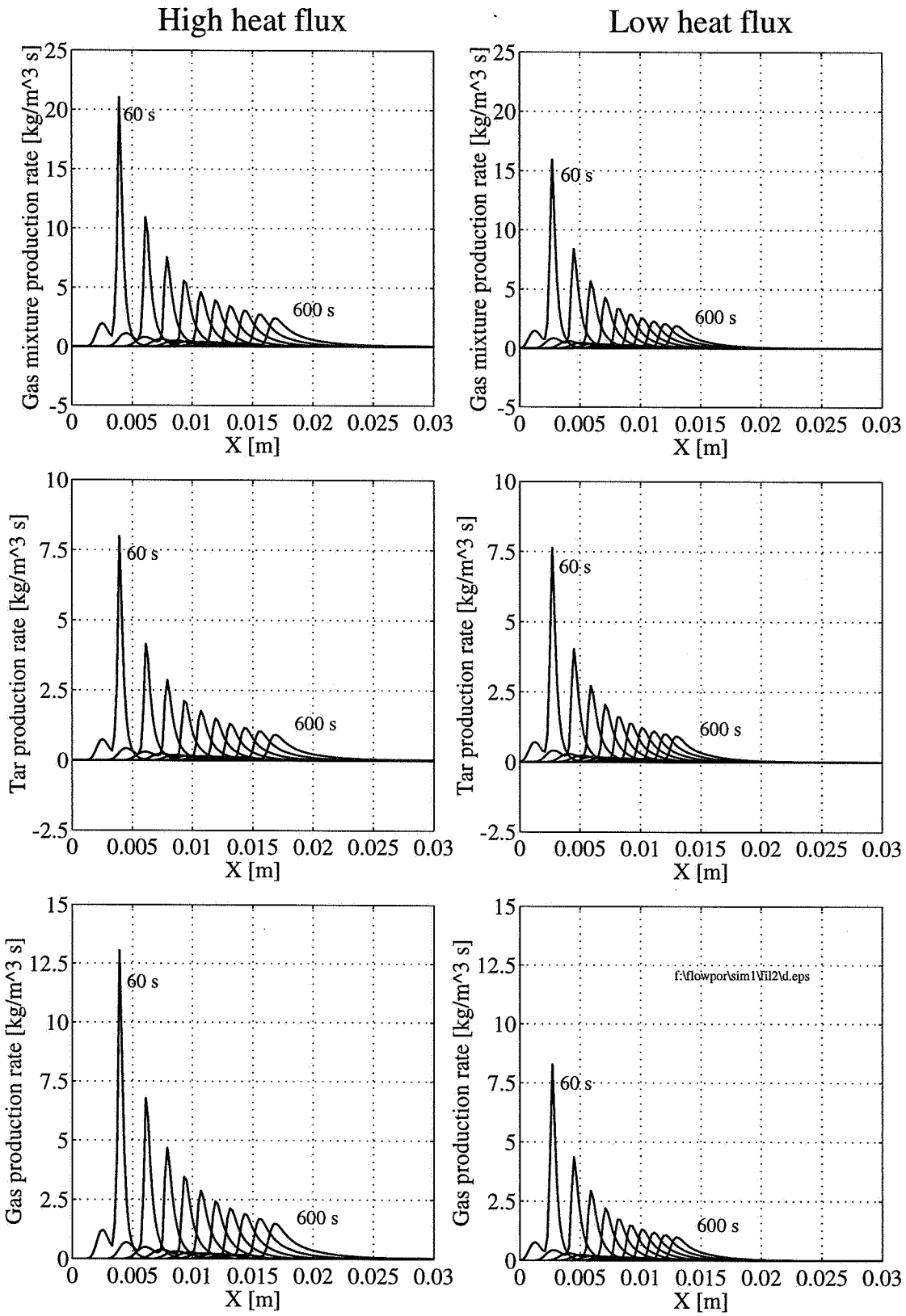

Figure 4.53 *Upper:* Predicted total gas mixture (gas + tar) production rate profiles.
Middle: Predicted tar production rate profiles.
Bottom: Predicted gas production rate profiles.

Table 4.29 Comparison of experimental percent reacted and product yields distribution and those predicted by using a the model of independent reactions.

		Low heat flux		High heat flux
		5 min	10 min	10 min
% Reacted	Experimental:	25.7 (±1.63)	45.5 (±3.61)	72.1 (±3.05)
	Predicted:	27.4	44.2	57.3
	Difference‡:	*1.7*	*-1.3*	*-14.8*
% Char	Experimental:	26.2 (±0.53)	28.7 (±1.06)	27.0 (±0.06)
	Predicted:	27.4	27.4	27.5
	Difference‡:	*1.2*	*-1.3*	*0.5*
% Tar	Experimental:	38.0 (±1.22)	31.3 (±5.06)	27.9 (±0.61)
	Predicted:	34.9	34.9	27.5
	Difference‡:	*-3.1*	*3.6*	*-0.4*
% Gas	Experimental:	35.9 (±1.44)	40.0 (±5.45)	45.2 (±0.62)
	Predicted:	37.8	37.8	44.9
	Difference‡:	*1.9*	*-2.2*	*-0.3*

‡ *Difference = Predicted - Experimental*

Although, simulations of spruce pyrolysis with the two reaction models presented so far give satisfactory predictions of the pyrolysis process for these particular set of experimental conditions, they are not applicable for simulating the pyrolysis of spruce under other conditions. This because they assume a constant ratio of the char to volatiles yield, i.e., they are simple correlation models that cannot be extended to systems different from the one which they were based. The experiments have proved that there exist a competition between the char, tar and gas formation which is dependent on the wood pellet's temperature history. This suggest that a competitive reaction model similar to the one proposed by Chan *et al.* (1985) and Glaister (1987) or by Di Blasi and Russo (1994) must be used.

Competitive Reactions

On of the most applied primary wood degradation mechanisms, originally proposed by Shafizadeh and Chin (1977), suggests that wood reacts through three competitive paths to form gases, tars and char.

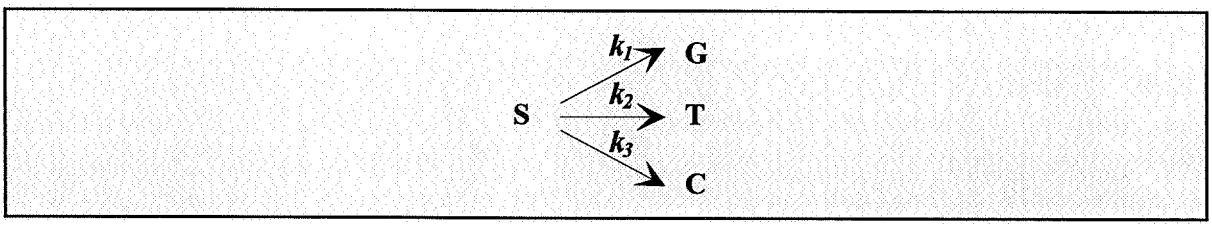

The reaction scheme does not take into account the initiation reaction of the widely used Broido-Shafizadeh model of cellulose pyrolysis in which the formation of an intermediate "active" substance precedes the formation of gas, tar and char. Disagreement exist about this intermediate "active" substance if it should it be included or not (ref: discussion at the conference on "Developments in Thermochemical Biomass Conversion", Banff, Canada, 1996). However, there are several reasons why this initiation step is omitted. First, the present research, neither on small nor large particles, can support any inclusion of an "active" intermediate substance. Second, the recent re-examination of the Broido-Shafizadeh model [Varhegyi *et al.* (1994)], previously discussed in Chapter 3, has raised some questions about the importance of the initiation reaction. New kinetic measurements seem to indicate that such a reaction is superfluous in the temperature range 250-370°C. Finally, even rough estimations of kinetic data for the formation of an intermediate "active" wood are not available in the literature. Experimental verification and determination of kinetic parameters for the model proposed by Shafizadeh and Chin (1977) require simultaneous collection of tar and gas and measurements of wood weight loss rate as a function of time. This have been done by Thurner and Mann (1981), and their estimated rate constants for oak wood pyrolysis in the temperature range 300-400°C are listed in Table 4.30.

Table 4.30 Kinetic data estimated for oak wood pyrolysis [Thurner and Mann (1981)].

Reaction *i*	A_i [s^{-1}]	E_i [kJ/mole]
1)	$1.43 \cdot 10^4$	88.6
2)	$4.13 \cdot 10^6$	112.7
3)	$7.38 \cdot 10^5$	106.5

Critics would (correctly) argue that this model suggests that certain experimental conditions permit the entire conversion of wood to an individual product species at the expense of the other two species. Ref: Antal (1985): "char cannot be formed without the simultaneous evolution of tar and/or gas" . However, it is highly unlikely that this will happen because the rates and the activation energies for the formation of the various product species shown in Table 4.30 are comparable. Chan *et al.* (1985) used the same model for the primary reaction step in their modeling of lodgepole pine pyrolysis, although, their kinetic data listed in Table 4.31 where not measured, but taken from the literature.

Table 4.31 Kinetic data estimated for lodgepole pine pyrolysis [Chan *et al.* (1985); Glaister (1987)].

Reaction *i*	A_i [s^{-1}]	E_i [kJ/mole]
1)	$1.30 \cdot 10^8$	140.3
2)	$2.00 \cdot 10^8$	133.1
3)	$1.10 \cdot 10^7$	121.3

Glaister (1987) modified Chan's model by including water vapour in the upper and lower branches (*solid → gas + water vapour, solid → char + water vapour*) to account for water vapour as a primary product of wood pyrolysis (see section 4.3.3). By doing so, the author eluded completely the possibility that char can be formed without the production of gas, although, the rate constants in Table 4.31 make this impossible. In a similar manner, the more general terms "gas" and/or "tar" could have been included in the lower branch as a byproduct of char formation, i.e., *solid → char + gas (+ tar)*, however, this would have required a rather comprehensive analysis. Hence, the competitive reaction model proposed by Shafizadeh and Chin (1977) has for simplicity been used in the following analysis, and the rate constants from both Thurner and Mann's (abbreviation: T&M) and Chan and Glaister's (abbreviation: C&G) study have been tested. Since less is known about the reaction heat of the three reactions, they have all been assumed equal in size and endothermic (Δh_i = 150 kJ/kg).

The results from the simulation with T&M's and C&G's kinetic data are presented in Figures 4.54 to 4.56 and Figures 4.57 to 4.59, respectively. A comparison of the experimental and predicted ultimate reacted fractions and product yields distribution for the two sets of data are presented in Table 4.32 (T&M) and Table 4.33 (C&G).

As revealed in Figure 4.54 and Figure 4.57 (upper), simulations with both T&M's and C&G's data give satisfactory predictions of the temperature history, both at high and low heat fluxes. However, the two sets of kinetic data yield somewhat different results, revealed in the density versus temperature profiles in Figures 4.54 and 4.57 (bottom), and the spatial density profiles in Figures 4.55 and 4.58 (bottom). As degradation proceeds, T&M's data give a constant char density while a successively larger char density is obtained with C&G's data. For both sets of data, the reactions occur at successively lower temperatures as the pyrolysis front propagates into the wood. This becomes obviously when the spatial temperature profiles, Figures 4.55 and 4.58 (upper), are being superimposed the spatial gas mixture production rate profiles in Figure 4.56 and 4.59 (upper). The maximum reaction temperature varies from 450 to 400°C with T&M's data and from 490 to 400°C with C&G's data, with a total temperature decrease of 50 and 90°C, respectively. Hence, the small temperature variations at the reaction front, as simulated by T&M's data, and the comparable values of the activation energies of tar and char formations (112.7 versus 106.5 kJ/mole) make the char density constant along

the particle thickness. On the contrary, the large temperature variations simulated by C&G's data and the relative large differences in activation energies between tar and char formations (133.1 versus 121.3 kJ/mole) may account for the variable char densities. In the work of Fredlund (1988), similar density profiles as simulated by C&G's kinetic data have been measured by a gamma ray assembly. That is, the char density is getting successively higher as the pyrolysis front propagates into the wood.

Table 4.32 Comparison of experimental percent reacted and product yields distribution and those predicted by using the kinetic data proposed by Thurner & Mann.

		Low heat flux		High heat flux
		5 min	10 min	10 min
% Reacted	Experimental:	25.7 (±1.63)	45.5 (±3.61)	72.1 (±3.05)
	Predicted:	26.0	42.2	53.3
	Difference‡:	*0.3*	*-3.3*	*-18.8*
% Char	Experimental:	26.2 (±0.53)	28.7 (±1.06)	27.0 (±0.06)
	Predicted:	29.5	30.0	29.8
	Difference‡:	*3.3*	*1.3*	*1.8*
% Tar	Experimental:	38.0 (±1.22)	31.3 (±5.06)	27.9 (±0.61)
	Predicted:	57.0	55.6	56.5
	Difference‡:	*19.0*	*24.3*	*26.8*
% Gas	Experimental:	35.9 (±1.44)	40.0 (±5.45)	45.2 (±0.62)
	Predicted:	13.0	14.4	13.3
	Difference‡:	*-22.9*	*-25.6*	*-31.3*

‡ *Difference = Predicted - Experimental*

As revealed in Table 4.32, T&M's kinetic data give, on the average, somewhat higher ultimate char-yields than those measured. The reacted fraction is fairly well predicted at low heat flux, but is under-predicted by almost 19 % at high heat flux. Simulations with C&G's kinetic data (Table 4.33) give very good predictions of the ultimate char-yields, both at low and high heat flux. Thus, it seems that the temperature dependency of the local char density may explain the increase in experimental char-yield observed when the total pyrolysis time was doubled from 5 to 10 minutes (low heat flux). The reacted fractions predicted with C&G's data are in accordance with those measured at low heat flux, but is under-predicted by 17 % at high heat flux. For these reasons, C&G's set of kinetic data are preferred and will be used in the continuation. Although, C&G's kinetic data does an good job in predicting the ultimate reacted fractions and char-yields, the ultimate tar-yields are over-predicted by almost 30 % at the

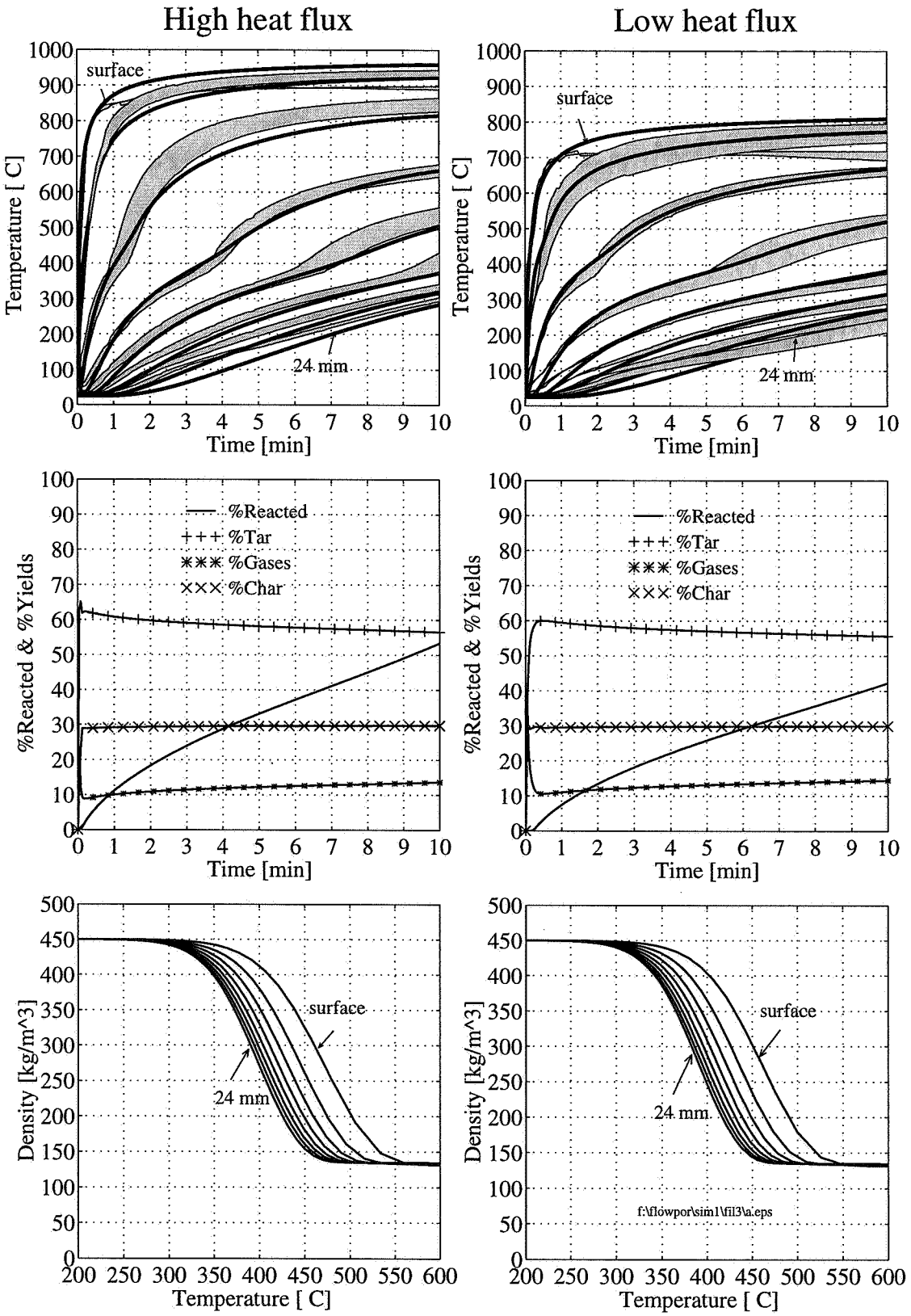

Figure 4.54 *Upper:* Predicted and experimental temperature histories. T&M's kinetic data. *Middle:* Predicted percentage reacted and product yields distribution versus time. *Bottom:* Predicted local density versus temperature.

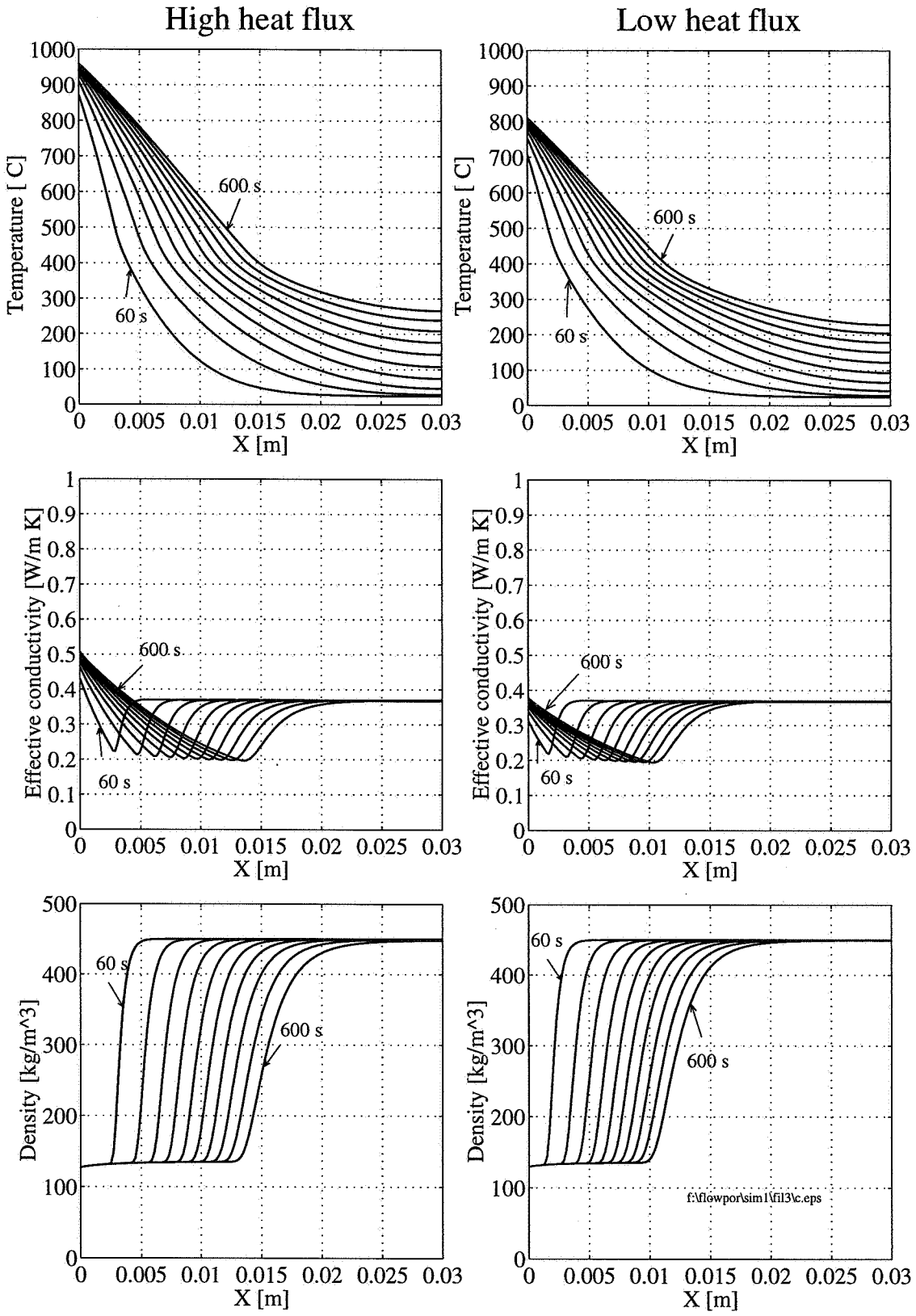

Figure 4.55 *Upper:* Predicted temperature profiles. T&M's kinetic data.
Middle: Predicted effective thermal conductivity profiles.
Bottom: Predicted density profiles.

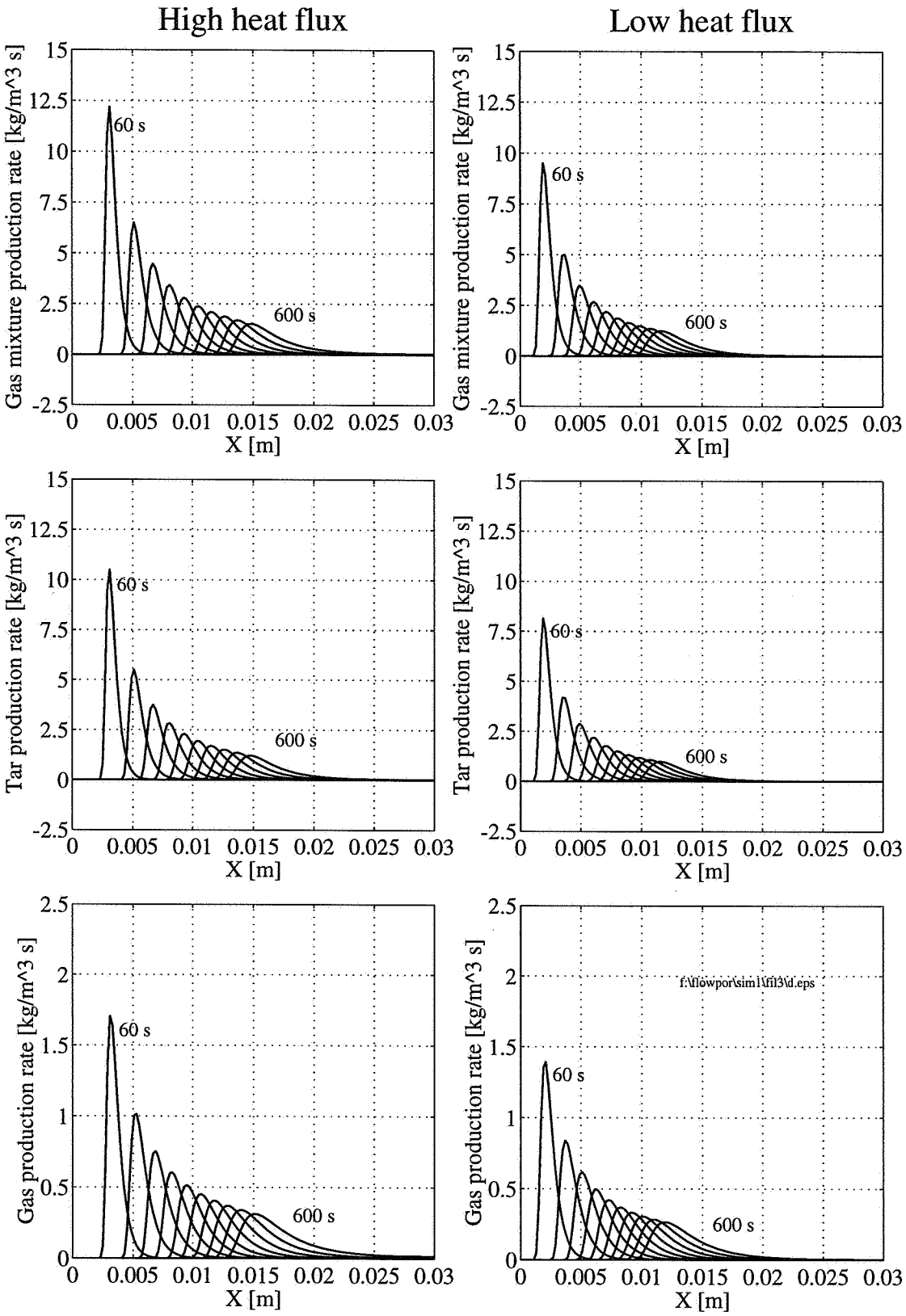

Figure 4.56 *Upper:* Predicted total gas mixture production rate profiles. T&M's kinetic data.
Middle: Predicted tar production rate profiles.
Bottom: Predicted gas production rate profiles.

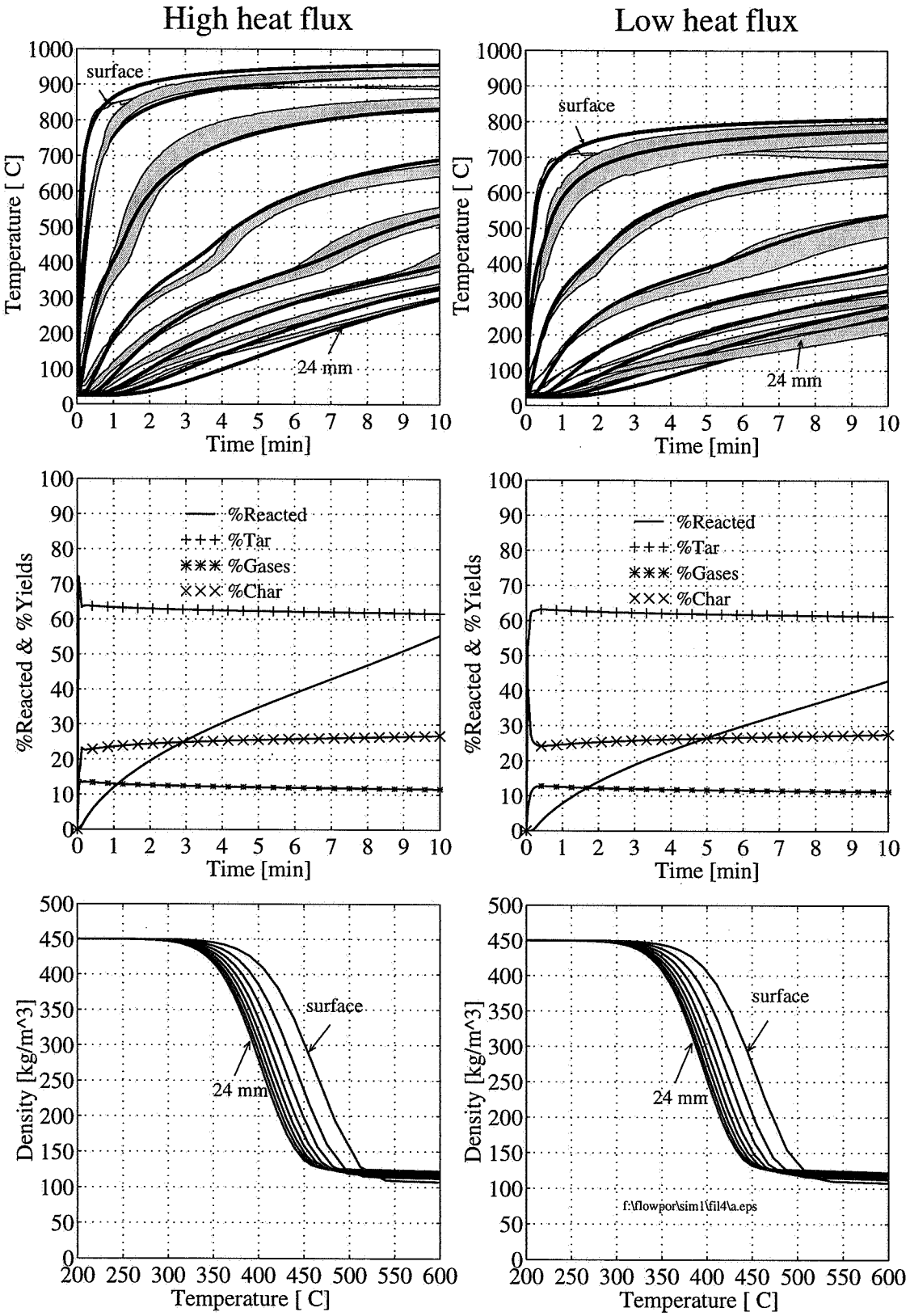

Figure 4.57 *Upper:* Predicted and experimental temperature histories. C&G's kinetic data. *Middle:* Predicted percentage reacted and product yields distribution versus time. *Bottom:* Predicted local density versus temperature.

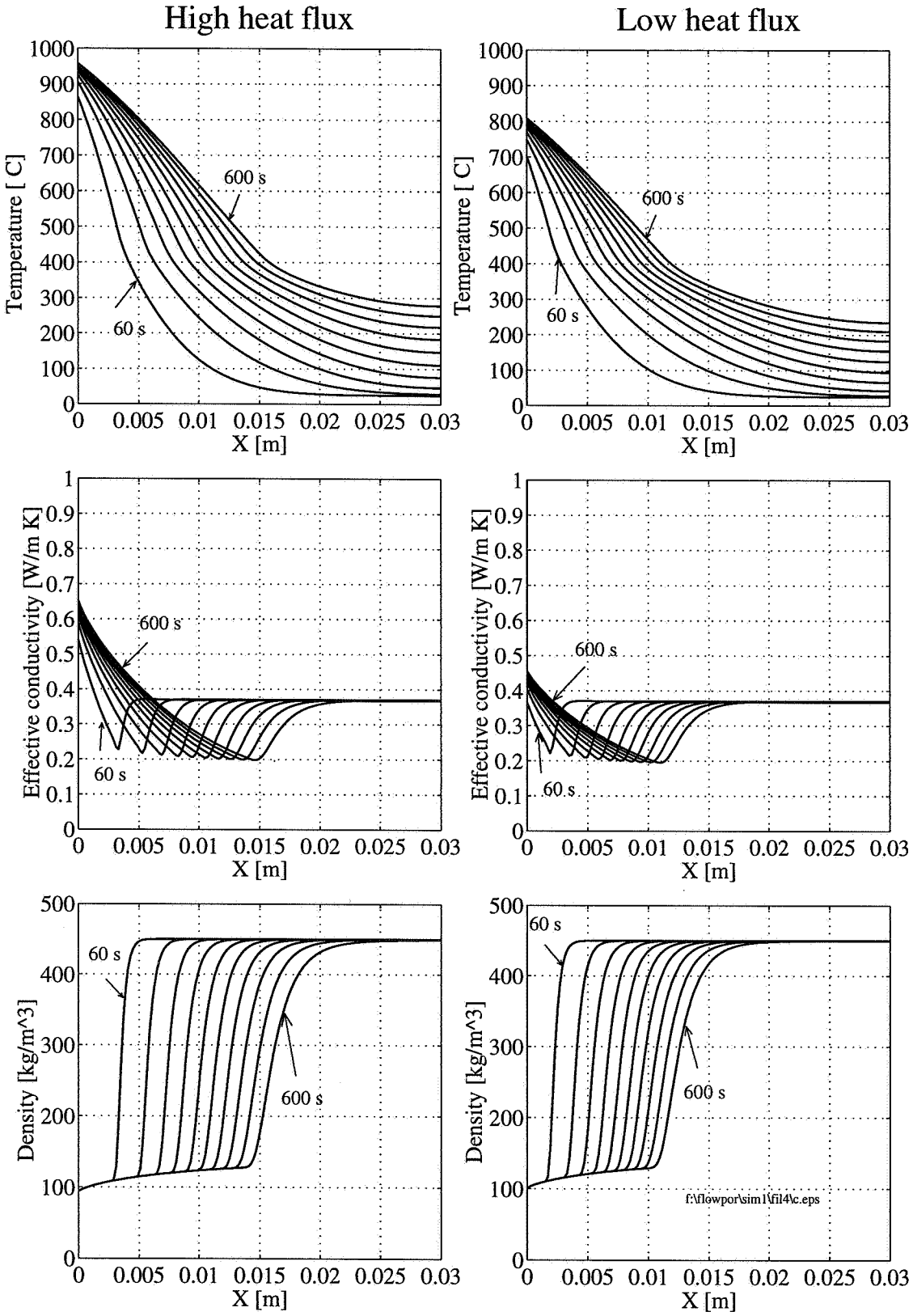

Figure 4.58 *Upper:* Predicted temperature profiles. C&G's kinetic data.
Middle: Predicted effective thermal conductivity profiles.
Bottom: Predicted density profiles.

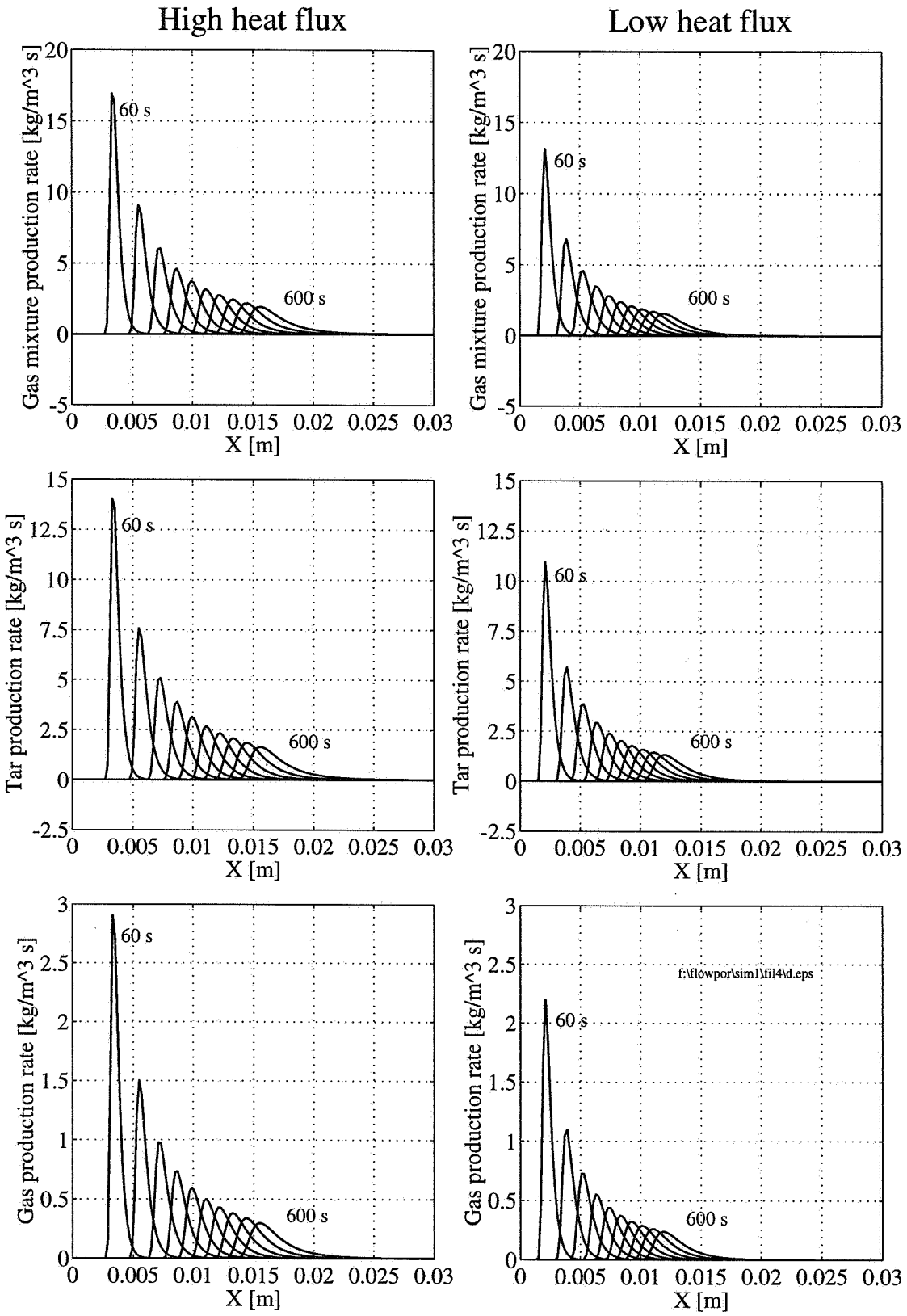

Figure 4.59 *Upper:* Predicted total gas mixture production rate profiles. C&G's kinetic data.
Middle: Predicted tar production rate profiles.
Bottom: Predicted gas production rate profiles.

expense of the ultimate gas-yields. The only way in which the kinetic model can be improved is by including a secondary cracking reaction of the tar components.

Table 4.33 Comparison of experimental percent reacted and product yields distribution and those predicted by using the kinetic data proposed by Chan & Glaister.

		Low heat flux		High heat flux
		5 min	10 min	10 min
% Reacted	Experimental:	25.7 (±1.63)	45.5 (±3.61)	72.1 (±3.05)
	Predicted:	26.5	42.9	55.4
	Difference‡:	*0.9*	*-2.6*	*-16.6*
% Char	Experimental:	26.2 (±0.53)	28.7 (±1.06)	27.0 (±0.06)
	Predicted:	26.5	27.5	26.8
	Difference‡:	0.3	-1.2	-0.2
% Tar	Experimental:	38.0 (±1.22)	31.3 (±5.06)	27.9 (±0.61)
	Predicted:	62.0	61.3	61.7
	Difference‡:	*24.0*	*30.0*	*33.8*
% Gas	Experimental:	35.9 (±1.44)	40.0 (±5.45)	45.2 (±0.62)
	Predicted:	12.0	11.2	11.5
	Difference‡:	*-23.9*	*-28.8*	*-33.7*

‡ *Difference = Predicted - Experimental*

Competitive Reactions with Secondary Tar Cracking

However, secondary reactions are very complex, being influenced by several factors such as type of wood, volatile residence time, heating rates, temperature, heat and mass transfer conditions interior and exterior to the solid, and the physical structure and structure failure of the reacting medium. Recall that Chan & Glaister assumed secondary tar, gas and water vapour to be the products of tar cracking, while Di Blasi and Russo (1994) (abbreviation: D&R) modeled secondary reactions as two competitive reactions to either give lighter hydrocarbons (gases) through a cracking reaction or char through a repolymerization reaction. C&G's and D&R's rate constants and heats of reaction for secondary tar cracking are listed in Table 4.34. Although, the pyrolysis of wood is generally accepted to be overall endothermic, tar cracking has in most cases been modeled as an exothermic process. Since the present experiments can neither support any secondary formation of tar nor char, tar cracking to form lighter gases has only been considered.

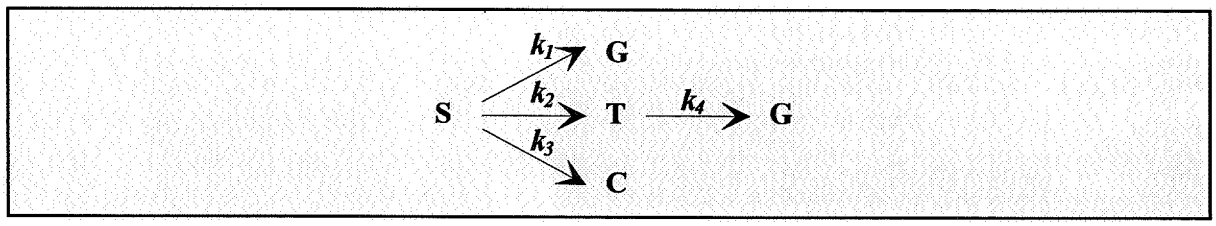

Table 4.34 Kinetic data and heat of reaction proposed for secondary tar cracking.

Reaction 4	A_i [s^{-1}]	E_i [kJ/mole]	Δh_i [kJ/kg]
Chan & Glaister's data	$1.50 \cdot 10^6$	114.3	-2009.7
Di Blasi &Russo's data	$4.28 \cdot 10^6$	108.0	-42.0
Adjusted data	$2.30 \cdot 10^4$	80.0	-50.0

Compared with the experimental results, simulations with D&R's data for secondary tar cracking resulted in a too high tar-to-gas conversion both at low and high heat flux, which means that the reaction rate is too fast. Simulations with C&G's data resulted in a thermal runaway, i.e., the in-depth temperature exceeded the surface temperature. This may be explained by the extremely high exothermic heat of reaction proposed by C&G. By reducing the heat of reaction of tar cracking to a more realistic level, 50 kJ/kg (exothermic), simulations with C&G's kinetic data gave satisfactory predictions of the ultimate tar and gas yields at low heat flux, but a too high tar-to-gas conversion at high heat flux. Through a parametric study, new rate constants for the secondary tar cracking reaction have been estimated that give better predictions of the experimental ultimate tar and gas yields at both heat fluxes. These are listed in Table 4.34 together with a reasonable value for the heat of reaction which is supposed to be slightly exothermic.

Finally, the results from the simulations with the complete reaction model are presented in Figures 4.60 to 4.62, that is, with Chan & Glaister's rate constants for the primary reactions and the adjusted rate constants for the secondary tar cracking reaction. A comparison of the experimental and predicted ultimate reacted fraction and product yields distribution are presented in Table 4.35.

As revealed in Figure 4.60 (upper), the predicted temporal temperature profiles agree reasonable well with the experimental results. Simulations with exothermic secondary tar cracking give somewhat higher ultimate surface and in-depth temperatures compared to those without tar cracking. Higher overall temperatures are, in turn, responsible for that more of the wood is reacted. The main difference between the two simulations, i.e., with and without tar cracking, is revealed in the temporal product yields distribution profiles (Figures 4.57 and 4.60 middle). In both cases, the gas and tar yields flatten after a few seconds at a low and high

level, respectively. In the case where tar cracking is not considered, these yields remain almost constant throughout the pyrolysis process, while a successively increasing gas yield and a reduction in tar yield may be seen when secondary tar cracking has been accounted for. Since char is a product of primary reactions only, tar cracking will have no influence on the final char-yield.

Table 4.35 Comparison of experimental percent reacted and product yields distribution and those predicted by using the competitive reaction model with secondary tar cracking.

		Low heat flux		High heat flux
		5 min	10 min	10 min
% Reacted	Experimental:	25.7 (±1.63)	45.5 (±3.61)	72.1 (±3.05)
	Predicted:	26.8	43.5	56.7
	Difference[‡]*:*	*1.1*	*-2.0*	*-15.4*
% Char	Experimental:	26.2 (±0.53)	28.7 (±1.06)	27.0 (±0.06)
	Predicted:	26.1	27.1	26.4
	Difference[‡]*:*	*-0.1*	*-1.6*	*-0.6*
% Tar	Experimental:	38.0 (±1.22)	31.3 (±5.06)	27.9 (±0.61)
	Predicted:	49.2	38.9	25.8
	Difference[‡]*:*	*11.2*	*7.6*	*-2.1*
% Gas	Experimental:	35.9 (±1.44)	40.0 (±5.45)	45.2 (±0.62)
	Predicted:	24.7	34.0	47.8
	Difference[‡]*:*	*-11.2*	*-6.0*	*2.6*

[‡] *Difference = Predicted - Experimental*

The effect of secondary tar cracking may also be seen in Figure 4.62, where the spatial gas mixture, tar and gas production rate profiles at several times are presented. Although, the gas mixture (gas + tar) production rate profiles are similar to those predicted without secondary reactions, the tar production, Figure 4.62 (middle), becomes negative after it has reached it's maximum value which means that the tar molecules are consumed as they flow towards the heated surface. The effect of this tar consumption is revealed in the gas production rate profiles in Figure 4.62 (bottom) which have two peaks. The innermost peak is due to primary reactions of the solid wood and the second peak, which is closer to the surface, is gas produced from secondary reactions of the tar. As revealed in Table 4.35, the ultimate reacted fraction is very well predicted at low heat flux but is under-predicted by almost 16 % at high heat flux. The model does an god job in predicting the experimental char-yields at both heat

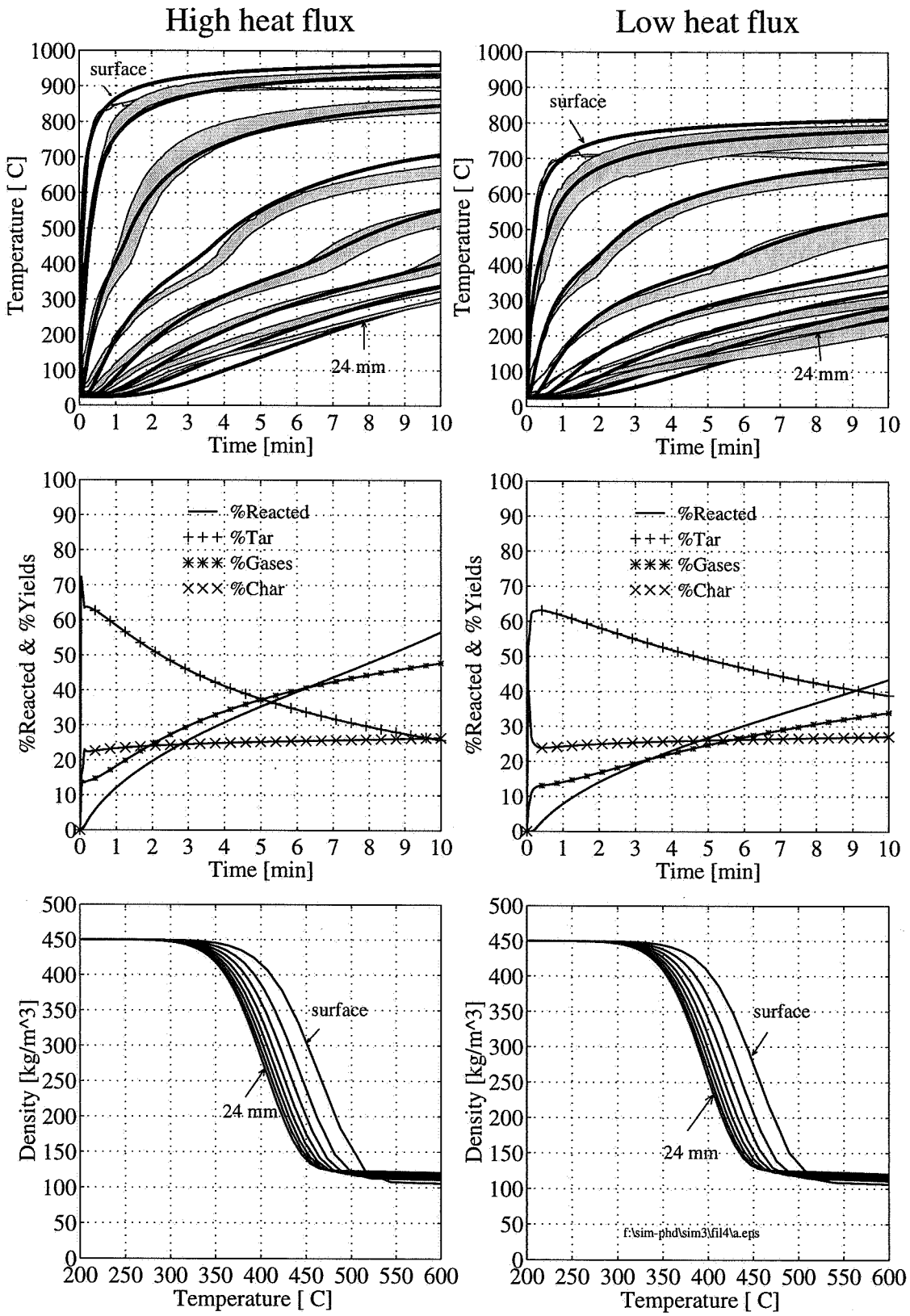

Figure 4.60 *Upper:* Predicted and experimental temperature histories.
Middle: Predicted percentage reacted and product yields distribution versus time.
Bottom: Predicted local density versus temperature.

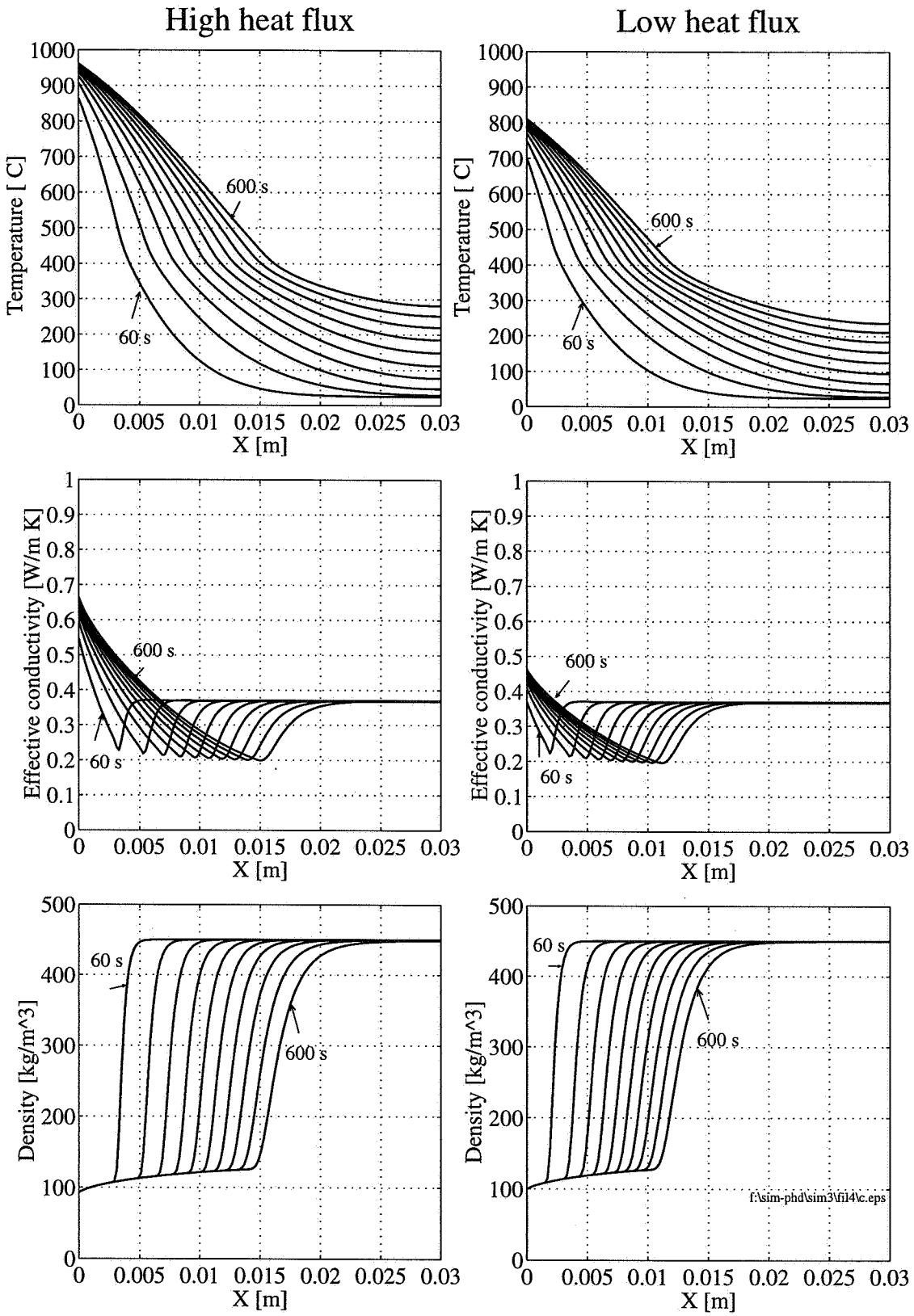

Figure 4.61 *Upper:* Predicted temperature profiles.
Middle: Predicted effective thermal conductivity profiles.
Bottom: Predicted density profiles.

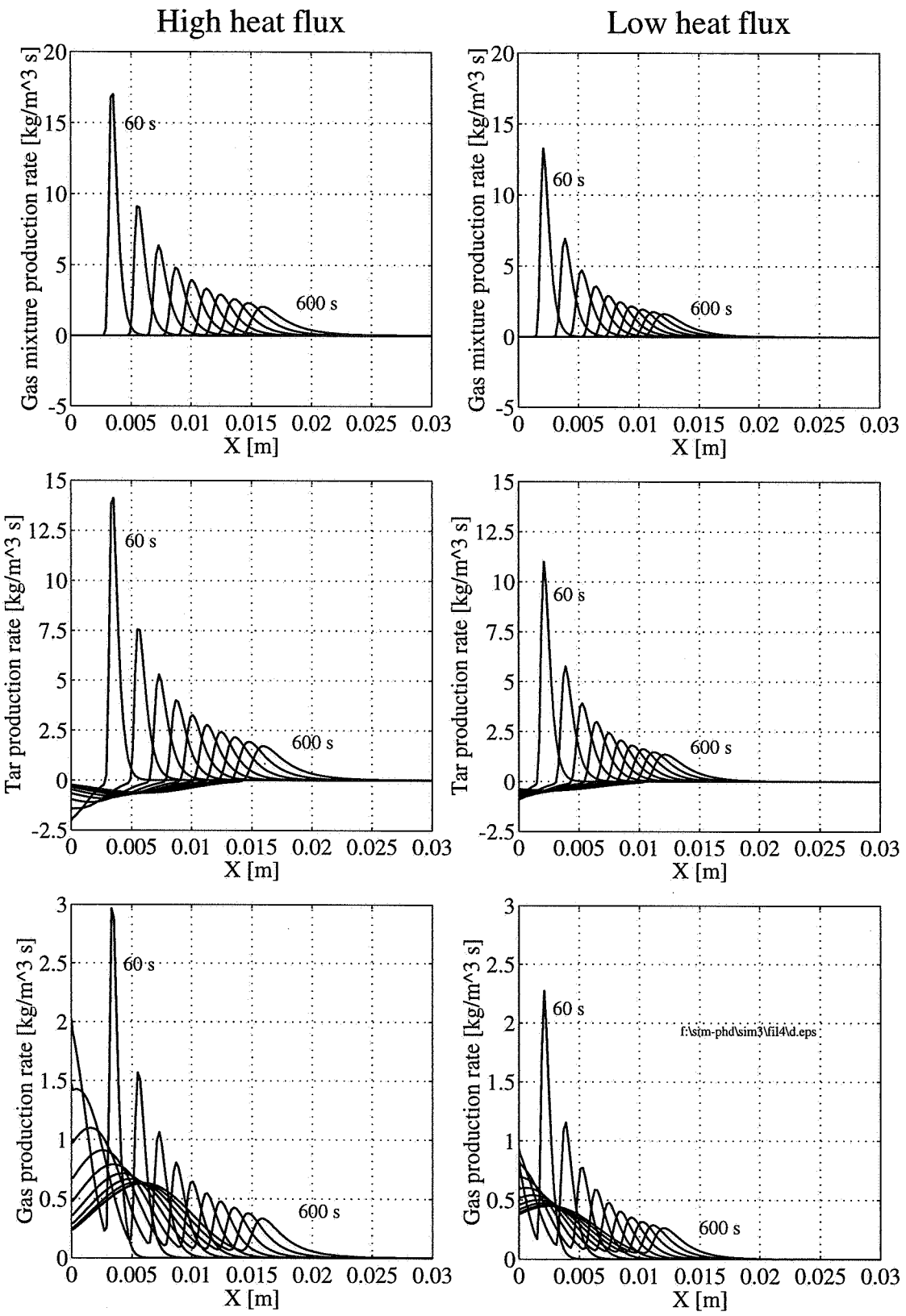

Figure 4.62 *Upper:* Predicted total gas mixture (gas + tar) production rate profiles.
Middle: Predicted tar production rate profiles.
Bottom: Predicted gas production rate profiles.

fluxes and the tar and gas-yields at high heat flux. The adjusted rate constants for secondary tar cracking give, however, a too low tar-to-gas conversion at low heat flux. By considering the uncertainties inherent in the experiments, e.g. in the mass-balance, and the simplifying assumptions used in the mathematical model, the predicted results must be regarded as satisfactory.

4.5.2 THEORETICAL PREDICTIONS WITH MOIST PELLETS

Due to resource and time limitations, no experiments were performed on moist wood pellets. Hence, the simulations that follows have not been compared with any experiments, although, a comparison with the simulations presented on dry samples in the previous section will be made. By this reasons, no attempt has been made to optimize any of the thermo-physical parameters involved in the drying model. The main objectives of this section will then be to demonstrate the model; to see what can be achieved by the model and by this, hopefully, give the reader further insight into the mechanisms of drying Before the results are presented, a brief discussion of the initial condition, boundary conditions and the thermo-physical parameters used will be given.

Except for the moisture content, the initial conditions are similar to those presented in section 4.5.1.1 for dry pellets. However, since evaporation/desorption and transport of bound water, liquid water and water vapour is included, the boundary conditions given in section 4.3.2 have to be used. The heat flux (F), heat transfer coefficient (h_T) and surface emissivity (ω_s) in equation (4.21) are equal to those used for dry pellets (see section 4.5.1.2). Given that h_T = 5 W/m^2 K, the mass transfer coefficient in equation (4.22) has been estimated to h_m = 0.03 m/s by using analogy between the Nusselt and Sherwood number:

$$Nu_L = \frac{h_T L}{k} = 0.664 Re_L^{1/2} Pr^{1/3}, \qquad Sh_L = \frac{h_m L}{D_{v-a}} = 0.664 Re_L^{1/2} Sc^{1/3} \tag{4.113}$$

where the Schmidt number (Sc) is defined by:

$$Sc = \frac{\mu}{\rho D_{v-a}} \tag{4.114}$$

Since the relative humidity in the surroundings is assumed zero, the partial water vapour pressure and hence, the vapour density, $<\rho_v>^g_\infty$, in the surroundings (equation (4.22)) will also be zero. The pyrolysis model that has been used is the competitive reaction model (Chan & Glaister's rate constants) with secondary tar cracking (adjusted rate constants). The thermo-physical parameters and kinetic data used are summarized in Tables 4.36 and 4.37, respectively.

Table 4.36 Thermo-physical parameters used for the combined drying and pyrolysis simulations.

Thermal conductivity: (*see section 4.3.4.6*)

$k_{eff,s} = \varepsilon_g k_g + (\varepsilon_b + \varepsilon_l) k_l + \eta k_{SD} + (1 - \eta) k_C + k_{rad}$

$k_{rad} = (4\varepsilon_g \sigma \omega d_{por} T^3)/(1 - \varepsilon_g)$

$d_{por} = \eta d_{por,SD} + (1 - \eta) d_{por,C}$

where: $k_g = 0.0258$ W/mK, $k_l = 0.658$ W/mK
$k_{SD} = 0.35$ W/mK, $k_C = 0.1$ W/mK
$d_{por,SD} = 50$ µm, $d_{por,C} = 100$ µm

Specific heats: (*see section 4.3.4.7*)

$C_{P,l} = 4.2$ kJ/kg K

$C_{P,s} = \eta C_{P,SD} + (1 - \eta) C_{P,C}$

$C_{P,g} \langle \rho_g \rangle = \sum C_{P,i} \langle \rho_i \rangle$

where: $C_{P,SD}$= f(T) see equation (4.80)
$C_{P,C}$= f(T) see equation (4.81)
$C_{P,i}$= f(T) see equation (4.83)-(4.86)

Permeabilities: (*see section 4.3.4.5*)

Relative: $K_r^g = 1 + (4S - 5)S^4$, $K_r^l = S^8$, $S = M_l/M_{l,sat}$

Intrinsic: $K_{g,s} = \eta K_{g,SD} + (1 - \eta) K_{g,C}$

where: $K_{g,SD} = 1.0 \cdot 10^{-14}$ m^2, $K_{g,C} = 1.0 \cdot 10^{-11}$ m^2

Dynamic viscosity: (*see section 4.3.4.9*)

$\mu_l = 1.40 \cdot 10^{-2} - 7.30 \cdot 10^{-5} T + 9.73 \cdot 10^{-8} T^2$ kg/ms

$\mu_g \langle \rho_g \rangle = \sum \mu_i \langle \rho_i \rangle$

where: μ_i= f(T) see equation (4.95)-(4.98)

Gas diffusion coefficient: (*see section 4.3.4.8*)

$D_{eff} = 20\, \varepsilon_g D_{v\text{-}a}$

where: $D_{v\text{-}a} = 1.192 \cdot 10^{-4} (T^{1.75}/P)$

Bound water diffusion coefficient: (*see section 4.3.4.8*)

$D_b = \exp(-9.9 - 4300/T + 9.8 \cdot M_b)$

Vapour pressure: (*see section 4.3.4.2*)

$M \geq M_{fsp}$: $\langle P_v \rangle^g = P_v^{sat}(T)$

$M < M_{fsp}$: $\langle P_v \rangle^g = P_v^{sat}(T)\, h(M_b, T)$

where: $P_v^{sat}(T) = \exp(24.1201 - 4671.3545/T)$
$h(M_b, T) = [1 - (1 - M_b/M_{fsp})^K$
$K = 6.453 \cdot 10^{-3} T$

Capillary pressure: (*see section 4.3.4.2*)

$P_C = 1.364 \cdot 10^5 \sigma (M_l + 1.2 \cdot 10^{-4})^{-0.63}$

where: $\sigma = (128.0 - 0.185T) \cdot 10^{-3}$

Heat of evaporation/desorption: (*see section 4.3.4.3*)

$M \geq M_{fsp}$: $\Delta h_v = \Delta h_l$

$M < M_{fsp}$: $\Delta h_v = \Delta h_l + \Delta h_{sorp}$

where: $\Delta h_l = 3179.0 - 2.5T$ kJ/kg
$\Delta h_{sorp} = 0.4 \Delta h_l (1 - M_b/M_{fsp})^2$ kJ/kg

Table 4.37 Reaction rate constants and heats of reaction for the competitive reaction model with secondary tar cracking

Reaction *i*	A_i [s^{-1}]	E_i [kJ/mole]	Δh_i [kJ/kg]
1	$1.3 \cdot 10^8$	140.3	150.0
2	$2.0 \cdot 10^8$	133.1	150.0
3	$1.1 \cdot 10^7$	121.3	150.0
4	$2.3 \cdot 10^4$	80.0	-50.0

The heat fluxes applied in the simulations of dry pellets (80 and 130 kW/m^2) have also been used for moist pellets. The initial moisture content has been varied between 10 and 40%, hence, the whole range from completely dry, through the bound water region into the region where both bound and liquid water exist, are covered.

The results from these simulations, given as percent reacted, ultimate product yields distribution and percent moisture evaporated, are presented in Table 4.38. Of comparative reasons, the results from the dry pellets simulations have been included.

Table 4.38 Results from simulation of moist wood pyrolysis after 10 minutes heating

Heat flux	%Initial moisture	%Reacted*	%Char*	%Tar*	%Gas*	%Moisture evaporated
Low	0	43.5	27.1	38.9	34.0	----
(80 kW/m^2)	10	33.6	27.0	49.5	23.5	78.1
	20	28.9	27.0	52.7	20.4	62.3
	30	25.9	27.0	54.5	18.5	52.9
	40	23.6	27.0	55.7	17.3	46.7
High	0	56.7	26.4	25.8	47.8	----
(130 kW/m^2)	10	44.2	26.1	38.7	35.2	88.0
	20	38.5	26.1	43.0	30.9	71.9
	30	34.6	26.1	46.1	27.8	61.2
	40	31.7	26.1	48.5	25.4	53.5

* based on dry wood

About the results presented in Table 4.38, there is not much to discuss, i.e., they are self-explainable. Obviously, as the initial moisture content increases, the reacted fraction and percent moisture evaporated decreases both at low and high heat flux. As consequence of

lower reacted fractions, the ultimate tar yields increase while the ultimate gas yields decrease. However, as the following discussion will show, a lot of interesting physics, thermodynamics and chemistry are buried in these results.

Figure 4.63 (UL = Upper Left) presents a comparison of predicted temperature histories for a dry pellet (dashed lines) and a pellet with an initial moisture content of 30% (solid lines) which both have been exposed to an heat flux of 130 kW/m^2 for 10 minutes. For the moist pellet, the predictions show prolonged plateaus of temperature near 100°C, indicative of the local drying process. The duration of the 100°C plateau depends on, of course, the initial moisture content and heating rate. In general, the length of the plateau increases with increasing moisture content, but decreases with increasing heating rate. Figure 4.63 (UR) presents temperature profiles as a function of depth and reaction times for the same simulations. A transition from drying to pyrolysis can be seen from the change in slope; for example, the drying front is 20 mm from the heated surface after 600 seconds. Water evaporation is a large sink compared to the net endothermic heat of reaction for the thermal degradation process (latent heat of 2250 kJ/kg at 100°C versus reaction heat of 100-150 kJ/kg). During the drying period, almost all of the energy received by the pellet is consumed by heating and evaporating water. After drying is complete at a location, the energy received rapidly increases the local temperature even though the pellet interior is still undergoing water evaporation. The temperature difference between the backside of the dry and moist pellet is approximately 200°C after 10 minutes heating, which highly reveals the delaying effect that moisture have on the pyrolysis process. This effect may also be seen in Figure 4.63 (MR), where the spatial density profiles for the two simulations are compared at different times. After 10 minutes of heating, the reaction front has progressed to a depth of 15 mm from the surface when the pellet is dry compared to "only" 10 mm for the pellet with an initial moisture content of 30%.

The evolution of the drying and pyrolysis processes are shown through product yields distribution, reacted fraction and percentage moisture evaporated versus time in Figure 4.63 (ML). After 10 minutes of exposure to a heat flux of 130 kW/m^2, about 61% of the moisture has been evaporated and almost 35% of the dry solid has been converted to char, tar and gases with a distribution of 26%, 46% and 28% based on dry wood, respectively. Based on moist mass, 40% of the wood has been converted to yield 35% water vapour, 18% char, 17% gases and 30% tar.

The predicted moisture content distributions are shown as a function of depth in Figure 4.63 (BR). The steep slopes correspond to the drying fronts in the pellet. It can be seen that the interior part of the pellet behind the drying front exhibits a moisture content greater than the

initial moisture content (M=0.3), an effect which has been experimentally observed by White and Schaffer (1981). It implies the existence of a inward flow of condensable water vapour, i.e., as drying proceeds, some of the water vapour produced moves into the relatively cooler interior part of the pellet behind the drying front and there it condense. This is confirmed by the water evaporation rate profiles shown as a function of depth in Figure 4.64 (ML). By following the evaporation rate profile from the surface, e.g. after 60 seconds, it can be seen that the evaporation rate reaches its maximum value at about 6 mm from the surface, after which it becomes negative indicating that condensation of water vapour occurs.

Figure 4.64 (BL) shows the predicted spatial overpressure at different times and reveals that the highest pressure is found near the maximum evaporation rate of water vapour. As time progresses, the pressure increases and reaches its maximum value after 600 seconds. This may be explained by the symmetry boundary conditions used at the right side of the calculation domain. The symmetry boundary condition implies that the velocities (for both liquid water and gas) and hence, the mass fluxes are zero at the non-heated surface. This means that all the gases, i.e., water vapour from drying, and gases and tars from pyrolysis, flowing into the interior of the pellet meet an impermeable surface and are then forced back to escape through the heated surface. The inward flow of water vapour may be seen in Figure 4.64 (BR), where the spatial superficial gas velocity profiles are presented it different times. Recall from Figure 4.12 that the x-coordinate was defined as positive in the direction from the heated surface and into the pellet. Hence, a negative velocity means that the gases flow towards the heated surface and to the contrary, i.e., an inward flow, if the gas velocity has a positive value. By superimposing the overpressure and superficial gas velocity profiles, it is seen that the gases flow towards the heated surface when the pressure gradients are positive and in the opposite direction when the pressure gradients are negative.

The predicted mass flux histories of volatile products, which include water vapour, tars and gases, are shown in Figure 4.63 (BL). As expected, the initial volatile species evolving from the heated surface is water vapour from drying. As time proceeds, the surface temperature rapidly increases and pyrolysis volatile products (tars and gases) start to take over as shown by the sharply increasing large peak indicated "tar flux" and the somewhat lower peak indicated "gas flux". It can be seen that the tar mass flux decays fast after reaching a maximum, while the gas mass flux first decreases slowly and then almost recovers its original value due to secondary cracking of the tar. The spatial tar and gas production rate profiles presented in Figures 4.64 (UL&UR) are similar to those presented for the dry pellets. However, the gas mixture (vapour + tar + gas) production rate profiles shown in Figure 4.64 (MR) have an additional peak which, of course, is the evaporation of water vapour.

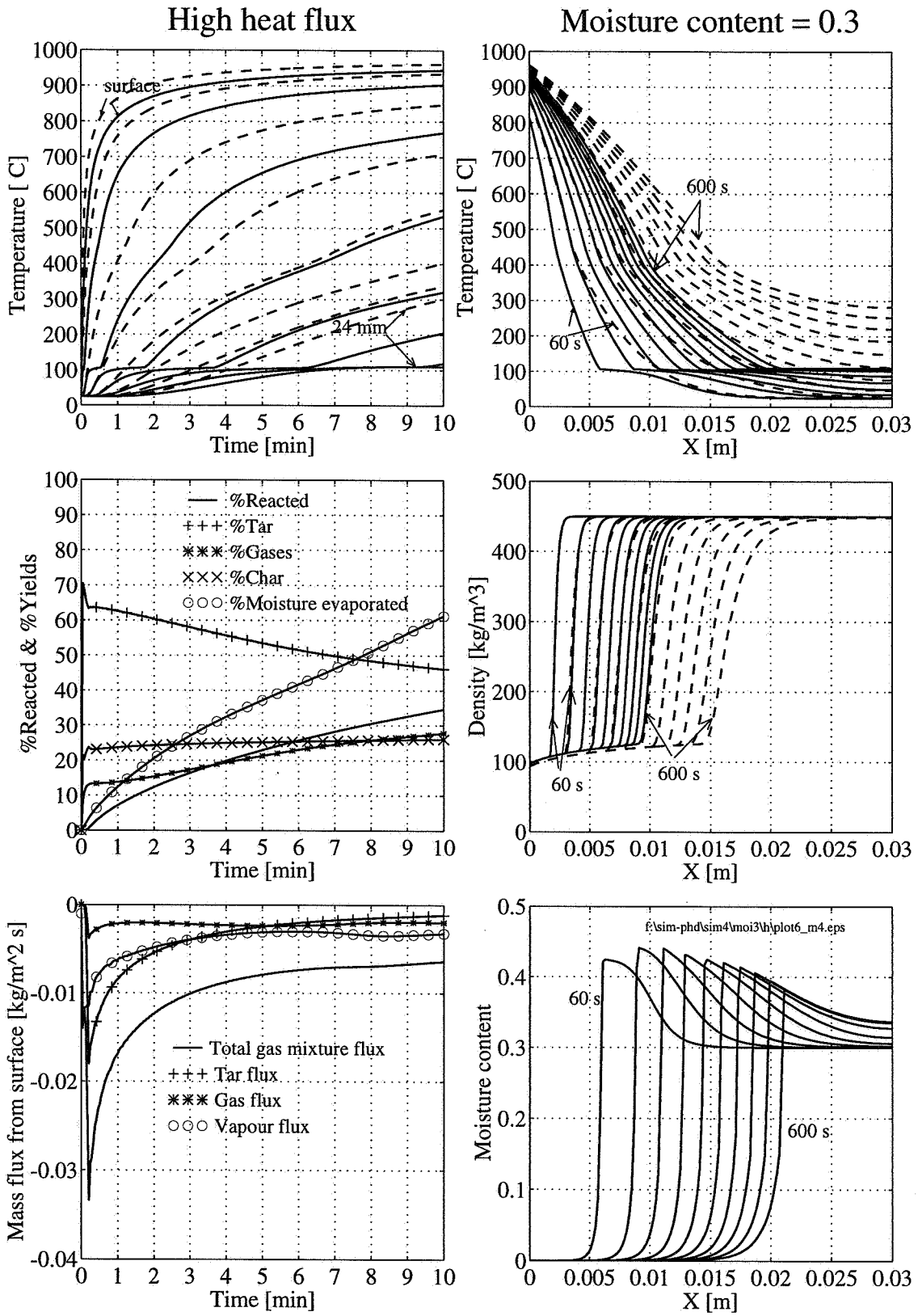

Figure 4.63 *UL:* Temperature vs time *UR:* Temperature vs pellet depth
ML: Product yields distribution *MR:* Density profiles
BL: Mass flux from surface *BR:* Moisture distribution

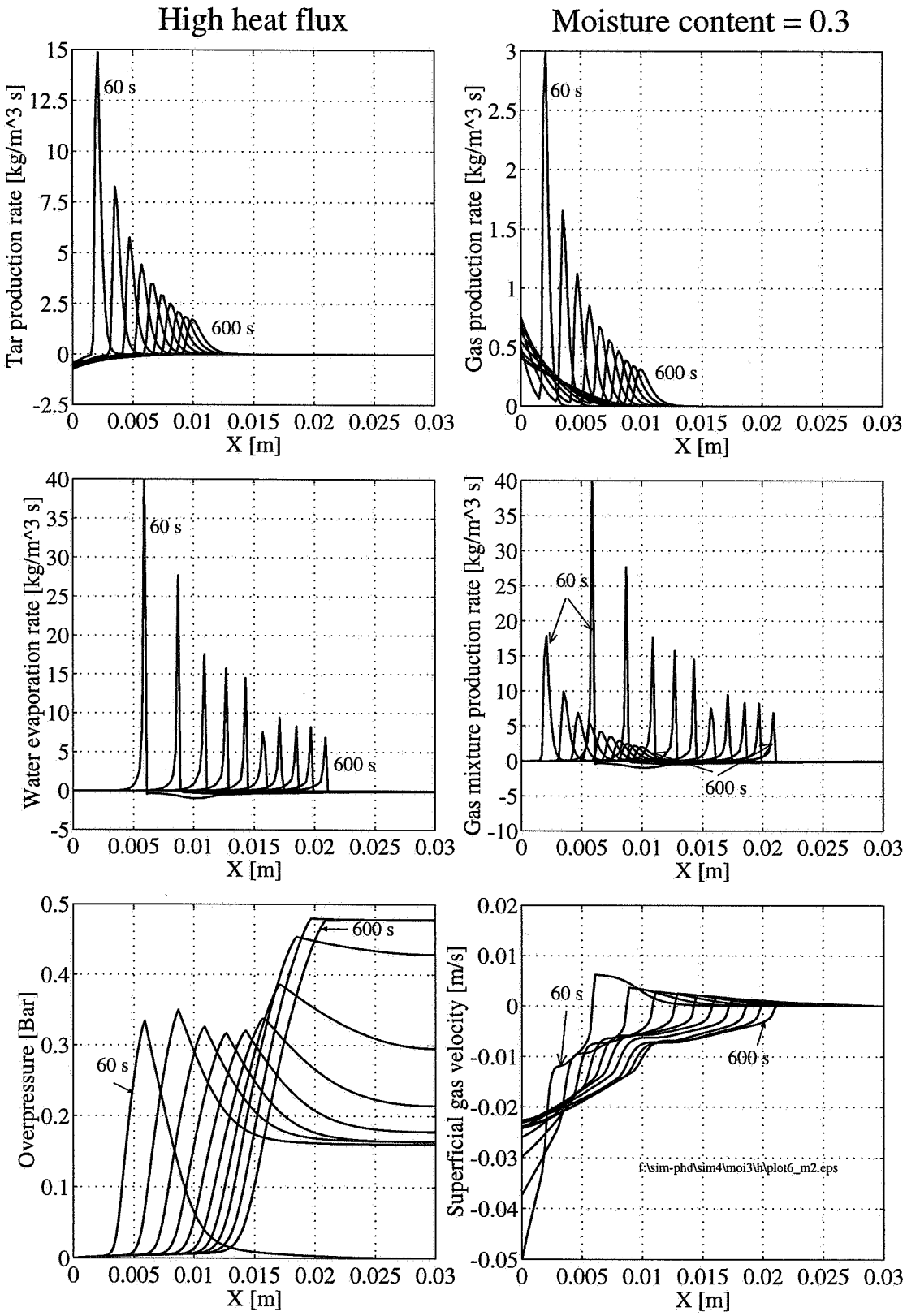

Figure 4.64 *UL:* Tar production rate *UR:* Gas production rate
ML: Water evaporation rate *MR:* Gas mixture production rate
BL: Pressure distribution *BR:* Superficial gas velocity

Since all the important mechanisms involved in the drying process, i.e., capillary water flow; bound water diffusion; and water vapour flow due to diffusion and pressure gradients, are included in the present simulations, i.e., with moisture content of 30%, it is decided to not present any of the predictions carried out at other moisture contents and heating rates.

4.5.3 SENSITIVITY ANALYSIS

The mathematical model that has been formulated to simulated one-dimensional drying and pyrolysis of wood requires many input parameters and properties of which values are highly uncertain. The purpose of this section is to study the effects of uncertainty in the model parameters on predictions and to identify those important parameters to which the model prediction is sensitive. The input parameters and characteristics studied are classified into the categories of: heat transfer properties; mass transfer properties; and decomposition properties. The sensitivity analysis has been performed by using the classical one-variable-at a-time approach, that is, one variable at a time is varied with the rest kept constant. Since the resources for this study are limited, the sensitivity of the parameters and properties involved in the drying model have been excluded from this analysis. To help evaluate the importance of various parameters, four predicted pyrolysis results from the mathematical model are compared with their reference values. They are: 1) The pellet fraction that reacted in the fixed pyrolysis time (10 min); 2) Tar yield (as weight percent of the pellet that reacted); 3) Gas yield (as weight percent of the pellet that reacted); and 4) Char yield (as weight percent of the pellet that reacted). The reference (ref) values are those presented in Table 4.35, which have been predicted by using the competitive reaction model with secondary tar cracking. To quantitatively evaluate the sensitivity of a predicted response to a parameter, a response value has been calculated for the reacted fraction, tar; gas and char yields which are equal to their predicted (new) values obtained by changing the input parameter minus their predicted reference values (=> *response value = new value - reference value*). If a change in the input parameter gives a negative response value, e.g., for the reacted fraction, this means that less of the substance is reacted compared to the reference case.

HEAT TRANSFER PROPERTIES

The category of heat transfer properties includes the effects of boundary conditions and thermal conductivity, the first of which is more important for agreement with the experiments than for general applications. The parameters and their values used to study model sensitivity to heat transfer properties are presented in Table 4.39 while the response values, or the model sensitivity to these parameters are summarized in Table 4.40.

Table 4.39 Parameters and their values used to study model sensitivity to heat transfer properties.

(*S1*)	**Boundary conditions**			
(*ref*)	h_T = 5 W/m^{2}K	ω_s=0.85	T_∞= 423 K	
(*S1a*)	h_T = 10 W/m^{2}K	ω_s=0.90	T_∞= 323 K	(higher heat losses from the surface)
(*S1b*)	h_T = 2 W/m^{2}K	ω_s=0.80	T_∞= 523 K	(lower heat losses from the surface)
(*S2*)	**Thermal conductivity**			
(*ref*)	$k_{eff,s} = \varepsilon_g k_g + \eta k_{SD} + (1 - \eta) k_C + k_{rad}$ k_g= 0.0258 W/mK, k_{SD}= 0.35 W/mK, k_C= 0.1 W/mK $d_{por,SD}$= 50 μm, $d_{por,C}$= 100 μm			
(*S2a*)	$k_{eff,s} = \varepsilon_g k_g + \eta k_{SD} + (1 - \eta) k_C$ k_g= 0.0258 W/mK, k_{SD}= 0.35 W/mK, k_C= 0.1 W/mK			(without radiation)
(*S2b*)	$k_{eff,s} = \varepsilon_g k_g + \eta k_{SD} + (1 - \eta) k_C$ k_g= 0.0258 W/mK, k_{SD}= 0.35 W/mK, k_C= 0.6 W/mK			(without radiation, higher k_C)
(*S2c*)	$k_{eff,s} = \varepsilon_g k_g + \eta k_{SD} + (1 - \eta) k_C + k_{rad}$ k_g= 0.0258 W/mK, k_{SD}= 0.35 W/mK, k_C= 0.1 W/mK $d_{por,SD}$= 75 μm, $d_{por,C}$= 125 μm			(with radiation, higher $d_{por,SD}$ & $d_{por,C}$)
(*S2d*)	$k_{eff,s} = \varepsilon_g k_g + \eta k_{SD} + (1 - \eta) k_C + k_{rad}$ k_g= 0.0258 W/mK, k_{SD}= 0.35 W/mK, k_C= 0.1 W/mK $d_{por,SD}$= 25 μm, $d_{por,C}$= 75 μm			(with radiation, lower $d_{por,SD}$ & $d_{por,C}$)
(*S2e*)	$k_{eff,s} = \varepsilon_g k_g + \eta k_{SD} + (1 - \eta) k_C + k_{rad}$ k_g= 0.0258 W/mK, k_{SD}= 0.175 W/mK, k_C= 0.05 W/mK $d_{por,SD}$= 25 μm, $d_{por,C}$= 50 μm $K_g = \eta K_{g,SD} + (1 - \eta) K_{g,C}$ $K_{g,SD}$= $1.0 \cdot 10^{-16}$ m^2, $K_{g,C}$= $1.0 \cdot 10^{-13}$ m^2			(radially heating, lower permeabilities)
(*S2f*)	$k_{eff,s} = \zeta k_{par} + (1 - \zeta) k_{ser}$ $k_{fiber,\parallel}$= 0.766 W/mK, $k_{fiber,\perp}$= 0.44 W/mK, ξ = 0.9			(parallel/serial conductivity model)

Boundary conditions

The heat loss to the surroundings is through convection and radiation; being influenced by the convective heat transfer coefficient (h_T), surface emissivity (ω_s) and surrounding temperature (T_∞). These parameters have been varied to study the effects of higher and lower heat losses from the surface, and are referred to as run *S1a* and run *S1b* in Table 4.39, Table 4.40 and

Figure 4.65. The reference parameters used were examined in section 4.5.1.2. The effects of changing the boundary conditions are shown through the temperature and density profiles in Figures 4.65 (UL&UR) and Figures 4.65 (ML&MR), where the dashed lines represent the reference case while the solid lines represent run *S1a* and run *S1b*. Obviously, higher heat losses to the surroundings, as simulated by run *S1a*, reduces the surface temperature. Less heat is then available for the thermal degradation and consequently, less of the substance (-2.7%) is reacted. The opposite occurs, i.e., higher surface temperature and more of the substance (+2.2%) is reacted when the heat losses are lower. By using the parameters (*ref*, *S1a*, *S1b*) specified in Table 4.39 and assuming an heat flux and surface temperature of 130 kW/m^2 and 950°C, respectively, the actual heat fluxes penetrating the pellet surface (that is available for conduction and thermal degradation) can be estimated to 7.4, 30.5 and 19.7 kW/m^2 for (*S1a*), (*S1b*) and the reference case, respectively. This highly reflects the importance of boundary conditions when model predictions shall be compared with experiments.

Thermal conductivity

In order to study the importance of its functional form, several thermal conductivity models, both with and without radiation, have been tested. These are referred to as (*S2a*) to (*S2f*) in Table 4.39. The results from these simulations are presented in Table 4.40 and Figures 4.65 to 4.67. The reference model used were examined in section 4.5.1.3.

Figure 4.65 (BL) presents a comparison of predicted temperature histories for the reference run (dashed lines) and run *S2a* (solid lines). In the latter case, radiation has been omitted and the thermal conductivity is dependent on density only. The corresponding comparison of effective conductivity profiles is shown in Figure 4.65 (BR). Since the effective thermal conductivity for run *S2a* is function of density which is decreasing as the virgin wood degrades to char, the temperature rise in the pellet interior is much slower than in the reference case and obviously, less of the substance is reacted.

Instead of using the usual temperature dependent radiative term to account for the increase in conductivity, the thermal conductivity of char has in run *S2b* been assumed two times greater than of the original wood. As Figures 4.66 (UL&UR) show, the temperature rise in the pellet interior becomes much faster for run *S2b* (solid lines) than predicted with the reference parameters (dashed lines), and approximately 30% more of the substance is reacted. These comparisons (run *S2a* and run *S2b*) show that it is necessary to take into consideration the contribution from radiative heat transfer when an effective thermal conductivity model is to be applicable to high temperatures.

The effects of an increase or a decrease in the radiative part of the effective conductivity are shown in Figures 4.66 (ML&MR) and Figures 4.66 (BL & BR), respectively. This has been done by respectively increasing (run *S2c*) and decreasing (run *S2d*) the pore diameter (= characteristic radiation length) of the virgin wood and char. By increasing the radiative thermal conductivity, the predicted intraparticle temperatures increase by as much as 50°C (dependent on position), compared to the reference run. The consequence of higher temperatures is of course that more of the substance is reacted. A similar decrease in the predicted intraparticle temperatures are observed when the radiative thermal conductivity is decreased and obviously, less of the substance is reacted.

In run *S2e* the thermal conductivity of virgin wood and char has been reduced by a factor of two from the reference case to simulate the effects of radially heating. Recall that the conductivity parallel with the grain is approximately two times that perpendicular to the grain. In addition, the pore diameter of virgin wood and char has been reduced to 25 and 50 microns, respectively, and the intrinsic permeabilities have been assumed 100 times lower. Figures 4.67 (UL&UR) present the resulting temperature histories and spatial effective conductivity profiles predicted by assuming radial heating (solid lines). The reference run (dashed lines), which intends to simulate longitudinal heating, has been included for comparison. Lower effective conductivity reduces the inward flow of heat. Consequently, the intraparticle temperatures becomes lower and approximately 17% less of the substance is reacting when the pellet is radially heated.

Finally, simulations with the effective conductivity model (*S2f*) based on weighting between parallel and serial heat transfer (outlined in section 4.3.4.6) are presented with solid lines in Figures 4.67 (ML&MR). The dashed lines are again representing the reference run. A comparison of the temperature profiles reveals that the conductivity for the unreacted substance in the parallel/serial model is too low. For example, the final temperature at position 24 mm from the heated surface is about 75°C lower than that predicted by the reference model. By this reason, about 5% less of the substance is reacting. However, closer to the surface where the temperatures are much higher, radiation is the most important heat transfer mechanism in both models and the predicted final temperatures at both 1 mm, 4 mm, 8 mm and 12 mm coincide fairly well.

Among the thermal conductivity models presented and discussed, the conclusion must be that the best prediction of the experimental temperature profiles is achieved with the original (*ref*) effective thermal conductivity expression. The current predictions and comparisons have also shown that the functional form of the thermal conductivity model is of great importance.

Table 4.40 Model sensitivity to changes in heat transfer properties.

	%Reacted	%Tar	%Gas	%Char	
Reference					
(*ref*)	56.7	25.8	47.8	26.4	
Boundary conditions					
(*S1a*)	-2.7	2.3	-2.3	0.0	Figures 4.65 UL&UR
(*S1b*)	2.2	-1.8	1.8	0.0	Figures 4.65 ML&MR
Thermal conductivity					
(*S2a*)	-23.4	3.8	-5.0	1.2	Figures 4.65 BL&BR
(*S2b*)	28.2	5.2	-4.9	-0.3	Figures 4.66 UL&UR
(*S2c*)	4.8	-0.3	0.3	0.0	Figures 4.66 ML&MR
(*S2d*)	-5.1	0.4	-0.4	0.0	Figures 4.66 BL&BR
(*S2e*)	-16.5	-1.0	1.3	-0.3	Figures 4.67 UL&UR
(*S2f*)	-5.4	-0.6	1.0	-0.4	Figures 4.67 ML&MR

response value = new value - reference value

MASS TRANSFER PROPERTIES

Since gaseous diffusion has been assumed to play a negligible role, the only parameters which may influence the mass transfer are the permeabilities and the dynamic viscosity. Both are included in Darcy's law calculation of the superficial gas velocity.

Permeabilities

In order to study the importance of mass-transfer of volatiles on the pyrolysis process, the effects of changing the wood and char permeabilities have been examined. The reference simulation (*ref*) with a virgin wood and char permeability of $K_{g,SD}=1.0\cdot10^{-14}$ m^2 and $K_{g,C}=1.0\cdot10^{-11}$ m^2, respectively, intends to describe a medium permeable wood with the resulting charred region, as a consequence of strong structural changes, 1000 times more permeable. The maximum overpressure calculated by using these permeabilities is 0.0008 bar. As the char permeability is decreased and finally reaches the value of the virgin wood, as simulated by run (*S4a*) to (*S4c*) (see Table 4.41), larger pressure peaks and lower velocities in the char region are computed. Hence, the residence time of the volatiles in the hot char region increase, promoting secondary cracking of the tar components. This is revealed in the ultimate tar and gas yields in Table 4.42. Less tar and more gas is calculated in run (*S4c*) compared to the

reference run. Although, the volatiles transfer some convective heat as they flow towards the heated surface, the gas pressure and velocity field in the wood pellet have negligible influence on the temperature distribution. By this reason, the permeabilities will have no influence on the reacted fraction and ultimate char yield. In reality, however, the char is due to its more porous structure, fissuration, etc. more permeable than in its origin state, and quasi steady-state approximation for the gas phase with no mass transfer resistance within the solid matrix, i.e., instantaneous outflow of gases [Kung (1972); Chan *et al.* (1985)], could for simplicity have been used. In this case, it is not necessary to solve the pressure equation.

Dynamic viscosity

Recall that for the reference run, a mass average dynamic viscosity of the gas mixture phase was used with temperature dependent expressions for the individual tar and gas components. In run (*S5a*) (see Table 4.41), the dynamic viscosity of tar and gas has been assumed constant (mass average for the gas mixture), while constant dynamic viscosity has been used for the gas mixture in run (*S5b*). As revealed in Table 4.42, none of these simplifications have influence on the predicted fraction reacted and ultimate product yields distribution. Hence, a constant dynamic viscosity for the gas mixture, which decrease the CPU time by as much as 10%, is preferable.

Table 4.41 Parameters and their values used to study model sensitivity to mass transfer properties.

(*S4*)	**Permeabilities**	
(*ref*)	$K_g = \eta K_{g,SD} + (1 - \eta) K_{g,C}$ $K_{g,SD} = 1.0 \cdot 10^{-14}$ m^2, $K_{g,C} = 1.0 \cdot 10^{-11}$ m^2	($K_{g,C} = 1000 \cdot K_{g,SD}$)
(*S4a*)	$K_{g,SD} = 1.0 \cdot 10^{-14}$ m^2, $K_{g,C} = 1.0 \cdot 10^{-12}$ m^2	($K_{g,C} = 100 \cdot K_{g,SD}$)
(*S4b*)	$K_{g,SD} = 1.0 \cdot 10^{-14}$ m^2, $K_{g,C} = 1.0 \cdot 10^{-13}$ m^2	($K_{g,C} = 10 \cdot K_{g,SD}$)
(*S4c*)	$K_{g,SD} = 1.0 \cdot 10^{-14}$ m^2, $K_{g,C} = 1.0 \cdot 10^{-14}$ m^2	($K_{g,C} = K_{g,SD}$)
(*S5*)	**Dynamic viscosity**	
(*ref*)	$\mu_g \langle \rho_g \rangle = \sum \mu_i \langle \rho_i \rangle$ $\mu_i = f(T)$	
(*S5a*)	$\mu_g \langle \rho_g \rangle = \sum \mu_i \langle \rho_i \rangle$ $\mu_G = 2.8 \cdot 10^{-5}$ kg m/s, $\mu_T = 1.5 \cdot 10^{-5}$ kg m/s	(mass average, μ_i= constant)
(*S5b*)	$\mu_g = 3 \cdot 10^{-5}$ kg m/s	(constant dynamic viscosity)

Table 4.42 Model sensitivity to changes in mass transfer properties.

	%Reacted	%Tar	%Gas	%Char
Reference				
(ref)	56.7	25.8	47.8	26.4
Permeabilities				
(S4a)	0.0	-0.2	0.2	0.0
(S4b)	0.0	-1.4	1.4	0.0
(S4c)	0.0	-6.6	6.6	0.0
Dynamic viscosity				
(S5a)	0.0	0.0	0.0	0.0
(S5b)	0.0	0.0	0.0	0.0

response value = new value - reference value

DECOMPOSITION PROPERTIES

The category of decomposition properties includes the effects of pyrolysis kinetics and heats of reactions. The effect of pyrolysis kinetics were studied by varying the activation energies of the four reaction by ±5 % (one at a time). Since the activation energy and frequency factor are strongly coupled (compensation effect), the activation energy should not be varied without simultaneously changing the frequency factor. Thus, the corresponding frequency factors were determined by using the following relation:

$$A = A_{ref} \exp\left[\frac{(E - E_{ref})}{(RT_{iso})}\right] \tag{4.115}$$

where A_{ref}, E_{ref} and A, E are the reference and new frequency factor and activation energy, respectively. T_{iso} = 591 K (318°C) is the isokinetic temperature calculated in Chapter 3.

The heats of reaction have in one of the simulations been assumed zero, that is, no heat produced or consumed during the thermal degradation process. In the other case, the heats of the primary reactions have been assumed more endothermic and the secondary tar cracking reaction more exothermic than in the reference case. The parameters and their values used to study model sensitivity to decomposition properties are presented in Table 4.43, while the resulting response values are summarized in Table 4.44.

Table 4.43 Parameters and their values used to study model sensitivity to decomposition properties.

(*S6*)	**Activation energy and frequency factor, gas-forming reaction**			
(*ref*)	E_1=140.3 kJ/mole	$A_1=1.3\cdot10^8$ s^{-1}		
(*S6a*)	E_1=147.3 kJ/mole	$A_1=5.4\cdot10^8$ s^{-1}	(5% increase in E_1)	
(*S6b*)	E_1=133.3 kJ/mole	$A_1=3.1\cdot10^7$ s^{-1}	(5% decrease in E_1)	
(*S7*)	**Activation energy and frequency factor, tar-forming reaction**			
(*ref*)	E_2=133.1 kJ/mole	$A_2=2.0\cdot10^8$ s^{-1}		
(*S7a*)	E_2=139.8 kJ/mole	$A_2=7.8\cdot10^8$ s^{-1}	(5% increase in E_2)	
(*S7b*)	E_2=126.4 kJ/mole	$A_2=5.1\cdot10^7$ s^{-1}	(5% decrease in E_2)	
(*S8*)	**Activation energy and frequency factor, char-forming reaction**			
(*ref*)	E_3=121.3 kJ/mole	$A_3=1.1\cdot10^7$ s^{-1}		
(*S8a*)	E_3=127.4 kJ/mole	$A_2=3.8\cdot10^7$ s^{-1}	(5% increase in E_3)	
(*S8b*)	E_3=115.3 kJ/mole	$A_2=3.2\cdot10^6$ s^{-1}	(5% decrease in E_3)	
(S9)	**Activation energy and frequency factor, tar-cracking reaction**			
(*ref*)	E_4=80.0 kJ/mole	$A_4=2.3\cdot10^4$ s^{-1}		
(*S9a*)	E_4=84.0 kJ/mole	$A_4=5.2\cdot10^4$ s^{-1}	(5% increase in E_4)	
(*S9b*)	E_4=76.0 kJ/mole	$A_4=1.0\cdot10^4$ s^{-1}	(5% decrease in E_4)	
(*S10*)	**Heats of reaction**			
(*ref*)	Δh_1=150.0 kJ/kg,	Δh_2=150.0 kJ/kg,	Δh_3=150.0 kJ/kg,	Δh_4=-50.0 kJ/kg
(*S10a*)	Δh_1=0.0 kJ/kg,	Δh_2=0.0 kJ/kg,	Δh_3=0.0 kJ/kg,	Δh_4=0.0 kJ/kg
(*S10b*)	Δh_1=250.0 kJ/kg,	Δh_2=250.0 kJ/kg,	Δh_3=250.0 kJ/kg,	Δh_4=-150.0 kJ/kg

Pyrolysis Kinetics

As Table 4.44 and Figures 4.67 (BL&BR) to Figures 4.70 (UL&UR) reveal, the compensation effect of kinetic data is not negligible; variation of kinetic data over a reasonable range causes a few percent change on the reacted fraction and relative product yields distribution. For example, a decrease in activation energy and frequency factor for the char formation reduce the char density by 25-30 kg/m^3 and the ultimate char yield by 3.3 %. Lower char density means higher porosity ($\varepsilon_g=1-\langle\rho_s\rangle/\langle\rho_s\rangle^s$). Recall that the porosity is included in both the numerator and denominator of the radiative conductivity term [$k_{rad}=(4\varepsilon_g\sigma\omega T^3)/(1-\varepsilon_g)$]. Hence, higher porosity will increase the radiative contribution to the effective thermal conductivity, and heat is transferred through the char region at a much faster rate and more of the substance is reacted (+3.7 %) will react. This decrease in char yield produces an increase in the yield

of other products owing to the necessity of a mass balance. The effect of an increase in the activation energy and frequency factor of the secondary reaction (*S9a*) is that less of the tar is cracked into gases, but no effect on the ultimate reacted fraction, char yield and temperature history is seen.

Heats of Reaction

The last parameters to be examined are the heats of reaction. As seen from Figures 4.70 (ML&MR) and Figures 4.70 (BL&BR), variation of the heats of reaction from zero, i.e., no heat consumed or produced, to an overall endothermic value of 100 kJ/kg, have moderate effects on temperature histories and reacted fraction, but small effects on product distribution.

Table 4.44 Model sensitivity to changes in decomposition properties.

	%Reacted	%Tar	%Gas	%Char	
Reference					
(*ref*)	56.7	25.8	47.8	26.4	
A_1 & E_1					
(*S6a*)	2.5	-2.0	4.0	-2.0	Figures 4.67 BL&BR
(*S6b*)	-0.7	0.6	-1.2	0.6	Figures 4.68 UL&UR
A_2 & E_2					
(*S7a*)	3.2	2.2	0.8	-3.1	Figures 4.68 ML&MR
(*S7b*)	-2.9	-2.5	-0.8	3.3	Figures 4.68 BL&BR
A_3 & E_3					
(*S8a*)	-3.1	-1.6	-2.1	3.7	Figures 4.69 UL&UR
(*S8b*)	3.7	1.3	2.0	-3.3	Figures 4.69 ML&MR
A_4 & E_4					
(*S9a*)	0.0	-4.2	4.2	0.0	Figures 4.69 BL&BR
(*S9b*)	0.0	5.0	-5.0	0.0	Figures 4.70 UL&UR
Heats of reaction					
(*S10a*)	3.9	-0.2	0.2	0.0	Figures 4.70 ML&MR
(*S10b*)	-2.0	0.0	0.0	0.0	Figures 4.70 BL&BR

response value = new value - reference value

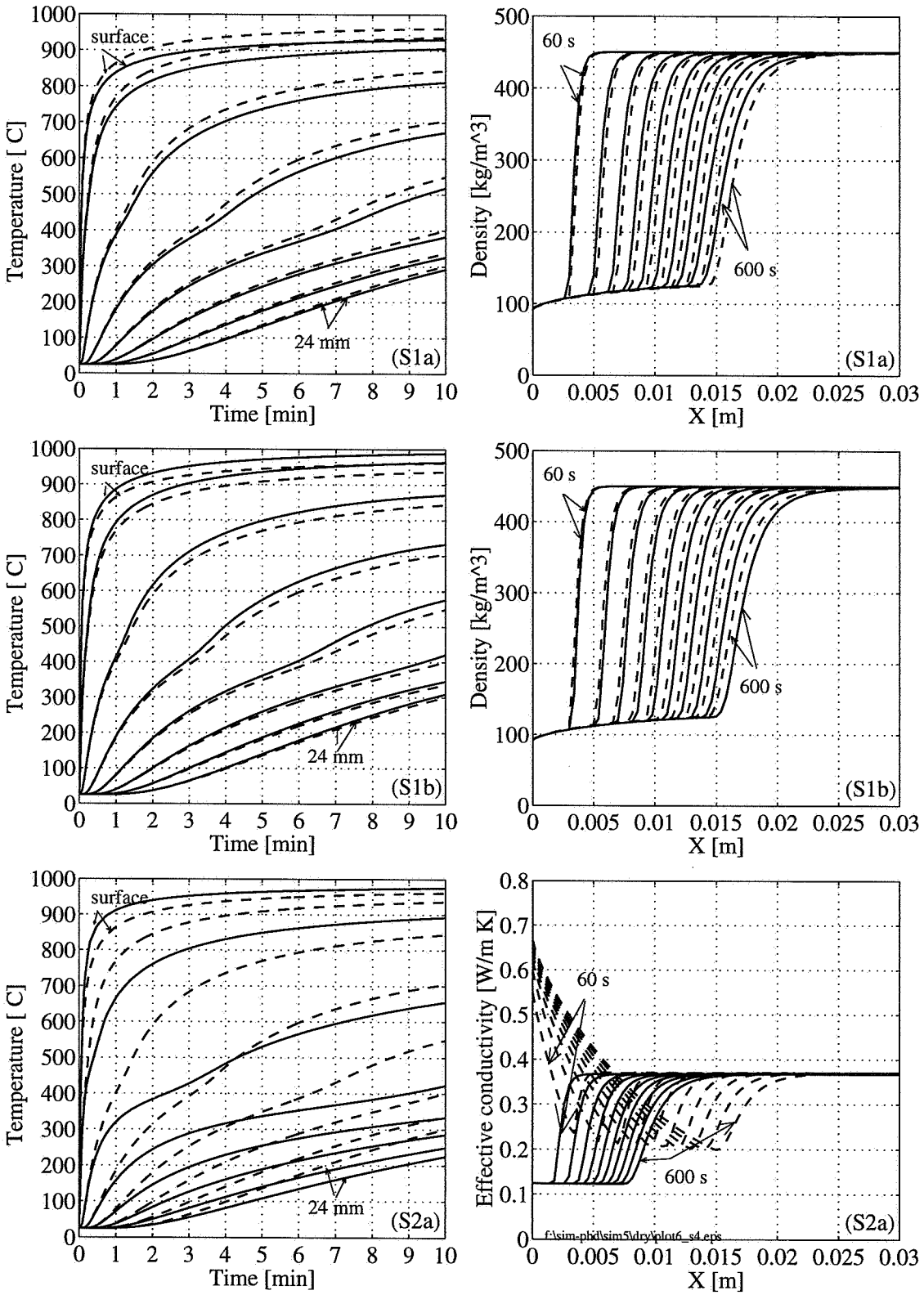

Figure 4.65 *UL:* Temperature vs time (*S1a*) *UR:* Density vs depth (*S1a*)
ML: Temperature vs time (*S1b*) *MR:* Density vs depth (S1b)
BL: Temperature vs time (*S2a*) *BR:* Effective conductivity vs depth (*S2a*)

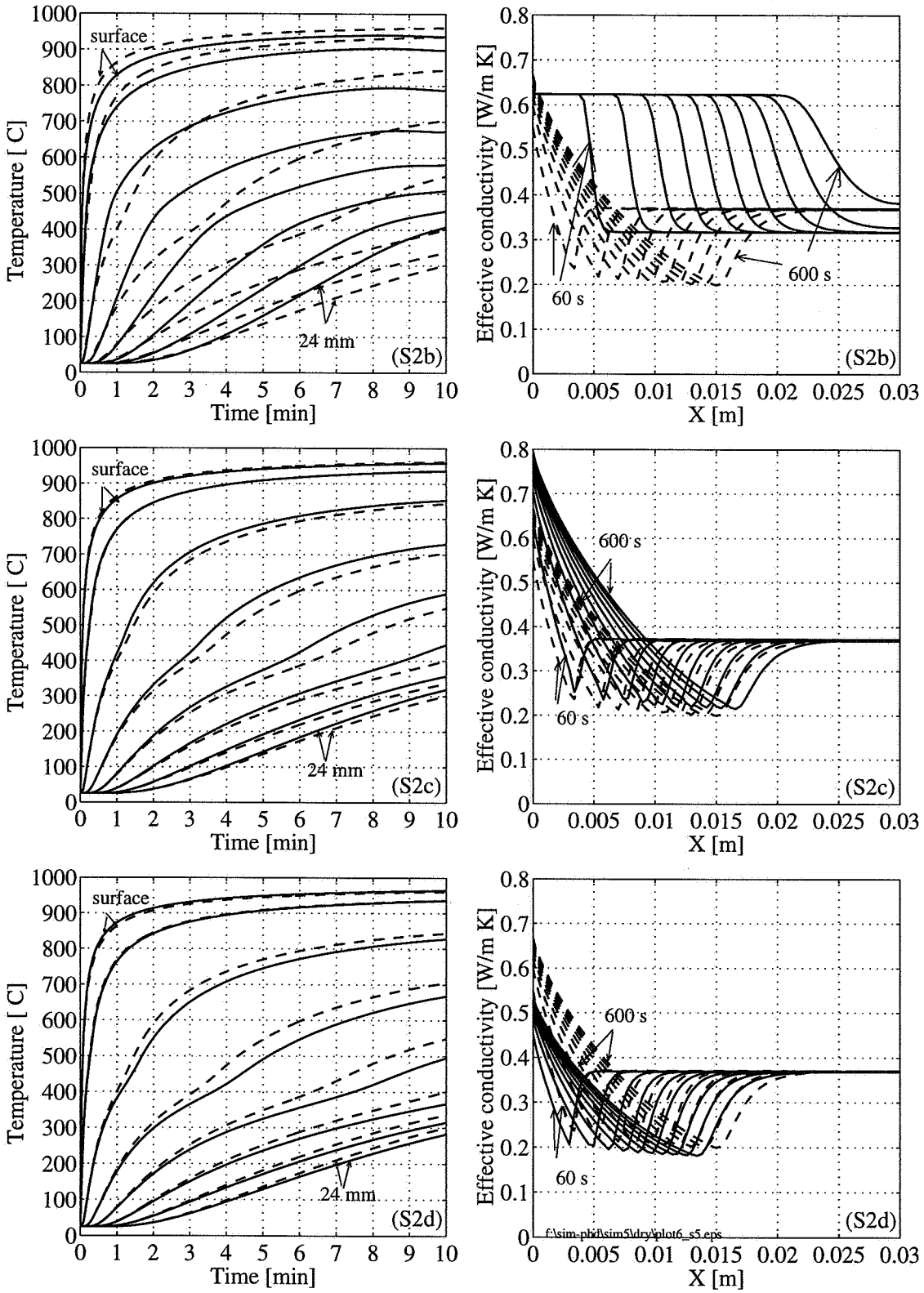

Figure 4.66 *UL:* Temperature vs time (*S2b*) *UR:* Effective conductivity vs depth (*S2b*)
ML: Temperature vs time (*S2c*) *MR:* Effective conductivity vs depth (*S2c*)
BL: Temperature vs time (*S2d*) *BR:* Effective conductivity vs depth (*S2d*)

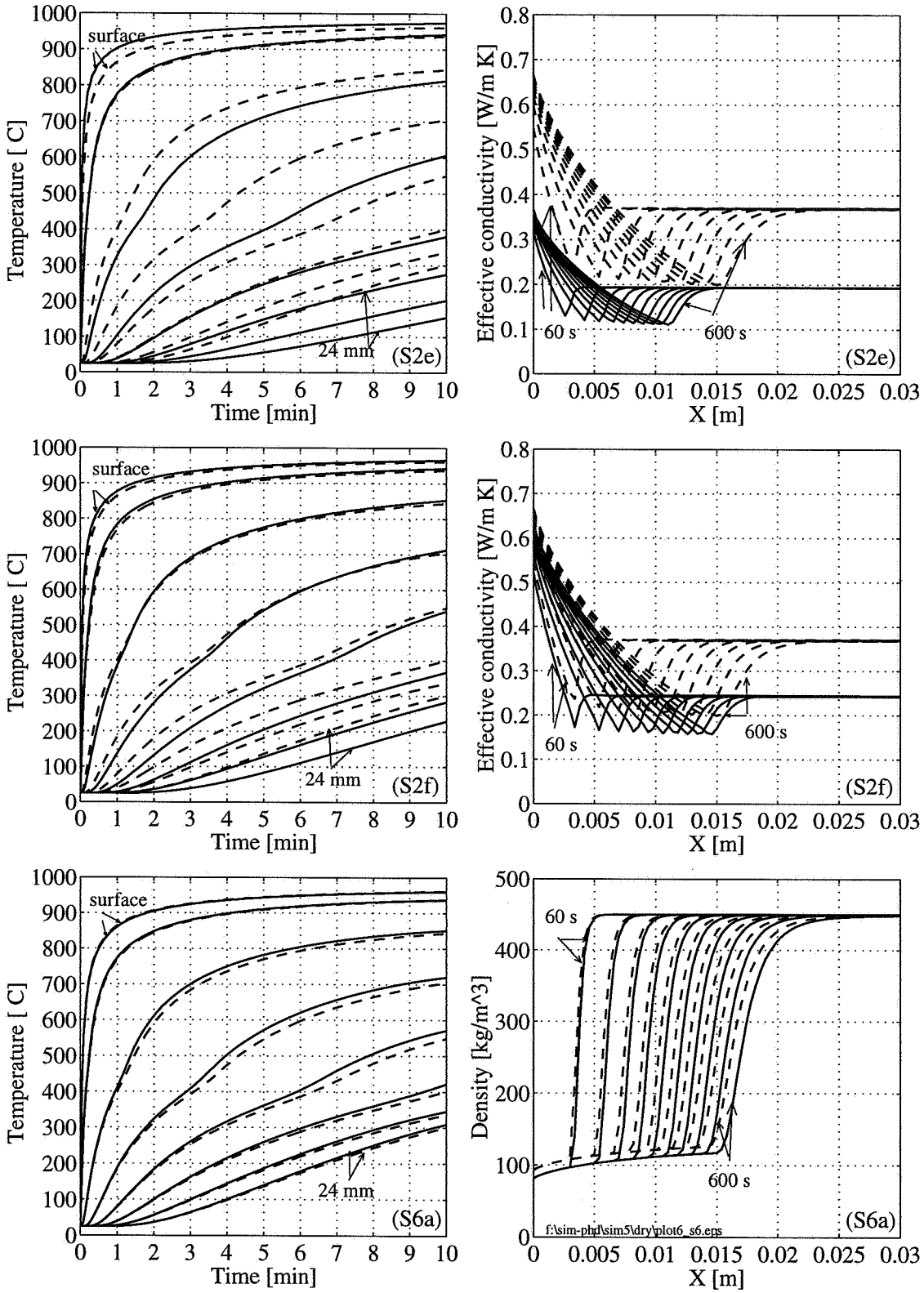

Figure 4.67 *UL:* Temperature vs time (*S2e*) *UR:* Effective conductivity vs depth (*S2e*)
ML: Temperature vs time (*S2f*) *MR:* Effective conductivity vs depth (*S2f*)
BL: Temperature vs time (*S6a*) *BR:* Density vs depth (*S6a*)

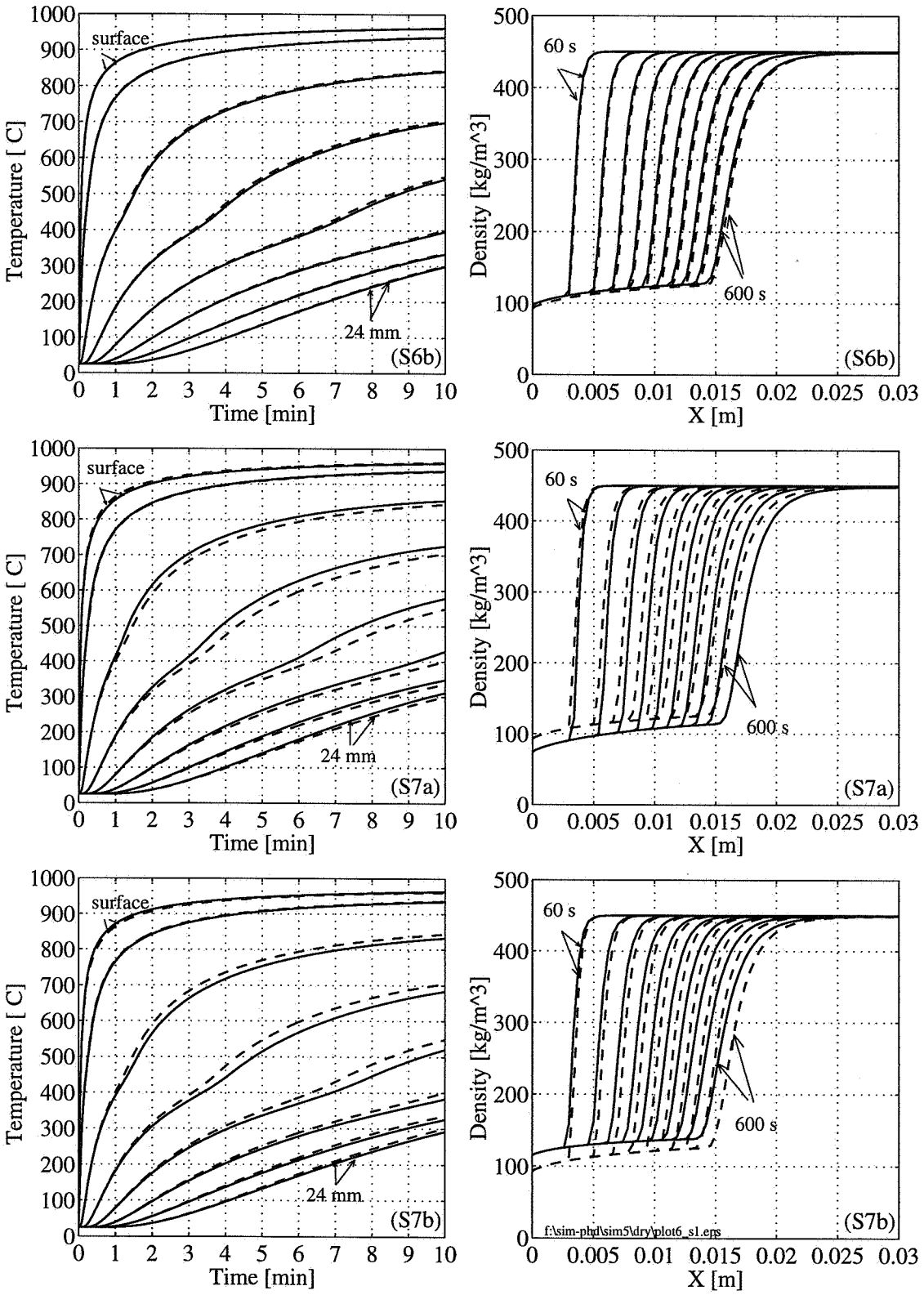

Figure 4.68 *UL:* Temperature vs time (*S6b*) *UR:* Density vs depth (*S6b*)
ML: Temperature vs time (*S7a*) *MR:* Density vs depth (*S7a*)
BL: Temperature vs time (*S7b*) *BR:* Density vs depth (*S7b*)

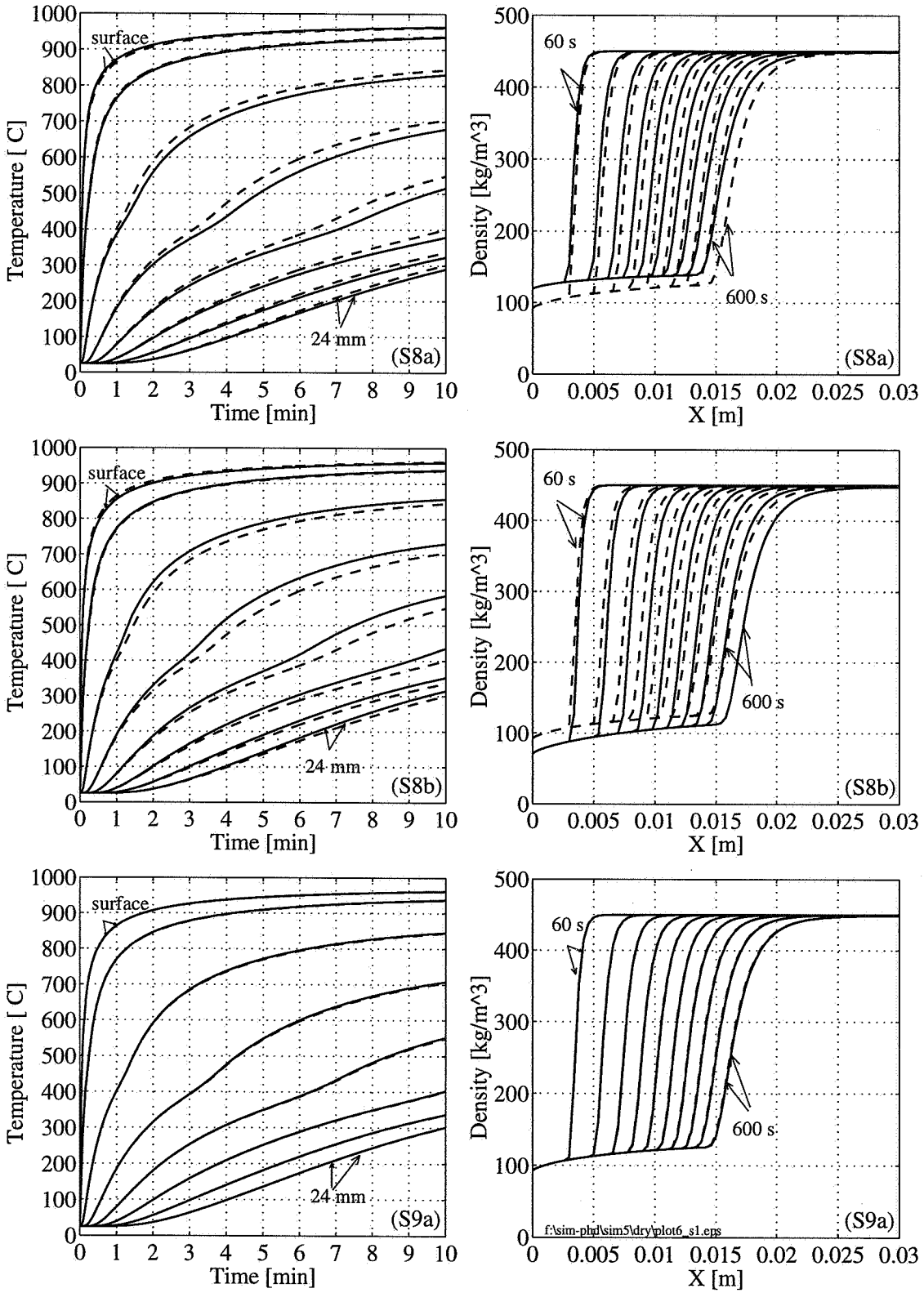

Figure 4.69 *UL:* Temperature vs time (*S8a*) *UR:* Density vs depth (*S8a*)
ML: Temperature vs time (*S8b*) *MR:* Density vs depth (*S8b*)
BL: Temperature vs time (*S9a*) *BR:* Density vs depth (*S9a*)

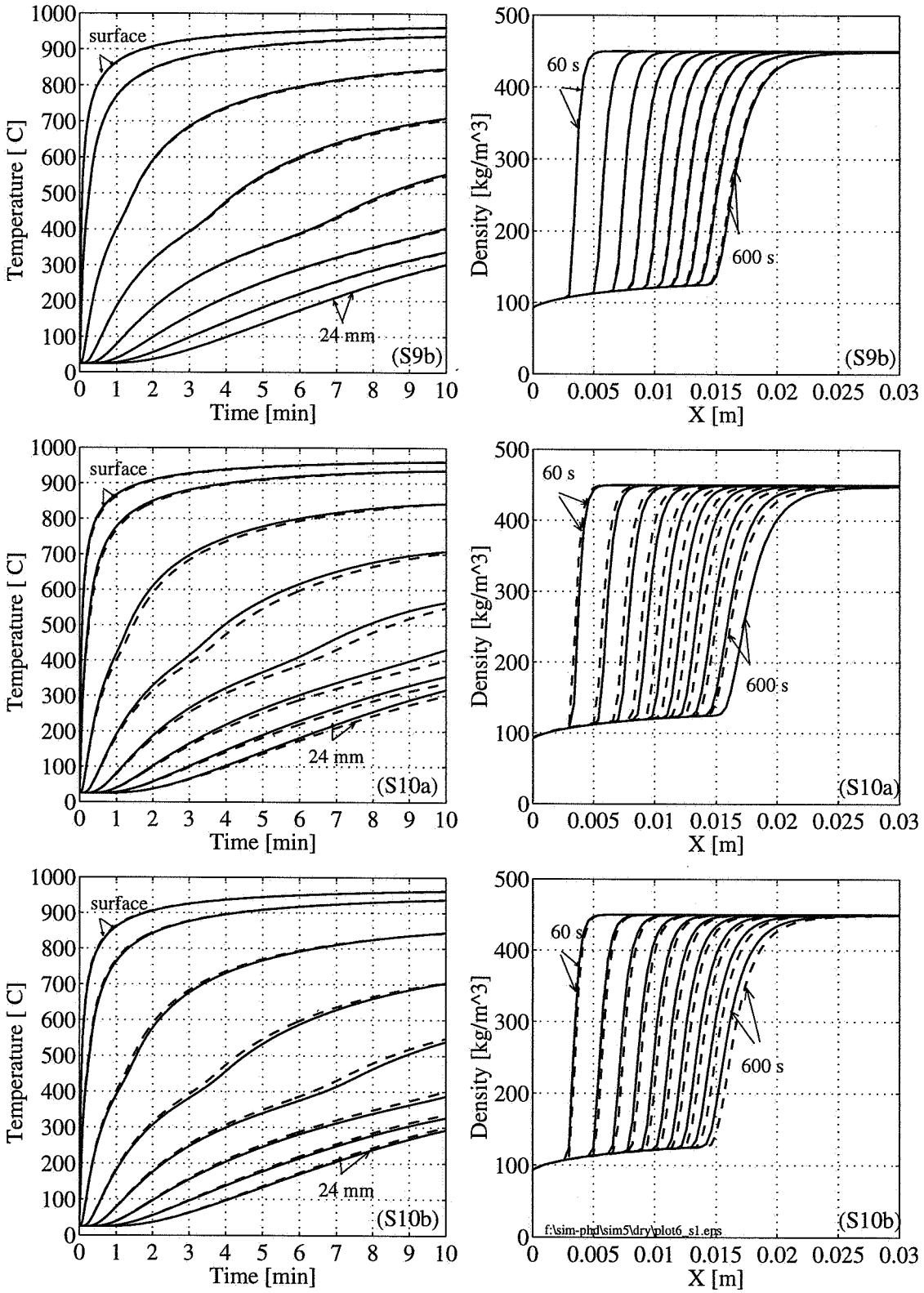

Figure 4.70 *UL:* Temperature vs time (*S9b*) *UR:* Density vs depth (*S9b*)
ML: Temperature vs time (*S10a*) *MR:* Density vs depth (*S10a*)
BL: Temperature vs time (*S10b*) *BR:* Density vs depth (*S10b*)

4.5.4 APPLICATION OF THE MODEL

After revising the model, and making satisfactory comparison of the model predictions to experiments, important pyrolysis conditions that have not been studied in the experiments will be simulated. Interesting predictions to make involve assessing the effects of particle size (thin versus thick particles) and heating conditions (longitudinal versus radial heating, low versus high heat fluxes) on the total time of conversion and ultimate product yields distribution. These effects are important to examine, since the understanding will aid in process design.

Dry pellets of spruce with particle size ranging from 1 mm to 100 mm are heated on both surfaces with hot (300°C) helium carrier gas as well as an radiative heat flux (ranging from 50 to 200 kW/m^2) from a hot reactor wall. Longitudinal and radial heating are simulated by using the effective thermal conductivity and permeability models in the reference run and run *(S2e)* of the previous section, respectively.

The time required for complete (100%) reaction strongly depends on particle size and applied heating conditions. Figure 4.71 shows the calculated time (note that the time axis is logarithmic) for the stipulated 100% reaction as a function of particle size at eight heating conditions, i.e., both longitudinal (solid lines) and radial (dashed lines) heating with applied heat fluxes of 50, 100, 150 and 200 kW/m^2. The time required to completely convert a 100 mm particle with an applied heat flux of 50 kW/m^2 is about 1 hour and 20 minutes when the heating is along with the grains and 2 hours and 15 minutes when the heating is perpendicular to the grain. The reaction time ratios (100% conversion) between the radially and longitudinally heated samples, ($\tau_{\perp}/\tau_{\parallel}$), are approximately 1.1, 1.3, 1.5, 1.6, 1.7 and 1.8 for the 1, 5, 10, 25, 50 and 100 mm particles, respectively. These ratios, ($\tau_{\perp}/\tau_{\parallel}$), are insensitive to the heat flux applied. An increase in heat flux from 50 to 200 kW/m^2 reduces the total time of conversion in both the longitudinal and radial heating case by a factor of 3.5 for the 1 mm particles, by a factor of 2.5 for the 5 and 10 mm particles and by a factor of 2 for the 25, 50 and 100 mm particles.

Figures 4.72 and 4.73 show the effect of heat flux and particle size on relative product yields for both longitudinal (solid lines) and radial (dashed lines) heating after 100% conversion. It can be seen that for the 1 mm particles, the product distribution is insensitive to grain orientation while the char yield slightly decreases and the tar and gas yields slightly increase as the heat flux applied is increased from 50 to 200 kW/m^2. When the particle size is increased, the product distribution becomes more sensitive to both grain orientation and heat flux. The following observations (and explanations) can be made:

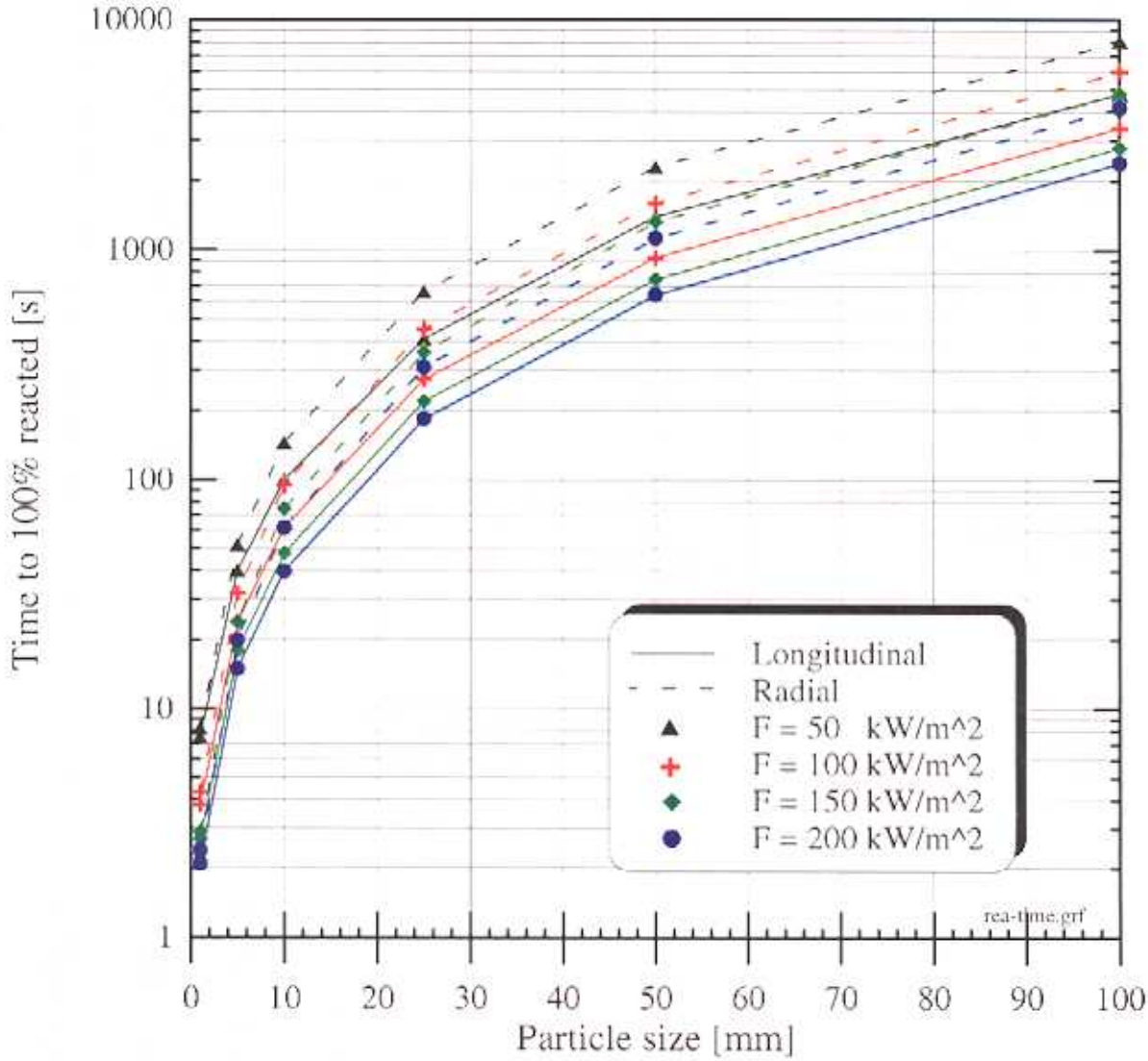

Figure 4.71 The calculated time for 100% reaction as a function of particle size and applied heat flux.

- For both longitudinal and radial heating, the char and gas yield increase with particle size while the tar yield decreases. The increase in ultimate char yield may be explained by the temperature-history dependency of the local char density, predicted by the competitive reaction model. For example, the char density in the centre of the 100 mm particle heated longitudinally with a heat flux of 50 kW/m^2 is about 150 kg/m^3 compared to 110 kg/m^3 at the surface. For comparison, the char density in the centre of the 1 mm particle (for the same heating conditions) is about 90 kg/m^3 and equal to the density at the surface. The char layer thickness will be larger as a consequence of longer particles. Hence, the distance which the volatiles must travel before they escape from the surface will be larger, i.e., the residence time in the hot char layer increases, promoting secondary reactions of the tar.

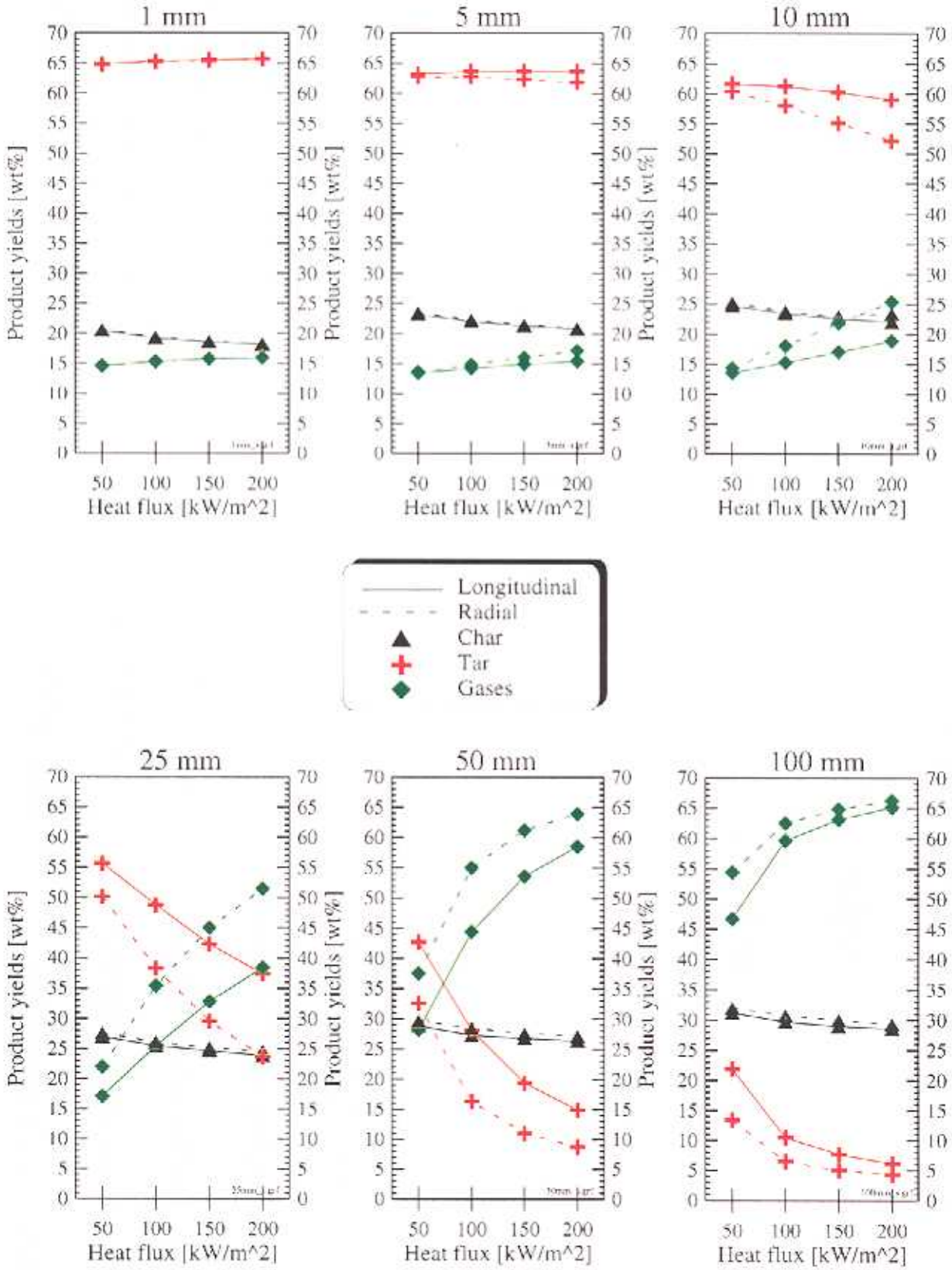

Figure 4.72 The effect of heat flux and particle size on relative product yields when 100% of the solid is reacted. Longitudinal and radial heating.

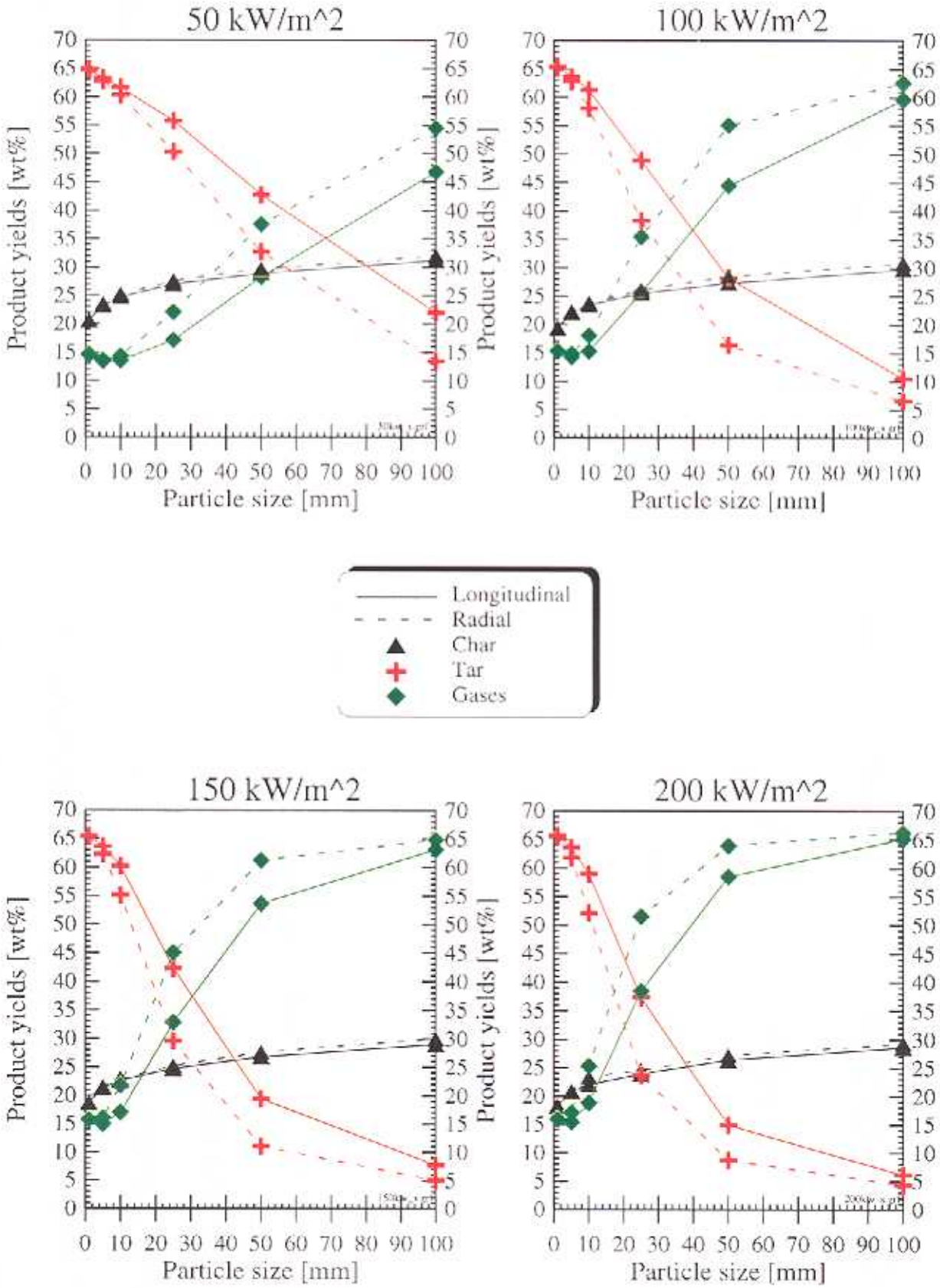

Figure 4.73 The effect of particle size and heat flux on relative product yields when 100% of the solid is reacted. Longitudinal and radial heating.

- Higher heat fluxes for the same particle size and grain orientation means higher surface and in-depth temperatures, faster heating and shorter reaction time. For example, the particle surface attains a temperature of 720°C when a 50 kW/m^2 heat flux is applied, while 1140°C is reached when the heat flux is increased to 200 kW/m^2. Obviously, higher surface and in-depth temperatures promote secondary reactions of the tar, thus, increasing the ultimate yield of gases. As previously discussed, the ultimate char-yield is dependent on the temperature-history of the particle. A more rapid heating, as a consequence of higher heat fluxes means that the ultimate yield of char will decrease.

- Since the particles heated longitudinally have an effective thermal conductivity which is about twice that of the radially heated particles, heat is transferred at a much faster rate and the time for complete conversion is much lower. Although, the radially heated particles finally reaches the temperature of those heated longitudinally, the temperature rise in the interior is much slower. Hence, the ultimate char yield becomes slightly higher and the longer intraparticle volatiles residence time increase the gas yield on the expense of tar.

These predictions show that particle size in combination with applied heat flux can significantly affect the final product distribution. The results suggest that in a thermal conversion process:

- Tar yield is maximized for thin particles and high heat fluxes because more rapid heating and shorter volatiles residence time in small particles will enhance tar yield and avoid tar cracking.

- Gas yield is maximized for large particles under high heating rate to enhance the tar cracking reactions.

- Char yield is maximized for large particles and low heat fluxes.

However, the experiments have demonstrated that wood often behaves in a very un-predictable way during the thermal degradation process, which cannot be simulated by an idealized one-dimensional mathematical model. Shrinkage and fissuration of the both the longitudinally and radially heated pellets reduces the volatiles residence time in the hot char layer and the possibilities for the tars to crack. During shrinkage, the char layer thickness is reduced and the heat transfer rate through the char layer will increases. Hence, the time required for complete reaction of the radial samples will in reality be approximately the same as for those heated longitudinally, and not nearly two times more as predicted by the model for the 100 mm particles.

The intention was also to study the impact of different moisture contents (10, 20 and 30 %) on the total time of conversion and ultimate product yields distribution. However, in many of these simulations, the model had convergence problems in the transition from "nearly" to completely dry, i.e., in the stage of the process where only a few water vapour molecules were left in the particle. The most likely reason for these problems is the very high heat fluxes (and temperatures) in combination with the diffusion model applied for the gas mixture phase. From the low heating (50 kW/m^2) simulations which did succeed, the following observations could be made: For particle sizes less than 5 mm, the drying and pyrolysis processes were consecutive, i.e., the particles were completely dried before the thermal degradation started. For particle sizes greater than 5 mm, the drying and pyrolysis occurred simultaneously.

4.6 CONCLUDING REMARKS

A theoretical and experimental study of the pyrolysis of large particles of wood have been presented. A single particle reactor was constructed and used to pyrolyse pellets of a realistic size and a mathematical model was developed to simulate intraparticle physical and chemical processes during the simultaneous drying and pyrolysis of wood.

In the experimental part, cylinders with a diameter of approximately 20 mm and a length of 30 mm prepared from birch, spruce and pine were one-dimensionally heated in bell-shaped glass reactor using a Xenon arc lamp as a heat source. Two heat fluxes: 80 kW/m^2 and 130 kW/m^2 were used and the effect of grain orientation relative to the heat flux (longitudinal and radial direction) was investigated. The following parameters were measured: surface and seven intraparticle temperatures, shrinkage, percentage reacted, gas concentrations (CO, CO_2 and HC) as a function of time, and the ultimate product yields distribution, i.e., char, condensable gases (tar+water) and non-condensable gases.

In the theoretical part, a transient, one-dimensional model which can simulate drying and pyrolysis of moist wood has been derived. The pyrolysis of moist wood involves the interaction in a porous media of heat, mass and momentum transfer with chemical reactions describing the thermal degradation. Heat is transported by convection, conduction and radiation. Water vapour from drying and volatiles (tars + gases) from pyrolysis are transported by diffusion and convection. Liquid water is transported due to a gradient in the liquid pressure while bound water movement is modeled as a diffusion process. The drying model is based on equilibrium between water vapour and bound/liquid water. Darcy's law has been used to calculate the pressure and velocity distributions within the wood. Several reaction models proposed in the literature for the pyrolysis of cellulose and wood, including a one-step

global model and models with competitive and consecutive reactions have been included in the simulation program. In addition, data and expressions for the thermo-physical properties have been extensively reviewed. The governing set of differential and algebraic equations have been solved by using an appropriate numerical code.

The following main conclusions can be drawn:

- Due to its heterogeneous and anisotropic structure, wood behaves in a very complicated and un-predictable way during the thermal degradation. The effects of a variation in thermal conductivity, say due to density (birch versus pine/spruce) or grain orientation (radial versus longitudinal), on the product distribution and ultimate reacted fraction are not obvious in this study. For example, heating the radial samples (lower thermal conductivity) would be expected to exhibit a slower pyrolysis rate and therefore a smaller amount of reacted substrate for the same time. Except for pine, the trends indicate the opposite results. This can be explained by the relatively higher axial shrinkage in the char layer of the radial samples. Shrinkage will increase the heat transfer rate through the insulating char layer since its thickness is being reduced.

- By comparing the two grain orientations for the same species and heat flux, it is evident that the condensable product fractions are lower for the longitudinally than the radially heated samples. From a theoretical point of view, heating the radial samples with lower permeability, i.e. higher mass transfer resistance to volatile outflow, would be expected to promote secondary reactions thus increasing the gas yield at the expense of tar. However, this counter intuitive result can again be explained by the relative higher axial and diametrical shrinkage in the char layer of the radial samples which makes it easier for the volatiles to escape.

- Heat flux arriving at the particle surface has a large effect on the reaction rates, product yields distribution as well as the intraparticle temperature distribution. In general, as the heat flux is increased, the yields of char and condensable gases (tar/water) decrease while the yield of non-condensable gases increases. Higher heat fluxes means higher surface and intraparticle temperatures. Heat is transferred at a much faster rate and more of the substance is reacting. For example, the final temperature close to the surface increases by approximately 150°C (800-950°C) when the heat flux is increased by 50 kW/m^2. Higher temperatures promote secondary cracking reactions of the tar thus increase the ultimate yield of non-condensable gases at the expense of tar.

- The simulation predictions revealed the importance of accurate heat transfer modeling. The thermal conductivity of wood is a function of density, temperature, moisture content and grain orientation. Variable thermal conductivity including radiative heat transfer is needed to predict the intraparticle temperature history throughout the pyrolysis process. For example, the temperature plateau evident around 380°C in the experiments is successfully predicted by the model and can be explained by a reduction in the local thermal conductivity. When the wood changes from its origin state to a more porous char, the local thermal conductivity decreases in a short period of time until the temperature reaches the level where the radiative contribution to the effective thermal conductivity becomes significant.

- Although, simulations of spruce pyrolysis with a one-step global model and a model of three independent parallel reactions give satisfactory predictions of the pyrolysis process under these particular set of experimental conditions, these models are not applicable for simulating the pyrolysis process under other conditions. This because they assume a constant ratio of the char to volatiles yield. The experiments evidence that there exist a competition between char, tar and gas formation which is dependent on the wood pellet's temperature history. Using three parallel competitive reactions to account for primary production of gas, tar and char, and a consecutive reaction for the secondary cracking of tar, the predicted ultimate product yields distribution and reacted fraction agree well with the experimental results.

- Prediction of drying behaviour has been demonstrated and drying is mainly controlled by water vapour flow and capillary water flow due to a pressure gradient. Bound water diffusion and diffusion in the gas mixture phase is not so important and plays a negligible role under the high heating conditions studied. Inclusion of water vapour flow due to a pressure gradient is indispensable in successfully predicting the 100°C temperature plateau and the evaporation rate during pyrolysis of moist wood. In the simulation of dry wood pyrolysis, however, the inclusion of Darcy's momentum equation is less important and steady-state approximation, i.e., instantaneous outflow of volatiles, can for simplicity be assumed.

- The combined effects of changing particle size and heating conditions simultaneously were studied in terms of the mathematical model over a large range. It was found that particle size in combination with applied heat flux could significantly alter the final product distribution. For example, the tar yield could be maximized by avoiding tar cracking, i.e., by using small particles.

CHAPTER 5

CONCLUSIONS AND RECOMMENDATIONS FOR FURTHER WORK

5.1 INTRODUCTION

A comprehensive theoretical and experimental study of the pyrolysis of biomass under regimes controlled by both chemical kinetics (Chapter 3), and heat and mass transfer (Chapter 4), have been presented. Since concluding remarks have been given separately in both these sections, the main purpose of the following discussion will be to sum up the achievements and to give some ideas and recommendations for further work. In other words, what have we learned from this study and which questions remain unanswered and invite further research.

5.2 SMALL PARTICLES

We have learned that:

- Thermogravimetry is a useful tool to distinguish different wood species from each other. That is, each species has its own thermal fingerprint which is dependent on the woods' chemical composition. For example, birch being a hardwood abound in hemicellulose (~ 39%) has a very distinct shoulder on the ascending part of the DTG curve as compared with pine and spruce (softwoods) where this shoulder is hardly visible. This may be explained by their comparatively lower hemicellulose (~ 27%) content. However, it is important to notice that the wood species investigated in this study have very low ash contents. Since inorganic impurities have strong catalytic effects and may alter the pyrolysis pathways, mild pretreatment of the wood such as washing with hot water is required to get a qualitative impression of its chemical composition.

- The TG and DTG curves associated with the pyrolysis of four different cellulose samples can be well described by a single step, first-order reaction model with activation

energies between 210 and 280 kJ/mol. The scattering in activation energy may be explained by different peak temperatures and width of the TG&DTG curves owing to impurities, differences in crystallinity and degree of polymerization.

- The TG and DTG curves associated with the pyrolysis of cellulose containing 15% hemicellulose and four different wood species can by using a model of independent parallel reactions be resolved into peaks associated with the pyrolysis of the sample's cellulose and hemicellulose components. In this way, it is possible to study the in situ decomposition of cellulose and hemicellulose in wood without breaking any chemical bonds which will occur during any extraction procedure. Such an evaluation gave an activation energy of 260±16 kJ/mol for the cellulose decomposition and a less reliable 119±23 kJ/mol for the hemicellulose decomposition in wood. Unfortunately, there is not possible to determine the kinetics of the lignin decomposition in wood since the mass loss of the lignin is concealed by the more protuberant DTG peaks associated with the cellulose and hemicellulose decomposition at lower temperatures. At higher temperature the slow charring of the residue of the cellulose and hemicellulose hinder the observation of the lignin decomposition. Likewise, it is not possible to quantitatively determine the actual concentrations of the hemicellulose and cellulose in wood since we do not know their individual contribution to the final char fraction.

Further work:

- In the present work it has been emphasized to understand the pyrolysis behaviour of three Scandinavian wood species. In further work, other wood species and biomass plants, such as herbaceous crops, food crops, high sugar/starch crops, short rotation energy crops etc. should be investigated in a similar way to learn more about the cellulose and hemicellulose pyrolysis in other biomass plants.

- Another interesting subject would be to see if one sample taken, for example, from the heartwood of a twenty year old tree behaves in a similar way as one sample taken from the sapwood, from the top or bottom of the stem or from the branches.

- Although, recent work (this work included) have shown that under conditions which minimize vapour-solid interactions and heat transfer intrusions, the weight loss curve of pure cellulose samples can be well fit by a single step, first order reaction with a high activation energy (> 200 kJ/mol), it is still the subject of controversy. One way to establish some sort of agreement in the community would be to make a TGA-round robin test.

- The kinetic model outlined in this study can probably be used to determine rate constants for other substances than biomass plants. For example, other polymers such as plastic (PVC, LDPE, HDPE, etc.) and other constituents found in municipal solid waste (MSW).

5.3 LARGE PARTICLES

We have learned that:

- For the pyrolysis of large biomass particles, the intraparticle temperatures determine the characteristics of pyrolysis reactions. Any parameter that affects the internal temperature distribution (heat flux, grain orientation) and intraparticle volatile residence time (shrinkage, fissuration) will also influence the product yields distribution.

- As indicated by the experimental results, the heat flux arriving the pellet surface has big influence on the reaction rates, product yields distribution as well as the intraparticle temperature distribution. As the heat flux is increased, the yields of char and condensable gases (tar/water) decrease while the yield of non-condensable gases increases. Higher heat fluxes means higher surface and intraparticle temperatures. Heat is transferred at a much faster rate and more of the substance is reacting. Higher temperatures promote secondary cracking reactions of the tar thus increase the ultimate yield of non-condensable gases at the expense of tar.

- It is impossible to conclude whether it is the chemical composition (cellulose, hemicellulose and lignin content) or the physical structure (density, permeability, thermal conductivity) of wood which dictates the product distribution, since shrinkage and deformation of the wood pellets make such an evaluation difficult. However, it seems that birch with the highest hemicellulose and lowest lignin content yields a lower char fraction than pine and spruce, similar to that observed in the TGA experiments. This suggest that lignin is responsible for much of the char formed during the pyrolysis of wood.

- The combined effects of changing particle size and heating conditions simultaneously were studied in terms of the mathematical model over a large range. It was found that particle size in combination with applied heat flux could significantly alter the final product distribution. The results suggested that in a thermal conversion process, tar yield is maximized for thin particles and high heat fluxes because more rapid heating and shorter volatiles residence time in small particles will enhance tar yield and avoid tar cracking. Gas yield is

maximized for large particles under high heating rate to enhance the tar cracking reactions. Char yield is maximized for large particles and low heat fluxes.

▸ The mathematical model that has been developed during this study to simulate drying and pyrolysis of wood is to the author's knowledge one of the most comprehensive models presented ever. From a mathematical point of view, it is quite satisfactory to include as many parameters as possible in a model and see that it works (!). However, the experiments have shown that wood during pyrolysis behaves in a very complicated and un-predictable way. In light of this, how complicated model is needed, from an engineering point of view, to satisfactorily simulate the pyrolysis of large biomass particles (?).

1) Variable thermal conductivity including the radiative heat transfer is needed to successfully predict the intraparticle temperature throughout the pyrolysis process.

2) A competitive reaction model including a secondary tar cracking reaction step is needed to be able to predict the effects of a variation in heat flux on the product yields distribution.

3) The sensitivity analysis revealed that mass transfer was not important in modeling of secondary tar cracking, and instantaneous outflow of volatiles can for simplicity be assumed. However, since the drying process is mainly controlled by water vapour flow and capillary water flow due to pressure gradients, modeling the mass transfer is indispensable in simulating the drying process.

Further work:

▸ Despite of the simplifications suggested above, it is still possible to make improvements to the mathematical model.

1) Since shrinkage occurs both during drying and pyrolysis, it should be included in the model.

2) The drying model needs to be verified, either separate in low temperature drying experiments or in pyrolysis experiments of moist wood pellets. However, the pyrolysis reactor cannot be used in such experiments without some modifications, since shrinkage in both the axial and radial directions will be problematic to handle (de-focused light, etc. see discussion in Section 4.4.4).

3) Some of the thermo-physical properties included in the model have been taken from the drying literature (diffusion coefficients, relative permeability, capillary pressure, etc.). It is not unlikely that some of these are responsible for the convergence problems that appeared in the transition from "nearly" to completely dry particles. Hence, a sensitivity analysis should be carried out.

4) Other mechanisms which can be included in the model are char combustion/gasification reactions and the external gas-phase reactions which occur during the combustion of volatiles. From a mathematical point of view, it could have been interesting to extend the model to two dimensions to account for the anisotropic structure of wood (permeability, diffusion coefficients, thermal conductivity, etc.). However, it is important to realize that although a two dimensional model for drying and pyrolysis may be more realistic in the combustion of solid fuels, the current one dimensional model can be used to approximate most of the pyrolysis situations. For example, wood logs or pellets used in fireplaces or wood boilers are normally long in the direction parallel to the grain and very short perpendicular to it. Hence, this type of combustion can be described by a one-dimensional model with heat flux perpendicular to the grain

REFERENCES

Agrawal, R.K. and R.J. McCluskey: "The Low Pressure Pyrolysis of Newsprint". *Journal of Applied Polymer Science, vol. 27, pp. 367-382, 1983.*

Agrawal, R.K., F. Gandhi and R.J. McCluskey: "Low-Pressure Pyrolysis of Newsprint Product Formation". *Journal of Analytical and Applied Pyrolysis, vol. 6, pp. 325-338, 1984a.*

Agrawal, R.K.: "Kinetics of Biomass and Coal Pyrolysis". *Ph.D-Thesis, Clarkson University, 1984b.*

Agrawal, R.K.: "Kinetic Analysis of Complex Reactions". *Journal of Thermal Analysis, vol. 31, pp. 1253-1262, 1986.*

Agrawal, R.K.: "Kinetics of Reactions Involved in Pyrolysis of Cellulose. 1. The Three Reaction Model". *The Canadian Journal of Chemical Engineering, vol. 66, pp. 403-411, 1988a.*

Agrawal, R.K.: "Kinetics of Reactions Involved in Pyrolysis of Cellulose. 2. The Modified Kilzer-Broido Model". *The Canadian Journal of Chemical Engineering, vol. 66, pp. 413-418, 1988b.*

Akita, K. and M. Kase: "Determination of Kinetic Parameters for Pyrolysis of Cellulose and Cellulose Treated with Ammonium Phosphate by Differential Thermal Analysis and Thermal Gravimetric Analysis". *Journal of Polymer Science: Part A-1, vol. 5, pp. 833-848, 1967.*

Alves, S.S. and J.L. Figueiredo: "Pyrolysis Kinetics of Lignocellulosic Materials by Multistage Isothermal Thermogravimetry". *Journal of Analytical and Applied Pyrolysis, vol. 13, pp. 123-134, 1988.*

Alves, S.S. and J.L. Figueiredo: "Interpreting Isothermal Thermogravimetric Data of Complex Reactions: Application to Cellulose Pyrolysis at Low Temperatures". *Journal of Analytical and Applied Pyrolysis, vol. 15, pp. 347-355, 1989a.*

Alves, S.S. and J.L. Figueiredo: "Kinetics of Cellulose Pyrolysis Modelled by Three Consecutive First Order Reactions". *Journal of Analytical and Applied Pyrolysis, vol. 17, pp. 37-46, 1989b.*

Alves, S.S., and J.L. Figueiredo: "A Model for Pyrolysis of Wet Wood". *Chemical Engineering Science. 44 : 2861-2869, 1989c.*

Antal, M.J., H.L. Friedman and F.E. Rogers: "Kinetics of Cellulose Pyrolysis in Nitrogen and Steam". *Combustion Science and Technology, vol. 21, pp. 141-152, 1980.*

Antal, M.J.: "Biomass Pyrolysis: A Review of the Literature Part I- Carbohydrate Pyrolysis". *In K.W. Boer and J.A. Duffie (eds): Advances in Solar Energy - American Solar Energy Society, pp. 61-110, 1983.*

Antal, M.J.: "Biomass Pyrolysis: A Review of the Literature Part II- Lignocellulose Pyrolysis". *In K.W. Boer and J.A. Duffie (eds): Advances in Solar Energy - American Solar Energy Society, pp. 175-255, 1985.*

Antal, M.J., W.S.-L. Mok, G. Varhegyi and T. Szekely: "Review of Methods for Improving the Yield of Charcoal from Biomass". *Energy & Fuels, vol. 4, pp. 221-225, 1990.*

Antal, M.J. and G. Varhegyi: "Cellulose Pyrolysis Kinetics: The Current State of Knowledge" *Ind. Eng. Chem. Res. vol. 34, pp. 703-717, 1995.*

Antal, M. J.: "Personal Communication". *Hawaii Natural Energy Institute, R^3L. University of Hawaii at Manoa, Honolulu, Hawaii, 1995.*

Anthony, D.B., J.B. Howard, H.C. Hottel and H.P.Meisner: "Rapid Devolatilization of Pulverized Coal". *Fifteenth Intern. Sump. on Combustion, pp. 1303-1317, 1974.*

Arseneau, D.F.: "The Differential Thermal Analysis of Wood". *Canadian Journal of Chemistry, vol. 39, pp. 1915-1919, 1961.*

Arseneau, D.F., "Competitive Reactions in the Thermal Decomposition of Cellulose". *Canadian Journal of Chemistry, vol. 49, pp. 633-638, 1971.*

Atreya, A.: "Pyrolysis, Ignition and Fire Spread on Horizontal Surfaces of Wood". *Ph.D - Thesis, Harvard University, 1983.*

Austegaard, A.: "Experimental and Numerical Study of a Jetfire Stop Material and a New Helical Flow Heat Exchanger" (provisional title). *Ph.D -Thesis, Norwegian University of Science and Technology, finished 1997.*

Avni, E., R.W. Coughlin, P.R. Solomon and H.H. King: "Mathematical Modelling of Lignin Pyrolysis". *Fuel, vol. 64, pp. 1495-1501, 1985.*

Bamford, C.H., J. Crank and D.H. Malan: "The Combustion of Wood. Part 1". *Proceedings of the Cambridge Philosophical Society, vol. 42, pp. 166-182, 1946.*

Beall, F.C. and H.W. Eickner: "Thermal Degradation of Wood Components: A Review of the Literature". *FPL Research Paper no.130, USDA Forest Products Laboratory, 1970.*

Beaumont, O. and Y. Schwob: "Influence of Physical and Chemical Parameters on Wood Pyrolysis". *Ind. Eng. Chem. Des. Dev, vol. 23, pp. 637-641, 1984.*

Ben Nasrallah, S. and P. Perre: "Detailed Study of a Model of Heat and Mass Transfer During Convective Drying of Porous Media". *International Journal of Heat and Mass Transfer, vol. 31, pp. 957-967, 1988.*

Birkebak, R.C. and E. Ozil: "Theoretical Consideration of Radiative Conductivities in Fibrous Insualation". *In J.P. Hartnett, T.F. Irvine, E. Pfender, and E.M. Sparrow (eds): Studies in Heat Transfer, A Festschrift for E.R.G. Eckert. McGraw-Hill Book Company, pp. 409-418, 1979.*

Blackshear, P.L. and M.A. Kanury: "Heat and Mass Transfer To, From and Within Cellulosic Solids Burning in Air". *Tenth Intern. Sump. on Combustion, pp. 911-923, 1965.*

Blackshear, P.L. and M.A. Kanury: "On the Combustion of Wood I: A Scale Effect in the Pyrolysis of Solids". *Combustion Science and Technology, vol. 2, pp. 1-4, 1970a.*

Blackshear, P.L. and M.A. Kanury: "On the Combustion of Wood II: The Influence of Internal Convection on the Transient Pyrolysis of Cellulose". *Combustion Science and Technology, vol. 2, pp. 5-9, 1970b.*

Bradbury, A.G.W., Y. Sakai and F. Shafizadeh: "A Kinetic Model for Pyrolysis of Cellulose". *Journal of Applied Polymer Science, vol. 23, pp. 3271-3280, 1979.*

Bridgwater, A. V. "An Overview of Thermochemical Biomass Conversion Technologies". *In G. E. Richards (ed): Proceedings of Wood, Fuel for Thought Conference held in Bristol, England 23-25 October, 1991.*

Broido, A.: "Effect of Fire-extinguishing Agents on Combustion of Sucrose". *Science, vol. 133, pp. 1701-1702, 1961.*

Broido, A. and S.B. Martin: "Effect of Potassium Bicarbonate on the Ignition of Cellulose by Radiation". *Fire Research Abstracts and Review, vol. 3, pp. 193-201, 1961.*

Broido, A. and F.J. Kilzer: "A Critique of the Present State of Knowledge of the Mechanism of Cellulose Pyrolysis". *Fire Research Abstracts and Review, vol. 5, pp. 157-161, 1963.*

Broido, A. and M.A. Nelson: "Ash Content: Its Effect on Combustion of Corn Plants". *Science, vol. 146, pp. 652-653, 1964.*

Broido, A.: "Thermogravimetric and Differential Thermal Analysis of Potassium Bicarbonate Contaminated Cellulose". *Pyrodynamics, vol. 4, pp. 243-251, 1966.*

Broido, A.: "A Simple, Sensitive Graphical Method of Treating Thermogravimetric Analysis Data". *Journal of Polymer Science, vol. 7, pp. 1761-1773, 1969.*

Broido, A. and M. Weinstein: "Thermogravimetric Analysis of Ammonia-Swelled Cellulose". *Combustion Science and Technology, vol. 1, pp. 279-285, 1970.*

Broido, A. and M. Weinstein: "Low Temperature Isothermal Pyrolysis of Cellulose".*Thermal Analysis, vol. 3, pp. 285-296, 1971.*

Broido, A. and F.A. Williams: "Use of Asymptotic Analysis of the Large Activation-energy Limited to Compare Graphical Methods of Treating Thermogravimetry Data". *Thermochimica Acta, vol. 6, pp. 245-253, 1973.*

Broido, A., A.C. Javier-Son and E.M. Barrall: "Molecular Weight Decrease in the Early Pyrolysis of Crystalline and Amorphous Cellulose". *Journal of Applied Polymer Science, vol. 17, pp. 3627-2635, 1973.*

Broido, A. and M.A. Nelson: "Char Yield on Pyrolysis of Cellulose". *Combustion and Flame, vol. 24, pp. 263-268, 1975.*

Broido, A: "Kinetics of Solid-Phase Cellulose Pyrolysis". *In F. Shafizadeh, K.V. Sarkanen, and D.A. Tillman (eds): Thermal Uses and Properties of Carbohydrates and Lignins, 172nd National Meeting of the American Chemical Society, Academic Press, pp. 19-36, 1976.*

Broido, A.: "Chemistry of Pyrolysis and Combustion of Cellulose". *In Proceedings from Nordic Workshop on Combustion of Biomass, Norway, 1991.*

Brown, L. E.: "An Experimental and Analytical Study of Wood Pyrolysis". *Ph.D.-Thesis. The University of Oklahoma, 1972.*

Butterfield, B. G. and B. A. Meylan: "Three-dimensional structure of Wood, An Ultrastructure Approach". *Chapman and Hall, 1980.*

Carrasco, F.: "The Evaluation of Kinetic Parameters From Thermogravimetric Data: Comparison Between Established Methods and the General Analytical Equation". *Thermochimica Acta, vol. 213, pp. 115-134, 1993.*

Chan, R.W.-C.: "Analysis of Chemical and Physical Processes During the Pyrolysis of Large Biomass Pellets". *Ph.D. - Thesis. University of Washington, 1983.*

Chan, W.-C.R., M. Kelbon and B. Krieger-Brockett: "Modelling and Experimental Verification of Physical and Chemical Processes During Pyrolysis of A Large Biomass Particle". *Fuel, vol. 64, pp. 1505-1513, 1985.*

Choong, E.T.: "Movement of Moisture Through a Softwood in the Hygroscopic Range". *Forest Products Journal, pp. 489-498, 1963.*

Choong, E.T. and F.O. Tesoro: "Relationship of Capillary Pressure and Water Saturation in Wood". *Wood Science, vol. 23, pp. 139-150, 1989.*

Chornet, E. and C. Roy: "Compensation Effect in the Thermal Decomposition of Cellulosic Materials". *Thermochimica Acta, vol. 35, pp. 389-393, 1980.*

Comstock, G.L.: "Directional Permeability of Softwoods". *Wood and Fiber., vol. 1, pp. 283-289, 1970.*

Cooly, S. and M.J. Antal: "Kinetics of Cellulose Pyrolysis in the Presence of Nitric Oxide". *Journal of Analytical and Applied Pyrolysis, vol. 14, pp. 149-161, 1988.*

Cordero, T., F. Carcia and J.J. Rodriguez: "A Kinetic Study of Holm Oak Wood Pyrolysis from Dynamic and Isothermal TG Experiment". *Thermochimica Acta, vol. 149, pp. 225-237, 1989.*

CRC Handbook of Chemistry and Physics, 1986-1987.

Curtis, L.J. and D.J. Miller: "Transport Model with Radiative Heat Transfer for Rapid Cellulose Pyrolysis". *Ind. Eng. Chem. Res., vol. 27, pp. 1775-1783, 1988.*

DeGroot, W. F. and F. Shafizadeh: "The Influence of Exchangeable Cations on the Carbonization of Biomass". *Journal of Analytical and Applied Pyrolysis., vol. 6, pp. 217-232, 1984.*

Di Blasi, C. and G. Russo: "Modeling of Transport Phenomena and Kinetics of Biomass Pyrolysis". *In A.V. Bridgwater (ed): Advances in Thermochemical Biomass Conversion. London: Blackie Academic & Professional, pp. 906-921, 1994.*

Di Blasi, C.: "Analysis of Convection and Secondary Reaction Effects Within Porous Solid Fuels Undergoing Pyrolysis". *Combustion Science and Technology, vol. 90, pp. 315-340, 1993a.*

Di Blasi, C.: "Modeling and Simulation of Combustion Processes of Charring and Non-Charring Solid Fuels". *Progress in Energy Combustion Science, vol. 19, pp. 71-104, 1993b.*

Diebold, J. P. and J. W. Scahill: "Entrained-Flow Fast Ablative Pyrolysis of Biomass". *Ann. Rep. SERI/PR-234-2144, 1984*

Elder, J. P.: "Proximate Analysis by Automated Thermogravimetry". *Fuel, vol. 62, 1983.*

Esping, B. "Trätorkning". *Trätek, 1992. (in Swedish)*

Faix, O., E. Jakab, F. Till and T. Szekely: "Study on Low Mass Thermal Degradation Products of Milled Wood Lignins by Thermogravimetric-Mass Spectrometry". *Wood Science and Technology, vol. 22, pp 323-334, 1988.*

Fairbridge, C., R.A. Ross and S.P. Sood: "A Kinetic and Surface Study of the Thermal Decomposition of Cellulose Powder in Inert and Oxidizing Atmospheres". *Journal of Applied Polymer Science, vol. 22, pp. 497-510, 1978.*

Figueiredo, J.L., C. Valenzuela, A. Bernalte and J.M. Encinar: "Pyrolysis of Holm-Oak Wood: Influence of Temperature and Particle Size". *Fuel, vol. 68, pp. 1012-1016, 1989.*

Flynn, J.H.: "The Iso-conversional Method for Determination of Energy of Activation at Constant Heating Rates". *Journal of Thermal Analysis, vol. 27, pp. 95-102, 1983.*

Fredlund, B.: "A Model for the Heat and Mass Transfer in Timber Structures During Fire". *Ph.D. Lund University, 1988.*

Fogler. H. S: "Elements of Chemical Reaction Engineering". *Prentice-Hall International Editions, 1986.*

Forest Products Laboratory: "The Encyclopedia of Wood". *Sterling Publishing Co. Inc, 1980.*

Fuller, E. N., P. D. Schettler and J. C. Giddings: "A new method for prediction of Binary Gas-Phase Diffusion Coefficients". *Industrial Engineering Chemistry, vol. 58, 1986*

Glaister, D.S.: "The Prediction of Chemical Kinetic, Heat and Mass Transfer Processes During the One- and Two-Dimensional Pyrolysis of a Large Wood Pellet". *M.Sc.-Thesis, University of Washington, 1987.*

Grønli, M., L. H. Sørensen and J. Hustad: "Thermogravimetric Analysis of Four Scandinavian Wood Species under Nonisothermal Conditions". *Paper Presented at the Nordic Seminar on Biomass Combustion, Trondheim, 1992*

Grønli, M. G: "Experimental and Modelling Work on the Pyrolysis and Combustion of Biomass - A Review of the Literature". *SINTEF Report STF12 A95013*

Hajaligol, M.R., J.B. Howard, J.P. Longwell and W.A. Peters: "Product Compositions and Kinetics for Rapid Pyrolysis of Cellulose". *Ind. Eng. Chem. Process Des. Dev., vol. 21, pp. 457-465, 1982.*

Hall, D. O., F. Rosillo-Calle, R. H. Williams and J. Woods: "Biomass for Energy: Supply Prospects", *In T. B. Johansson, H. Kelly, A. M. K. Reddy and R. H. Williams (eds): Renewable Energy - Sources for Fuel and Electricity. Earthscan Publictions Ltd, 1993.*

Havens, J.A., H.T. Hashemi, L.E. Brown and J.R. Welker: "A Mathematical Model of The Thermal Decomposition of Wood". *Combustion Science and Technology, vol. 5, pp. 91-98, 1972.*

Hottel, H. C. and A. F. Sarofim: "Radiative Transfer". *McGraw- Hill Book Company, New York, 1967.*

Hustad, J. E. and O. K. Sønju: "Biomass Combustion in IEA Countries". *Biomass and Bioenergy, vol. 2 Nos 1-6, pp. 239-261, 1992.*

Kansa, E.J., H.E. Perlee and R.F. Chaiken: "Mathematical Model of Wood Pyrolysis Including Internal Forced Convection". *Combustion and Flame, vol. 29, pp. 311-324, 1977.*

Kanury, M.A.: "An Evaluation of the Physio-Chemical Factors Influencing the Burning Rate of Cellulosic Fuels and a Comprehensive Model for Solid". *Ph.D.-Thesis. University of Minnesota, 1969.*

Kanury, M.A.: "Thermal Decomposition Kinetics of Wood Pyrolysis". *Combustion and Flame, vol. pp. 75-83, 1972.*

Kanury, M.A.: "Rate of Charring Combustion in a Fire". *Fourteenth Intern. Sump. on Combustion, pp. 1131-1142, 1973.*

Kanury, M.A. and P.L. Blackshear: "An X-Ray Photographic Study of the Reaction Kinetics of Alpha-Cellulose Decomposition". *Pyrodynamics, vol. 4, pp. 285-298, 1966.*

Kanury, M.A. and P.L. Blackshear: "Pyrolysis Effects in the Transfer of Heat and Mass in Thermally Decomposing Organic Solids". *Eleventh Intern. Sump. on Combustion, pp. 517-523, 1967.*

Kays, W. M. and M. E. Crawford: "Convective Heat and Mass Transfer". *McGraw-Hill Publishing Company, (second edition), 1980.*

Kreith, F and W. Z. Black: "Basic Heat Transfer". *Harper & Row Publishers, 1980*

Koch, P.: "Specific Heat of Ovendry Spruce Pine Wood and Bark". *Wood Science, vol. 1, pp. 203-214, 1969.*

Kollmann, F.F.P. and W.A. Cote: "Principles of Wood Science and Technology - I Solid Wood". *Springer-Verlag, 1968.*

Koufopanos, C.A., G. Maschio and A. Lucchesi: "Kinetic Modelling of the Pyrolysis of Biomass and Biomass Components". *The Canadian Journal of Chemical Engineering, vol. 67, pp. 75-84, 1989.*

Kung, H.-C. and A.S. Kalelkar: "On the Heat of Reaction in Wood Pyrolysis". *Combustion and Flame, vol. 20, pp. 91-103, 1973.*

Kung, H.-C.: "A Mathematical Model of Wood Pyrolysis". *Combustion and Flame. vol. 18, pp. 185-195, 1972.*

Lai, W-C.: "Reaction Engineering of Heterogeneous Feeds: Municipal Solid Waste as a Model". *Ph.D.-Thesis, University of Washington, 1991.*

Lee, C.K., R.F. Chaiken and J.M. Singer: "Charring Pyrolysis of Wood in Fires by Laser Simulation". *Sixteenth Intern. Sump. on Combustion, pp. 1459-1470, 1976.*

Lee, V.T.: "Kinetic Analysis and Modeling of Wood Pyrolysis under Nonisothermal Conditions". *Ph.D. - Thesis Texas Tech University, 1982.*

Leu, J.C.: "Modelling of the Pyrolysis and Ignition of Wood". *Ph.D.-Thesis University of Oklahoma, 1975.*

Lewellen, P.C., W.A. Peters and J.B. Howard: "Cellulose Pyrolysis Kinetics and Char Formation Mechanism". *Sixteenth Intern. Sump. on Combustion, pp. 1471-1480, 1977.*

Liden, A. G. Berruti, F. and D. S. Scott: "A Kinetic Model for the Production of Liquids from the Flash Pyrolysis of Biomass " *Chem. Eng. Comm., vol. 65, pp. 207-221, 1988.*

Lipska, A.E. and W.J. Parker: "Kinetics of the Pyrolysis of Cellulose in the Temperature Range 250-300°C". *Journal of Applied Polymer Science, vol. 10, pp. 1439-1453, 1966.*

Lipska, A.E. and F.A. Wodley: "Isothermal Pyrolysis of Cellulose: Kinetics and Gas Chromatographic Mass Spectrometric Analysis of the Degradation Products". *Journal of Applied Polymer Science, vol. 13, pp. 851-865, 1969.*

MacLean, J.D.: "Thermal Conductivity of Wood". *Transaction American Society of Heating and Ventilation Engineers, vol. 47, pp. 323-354, 1941.*

Maku, T.: "Studies on the Heat Conduction in Wood". *Kyote University, Bulletin of the Wood Research Institute, No 13, pp. 1-80, 1957.*

Melaaen, M. C. and M. G. Grønli: "Mathematical Modelling and Numerical Analysis of Drying and Pyrolysis of Porous Media With Emphasis on Wood". *SINTEF Report STF15 F94047, 1994.*

Melaaen, M. C.: "Simulation of Drying and Pyrolysis in Porous Media". *SINTEF Report STF15 F94048, 1994.*

Melaaen, M.C. and M. G. Grønli: "Modelling and Simulation of Moist Wood Drying and Pyrolysis". *Presented at Developments in Thermochemical Biomass Conversion, Banff, Canada, May 1996.*

Melaaen, M.C.: "Numerical Analysis of Heat and Mass Transfer in Drying and Pyrolysis of Porous Media". *Numerical Heat Transfer, Part A, vol. 29, pp. 331-355, 1996.*

Milne, T. A.: "Pyrolysis - The Thermal Behaviour of Biomass Below 600°C". *In A Survey of Biomass Gasification. Volume II - Principles of Gasification, SERI/TR-33-239 July 1979.*

Min, K.: "Vapor-Phase Thermal Analysis of Pyrolysis Products from Cellulosic Materials". *Combustion and Flame, vol. 30, pp. 285-294, 1977.*

Mok, W.S.-L. and M.J. Antal, "Effect of Pressure on Biomass Pyrolysis. I. Cellulose Pyrolysis Products". *Thermochimica Acta, vol. 68, pp. 155-164, 1983a.*

Mok, W.S.-L. and M.J. Antal, "Effects of Pressure on Biomass Pyrolysis. II. Heats of Reaction of Cellulose Pyrolysis". *Thermochimica Acta, vol. 68, pp. 165-186, 1983b.*

Mok, W.S.-L., M.J. Antal, P. Szabo, G. Varhegyi and B. Zelei, "Formation of Charcoal from Biomass in a Sealed Reactor". *Ind. Eng. Chem. Res, vol. 31, pp. 1162-1167, 1992.*

Moyne, C. and P. Perre: "Processes Related to Drying: Part I, Theoretical Model". *Drying Technology, vol. 9, pp. 1135-1152, 1991.*

Narayan, R. and M. J. Antal: "Thermal Lag, Fusion, and the Compensation Effect during Biomass Pyrolysis". *Ind. Eng. Chem. Res, vol. 35, pp. 1711-1721, 1996.*

Nunn, T.R., J.B. Howard, J.P. Longwell and W.A. Peters: "Product Composition and Kinetics in the Rapid Pyrolysis of Milled Wood Lignin". *Ind. Eng. Chem. Process Des. Dev., vol. 24, pp. 844-852, 1985.*

Ouelhazi, N., G. Arnaud and J.P. Fohr: "A Two-Dimensional Study of Wood Plank Drying. The Effect of Gaseous Pressure Below Boiling Point". *Transport in Porous Media., vol. 7, pp. 39-61, 1992.*

Panton, R.L. and J.G. Rittmann: "Pyrolysis of a Slab of Porous Material". *Thirteenth Intern. Sump. on Combustion, pp. 881-891, 1971.*

Patankar, S. V.: "Numerical Heat Transfer and Fluid Flow". *Hemisphere Publishing Corporation, McGraw-Hill Book Company, 1980.*

Perre, P. and A. Degiovanni: "Control-Volume Formulation of Simultaneous Transfer in Anisotropic Porous Media:Simulations of Softwood Drying at Low and High Temperature". *International Journal of Heat and Mass Transfer, vol. 33, pp. 2463-2478, 1990.*

Perre, P. and C. Moyne: "Processes Related to Drying: Part II. Use of the Same Model to Solve Transfer Both in Saturated and Unsaturated Porous Media". *Drying Technology, vol. 9, pp. 1153-1179, 1991.*

Perre, P., M. Moser and M. Martin: "Advances in Transport Phenomena Drying Convective Drying With Superheated Steam and Moist Air". *International Journal of Heat and Mass Transfer, vol. 36, pp. 2725-2746, 1993.*

Piskorz, J., D. Radlein, D. Scott and S. Czernik.: "Pretreatment of Wood and Cellulose for Production of Sugars by Fast Pyrolysis". *Journal of Analytical and Applied Pyrolysis, vol. 16, pp. 127-142, 1989.*

Plumb, O.A., G.A. Spolek and B.A. Olmstead: "Heat and Mass Transfer in Wood During Drying". *International Journal of Heat and Mass Transfer, vol. 28, pp. 1669-1678, 1985.*

Pokol, G. and G. Varhegyi: "Kinetic Aspects of Thermal Analysis". *CRC Critical Reviews in Analytical Chemistry, vol. 19, Issue 1, 1988.*

Pyle, D.L. and C.A. Zaror, "Heat Transfer and Kinetics in the Low Temperature Pyrolysis of Solids". *Chemical Engineering Science, vol. 39, pp. 147-158, 1984.*

Ramiah, M.V., "Thermogravimetric and Differential Thermal Analysis of Cellulose, Hemicellulose and Lignin". *Journal of Applied Polymer Science, vol. 14, pp. 1323-1337, 1970.*

Raznjevik. K.: "Handbook of Thermodynamic Tables and Charts". *Hemisphere Publishing Corporation, McGraw-Hill Book Company, 1976.*

Richards, G. N. and G. Zheng: "Influence of Metal Ions and of Salts on Products from Pyrolysis of Wood: Applications to Thermochemical Processing of Newsprint and Biomass". *Journal of Analytical and Applied Pyrolysis, vol. 21, pp. 133-146, 1991.*

Roberts, A.F. and G. Clough: "Thermal Decomposition of Wood in an Inert Atmosphere". *Ninth Intern. Sump. on Combustion, pp. 158-166, 1963.*

Roberts, A.F.: "A Review of Kinetics Data for the Pyrolysis of Wood and Related Substances". Combustion and Flame, vol. 14, pp. 261-272, 1970.

Rogers, F.E. and T.J. Ohlemiller: "Cellulosic Insulation Material- I. Overall Degradation Kinetics and Reaction Heats". *Combustion Science and Technology, vol. 24, pp. 129-137, 1980.*

Sadakata, M., K. Takahasi, M. Saito and T. Sakai: "Production of Fuel Gas and Char from Wood, Lignin and Holocellulose by Carbonization". *Fuel, vol. 66, pp. 1667-1671, 1987.*

Saastamoinen, J., and M. Aho: "The Simultaneous Drying and Pyrolysis of Single Wood Particles and Pellets Made of Peat". *Paper Presented at the American Flame Research Committee, 1984, International Symposium on Alternative Fuels and Hazardous Wastes. pp 1-29, 1984.*

Shafizadeh, F.: "Pyrolysis and Combustion of Cellulosic Materials". *Advances in Carbohydrate Chemistry, vol. 23, pp. 419-474, 1968.*

Shafizadeh, F. and G.D. McGinnis: "Chemical Composition and Thermal Analysis of Cottonwood". *Carbohydrate Research, vol. 16, pp. 273-277, 1971.*

Shafizadeh, F., G.D. McGinnis, R.A. Susott and H.W. Tatton: "Thermal Reactions of Alpha-D-Xylopyranose and Beta-D-Xylopyranosides". *Journal of Org. Chem., vol. 36, pp. 2813-2818, 1971.*

Shafizadeh, F., R.A. Susott and G.D. McGinnis: "Pyrolysis of Substituted Phenyl beta-D-Glycopyranosides and 2-Deoxy-alph-D-arabino-Hexopyranosides". *Carbohydrate Research, vol. 22, pp. 63-73, 1972.*

Shafizadeh, F. and Y.L. Fu: "Pyrolysis of Cellulose". *Carbohydrate Research, vol. 29, pp. 113-122, 1973.*

Shafizadeh, F.: "Industrial Pyrolysis of Cellulosic Materials". *Applied Polymer Symposium, vol. 28, pp. 153-174, 1975.*

Shafizadeh, F. and W.F. DeGroot: "Combustion Characteristics of Cellulosic Fuels". *In F. Shafizadeh, K.V. Sarkanen, and D.A. Tillman (eds): Thermal Uses and Properties of Carbohydrates and Lignins, 172nd National Meeting of the American Chemical Society, Academic Press, pp. 1-18, 1976.*

Shafizadeh, F. and P.S. Chin: "Thermal Deterioration of Wood". *Wood Technology: Chemical Aspects, ACS Symp. Ser. 43, 57-81, 1977.*

Shafizadeh, F.: "Combustion, Combustibility, and Heat Release of Forest Fuels". *AIChE Symposium Series, vol. 74, pp. 76-82, 1978.*

Shafizadeh, F. and A.G.W. Bradbury: "Thermal Degradation of Cellulose in Air and Nitrogen at Low Temperatures". *Journal of Applied Polymer Science, vol. 23, pp. 1431-1442, 1979.*

Shafizadeh, F., R.H. Furneaux, T.G. Cochran, J.P. Scholl and Y. Sakai: "Production of Levoglucosan and Glucose from Pyrolysis of Cellulosic Materials". *Journal of Applied Polymer Science, vol. 23, pp. 3525-3539, 1979.*

Shafizadeh, F.: "Introduction to pyrolysis of Biomass". *Journal of Analytical and Applied Pyrolysis, vol. 3, pp. 283-385, 1982.*

Shafizadeh, F.: "The Chemistry of Pyrolysis and Combustion". *In R. Rowell (ed): The Chemistry of Solid Wood. American Chemical Society, pp. 489-529, 1984.*

Shafizadeh, F.: "Pyrolytic Reactions and Products of Biomass". *In R.P. Overend, T.A. Milne, and L.K. Mudge (eds): Fundamentals of Thermochemical Biomass Conversion. Elsevier Applied Science Publisher, pp. 183-217, 1985.*

Siau, J.F.: "Nonisothermal Moisture Movement in Wood". *Wood Science, vol. 13, pp. 11-13, 1980.*

Siau, J. F.: "Transport Processes in Wood" *Springer-Verlag Series in Wood Science, 1984.*

Simkovic, I., G. Varhegyi, M.J. Antal, A. Ebringerova, T. Szekely and P. Szabo: "Thermogravimetric/Mass Spectrometric Characterization of the Thermal Decomposition of (4-O-Methyl-D-Glucurono)-D-Xylan". *Journal of Applied Polymer Science, vol. 36, pp. 721-728, 1988.*

Simpson, W.T.: "Predicting Equilibrium Moisture Content of Wood By Mathematical Models". *Wood and Fiber, vol. 5, pp. 41-49, 1973.*

Simpson, W.T.: "Sorption Theories Applied to Wood". *Wood and Fiber, vol. 12, pp. 183-195, 1980.*

Simpson, W.T.: "Drying Wood: A Review - Part I". *Drying Technology, vol. 2, pp. 235-264, 1983a.*

Simpson, W.T.: "Drying Wood: A Review - Part II". *Drying Technology, vol. 2, pp. 353-368, 1983b.*

Simpson, W.T.: "Determination and Use of Moisture Diffusion Coefficient to Characterize Drying of Northern Red Oak". *Wood Science and Technology, vol. 27, pp. 409-420, 1993.*

Sjöström, E. "Wood Chemistry - Fundamentals and Applications". *Academic Press, 1981.*

Skaar, C. and J.F. Siau: "Thermal Diffusion of Bound Water in Wood". *Wood Science and Technology, vol. 15, pp. 105-112, 1981.*

Skaar, C. and M. Babiak: "A Model for Bound-Water Transport in Wood". *Wood Science and Technology, pp. 123-138, 1982.*

Skaar, C.: "Wood-Water Relationships". *In R. Rowell (ed): The Chemistry of Solid Wood, American Chemical Society, pp. 127-174, 1984.*

Skaar, C.: "Wood-Water Relations". *Springer-Verlag Series in Wood Science, 1988.*

Skaar, C.: "Hygroscopicity and Water Sorption". *In: Concise Encyclopedia of Wood and Wood-Based Materials, Pergamon Press, pp. 143-147, 1989.*

Skille, J.: "Production of Activated Carbon from Biomass". *Diploma Thesis, Norwegian University of Technology, Department of Thermal Energy and Hydropower and University of Hawaii at Manoa, Hawaii Natural Energy Institute, 1995*

Sonntag R. E. and G. J. Van Wylen: "Introduction to Thermodynamics, Classical & Statistical". *John Wiley & Sons, Second Edition, 1982.*

Spolek, G.A. and O.A. Plumb: "Capillary Pressure in Softwoods". *Wood Science and Technology, vol. 15, pp. 189-199, 1981*

Spolek, G.A.: "A Model of Simultaneous Convective, Diffusive and Capillary Heat and Mass Transport in Drying Wood". *Ph.D-Thesis, Washington State University, 1981.*

Stamm, A. J. and R. M. Seeborg: "Absorption Compression on Cellulose and Wood. I Density Measurement in Benzene". *Journal of Physical Chemistry, vol. 39, pp. 133-142, 1934.*

Stamm, A.J. and N.C. Raleigh: "Diffusion". *Wood Science and Technology, vol. 1, pp. 205-230, 1967.*

Stamm, A. J.: "Wood and Cellulose Science". *Ronald New York, pp 1-549, 1964.*

Stanish, M.A.: "The Roles of Bound Water Chemical Potential and Gas Phase Diffusion in Moisture Transport Through Wood". *Wood Science and Technology, vol. 19, pp. 53-70, 1986a.*

Stanish, M.A., G.S. Schajer and F. Kayihan: "A Mathematical Model of Drying for Hygroscopic Porous Media". *AIChE Journal, vol. 32, pp. 1301-1311, 1986.*

Strumillo, C. and T. Kudra: "Drying: Principles, Applications and Design". *Gordon and Breach Science Publishers, 1986.*

Tang, W.K.: "Effect of Inorganic Salts on Pyrolysis of Wood, Alpha-Cellulose and Lignin". *FPL Research Paper no.71, USDA Forest Products Laboratory, 1967.*

Tesoro, F.O., E.T. Choong and O.K. Kimbler: "Relative Permeability and the Gross Pore Structure of Softwoods". *Wood and Fiber, vol. 6, pp. 226-236, 1974.*

Thurner, F. and U. Mann: "Kinetic Investigation of Wood Pyrolysis". *Ind. Eng. Chem. Process Des. Dev, vol. 20, pp. 482-488, 1981.*

Tillman, D.A., A.J. Rossi, and W.D. Kitto "Wood Combustion - Principles, Processes and Economics". *Academic Press, 1981.*

Tinney, E.R.: "The Combustion of Wooden Dowels in Heated Air". *Tenth Intern. Sump. on Combustion, pp. 925-930, 1965.*

Varhegyi, G.: "Kinetic Evaluation of Non-Isothermal Thermoanalytical Curves in the Case of Independent Thermal Reactions". *Thermochimica Acta, vol. 28, pp. 367-376, 1979.*

Varhegyi, G. and T. Szekely: "Reaction Kinetics in Thermal Analysis. Part 1. The Sensitivity of Kinetic Equations to Experimental Errors. A Mathematical Analysis". *Thermochimica Acta, vol. 57, pp. 13-28, 1982.*

Varhegyi, G., M.J. Antal, T. Szekely, F. Till and E. Jakab: "Simultaneous Thermogravimetric-Mass Spectrometric Studies of the Thermal Decomposition of Biopolymers. 1) Avicel Cellulose in the Presence and Absence of Catalysts. 2) Sugar Cane Bagasse in the Presence and Absence of Catalysts". *Energy & Fuels, vol. 2, pp. 267-272, 1988.*

Varhegyi, G., M.J. Antal, T. Szekely and P. Szabo: "Kinetics of the Thermal Decomposition of Cellulose, Hemicellulose, and Sugar Cane Bagasse". *Energy & Fuels, vol. 3, pp. 329-335, 1989.*

Varhegyi, G., E. Jakab, F. Till and T. Szekely: "Thermogravimetric-Mass Spectrometric Characterization of the Thermal Decomposition of SunFlower Stem". *Energy & Fuels, vol. 3, pp. 755-760, 1989.*

Varhegyi, G., P. Szabo and M.J. Antal: "Reaction Kinetics of the Thermal Decomposition of Cellulose and Hemicellulose in Biomass Materials". *In A.V. Bridgwater (ed): Advances in Thermochemical Biomass Conversion. London: Blackie Academic & Professional, pp. 760-770, 1994a.*

Varhegyi, G., P. Szabo and M.J. Antal: " Kinetics of the Thermal Decomposition of Cellulose Under the Experimental Conditions of Thermal Analysis. Theoretical Extrapolations to Higher Heating Rates". *Biomass and Bioenergy, vol. 7, Nos 1-6, pp. 69-74, 1994b.*

Varhegyi, G., E. Jakab, and M. J. Antal: "Is the Broido-Shafizadeh Model for Cellulose Pyrolysis True?". *Energy & Fuels, vol. 8, pp. 1345-1352, 1994.*

Varhegyi, G. "Personal Communication". *1996.*

Vovelle, C., H. Mellottee and R. Delbourgo: "Kinetics of The Thermal Degradation of Cellulose and Wood in Inert and Oxidative Atmospheres". *Nineteenth Intern. Sump. on Combustion, pp. 797-805, 1982.*

Wendlandt, W.: "Thermal Methods of Analysis". *John Wiley & Sons, 1974.*

Wessling, S.: "An Experimental Study of the Pyrolysis of Biomass and Municipal Solid Waste Pellets". *Diploma Thesis, Norwegian University of Science and Technology, 1994*

Whitaker, S.: "Diffusion and Dispersion in Porous Media". *AIChE Journal, vol. 13, pp. 420-427, 1967.*

Whitaker, S.: "Advances in Theory of Fluid Motion in Porous Media". *Industrial and Engineering Chemistry, vol. 61, pp. 14-28, 1969.*

Whitaker, S.: "Simultaneous Heat, Mass and Momentum Transfer in Porous Media: A Theory of Drying". *Advances in Heat Transfer, vol. 13, pp. 119-203, 1977.*

White, R. H. and E. L. Schaffer: "Transient Moisture Gradient in Fire-Exposed Wood Slab". *Wood and Fiber, vol. 13, pp. 17-38, 1981.*

Wichman, I. S. and M. C. Melaaen: "Modelling The Pyrolysis of Cellulosic Materials". *In A.V. Bridgwater (ed): Advances in Thermochemical Biomass Conversion. London: Blackie Academic & Professional, pp. 887-905, 1994.*

Williams, P.T. and S. Besler: "Thermogravimetric Analysis of the Components of Biomass". *In A.V. Bridgwater (ed): Advances in Thermochemical Biomass Conversion. London: Blackie Academic & Professional, 1994.*

Zaror, C. A. and D. L. Pyle: " " *Journal of Analytical an Applied Pyrolysis, vol. 10, pp. 1-12, 1986*

Zsako, J.: "The Kinetic Compensation Effect". *Journal of Thermal Analysis, vol. 9, pp. 101-108, 1976.*

APPENDIX A
KINETIC ANALYSIS

CELLULOSE

LIGNIN - 5 mg sample size and 5°C/min heating rate

BIRCH - 5 mg sample size and 5°C/min heating rate

SPRUCE - 5 mg sample size and 5°C/min heating rate

PINE - 5 mg sample size and 5°C/min heating rate

PINEROOT - 5 mg sample size and 5°C/min heating rate

In all figures, dots, the bold solid line and thin solid lines represents the experimental data $(m)^{exp}$ and $(-dm/dt)^{exp}$, the calculated data $(m)^{calc}$ and $(-dm/dt)^{calc}$ and the contributions of the partial reactions to $(-dm/dt)^{calc}$, respectively.

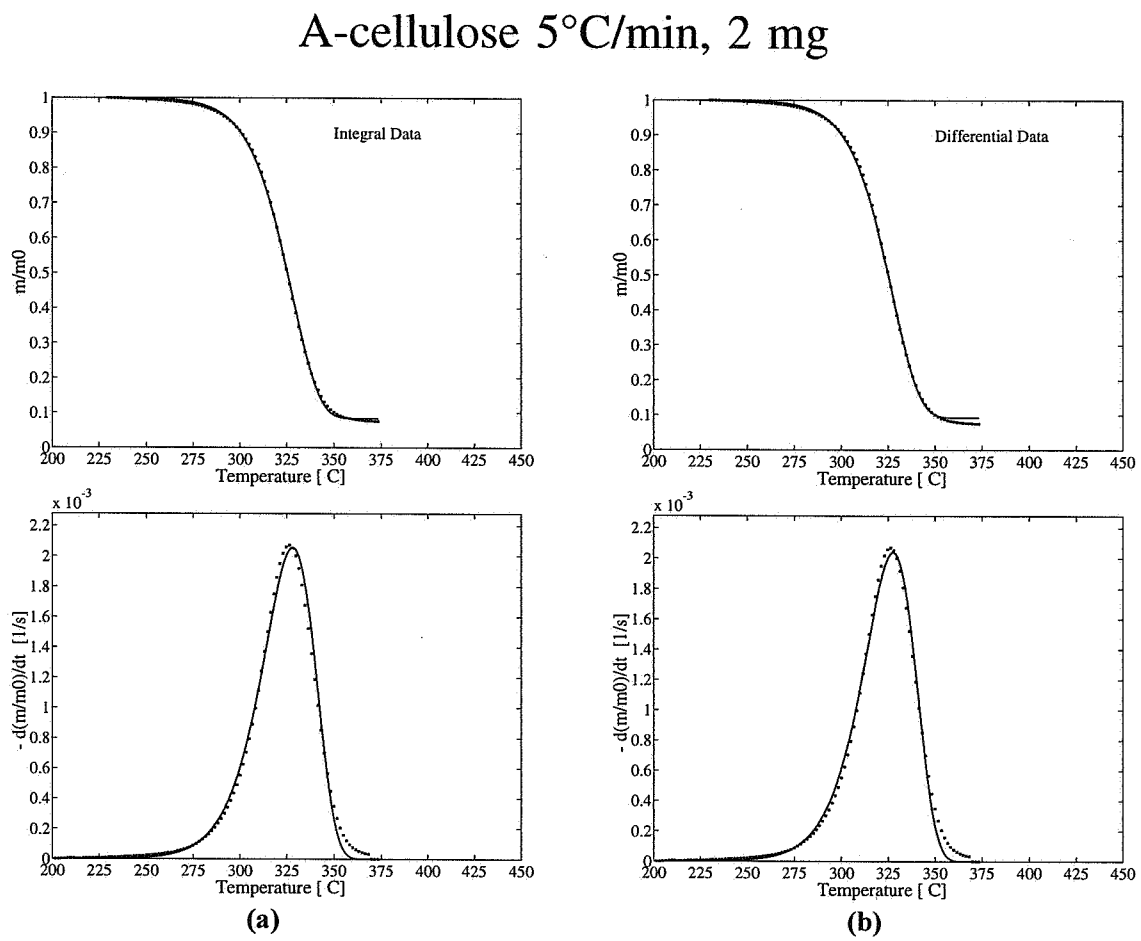

Figure A.1 Kinetic evaluation of A-cellulose assuming a single first order reaction. Evaluation methods: (a) Fit of TG curve; (b) fit of DTG curve.

Table A.1 Kinetic parameters for A-cellulose evaluated by a single first order reaction.

	first peak	
Evaluated Curve	E_1 [kJ/mol] $\log A_1$ [log s^{-1}] c_1 [%] n	dev1 [%] dev2 [%] $(T_{peak})^{calc}$ $(T_{peak})^{exp}$
TG	211.3 16.13 91.7 1.0	1.9 9.9 328.1 326.7
DTG	211.5 16.16 90.7 1.0	1.8 18.9 327.4 326.7

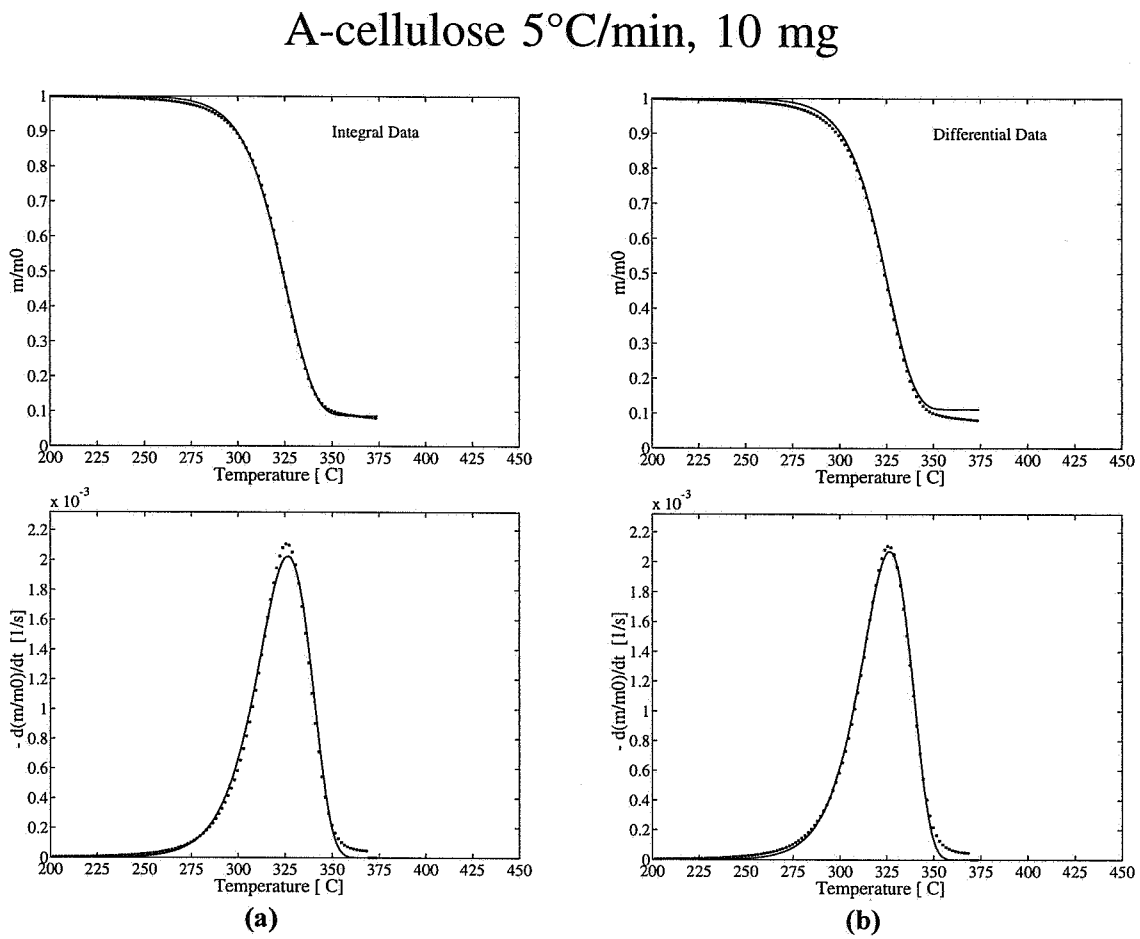

Figure A.2 Kinetic evaluation of A-cellulose assuming a single first order reaction. Evaluation methods: (a) Fit of TG curve; (b) fit of DTG curve.

Table A.2 Kinetic parameters for A-cellulose evaluated by a single first order reaction.

	first peak	
Evaluated Curve	E_1 [kJ/mol] $\log A_1$ [log s^{-1}] c_1 [%] n	dev1 [%] dev2 [%] $(T_{peak})^{calc}$ $(T_{peak})^{exp}$
TG	211.0 16.15 91.3 1.0	1.6 8.1 326.9 327.0
DTG	222.3 17.16 88.8 1.0	1.2 28.3 326.9 327.0

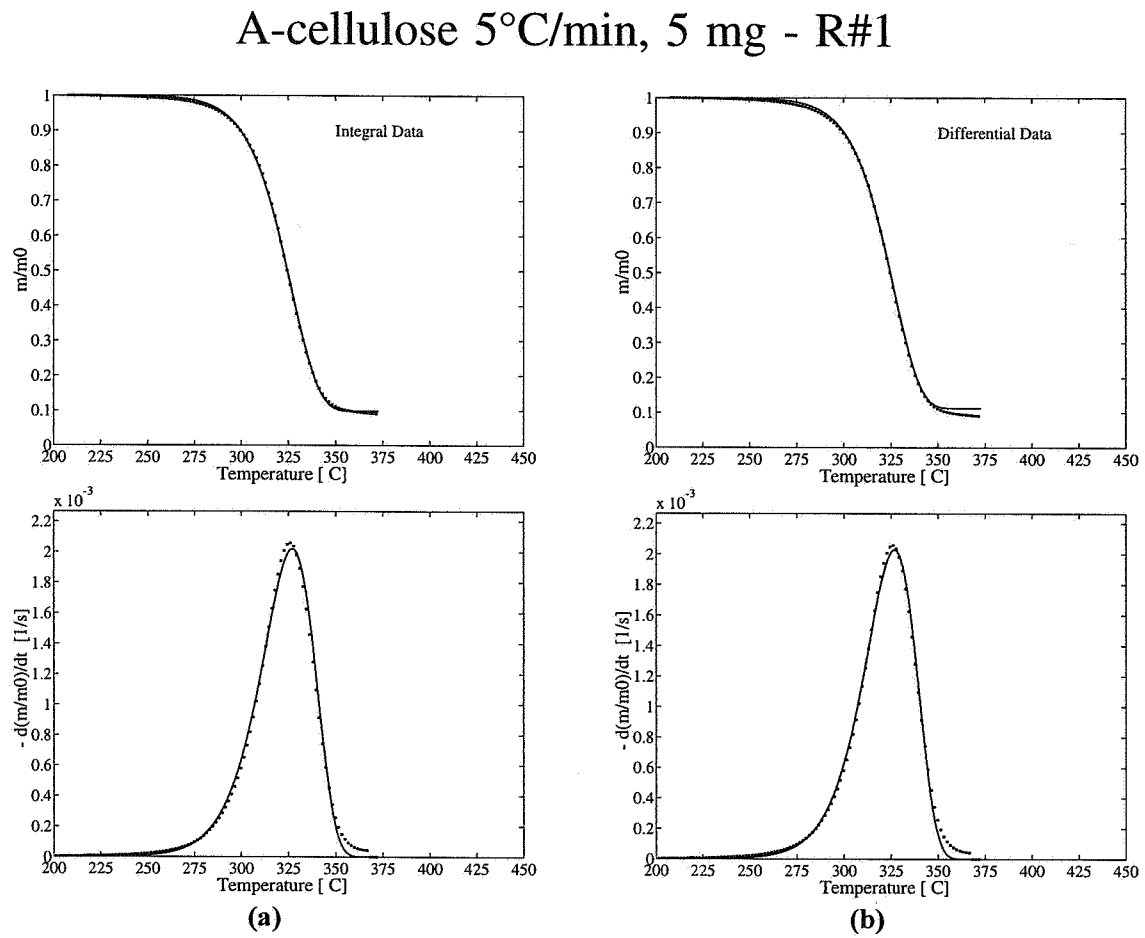

Figure A.3 Kinetic evaluation of A-cellulose assuming a single first order reaction. Evaluation methods: (a) Fit of TG curve; (b) fit of DTG curve.

Table A.3 Kinetic parameters for A-cellulose evaluated by a single first order reaction.

	first peak	
Evaluated Curve	E_1 [kJ/mol]	dev1 [%]
	$\log A_1$ [log s^{-1}]	dev2 [%]
	c_1 [%]	$(T_{peak})^{calc}$
	n	$(T_{peak})^{exp}$
TG	211.1	1.5
	16.14	7.6
	90.2	327.1
	1.0	325.7
DTG	215.6	1.4
	16.56	19.7
	88.8	327.1
	1.0	325.7

A-cellulose 5°C/min, 5 mg - R#1

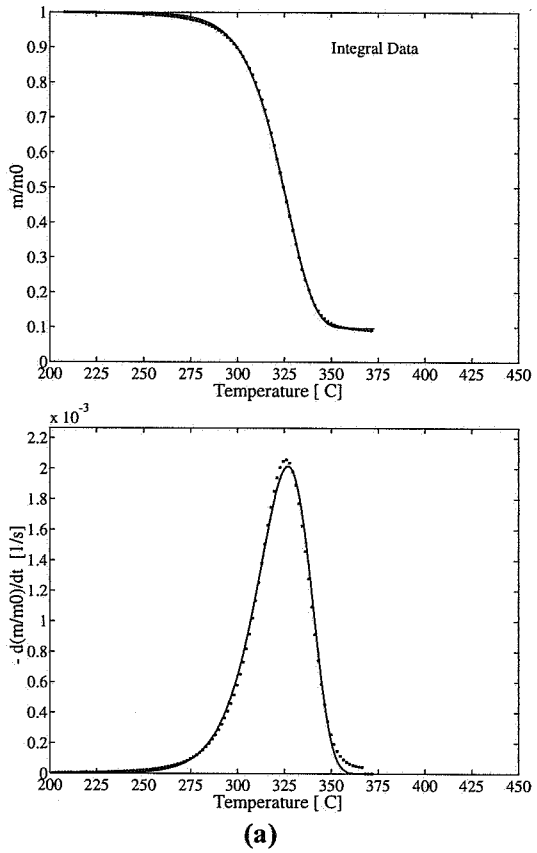

(a)

Figure A.4 Kinetic evaluation of A-cellulose assuming a single n'the order reaction. Evaluation methods: (a) Fit of TG curve.

Table A.4 Kinetic parameters for A-cellulose evaluated by a single n'the order reaction.

	first peak	
Evaluated Curve	E_1 [kJ/mol]	dev1 [%]
	$\log A_1$ [log s^{-1}]	dev2 [%]
	c_1 [%]	$(T_{peak})^{calc}$
	n	$(T_{peak})^{exp}$
TG	212.5	1.4
	16.27	7.1
	90.3	327.1
	1.018	325.7

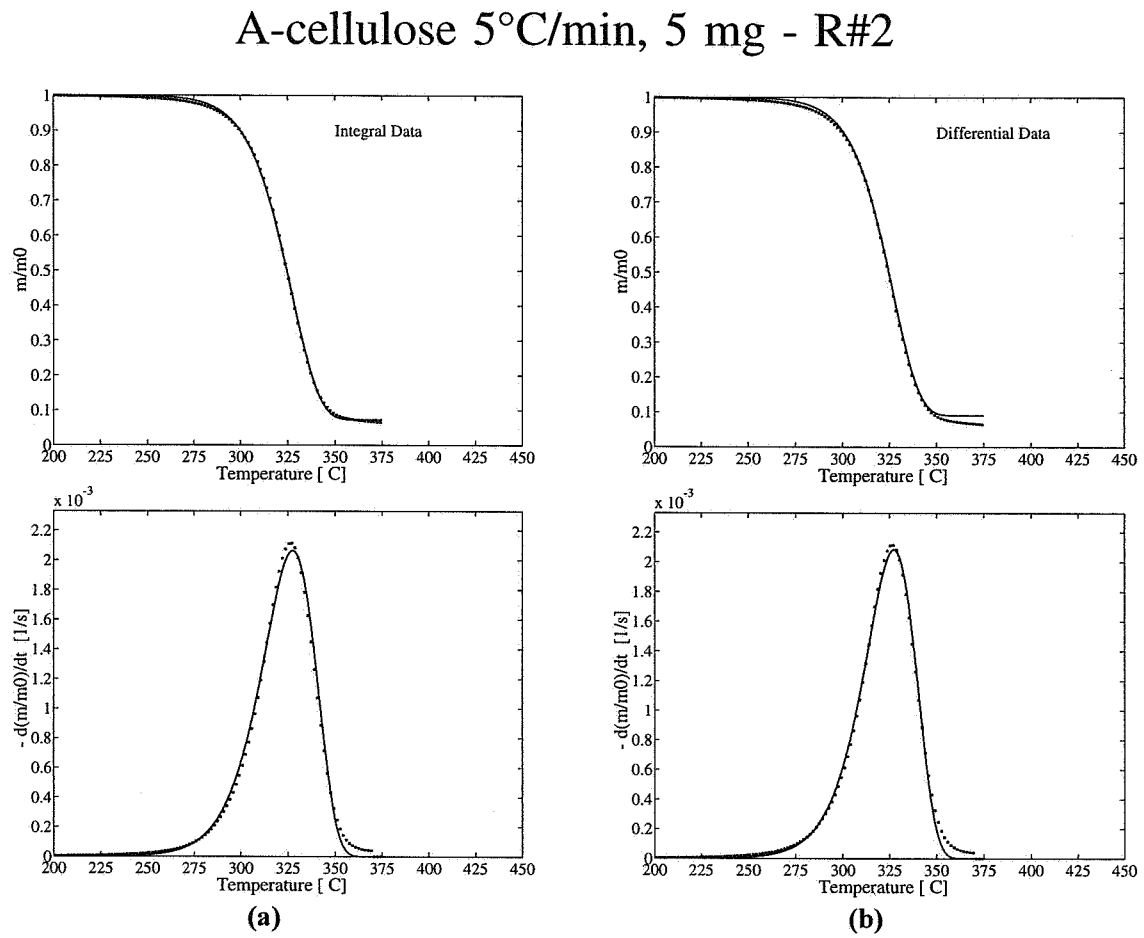

Figure A.5 Kinetic evaluation of A-cellulose assuming a single first order reaction. Evaluation methods: (a) Fit of TG curve; (b) fit of DTG curve.

Table A.5 Kinetic parameters for A-cellulose evaluated by a single first order reaction.

	first peak	
Evaluated Curve	E_1 [kJ/mol]	dev1 [%]
	$\log A_1$ [log s^{-1}]	dev2 [%]
	c_1 [%]	$(T_{peak})^{calc}$
	n	$(T_{peak})^{exp}$
TG	210.4	1.6
	16.07	10.5
	92.7	327.4
	1.0	326.4
DTG	216.7	1.4
	16.64	28.5
	90.9	327.1
	1.0	326.4

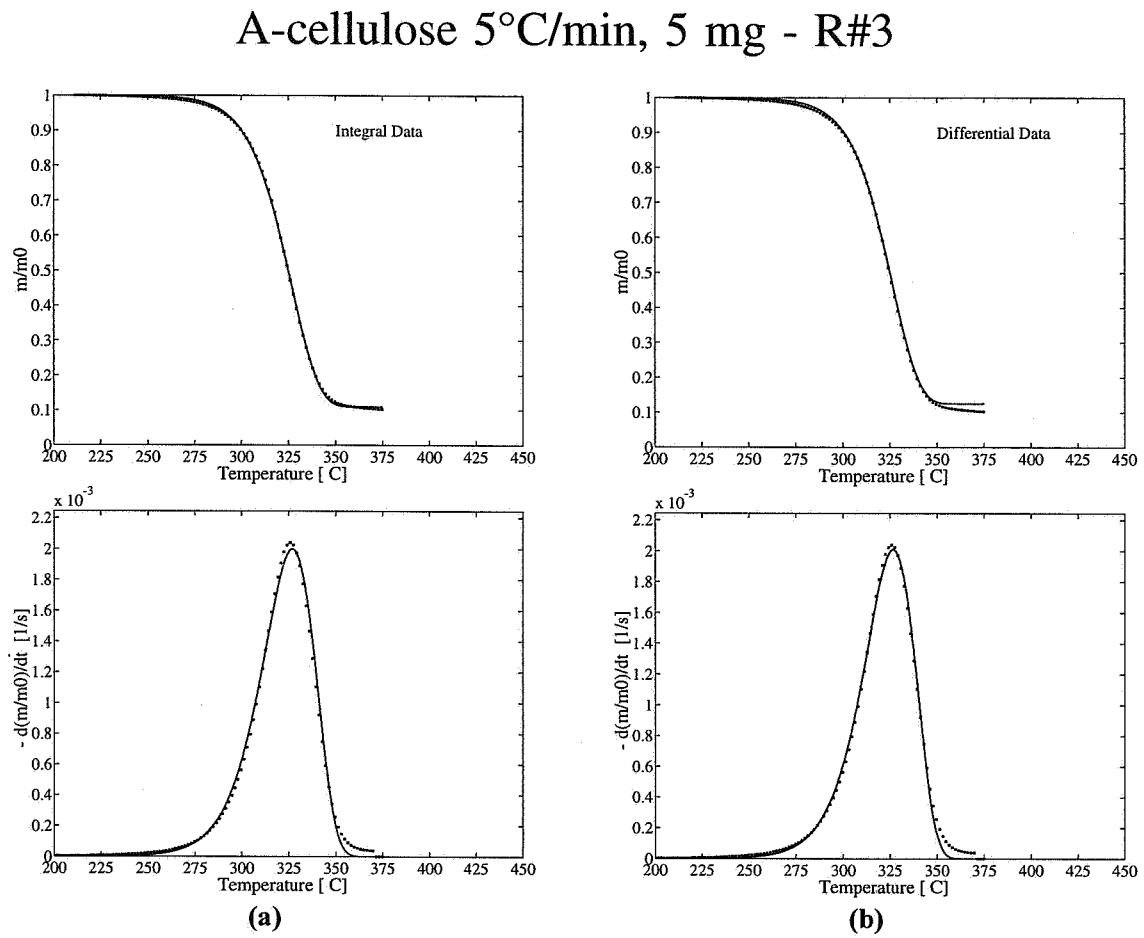

Figure A.6 Kinetic evaluation of A-cellulose assuming a single first order reaction. Evaluation methods: (a) Fit of TG curve; (b) fit of DTG curve.

Table A.6 Kinetic parameters for A-cellulose evaluated by a single first order reaction.

	first peak	
Evaluated Curve	E_1 [kJ/mol]	dev1 [%]
	$\log A_1$ [log s^{-1}]	dev2 [%]
	c_1 [%]	$(T_{peak})^{calc}$
	n	$(T_{peak})^{exp}$
TG	212.0	1.5
	16.22	6.7
	89.0	327.2
	1.0	326.6
DTG	217.1	1.3
	16.69	18.5
	87.5	326.6
	1.0	326.6

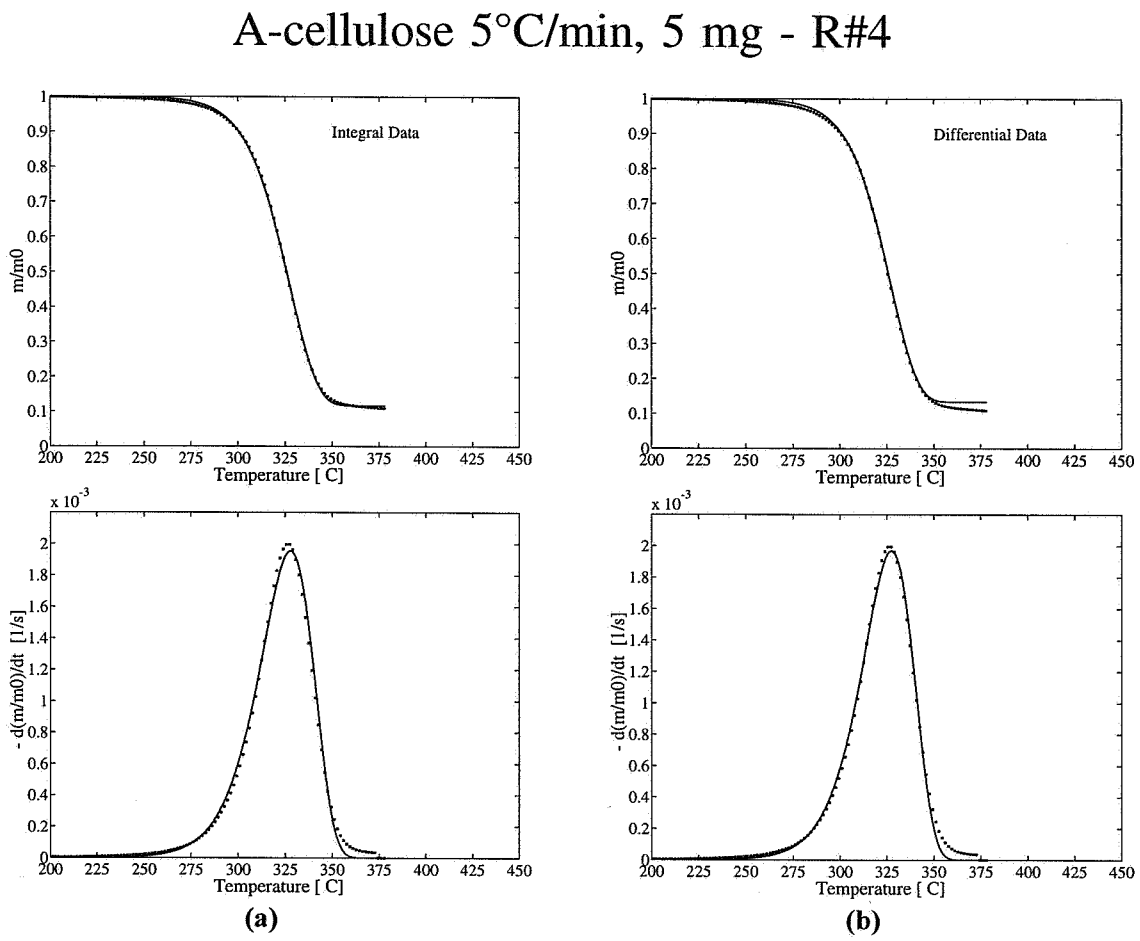

Figure A.7 Kinetic evaluation of A-cellulose assuming a single first order reaction. Evaluation methods: (a) Fit of TG curve; (b) fit of DTG curve.

Table A.7 Kinetic parameters for A-cellulose evaluated by a single first order reaction.

	first peak	
Evaluated Curve	E_1 [kJ/mol] $\log A_1$ [log s^{-1}] c_1 [%] n	dev1 [%] dev2 [%] $(T_{peak})^{calc}$ $(T_{peak})^{exp}$
TG	208.8 15.92 88.3 1.0	1.7 6.7 327.6 328.0
DTG	214.6 16.45 86.6 1.0	1.5 18.6 327.3 328.0

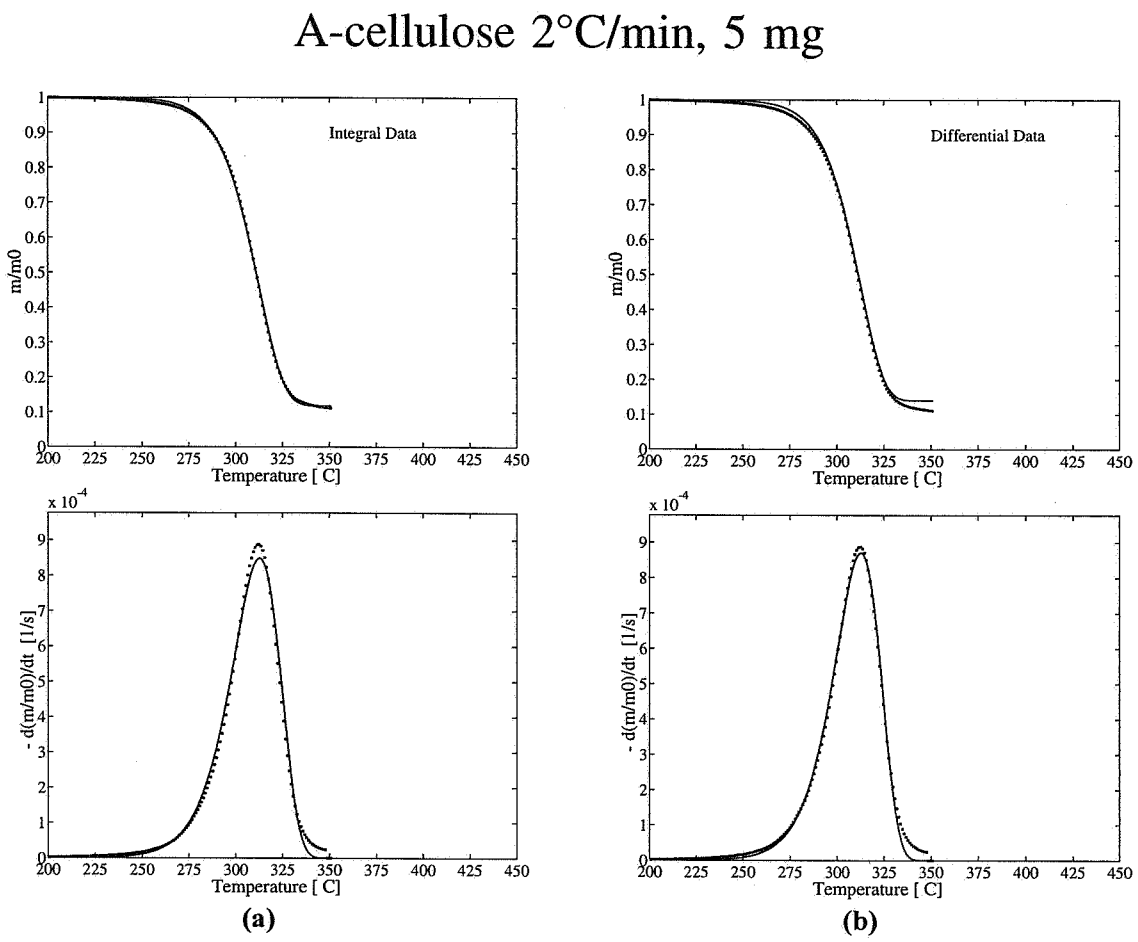

Figure A.8 Kinetic evaluation of A-cellulose assuming a single first order reaction. Evaluation methods: (a) Fit of TG curve; (b) fit of DTG curve.

Table A.8 Kinetic parameters for A-cellulose evaluated by a single first order reaction.

	first peak	
Evaluated Curve	E_1 [kJ/mol] $\log A_1$ [log s^{-1}] c_1 [%] n	dev1 [%] dev2 [%] $(T_{peak})^{calc}$ $(T_{peak})^{exp}$
TG	216.3 16.69 88.1 1.0	1.8 6.3 312.9 313.4
DTG	227.8 17.75 86.0 1.0	1.4 20.7 312.9 313.4

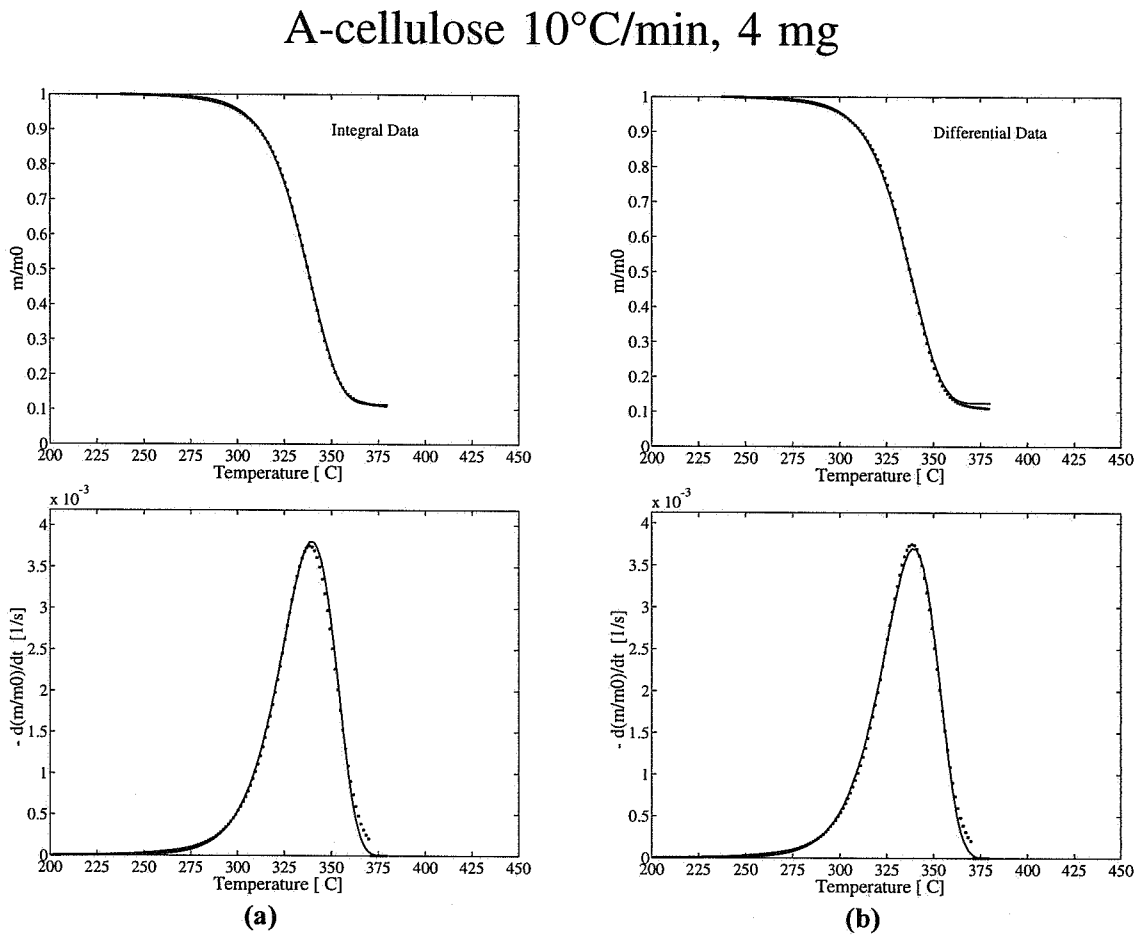

Figure A.9 Kinetic evaluation of A-cellulose assuming a single first order reaction. Evaluation methods: (a) Fit of TG curve; (b) fit of DTG curve.

Table A.9 Kinetic parameters for A-cellulose evaluated by a single first order reaction.

	first peak	
Evaluated Curve	E_1 [kJ/mol] $\log A_1$ [log s^{-1}] c_1 [%] n	dev1 [%] dev2 [%] $(T_{peak})^{calc}$ $(T_{peak})^{exp}$
TG	212.2 16.15 88.6 1.0	1.3 4.2 339.1 340.2
DTG	208.4 15.82 87.6 1.0	1.1 12.1 339.1 340.2

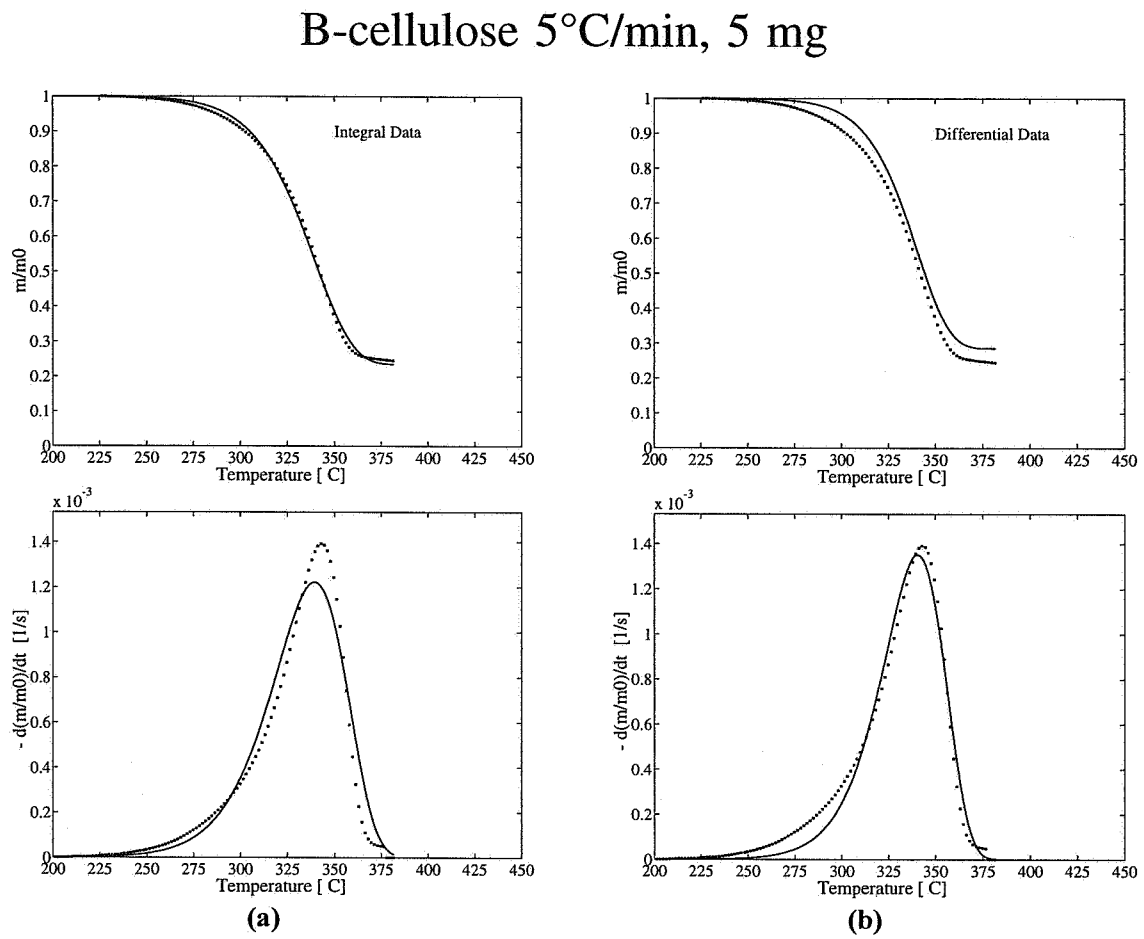

Figure A.10 Kinetic evaluation of B-cellulose assuming a single first order reaction. Evaluation methods: (a) Fit of TG curve; (b) fit of DTG curve.

Table A.10 Kinetic parameters for B-cellulose evaluated by a single first order reaction.

	first peak	
Evaluated Curve	E_1 [kJ/mol] $\log A_1$ [log s^{-1}] c_1 [%] n	dev1 [%] dev2 [%] $(T_{peak})^{calc}$ $(T_{peak})^{exp}$
TG	153.4 10.69 76.6 1.0	5.0 4.2 338.9 344.6
DTG	184.5 13.39 71.4 1.0	3.4 14.2 340.3 344.6

B-cellulose 5°C/min, 5 mg

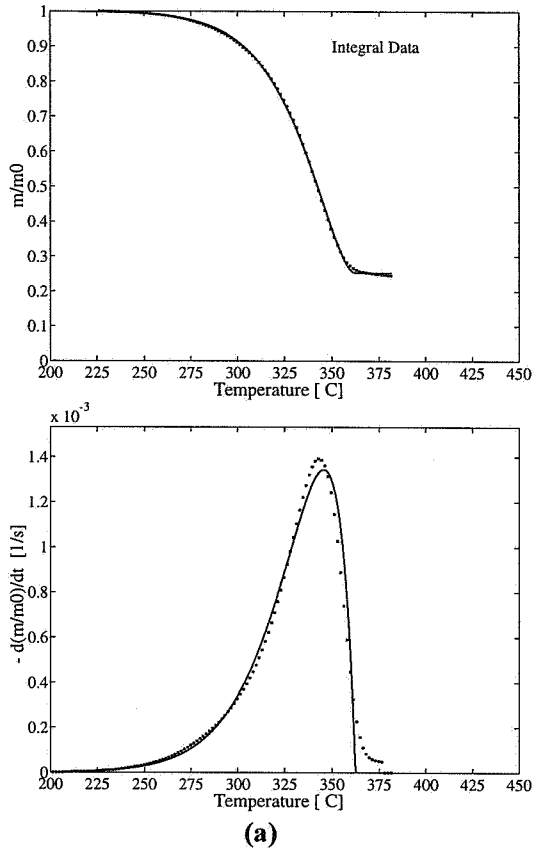

(a)

Figure A.11 Kinetic evaluation of B-cellulose assuming a single n'the order reaction. Evaluation methods: (a) Fit of TG curve.

Table A.11 Kinetic parameters for B-cellulose evaluated by a single n'the order reaction.

	first peak	
Evaluated Curve	E_1 [kJ/mol]	dev1 [%]
	$\log A_1$ [log s^{-1}]	dev2 [%]
	c_1 [%]	$(T_{peak})^{calc}$
	n	$(T_{peak})^{exp}$
TG	126.1	3.4
	8.18	3.2
	74.7	345.9
	0.481	344.6

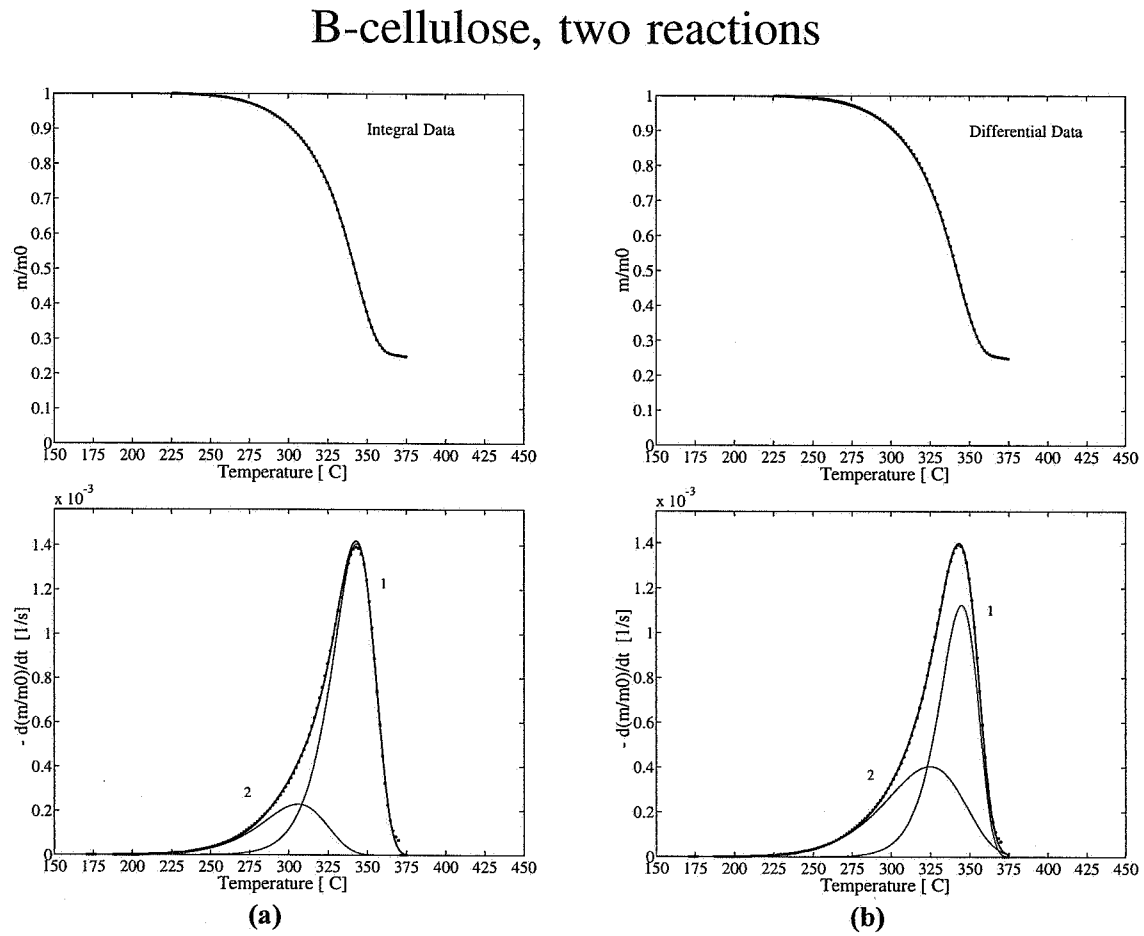

Figure A.12 Kinetic evaluation of B-cellulose assuming two independent parallel reactions. Evaluation methods: (a) Fit of TG curve; (b) fit of DTG curve.

Table A.12 Kinetic parameters for B-cellulose evaluated by two independent parallel reactions.

	first peak (reaction 2)	second peak (reaction 1)	
Evaluated Curve	E_2 [kJ/mol] $\log A_2$ [log s^{-1}] c_2 [%] $(T_{peak,\,2})^{calc}$	E_1 [kJ/mol] $\log A_1$ [log s^{-1}] c_1 [%] $(T_{peak,\,1})^{calc}$	dev1 [%] dev2 [%] $(T_{peak})^{exp}$
TG	132.3 9.53 14.8 306.1	232.4 17.39 60.2 343.2	0.6 0.9 344.6
DTG	115.2 7.57 31.6 325.0	258.8 19.72 43.6 344.9	0.3 0.2 344.6

Birch cellulose 5°C/min, 5 mg

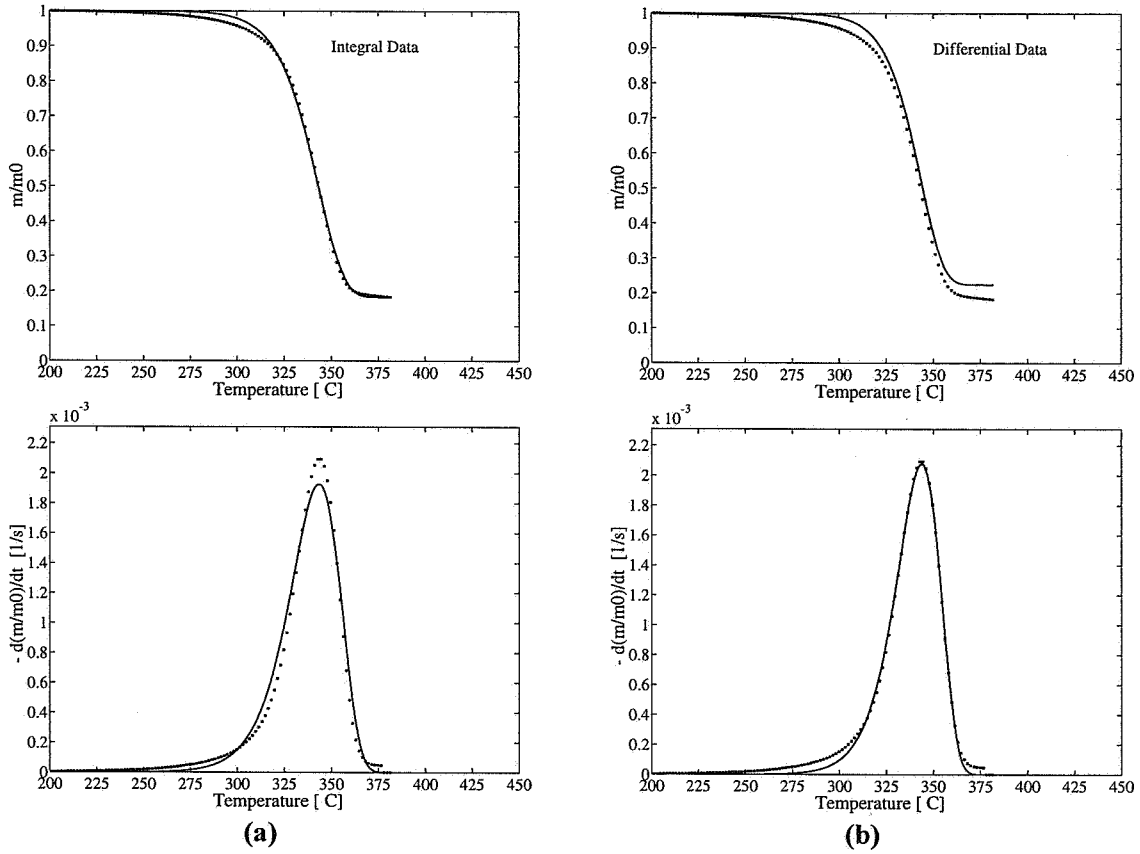

Figure A.13 Kinetic evaluation of birch-cellulose assuming a single first order reaction. Evaluation methods: (a) Fit of TG curve; (b) fit of DTG curve.

Table A.13 Kinetic parameters for birch-cellulose evaluated by a single first order reaction.

	first peak	
Evaluated Curve	E_1 [kJ/mol] $\log A_1$ [log s^{-1}] c_1 [%] n	dev1 [%] dev2 [%] $(T_{peak})^{calc}$ $(T_{peak})^{exp}$
TG	235.5 17.75 81.7 1.0	2.7 0.1 343.2 343.8
DTG	269.4 20.67 77.5 1.0	1.3 18.8 343.8 343.8

Birch cellulose 5°C/min, 5 mg

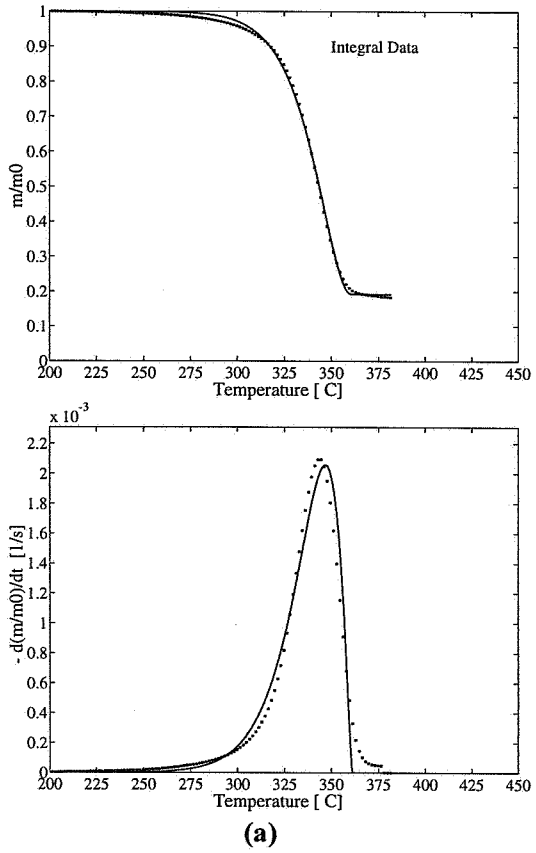

(a)

Figure A.14 Kinetic evaluation of birch-cellulose assuming a single n'the order reaction. Evaluation methods: (a) Fit of TG curve.

Table A.14 Kinetic parameters for birch-cellulose evaluated by a single n'the order reaction.

	first peak	
Evaluated Curve	E_1 [kJ/mol]	dev1 [%]
	$\log A_1$ [log s^{-1}]	dev2 [%]
	c_1 [%]	$(T_{peak})^{calc}$
	n	$(T_{peak})^{exp}$
TG	199.9	3.7
	14.57	4.7
	80.8	346.8
	0.588	343.8

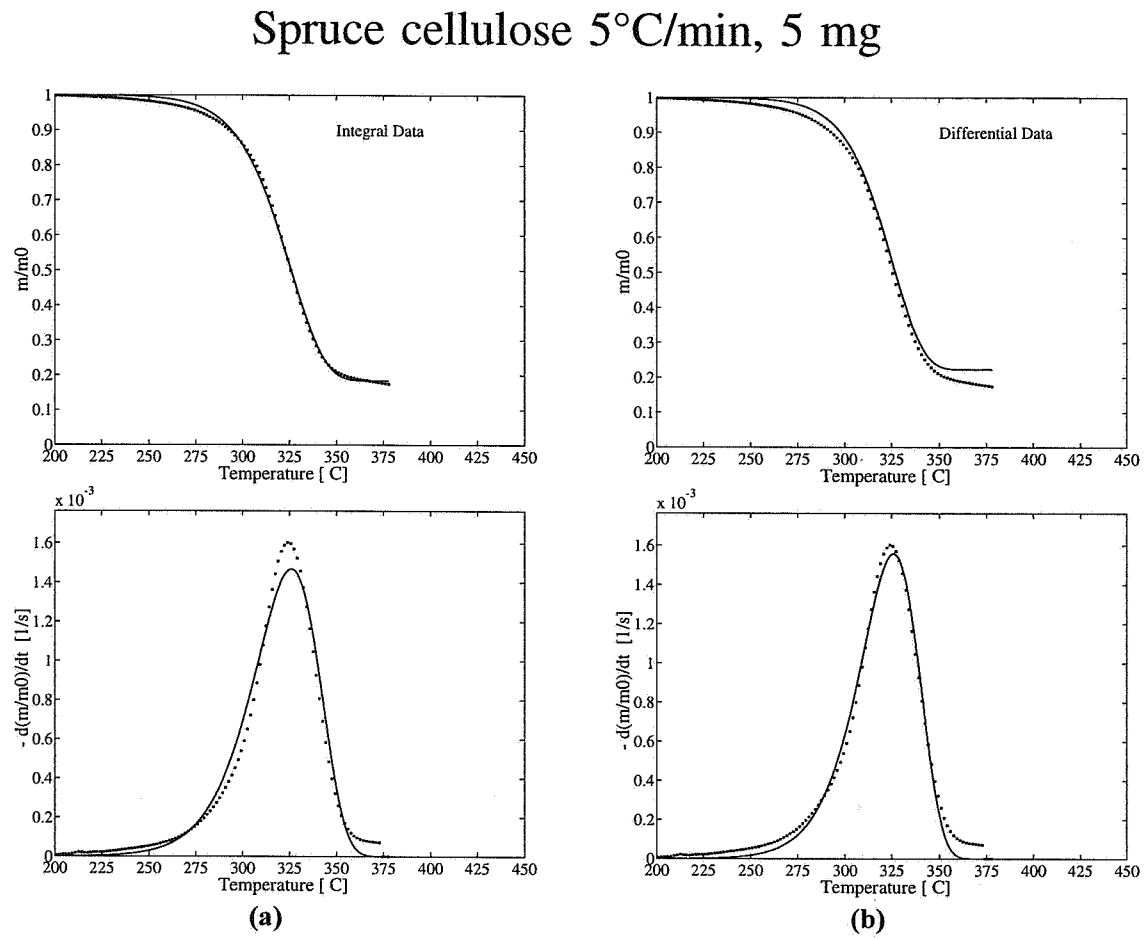

Figure A.15 Kinetic evaluation of spruce-cellulose assuming a single first order reaction. Evaluation methods: (a) Fit of TG curve; (b) fit of DTG curve.

Table A.15 Kinetic parameters for spruce-cellulose evaluated by a single first order reaction.

	first peak	
Evaluated Curve	E_1 [kJ/mol]	dev1 [%]
	$\log A_1$ [log s^{-1}]	dev2 [%]
	c_1 [%]	$(T_{peak})^{calc}$
	n	$(T_{peak})^{exp}$
TG	166.4	3.4
	12.18	5.0
	81.6	326.4
	1.0	325.6
DTG	186.4	2.4
	13.98	21.7
	77.7	325.4
	1.0	325.6

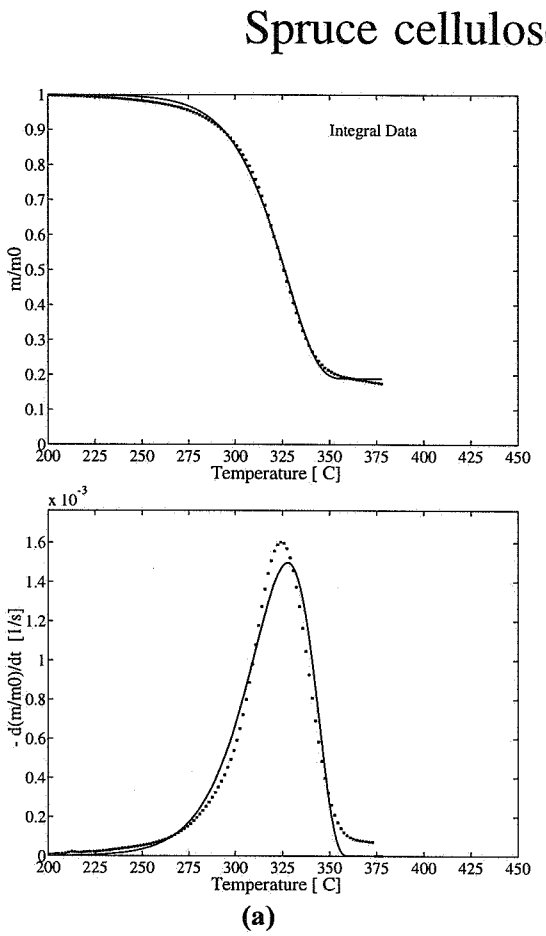

Figure A.16 Kinetic evaluation of spruce-cellulose assuming a single n'the order reaction. Evaluation methods: (a) Fit of TG curve.

Table A.16 Kinetic parameters for spruce-cellulose evaluated by a single n'the order reaction.

	first peak	
Evaluated Curve	E_1 [kJ/mol] $\log A_1$ [log s^{-1}] c_1 [%] n	dev1 [%] dev2 [%] $(T_{peak})^{calc}$ $(T_{peak})^{exp}$
TG	155.0 11.11 81.1 0.816	3.9 7.4 327.7 325.6

Whatman filter paper 5°C/min, 5 mg - Run 1

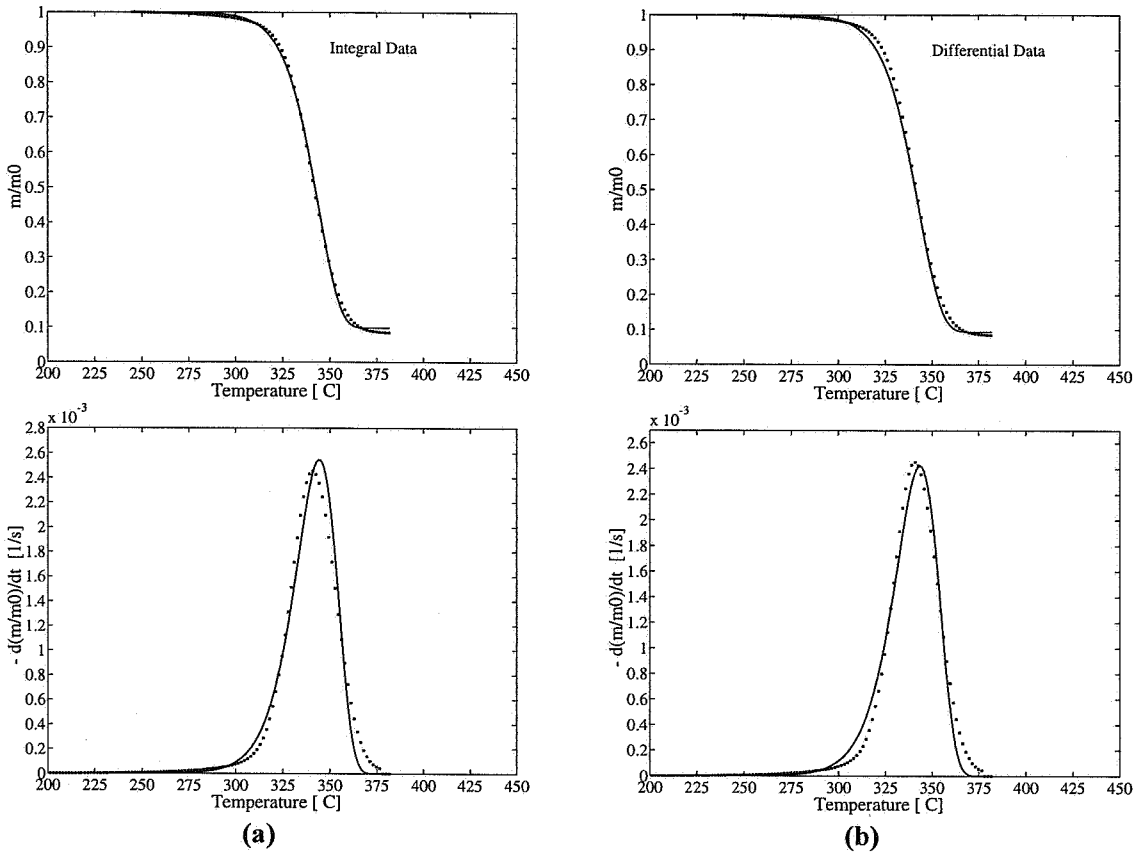

Figure A.17 Kinetic evaluation of Whatman filter paper assuming a single first order reaction. Evaluation methods: (a) Fit of TG curve; (b) fit of DTG curve.

Table A.17 Kinetic parameters for Whatman filter paper evaluated by a single first order reaction.

	first peak	
Evaluated Curve	E_1 [kJ/mol] $\log A_1$ [log s^{-1}] c_1 [%] n	dev1 [%] dev2 [%] $(T_{peak})^{calc}$ $(T_{peak})^{exp}$
TG	284.8 21.97 90.2 1.0	3.6 13.9 344.6 341.2
DTG	269.0 20.65 90.7 1.0	3.2 10.0 343.6 341.2

Whatman filter paper 5°C/min, 5 mg - Run 1

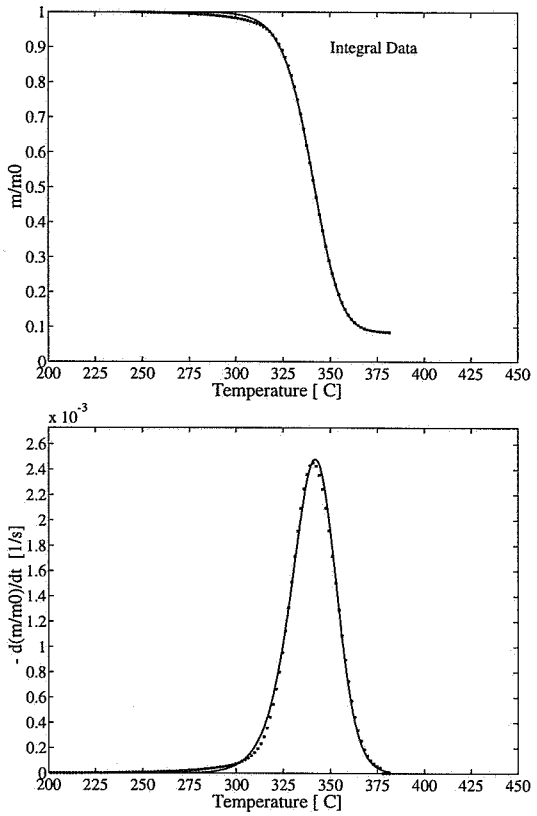

(a)

Figure A.18 Kinetic evaluation of Whatman filter paper assuming a single n'the order reaction. Evaluation methods: (a) Fit of TG curve.

Table A.18 Kinetic parameters for Whatman filter paper evaluated by a single n'the order reaction.

	first peak	
Evaluated Curve	E_1 [kJ/mol]	dev1 [%]
	$\log A_1$ [log s^{-1}]	dev2 [%]
	c_1 [%]	$(T_{peak})^{calc})_{max}$
	n	$(T_{peak})^{exp})_{max}$
TG	334.1	1.2
	26.32	1.7
	91.5	341.6
	1.452	341.2

Whatman filter paper 5°C/min, 5 mg - Run 2

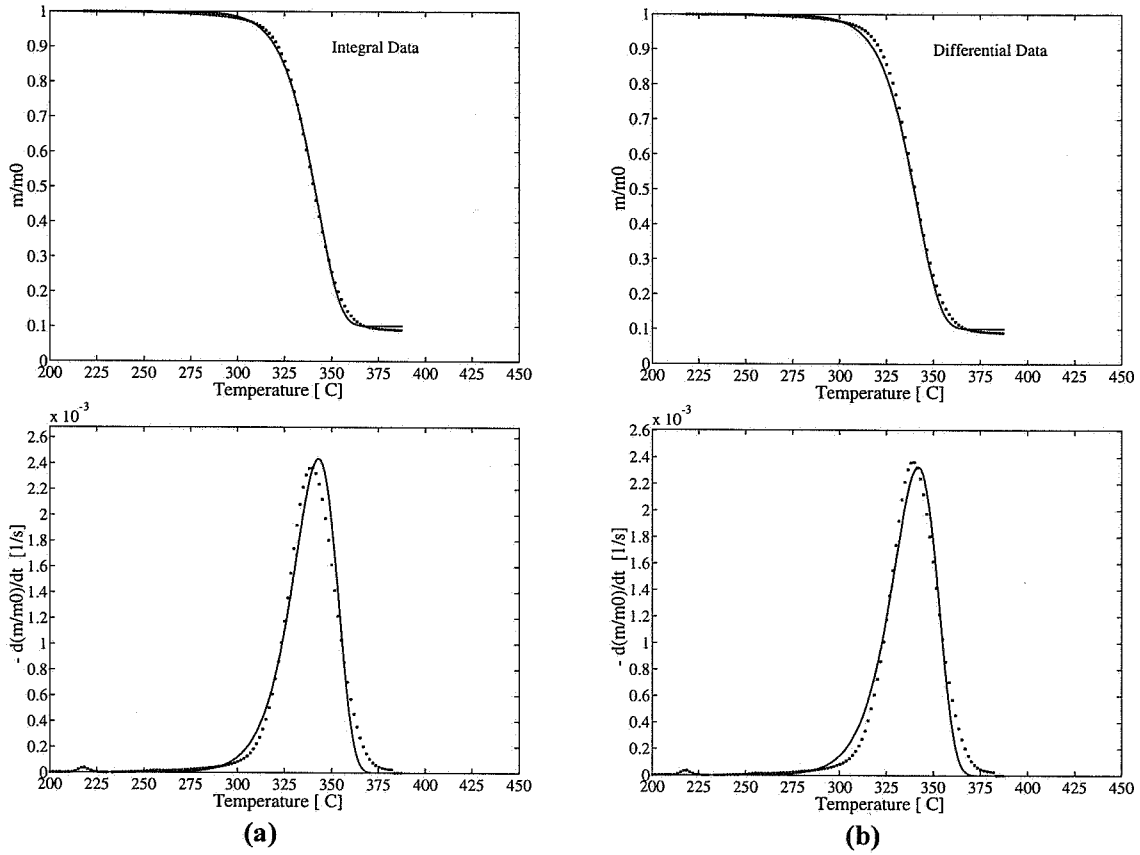

Figure A.19 Kinetic evaluation of Whatman filter paper assuming a single first order reaction. Evaluation methods: (a) Fit of TG curve; (b) fit of DTG curve.

Table A.19 Kinetic parameters for Whatman filter paper evaluated by a single first order reaction.

	first peak	
Evaluated Curve	E_1 [kJ/mol] $\log A_1$ [log s^{-1}] c_1 [%] n	dev1 [%] dev2 [%] $(T_{peak})^{calc}$ $(T_{peak})^{exp}$
TG	271.3 20.86 89.9 1.0	3.6 12.2 342.9 339.9
DTG	258.4 19.78 89.9 1.0	3.1 12.0 341.9 339.9

Birch lignin, one reaction

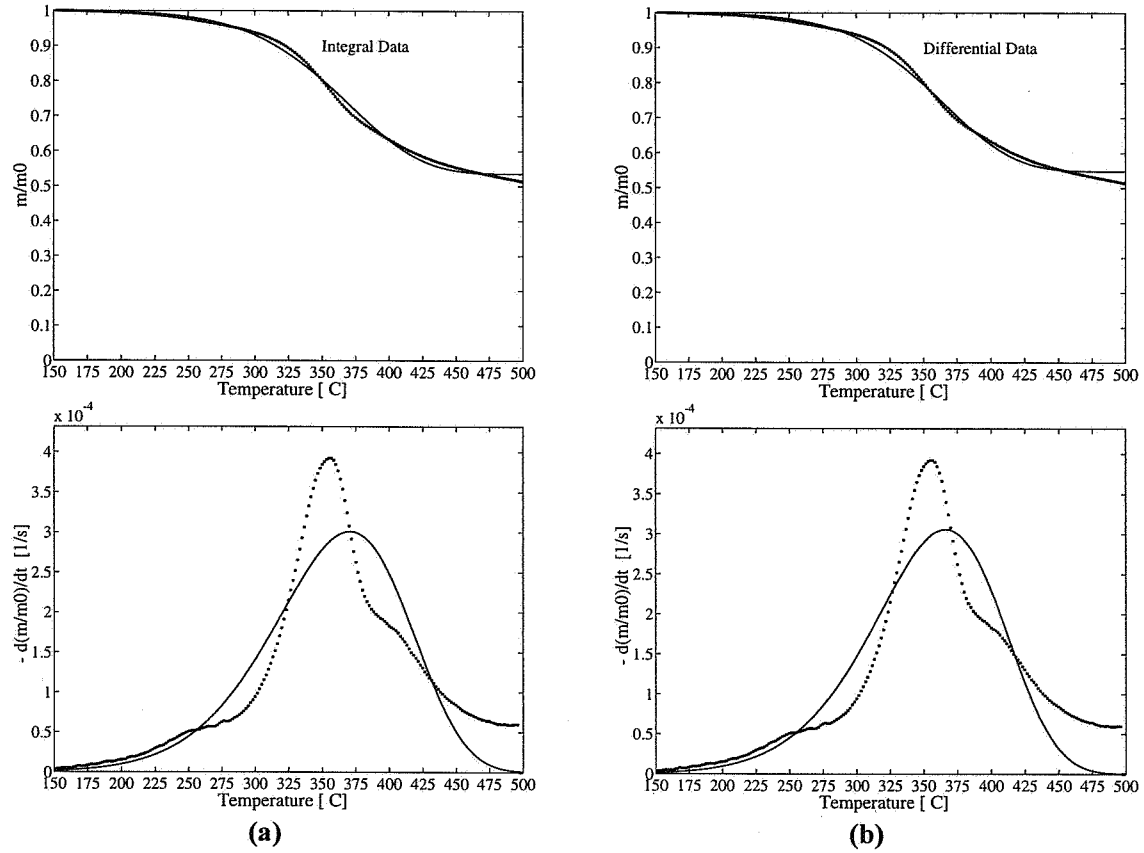

Figure A.20 Kinetic evaluation of birch-lignin assuming a single first order reaction. Evaluation methods: (a) Fit of TG curve; (b) fit of DTG curve.

Table A.20 Kinetic parameters for birch-lignin evaluated by a single first order reaction.

	first peak	
Evaluated Curve	E_1 [kJ/mol]	dev1 [%]
	$\log A_1$ [log s^{-1}]	dev2 [%]
	c_1 [%]	$(T_{peak})^{calc}$
	n	$(T_{peak})^{exp}$
TG	63.4	10.4
	2.33	4.1
	46.5	370.3
	1.0	354.7
DTG	65.5	10.2
	2.56	6.3
	45.3	366.3
	1.0	354.7

Spruce lignin, one reaction

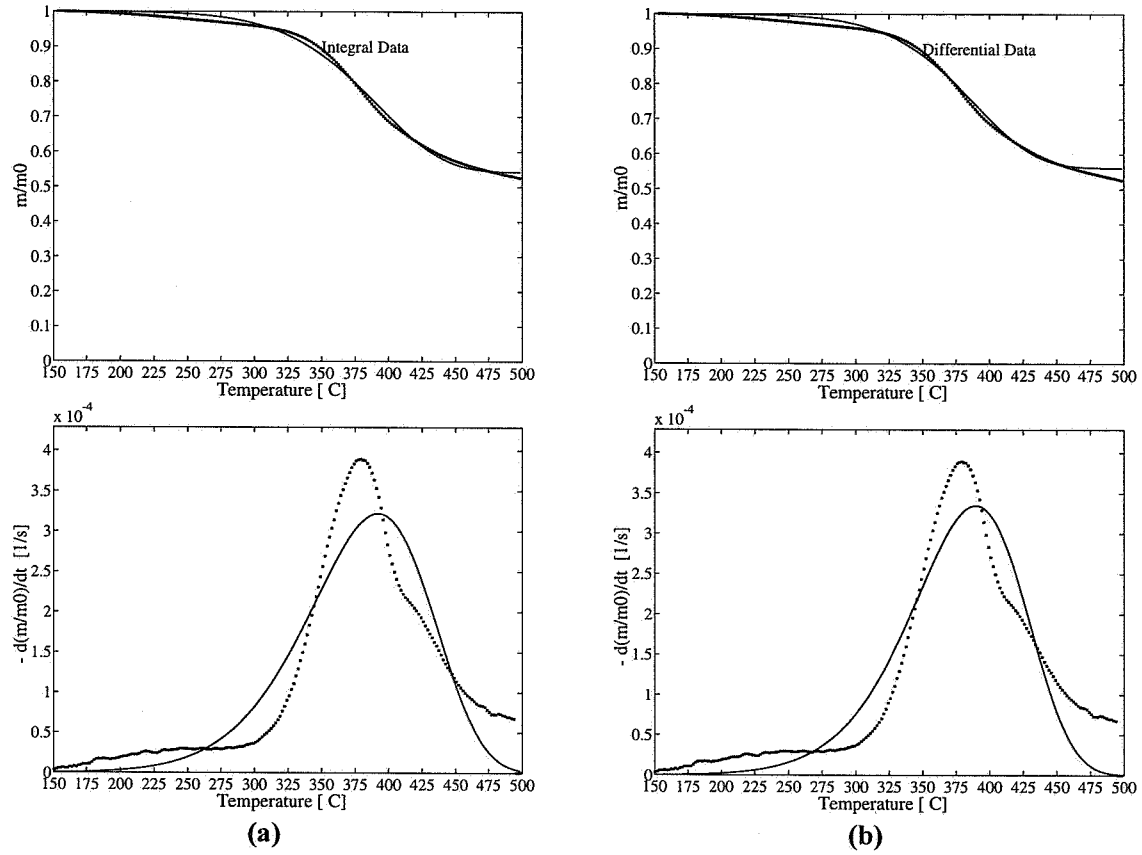

Figure A.21 Kinetic evaluation of spruce-lignin assuming a single first order reaction. Evaluation methods: (a) Fit of TG curve; (b) fit of DTG curve.

Table A.21 Kinetic parameters for spruce-lignin evaluated by a single first order reaction.

	first peak	
Evaluated Curve	E_1 [kJ/mol]	dev1 [%]
	$\log A_1$ [log s^{-1}]	dev2 [%]
	c_1 [%]	$(T_{peak})^{calc}$
	n	$(T_{peak})^{exp}$
TG	74.7	9.6
	3.09	3.1
	45.8	391.5
	1.0	378.1
DTG	80.9	9.4
	3.65	6.3
	43.9	389.5
	1.0	378.1

Birch, one reaction

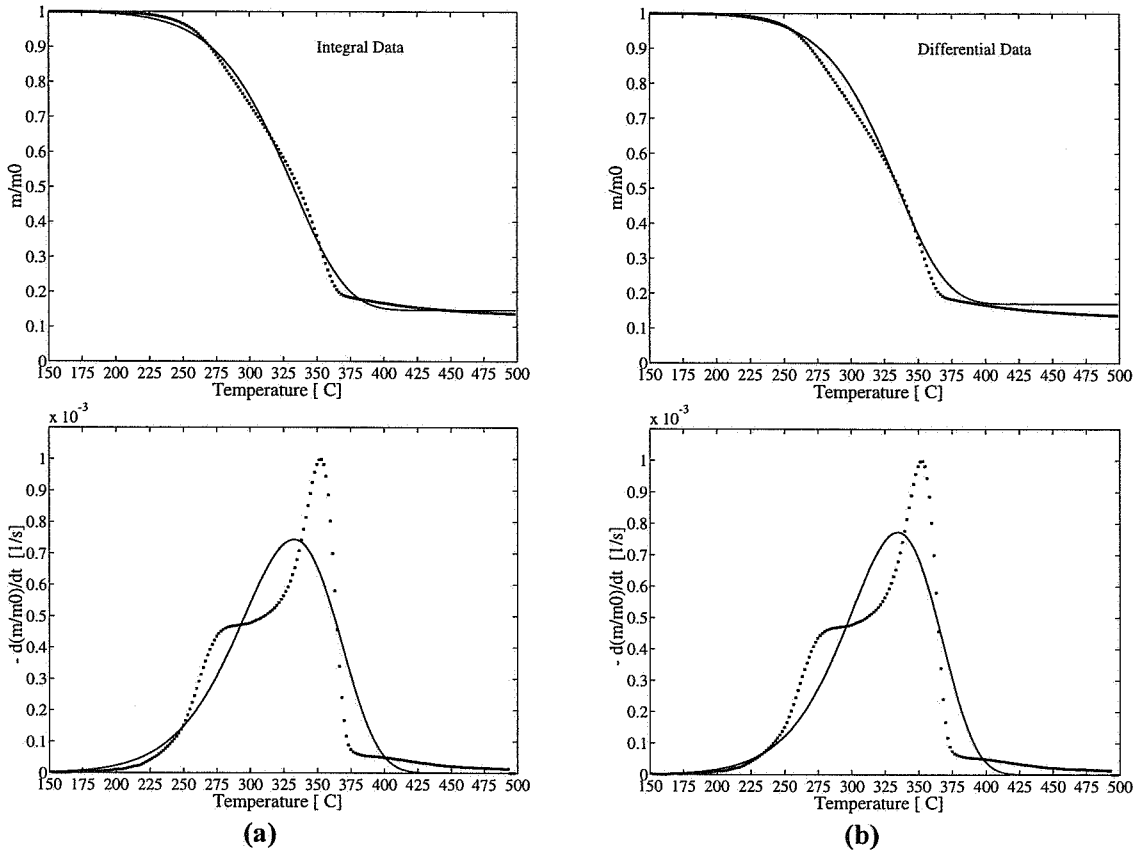

Figure A.22 Kinetic evaluation of birch assuming a single first order reaction. Evaluation methods: (a) Fit of TG curve; (b) fit of DTG curve.

Table A.22 Kinetic parameters for birch evaluated by a single first order reaction.

	first peak	
Evaluated Curve	E_1 [kJ/mol] $\log A_1$ [log s^{-1}] c_1 [%] n	dev1 [%] dev2 [%] $(T_{peak})^{calc}$ $(T_{peak})^{exp}$
TG	77.8 4.03 85.3 1	9.0 6.9 332.5 352.3
DTG	84.2 4.60 83.0 1	9.8 19.9 334.2 352.3

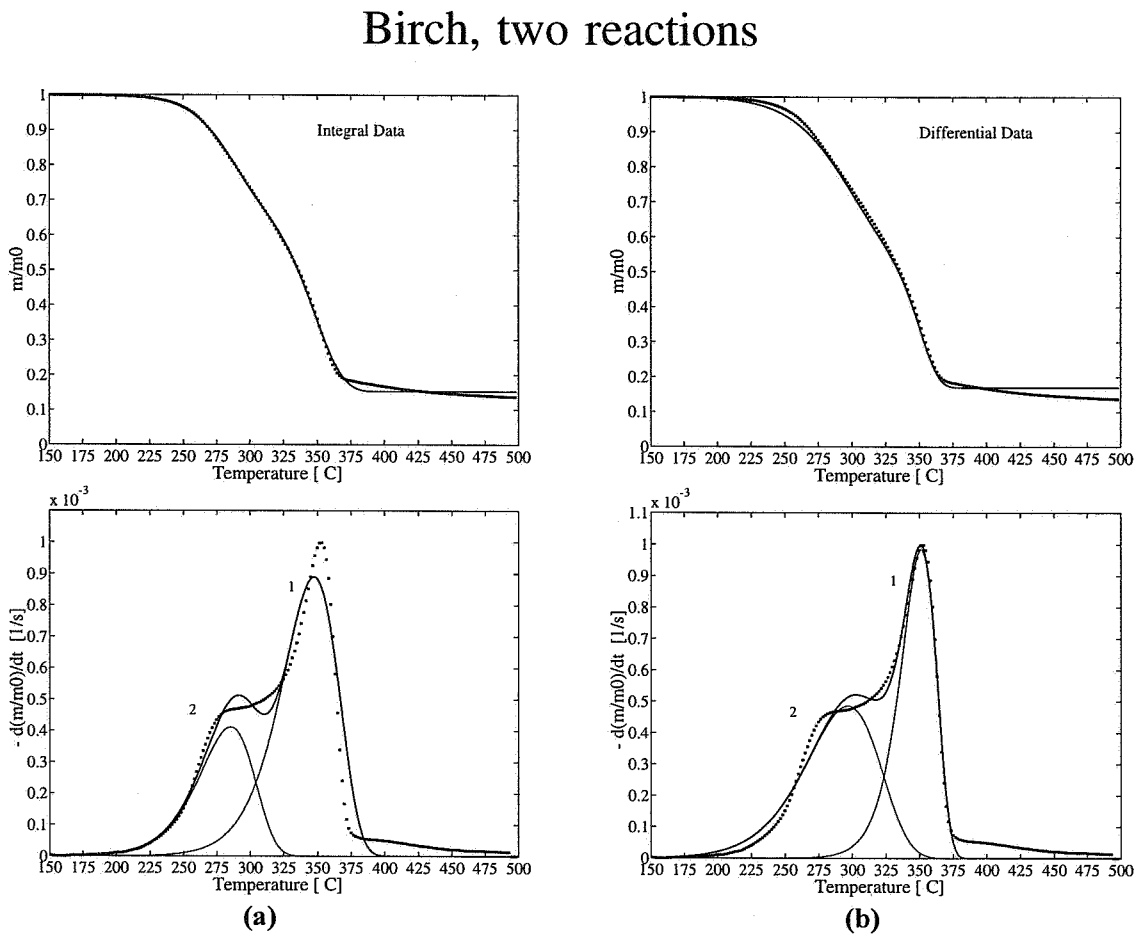

Figure A.23 Kinetic evaluation of birch assuming two independent parallel reactions. Evaluation methods: (a) Fit of TG curve; (b) fit of DTG curve.

Table A.23 Kinetic parameters for birch evaluated by two independent parallel reactions.

	first peak (reaction 2)	second peak (reaction 1)	
Evaluated Curve	E_2 [kJ/mol] $\log A_2$ [log s^{-1}] c_2 [%] $(T_{peak,\,2})^{calc}$	E_1 [kJ/mol] $\log A_1$ [log s^{-1}] c_1 [%] $(T_{peak,\,1})^{calc}$	dev1 [%] dev2 [%] $(T_{peak})^{exp}$
TG	122.2 9.03 26.6 285.2	150.3 10.24 58.2 347.2	5.0 10.3 352.3
DTG	93.7 6.06 41.8 297.2	243.1 18.13 41.3 351.1	2.8 19.5 352.3

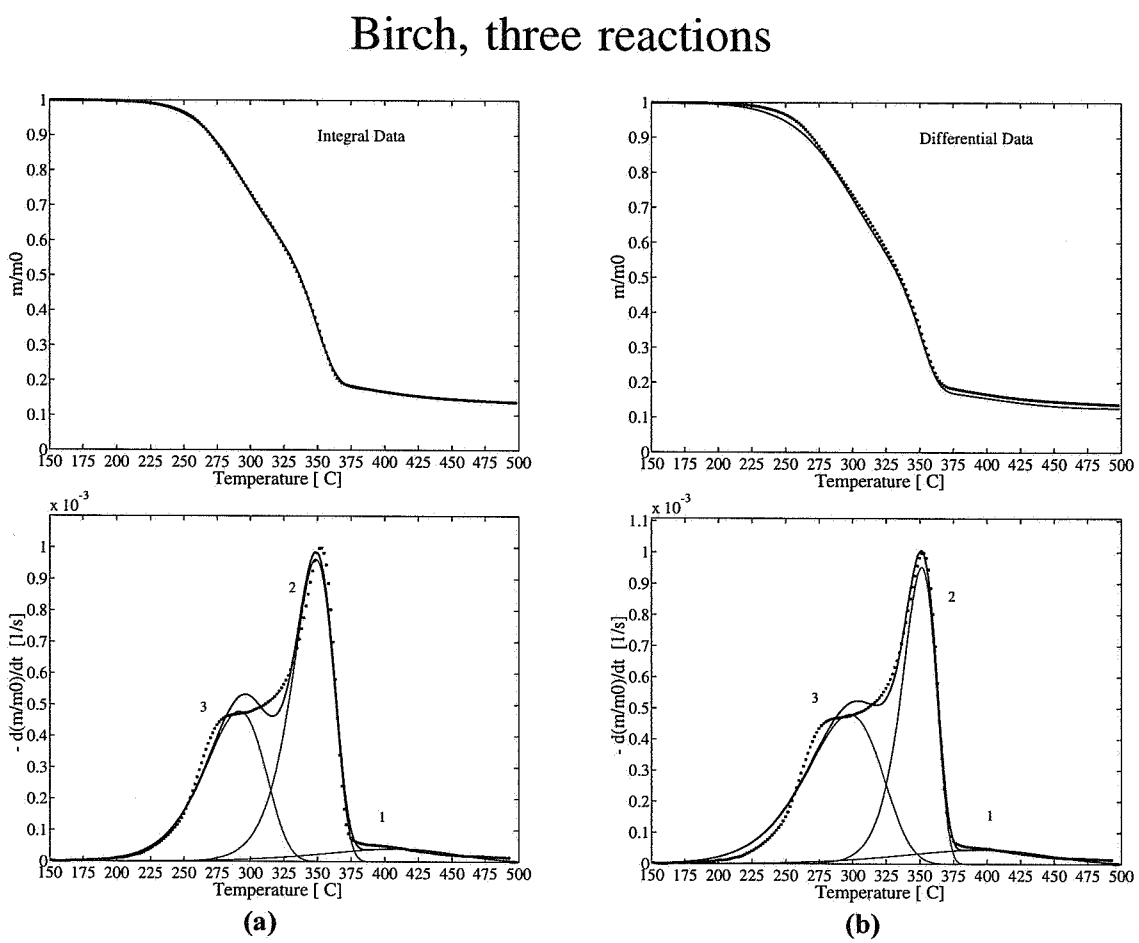

Figure A.24 Kinetic evaluation of birch assuming three independent parallel reactions. Evaluation methods: (a) Fit of TG curve; (b) fit of DTG curve.

Table A.24 Kinetic parameters for birch evaluated by three independent parallel reactions.

	first peak (reaction 3)	second peak (reaction 2)	third peak (reaction 1)	
Evaluated Curve	E_3 [kJ/mol] $\log A_3$ [log s^{-1}] c_3 [%] $(T_{peak,3})^{calc}$	E_2 [kJ/mol] $\log A_2$ [log s^{-1}] c_2 [%] $(T_{peak,2})^{calc}$	E_1 [kJ/mol] $\log A_1$ [log s^{-1}] c_1 [%] $(T_{peak,1})^{calc}$	dev1 [%] dev2 [%] $(T_{peak})^{exp}$
TG	113.2 8.03 33.9 291.2	209.1 15.30 46.3 349.1	75.6 3.01 6.0 408.1	2.8 1.4 352.3
DTG	92.4 5.91 42.0 297.6	256.4 19.26 38.0 351.1	65.6 2.29 7.4 396.2	2.1 7.2 352.3

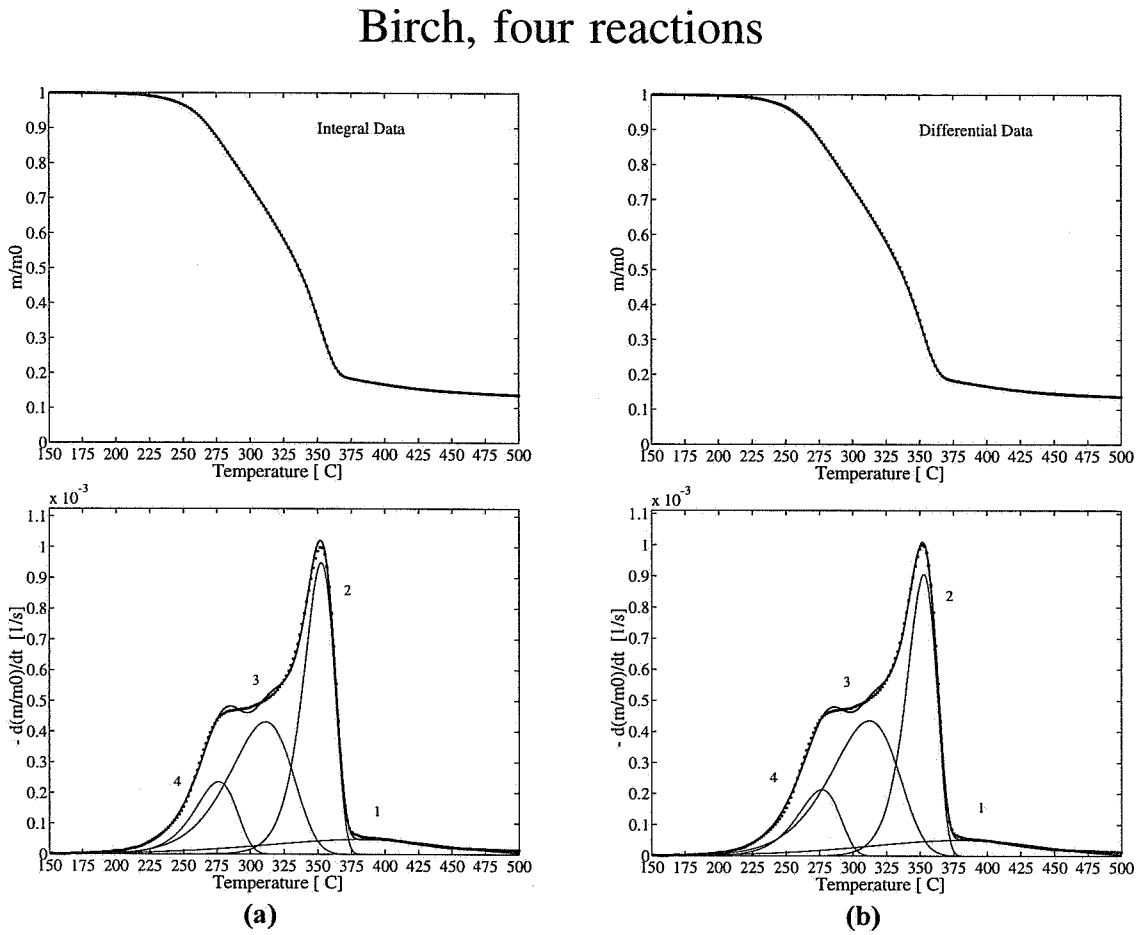

Figure A.25 Kinetic evaluation of birch assuming four independent parallel reactions. Evaluation methods: (a) Fit of TG curve; (b) fit of DTG curve.

Table A.25 Kinetic parameters for birch evaluated by four independent parallel reactions.

	first peak (reaction 4)	second peak (reaction 3)	third peak (reaction 2)	fourth peak (reaction 1)	
Evaluated Curve	E_4 [kJ/mol] $\log A_4$ [log s^{-1}] c_4 [%] $(T_{peak,4})^{calc}$	E_3 [kJ/mol] $\log A_3$ [log s^{-1}] c_3 [%] $(T_{peak,3})^{calc}$	E_2 [kJ/mol] $\log A_2$ [log s^{-1}] c_2 [%] $(T_{peak,2})^{calc}$	E_1 [kJ/mol] $\log A_1$ [log s^{-1}] c_1 [%] $(T_{peak,1})^{calc}$	dev1 [%] dev2 [%] $(T_{peak})^{exp}$
TG	159.2 12.86 11.5 276.2	118.2 8.10 31.4 311.2	287.6 21.88 34.0 352.4	49.9 1.05 9.5 381.2	0.7 1.27 352.3
DTG	159.2 12.85 10.4 276.5	108.2 7.16 34.5 312.2	294.0 22.41 31.8 353.1	50.8 1.14 9.8 380.2	0.6 0.1 352.3

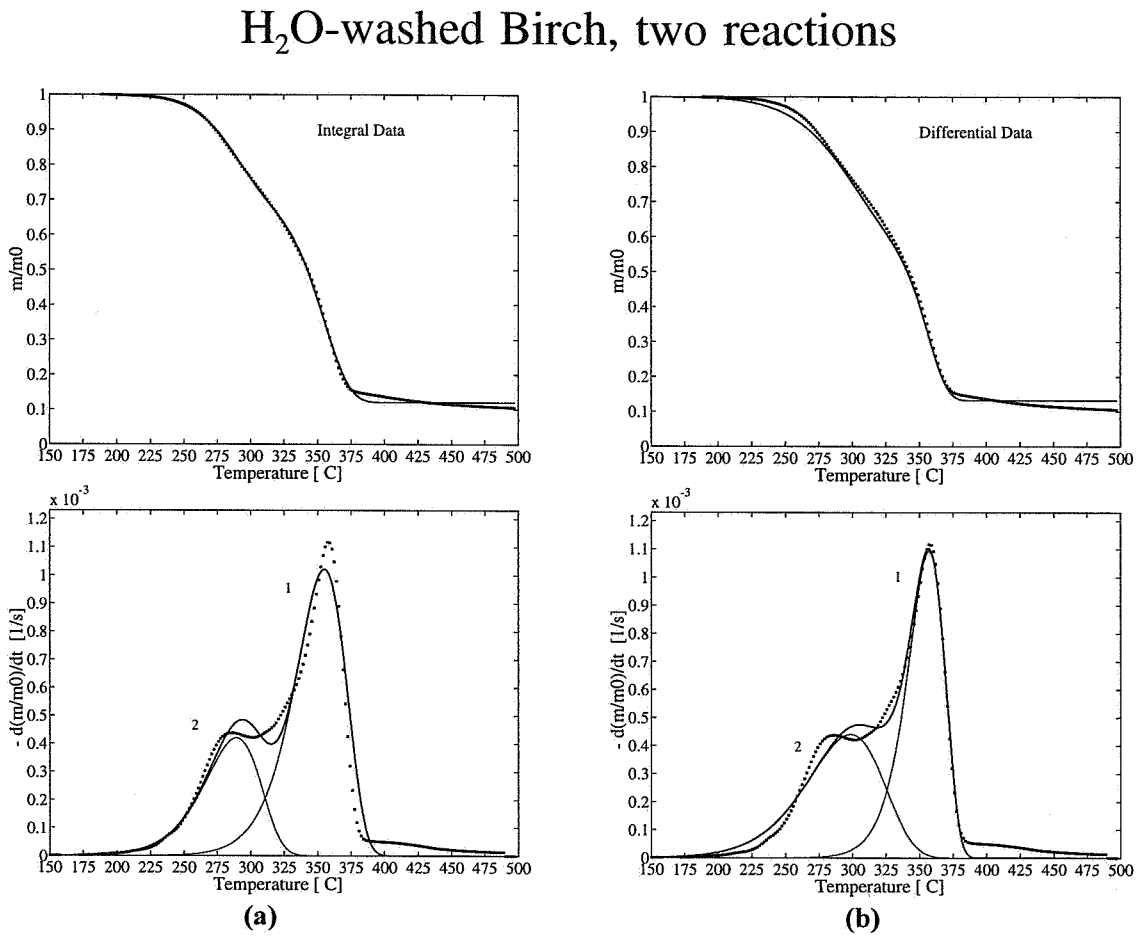

Figure A.26 Kinetic evaluation of H_2O-washed birch assuming two independent parallel reactions. Evaluation methods: (a) Fit of TG curve; (b) fit of DTG curve.

Table A.26 Kinetic parameters for H_2O-washed birch evaluated by two independent parallel reactions.

	first peak (reaction 2)	second peak (reaction 1)	
Evaluated Curve	E_2 [kJ/mol] $\log A_2$ [log s^{-1}] c_2 [%] $(T_{peak,\,2})^{calc}$	E_1 [kJ/mol] $\log A_1$ [log s^{-1}] c_1 [%] $(T_{peak,\,1})^{calc}$	dev1 [%] dev2 [%] $(T_{peak})^{exp}$
TG	122.3 8.95 27.5 289.8	171.4 11.90 60.5 354.7	4.1 12.3 358.5
DTG	91.1 5.78 39.1 298.1	237.6 17.47 47.7 357.7	2.6 20.1 358.5

H_2O-washed Birch, three reactions

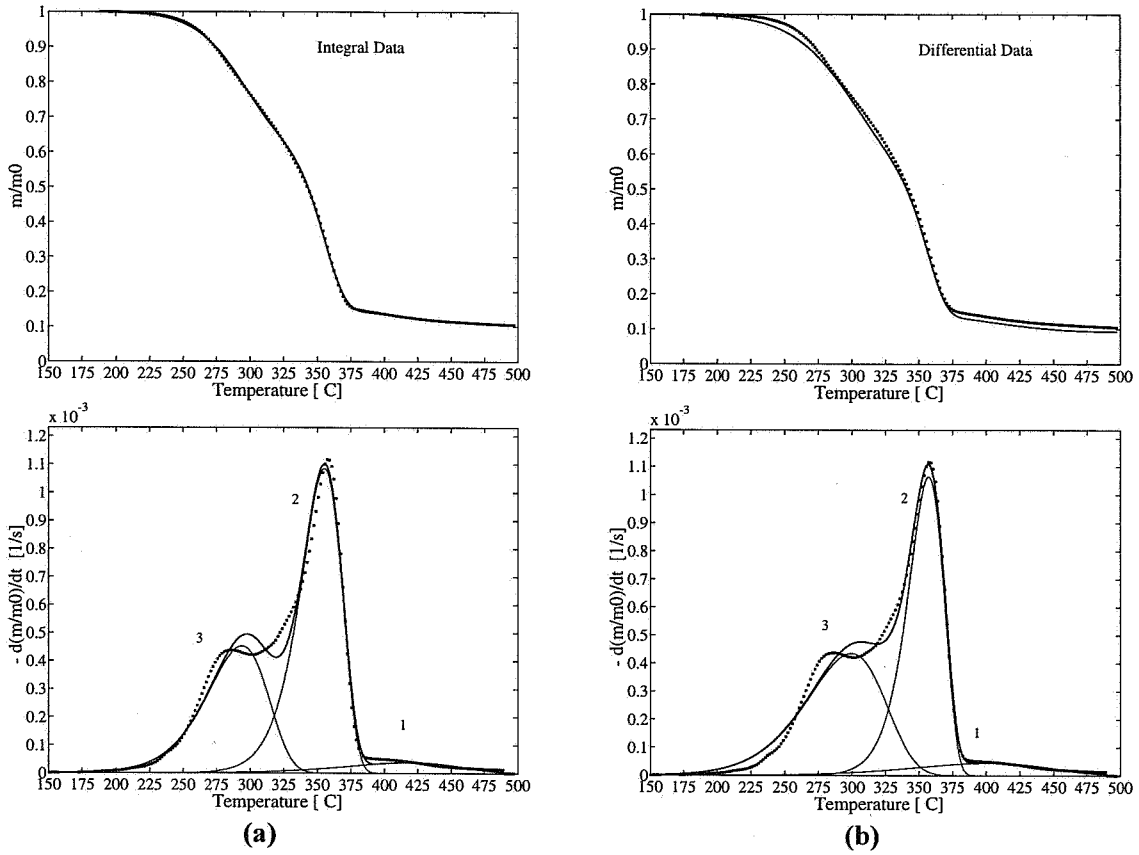

Figure A.27 Kinetic evaluation of H_2O-washed birch assuming three independent parallel reactions. Evaluation methods: (a) Fit of TG curve; (b) fit of DTG curve.

Table A.27 Kinetic parameters for H_2O-washed birch evaluated by three independent parallel reactions.

	first peak (reaction 3)	second peak (reaction 2)	third peak (reaction 1)	
Evaluated Curve	E_3 [kJ/mol] $\log A_3$ [log s^{-1}] c_3 [%] $(T_{peak,3})^{calc}$	E_2 [kJ/mol] $\log A_2$ [log s^{-1}] c_2 [%] $(T_{peak,2})^{calc}$	E_1 [kJ/mol] $\log A_1$ [log s^{-1}] c_1 [%] $(T_{peak,1})^{calc}$	dev1 [%] dev2 [%] $(T_{peak})^{exp}$
TG	114.3 8.09 32.1 293.8	213.0 15.45 52.3 355.7	89.6 4.04 5.0 418.8	2.8 1.5 358.5
DTG	89.7 5.63 39.3 298.8	248.6 18.40 44.5 357.7	70.1 2.62 6.9 400.8	2.1 11.6 358.5

H_2O-washed Birch, four reactions

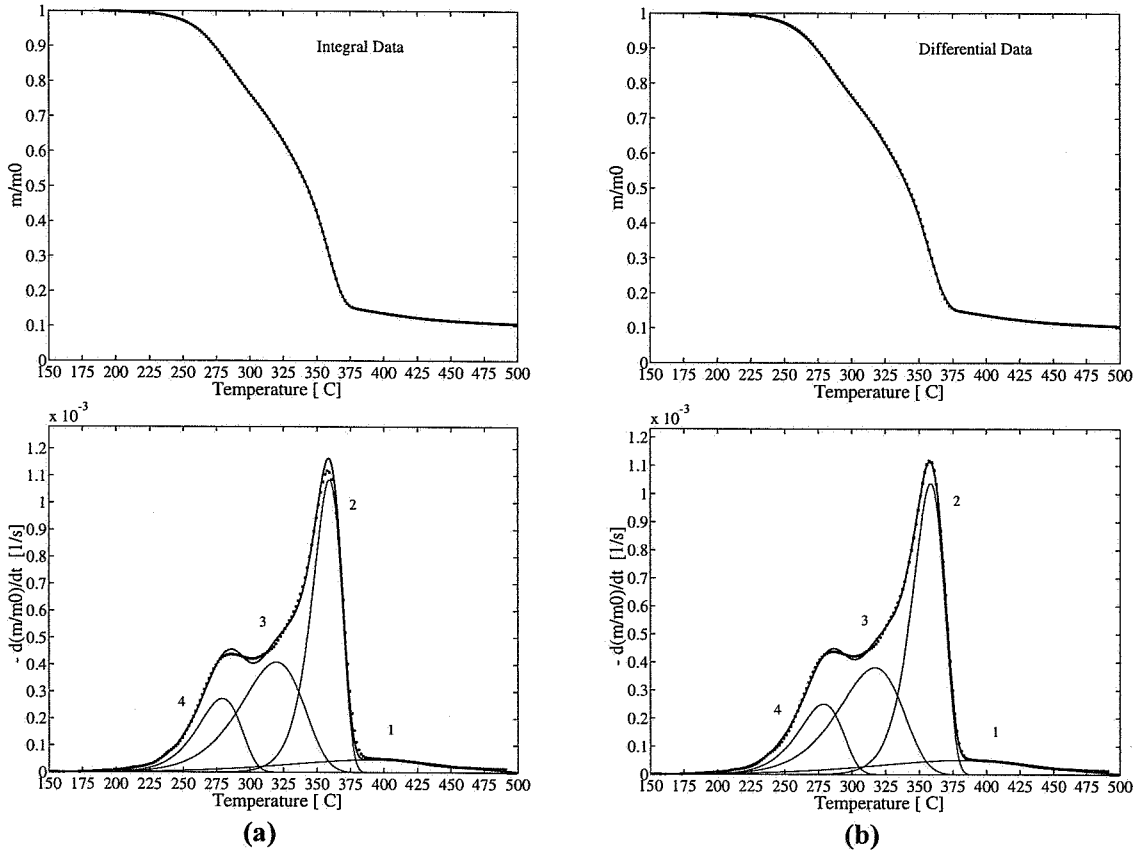

Figure A.28 Kinetic evaluation of H_2O-washed birch assuming four independent parallel reactions. Evaluation methods: (a) Fit of TG curve; (b) fit of DTG curve.

Table A.28 Kinetic parameters for H_2O-washed birch evaluated by four independent parallel reactions.

	first peak (reaction 4)	second peak (reaction 3)	third peak (reaction 2)	fourth peak (reaction 1)	
Evaluated Curve	E_4 [kJ/mol] $\log A_4$ [log s^{-1}] c_4 [%] $(T_{peak,\,4})^{calc}$	E_3 [kJ/mol] $\log A_3$ [log s^{-1}] c_3 [%] $(T_{peak,\,3})^{calc}$	E_2 [kJ/mol] $\log A_2$ [log s^{-1}] c_2 [%] $(T_{peak,\,2})^{calc}$	E_1 [kJ/mol] $\log A_1$ [log s^{-1}] c_1 [%] $(T_{peak,\,1})^{calc}$	dev1 [%] dev2 [%] $(T_{peak})^{exp}$
TG	155.4 12.40 13.8 279.1	121.3 8.23 29.9 319.8	304.7 23.06 37.5 359.0	58.41 1.71 8.2 391.8	1.0 1.5 358.5
DTG	152.3 12.11 12.9 278.8	117.9 7.96 28.4 317.1	279.7 20.98 38.9 358.6	54.2 1.42 9.4 383.8	0.4 0.1 358.5

Spruce - one reaction

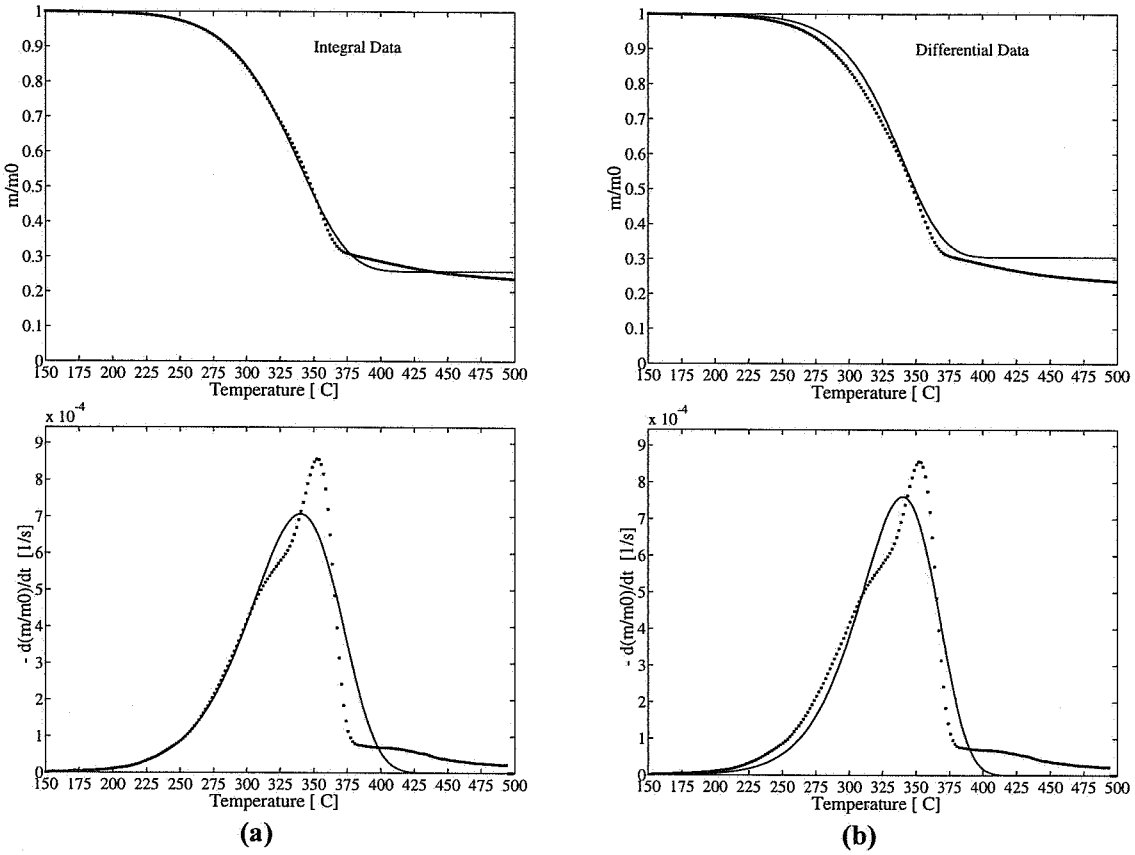

Figure A.29 Kinetic evaluation of spruce assuming a single first order reaction. Evaluation methods: (a) Fit of TG curve; (b) fit of DTG curve.

Table A.29 Kinetic parameters for spruce evaluated by a single first order reaction.

	first peak	
Evaluated Curve	E_1 [kJ/mol] $\log A_1$ [log s^{-1}] c_1 [%] n	dev1 [%] dev2 [%] $(T_{peak})^{calc}$ $(T_{peak})^{exp}$
TG	88.0 4.87 74.3 1	7.3 8.0 340.2 353.5
DTG	102.6 6.18 69.5 1	6.6 22.5 340.2 353.5

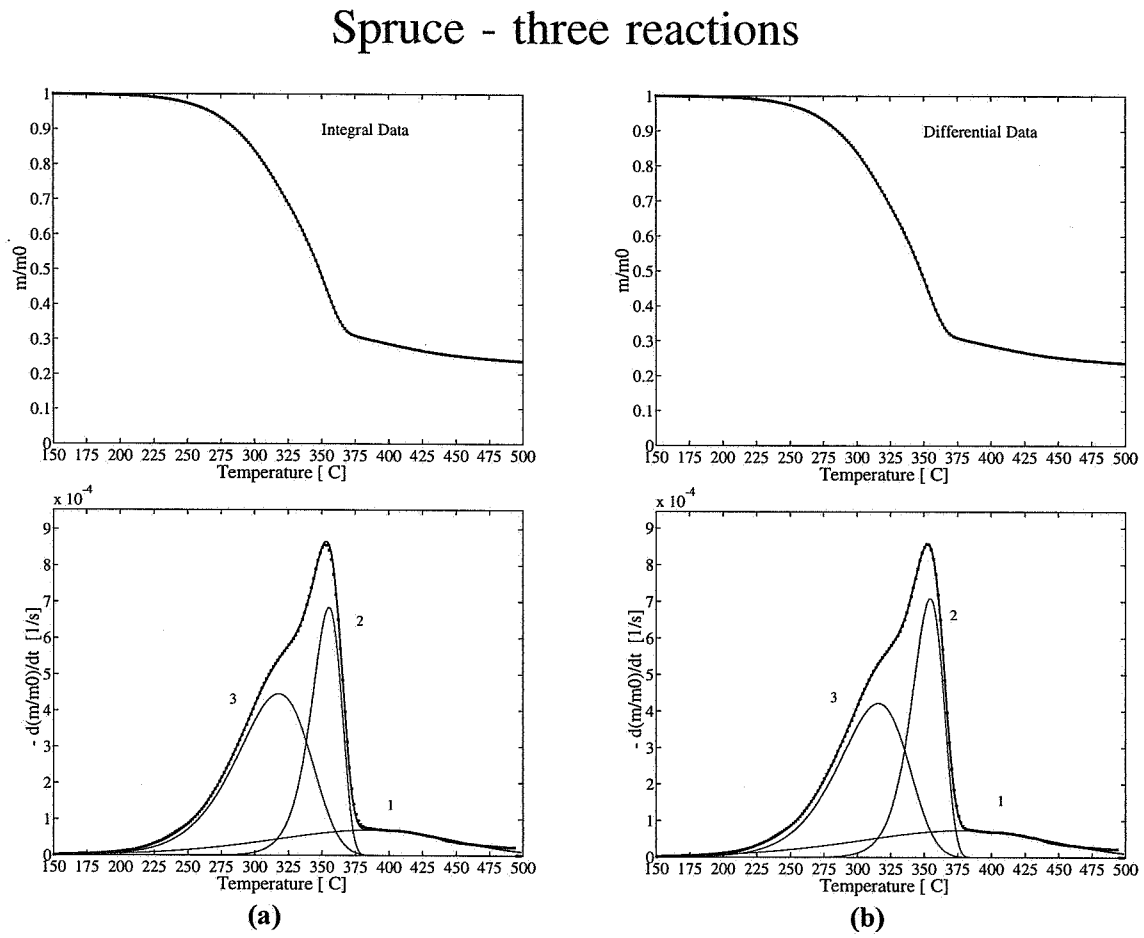

Figure A.30 Kinetic evaluation of spruce assuming three independent parallel reactions. Evaluation methods: (a) Fit of TG curve; (b) fit of DTG curve.

Table A.30 Kinetic parameters for spruce evaluated by three independent parallel reactions.

	first peak (reaction 3)	second peak (reaction 2)	third peak (reaction 1)	
Evaluated Curve	E_3 [kJ/mol] $\log A_3$ [log s^{-1}] c_3 [%] $(T_{peak,3})^{calc}$	E_2 [kJ/mol] $\log A_2$ [log s^{-1}] c_2 [%] $(T_{peak,2})^{calc}$	E_1 [kJ/mol] $\log A_1$ [log s^{-1}] c_1 [%] $(T_{peak,1})^{calc}$	dev1 [%] dev2 [%] $(T_{peak})^{exp}$
TG	102.3 6.51 37.9 317.6	292.9 22.22 24.2 355.2	48.9 0.93 14.2 387.4	0.4 0.7 353.5
DTG	106.9 6.98 34.2 316.3	276.5 20.86 26.2 354.5	44.2 0.56 15.9 378.3	0.3 0.1 353.5

H_2O-washed Spruce, three reactions

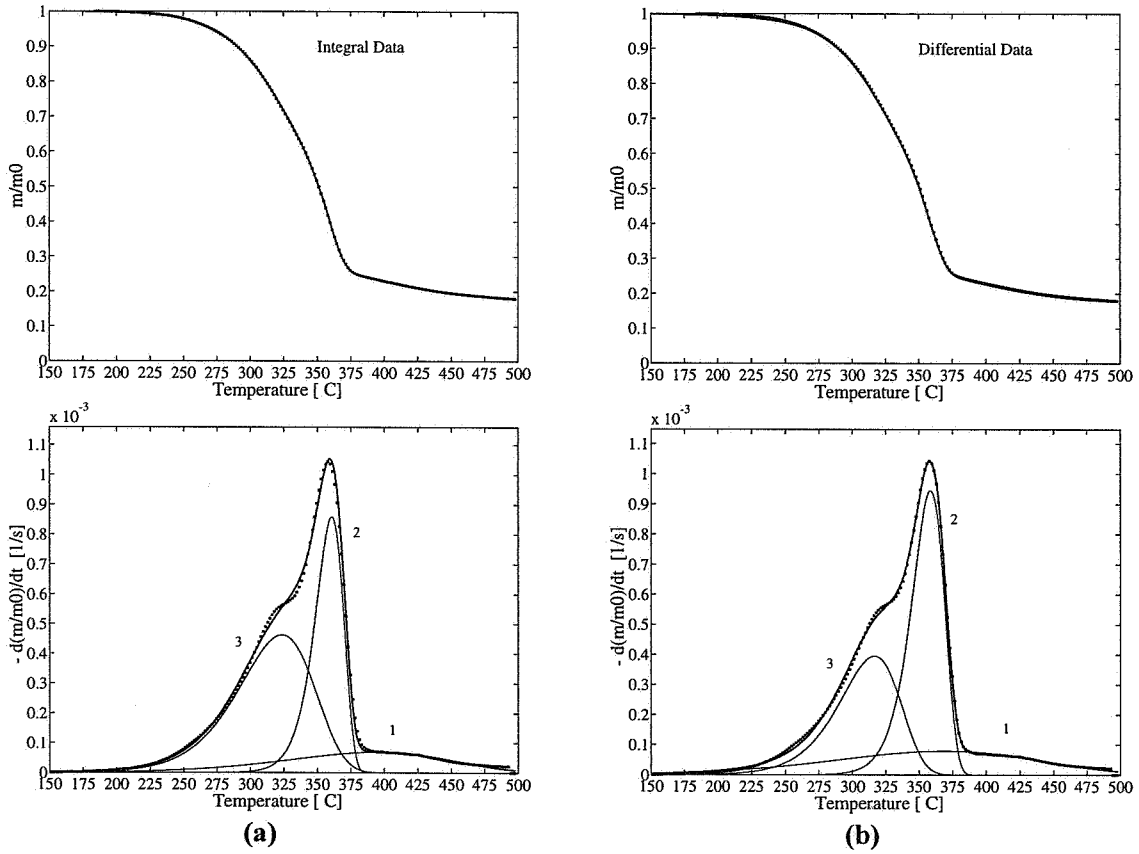

Figure A.31 Kinetic evaluation of H_2O-washed spruce assuming three independent parallel reactions. Evaluation methods: (a) Fit of TG curve; (b) fit of DTG curve.

Table A.31 Kinetic parameters for H_2O-washed spruce, three independent parallel reactions.

	first peak (reaction 3)	second peak (reaction 2)	third peak (reaction 1)	
Evaluated Curve	E_3 [kJ/mol] $\log A_3$ [log s^{-1}] c_3 [%] $(T_{peak,3})^{calc}$	E_2 [kJ/mol] $\log A_2$ [log s^{-1}] c_2 [%] $(T_{peak,2})^{calc}$	E_1 [kJ/mol] $\log A_1$ [log s^{-1}] c_1 [%] $(T_{peak,1})^{calc}$	dev1 [%] dev2 [%] $(T_{peak})^{exp}$
TG	101.1 6.30 40.5 323.3	316.4 23.98 28.8 360.5	56.2 1.49 12.7 394.3	1.0 1.0 357.9
DTG	122.8 8.43 28.3 316.3	273.2 20.43 36.3 358.5	40.0 0.24 18.1 369.2	0.6 1.1 357.9

Pine - one reaction

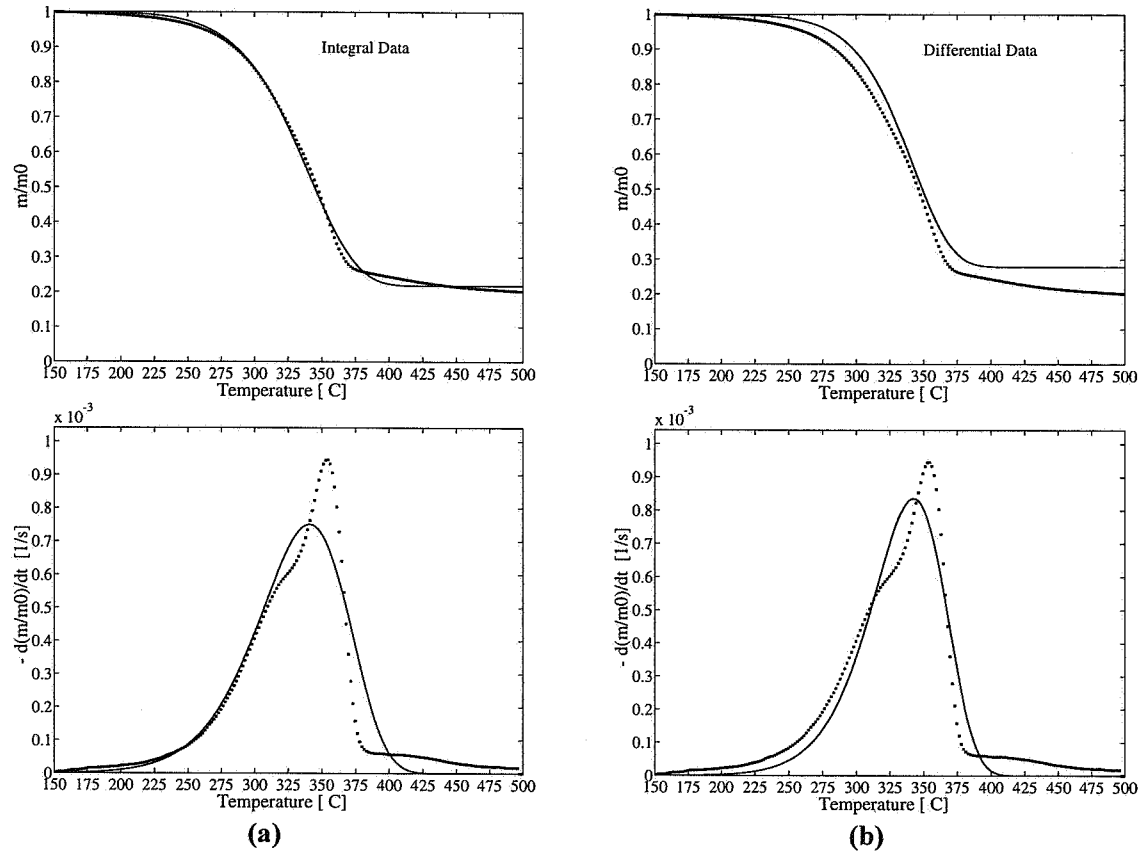

Figure A.32 Kinetic evaluation of pine assuming a single first order reaction. Evaluation methods: (a) Fit of TG curve; (b) fit of DTG curve.

Table A.32 Kinetic parameters for pine evaluated by a single first order reaction.

	first peak	
Evaluated Curve	E_1 [kJ/mol]	dev1 [%]
	$\log A_1$ [log s^{-1}]	dev2 [%]
	c_1 [%]	$(T_{peak})^{calc}$
	n	$(T_{peak})^{exp}$
TG	89.0	7.4
	4.95	7.2
	78.2	340.9
	1	353.5
DTG	110.0	6.4
	6.80	27.7
	72.1	342.9
	1	353.5

Pine - three reactions

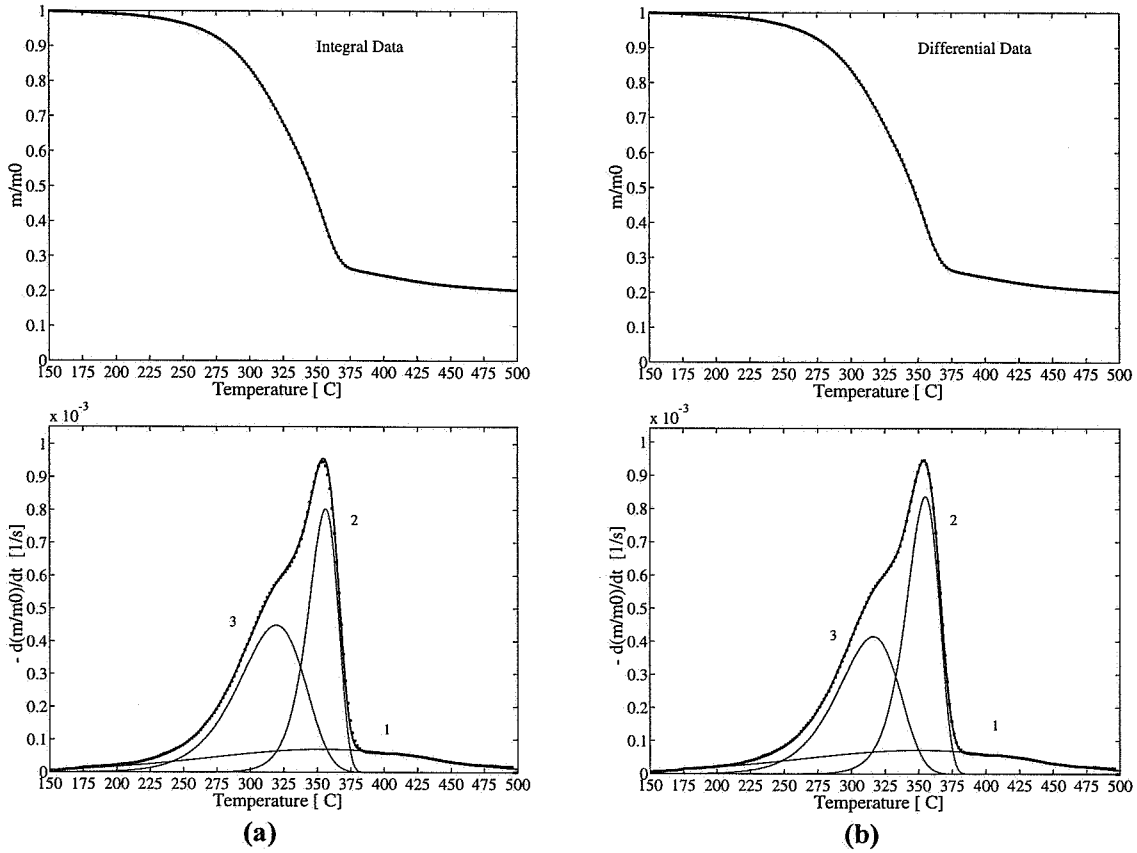

Figure A.33 Kinetic evaluation of pine assuming three independent parallel reactions. Evaluation methods: (a) Fit of TG curve; (b) fit of DTG curve.

Table A.33 Kinetic parameters for pine evaluated by three independent parallel reactions.

	first peak (reaction 3)	second peak (reaction 2)	third peak (reaction 1)	
Evaluated Curve	E_3 [kJ/mol] $\log A_3$ [log s^{-1}] c_3 [%] $(T_{peak,3})^{calc}$	E_2 [kJ/mol] $\log A_2$ [log s^{-1}] c_2 [%] $(T_{peak,2})^{calc}$	E_1 [kJ/mol] $\log A_1$ [log s^{-1}] c_1 [%] $(T_{peak,1})^{calc}$	dev1 [%] dev2 [%] $(T_{peak})^{exp}$
TG	115.3 7.68 34.3 319.3	295.0 22.36 28.3 356.2	34.2 -0.21 17.5 354.8	0.5 0.4 353.5
DTG	122.7 8.42 29.6 316.0	267.8 20.10 32.3 354.8	32.8 -0.32 18.3 349.8	0.3 0.1 353.5

H_2O-washed Pine, three reactions

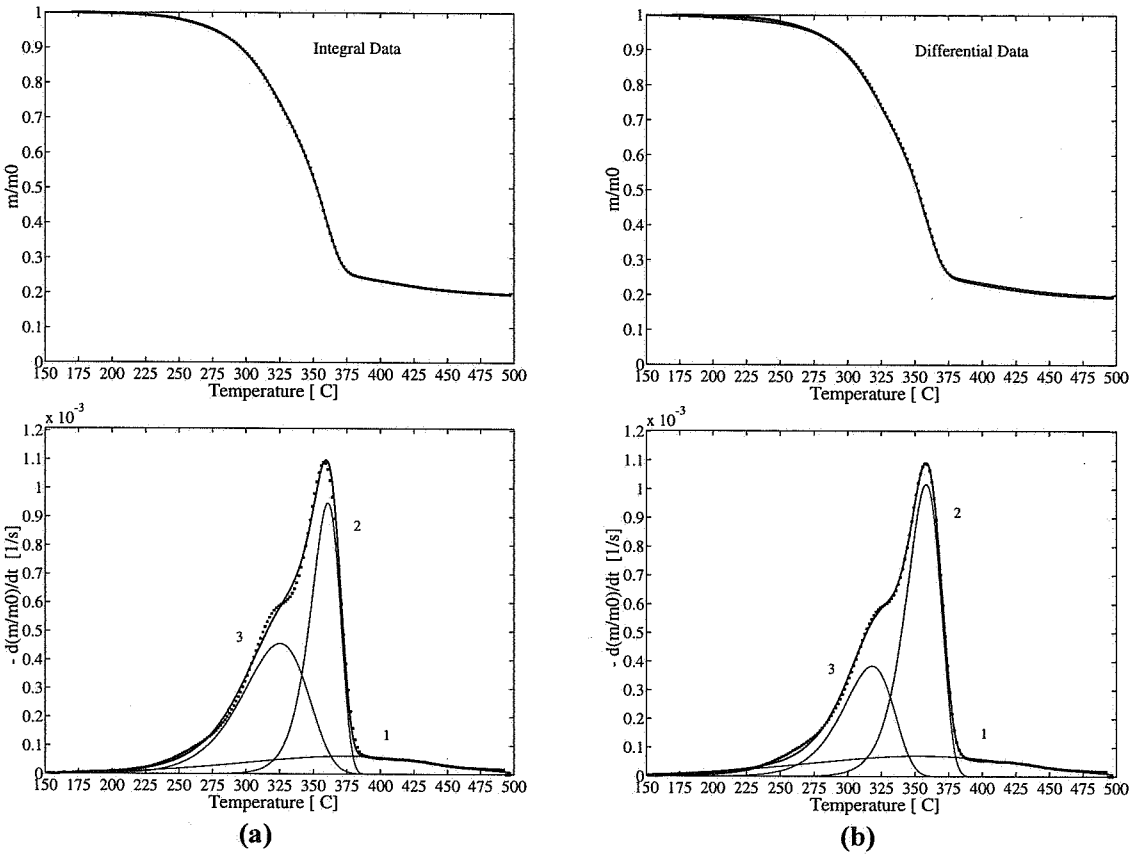

Figure A.34 Kinetic evaluation of H_2O-washed pine assuming three independent parallel reactions. Evaluation methods: (a) Fit of TG curve; (b) fit of DTG curve.

Table A.34 Kinetic parameters for H_2O-washed pine, three independent parallel reactions.

	first peak (reaction 3)	second peak (reaction 2)	third peak (reaction 1)	
Evaluated Curve	E_3 [kJ/mol] $\log A_3$ [log s^{-1}] c_3 [%] $(T_{peak,3})^{calc}$	E_2 [kJ/mol] $\log A_2$ [log s^{-1}] c_2 [%] $(T_{peak,2})^{calc}$	E_1 [kJ/mol] $\log A_1$ [log s^{-1}] c_1 [%] $(T_{peak,1})^{calc}$	dev1 [%] dev2 [%] $(T_{peak})^{exp}$
TG	119.7 7.97 34.4 325.0	305.9 23.10 32.8 360.8	43.9 0.57 13.4 375.3	1.1 0.7 357.9
DTG	150.3 10.91 22.9 318.0	257.5 19.12 41.2 358.2	36.2 -0.01 16.9 352.9	0.6 1.5 357.9

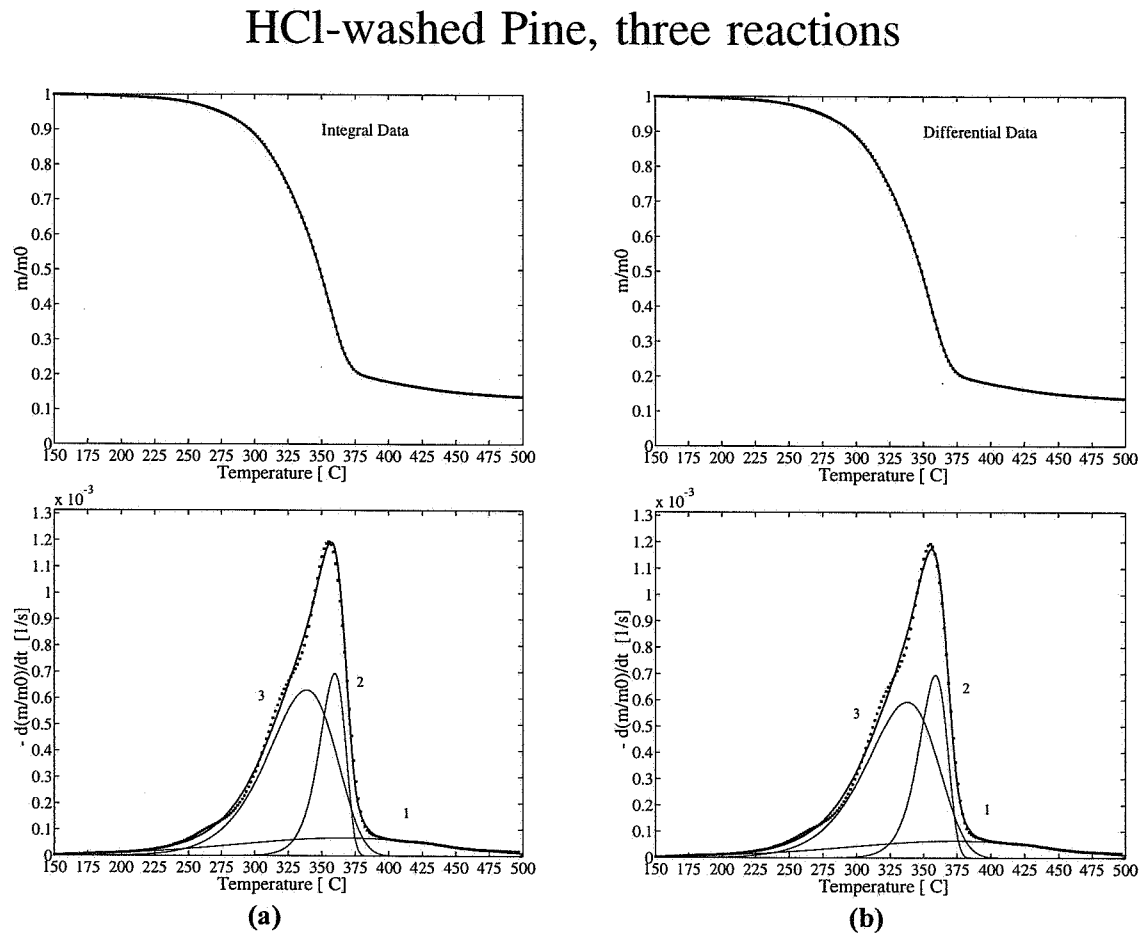

Figure A.35 Kinetic evaluation of HCl-washed pine assuming three independent parallel reactions. Evaluation methods: (a) Fit of TG curve; (b) fit of DTG curve.

Table A.35 Kinetic parameters for HCl-washed pine, three independent parallel reactions.

	first peak (reaction 3)	second peak (reaction 2)	third peak (reaction 1)	
Evaluated Curve	E_3 [kJ/mol] $\log A_3$ [log s^{-1}] c_3 [%] $(T_{peak,3})^{calc}$	E_2 [kJ/mol] $\log A_2$ [log s^{-1}] c_2 [%] $(T_{peak,2})^{calc}$	E_1 [kJ/mol] $\log A_1$ [log s^{-1}] c_1 [%] $(T_{peak,1})^{calc}$	dev1 [%] dev2 [%] $(T_{peak})^{exp}$
TG	119.1 7.68 50.0 338.4	352.3 27.04 20.8 359.6	39.2 0.18 15.8 368.4	1.2 0.8 355.1
DTG	114.0 7.23 48.8 357.7	318.8 24.26 23.0 359.3	40.2 0.24 14.8 373.4	1.0 1.0 355.1

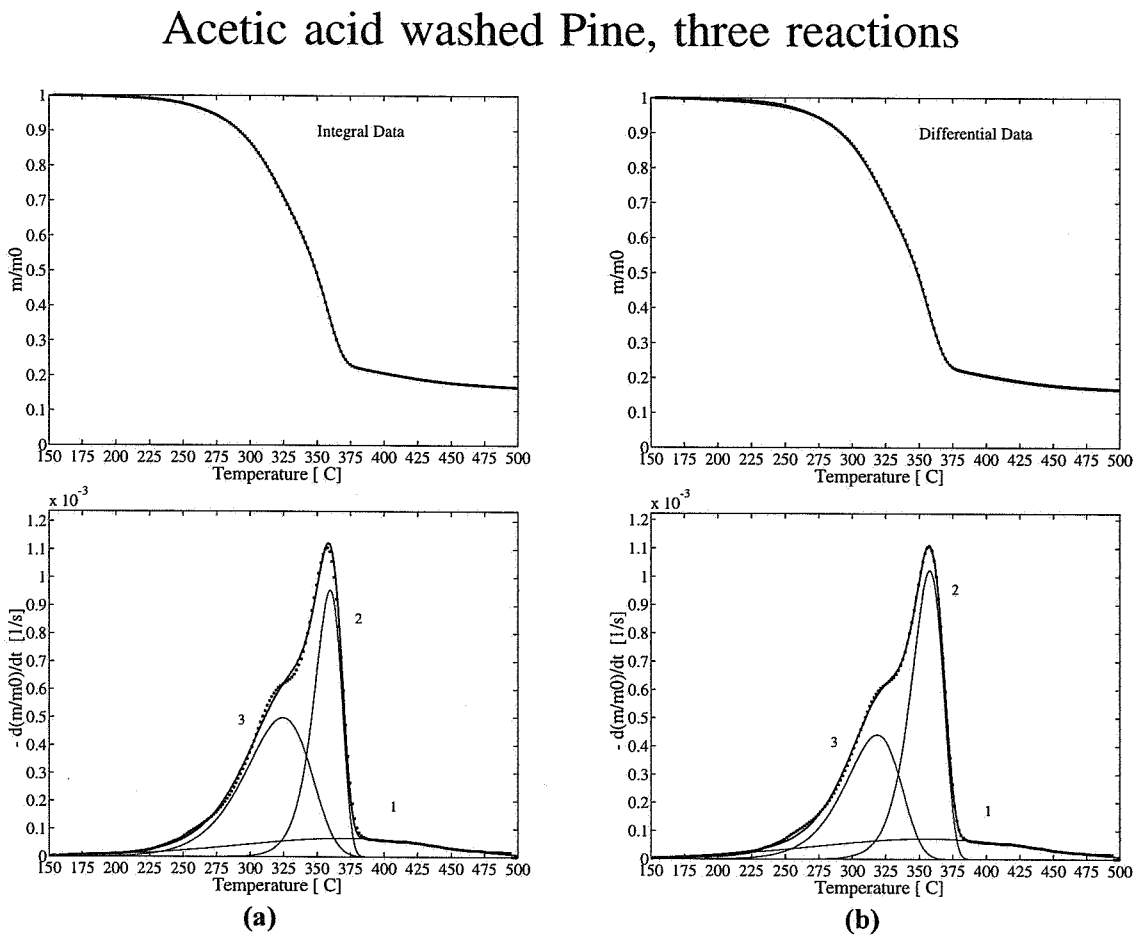

Figure A.36 Kinetic evaluation of acetic acid-washed pine assuming three independent parallel reactions. Evaluation methods: (a) Fit of TG curve; (b) fit of DTG curve.

Table A.36 Kinetic parameters for acetic acid-washed pine, three independent parallel reactions.

	first peak (reaction 3)	second peak (reaction 2)	third peak (reaction 1)	
Evaluated Curve	E_3 [kJ/mol] $\log A_3$ [log s^{-1}] c_3 [%] $(T_{peak,3})^{calc}$	E_2 [kJ/mol] $\log A_2$ [log s^{-1}] c_2 [%] $(T_{peak,2})^{calc}$	E_1 [kJ/mol] $\log A_1$ [log s^{-1}] c_1 [%] $(T_{peak,1})^{calc}$	dev1 [%] dev2 [%] $(T_{peak})^{exp}$
TG	118.4 7.87 37.8 324.2	326.9 24.90 30.9 359.7	41.6 0.39 14.7 370.2	0.9 0.7 357.4
DTG	137.9 9.78 28.4 318.6	280.8 21.09 38.1 358.1	36.3 -0.02 17.2 355.1	0.5 1.1 357.4

Pineroot - one reaction

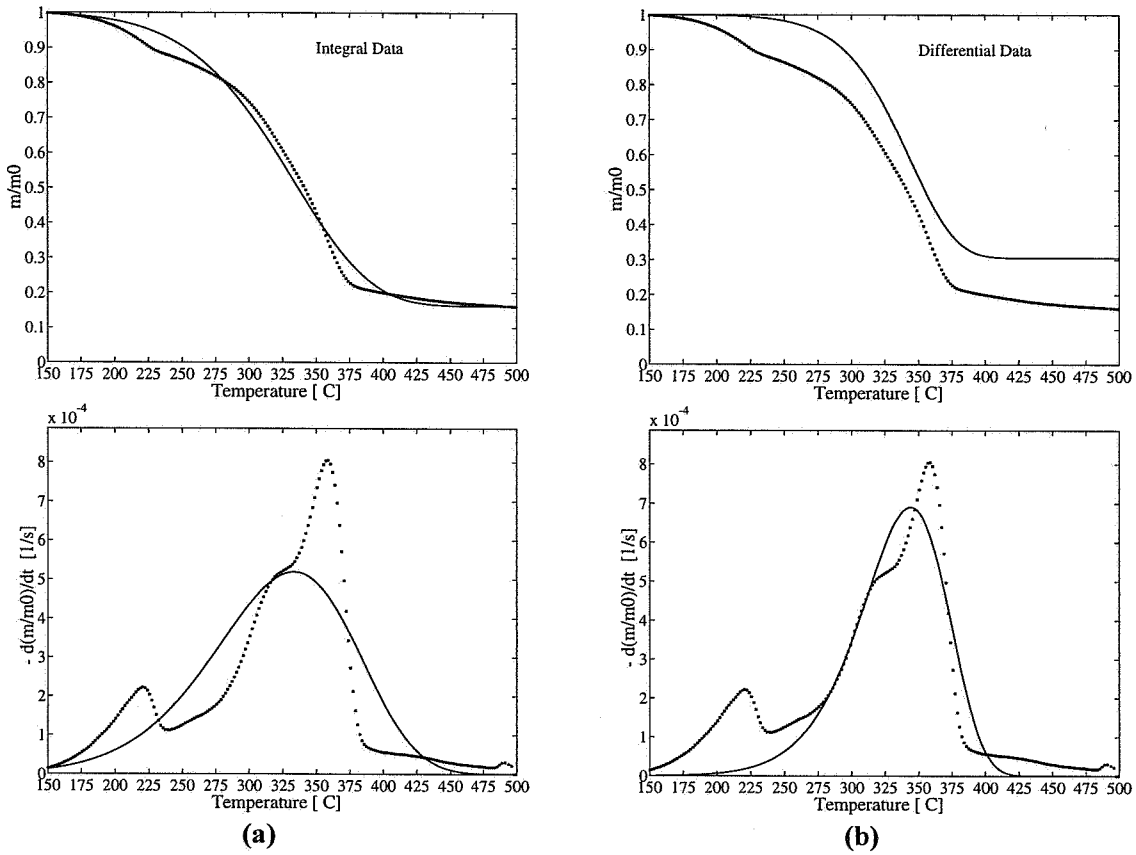

Figure A.37 Kinetic evaluation of pineroot assuming a single first order reaction. Evaluation methods: (a) Fit of TG curve; (b) fit of DTG curve.

Table A.37 Kinetic parameters for pineroot evaluated by a single first order reaction.

	first peak	
Evaluated Curve	E_1 [kJ/mol] $\log A_1$ [log s^{-1}] c_1 [%] n	dev1 [%] dev2 [%] $(T_{peak})^{calc}$ $(T_{peak})^{exp}$
TG	53.1 1.73 83.8 1	12.9 1.9 332.9 358.9
DTG	93.5 5.31 69.4 1	9.9 48.1 344.6 358.9

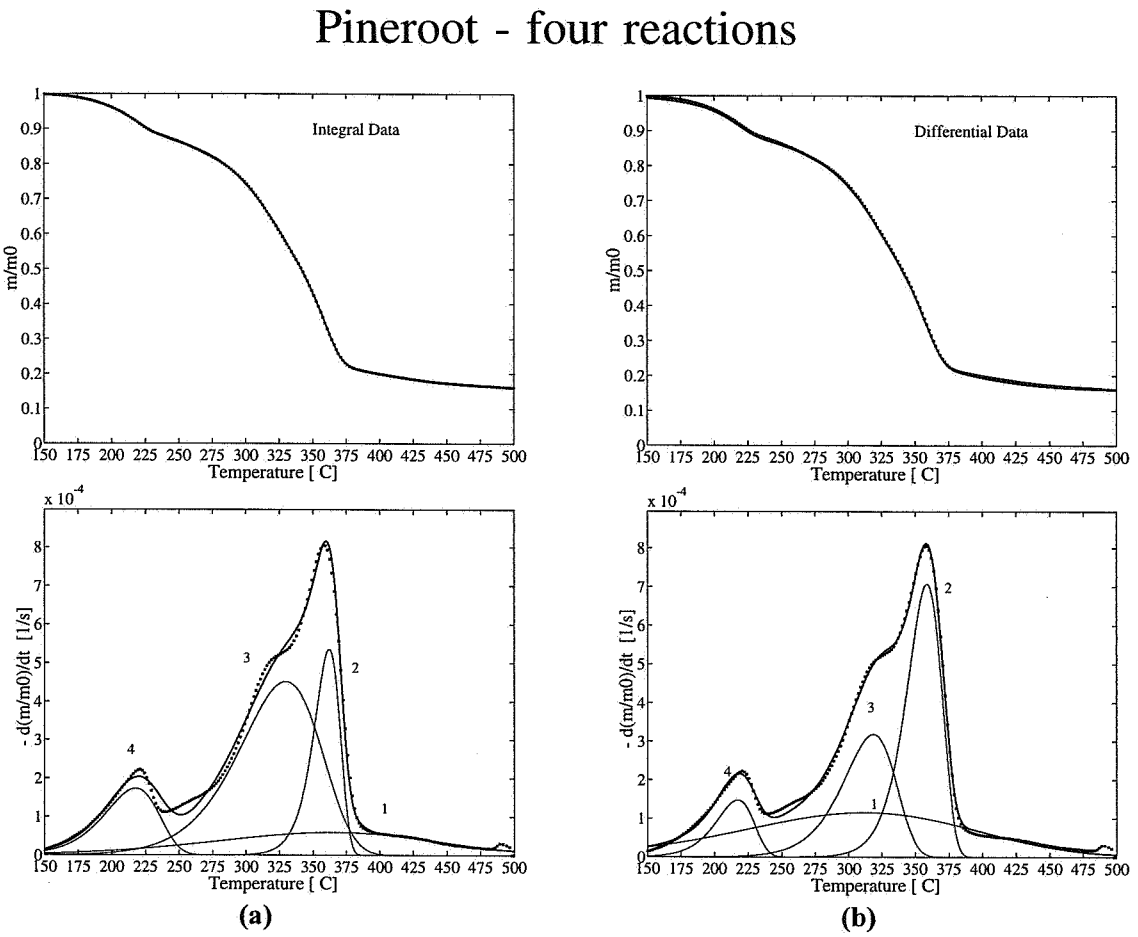

Figure A.38 Kinetic evaluation of pineroot assuming four independent parallel reactions. Evaluation methods: (a) Fit of TG curve; (b) fit of DTG curve.

Table A.38 Kinetic parameters for pineroot evaluated by four independent parallel reactions.

	first peak (reaction 4)	second peak (reaction 3)	third peak (reaction 2)	fourth peak (reaction 1)	
Evaluated Curve	E_4 [kJ/mol] $\log A_4$ [log s^{-1}] c_4 [%] $(T_{peak,4})^{calc}$	E_3 [kJ/mol] $\log A_3$ [log s^{-1}] c_3 [%] $(T_{peak,3})^{calc}$	E_2 [kJ/mol] $\log A_2$ [log s^{-1}] c_2 [%] $(T_{peak,2})^{calc}$	E_1 [kJ/mol] $\log A_1$ [log s^{-1}] c_1 [%] $(T_{peak,1})^{calc}$	dev1 [%] dev2 [%] $(T_{peak})^{exp}$
TG	96.8 7.91 10.8 217.6	95.5 5.70 42.5 329.6	344.5 26.26 16.5 362.2	36.6 -0.05 14.4 365.6	1.6 0.9 358.9
DTG	139.6 12.64 6.5 217.6	144.3 10.36 19.7 318.6	254.3 18.83 29.0 358.5	28.6 -0.52 29.0 311.6	1.1 0.1 358.9

H_2O-washed Pineroot, four reactions

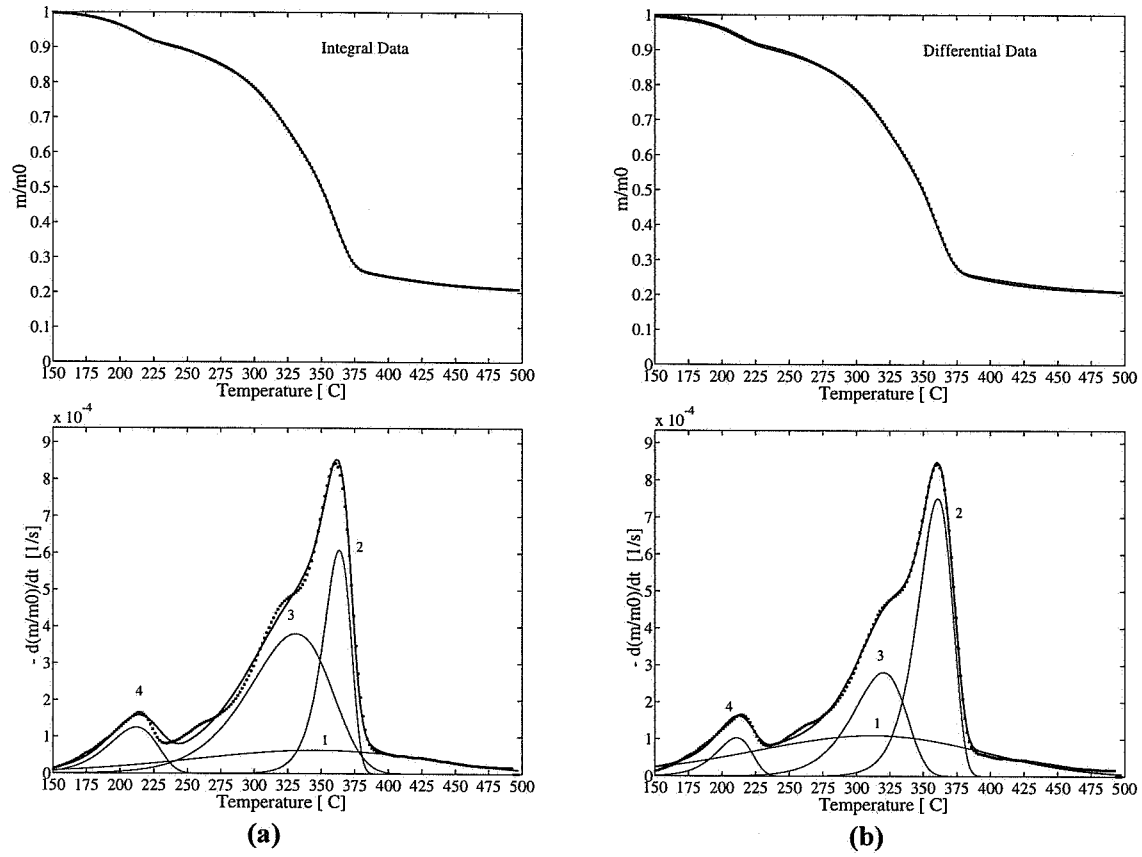

Figure A.39 Kinetic evaluation of H_2O-washed pineroot assuming four independent parallel reactions. Evaluation methods: (a) Fit of TG curve; (b) fit of DTG curve.

Table A.39 Kinetic parameters for H_2O-washed pineroot, four independent parallel reactions.

	first peak (reaction 4)	second peak (reaction 3)	third peak (reaction 2)	fourth peak (reaction 1)	
Evaluated Curve	E_4 [kJ/mol] $\log A_4$ [log s^{-1}] c_4 [%] $(T_{peak,4})^{calc}$	E_3 [kJ/mol] $\log A_3$ [log s^{-1}] c_3 [%] $(T_{peak,3})^{calc}$	E_2 [kJ/mol] $\log A_2$ [log s^{-1}] c_2 [%] $(T_{peak,2})^{calc}$	E_1 [kJ/mol] $\log A_1$ [log s^{-1}] c_1 [%] $(T_{peak,1})^{calc}$	dev1 [%] dev2 [%] $(T_{peak})^{exp}$
TG	106.4 9.11 7.0 212.3	95.5 5.67 36.0 330.7	327.7 24.80 19.8 363.6	31.3 -0.45 16.6 345.7	1.3 0.4 360.9
DTG	145.8 13.53 4.3 210.6	145.1 10.39 17.4 320.7	261.4 19.35 30.2 360.6	28.8 -0.50 27.4 312.7	0.9 0.0 360.9

H_2O-washed Pineroot, five reactions

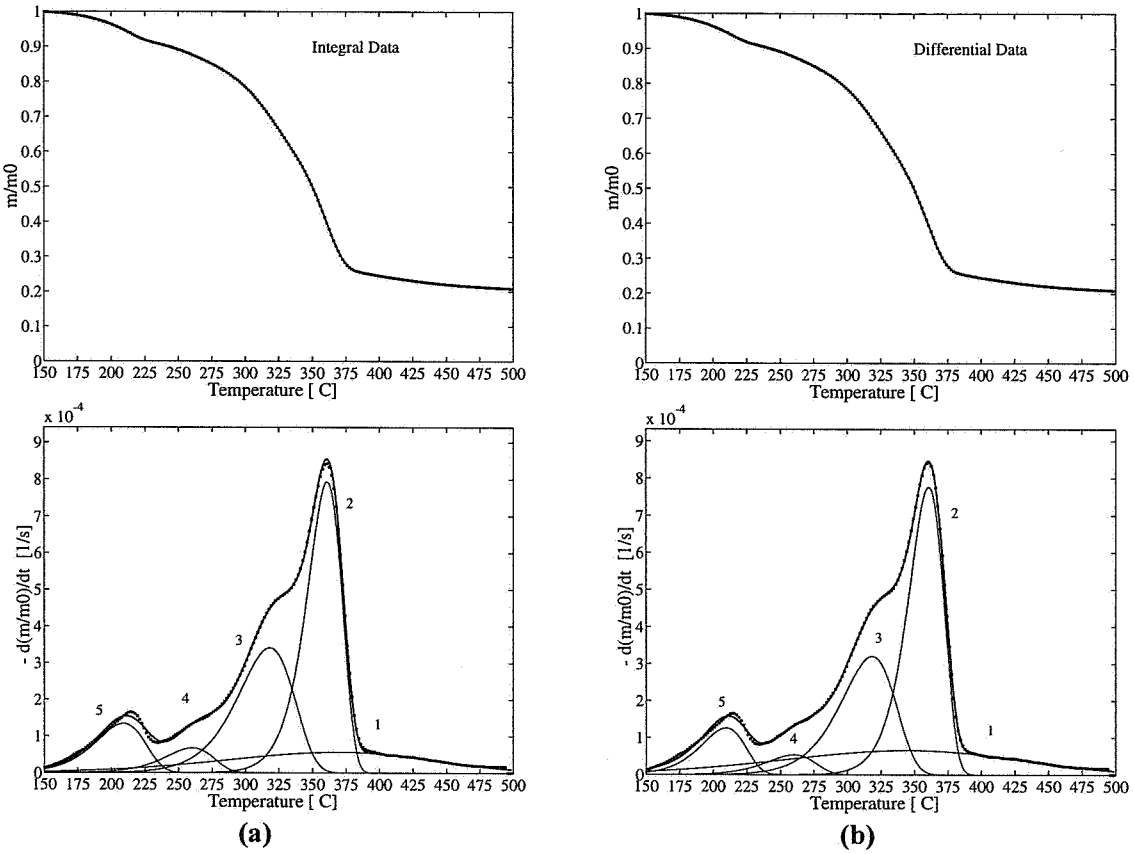

Figure A.40 Kinetic evaluation of H_2O-washed pineroot assuming five independent parallel reactions. Evaluation methods: (a) Fit of TG curve; (b) fit of DTG curve.

Table A.40 Kinetic parameters for H_2O-washed pineroot, five independent parallel reactions.

	first peak (reaction 5)	second peak (reaction 4)	third peak (reaction 3)	fourth peak (reaction 2)	fifth peak (reaction 1)	
Evaluated Curve	E_5 [kJ/mol] $\log A_5$ [log s^{-1}] c_5 [%] $(T_{peak,5})^{calc}$	E_4 [kJ/mol] $\log A_4$ [log s^{-1}] c_4 [%] $(T_{peak,4})^{calc}$	E_3 [kJ/mol] $\log A_3$ [log s^{-1}] c_3 [%] $(T_{peak,3})^{calc}$	E_2 [kJ/mol] $\log A_2$ [log s^{-1}] c_2 [%] $(T_{peak,2})^{calc}$	E_1 [kJ/mol] $\log A_1$ [log s^{-1}] c_1 [%] $(T_{peak,1})^{calc}$	dev1 [%] dev2 [%] $(T_{peak,1})^{exp}$
TG	103.0 8.81 7.6 208.9	129.2 10.32 3.8 260.7	136.1 9.61 22.3 318.7	256.9 18.98 32.5 360.6	38.9 0.14 13.2 368.6	0.6 0.4 360.9
DTG	114.5 10.08 6.5 209.6	128.9 10.29 3.0 259.7	139.9 9.96 20.4 318.7	252.1 18.57 32.4 360.6	31.2 -0.45 17.2 344.7	0.5 0.2 360.9

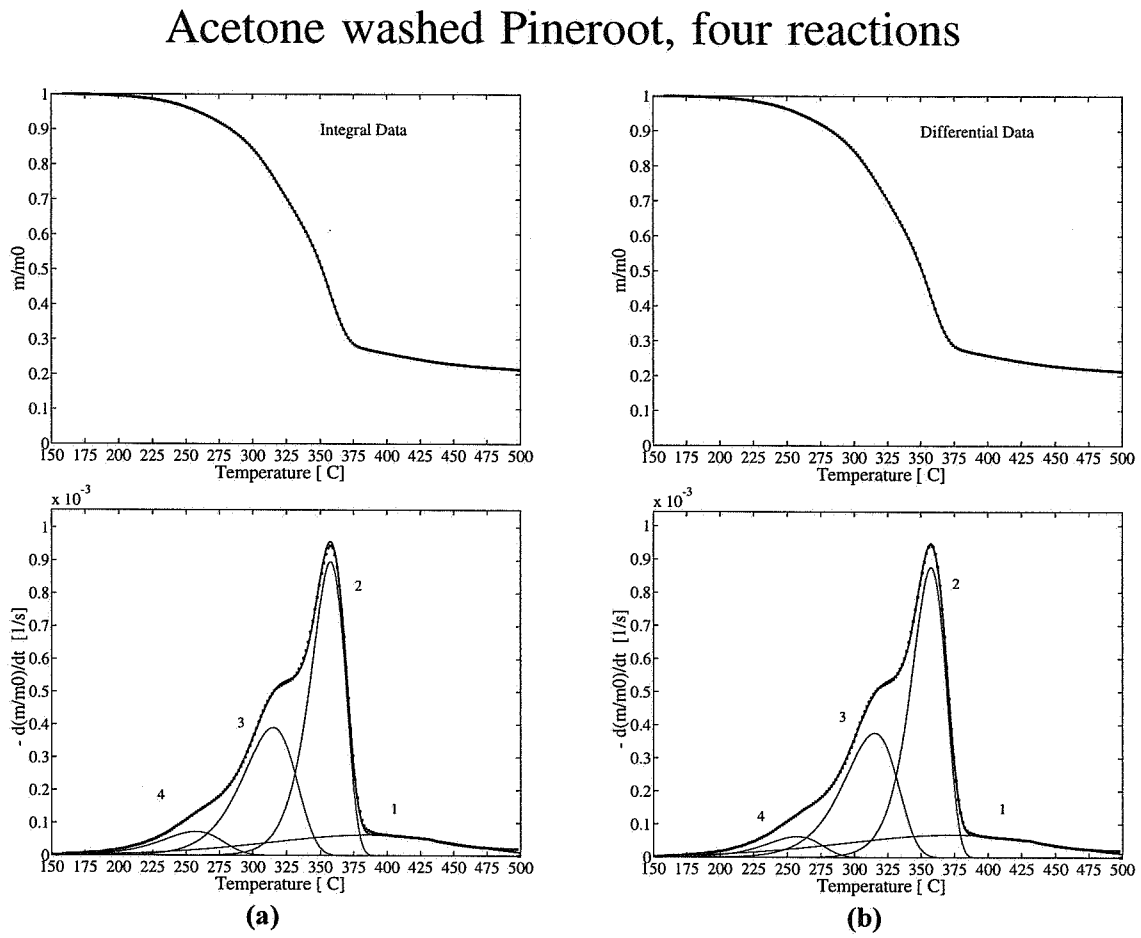

Figure A.41 Kinetic evaluation of acetone-washed pineroot assuming four independent parallel reactions. Evaluation methods: (a) Fit of TG curve; (b) fit of DTG curve.

Table A.41 Kinetic parameters for acetone-washed pineroot, four independent parallel reactions.

	first peak (reaction 4)	second peak (reaction 3)	third peak (reaction 2)	fourth peak (reaction 1)	
Evaluated Curve	E_4 [kJ/mol] $\log A_4$ [log s^{-1}] c_4 [%] $(T_{peak,4})^{calc}$	E_3 [kJ/mol] $\log A_3$ [log s^{-1}] c_3 [%] $(T_{peak,3})^{calc}$	E_2 [kJ/mol] $\log A_2$ [log s^{-1}] c_2 [%] $(T_{peak,2})^{calc}$	E_1 [kJ/mol] $\log A_1$ [log s^{-1}] c_1 [%] $(T_{peak,1})^{calc}$	dev1 [%] dev2 [%] $(T_{peak})^{exp}$
TG	100.3 7.44 5.1 256.7	143.0 10.32 24.1 314.7	256.1 19.02 36.5 357.6	46.7 0.74 13.2 385.7	0.4 0.6 358.3
DTG	111.2 8.55 4.0 256.7	140.6 10.10 23.6 314.7	255.4 18.96 35.8 357.6	40.2 0.24 15.7 372.7	0.3 0.1 358.3

APPENDIX B

EXPERIMENTAL RESULTS FROM PYROLYSIS OF LARGE PARTICLES

In the following appendix, the data from the pyrolysis experiments of large particles are presented.

For the data concerning axial shrinkage, reacted fraction and ultimate product yields, an average value:

$$\bar{y} = \sum_{i=1}^{n} \frac{y_i}{n} \tag{B.1}$$

with the standard deviation:

$$s = \sqrt{\sum_{i=1}^{n} \frac{(y_i - \bar{y})^2}{n - 1}} \tag{B.2}$$

are calculated, where n is the number of experiments and y_i is one single data point.

Those experiments which are not included in the calculation, are marked with grey columns. Obviously there is something wrong with those experiments, and the values which give a hint about the reason are all marked with bold letters.

Table B.1 Experimental results from pyrolysis of spruce, longitudinal fiber direction, high heat flux.

Wood Species Fiber Direction Heat Flux Filename Date Total Time	Spruce Longitudinal 130 kW/m^2 SPHHLD1.PRN 31.08.94 10 min	Spruce Longitudinal 130 kW/m^2 SPHHLD2.PRN 17.09.94 10 min	Spruce Longitudinal 130 kW/m^2 SPHHLD3.PRN 20.09.94 10 min	Spruce Longitudinal 130 kW/m^2 SPHHLD4.PRN 24.09.94 10 min
Sample weight [g]	3.703	3.306	3.766	3.880
Sample diam.[mm]	18.3	18.3	18.4	18.4
Sample length [mm]	30.0	27.6	30.0	30.0
Surface area [m^2]	$2.629 \cdot 10^{-2}$	$2.629 \cdot 10^{-2}$	$2.658 \cdot 10^{-2}$	$2.658 \cdot 10^{-2}$
Char-yield [wt%]	28.8	27.0	27.0	26.9
Tar/water-yield [wt%]	**35.9**	28.0	27.2	28.4
Gas-yield [wt%]	35.3	45.0	45.9	44.7
Pyrolyzed [wt%]	83.5	75.2	72.1	69.1
Non-pyrolyzed [wt%]	16.5	24.8	27.9	30.9
Pyrolyzed [lt%]	73.3	69.6	65.7	63.3
Non-pyrolyzed [lt%]	26.7	30.4	34.3	36.7
Shrinkage [lt%]	**10.0**	0.4	2.0	2.0
Max O_2 [vol%]	0.00	0.00	0.00	0.00
Max CO [vol%]	0.80	0.90	0.85	0.90
Max CO_2 [vol%]	0.30	0.40	0.40	0.40
Max HC [ppm]	4500	3300	5300	5300
Flowrate [l/min]	4.511	4.511	4.556	4.556
$T_{Max\ (1mm)}$ [°C]	930	945	925	935
$T_{Condensator}$ [°C]	- 75	- 75	- 75	- 75
Comments:	40.0 - 38.2 W 8 mm	40.1 - 40.2 W 8.4 mm	40.2 - 39.9 W 10.3 mm	40.1 - 40.1 W 11.0 mm

Spruce Longitudinal 130 kW/m^2	Mean value	Standard deviation
Char-yield [wt%]	27.0	0.06
Tar/water-yield [wt%]	27.9	0.61
Gas-yield [wt%]	45.2	0.62
Reacted fraction [wt%]	72.1	3.05
Shrinkage [lt%]	1.5	0.92

Table B.2 Experimental results from pyrolysis of pine, longitudinal fiber direction, high heat flux.

Wood Species Fiber Direction Heat Flux Filename Date Total Time	Pine Longitudinal 130 kW/m^2 PIHHLD1.PRN 31.08.94 10 min	Pine Longitudinal 130 kW/m^2 PIHHLD2.PRN 17.09.94 10 min	Pine Longitudinal 130 kW/m^2 PIHHLD3.PRN 20.09.94 10 min	Pine Longitudinal 130 kW/m^2 PIHHLD4.PRN 27.09.94 10 min
Sample weight [g]	3.677	3.821	3.850	3.811
Sample diam.[mm]	18.3	18.4	18.5	18.4
Sample length [mm]	29.8	29.0	30.0	30.0
Surface area [m^2]	$2.623 \cdot 10^{-2}$	$2.658 \cdot 10^{-2}$	$2.687 \cdot 10^{-2}$	$2.658 \cdot 10^{-2}$
Char-yield [wt%]	24.6	25.9	23.9	23.8
Tar/water-yield [wt%]	**39.7**	24.2	26.1	26.2
Gas-yield [wt%]	35.7	49.9	50.0	50.0
Pyrolyzed [wt%]	79.7	100.0	86.2	93.1
Non-pyrolyzed [wt%]	20.3	0.0	13.8	6.9
Pyrolyzed [lt%]	71.5	100.0	82.3	88.7
Non-pyrolyzed [lt%]	28.5	0.0	17.7	11.3
Shrinkage [lt%]	12.8	17.2	13.3	13.3
Max O_2 [vol%]	0.00	0.00	0.00	0.00
Max CO [vol%]	1.00	1.00	1.05	1.10
Max CO_2 [vol%]	0.43	0.50	0.43	0.50
Max HC [ppm]	5000	5000	5500	5500
Flowrate [l/min]	4.511	4.511	4.556	4.556
$T_{Max\ (1mm)}$ [°C]	880	940	920	950
$T_{Condensator}$ [°C]	-75	-75	-75	- 75
Comments:	40.0 - W **6.0 - 11 mm**	40.2 - 39.9 W 0.0 mm	40.1 - 39.6 W 4.4 - 7.1 mm	40.1 - 39.8 W 3.4 mm

Pine Longitudinal 130 kW/m^2	Mean value	Standard deviation
Char-yield [wt%]	24.5	1.18
Tar/water-yield [wt%]	25.5	1.13
Gas-yield [wt%]	50.0	0.06
Reacted fraction [wt%]	93.1	6.90
Shrinkage [lt%]	14.6	2.25

Table B.3 Experimental results from pyrolysis of birch, longitudinal fiber direction, high heat flux.

Wood Species Fiber Direction Heat Flux Filename Date Total Time	Birch Longitudinal 130 kW/m^2 BIHHLD1.PRN 30.08.94 10 min	Birch Longitudinal 130 kW/m^2 BIHHLD2.PRN 16.09.94 10 min	Birch Longitudinal 130 kW/m^2 BIHHLD3.PRN 20.09.94 10 min	Birch Longitudinal 130 kW/m^2 BIHHLD4.PRN 28.09.94 10 min
Sample weight [g]	4.142	4.196	4.342	5.307
Sample diam.[mm]	18.5	18.5	18.4	18.4
Sample length [mm]	29.5	29.6	30.0	30.4
Surface area [m^2]	$2.687 \cdot 10^{-2}$	$2.687 \cdot 10^{-2}$	$2.658 \cdot 10^{-2}$	$2.658 \cdot 10^{-2}$
Char-yield [wt%]	25.4	24.6	21.8	19.2
Tar/water-yield [wt%]	**38.6**	27.8	27.1	28.4
Gas-yield [wt%]	36.0	47.6	51.1	52.4
Pyrolyzed [wt%]	74.6	87.8	78.7	84.5
Non-pyrolyzed [wt%]	25.4	12.2	21.3	15.5
Pyrolyzed [lt%]	68.5	81.8	70.0	75.0
Non-pyrolyzed [lt%]	31.5	18.2	30.0	25.0
Shrinkage [lt%]	8.5	14.5	10.7	14.5
Max O_2 [vol%]	0.00	0.00	0.00	0.00
Max CO [vol%]	1.00	1.00	1.00	1.20
Max CO_2 [vol%]	0.42	0.43	0.43	0.50
Max HC [ppm]	5700	5800	5000	5000
Flowrate [l/min]	4.511	4.511	4.556	4.556
$T_{Max\ (1mm)}$ [°C]	940	930	920	965
$T_{Condensator}$ [°C]	- 75	- 75	- 75	- 75
Comments:	40.2 - 40.2 W **5.7 - 13.0 mm**	40.2 - 39.7 W 2.2 - 8.4 mm	40.2 - 39.8 W 5.3 - 11.1 mm	40.2 -40.0 W 7.6 mm HC-analyser not properly closed

Birch Longitudinal 130 kW/m^2	Mean value	Standard deviation
Char-yield [wt%]	21.9	2.70
Tar/water-yield [wt%]	27.8	0.65
Gas-yield [wt%]	50.4	2.48
Reacted fraction [wt%]	83.7	4.61
Shrinkage [lt%]	13.2	2.19

Table B.4 Experimental results from pyrolysis of spruce, longitudinal fiber direction, low heat flux.

Wood Species	Spruce	Spruce	Spruce
Fiber Direction	Longitudinal	Longitudinal	Longitudinal
Heat Flux	80 kW/m^2	80 kW/m^2	80 kW/m^2
Filename	SPLHLD1.PRN	SPLHLD2.PRN	SPLHLD3.PRN
Date	05.09.94	10.09.94	15.09.94
Total Time	10 min	10 min	10 min
Sample weight [g]	3.516	3.519	3.565
Sample diam.[mm]	18.2	18.3	18.4
Sample length [mm]	30.8	30.7	29.0
Surface area [m^2]	$2.600 \cdot 10^{-2}$	$2.629 \cdot 10^{-2}$	$2.658 \cdot 10^{-2}$
Char-yield [wt%]	29.9	28.3	27.9
Tar/water-yield [wt%]	34.0	25.5	34.5
Gas-yield [wt%]	36.1	46.2	37.6
Pyrolyzed [wt%]	41.6	48.7	46.3
Non-pyrolyzed [wt%]	58.4	51.3	53.7
Pyrolyzed [lt%]	36.4	43.3	41.0
Non-pyrolyzed [lt%]	63.6	56.7	59.0
Shrinkage [lt%]	4.2	3.9	0.0
Max O_2 [vol%]	0.00	0.00	0.00
Max CO [vol%]	0.20	0.40	0.40
Max CO_2 [vol%]	0.08	0.20	0.20
Max HC [ppm]	2000	2800	2500
Flowrate [l/min]	4.511	4.398	4.488
$T_{Max\ (1mm)}$ [°C]	750	800	800
$T_{Condensator}$ [°C]	- 75	- 75	- 75
Comments:	25.0 - 24.4 W 19.5 mm	25.1 - 25.2 W 17.4 mm Smoke first 120 sec	25.1 - 25.0 W 17.1 mm

Spruce Longitudinal 80 kW/m^2	Mean value	Standard deviation
Char-yield [wt%]	28.7	1.06
Tar/water-yield [wt%]	31.3	5.06
Gas-yield [wt%]	40.0	5.45
Reacted fraction [wt%]	45.5	3.61
Shrinkage [lt%]	2.7	2.34

Table B.5 Experimental results from pyrolysis of spruce, longitudinal fiber direction, low heat flux, 5 minutes run

Wood Species	Spruce	Spruce	Spruce
Fiber Direction	Longitudinal	Longitudinal	Longitudinal
Heat Flux	80 kW/m^2	80 kW/m^2	80 kW/m^2
Filename	SPLHLD6.PRN	SPLHLD7.PRN	SPLHLD8.PRN
Date	06.10.94	06.10.94	06.10.94
Total Time	5 min	5 min	5 min
Sample weight [g]	3.757	3.851	3.846
Sample diam.[mm]	18.3	18.4	18.5
Sample length [mm]	30.0	30.0	30.0
Surface area [m^2]	$2.629 \cdot 10^{-2}$	$2.658 \cdot 10^{-2}$	$2.687 \cdot 10^{-2}$
Char-yield [wt%]	25.6	26.4	26.6
Tar/water-yield [wt%]	37.7	36.9	39.3
Gas-yield [wt%]	36.7	36.7	34.2
Pyrolyzed [wt%]	27.5	25.1	24.4
Non-pyrolyzed [wt%]	72.5	74.9	75.6
Pyrolyzed [lt%]	25.0	21.7	24.7
Non-pyrolyzed [lt%]	75.0	78.3	75.3
Shrinkage [lt%]	3.3	3.3	2.0
Max O_2 [vol%]	0.00	0.00	0.00
Max CO [vol%]	0.40	0.37	0.35
Max CO_2 [vol%]	0.25	0.19	0.18
Max HC [ppm]	2500	2500	2500
Flowrate [l/min]	4.556	4.556	4.556
$T_{Max\ (1mm)}$ [°C]	735	760	760
$T_{Condensator}$ [°C]	- 75	- 75	- 75
Comments:	25.1 - 25.0 W 21.4 - 23.6 mm 5 min expe.	25.1 - 24.8 W 22.4 - 24.6 mm 5 min exper.	25.0 - 24.8 W 22.4 - 25.0 mm 5 min exper.

Spruce 5 minute experiments Longitudinal 80 kW/m^2	Mean value	Standard deviation
Char-yield [wt%]	26.2	0.53
Tar/water-yield [wt%]	38.0	1.22
Gas-yield [wt%]	35.9	1.44
Reacted fraction [wt%]	25.7	1.63
Shrinkage [lt%]	2.9	0.75

Table B.6 Experimental results from pyrolysis of pine, longitudinal fiber direction, low heat flux.

Wood Species Fiber Direction Heat Flux Filename Date Total Time	Pine Longitudinal 80 kW/m^2 PILHLD1.PRN 06.09.94 10 min	Pine Longitudinal 80 kW/m^2 PILHLD2.PRN 09.09.94 10 min	Pine Longitudinal 80 kW/m^2 PILHLD3.PRN 13.09.94 10 min	
Sample weight [g]	3.818	3.736	3.781	
Sample diam.[mm]	18.4	18.3	18.5	
Sample length [mm]	30.0	29.8	30.0	
Surface area [m^2]	$2.658 \cdot 10^{-2}$	$2.629 \cdot 10^{-2}$	$2.687 \cdot 10^{-2}$	
Char-yield [wt%]	27.4	25.0	24.6	
Tar/water-yield [wt%]	31.1	37.6	34.6	
Gas-yield [wt%]	41.5	37.4	40.8	
Pyrolyzed [wt%]	47.6	50.9	46.0	
Non-pyrolyzed [wt%]	52.4	49.1	54.0	
Pyrolyzed [lt%]	43.3	46.3	42.0	
Non-pyrolyzed [lt%]	56.7	53.7	58.0	
Shrinkage [lt%]	6.7	6.0	8.0	
Max O_2 [vol%]	0.00	0.00	0.00	
Max CO [vol%]	0.37	0.32	0.40	
Max CO_2 [vol%]	0.25	0.20	0.23	
Max HC [ppm]	2500	2500	2500	
Flowrate [l/min]	4.420	4.420	4.488	
$T_{Max\ (1mm)}$ [°C]	780	720	760	
$T_{Condensator}$ [°C]	-75	-75	-75	
Comments:	25.2 - 25.3 W 17.0 mm	25.0 - 25.1 W 13 - 19 mm HC-Analyzer not properly closed in 240 s	25.1 -25.3 W 15.7 - 18.8 mm	

Pine Longitudinal 80 kW/m^2	Mean value	Standard deviation
Char-yield [wt%]	25.7	1.51
Tar/water-yield [wt%]	34.4	3.25
Gas-yield [wt%]	39.9	2.19
Reacted fraction [wt%]	48.2	2.50
Shrinkage [lt%]	6.9	1.01

Table B.7 Experimental results from pyrolysis of birch, longitudinal fiber direction, low heat flux.

Wood Species Fiber Direction Heat Flux Filename Date Total Time	Birch Longitudinal 80 kW/m^2 BILHLD1.PRN 07.09.94 10 min	Birch Longitudinal 80 kW/m^2 BILHLD2.PRN 10.09.94 10 min	Birch Longitudinal 80 kW/m^2 BILHLD3.PRN 13.09.94 10 min	Birch Longitudinal 80 kW/m^2 BILHLD4.PRN 25.09.94 10 min
Sample weight [g]	4.504	3.769	3.705	5.193
Sample diam.[mm]	18.5	18.5	18.6	18.4
Sample length [mm]	30.0	29.6	30.0	30.0
Surface area [m^2]	$2.687 \cdot 10^{-2}$	$2.687 \cdot 10^{-2}$	$2.716 \cdot 10^{-2}$	$2.658 \cdot 10^{-2}$
Char-yield [wt%]	25.6	25.3	23.3	22.6
Tar/water-yield [wt%]	25.6	30.0	28.5	33.0
Gas-yield [wt%]	48.8	44.7	48.2	44.4
Pyrolyzed [wt%]	51.5	48.0	54.0	**39.7**
Non-pyrolyzed [wt%]	48.5	52.0	46.0	60.3
Pyrolyzed [lt%]	46.3	41.2	45.3	33.3
Non-pyrolyzed [lt%]	53.7	58.8	54.7	66.7
Shrinkage [lt%]	4.7	5.4	6.7	5.0
Max O_2 [vol%]	0.00	0.00	0.00	0.00
Max CO [vol%]	0.42	0.25	0.38	0.37
Max CO_2 [vol%]	0.22	0.30	0.18	0.27
Max HC [ppm]	2800	2000	2800	2500
Flowrate [l/min]	4.466	4.398	4.488	4.579
$T_{Max\ (1mm)}$ [°C]	750	770	780	772
$T_{Condensator}$ [°C]	- 75	- 75	- 75	- 75
Comments:	25.2 - 25.1 W 14.7 - 17.9 mm	25.2 - 25.1 W 17.4 mm CO-CO_2 anal. not connected first180 sec	25.0 - 25.0 W 14.1 - 17.4 mm	25.0 - 24.8 W **18.0 - 22.5 mm**

Birch Longitudinal 80 kW/m^2	Mean value	Standard deviation
Char-yield [wt%]	24.7	1.25
Tar/water-yield [wt%]	28.0	2.24
Gas-yield [wt%]	47.2	2.21
Reacted fraction [wt%]	51.2	3.01
Shrinkage [lt%]	5.6	1.02

Table B.8 Experimental results from pyrolysis of spruce, radial fiber direction, high heat flux.

Wood Species Fiber Direction Heat Flux Filename Date Total Time	Spruce Radial 130 kW/m^2 SPHHRD1.PRN 29.08.94 10 min	Spruce Radial 130 kW/m^2 SPHHRD2.PRN 01.09.94 10 min	Spruce Radial 130 kW/m^2 SPHHRD3.PRN 18.09.94 10 min	Spruce Radial 130 kW/m^2 SPHHRD4.PRN 28.09.94 10 min
Sample weight [g]	3.039	2.965	2.871	2.762
Sample diam.[mm]	18.4	18.3	18.4	18.4
Sample length [mm]	30.0	29.7	28.1	29.3
Surface area [m^2]	$2.658 \cdot 10^{-2}$	$2.629 \cdot 10^{-2}$	$2.658 \cdot 10^{-2}$	$2.658 \cdot 10^{-2}$
Char-yield [wt%]	23.4	23.2	23.1	23.4
Tar/water-yield [wt%]	37.7	36.5	29.5	31.8
Gas-yield [wt%]	38.9	40.3	47.4	44.8
Pyrolyzed [wt%]	65.5	85.0	95.4	85.0
Non-pyrolyzed [wt%]	34.5	15.0	4.6	15.0
Pyrolyzed [lt%]	61.7	79.8	92.9	81.9
Non-pyrolyzed [lt%]	38.3	20.2	7.1	18.1
Shrinkage [lt%]	8.7	**19.2**	0.4	3.1
Max O_2 [vol%]	0.00	0.00	0.00	0.00
Max CO [vol%]	0.60	0.60	0.90	0.65
Max CO_2 [vol%]	0.23	0.43	0.35	0.30
Max HC [ppm]	4500	4500	4300	3500
Flowrate [l/min]	4.466	4.511	4.556	4.556
$T_{Max\ (1mm)}$ [°C]	950	925	960	920
$T_{Condensator}$ [°C]	- 75	- 75	- 75	- 75
Comments:	40.0 - 39.3 W 1.0 - 1.3 mm	**40.0 - 35.0 W** 6.0 mm Smoke first 60 sec	40.2 - 39.9 W 2.0 mm	40.2 - 39.5 W 5.3 mm

Spruce Radial 130 kW/m^2	Mean value	Standard deviation
Char-yield [wt%]	23.3	0.17
Tar/water-yield [wt%]	33.0	4.23
Gas-yield [wt%]	43.7	4.36
Reacted fraction [wt%]	82.0	15.18
Shrinkage [lt%]	4.1	4.23

Table B.9 Experimental results from pyrolysis of pine, radial fiber direction, high heat flux.

Wood Species Fiber Direction Heat Flux Filename Date Total Time	Pine Radial 130 kW/m^2 PIHHRD1.PRN 02.09.94 10 min	Pine Radial 130 kW/m^2 PIHHRD2.PRN 19.09.94 10 min	Pine Radial 130 kW/m^2 PIHHRD3.PRN 20.09.94 10 min	
Sample weight [g]	3.394	3.218	3.438	
Sample diam.[mm]	18.7	18.5	18.6	
Sample length [mm]	30.0	29.6	30.0	
Surface area [m^2]	$2.745 \cdot 10^{-2}$	$2.687 \cdot 10^{-2}$	$2.716 \cdot 10^{-2}$	
Char-yield [wt%]	25.7	23.6	23.8	
Tar/water-yield [wt%]	29.9	30.0	32.1	
Gas-yield [wt%]	44.4	46.3	44.2	
Pyrolyzed [wt%]	72.3	83.2	80.8	
Non-pyrolyzed [wt%]	27.7	16.8	19.2	
Pyrolyzed [lt%]	63.3	77.4	76.0	
Non-pyrolyzed [lt%]	36.7	22.6	24.0	
Shrinkage [lt%]	0.0	0.7	0.0	
Max O_2 [vol%]	0.00	0.00	0.00	
Max CO [vol%]	0.80	0.75	0.80	
Max CO_2 [vol%]	0.30	0.30	0.30	
Max HC [ppm]	5000	4300	4500	
Flowrate [l/min]	4.511	4.556	4.556	
$T_{Max\ (1mm)}$ [°C]	980	933	925	
$T_{Condensator}$ [°C]	- 75	- 75	- 75	
Comments:	40.4 - 40.7 W 11 mm Smoke first 45 sec	40.1 - 40.2 W 6.7 mm Smoke first 30 sec	40.1 - 40.4 W 7.2 mm	

Pine Radial 130 kW/m^2	Mean value	Standard deviation
Char-yield [wt%]	24.4	1.16
Tar/water-yield [wt%]	30.7	1.24
Gas-yield [wt%]	45.0	1.16
Reacted fraction [wt%]	78.8	5.73
Shrinkage [lt%]	0.2	0.40

Table B.10 Experimental results from pyrolysis of birch, radial fiber direction, high heat flux.

Wood Species Fiber Direction Heat Flux Filename Date Total Time	Birch Radial 130 kW/m^2 BIHHRD1.PRN 31.08.94 10 min	Birch Radial 130 kW/m^2 BIHHRD2.PRN 19.09.94 10 min	Birch Radial 130 kW/m^2 BIHHRD3.PRN 21.09.94 10 min	Birch Radial 130 kW/m^2 BIHHRD4.PRN 27.09.94 10 min
Sample weight [g]	4.434	4.032	4.470	4.323
Sample diam.[mm]	18.6	18.4	18.3	18.4
Sample length [mm]	30.0	28.8	30.0	28.4
Surface area [m^2]	$2.716 \cdot 10^{-2}$	$2.658 \cdot 10^{-2}$	$2.629 \cdot 10^{-2}$	$2.658 \cdot 10^{-2}$
Char-yield [wt%]	21.2	20.8	24.9	18.6
Tar/water-yield [wt%]	35.8	26.7	25.2	34.4
Gas-yield [wt%]	43.0	52.5	49.9	46.9
Pyrolyzed [wt%]	94.1	100.0	100.0	100.0
Non-pyrolyzed [wt%]	5.9	0.0	0.0	0.0
Pyrolyzed [lt%]	91.7	100.0	100.0	100.0
Non-pyrolyzed [lt%]	8.3	0.0	0.0	0.0
Shrinkage [lt%]	26.7	30.6	30.0	33.1
Max O_2 [vol%]	0.00	0.00	0.00	0.00
Max CO [vol%]	1.10	1.20	1.05	1.20
Max CO_2 [vol%]	0.42	0.62	0.42	0.55
Max HC [ppm]	6000	6000	6500	5500
Flowrate [l/min]	4.511	4.566	4.556	4.556
$T_{Max\ (1mm)}$ [°C]	960	927	920	965
$T_{Condensator}$ [°C]	- 75	- 75	- 75	- 75
Comments:	40.0 - 39.7 W 2.5 mm Smoke first 120 sec	40.1 - 40.3 W 0.0 mm Smoke first 45 sec	40.2 - 39.5 W 0.0 mm	40.1 -39.9 W 0.0 mm

Birch Radial 130 kW/m^2	Mean value	Standard deviation
Char-yield [wt%]	21.4	2.61
Tar/water-yield [wt%]	30.5	5.35
Gas-yield [wt%]	48.1	4.08
Reacted fraction [wt%]	98.5	2.95
Shrinkage [lt%]	30.1	2.63

Table B.11 Experimental results from pyrolysis of spruce, radial fiber direction, low heat flux

Wood Species Fiber Direction Heat Flux Filename Date Total Time	Spruce Radial 80 kW/m^2 SPLHRD1.PRN 09.09.94 10 min	Spruce Radial 80 kW/m^2 SPLHRD2.PRN 12.09.94 10 min	Spruce Radial 80 kW/m^2 SPLHRD3.PRN 15.09.94 10 min	Spruce Radial 80 kW/m^2 SPLHRD4.PRN 25.09.94 10 min
Sample weight [g]	3.180	2.973	3.922	2.992
Sample diam.[mm]	18.5	18.4	18.4	18.4
Sample length [mm]	29.9	29.3	29.8	30.0
Surface area [m^2]	$2.687 \cdot 10^{-2}$	$2.658 \cdot 10^{-2}$	$2.658 \cdot 10^{-2}$	$2.658 \cdot 10^{-2}$
Char-yield [wt%]	27.2	27.0	25.4	24.2
Tar/water-yield [wt%]	33.0	28.5	39.7	42.1
Gas-yield [wt%]	39.8	44.5	34.9	33.7
Pyrolyzed [wt%]	61.8	71.3	68.3	69.9
Non-pyrolyzed [wt%]	38.2	28.7	31.7	30.1
Pyrolyzed [lt%]	61.2	65.9	66.4	66.7
Non-pyrolyzed [lt%]	38.8	34.1	33.6	33.3
Shrinkage [lt%]	7.7	**3.1**	13.8	16.7
Max O_2 [vol%]	0.00	0.00	0.00	0.00
Max CO [vol%]	0.25	0.20	0.31	0.30
Max CO_2 [vol%]	0.15	0.07	0.23	0.23
Max HC [ppm]	1850	2000	2000	2200
Flowrate [l/min]	4.420	4.398	4.488	4.556
$T_{Max\ (1mm)}$ [°C]	710	780	780	803
$T_{Condensator}$ [°C]	- 75	- 75	- 75	- 75
Comments:	25.2- 25.5 W 11.6 mm Smoke after 45 sec	25.1 - 25.1 W 10.0 mm **Much tar/water in sample holder**	25.1 - 25.5 W 10.0 mm Smoke first 90 sec	25.0 - 24.9 W 8.0 - 12 mm

Spruce Radial 80 kW/m^2	Mean value	Standard deviation
Char-yield [wt%]	25.6	1.51
Tar/water-yield [wt%]	38.3	4.72
Gas-yield [wt%]	36.1	3.23
Reacted fraction [wt%]	66.7	4.29
Shrinkage [lt%]	12.7	4.59

Table B.12 Experimental results from pyrolysis of birch, radial fiber direction, low heat flux.

Wood Species Fiber Direction Heat Flux Filename Date Total Time	Pine Radial 80 kW/m^2 PILHRD1.PRN 08.09.94 10 min	Pine Radial 80 kW/m^2 PILHRD2.PRN 12.09.94 10 min	Pine Radial 80 kW/m^2 PILHRD3.PRN 14.09.94 10 min	Pine Radial 80 kW/m^2 PILHRD4.PRN 21.09.94 10 min
Sample weight [g]	3.343	3.392	3.417	3.125
Sample diam.[mm]	18.5	18.5	18.6	18.5
Sample length [mm]	29.6	29.4	29.5	29.6
Surface area [m^2]	$2.687 \cdot 10^{-2}$	$2.687 \cdot 10^{-2}$	$2.716 \cdot 10^{-2}$	$2.687 \cdot 10^{-2}$
Char-yield [wt%]	29.8	28.5	29.7	28.0
Tar/water-yield [wt%]	48.0	36.7	**17.9**	37.1
Gas-yield [wt%]	22.2	34.9	52.5	34.9
Pyrolyzed [wt%]	45.5	56.0	54.9	53.2
Non-pyrolyzed [wt%]	54.5	44.0	45.1	46.8
Pyrolyzed [lt%]	42.6	51.7	52.5	49.3
Non-pyrolyzed [lt%]	57.4	48.3	47.5	50.7
Shrinkage [lt%]	2.0	1.4	0.3	3.7
Max O_2 [vol%]	0.00	0.00	0.00	0.00
Max CO [vol%]	0.20	0.30	0.20	0.25
Max CO_2 [vol%]	0.15	0.15	0.10	0.17
Max HC [ppm]	1800	2500	2500	2300
Flowrate [l/min]	4.433	4.398	4.466	4.556
$T_{Max\ (1mm)}$ [°C]	770	780	740	780
$T_{Condensator}$ [°C]	- 75	- 75	- 75	- 75
Comments:	25.2 - 25.1 W 17.0 mm A lot of smoke after 60 sec	25.0 - 25.0 W 13.0 - 19.0 mm Perfect Experiment	25.0 - 25.0 W 14.0 mm **Much tar in sample tube**	25.1 - 25.0 W 15.0 mm

Pine Radial 80 kW/m^2	Mean value	Standard deviation
Char-yield [wt%]	28.8	0.93
Tar/water-yield [wt%]	40.6	6.41
Gas-yield [wt%]	30.7	7.33
Reacted fraction [wt%]	51.6	5.44
Shrinkage [lt%]	2.4	1.19

Table B.13 Experimental results from pyrolysis of pine, radial fiber direction, low heat flux.

Wood Species Fiber Direction Heat Flux Filename Date Total Time	Birch Radial 80 kW/m^2 BILHRD1.PRN 07.09.94 10 min	Birch Radial 80 kW/m^2 BILHRD2.PRN 11.09.94 10 min	Birch Radial 80 kW/m^2 BILHRD3.PRN 14.09.94 10 min	Birch Radial 80 kW/m^2 BILHRD4.PRN 23.09.94 10 min
Sample weight [g]	4.142	4.388	3.868	4.059
Sample diam.[mm]	18.5	18.4	18.5	18.6
Sample length [mm]	29.5	29.5	29.9	30.0
Surface area [m^2]	$2.687 \cdot 10^{-2}$	$2.658 \cdot 10^{-2}$	$2.687 \cdot 10^{-2}$	$2.716 \cdot 10^{-2}$
Char-yield [wt%]	22.8	23.3	22.3	22.8
Tar/water-yield [wt%]	41.9	**24.7**	37.5	41.4
Gas-yield [wt%]	35.3	52.0	40.2	35.5
Pyrolyzed [wt%]	60.1	74.7	61.0	65.9
Non-pyrolyzed [wt%]	39.9	25.3	39.0	34.1
Pyrolyzed [lt%]	58.0	66.1	59.9	61.7
Non-pyrolyzed [lt%]	42.0	33.5	40.1	38.3
Shrinkage [lt%]	18.6	**25.4**	19.7	16.7
Max O_2 [vol%]	0.00	0.00	0.00	0.00
Max CO [vol%]	0.40	0.40	0.40	0.30
Max CO_2 [vol%]	0.25	0.20	0.28	0.30
Max HC [ppm]	2400	2800	3300	2300
Flowrate [l/min]	4.466	4.398	4.488	4.566
$T_{Max\ (1mm)}$ [°C]	750	785	780	790
$T_{Condensator}$ [°C]	- 75	- 75	- 75	- 75
Comments:	25.1 - 24.7 W 8.5 - 14.4 mm Smoke after 60 sec	25.0 - 25.1 W 14.0 mm	25.0 - 25.0 W 12.0 mm	25.2 - 25.0 W 10.0 - 13.0 mm

Birch Radial 80 kW/m^2	Mean value	Standard deviation
Char-yield [wt%]	22.6	0.29
Tar/water-yield [wt%]	40.3	2.41
Gas-yield [wt%]	37.0	2.77
Reacted fraction [wt%]	62.3	3.12
Shrinkage [lt%]	18.3	1.52